PhD Course

Chemical Science and Technologies

XXXIV cycle

Thesis Title

Metal complexes of environmental and biological interest

Scientific Disciplinary Sector

CHIM/01

PhD candidate   Sebastiano Masuri

PhD course coordinator   Prof.ssa Carla Cannas

Supervisor   Prof.ssa Tiziana Pivetta

Final exam. Academic Year: 2021 – 2022
Thesis defence: June 2022 session

Index

Abstract

This work reports on the research activities that I've carried out during these three years, which covered the following topics: *i*) Fluorescent probes for environmental and biological applications; *ii*) Bioactive ligands and metal complexes.

As regards the first research line (**Part 1** of the present work) I've prepared a series substituted derivatives of 3-(pyridin-2-yl)coumarin and evaluated their potential application as fluorescent chemosensors for the recognition and quantitation of environmentally and biologically relevant analytes. Interestingly, I've found out how these compounds show a "ratiometric" and "turn-on" fluorescent behaviour towards Fe(III), a paramagnetic metal ion that usually quenches the fluorescence of organic molecules. The most promising ligand of the series shows selectivity towards this metal ion, with a limit of detection in the micromolar concentration range and a fluorescent response that has been observed both in solution and on cellulose paper strip. These results suggest a potential application of this chemosensor for the determination of Fe(III) in liquid samples.

As regards the second research line (**Part 2** of this PhD thesis), I've designed, synthesized, and characterized a series of ternary Cu(II) bis-phenanthroline complexes bearing different classes of organic auxiliary ligands, (e.g., imidazolidine-2-thiones, coumarin-based oxylacetic acids, ER-stress modulators) with the aim of obtaining novel potential anticancer metallodrugs that might overcome currently approved Pt(II)-based chemotherapeutics. These studies were carried out in collaboration with Prof. Vanhara's Group, Masaryk University, Brno (CZ). These complexes show high anticancer potency (at micromolar/sub-micromolar) level *in-vitro* on different cancer cell lines. Interestingly, these compounds

induce cell death by activating the pro-apoptotic branch of the Unfolded Protein Response (UPR), a signalling pathway that is activated in cells that undergo to a prolonged or severe condition of Endoplasmic Reticulum (ER) stress.

I've also prepared a series of hydroxylated derivatives of 3-(pyridin-2-yl)coumarin and evaluated their antioxidant and inhibitory activity towards lipoxygenases, a class of enzymes that are commonly known to be involved in the pathogenesis of several inflammatory disorders and cancers. These compounds have proved to possess potent lipoxygenase inhibitory activity, with tuneable antioxidant properties according to the number and relative position of the hydroxyl groups in the coumarinic backbone. In addition, I've evaluated the potential sites of absorption and distribution properties of these molecules by merging the protonation constants, determined experimentally, with selected *in-silico* molecular descriptors.

Finally, I'll report on the preliminary data regarding the antioxidant and anti-tyrosinase activity of a panel of thiosemicarbazones of 3-acetylcoumarin that I've prepared and characterized (in collaboration with Prof. Fais's Group, University of Cagliari). These compounds show promising anti-tyrosinase activity, with variable antioxidant properties according to the substituents in the coumarinic skeleton.

List of publications

Published articles

- T. Pivetta, **S. Masuri**, M.G. Cabiddu, C. Caltagirone, A. Pintus, M. Massa, F. Isaia, E. Cadoni, A novel ratiometric and TURN-ON fluorescent coumarin-based probe for Fe(III), *New Journal of Chemistry*, **2019**, 43, 12032-12041 (**Article 1**).

- L. Moráň, T. Pivetta, **S. Masuri**, K. Vašíčková, F. Walter, J. Prehn, J. Havel, P. Vaňhara, Mixed copper (II)-phenanthroline complexes induce cell death of ovarian cancer cells by evoking the unfolded protein response, *Metallomics*, **2019**, 11, 1481-1489 (**Article 2**).

- **S. Masuri**, E. Cadoni, M.G. Cabiddu, F. Isaia, M.G. Demuru, L. Moráň, D. Buček, P. Vaňhara, J. Havel, T. Pivetta, The first copper(II) complex with 1,10-phenanthroline and salubrinal with interesting biochemical properties, *Metallomics*, **2020**, 12, 891-901 (**Article 3**).

- **S. Masuri**, M.G. Cabiddu, E. Cadoni, T. Pivetta, Hydroxylated 3-(pyridin-2-yl)coumarins as radical scavengers with potent lipoxygenase inhibitor activity, *New Journal of Chemistry*, **2021**, 45, 10749-10760 (**Article 7**).

- **S. Masuri**, P. Vaňhara, M. G. Cabiddu, L. Moráň, J. Havel, E. Cadoni, T. Pivetta, Copper(II) Phenanthroline-Based Complexes as Potential AntiCancer Drugs: A Walkthrough on the Mechanisms of Action, *Molecules*, **2022**, 27(1), 49 (**Article 6**).

Articles in preparation/submitted

- **S. Masuri,** L. Moráň, T. Vesselá E. Cadoni, M.G. Cabiddu, F. Isaia, F. Simeoni, L. Puddu, P. Vaňhara, J. Havel, T. Pivetta, A novel heteroleptic Cu(II)-phenanthroline complex with the ER-stress modulator Ursodeoxycholic Acid with anticancer properties (**Article 4**).

- **S. Masuri**, M. G. Cabiddu, L. Moráň, T. Vesselá, E. Cadoni, M. Bartosik, J. Havel, P. Vaňhara, T. Pivetta, Ternary Copper (II) complexes of 1,10-phenanthroline and coumarin-based oxylacetates as potential anticancer metallodrugs (**Article 5**).

- M.G. Cabiddu, B. Era, **S. Masuri**, E. Cadoni, T. Pivetta, A. Fais, Coumarin-based thiosemicarbazones as potent antioxidants and tyrosinase inhbitors (**Article 8**).

Articles not included in this PhD thesis

- P. Vaňhara, L. Moráň, L. Pečinka, V. Porokh, T. Pivetta, **S. Masuri**, E. M. Peña-Méndez, J. E. Conde González, A. Hampl , J. Havel, Intact Cell Mass Spectrometry for Embryonic Stem Cell Biotyping, *Mass Spectrometry in Life Sciences and Clinical Laboratory*, IntechOpen, **2021**.

Part 1. Fluorescent probes for environmental and biological applications

Introduction

Chemosensors as tools for metal ions sensing and quantitation

A chemosensor is typically defined as a molecule that undergoes to a change of one or more properties (e.g., redox potential, absorption and/or fluorescence spectra) upon selective and reversible binding with an analyte.[1]

The design of these molecules might follow two different methodologies. In the first one ("receptor – spacer - active unit "approach), chemosensors are schematized as the sum of three main components (**Figure 1A**): *i*) a receptor, which is the moiety that selectively interacts with the analyte (e.g., complexation); *ii*) an active unit, whose properties might vary upon interaction with the analyte; *iii*) a spacer, that influence the 3D arrangement and the electronic interaction between the other two components. In the second one ("integrated system" approach), the roles of receptor and active unit will be covered by the same functional groups in the chemosensor structure (**Figure 1B**).[1,2]

Figure 1. Schematic representation of a generic chemosensor designed following the "receptor – spacer - active unit" (**A**) and "integrated system" (**B**) approaches.

Detection and quantitation of metal ions in complex samples constitute an important (and often challenging) task with applications in many fields (e.g., chemistry, geology, biology, medicine, environmental sciences): the presence of exogenous metal ions (e.g., Pb(II), Hg(II), Cr(VI)), but also essential ones (e.g., Cu(II), Fe(III)) in high concentrations could lead to serious consequences for living organisms (diseases) and the ecosystems (pollution).

Traditional instrumental analytical techniques (e.g., inductively coupled plasma-mass spectrometry, atomic absorption spectroscopy, electrochemical-based methods) generally offer good detection and quantitation limits, which makes them suitable for both qualitative and quantitative analysis of trace metal ions. However, they usually require expensive instrumentation, and the sample preparation process might be complex and time-consuming.

On the contrary, fluorescence-based analytical methods are commonly cheaper while offering high selectivity and sensibility, with detection limit in micromolar or nanomolar concentration range.[3] Thanks to these features, the interest towards fluorescence-based chemosensors has been increasing over the years, with applications that include not only the detection and quantitation of cationic, anionic, and neutral analytes, but also as probes for imaging studies in medicine.[2,4,5]

The fluorescence properties of such chemosensors might be altered in the following ways upon interaction with an analyte (**Figure 2**): *i*) increase of the fluorescence intensity ("turn-on" mode); *ii*) decrease of the fluorescent intensity ("turn-off" mode); *iii*) shift of the fluorescent emission maximum towards higher/lower wavelengths ("ratiometric" mode).
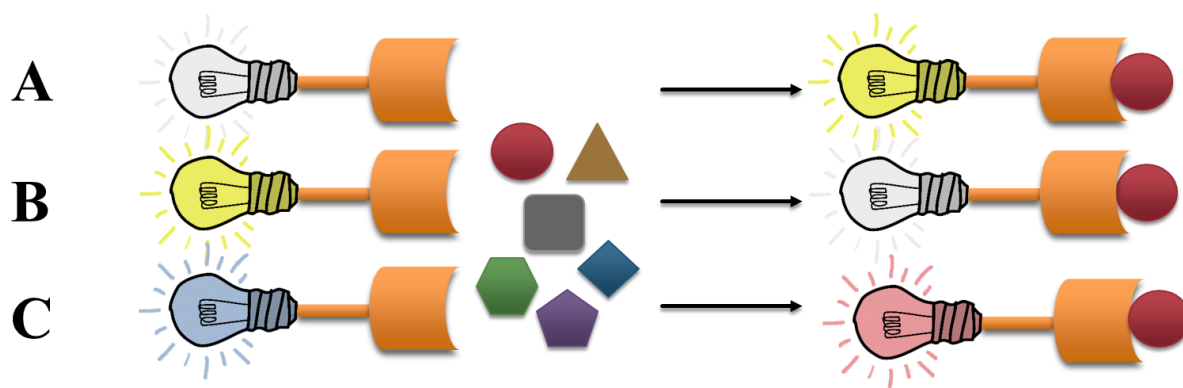
Figure 2. Representations of "turn-on" (**A**), "turn-off" (**B**) and "ratiometric" (**C**) mechanisms for a generic fluorescent chemosensor.

These different behaviours might be originated by one of the following mechanistic pathways: [1,6]

Paramagnetic fluorescence quenching, where the rate of the formally forbidden intersystem crossing (isc) is increased when the chemosensor binds to a paramagnetic species (the metal ion). This is the reason why the intensity of many fluorescent chemosensors is usually quenched upon binding to paramagnetic Cu(II), Fe(III), Co(II) species (**Figure 3**).

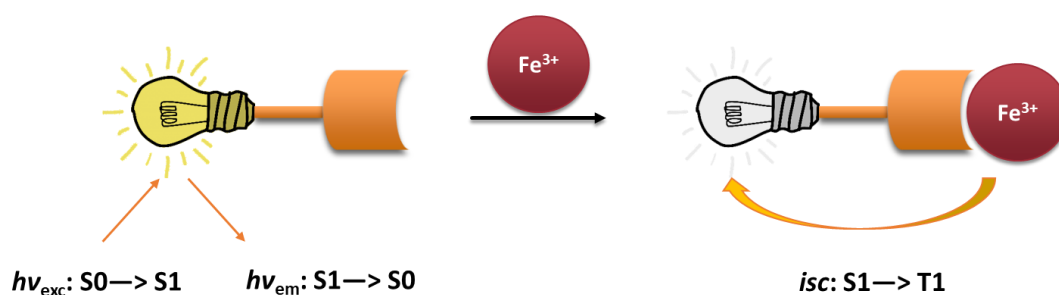$h\nu_{exc}$: S0—> S1 $h\nu_{em}$: S1—> S0 isc: S1—> T1

Figure 3. Schematic representation of Paramagnetic fluorescence quenching. Adapted from Ref.[6]

Photoinduced Electron Transfer (PET), a deactivation pathway that is originated by an internal redox process between the excited state of the fluorophore and another species

having electron donating/accepting ability. A key point that explains this pathway is the different behaviour of species at their excited states compared to the ground state itself. In fluorescent probes for cations, PET generally takes place from the lone pair of the coordinating atoms (e.g., N, O, S, P) to the HOMO of the fluorophore at the excited state. The coordination of a metal ion determines the stabilization of the orbital containing the lone pair, thus making such electron transfer not feasible and determining an increase in fluorescent intensity (**Figure 4**).
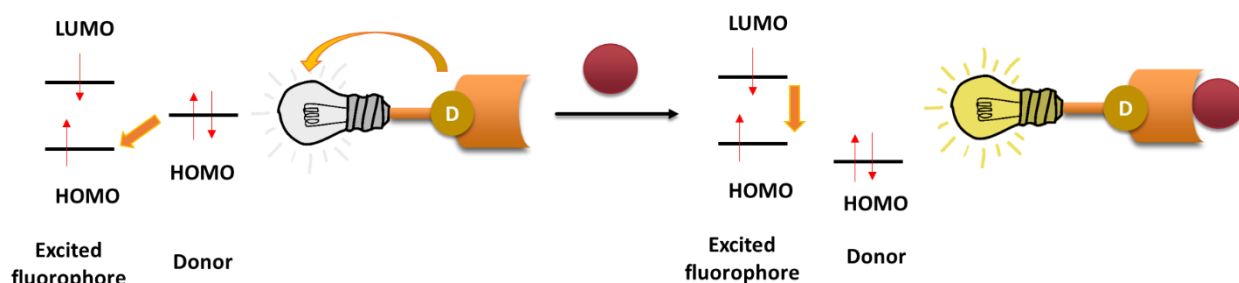
Figure 4. Schematic representation of Photoinduced Electron Transfer. Adapted from Ref.[1]

Photoinduced Charge Transfer (PCT), which requires the presence of an electron releasing group (ERG) and an electron withdrawing group (EWG) in a π-conjugated system. The fluorescence phenomenon takes place thanks to the charge transfer from the donor to the acceptor of the molecule at its excited state, which produces a variation of the dipole moment. When the chemosensor binds to a metal ion, the entity of this charge transfer might be altered according to the "site" (donor or acceptor) of interaction with this analyte. In general, when the ion interacts with the ERGs, the frontier molecular orbitals (FOM) of these functional groups are increased in energy, with a consequent reduction of their electron donating ability and the blue shift of fluorescent wavelengths (**Figure 5**). The exact opposite

will happen when the metal interacts with the EWGs, since the electron accepting ability of these functional groups will be accentuated.
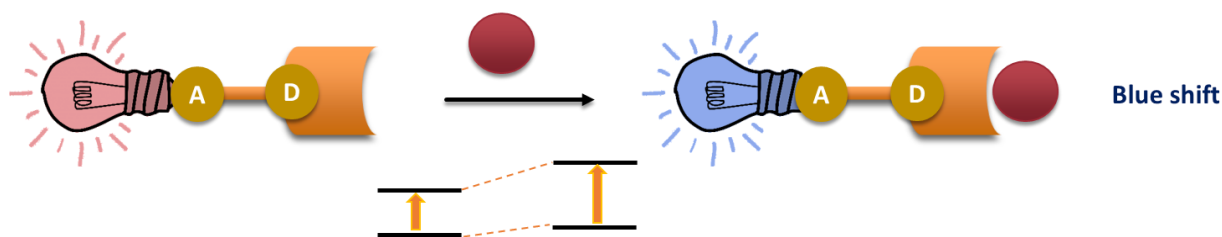

Figure 5. Photoinduced Charge Transfer upon interaction of the metal ion with the donor group. Adapted from Ref.[1]

Fluorescent Resonance Energy Transfer (FRET). This is a distance-dependent phenomenon that takes place thanks to the energy transfer from an excited fluorophore to another one, in which the exciting energy is transferred from a donor to an acceptor without the emission of photons. When FRET takes place, the excitation of the donor fluorophore determines the emission of the acceptor one. FRET requires some conditions to be observed: *i*) both donor and acceptor must be in proximity (10-100 Å are commonly required); *ii*) there must be an overlapping between the absorption spectrum of the acceptor and the emission spectrum of the donor; *iii*) dipole moments of both donor and acceptor must be close to parallel. The presence of a metal ion can modify the geometry of the ligand (through complexation), thus influencing the efficiency of the FRET according to the initial spatial arrangement of the probe (**Figure 6**).
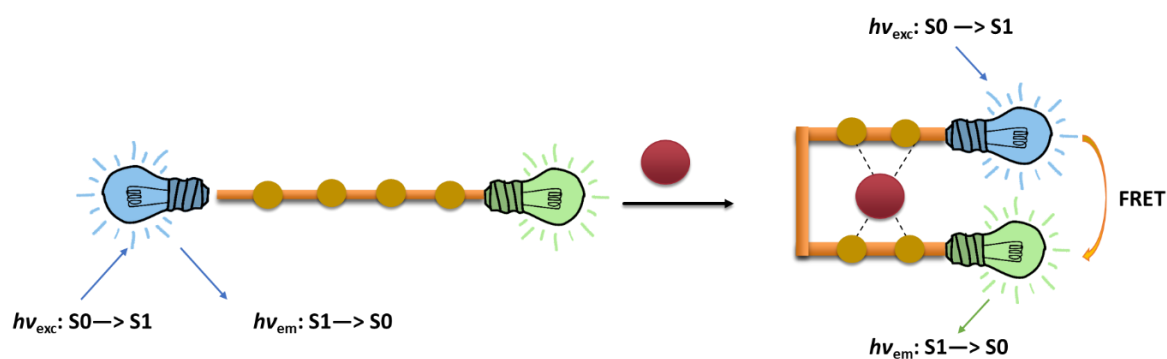
Figure 6. Activation of Fluorescent Resonance Energy Transfer upon metal ion binding. Adapted from Ref.[6]

Coumarins as fluorescent chemosensors

Coumarins constitute a widespread class of molecules, of both natural and synthetic origin, that share a 2-*H*-chromen-2-one moiety (**Figure 7**). Thanks to their synthetic accessibility and degree of biocompatibility (for both living organisms and the environment), many coumarin-based derivatives have found numerous biological and technological applications.[7–9]
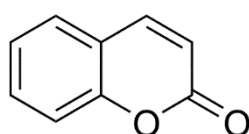
Figure 7. Structure of 2-*H*-chromen-2-one (coumarin).

Several of these molecules have shown to possess interesting photophysical properties, such as high fluorescent emission, quantic yield and photostability, that has them allowed to be employed in the production of lasers, probes for imaging studies, chemosensors for the recognition of charged and neutral species. From a structural perspective, these feature are attributed to the lack of photoisomerization (under UV light) of the C3-C4 double bond in the 2-pyrone portion, which is guaranteed thanks to the presence of the lactonic structure.[9]

Many coumarin-based molecules have been proposed as fluorescent chemosensor for metal ion sensing. For instance, *Wang et al.* tested the fluorescence properties of the coumarin derivative **A1** (**Figure 8**) towards many metal ions in EtOH:H_2O (95:5, V:V), evidencing that the studied probe shows a selective and reversible turn-off behaviour towards Fe(III) (even in excess of competing metal ions), with a fast response in the pH 3.3 – 9.2 range, and linearity in the micromolar range (3.3 – 16.7 µM). The authors proposed the formation of a 1:1 complex between Fe(III) and the ligand as the possible cause for the fluorescence quenching observed. The reported molecule was proposed as potential probe for Fe(III) imaging studies by cultivating single mice microglia in presence of Fe(III), the ligand and EDTA.[10]
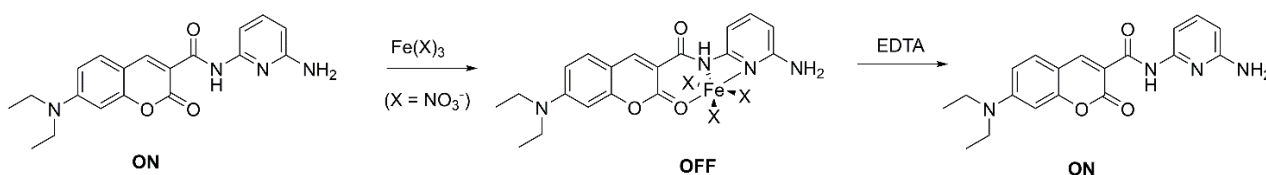
Figure 8. Schematic representation of fluorescence behaviour of **A1** towards Fe(III) and reversibility in presence of EDTA.

Mizukami et al. have prepared a series of 7-hydroxycoumarin derivatives (**A2-6**, **Figure 9**) having a selective ratiometric response towards Zn(II). The observed fluorescent behaviour could be attributed to the formation of 1:1 Zn(II):ligands complexes in solution, as experimentally observed. One of this derivatives (**A6**) was proposed as probe for intracellular Zn(II) detection in RAW264 cells thanks to its ability at crossing cellular membranes.[11]
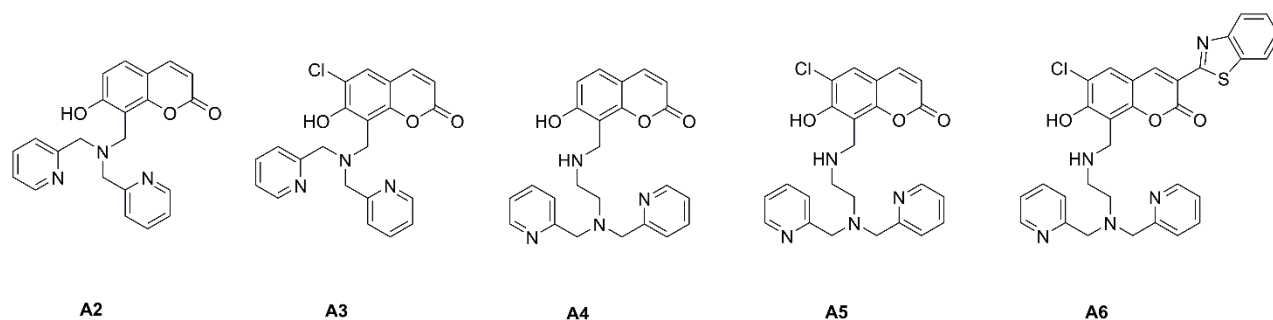
Figure 9. Structures of **A2-6** fluorescent probes.

The coumarin-based probe **A7** (**Figure 10**), developed by *Maity et al.*, shows a selective "turn-on" behaviour towards Al(III) (even in excess of competing metal ions) with a limit of detection (LOD) in the sub-micromolar concentration range ($1.0 \cdot 10^{-7}$ M). The formation of a 1:1 Al(III):ligand complex, as evidenced by merging results from different spectroscopic techniques, determines the fluorescence increase in intensity observed by suppressing the PET in the ligand.[12]
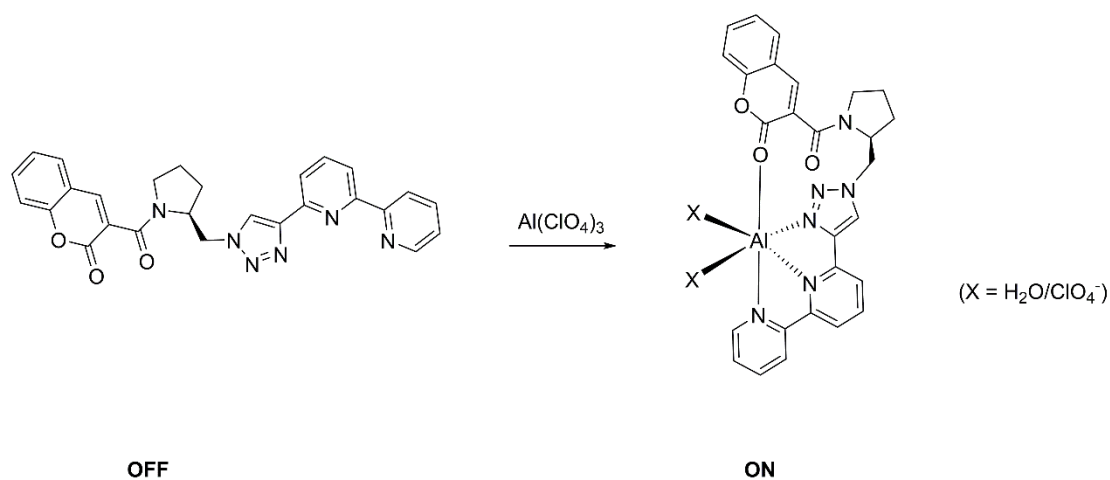
Figure 10. Schematic representation of fluorescence behaviour of **A7** towards Al(III).

The two coumarin-based derivatives **A8** and **A9** (**Figure 11**) of *Sakamoto et al.* shows a selective turn-off fluorescence response towards Ag(I), which is attributable to the formation of a 1:1 complex with this metal ion. The authors demonstrated the feasibility of

this probes in liquid-liquid (water-dichloromethane) extraction of Ag(I), showing that these

probes can extract this metal ion up to $2 \cdot 10^{-8}$ M concentration level.[13]

A8　　　　　　　**A9**
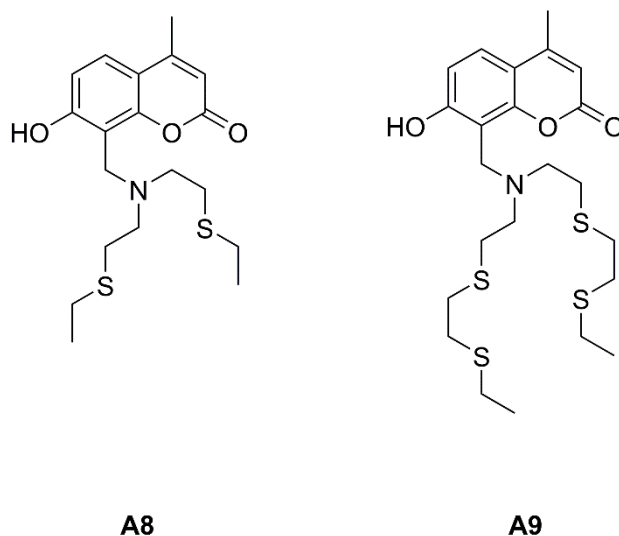
Figure 9. Structures of **A8** and **A9** fluorescent probes.

References

1　　B. Valeur, *Coord. Chem. Rev.*, 2000, **205**, 3–40.

2　　X. Li, X. Gao, W. Shi and H. Ma, *Chem. Rev.*, 2014, **114**, 590–659.

3　　B. Valeur, *Molecular Fluorescence Principles and Applications*, 2001, vol. 8.

4　　K. P. Carter, A. M. Young and A. E. Palmer, *Chem. Rev.*, 2014, **114**, 4564–4601.

5　　L. Prodi, F. Bolletta, M. Montalti and N. Zaccheroni, *Coord. Chem. Rev.*, 2000, **205**, 59–83.

6　　M. Formica, V. Fusi, L. Giorgi and M. Micheloni, *Coord. Chem. Rev.*, 2012, **256**, 170–192.

7　　Y. Bansal, P. Sethi and G. Bansal, *Med. Chem. Res.*, 2013, **22**, 3049–3060.

8　　A. Thakur, R. Singla and V. Jaitak, *Eur. J. Med. Chem.*, 2015, **101**, 476–495.

9　　L. C. and Z. C. Hongqi Li, *Cumarin derived fluorescence chemosensors*, InTech, 2012.

10　　R. Wang, Q. Wan, F. Feng and Y. Bai, *Chem. Res. Chinese Univ.*, 2014, **30**, 560–565.

11   S. Mizukami, S. Okada, S. Kimura and K. Kikuchi, *Inorg. Chem.*, 2009, **48**, 7630–7638.

12   D. Maity and T. Govindaraju, *Inorg. Chem.*, 2010, **49**, 7229–7231.

13   H. Sakamoto, J. Ishikawa, H. Osuga, K. Doi and H. Wada, *Analyst*, 2010, **135**, 550–558.

Aim of the Work

With the aim of developing the first research line of my PhD project (*"Fluorescent probes for environmental and biological applications"*), I focused my attention on the preparation of a series of variably substituted derivatives of 3-(pyridin-2-yl)-2-*H*-chromen-2-one, whose fluorescent properties were evaluated.

Since their fluorescence properties appear to be altered upon interaction with Fe(III), I decided to investigate more in depth the nature of this interaction at both solid and solution state. For this reason, I synthesized the Fe(III) complexes with the studied ligands and hypothesized their structure by combining experimental and computational results. Then, I extended these studies at solution state by determining formation constants of Fe(III) complexes by means of spectrophotometric titrations.

I chose the most promising ligand of the series and used fluorescence spectroscopy to assess a series of important analytical parameters, such as selectivity, reversibility, range of linearity, limit of detection (LOD). Based on these results I deemed interesting to evaluate the potential analytical applications in solution and on cellulose paper strips.

Results and discussion

Article 1.

A novel ratiometric and turn-on fluorescent coumarin-based probe for Fe(III).

A novel ratiometric and turn-on fluorescent coumarin-based probe for Fe(III)†

Tiziana Pivetta, * Sebastiano Masuri, Maria Grazia Cabiddu, Claudia Caltagirone, Anna Pintus, Michela Massa, Francesco Isaia and Enzo Cadoni

Five coumarin derivatives, able to coordinate Fe(III) and exhibit a ratiometric and turn-on fluorescence response, were prepared and tested. The derivative with the –OCH$_3$ substituent exhibited a high fluorescence enhancement in the presence of Fe(III), Ga(III), Au(III) and Y(III). Thanks to the higher stability of the Fe(III) complexes, this molecule could be proposed as a selective fluorescent sensor for the detection of Fe(III) in CH$_3$CN and CH$_3$CN : H$_2$O (1 : 1, v/v) solutions, showing a linear response up to 35.0 μM Fe(III) concentration and a limit of detection of 2.4 μM Fe(III) concentration. The fluorescence response towards this ion was also tested on a solid surface with a simple cellulose paper-strip test. The peculiarity of the proposed sensor lies in its easy and low-cost synthesis, relevant ratiometric response and, since it is derived from a natural product, low impact on the environment and its organisms.

Introduction

The recognition and quantitation of metal ions are of great importance in various fields, and the interactions between metals and ligands may be exploited for both biomedical[1] and environmental applications.[2] The most common instrumental analytical techniques such as atomic absorption spectroscopy, inductively coupled plasma–mass spectrometry and electrochemical methods, exhibit a good detection limit; however, they require expensive instrumentation and very often the sample preparation is complex and time-consuming. Conversely, the analytical methods based on fluorescence emission spectroscopy are relatively inexpensive, providing at the same time a high sensitivity and selectivity and a detection limit of the order of micromolar or nanomolar concentration.[3] The design of fluorescent chemosensors can follow two different pathways: the "receptor-spacer-active unit" paradigm or the conjugated active-receptor units.[4] When the recognition of the analyte occurs, three behaviours could be expected: (i) an increase of the emission intensity (turn-on mode), (ii) a reduction or quenching of the emission intensity (turn-off mode) and (iii) a variation of the emission wavelength, i.e. a ratiometric response. The quenching is due, in most cases, to the intersystem crossing, which becomes more probable when the paramagnetic metallic ion is located near the fluorophore.[3] This phenomenon is called the paramagnetic effect and it is the main cause of the fluorescence quenching in

the presence of odd electron ions, as Cu(II), Fe(III) and Co(III). Generally, for analytical applications, to increase the sensitivity and decrease the detection limit, fluorescence enhancement systems (TURN-ON) and/or ratiometric ones are preferred.

Among metal ions, Fe(III) is one of the most studied, due to its biological importance, being an essential metal ion, and for environmental applications, in particular for steel industry pollution evaluation. For these reasons, the development of analytical techniques for iron detection is always up-to-date. At present, a wide number of iron detection systems have been developed, based on chelators and on the measurement of the fluorescence emission. However, most of these systems are based on the quenching of fluorescence, i.e. turn-off mode,[5–16] while the few examples of turn-on and ratiometric sensors reported in the literature are based on molecules that require an elaborate and expensive synthesis.[17–23] Among the different classes of fluorophores, coumarins are of great importance, since they are able to coordinate different metal ions and, thanks to their natural origin, show low toxicity and a good biocompatibility for organisms and the environment.[5,11,13,17,18,24–30] Coumarins belong to the class of benzopyrones and have different fields of application, from biological to therapeutic ones. The most well-known example is "warfarin",[31] currently used as an anticoagulant. Coumarin derivatives emit, under proper excitation, a fluorescence radiation whose wavelength and intensity depend on the substituents present on the molecular skeleton. Following our interest in metal ion recognition and sensing and in Fe(III) equilibria in solution,[32–38] we report here the synthesis of five coumarin derivatives (L1–L5, Scheme 1) with a pyridinyl ring at the 3rd position of the coumarin ring and a chlorine, fluorine, methoxyl and hydroxyl

Dipartimento di Scienze Chimiche e Geologiche, Università degli Studi di Cagliari, Cittadella Universitaria, 09042 Monserrato, CA, Italy. E-mail: tpivetta@unica.it
† Electronic supplementary information (ESI) available. See DOI: 10.1039/c9nj02044f

Abstract

With the aim of preparing novel fluorescent probes for the recognition of analytes of environmental and/or biological interest, I prepared 5 coumarin-based derivatives based on the structure of 3-(pyridin-2-yl)-2-*H*-chromen-2-one (**L1-L5**, **Figure 12**) and evaluated their fluorescence properties.
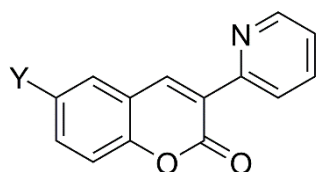
Figure 12. Structure and acronyms of the studied molecules: **L1** (Y = -H), **L2** (Y = -Cl), **L3** (Y = -OCH₃), **L4** (Y = -F), **L5** (Y = -OH).

Interestingly, all of them showed a ratiometric and turn-on behaviour towards Fe(III) (**Figure 13**), a metal ion commonly known to deactivate the fluorescence emission of organic molecules through the "paramagnetic fluorescence quenching" mechanism.
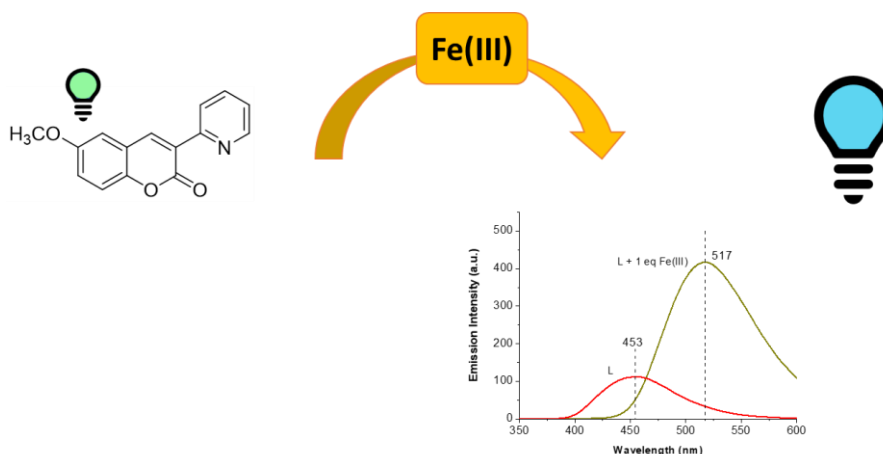
Figure 13. Ratiometric and turn-on fluorescence behaviour observed for **L3** upon interaction with Fe(III).

Based on these results and considering that the formation of metal complexes could be related with the fluorescence response observed, I decided to study the complex formation

processes with this analyte at both solid and solution states. In particular, I prepared Fe(III) complexes of different stoichiometries (1:2 and 1:3 metal:ligand molar ratio) and hypothesized their structure by merging experimental (elemental analysis, IR, mass spectrometry) and theoretical (DFT calculations)* results. In addition, I determined the complex formation constants in solution by means of UV-Vis spectroscopy.

I then selected the most promising ligand of the series (**L3**) and evaluated its analytical applications, evidencing that **L3** shows selectivity towards Fe(III) even in presence of excess competing metal ions, with an LOD of 2.4 µM and a linear response towards Fe(III) up to 35 µM. The fluorescence response towards Fe(III) in solution was further confirmed on simple cellulose paper-strip (**Figure 14**). The results obtained suggest a potential application of this chemosensor for the determination of Fe(III) in liquid samples.
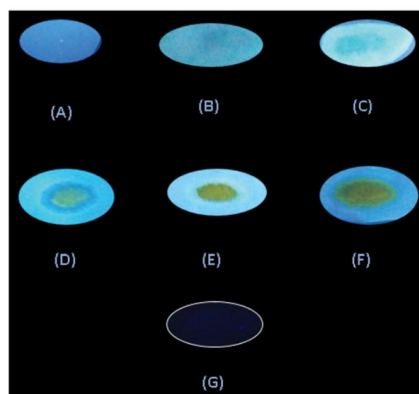
Figure 13. Fluorescence response of **L3**-coated strips alone (**A**) and in the presence of 1 mM (**B**), 10 mM (**C**), 20 mM (**D**), 50 mM (**E**), and 70 mM (**F**) Fe(III) water solutions. Fluorescence response of Fe(III)-coated strip (**G**) is reported for comparison. The outline of (**G**) is highlighted to make it more visible (emission wavelength 365 nm).

---

* DFT calculations were performed in collaboration with Dr. Anna Pintus, Department of Chemical and Geological Sciences, University of Cagliari.

A novel ratiometric and turn-on fluorescent coumarin-based probe for Fe(III).

Tiziana Pivetta[1]*, Sebastiano Masuri[1], Maria Grazia Cabiddu[1], Claudia Caltagirone[1], Anna Pintus[1], Michela Massa[1], Francesco Isaia[1], Enzo Cadoni[1].

[1]Department of Chemical and Geological Sciences, University of Cagliari, 09042, Cittadella Universitaria, Monserrato, Cagliari, Italy

* Corresponding author: tpivetta@unica.it

Check for updates

A novel ratiometric and turn-on fluorescent coumarin-based probe for Fe(III)†

Tiziana Pivetta, ID * Sebastiano Masuri, ID Maria Grazia Cabiddu, ID Claudia Caltagirone, ID Anna Pintus, ID Michela Massa, Francesco Isaia ID and Enzo Cadoni ID

Five coumarin derivatives, able to coordinate Fe(III) and exhibit a ratiometric and turn-on fluorescence response, were prepared and tested. The derivative with the $-OCH_3$ substituent exhibited a high fluorescence enhancement in the presence of Fe(III), Ga(III), Au(III) and Y(III). Thanks to the higher stability of the Fe(III) complexes, this molecule could be proposed as a selective fluorescent sensor for the detection of Fe(III) in CH_3CN and $CH_3CN : H_2O$ (1:1, v/v) solutions, showing a linear response up to 35.0 μM Fe(III) concentration and a limit of detection of 2.4 μM Fe(III) concentration. The fluorescence response towards this ion was also tested on a solid surface with a simple cellulose paper-strip test. The peculiarity of the proposed sensor lies in its easy and low-cost synthesis, relevant ratiometric response and, since it is derived from a natural product, low impact on the environment and its organisms.
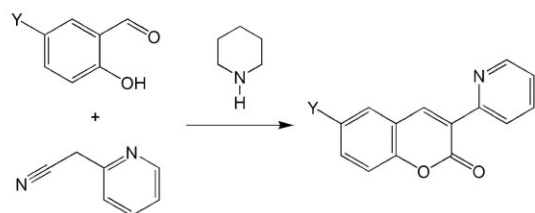
Introduction

The recognition and quantitation of metal ions are of great importance in various fields, and the interactions between metals and ligands may be exploited for both biomedical[1] and environmental applications.[2] The most common instrumental analytical techniques such as atomic absorption spectroscopy, inductively coupled plasma–mass spectrometry and electrochemical methods, exhibit a good detection limit; however, they require expensive instrumentation and very often the sample preparation is complex and time-consuming. Conversely, the analytical methods based on fluorescence emission spectroscopy are relatively inexpensive, providing at the same time a high sensitivity and selectivity and a detection limit of the order of micromolar or nanomolar concentration.[3] The design of fluorescent chemosensors can follow two different pathways: the "receptor-spacer-active unit" paradigm or the conjugated active-receptor units.[4] When the recognition of the analyte occurs, three behaviours could be expected: (i) an increase of the emission intensity (turn-on mode), (ii) a reduction or quenching of the emission intensity (turn-off mode) and (iii) a variation of the emission wavelength, *i.e.* a ratiometric response. The quenching is due, in most cases, to the intersystem crossing, which becomes more probable when the paramagnetic metallic ion is located near the fluorophore.[3] This phenomenon is called the paramagnetic effect and it is the main cause of the fluorescence quenching in

the presence of odd electron ions, as Cu(II), Fe(III) and Co(III). Generally, for analytical applications, to increase the sensitivity and decrease the detection limit, fluorescence enhancement systems (TURN-ON) and/or ratiometric ones are preferred.

Among metal ions, Fe(III) is one of the most studied, due to its biological importance, being an essential metal ion, and for environmental applications, in particular for steel industry pollution evaluation. For these reasons, the development of analytical techniques for iron detection is always up-to-date. At present, a wide number of iron detection systems have been developed, based on chelators and on the measurement of the fluorescence emission. However, most of these systems are based on the quenching of fluorescence, *i.e.* turn-off mode,[5–16] while the few examples of turn-on and ratiometric sensors reported in the literature are based on molecules that require an elaborate and expensive synthesis.[17–23] Among the different classes of fluorophores, coumarins are of great importance, since they are able to coordinate different metal ions and, thanks to their natural origin, show low toxicity and a good biocompatibility for organisms and the environment.[5,11,13,17,18,24–30] Coumarins belong to the class of benzopyrones and have different fields of application, from biological to therapeutic ones. The most well-known example is "warfarin",[31] currently used as an anticoagulant. Coumarin derivatives emit, under proper excitation, a fluorescence radiation whose wavelength and intensity depend on the substituents present on the molecular skeleton. Following our interest in metal ion recognition and sensing and in Fe(III) equilibria in solution,[32–38] we report here the synthesis of five coumarin derivatives (L1–L5, Scheme 1) with a pyridinyl ring at the 3rd position of the coumarin ring and a chlorine, fluorine, methoxyl and hydroxyl

Dipartimento di Scienze Chimiche e Geologiche, Università degli Studi di Cagliari, Cittadella Universitaria, 09042 Monserrato, CA, Italy. E-mail: tpivetta@unica.it

† Electronic supplementary information (ESI) available. See DOI: 10.1039/c9nj02044f

Scheme 1 Reaction scheme for **L1–L5** (Y = H, Cl, OCH₃, F, and OH).

substituent at the 6th position. These systems were able to coordinate Fe(III) showing a ratiometric and TURN ON behaviour in CH_3CN and $CH_3CN:H_2O$ solutions. The molecule 6-methoxy-3-(pyridin-2-yl)-2*H*-chromen-2-one (**L3**) was shown to be the most promising sensor for Fe(III) recognition, both due to its ratiometric behaviour and its selectivity at micromolar concentration. The proposed sensor is characterised by an easy and low-cost synthesis, a relevant ratiometric response and, since it is derived from a natural product, a low impact on the environment and its organisms.

Results and discussion

Synthesis

All the derivatives of 3-(pyridin-2-yl)coumarins, **L1–L5**, were prepared according to a reported method[39] from substituted salicylaldehydes and 2-pyridylacetonitrile *via* a Knoevenagel condensation and subsequent acid hydrolysis of the imines. The synthetic pathway is depicted in Scheme 1. Compounds **L1–L4** were previously prepared and characterized.[40] The novel derivative **L5** was obtained with moderate yield (50%). Details of the synthesis as well as ESI-MS, IR, ¹H NMR and ¹³C NMR spectra of **L5** are reported in the ESI† (Fig. S1–S12).

Fe(III) complexes **C1–C10** were prepared by reacting Fe(ClO₄)₃·H₂O and **L1–L5** in 1 : 2 or 1 : 3 metal : ligand molar ratios, and complexes of general formula Fe(L)₂(ClO₄)₃ or Fe(L)₃(ClO₄)₃ were obtained, respectively. Their stoichiometries were assessed through elemental analysis, ESI-MS and IR spectrometry (ESI-MS spectra of [Fe(**L1**)₃](ClO₄)₃ and [Fe(**L3**)₃](ClO₄)₃ are reported in the ESI,† Fig. S17). Coordination of the metal ion was proposed considering the variations of the carbonyl group's IR stretching frequencies, observed upon complexation. In the IR spectra of ligand **L3** and complex **C8** (see ESI,† Fig. S11 and S12), the C=O frequency is red-shifted from 1730 cm⁻¹ to 1691 cm⁻¹, suggesting the involvement of the carbonyl group in the metal coordination. The multitude of peaks in the IR spectra of the complexes, in the range of 1600–1200 cm⁻¹ (due to the presence of both the Λ and Δ stereoisomers in the isolated products), prevented the attribution of the nitrogen pyridine signals. No coordinated water signal was observed in the IR spectra of the 1 : 2 complexes, where the octahedral coordination sphere might be completed in the solid state by the perchlorate anions.

In agreement with the reported structure of **L3**·HClO₄,[40] in which the proton could be considered as a metal vicariant, Fe(III) was supposed to be coordinated by the pyridine nitrogen

atom and the coumarin carbonyl group. This hypothesis was further confirmed by theoretical calculations. Any attempt to isolate the 1 : 1 complex in the solid state was unsuccessful.

Theoretical calculations

Theoretical calculations at the DFT level were performed to confirm the hypothesized coordination around the metal ion and the related geometries of the complexes. **L3** was chosen as the model ligand.

Ligands. In the previously reported crystal structure of ligand **L3**,[40] the pyridine pendant was observed to lie outside the plane described by the coumarin rings by about 30°, in a distorted antiperiplanar conformation. On the other hand, **L3** was hypothesized to act as a bidentate ligand towards metal ions through the pyridine nitrogen and the coumarin carbonyl, in a distorted periplanar conformation, in agreement with the structural data reported in the literature for similar systems[41–46] and with the crystal structure of **L1**·HClO₄, where the periplanar conformation was due to the pyridinic ring N–H⋯O intramolecular hydrogen bond and the N–H⋯O intermolecular hydrogen bond with the perchlorate ion.[40] The rotational barrier of the pyridine ring was thus evaluated through a potential electronic energy scan (PES), as a function of the dihedral angle C7–C6–C5–N1 ($\tau = 0.00°$ and 180.00° for the periplanar and antiperiplanar conformation, respectively; C_s point group for both conformations, Fig. S13, ESI†). The resulting antiperiplanar conformation was more stable than the periplanar one by about 7 kcal mol⁻¹ (see ESI,† Fig. S14), thus indicating the rotational barrier to be modest.

The metric parameters of ligand **L3** were in very good agreement with the corresponding structural data obtained by single crystal X-ray diffraction (bond distances and angles differ by less than 0.04 Å and 3°, respectively, for both the periplanar and antiperiplanar conformations, see ESI,† Table S1). An examination of the highest occupied Kohn–Sham (KS) molecular orbitals (MOs) calculated for the free ligand shows the localization of the lone pairs available for metal coordination on the pyridine nitrogen (KS-MO HOMO−2 for both the periplanar and antiperiplanar conformations) and the carbonyl group of coumarin (KS-MOs HOMO−4 and HOMO−5 for the antiperiplanar and periplanar conformations, respectively; Fig. 1).

Fe(III) complexes. The mononuclear Fe(III) complexes of **L3** were optimized in different binding stoichiometries (3 : 1, 2 : 1 and 1 : 1, respectively). In all the optimizations, **L3** was designed to act as a bidentate ligand in its periplanar conformation (*via* the N1 and O1 donor atoms), and a hexacoordinated sphere was considered for the central iron ion. Water molecules were employed to complete the coordination sphere in the 2 : 1 and 1 : 1 complexes, in agreement with what was observed for other iron complexes featuring bidentate ligands.[47–55] The 3 : 1 complex [Fe(**L3**)₃]³⁺ was optimized as the Λ enantiomer, while the 2 : 1 complex [Fe(**L3**)₂(H₂O)₂]³⁺ was modelled in its *cis* conformation.

Given the ability of octahedral Fe(III) complexes to display spin crossover (SCO) behaviour,[56] the complexes were optimized both in their low spin (LS, $S = 1/2$) and high spin (HS, $S = 5/2$) configurations. For all complexes, the HS configuration was
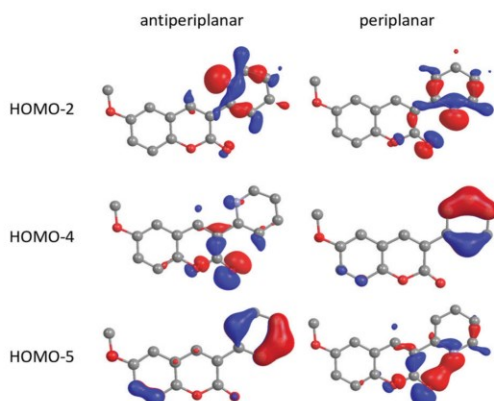
25

Fig. 1 Isosurface drawings of selected Kohn–Sham frontier molecular orbitals calculated for **L3** in its antiperiplanar and periplanar conformations. Cutoff value = 0.05 |e|. Hydrogen atoms are omitted for clarity.

Fig. 2 Molecular drawings and atom labelling schemes for $[Fe(\mathbf{L3})_3]^{3+}$, $[Fe(\mathbf{L3})_2(H_2O)_2]^{3+}$ and $[Fe(\mathbf{L3})(H_2O)_4]^{3+}$ at the DFT-optimized geometries in their high spin configurations.

slightly more stable than the LS one: in particular, the difference in the Gibbs free energy/total electronic energy for the two conformations was about 9/14, 13/18, and 17/23 kcal mol^{-1} for the 3:1, 2:1, and 1:1 complexes, respectively (ΔE_{tot} = 8.86 kcal mol^{-1} for $[Fe(\mathbf{L3})_3]^{3+}$; 13.45 kcal mol^{-1} for $[Fe(\mathbf{L3})_2(H_2O)_2]^{3+}$; 17.44 kcal mol^{-1} for $[Fe(\mathbf{L3})(H_2O)_4]^{3+}$; ΔG = 13.38 kcal mol^{-1} for $[Fe(\mathbf{L3})_3]^{3+}$; 18.01 kcal mol^{-1} for $[Fe(\mathbf{L3})_2(H_2O)_2]^{3+}$; 23.30 kcal mol^{-1} for $[Fe(\mathbf{L3})(H_2O)_4]^{3+}$. In all complexes, the central iron ion features a slightly distorted octahedral coordination geometry (Tables S2–S4, ESI†), and in the **L3** ligand, the pyridine ring is twisted with respect to the coumarin fragment by an average of about 26°. Average Fe–N, Fe–O$_{coum}$, and Fe–O$_{water}$ distances of 1.979, 1.886, and 1.954 Å, respectively, were calculated for the LS complexes (Fe–O$_{coum}$ and Fe–O$_{water}$ = bonds between the central iron ion and the oxygen atoms of the coumarin ligands and the water molecules, respectively); the Fe–N and Fe–O$_{coum}$ bonds were calculated to be slightly shorter in the 1:1 complexes compared to the 2:1 and 3:1 systems (Fe–N distances in the range 1.976–1.996 Å for the 3:1 and 2:1 complexes, and 1.939–1.943 Å for the 1:1 complexes; Fe–O$_{coum}$ distances in the range 1.871–1.924 Å for the 3:1 and 2:1 complexes, and 1.839–1.843 Å for the 1:1 complex). In agreement with what was previously reported for other iron(III) octahedral complexes,[57] the bond lengths in the coordination sphere were systematically longer in the HS compounds compared to the LS systems. This is consistent with the movement of electrons from the bonding t$_{2g}$ set to the anti-bonding e$_g$ set of orbitals.[58] In particular, the average Fe–N, Fe–O$_{coum}$ and Fe–O$_{water}$ distances were calculated to be longer by 0.152, 0.078, and 0.114 Å, respectively, in the HS compounds. Also, the significant variation involving the Fe–N distances is consistent with the literature reports on iron(III) SCO systems.[58] In Fig. 2, the most stable hypothesized structures of Fe(III) complexes with **L3** are shown.

The difference in spin configuration for all complexes is also reflected in the charge distribution, which was calculated at both the Mulliken and NBO level[59] (see ESI,† Tables S5–S7).
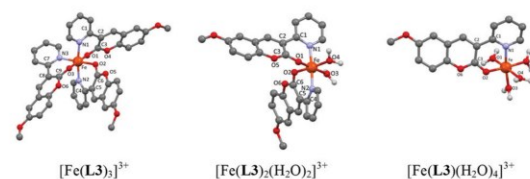
An examination of the calculated frontier MOs shows that, for all the complexes, the highest singly occupied molecular orbital (SOMO) is mainly localized on **L3**, while the lowest unoccupied molecular orbital (LUMO) is mostly centred on the metal ion, thus indicating that the SOMO–LUMO electronic excitation should be considered ligand-to-metal charge-transfer (LMCT) in nature (Fig. 3).

Spectrophotometric measurements. To determine the number and stoichiometry of the complexes formed between Fe(III) and the studied sensors, the method of continuous variation, also called Job's method, was applied.[60,61] For the **L1**–**L5** sensors, the formation of three complexes was evidenced, with stoichiometry FeL, FeL$_2$ and FeL$_3$ (charges are omitted). In Fig. 4 (top), the absorption spectra collected varying the ligand molar fraction from 0 to 1 are reported for the system Fe(III)-**L3** as an example. Absorbance data at 438, 387 and 308 nm, corrected for the absorbance of the pure reactants, reported as a function of the ligand molar fraction (Fig. 4 bottom), clearly indicate 1:1 (χ_L = 0.5), 2:1 (χ_L = 0.66) and 3:1 (χ_L = 0.75) ligand:metal complexes. Uncorrected absorbance data are reported in the ESI† (Fig. S15). Once the complexation model was defined, the complex formation constants were determined by spectrophotometric titration. By adding increasing amounts of the ligands, new absorption bands were evidenced, a feature consistent with an interaction altering the solvated cationic core. Two or three isosbestic points appeared consecutively during the titration, providing evidence for more than one equilibrium. From eigenvalue analysis of the spectrophotometric data in the 200–450 nm
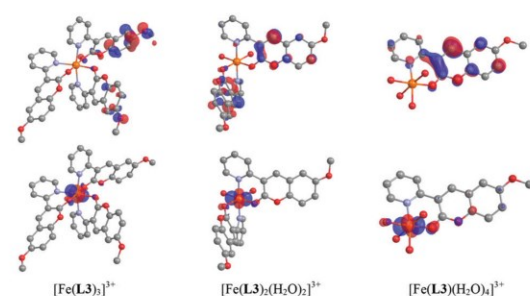

Fig. 3 Isosurface drawings of Kohn–Sham SOMO (top) and LUMO (bottom) beta molecular orbitals calculated for $[Fe(\mathbf{L3})_3]^{3+}$, $[Fe(\mathbf{L3})_2(H_2O)_2]^{3+}$ and $[Fe(\mathbf{L3})(H_2O)_4]^{3+}$ in their high spin configurations. Cutoff value = 0.05 |e|. Hydrogen atoms are omitted for clarity.
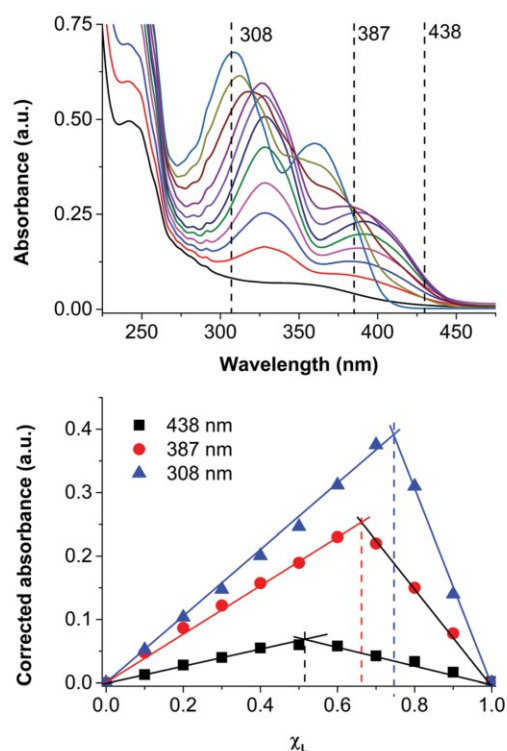
26

Fig. 4 Absorption spectra collected varying the ligand molar fraction from 0 to 1 for the system Fe(III)-L3 (top) and Job's plots for absorbance data at 438, 387 and 308 nm reported as a function of the ligand molar fraction (bottom). Absorbance data in the Job's plots were corrected for the absorbance of the pure reactant (concentration of Fe(III) = L = 5.27 × 10^{-5} M, 0.01 M NaClO$_4$, T 25 °C, and optic path length 1 cm).

range, five significant eigenvalues were found, indicating five linearly independent absorbing species in solution. By fitting the experimental data considering the species $[Fe(III)]_{free}$, $[FeL]^{3+}$, $[FeL_2]^{3+}$, $[FeL_3]^{3+}$ and $[L]_{free}$, the complex formation constants were calculated (Table 1). To compare the ability of the ligands to coordinate Fe(III), the concentration of the free metal ion in the presence of ligand at 1:1 and 1:10 metal:ligand molar ratios,

has been calculated (Table 1). Considering the 1:10 ratio, the concentration of free Fe(III) varies with the ligands in the order **L2** < **L5** < **L3** < **L4** < **L1**. The ligands **L2**, **L5** and **L3** show the highest stability ($[Fe(III)_{free}]$ ranging from 5.9 × 10^{-18} to 9.6 × 10^{-16} M). Selected spectra recorded during the titrations are reported in the ESI† (Fig. S16). The complex formation was also studied in solution by ESI-MS measurements. Several complexes containing metal and ligand in 1:1, 1:2 and 1:3 molar ratios were observed, as adducts with the solvent. Some mass spectra are reported as an example in the ESI† (Fig. S17).

Spectrofluorimetric measurements

Ligands. In CH$_3$CN, all the ligands showed fluorescence emission in the 350–550 nm wavelength range. The highest quantum yield was observed for **L4** (Φ = 0.342). The other ligands showed a quantum yield ≤ 0.1 (Table 2). The spectral shape was similar for all the ligands, as can be seen in the ESI† (Fig. S18).

Complexes. Spectrofluorimetric titrations were performed in CH$_3$CN solution by adding aliquots of Fe(III) perchlorate to the ligand solution. Selected spectra recorded during the titrations are reported in Fig. 5. For all the studied ligands, a ratiometric behaviour was observed. The differences between the two emission maxima were 23 nm for **L1**, 36 nm for **L2**, 31 nm for **L3**, 64 nm for **L4** and approx. 67 nm for **L5**. In the case of **L5**, the emission band of the Fe(III) complex fell in the same region as the ligand overtone band and the spectral recording was inevitably ended at 525 nm (Fig. 5E). The intensity of the formed band was higher than that of the ligand alone, in the order **L3** (ratio was 3.75) > **L1** (ratio was 1.4) > **L5** (ratio was approx. 1.3) > **L4** (ratio was 1.1). Since turn-on and ratiometric systems are preferred for the enhancement of the sensitivity and then for the decrease of the detection limit, ligand **L3** was chosen as the best sensor for Fe(III) and further experiments, on its selectivity and competition with other metal ions, were carried out. The analytical procedure for quantification of Fe(III) with **L3** was also undertaken. Excitation and emission wavelengths and quantum yields for the studied complexes are reported in Table 3. A structure–function correlation suitable to explain the high quantum efficiency of the fluorinated derivative **L4** and its low fluorescence rising after complexation, in comparison with the behaviour shown by **L3**, would require the

Table 1 Complex formation constants for the studied systems and concentrations of the free Fe(III) in the presence of the ligands at 1:1 and 1:10 metal:ligand molar ratios (25 °C, 0.05 M NaClO$_4$, and CH$_3$CN solution; the standard deviation to the last significant figure is reported in parentheses)

Species	Substituent				
	L1	**L2**	**L3**	**L4**	**L5**
	H	6-Cl	6-OMe	6-F	6-OH
	$\log \beta$				
$[FeL]^{3+}$	7.90(1)	9.44(1)	9.05(1)	7.61(1)	9.29(2)
$[FeL_2]^{3+}$	15.45(4)	18.08(1)	17.13(1)	15.0(1)	18.1(1)
$[FeL_3]^{3+}$	21.89(1)	26.69(2)	24.48(2)	22.3(2)	26.3(1)
	$[Fe(III)free]$ (M)				
L = 1.0 × 10^{-5} M Fe(III) = 1.0 × 10^{-5} M	3.0 × 10^{-6}	2.6 × 10^{-6}	2.1 × 10^{-6}	3.7 × 10^{-6}	2.9 × 10^{-6}
L = 1.0 × 10^{-5} M Fe(III) = 1.0 × 10^{-6} M	3.5 × 10^{-13}	5.9 × 10^{-18}	9.6 × 10^{-16}	1.5 × 10^{-13}	1.5 × 10^{-17}

27

Table 2 Excitation/emission wavelengths and quantum yield (Φ) of the studied sensors (reference was quinine sulphate in sulfuric acid 0.5 M, Φ is 0.5469)

Compound	λ_{exc} (nm)	λ_{em} (nm)	Φ
L1	309	405	0.082
L2	301	416	0.032
L3	310	453	0.031
L4	261	418	0.342
L5	267	460	0.027

Table 3 Excitation/emission wavelengths and quantum yield (Φ) of the studied Fe(III) complexes (reference was quinine sulphate in sulfuric acid 0.5 M, Φ is 0.5469)

Compound	λ_{exc} (nm)	λ_{em} (nm)	Φ
Fe(**L1**)$^{3+}$	309	428	0.104
Fe(**L1**)$_2$$^{3+}$			0.092
Fe(**L1**)$_3$$^{3+}$			0.086
Fe(**L2**)$^{3+}$	301	455	0.032
Fe(**L2**)$_2$$^{3+}$			0.035
Fe(**L2**)$_3$$^{3+}$			0.033
Fe(**L3**)$^{3+}$	310	517	0.099
Fe(**L3**)$_2$$^{3+}$			0.069
Fe(**L3**)$_3$$^{3+}$			0.051
Fe(**L4**)$^{3+}$	261	449	0.047
Fe(**L4**)$_2$$^{3+}$			0.046
Fe(**L4**)$_3$$^{3+}$			0.050
Fe(**L5**)$^{3+}$	267	460	n.d.^{a}
Fe(**L5**)$_2$$^{3+}$			n.d.
Fe(**L5**)$_3$$^{3+}$			n.d.

^{a} Quantum yields for Fe(**L5**)$^{3+}$, Fe(**L5**)$_2$$^{3+}$ and Fe(**L5**)$_3$$^{3+}$ were not calculated due to the overlapping of the ligand overtone band.
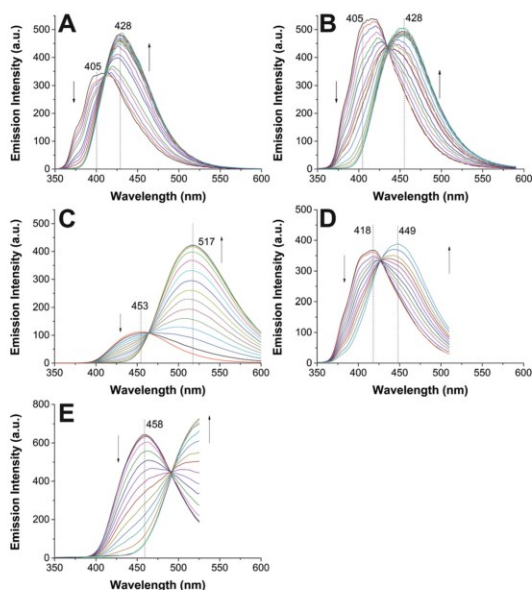

Fig. 5 Selected emission spectra of the titrations of the ligands (6.7 × 10^{-5} mmol) with Fe(III) (2.5 × 10^{-3} M) in CH$_3$CN solution, T 25 °C, 1 cm optical path length: (A) **L1** λ_{exc} 309 nm, slits 2.5 × 2.5 nm, and PMT 600 V; (B) **L2** λ_{exc} 301 nm, slits 5.0 × 5.0 nm, and PMT 600 V; (C) **L3** λ_{exc} 310 nm, slits 2.5 × 5.0 nm, and PMT 600 V; (D) **L4** λ_{exc} 261 nm, slits 5.0 × 2.5 nm, and PMT 600 V; (E) **L5** λ_{exc} 267 nm, slits 5.0 × 5.0 nm, and PMT 650 V.
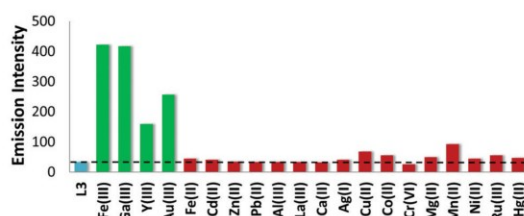

Fig. 6 Fluorescence emission intensity of systems containing **L3** and different metal ions in 1:1 molar ratio. The dotted line indicates the emission intensity due to the ligand alone (6.7 × 10^{-5} mmol, CH$_3$CN solution, T 25 °C, 1 cm optical path length, λ_{exc} 310 nm, slits 2.5 × 5.0 nm, PMT 600 V, and λ_{em} 517 nm).

computation of all the MOs in fundamental and excited states; however, such a theoretical approach is beyond the scope of this work. Tentatively, it could be assumed that the high quantum yield of **L4** was attributable to the high electronegativity and the low dimensions of the fluorine substituent, when compared to the others.

Selectivity studies. To define the selectivity of **L3** towards Fe(III), the fluorescence emission at 517 nm in the presence of other divalent (copper, mercury, iron, cadmium, zinc, lead, calcium, magnesium, cobalt, zinc, manganese, and nickel), trivalent (gallium, aluminium, lanthanum, gold, yttrium, and ruthenium) and hexavalent (chromium) metal ions was evaluated. An emission comparable to that observed with Fe(III) was observed with Ga(III), Au(III) and Y(III) while no significant emission was observed with the other metal ions, not even with Fe(II). The results are summarized in Fig. 6.

From eigenvalue analysis in the range of 200–450 nm, Ga(III) complexes [GaL]$^{3+}$, [GaL$_2$]$^{3+}$, and [GaL$_3$]$^{3+}$ were suggested, while for the Y(III) and Au(III) complexes, [YL]$^{3+}$, [YL$_2$]$^{3+}$ and [AuL]$^{3+}$ were identified, respectively. Complex formation constants are reported in Table 4. In order to define the real selectivity of **L3** towards Fe(III), the concentrations of the remaining free Fe(III) in the presence of the other metal ion(s) were calculated. In the ESI,† the calculated concentrations of each complex species for systems containing **L3**, Fe(III) and, in turn, Ga(III), Au(III) or Y(III), and **L3** with all the four metal ions, in 1:1:1 and 1:1:10 or 1:1:1:1 and 1:1:1:10 molar ratios, are reported (Table S8, ESI†). As can be seen on comparing [Fe(III)]$_{free}$ for all the different studied systems, **L3** shows higher affinity towards Fe(III) than towards the other metal ions, even in a large excess of Ga(III), Au(III) and Y(III), as well-evidenced in Fig. S20 (ESI†).

Competition studies. To a solution containing **L3** and Fe(III) in 1:1 molar ratio, other potential competitive metal ions were added and the variation of the fluorescence emission intensity at 517 nm was monitored. When the metal competitor was added in 1:1:1 **L3**:Fe(III):metal molar ratio, no significant change was observed. It was necessary to reach the 1:1:10 ratio to detect some changes, i.e. a diminishing of the intensity in

28

Table 4 Complex formation constants for **L3** and Ga(III), Y(III) and Au(III) (25 °C, 0.05 M NaClO$_4$, and CH$_3$CN solution; the standard deviation to the last significant figure is reported in parentheses)

Species	M		
	Ga(III)	Y(III)	Au(III)
	log β		
[ML]$^{3+}$	6.74(2)	7.51(2)	5.09(2)
[ML$_2$]$^{3+}$	13.3(1)	14.31(2)	—
[ML$_3$]$^{3+}$	19.45(2)	—	—

the presence of Cd(II), Cu(II), Ag(I), Au(III), Cr(VI) and Ru(III), and a slight increase with Ga(III) (Fig. 7).

Reversibility studies. To examine the reversibility of the probe's fluorescence behaviour towards Fe(III), a solution containing **L3** and Fe(III) in 1 : 1 molar ratio was titrated with EDTA. A progressive decrease in fluorescence emission intensity along with a hypsochromic shift was observed. After *ca.* 1.0 eq. of EDTA was added, both the spectral shape and the emission maxima of **L3** were fully restored, suggesting a sequestering action of EDTA for the formation of a more stable Fe(III)–EDTA complex, hence confirming the reversibility of **L3** as a fluorescent chemosensor for Fe(III) recognition (Fig. S21, ESI†).

Analytical applications. The applicability of **L3** as a fluorescent chemosensor for the quantitative determination of Fe(III) was investigated. Several solutions containing ligand and metal were prepared and the related emission intensity was measured. A linear response between emission intensity and Fe(III) concentration was found in the 2.4–35.0 μM Fe(III) concentration range. The limit of detection (LOD) was quantified as 2.4 μM Fe(III) at middle photomultiplier voltage (PMT). A lower LOD (0.1 μM)
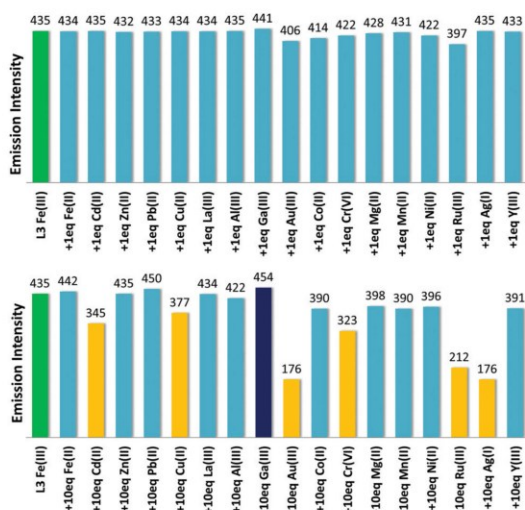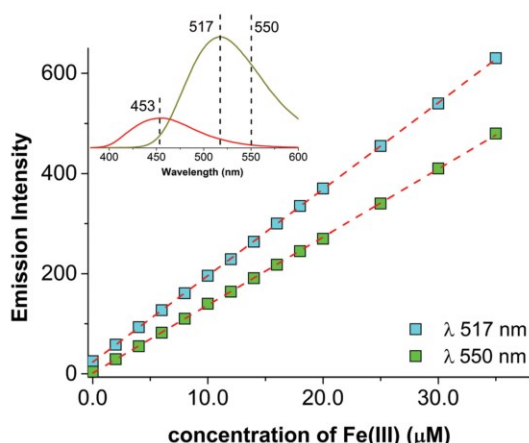

Fig. 8 Linear response between emission intensity measured at 517 (cyan squares) and 550 (green squares) nm and the analytical Fe(III) concentration. Limit of detection (LOD) for Fe(III) was 2.4 μM under the following experimental conditions: **L3** concentration 35 μM, CH$_3$CN solution, T 25 °C, 1 cm optical path length, λ_{exc} 310 nm, slits 2.5 × 5.0 nm, PMT 600 V, slits 2.5 × 5.0 nm, $Y_{517nm} = 15.53(6)X + 21(1)$, $R^2 = 0.9999$, $Y_{550nm} = 13.571(2)X$, and $R^2 = 0.9999$. In the inset, the emission of **L3** (red line) and **L3** with Fe(III) in 1 : 1 molar ratio (green line, 6.7×10^{-5} M) is reported to remind the positions of the maxima.

was observed upon increasing the PMT voltage and/or changing the slits; however, to avoid the loss of resolution and to increase the signal to noise ratio, repeated measures were recorded with an increase of the experimental time (this procedure is suggested for very low Fe(III) content). The linear correlation was assessed at 517 nm, *i.e.* at the emission maximum; however, at this wavelength, the emission of the ligand is still present (Fig. 8, cyan squares).‡ The emission at 550 nm was also considered, since at this wavelength the ligand contribution is negligible, and the linear response was still verified (Fig. 8, green squares) even if the emission of the complex is slightly lower.

Since **L3** could be proposed as a fluorescent chemosensor for the determination of Fe(III) in aqueous matrices, the linear response was also studied in water–acetonitrile solutions (ESI,† Fig. S22). The presence of CH$_3$CN was necessary for the ligand solubilization. As can be seen in Fig. S22 (ESI†), the emission spectra of the solutions containing ligand and Fe(III) in CH$_3$CN–H$_2$O (1 : 1) were slightly different from those recorded in pure CH$_3$CN. The linear response was verified for the same concentration range, but the ligand emission contribution was not negligible; however, this did not prevent the quantitative determination of Fe(III).

The sensors were efficiently tested in the 5–7 pH interval. At higher pH, the competition between ligand and hydroxyl ion for the metal ion becomes concurrent, while at lower pH, the protonation of the pyridinyl nitrogen was observed.

Fig. 7 Competition studies for the **L3**–Fe(III) system. Metal competitor was added in 1 : 1 : 1 (top) and 1 : 1 : 10 (bottom) molar ratios to a solution containing **L3** and Fe(III) in 1 : 1 molar ratio (6.7×10^{-5} mmol, CH$_3$CN solution, T 25 °C, 1 cm optical path length, λ_{exc} 310 nm, slits 2.5 × 5.0 nm, PMT 600 V, and λ_{em} 517 nm).

‡ The experimental emission at 517 nm could be corrected for the ligand contribution so the linear trendline goes through the origin.
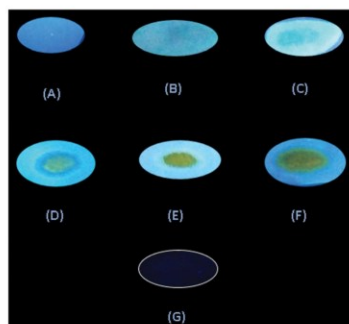
29

Finally, to examine the fluorescence emission of **L3** on a solid surface, cellulose paper test strips (Whatman™) were prepared by spotting a solution of **L3** (1 mM) dissolved in CH_3CN. The strips were air dried and water solutions of Fe(ɪɪɪ) at different concentrations (1, 10, 20, 50 and 70 mM) were deposited at the centre of the ligand spots. A fluorescence response was observed under a UV lamp. The results are shown in Fig. 9. As can be seen, an increase in fluorescence emission is observed upon an increase in Fe(ɪɪɪ) solution concentration, while in the absence of **L3**, as expected, a dramatic quenching of fluorescence by Fe(ɪɪɪ) is observed. These results suggest a potential application of **L3** for the determination of Fe(ɪɪɪ) in aqueous samples by means of a simple paper strip test.

Conclusions

The coordination ability towards Fe(ɪɪɪ) of a family of 3-(pyridin-2-yl)coumarin derivatives was studied using spectrophotometric and spectrofluorimetric measurements. Complexes $[FeL_2](ClO_4)_3$ and $[FeL_3](ClO_4)_3$ were isolated in the solid state. Spectrofluorimetric studies evidenced that these derivatives showed a ratiometric and turn-on behavior in the presence of Fe(ɪɪɪ). The derivative with the –OCH_3 substituent at the 6th position (6-methoxy-3-(pyridin-2-yl)-2*H*-chromen-2-one) exhibited the highest fluorescence enhancement in the presence of Fe(ɪɪɪ). This sensor showed a ratiometric behaviour also with Ga(ɪɪɪ), Au(ɪɪɪ) and Y(ɪɪɪ), however, thanks to the greater stability of the Fe(ɪɪɪ) complexes, with respect to those of the other metal ions, and to their limited diffusion in both environmental and biological systems, 6-methoxy-3-(pyridin-2-yl)-2*H*-chromen-2-one could be proposed as a selective fluorescent chemosensor for the detection of Fe(ɪɪɪ) in CH_3CN and CH_3CN : H_2O (1 : 1) solutions and on coated paper strips.

Experimental

Materials and measurements

Reagents. Ethanol, methanol, hydrochloric acid, anhydrous ethanol, EDTA, Fe(ɪɪɪ) perchlorate monohydrate, Fe(ɪɪ) perchlorate

monohydrate, Ga(ɪɪɪ) perchlorate monohydrate, Cu(ɪɪ) perchlorate hexahydrate, La(ɪɪɪ) chloride, Al(ɪɪɪ) chloride, Cd(ɪɪ) nitrate monohydrate, Zn(ɪɪ) chloride, Pb(ɪɪ) chloride, Hg(ɪɪ) chloride, Ca(ɪɪ) chloride, Ag(ɪ) nitrate, Mg(ɪɪ) perchlorate hexahydrate, Mn(ɪɪ) perchlorate hexahydrate, Ni(ɪɪ) perchlorate hexahydrate, Y(ɪɪɪ) nitrate hexahydrate, Co(ɪɪ) perchlorate hexahydrate, tetrachloroauric(ɪɪɪ) acid, potassium chromate, Ru(ɪɪɪ) chloride hydrate and piperidine were purchased from Aldrich (Milan, Italy). Pyridine acetonitrile, salicylic aldehyde and its derivatives were purchased from Alfa-Aesar. The commercial reagents were used as received, without any further purification.

NMR

^{1}H and ^{13}C NMR spectra were recorded on a Varian 500 spectrometer at room temperature with trimethylsilane (TMS) as internal standard in DMSO or $CDCl_3$. Chemical shifts, multiplicity and coupling constants were reported.

Mass spectrometry

Mass spectra were recorded on a triple quadruple QqQ Varian 310-MS mass spectrometer using the electrospray ionisation technique. The mass spectra were recorded in positive ion mode in the *m/z* 50–550 range. The experimental conditions were: needle voltage 4500 V, shield voltage 800 V, housing temperature 60 °C, drying gas temperature 150 °C, nebuliser gas pressure 40 PSI, drying gas pressure 40 PSI, and detector voltage 1650 V.

Theoretical calculations

Theoretical calculations were carried out at the density functional theory (DFT)[62] level with the Gaussian 16 commercial suite of programs (rev. A.03).[63] The PBE0 hybrid functional[64] was adopted, along with the Ahlrichs single-ζ basis sets (BSs), in the recent Weigend's formulation (def2-SVP).[65] Acetonitrile was implicitly taken into account by using the integral equation formalism of the polarizable continuous model (IEF-PCM) within the self-consistent reaction field (SCRF) approach.[66] The molecular geometry optimizations were performed starting from structural data, when available. Harmonic frequency calculations (keyword freq = Raman) were carried out to verify the nature of the minima of each optimization by verifying the absence of calculated negative frequencies. A potential energy surface (PES; keyword opt = modredundant) study was carried out to evaluate the rotational barrier between the pyridine and coumarin fragments in the free ligand **L3**. Thermochemical data, including zero-point energy corrections, and natural atomic charges[59] were calculated at the optimized geometries at the same level of theory. The programs GaussView 6.0.16,[67] Molden 5.7,[68] and Chemissian 4.53[69] were used to investigate the optimized structures, molecular orbital shapes, and spin density maps.

Spectrophotometric measurements

UV-visible spectrophotometric measurements were carried out on a Varian Cary 60 UV-vis spectrophotometer in the 200–450 nm wavelength range using a 1 cm quartz cell, at 25 °C. The formation constants of the complexes formed by **L1–L5** with metal ions were determined at 25 °C by spectrophotometric titration of the metal

ions with the ligands in acetonitrile solution in 0.05 M $NaClO_4$ ionic buffer. The number of linearly independent absorbing species was obtained by applying eigenvalue analysis on the absorbance data matrix.[70] The complex formation constants were obtained using the Hyperquad 2006 program.[71] The equilibrium constants were expressed as overall association constants. IR spectra were acquired using a Bruker Vector 22 spectrophotometer, preparing the samples as KBr pellets.

Spectrofluorimetric measurements

Spectrofluorimetric measurements were recorded in CH_3CN and in CH_3CN–H_2O 1 : 1 solution on a Varian Cary Eclipse (optical path length 1 cm). Titrations were performed at 25 °C by adding aliquots of metal ion solution to the ligands. Quantitative yields were determined using quinine sulphate as a reference (quinine sulphate in sulfuric acid 0.5 M, Φ is 0.546).[72] Screening studies were performed recording the emission spectra of solutions containing ligand and metal in a 1 : 1 ratio. Competitive studies were performed recording the emission spectra of solutions containing ligand, Fe(III) and another metal ion in 1 : 1 : 1 and 1 : 1 : 10 ratios.

Solid state sensor application

Fluorescence emission was observed with a UV lamp (Spectroline ENF-240CD/E, emission wavelength 365 nm). $Fe(ClO_4)_3H_2O$ was used.

Synthesis

General procedure for the preparation of chromen-2-one derivatives. Salicylaldehyde derivatives (0.0072 mol) and pyridine-2-acetonitrile (0.76 mL, 0.0072 mol) were dissolved in 14 mL of anhydrous ethanol, and piperidine (0.26 mL) was added dropwise in an ice bath. The mixture was stirred for 20 h at room temperature, treated with HCl (23 mL, 3.5%) and refluxed for 10 h to hydrolyze the iminocoumarin. When the reaction was completed, the acidic solution was neutralized with aqueous ammonia until pH 7. The precipitate was filtered off and recrystallized from methanol to yield the desired product. Compounds **L1**–**L4** were previously prepared and characterized.[1]

L5 (6-Hydroxy-3-(pyridin-2-yl)-2H-chromen-2-one): yield: 50%. M.p. 245–255 °C. ^1H NMR (500 MHz, DMSO d_6, δ, ppm): 8.85 (d, 1H, J = 5.14 Hz), 8.82 (s, 1H), 8.39 (d, 1H, J = 8.00 Hz) 8.32 (td, 1H, J = 7.85 Hz, J = 1.23 Hz), 7.78 (dd, 1H, J = 6.23 Hz, J = 0.86 Hz), 7.35 (d, 1H, J = 8.81 Hz) 7.23 (d 1H, J = 2.70 Hz), 7.21 (dd, 1H, J = 8.81 Hz, J = 2.81 Hz). ^{13}C NMR (125 MHz, DMSO d_6, δ, ppm): 162.80, 157.07, 154.31, 152.52, 149.93, 145.56, 139.81, 127.83, 126.68, 126.63, 123.83, 122.79, 119.89, 116.32 ESI-MS (calcd, found, m/z): 240.1, 239.9 $[L + H]^+$; 262.0, 261.9 $[L + Na]^+$; 501.1, 501.0 $[2L + Na]^+$. IR (KBr, cm^{-1}): 1700 (C=O); UV-vis (MeCN, λ_{max} nm, log ε): 225 (4.113), 327 (4.010).

Fe(III) complexes C1–C10. An ethanolic solution of $Fe(ClO_4)_3$·H_2O (0.5 g, 10 mL) was slowly added to an ethanolic solution (10 mL) of the ligands in 1 : 2 and 1 : 3 metal : ligand molar ratios, under stirring and at room temperature. A microcrystalline precipitate was immediately formed. The mixture was stirred for two hours and then the solid product was recovered by centrifuging. Elemental analysis: $Fe(L1)_2(ClO_4)_3$ (**C1**) found C% 40.25, H% 2.63, N% 3.30, calculated C% 40.19, H% 2.65, N% 3.35; $Fe(L2)_2(ClO_4)_3$ (**C2**) found C% 37.24, H% 2.29, N% 3.11, calculated C% 37.14, H% 2.23, N% 3.09; $Fe(L3)_2(ClO_4)_3$ (**C3**) found C% 41.79, H% 3.00, N% 3.26, calculated C% 41.67, H% 3.03, N% 3.24; $Fe(L4)_2(ClO_4)_3$ (**C4**) found C% 38.94, H% 2.33, N% 3.19, calculated C% 38.54, H% 2.31, N% 3.21; $Fe(L5)_2(ClO_4)_3$ (**C5**) found C% 40.89, H% 2.25, N% 3.42, calculated C% 40.39, H% 2.18, N% 3.36; $Fe(L1)_3(ClO_4)_3$ (**C6**) found C% 49.01, H% 2.62, N% 4.08, calculated C% 49.27, H% 2.66, N% 4.10; $Fe(L2)_3(ClO_4)_3$ (**C7**) found C% 44.78, H% 2.15, N% 3.71, calculated C% 44.75, H% 2.15, N% 3.73; $Fe(L3)_3(ClO_4)_3$ (**C8**) found C% 50.77, H% 3.14, N% 3.92, calculated C% 50.70, H% 3.12, N% 3.94; $Fe(L4)_3(ClO_4)_3$ (**C9**) found C% 46.78, H% 2.20, N% 3.87, calculated C% 46.80, H% 2.24, N% 3.90.; $Fe(L5)_3(ClO_4)_3$ (**C10**) found C% 47.12, H% 2.61, N% 3.93, calculated C% 47.06, H% 2.54, N% 3.92. FT-IR (C=O, cm^{-1}): **C1** 1711, **C2** 1701, **C3** 1691, **C4** 1701, **C5** 1684, **C6** 1708, **C7** 1701, **C8** 1691, **C9** 1701, **C10** 1686.

Conflicts of interest

There are no conflicts to declare.

Acknowledgements

Notes and references

1 T. Pivetta, V. Lallai, E. Valletta, F. Trudu, F. Isaia, D. Perra, E. Pinna and A. Pani, *J. Inorg. Biochem.*, 2015, **15**, 107–114.

2 E. Merian and T. W. Clarkson, *Metals and Their Compounds in the Environment*, VCH, 1991.

3 J. R. Lakowicz, *Principles of Fluorescence Spectroscopy*, Plenum, New York, 1983.

4 B. Valeur and I. Leray, *Coord. Chem. Rev.*, 2000, **205**, 3–40.

5 R. Wang, Q. Wan, F. Feng and Y. Bai, *Chem. Res. Chin. Univ.*, 2014, **30**, 560–565.

6 O. García-Beltrán, N. Mena, O. Yañez, J. Caballero, V. Vargas, M. T. Nuñez and B. K. Cassels, *Eur. J. Med. Chem.*, 2013, **67**, 60–63.

7 C. Wolf, X. Mei and H. K. Rokadia, *Tetrahedron Lett.*, 2004, **45**, 7867–7871.

8 N. Kaur, M. Kaur, S. Chopra, J. Singh, A. Kuwar and N. Singh, *Food Chem.*, 2018, **245**, 1257–1261.

9 H. Xu, Y. Dong, Y. Wu, W. Ren, T. Zhao, S. Wang and J. Gao, *J. Solid State Chem.*, 2018, **258**, 441–446.

31

10 Y. He, Z. Yu, J. He, H. Zhang, Y. Liu and B. Lei, *Sens. Actuators, B*, 2018, **262**, 228–235.

11 J. Yao, W. Dou, W. Qin and W. Liu, *Inorg. Chem. Commun.*, 2009, **12**, 116–118.

12 Y. Xiang and A. Tong, *Org. Lett.*, 2006, **8**, 1549–1552.

13 D. En, Y. Guo, B.-T. Chen, B. Dong and M.-J. Peng, *RSC Adv.*, 2014, **4**, 248–253.

14 S. Joshi, S. Kumari, R. Bhattacharjee, A. Sarmah, R. Sakhuja and D. D. Pant, *Sens. Actuators, B*, 2015, **220**, 1266–1278.

15 S. Warrier and P. S. Kharkar, *Spectrochim. Acta, Part A*, 2018, **188**, 659–665.

16 N. Singh, N. Kaur, J. Dunn, M. MacKay and J. F. Callan, *Tetrahedron Lett.*, 2009, **50**, 953–956.

17 Z. Zhang, H. Wang, H. Zhang and Y. Liu, *Chin. J. Chem.*, 2013, **31**, 598–602.

18 L. J. Fan and W. E. Jones, *J. Am. Chem. Soc.*, 2006, **128**, 6784–6785.

19 N. C. Lim, S. V. Pavlova and C. Brückner, *Inorg. Chem.*, 2009, **48**, 1173–1182.

20 Z. Mu, J. Hua, S. Feng and Y. Yang, *Spectrochim. Acta, Part A*, 2019, **219**, 248–256.

21 H. Chen, X. Bao, H. Shu, B. Zhou, R. Ye and J. Zhu, *Sens. Actuators, B*, 2017, **242**, 921–931.

22 S. Adhikari, A. Ghosh, M. Ghosh, S. Guria and D. Das, *Sens. Actuators, B*, 2017, **251**, 942–950.

23 P. Sirajuddin Nayab, M. Shkir, P. Gull and S. AlFaify, *J. Photochem. Photobiol., A*, 2017, **347**, 209–217.

24 O. García-Beltrán, B. K. Cassels, C. Pérez, N. Mena, M. T. Núñez, N. P. Martínez, P. Pavez and M. E. Aliaga, *Sensors*, 2014, **14**, 1358–1371.

25 S. Voutsadaki, G. K. Tsikalas, E. Klontzas, G. E. Froudakis and H. E. Katerinopoulos, *Chem. Commun.*, 2010, **46**, 3292.

26 D. Ray and P. K. Bharadwaj, *Inorg. Chem.*, 2008, **47**(7), 2252–2254.

27 C. P. Kulatilleke, S. A. de Silva and Y. Eliav, *Polyhedron*, 2006, **25**, 2593–2596.

28 N. C. Lim, J. V. Schuster, M. C. Porto, M. A. Tanudra, L. Yao, H. C. Freake and C. Brückner, *Inorg. Chem.*, 2005, **44**, 2018–2030.

29 D. Ray, A. Nag, A. Jana, D. Goswami and P. K. Bharadwaj, *Inorg. Chim. Acta*, 2010, **363**, 2824–2832.

30 J. S. Wu, W. M. Liu, X. Q. Zhuang, F. Wang, P. F. Wang, S. L. Tao, X. H. Zhang, S. K. Wu and S. T. Lee, *Org. Lett.*, 2007, **9**, 33–36.

31 J. Ansell, J. Hirsh, E. Hylek, A. Jacobson, M. Crowther and G. Palareti, *Chest*, 2008, **133**, 160–198.

32 M. C. Aragoni, M. Arca, A. Bencini, C. Caltagirone, A. Garau, F. Isaia, M. E. Light, V. Lippolis, C. Lodeiro, M. Mameli, R. Montis, M. C. Mostallino, A. Pintus and S. Puccioni, *Dalton Trans.*, 2013, **42**, 14516–14530.

33 C. Bazzicalupi, C. Caltagirone, Z. Cao, Q. Chen, C. Dinatale, A. Garau, V. Lippolis, L. Lvova, H. Liu, I. Lundström, M. C. Mostallino, M. Nieddu, R. Paolesse, L. Prodi, M. Sgarzi and N. Zaccheroni, *Chem. – Eur. J.*, 2013, **19**, 14639–14653.

34 A. Bettoschi, A. Bencini, D. Berti, C. Caltagirone, L. Conti, D. Demurtas, C. Giorgi, F. Isaia, V. Lippolis, M. Mamusa and S. Murgia, *RSC Adv.*, 2015, **5**, 37385–37391.

35 G. Crisponi, V. M. Nurchi, T. Pivetta, J. Gałęzowska, E. Gumienna-Kontecka, T. Bailly, R. Burgada and H. Kozłowski, *J. Inorg. Biochem.*, 2008, **102**, 1486–1494.

36 V. M. Nurchi, G. Crisponi, J. I. Lachowicz, S. Murgia, T. Pivetta, M. Remelli, A. Rescigno, J. Niclós-Gutiérrez, J. M. González-Pérez, A. Domínguez-Martín, A. Castiñeiras and Z. Szewczuk, *J. Inorg. Biochem.*, 2010, 104.

37 V. M. Nurchi, T. Pivetta, J. I. Lachowicz and G. Crisponi, *J. Inorg. Biochem.*, 2009, 103.

38 M. C. Aragoni, M. Arca, A. Bencini, A. J. Blake, C. Caltagirone, A. Danesi, F. A. Devillanova, A. Garau, T. Gelbrich, F. Isaia, V. Lippolis, M. B. Hursthouse, B. Valtancoli and C. Wilson, *Inorg. Chem.*, 2007, **46**, 8088–8097.

39 T. Yu, S. Yang, J. Meng, Y. Zhao, H. Zhang, D. Fan, X. Han and Z. Liu, *Inorg. Chem. Commun.*, 2011, **14**, 159–161.

40 T. Pivetta, E. Valletta, G. Ferino, F. Isaia, A. Pani, S. Vascellari, C. Castellano, F. Demartin, M. G. Cabiddu and E. Cadoni, *J. Inorg. Biochem.*, 2017, 177.

41 P. Ganis, A. Saporito, A. Vitagliano and G. Valle, *Inorg. Chim. Acta*, 1988, **142**, 75–79.

42 C. R. Turlington, P. S. White, M. Brookhart and J. L. Templeton, *J. Am. Chem. Soc.*, 2014, **136**, 3981–3994.

43 B. M. Holligan, J. C. Jeffery, M. K. Norgett, E. Schatz and M. D. Ward, *J. Chem. Soc., Dalton Trans.*, 1992, 3345–3351.

44 K. Kim, J. Hyun, J. Kim and H. Kim, *Asian J. Org. Chem.*, 2017, **6**, 907–912.

45 D. A. Bardwell, D. Black, J. C. Jeffery, E. Schatz and M. D. Ward, *J. Chem. Soc., Dalton Trans.*, 1993, 2321–2327.

46 D. A. Bardwell, J. C. Jeffery and M. D. Ward, *Inorg. Chim. Acta*, 1995, **236**, 125–130.

47 Z. Setifi, F. Setifi, B. M. Francuski, S. B. Novaković and H. Merazig, *Acta Crystallogr., Sect. E: Crystallogr. Commun.*, 2015, **71**, 346–349.

48 X. Sui, X. Lu, J. Feng, S. Wang and P. Li, *J. Coord. Chem.*, 2008, **61**, 1568–1574.

49 B. F. Abrahams, B. F. Hoskins and R. Robson, *Acta Crystallogr., Sect. C: Cryst. Struct. Commun.*, 1996, **52**, 2766–2768.

50 E. D. Djomo, M. Foulon, N. Justin, M. M. Bélombé and F. Michel, *Acta Crystallogr., Sect. E: Struct. Rep. Online*, 2015, **71**, 934–936.

51 Y.-Z. Tang, J. Huang, M. Zhou, J.-S. Wu, Y.-H. Tan and H.-R. Wen, *Z. Anorg. Allg. Chem.*, 2013, **639**, 409–413.

52 K. Nagayoshi, M. K. Kabir, H. Tobita, K. Honda, M. Kawahara, M. Katada, K. Adachi, H. Nishikawa, I. Ikemoto, H. Kumagai, Y. Hosokoshi, K. Inoue, S. Kitagawa and S. Kawata, *J. Am. Chem. Soc.*, 2003, **125**, 221–232.

53 O. K. Kwak, K. S. Min and B. G. Kim, *Acta Crystallogr., Sect. E: Struct. Rep. Online*, 2007, **63**, m17–m19.

54 M. Hu, S.-T. Ma, L.-Q. Guo and S.-M. Fang, *Acta Crystallogr., Sect. E: Struct. Rep. Online*, 2009, **65**, m382.

55 M. K. Kabir, N. Miyazaki, S. Kawata, K. Adachi, H. Kumagai, K. Inoue, S. Kitagawa, K. Iijima and M. Katada, *Coord. Chem. Rev.*, 2000, **198**, 157–169.

56 M. Nihei, T. Shiga, Y. Maeda and H. Oshio, *Coord. Chem. Rev.*, 2007, **251**, 2606–2621.

32

57 S. Ashoka Sahadevan, E. Cadoni, N. Monni, C. Sáenz De Pipaón, J. R. Galan Mascaros, A. Abhervé, N. Avarvari, L. Marchiò, M. Arca and M. L. Mercuri, *Cryst. Growth Des.*, 2018, **18**, 4187–4199.

58 D. J. Harding, P. Harding and W. Phonsri, *Coord. Chem. Rev.*, 2016, **313**, 38–61.

59 A. E. Reed, R. B. Weinstock and F. Weinhold, *J. Chem. Phys.*, 1985, **83**, 735–746.

60 P. Job, *Ann. Chim. Appl.*, 1928, **9**, 113–203.

61 J. S. Renny, L. L. Tomasevich, E. H. Tallmadge and D. B. Collum, *Angew. Chem., Int. Ed.*, 2013, **52**, 11998–12013.

62 W. Koch and M. C. Holthausen, *A Chemist's Guide to Density Functional Theory*, Wiley-VCH Verlag GmbH, Weinheim, FRG, 2001, vol. 3.

63 M. J. Frisch, G. W. Trucks, H. B. Schlegel, G. E. Scuseria, M. A. Robb, J. R. Cheeseman, G. Scalmani, V. Barone, G. A. Petersson, H. Nakatsuji, X. Li, M. Caricato, A. V. Marenich, J. Bloino, B. G. Janesko, R. Gomperts, B. Mennucci, H. P. Hratchian, J. V. Ortiz, A. F. Izmaylov, J. L. Sonnenberg, D. Williams-Young, F. Ding, F. Lipparini, F. Egidi, J. Goings, B. Peng, A. Petrone, T. Henderson, D. Ranasinghe, V. G. Zakrzewski, J. Gao, N. Rega, G. Zheng, W. Liang, M. Hada, M. Ehara, K. Toyota, R. Fukuda, J. Hasegawa, M. Ishida, T. Nakajima, Y. Honda, O. Kitao, H. Nakai, T. Vreven, K. Throssell, J. E. Peralta, J. A. Montgomery Jr., F. Ogliaro, M. J. Bearpark, J. J. Heyd, E. N. Brothers, K. N. Kudin, V. N. Staroverov, T. A. Keith, R. Kobayashi, J. Normand, K. Raghavachari, A. P. Rendell, J. C. Burant, S. S. Iyengar, J. Tomasi, M. Cossi, J. M. Millam, M. Klene, C. Adamo, R. Cammi, J. W. Ochterski, R. L. Martin, K. Morokuma, O. Farkas, J. B. Foresman and D. J. Fox, *Gaussian 16, Revision B.01*, Gaussian, Inc., Wallingford CT, 2016.

64 C. Adamo and V. Barone, *J. Chem. Phys.*, 1999, **110**, 6158–6170.

65 F. Weigend and R. Ahlrichs, *Phys. Chem. Chem. Phys.*, 2005, **7**, 3297–3305.

66 J. Tomasi, B. Mennucci and R. Cammi, *Chem. Rev.*, 2005, **105**, 2999–3093.

67 T. A. Keith and J. M. Millam, *GaussView, Version 6, Roy Dennington*, Semichem Inc., Shawnee Mission, KS, 2016.

68 G. Schaftenaar and J. H. Noordik, *J. Comput.-Aided Mol. Des.*, 2000, **14**, 123–134.

69 See http://www.chemissian.com.

70 M. Meloun, J. Čapek, P. Mikšík and R. G. Brereton, *Anal. Chim. Acta*, 2000, **423**, 51–68.

71 P. Gans, A. Sabatini and A. Vacca, *Talanta*, 1996, **43**, 1739–1753.

72 B. Valeur, *Molecular Fluorescence Principles and Applications*, 2001, vol. 8.

33

A novel ratiometric and TURN-ON fluorescent coumarin-based probe for Fe(III)

Tiziana Pivetta[1*], Sebastiano Masuri[1], Maria Grazia Cabiddu[1], Claudia Caltagirone[1], Anna Pintus[1],

Michela Massa[1], Francesco Isaia[1], Enzo Cadoni[1]

[1] Dipartimento di Scienze Chimiche e Geologiche, Università degli Studi di Cagliari, Cittadella

Universitaria, 09042 Monserrato CA – ITALY

Address reprints requests to:

Tiziana Pivetta

Dipartimento di Scienze Chimiche e Geologiche

Università degli Studi di Cagliari, Cittadella Universitaria

09042 Monserrato CA – ITALY

Tel. 0039 070 675 4473

mail: tpivetta@unica.it

Supplementary Information
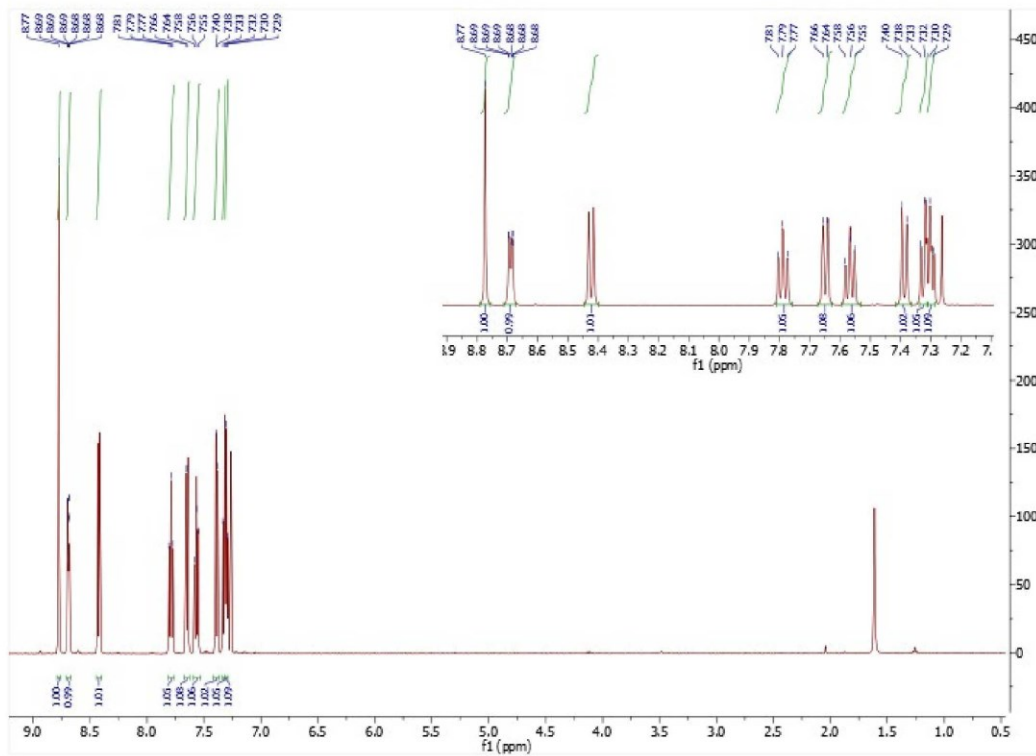
Figure S1: ^{1}H NMR of ligand L1, 3-(pyridin-2-yl)-2*H*-chromen-2-one. NMR spectra were recorded on a Varian 500 spectrometer at room temperature with trimethylsilane (TMS) as internal standard in CDCl$_3$.
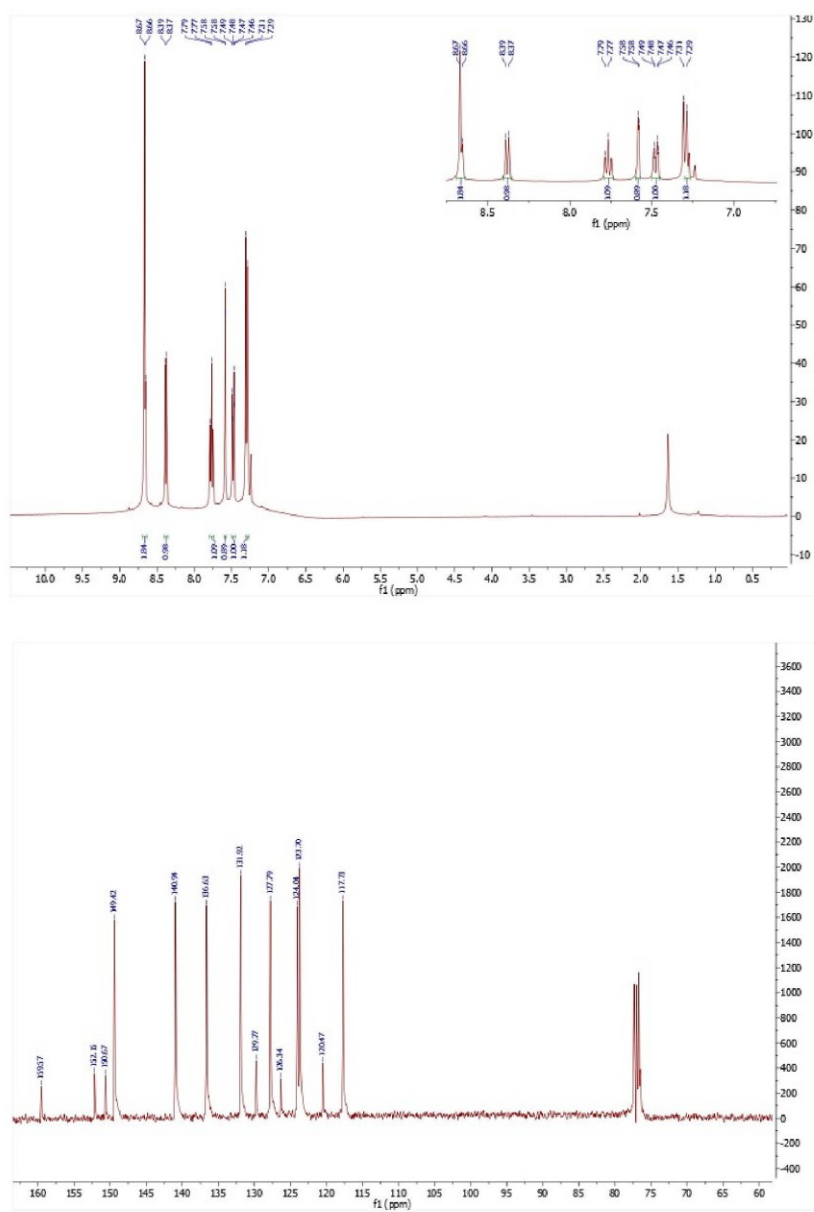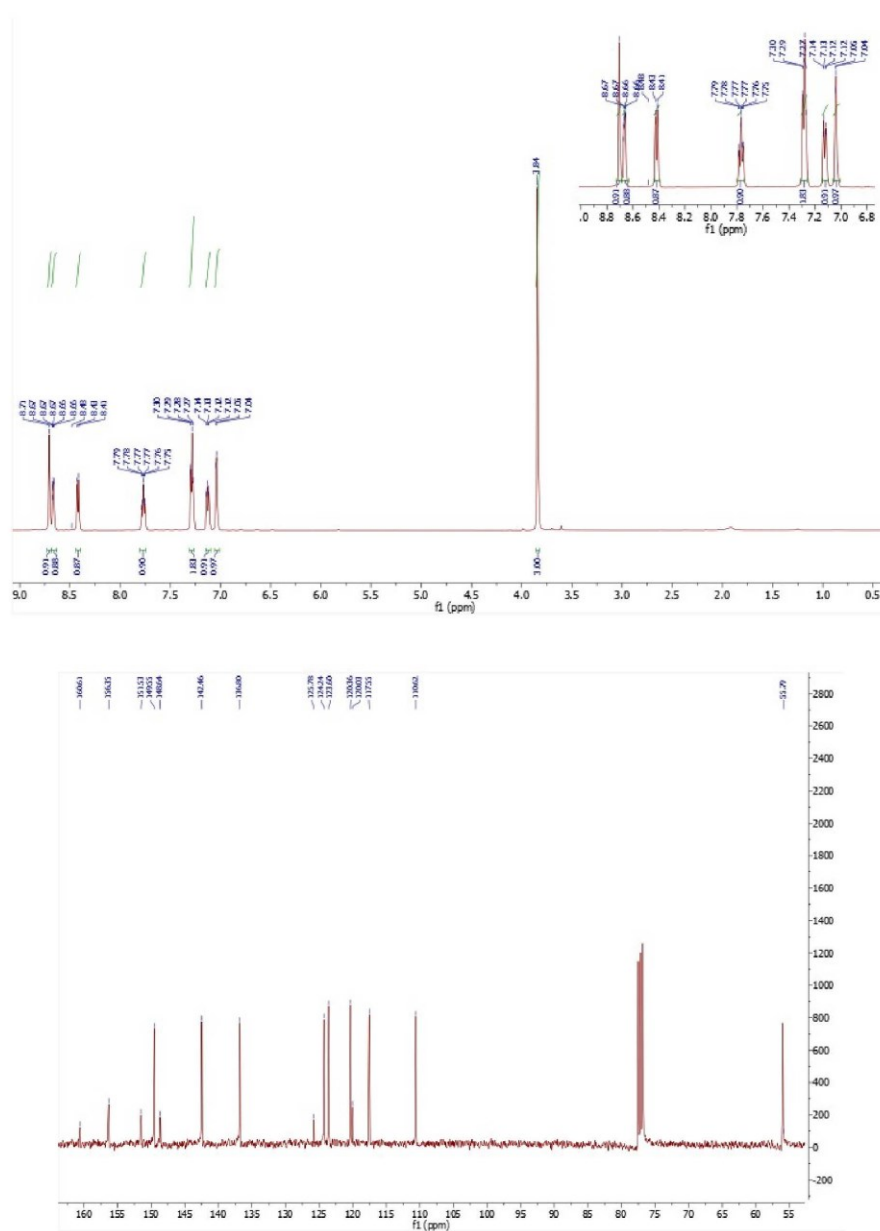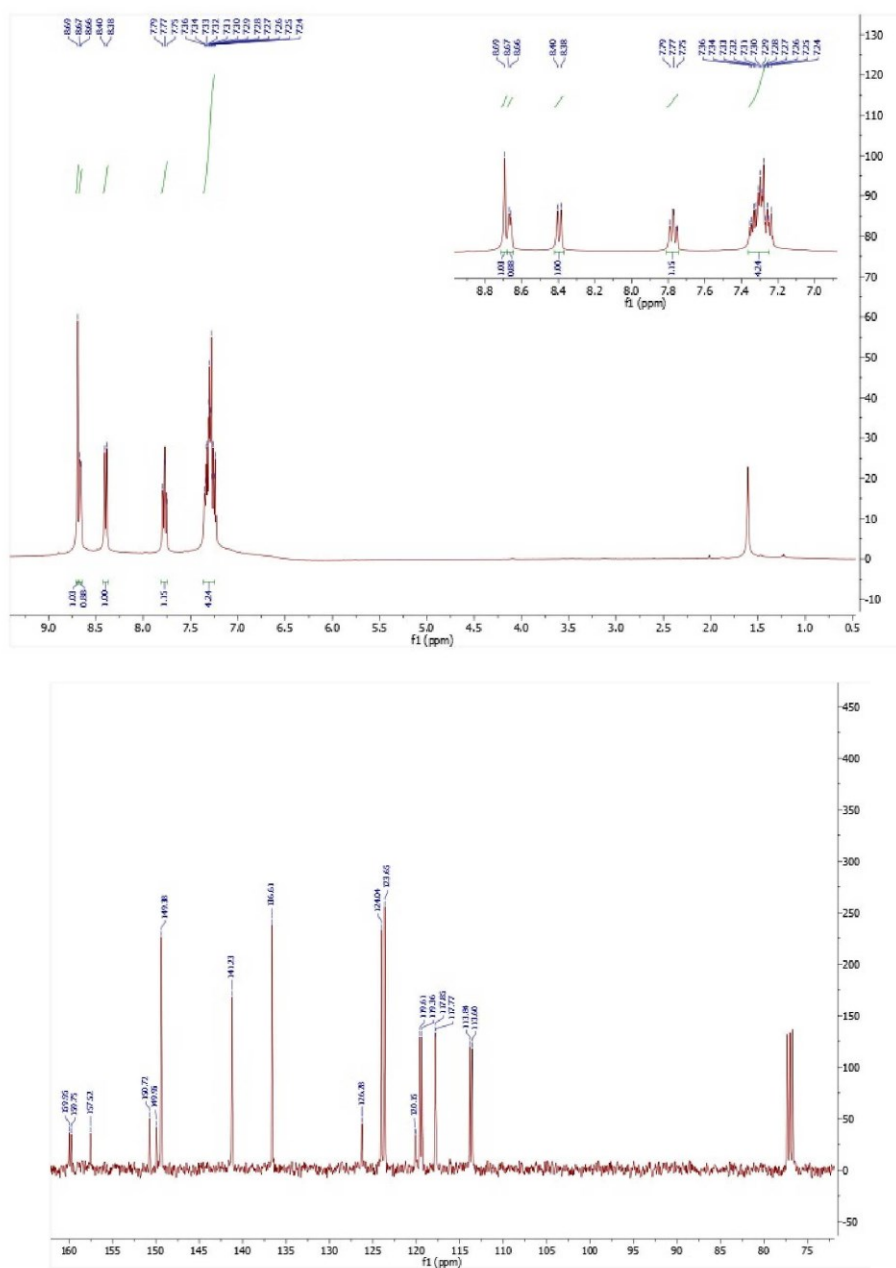
Figure S2: ^{1}H NMR (top) and ^{13}C NMR spectrum (bottom) of ligand L2, 6-chloro-3-(pyridin-2-yl)-2H-chromen-2-one. NMR spectra were recorded on a Varian 500 spectrometer at room temperature with trimethylsilane (TMS) as internal standard in CDCl₃.
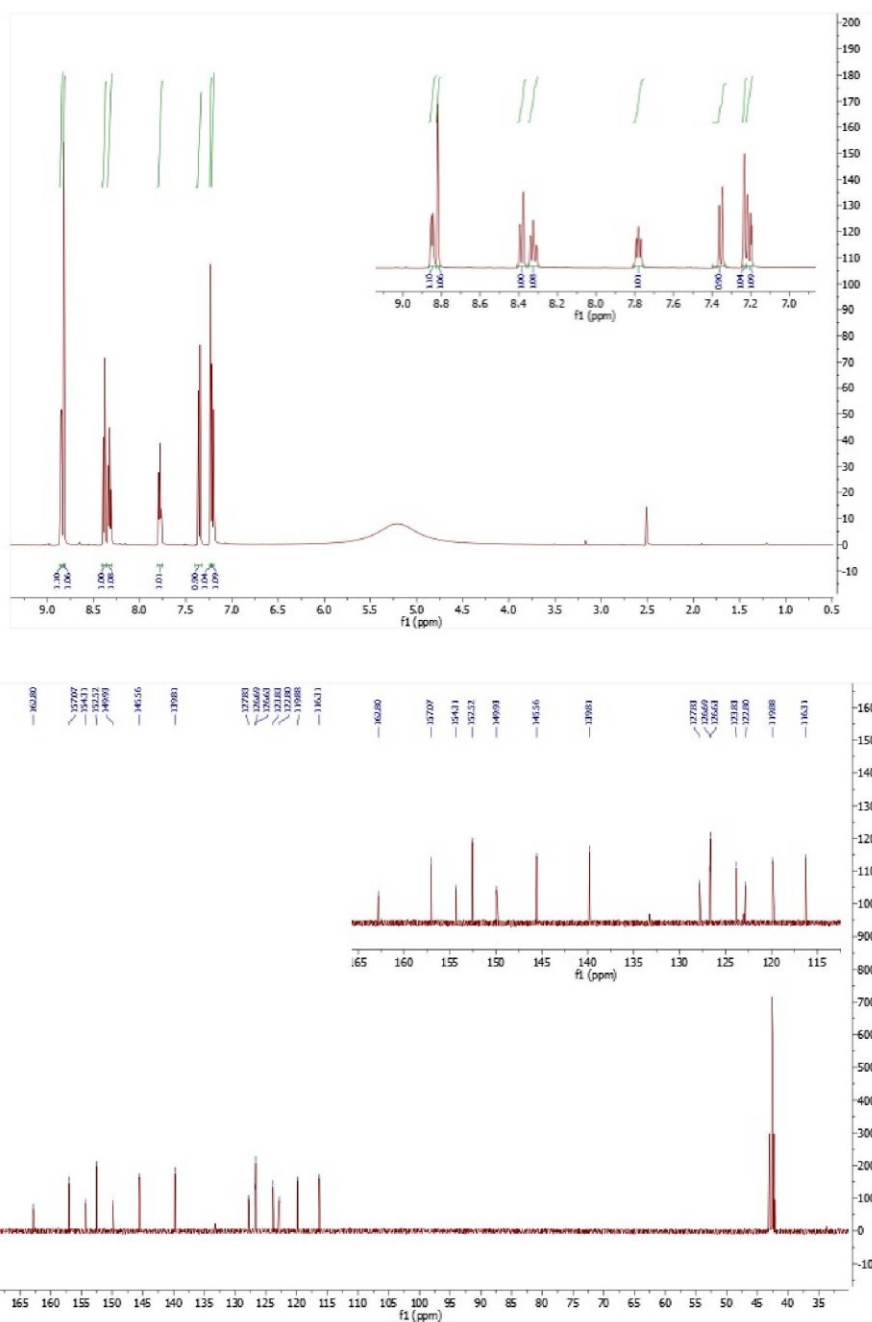
Figure S3: ^{1}H NMR (top) and ^{13}C NMR spectrum (bottom) of ligand L3, 6-methoxy-3-(pyridin-2-yl)-2*H*-chromen-2-one. NMR spectra were recorded on a Varian 500 spectrometer at room temperature with trimethylsilane (TMS) as internal standard in CDCl$_3$.

Figure S4: ^{1}H NMR (top) and ^{13}C NMR spectrum (bottom) of ligand L4, 6-fluoro-3-(pyridin-2-yl)-2*H*-chromen-2-one. NMR spectra were recorded on a Varian 500 spectrometer at room temperature with trimethylsilane (TMS) as internal standard in CDCl$_3$.
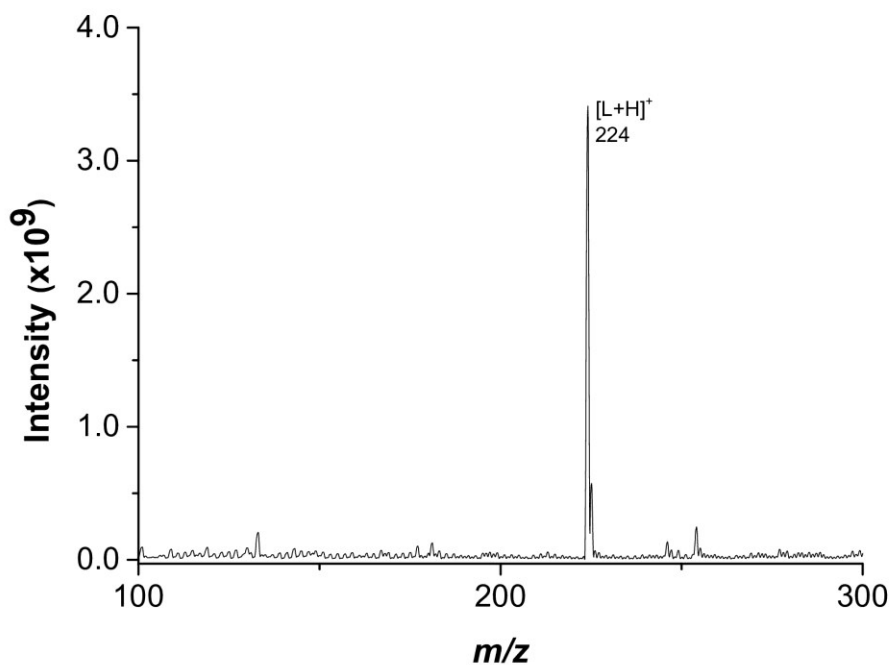
Figure S5: ^{1}H NMR (top) and ^{13}C NMR spectrum (bottom) of ligand L5, 6-hydroxy-3-(pyridin-2-yl)-2*H*-chromen-2-one. NMR spectra were recorded on a Varian 500 spectrometer at room temperature with trimethylsilane (TMS) as internal standard in DMSO.

Figure S6: ESI-MS spectrum of ligand L1, 3-(pyridin-2-yl)-2*H*-chromen-2-one. Mass spectra were recorded on a triple quadruple QqQ Varian 310-MS mass spectrometer using electrospray ionisation (ESI) technique. The mass spectra were recorded in positive ion mode in the m/z 50–550 range. The experimental conditions were: needle voltage 4500 V, shield voltage 800 V, housing temperature 60 °C, drying gas temperature 150 °C, nebuliser gas pressure 40 PSI, drying gas pressure 40 PSI, and detector voltage 1650 V.
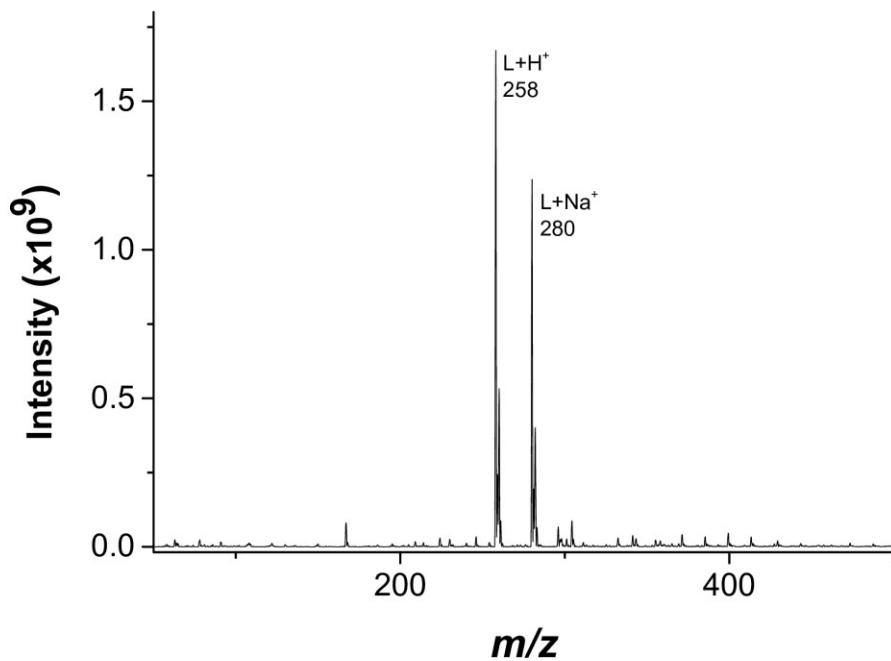
Figure S7: ESI-MS spectrum of ligand L2, 6-chloro-3-(pyridin-2-yl)-2*H*-chromen-2-one. Mass spectra were recorded on a triple quadruple QqQ Varian 310-MS mass spectrometer using electrospray ionisation (ESI) technique. The mass spectra were recorded in positive ion mode in the m/z 50–550 range. The experimental conditions were: needle voltage 4500 V, shield voltage 800 V, housing temperature 60 °C, drying gas temperature 150 °C, nebuliser gas pressure 40 PSI, drying gas pressure 40 PSI, and detector voltage 1650 V.
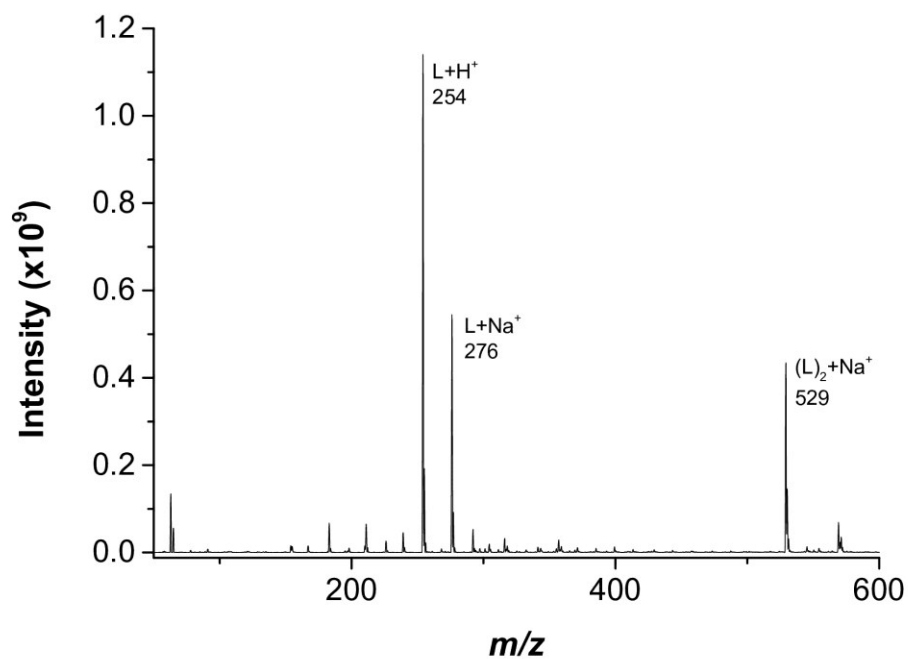
Figure S8: ESI-MS spectrum of ligand L3, 6-methoxy-3-(pyridin-2-yl)-2*H*-chromen-2-one. Mass spectra were recorded on a triple quadruple QqQ Varian 310-MS mass spectrometer using electrospray ionisation (ESI) technique. The mass spectra were recorded in positive ion mode in the m/z 50–550 range. The experimental conditions were: needle voltage 4500 V, shield voltage 800 V, housing temperature 60 °C, drying gas temperature 150 °C, nebuliser gas pressure 40 PSI, drying gas pressure 40 PSI, and detector voltage 1650 V.
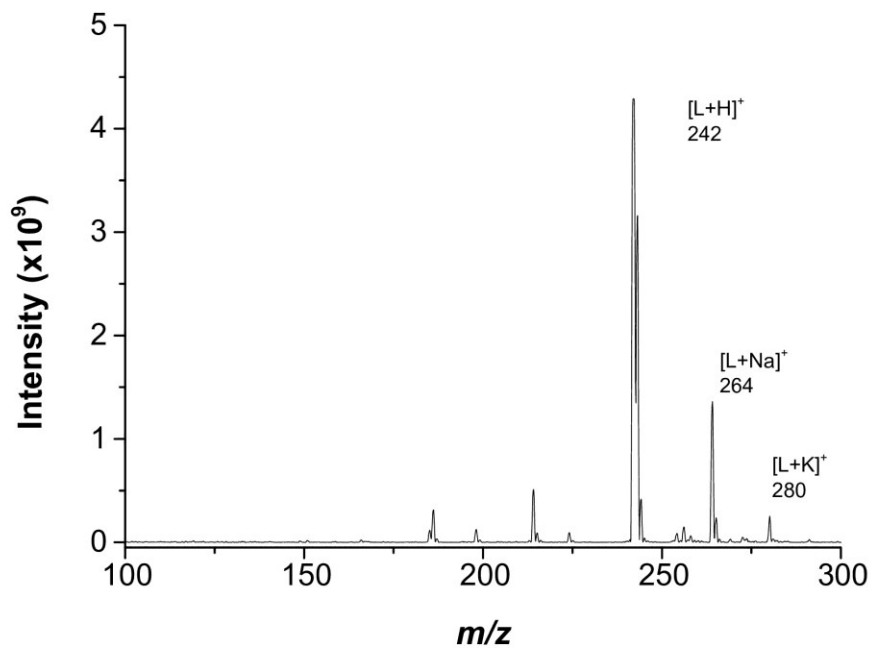
Figure S9: ESI-MS spectrum of ligand L4, 6-fluoro-3-(pyridin-2-yl)-2*H*-chromen-2-one. Mass spectra were recorded on a triple quadruple QqQ Varian 310-MS mass spectrometer using electrospray ionisation (ESI) technique. The mass spectra were recorded in positive ion mode in the m/z 50–550 range. The experimental conditions were: needle voltage 4500 V, shield voltage 800 V, housing temperature 60 °C, drying gas temperature 150 °C, nebuliser gas pressure 40 PSI, drying gas pressure 40 PSI, and detector voltage 1650 V.
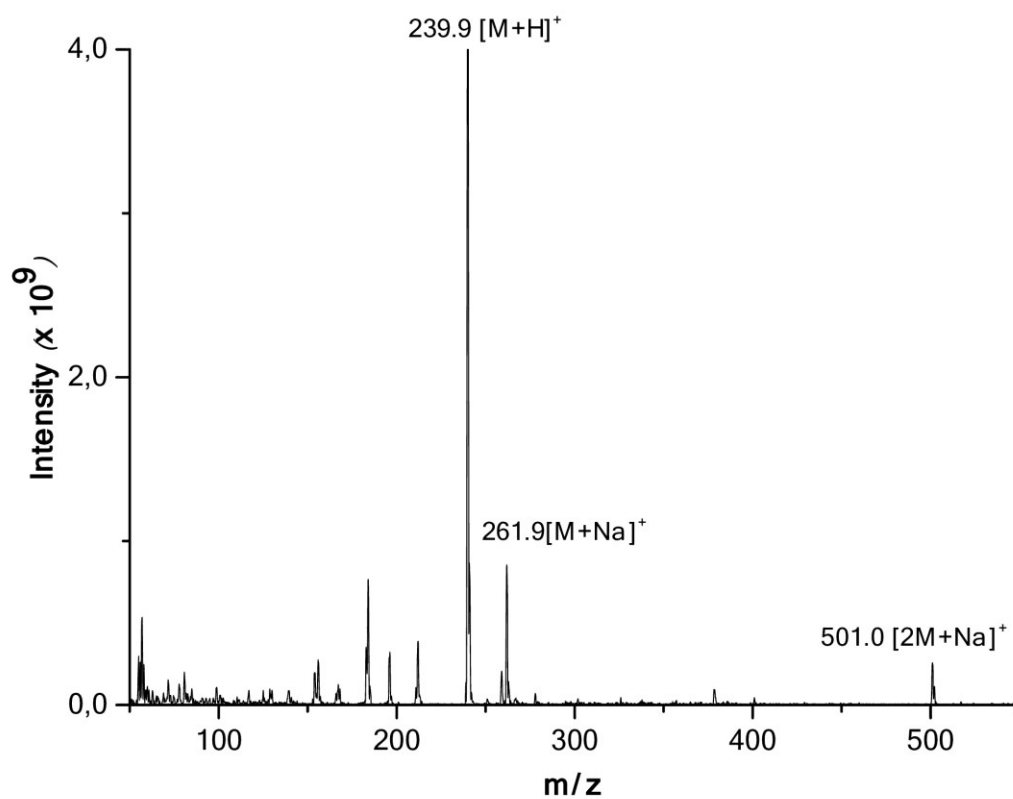
Figure S10: ESI-MS spectrum of ligand L5, 6-Hydroxy-3-(pyridin-2-yl)-2*H*-chromen-2-one. Mass spectra were recorded on a triple quadruple QqQ Varian 310-MS mass spectrometer using electrospray ionisation (ESI) technique. The mass spectra were recorded in positive ion mode in the m/z 50–550 range. The experimental conditions were: needle voltage 4500 V, shield voltage 800 V, housing temperature 60 °C, drying gas temperature 150 °C, nebuliser gas pressure 40 PSI, drying gas pressure 40 PSI, and detector voltage 1650 V.
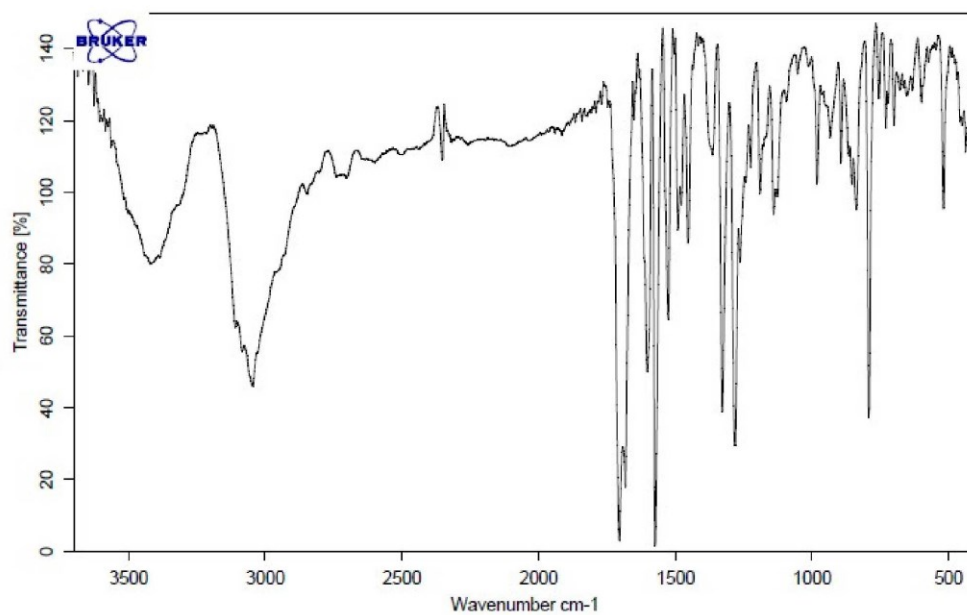
Figure S11: IR spectrum of ligand L5, 6-Hydroxy-3-(pyridin-2-yl)-2*H*-chromen-2-one. IR spectra were acquired with a Bruker Vector 22 spectrophotometer, preparing the samples as KBr pellets.
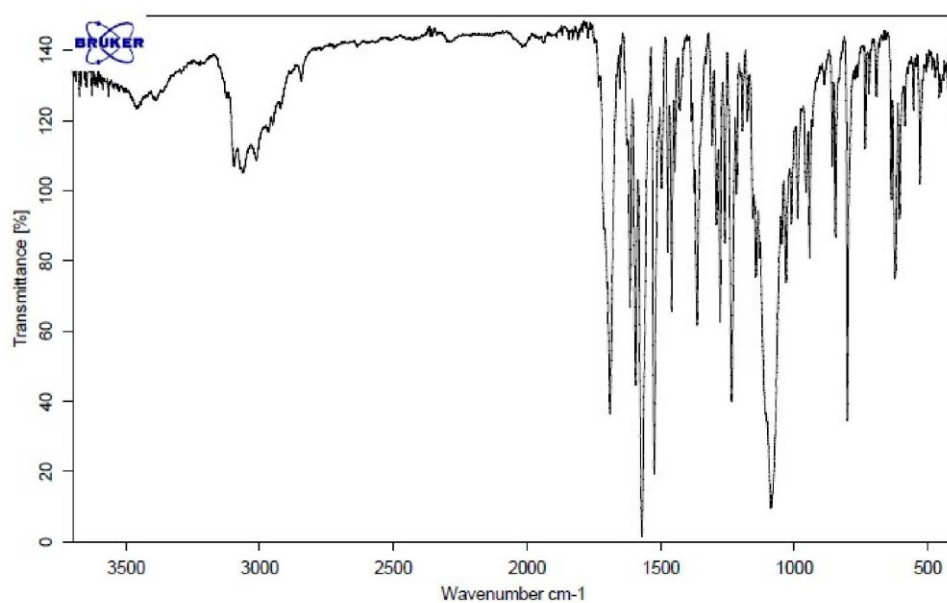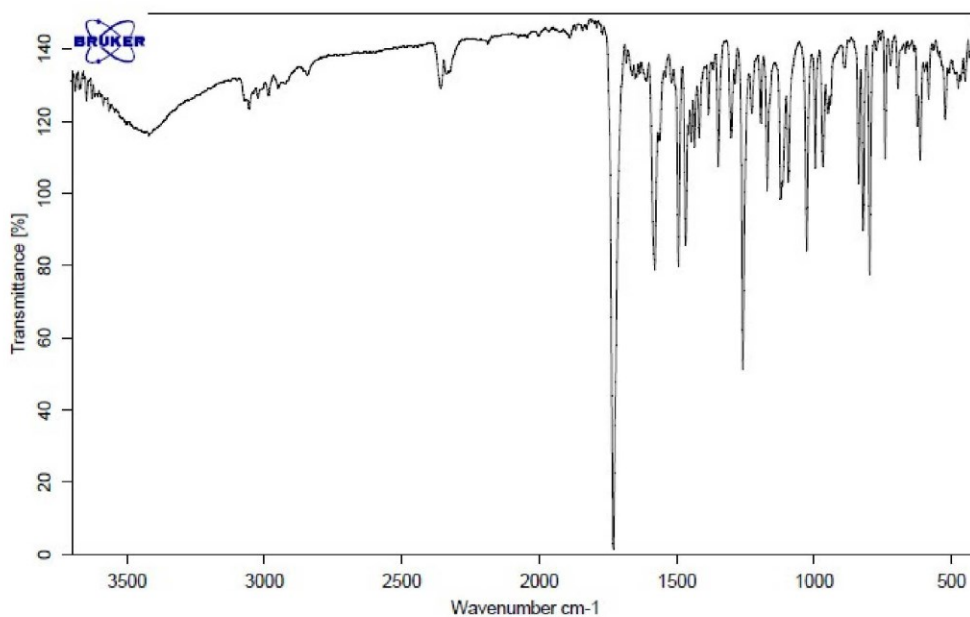
Figure S12: IR spectrum of ligand L3 (up), 6-Methoxy-3-(pyridin-2-yl)-2*H*-chromen-2-one and C8, Fe(L3)₃(ClO₄)₃. (bottom). IR spectra were acquired with a Bruker Vector 22 spectrophotometer, preparing the samples as KBr pellets.
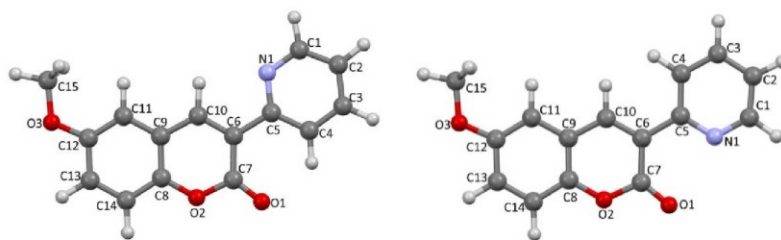
Figure S13. Molecular drawings and atom labelling schemes for **L3** in antiperiplanar (right) and periplanar (left) conformations at the DFT-optimized geometries (data are reported in Table S1)
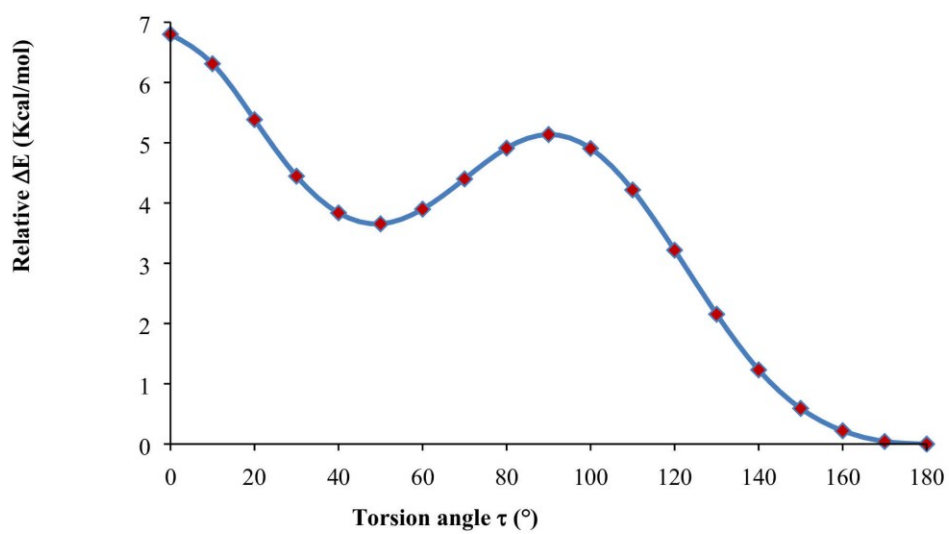
Fig. S14. Relative variation ΔE of the total electronic energy as a function of torsion angle τ (C7–C6–C5–N1 dihedral) calculated for **L3** at the DFT level.
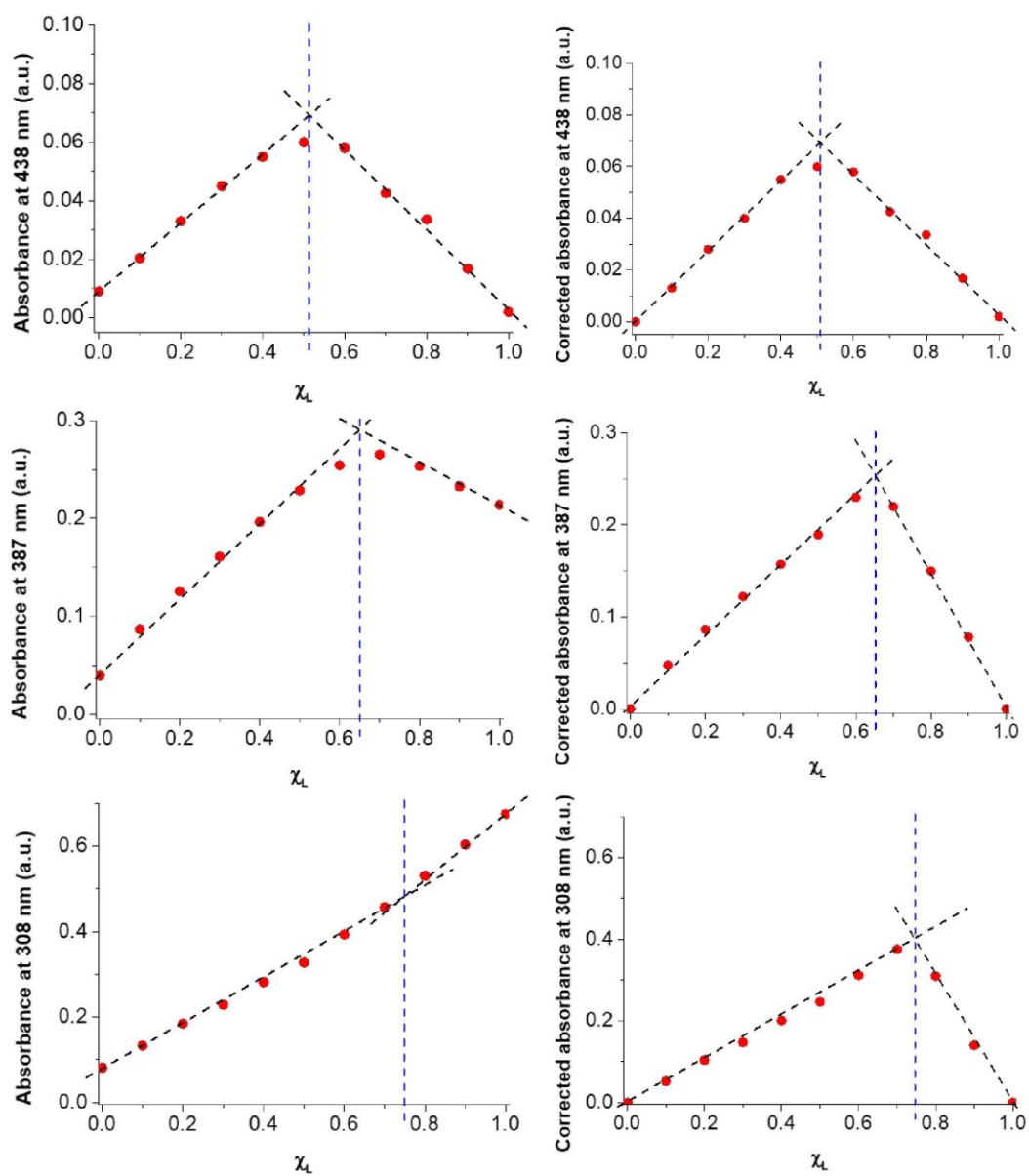
Figure S15. Job's plot for the system Fe(III)-L3. Uncorrected (left) and corrected (right) absorbances measured at different ligand:metal molar ratio at 438, 387 and 308 nm (concentration of Fe(III) = L = $5.27 \cdot 10^{-5}$ M, 0.01M NaClO$_4$, T 25°C, optic path length 1 cm).
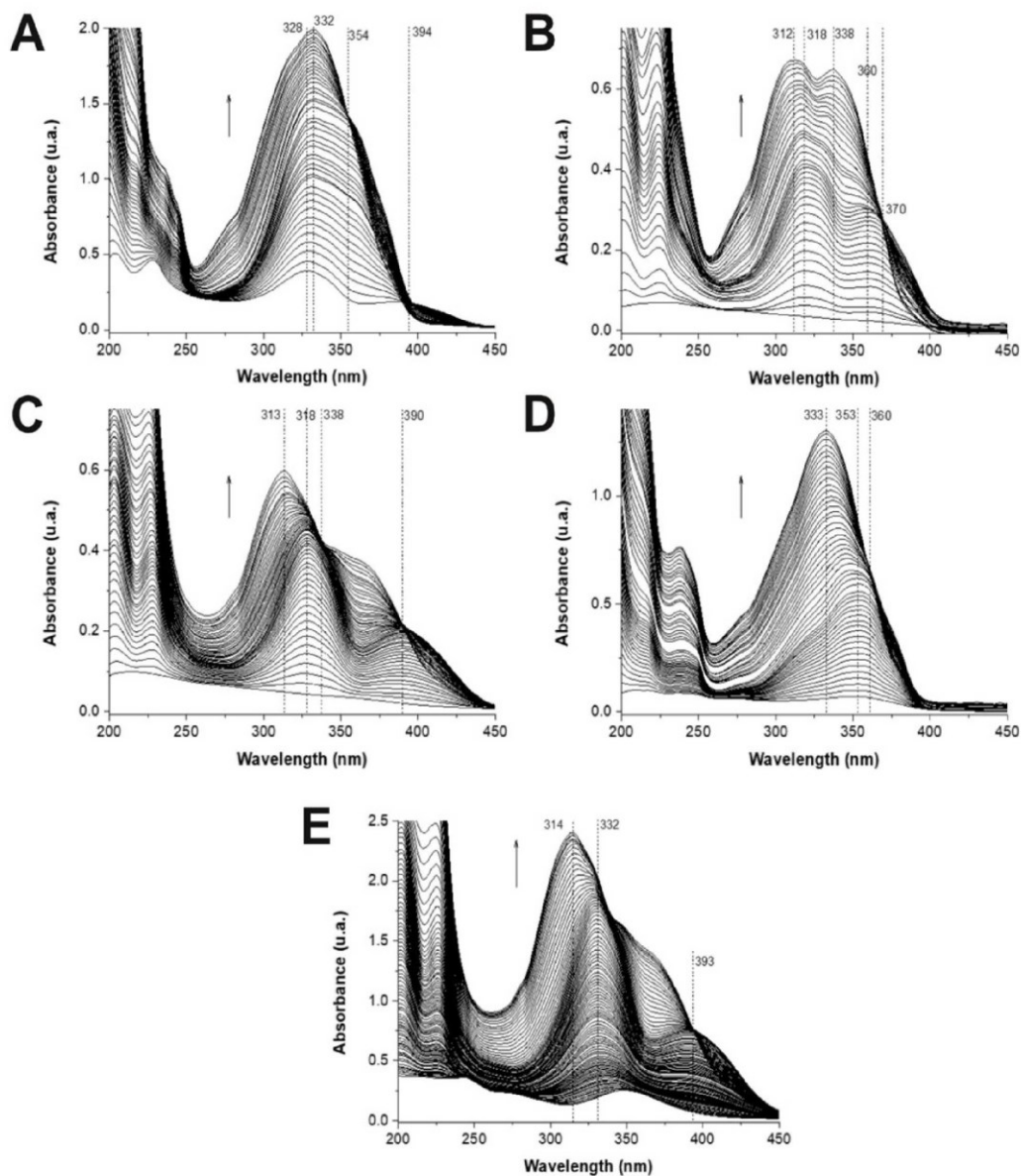
Figure S16. Selected spectra collected during the spectrophotometric titration of Fe(III) with **L1** (**A**) (Fe(III) $8.4 \cdot 10^{-5}$ mmoles, L $4.2 \cdot 10^{-5}$ M), **L2** (**B**) (Fe(III) $4.6 \cdot 10^{-5}$ mmoles, L $4.5 \cdot 10^{-5}$ M), **L3** (**C**) (Fe(III) $4.6 \cdot 10^{-5}$ mmoles, L $4.3 \cdot 10^{-5}$ M), **L4** (**D**) (Fe(III) $4.6 \cdot 10^{-5}$ mmoles, L $4.5 \cdot 10^{-5}$ M), **L5** (**E**) (Fe(III) $5.7 \cdot 10^{-5}$ mmoles, L $4.6 \cdot 10^{-5}$ M); NaClO$_4$ 0.05 M ionic strength buffer, 1 cm optical path length, 25 °C, CH$_3$CN solution.
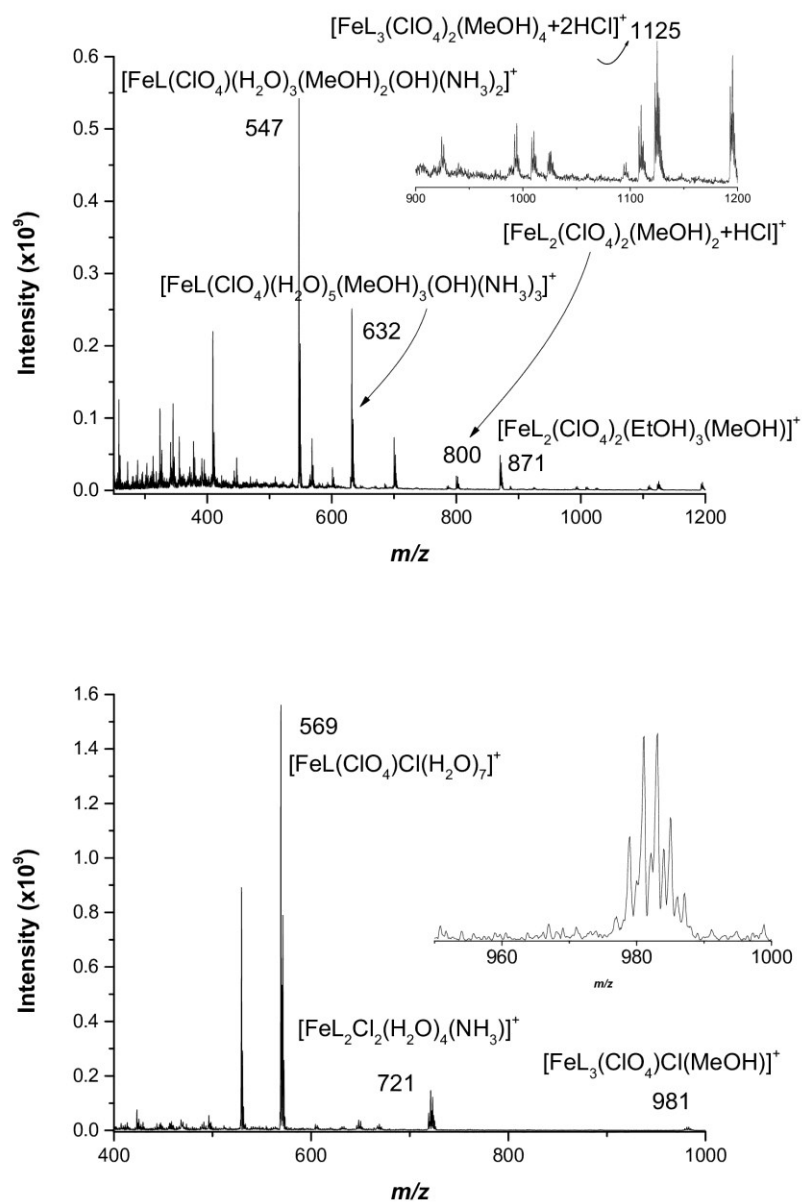
Figure S17. ESI mass spectra of solution containing Fe(III) and L1 (up) or L3 (down) in 1:3 metal:ligand molar ratio. Several adducts with solvent were evidenced. The stoichiometry was proposed on the basis of the fitting of the isotopic pattern and on MS-MS experiments (Fe(III) 1mM, H_2O:MeOH:EtOH 50:40:10).
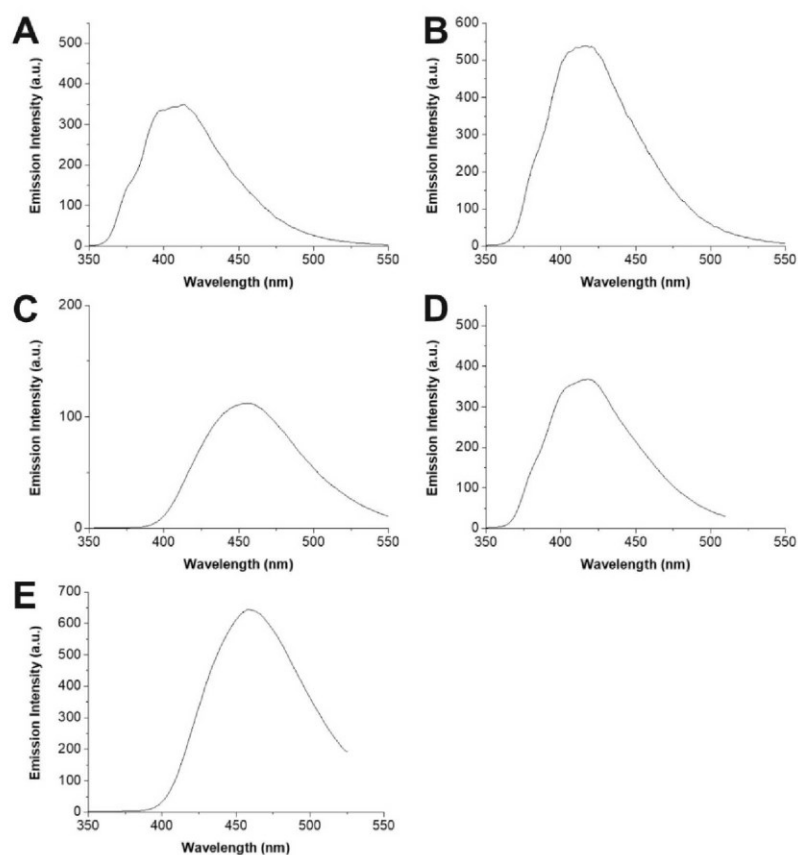
Figure S18. Fluorescence emission spectra of L1-L5 in CH_3CN solution (concentration $6.7 \cdot 10^{-5}$ mmol, quinine sulphate as reference, 25°C), (**A**) **L1** λ_{exc} 309 nm, slits 2.5 × 2.5 nm, PMT 600V, Φ 0.0820; (**B**) **L2** λ_{exc} 301 nm, slits 5.0 × 5.0 nm , PMT 600V, Φ 0.0322; (**C**) **L3** λ_{exc} 310 nm, slits 2.5 × 5.0 nm , PMT 600V, Φ 0.0310; (**D**) **L4** λ_{exc} 261 nm, slits 5.0 × 2.5 nm , PMT 600V, Φ 0.342; (**E**) **L5** λ_{exc} 267 nm, slits 5.0 × 5.0 nm , PMT 650 V, Φ 0.0266.

A

B

C

D

52

Figure S19. Selected spectra collected during the spectrophotometric titration of Ga(III) with **L3** **(A)** (Ga(III) $5.2 \cdot 10^{-5}$ mmoles, L $6.7 \cdot 10^{-5}$ M), Au(III) with **L3 (B)** (Au(III) $5.2 \cdot 10^{-5}$ mmoles, L $6.7 \cdot 10^{-5}$ M) and Y(III) with **L3 (C)** (Y(III) $5.3 \cdot 10^{-5}$ mmoles, L $6.7 \cdot 10^{-5}$ M) ; NaClO$_4$ 0.05 M ionic strength buffer, 1 cm optical path length, 25 °C, CH$_3$CN solution. In the left, solutions containing ligand and metal at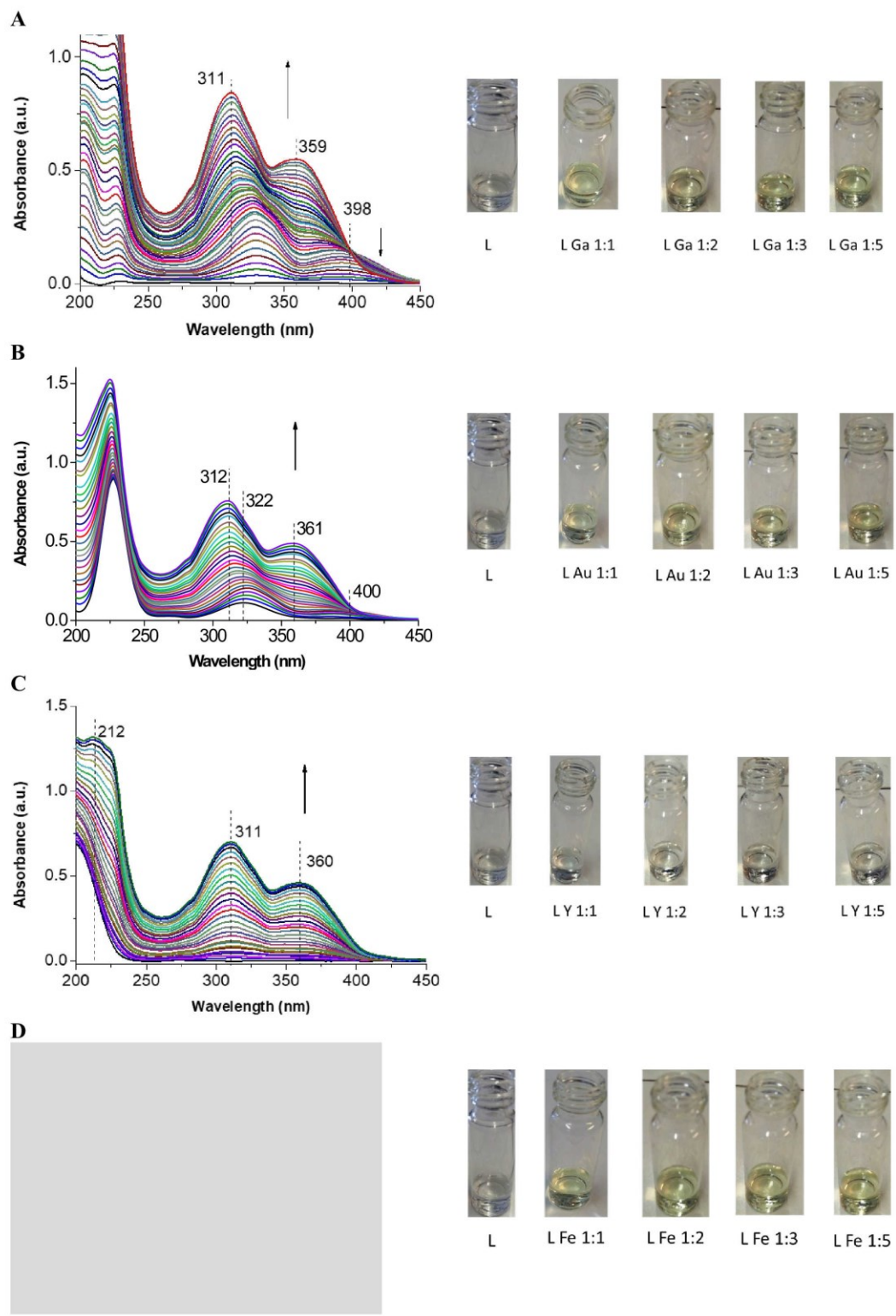 different molar ratios are shown to evidence the colorimetric response of the sensor. In **D** the spectrophotometrical titration of Fe(III) with **L1** is recalled for comparison.

Ga(III)-L3: by adding increasing amount of the ligand, the progressive formation of a band centred at 311 cm and a shoulder at 359 nm was observed. In addition, an isosbestic point at 398 nm was evidenced.

Au(III)-L3: the absorption maxima of Au(III) at 322 nm was gradually shifted at 312 nm by ligand addition. The presence of a shoulder at 361 nm and an isosbestic point at 400 nm were also put into evidence.

Y(III)-L3: solvated cationic core of the metal ion was progressively altered during ligand addition, as evidenced by absorption maxima shift from 200 nm to 212 nm, along with the formation of a band at 311 nm and a shoulder at 360 nm.
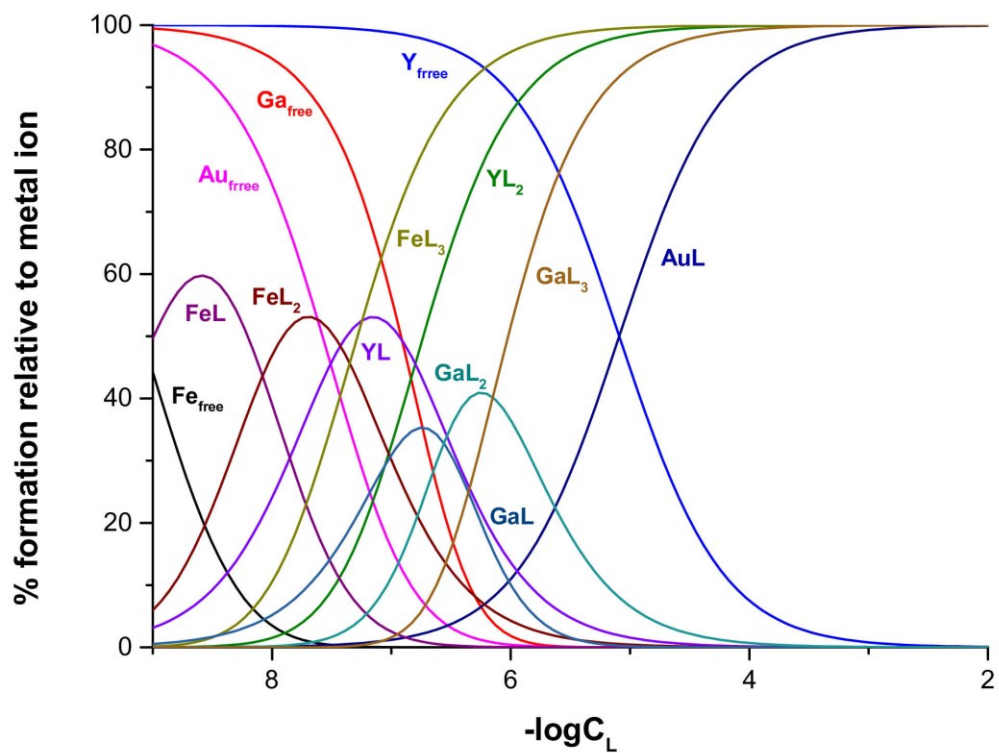
Figure S20. Calculated distribution curves for the **L3**-Fe(III)-Ga(III)-Au(III)-Y(III) system as a function of the minus logarithm of the **L3** concentration when Fe(III) is $1 \cdot 10^{-6}$ M and the other metal ions are $1 \cdot 10^{-5}$ M (L is **L3**)
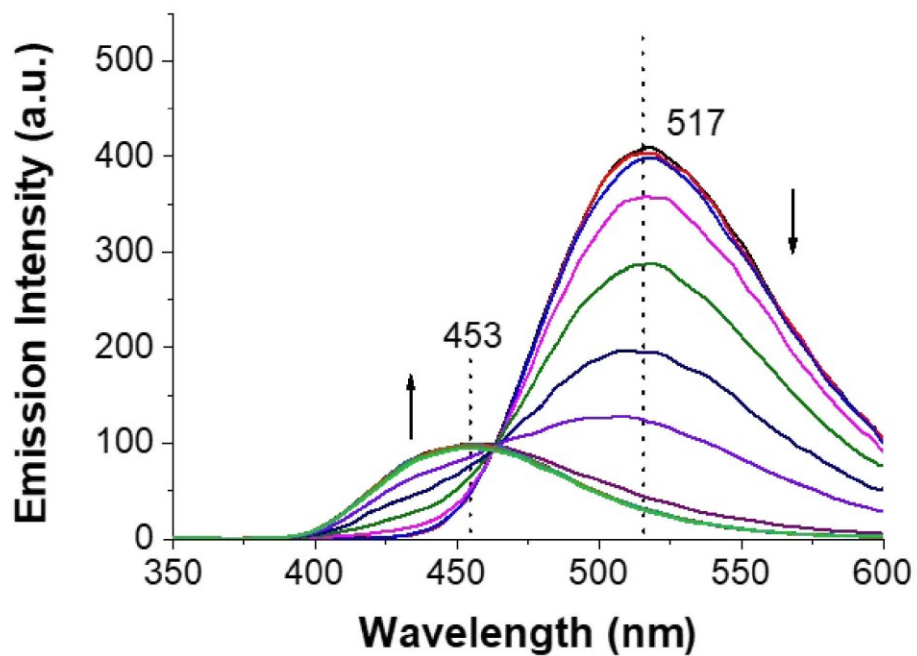
Figure S21 Selected emission spectra collected during the titration of a CH_3CN solution containing L3 ($6.7 \cdot 10^{-5}$ mmol) and Fe(III) in 1:1 molar ratio with EDTA ($2.48 \cdot 10^{-3}$ M), T 25 °C, 1 cm optical path length, λ_{exc} 310 nm, slits 2.5 × 5.0 nm , PMT 600V.
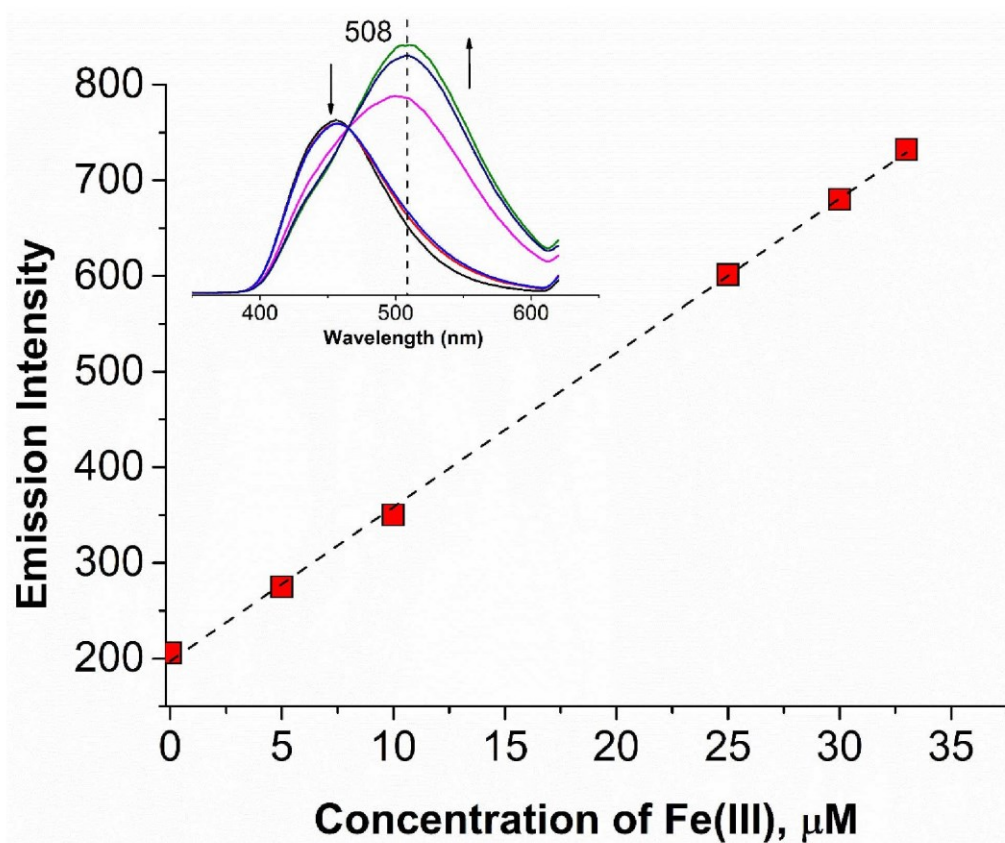
Figure S22. Linear response between emission intensity measured at 508 nm and the analytical Fe(III) concentration (**L3** concentration 35 µM, 1:1 H_2O: CH_3CN solution, T 25 °C, 1 cm optical path length, λ_{exc} 310 nm, slits 2.5 × 5.0 nm, PMT 600V, slits 2.5 x 5.0 nm). Y_{508nm} = 15.1(1)X + 203(2), R^2 = 0.9999. In the onset, the emission of **L3** and **L3** with Fe (III) in different molar ratios are reported to show the positions of the maxima.

Table S1. Selected optimized bond distances (Å) and angles (°) for the antiperiplanar and periplanar conformations of **L3** in acetonitrile (IEF-PCM SCRF model), and corresponding structural data for **L3**. Atom labelling scheme as in Figure S13.

		L3	
	Structural parameters	Optimized geometry	
		Antiperiplanar	Periplanar
C8-O2	1.382	1.352	1.348
O2-C7	1.368	1.368	1.379
C7-O1	1.201	1.209	1.201
C7-C6	1.483	1.469	1.480
C6-C5	1.474	1.487	1.490
C5-N1	1.331	1.342	1.337
N1-C1	1.330	1.325	1.329
C12-O3	1.369	1.345	1.346
C13-O3	/	/	/
O3-C15	1.423	1.407	1.407
C8-O2-C7	123.29	124.76	125.40
O2-C7-C6	117.09	116.38	115.87
O2-C7-O1	116.64	116.23	115.62
C7-C6-C5	119.79	121.69	120.82
C6-C5-N1	114.51	115.29	118.55
C5-N1-C1	117.97	119.46	119.58
C12-O3-C15	116.78	118.73	118.73
C13-O3-C15	/	/	/
C7-C6-C5-N1	150.82	180.00	0.00
C8-O2-C7-O1	178.57	180.00	180.00
C11-C12-O3-C15	0.56	0.00	0.00
C14-C13-O3-C15	/	/	/

Table S2. Selected optimized bond distances (Å) and angles (°) for the low spin (LS) and high spin (HS) configurations of $[Fe(\textbf{L3})_3]^{3+}$ in acetonitrile (IEF-PCM SCRF model). Atom labelling scheme as in Figure S13.

	$[Fe(\textbf{L3})_3]^{3+}$	
	LS	HS
Fe-N1	1.994	2.133
Fe-O1	1.901	1.976
Fe-O2	1.921	2.002
Fe-N2	1.988	2.152
Fe-O3	1.902	1.992
Fe-N3	1.976	2.139
N1-Fe-O1	89.05	84.75
N1-Fe-O2	85.09	87.22
N1-Fe-N2	173.71	168.75
N1-Fe-O3	92.92	95.65
N1-Fe-N3	92.06	95.69
O1-Fe-O2	90.51	93.60
O1-Fe-N2	87.75	89.41
O1-Fe-O3	177.33	178.42
O1-Fe-N3	92.03	93.97
O2-Fe-N2	89.52	83.54
O2-Fe-O3	87.85	89.94
O2-Fe-N3	176.15	172.10
N2-Fe-O3	90.12	90.44
N2-Fe-N3	93.47	94.30
O3-Fe-N3	92.06	84.78
Fe-O1-C3	121.43	124.07
Fe-O2-C6	120.26	122.63
Fe-O3-C9	122.00	126.32
N1-C1-C2-C3	24.24	26.56
N2-C4-C5-C6	28.27	30.37
N3-C7-C8-C9	27.07	28.19
Fe-O1-C3-O4	145.25	141.06
Fe-O2-C6-O5	146.06	138.43
Fe-O3-C9-O6	146.94	143.41

Table S3. Selected optimized bond distances (Å) and angles (°) for the low spin (LS) and high spin (HS) configurations of $[Fe(\mathbf{L3})_2(H_2O)_2]^{3+}$ in acetonitrile (IEF-PCM SCRF model). Atom labelling scheme as in Figure S13.

	$[Fe(\mathbf{L3})_2(H_2O)_2]^{3+}$	
	LS	HS
Fe-N1	1.991	2.133
Fe-O1	1.882	1.949
Fe-O2	1.871	1.953
Fe-N2	1.982	2.131
Fe-O3	1.967	2.065
Fe-O4	1.956	2.065
N1-Fe-O1	88.63	84.96
N1-Fe-O2	86.63	88.77
N1-Fe-N2	176.53	175.16
N1-Fe-O3	93.98	93.37
N1-Fe-O4	89.33	90.04
O1-Fe-O2	92.14	93.70
O1-Fe-N2	89.01	92.64
O1-Fe-O3	175.49	176.78
O1-Fe-O4	87.09	89.18
O2-Fe-N2	90.91	86.18
O2-Fe-O3	91.68	89.04
O2-Fe-O4	175.90	177.08
N2-Fe-O3	88.53	89.22
N2-Fe-O4	93.10	94.14
O3-Fe-O4	89.27	88.06
Fe-O1-C3	121.66	123.26
Fe-O2-C6	123.49	126.46
N1-C1-C2-C3	24.62	27.47
N2-C4-C5-C6	24.72	28.69
Fe-O1-C3-O5	146.13	140.63
Fe-O2-C6-O6	150.92	145.61

Table S5. Selected Mulliken and Natural Charges Q ($|e|$) Calculated on the low spin (LS) and high spin (HS) configurations of $[Fe(\mathbf{L3})_3]^{3+}$ in acetonitrile (IEF-PCM SCRF model). Atom labelling scheme as in Figure S13.

| | Mulliken | | NBO | |
| | $[Fe(\mathbf{L3})_3]^{3+}$ | | $[Fe(\mathbf{L3})_3]^{3+}$ | |
	LS	HS	LS	HS
Fe	0.642	0.981	0.826	1.470
O1	-0.344	-0.388	-0.592	-0.682
O2	-0.331	-0.365	-0.590	-0.670
O3	-0.344	-0.383	-0.592	-0.684
N1	-0.292	-0.353	-0.452	-0.562
N2	-0.309	-0.344	-0.464	-0.564
N3	-0.323	-0.373	-0.470	-0.684
O4	-0.195	-0.194	-0.451	-0.452
O5	-0.198	-0.197	-0.454	-0.455
O6	-0.196	-0.197	-0.449	-0.453

Table S6. Selected Mulliken and Natural Charges Q ($|e|$) Calculated on the low spin (LS) and high spin (HS) configurations of $[Fe(\mathbf{L3})_2(H_2O)_2]^{3+}$ in acetonitrile (IEF-PCM SCRF model). Atom labelling scheme as in Figure S13.

| | Mulliken | | NBO | |
| | $[Fe(\mathbf{L3})_2(H_2O)_2]^{3+}$ | | $[Fe(\mathbf{L3})_2(H_2O)_2]^{3+}$ | |
	LS	HS	LS	HS
Fe	0.737	1.061	0.913	1.507
O1	-0.332	-0.378	-0.575	-0.667
O2	-0.338	-0.377	-0.58	-0.671
O3	-0.234	-0.277	-0.843	-0.919
O4	-0.224	-0.268	-0.836	-0.914
N1	-0.3	-0.352	-0.457	-0.564
N2	-0.321	-0.366	-0.464	-0.57
O5	-0.191	-0.189	-0.448	-0.448
O6	-0.187	-0.189	-0.444	-0.447

conditions	point 1
total Fe	1.000E-05
total Au	1.000E-05
total Y	1.000E-05
total Ga	1.000E-05
total L	1.000E-05
p(Fe)	(set pX)
p(Au)	(set pX)
p(Y)	(set pX)
p(Ga)	(set pX)
p(L)	(set pX)

results	concn./M
free Fe	2.41057E-06
free Au	9.99730E-06
free Y	9.32764E-06
free Ga	1.00000E-05
free L	2.19710E-09
AuL	2.70229E-09
FeL	5.94251E-06
FeL$_2$	1.56971E-06
FeL$_3$	7.72090E-08
YL	6.63164E-07
YL$_2$	9.19328E-09
YGaL	1.12621E-12
YGaL$_2$	8.98401E-15
YGaL$_3$	2.78818E-17

G

conditions	point 1
total Fe	1.000E-06
total Au	1.000E-06
total Y	1.000E-06
total Ga	1.000E-06
total L	1.000E-05
p(Fe)	(set pX)
p(Au)	(set pX)
p(Y)	(set pX)
p(Ga)	(set pX)
p(L)	(set pX)

results	concn./M
free Fe	3.20511E-15
free Au	6.34739E-07
free Y	2.16481E-10
free Ga	9.99999E-07
free L	4.67743E-06
AuL	3.65261E-07
FeL	1.68210E-11
FeL$_2$	9.45926E-09
FeL$_3$	9.90524E-07
YL	3.27662E-08
YL$_2$	9.67017E-07
YGaL	5.56449E-15
YGaL$_2$	9.45003E-14
YGaL$_3$	6.24369E-13

H

61

Part 2. Bioactive ligands and metal complexes

Introduction

Cancer: definition, features, and incidence

Cancer (neoplasia) comprises a large group of diseases that share some common traits, such as a high cell division rate and the inhibition of cell death (apoptosis), which results in the constitution of abnormal masses, commonly named as tumours (neoplasms). These tissue masses could persist in the region where they have developed of invade other compartments of human body through a process commonly known as metastasis.[1]

The formation of tumoral masses generally arises from repeated mutations at DNA level, which can originate from inherited genetical factors or being caused by external ones, such as the prolonged exposition to pollutants or other toxic substances (mutagens). Moreover, it is known that certain viruses can be involved in the pathogenesis of at least 6 types of cancers: for instance, exposition to Human papillomavirus can lead to cervix cancer.[2,3]

All those genes that are involved in the transcription of proteins that regulate the cell division or differentiation are called proto-oncogenes. When the same genes are mutated, they then become oncogenes. When DNA damage occurs in a healthy cell, its division is purposely interrupted to repair it prior to next cell division. If the repairing system fails at its scope, then the cell commits suicide undergoing to apoptosis. In a cell having a highly damaged DNA, the repairing system becomes less efficient, and the defects are transferred to the next generation. A cell having a high degree of DNA damage have more chances to become cancerous.[2]

The casualty of these mutations results in a high degree of heterogeneity among cancer cells, even when deriving from the same tissue or organ. That's the reason why, from the same tissue/organ, there are many cancer cell lines having their own morphological and molecular profile.

At present days, cancer still represents one of the leading causes of death in our society: according to the GLOBOCAN statistics of the International Agency for Research of Cancer (IARC), 19.3 million new cases and 10 million deaths were estimated in 2020. Breast cancer has become the most diagnosed (11.7 % new cases last year), thus surpassing lung cancer which became the second one (11.4 %) while still remaining the main cause of cancer death (18% deaths in 2020).[4]

Cancer treatments include many methods, such as surgical removal, chemotherapy, radiotherapy, and immunotherapy, that are commonly chosen considering the type, location, severity of the cancer, but also and patience's health. These treatments are often combined: for instance, surgical removal coupled by chemotherapy represents one of the first treatments for many cancers, such as ovarian ones.

Anticancer chemotherapy strategies

Anticancer chemotherapy (commonly abbreviated as chemotherapy) consists of the use of one or more anticancer drugs with the aim of curing the patient or alleviating the symptoms. Chemotherapeutic treatments are often administered after surgical removal of the primary tumoral mass to reduce the risks of relapse. Anticancer chemotherapeutics are commonly designed as cytotoxic molecules that can interfere at specific targets, such as DNA, key proteins, or enzymes.[1]

The simultaneous use of drugs having different molecular targets (combinatorial therapy) is often preferred since it usually results in higher efficacy with lower side effects and drug-resistance phenomena. However, the identification of specific targets for cancerous cells is quite challenging since cancer cells derive from healthy ones. That's the reason why most anticancer agents will target both types of cells, especially those having high proliferation rates since they tend to accumulate nutrients and drugs more rapidly.[2]

Many cancer cells tend to grow rapidly, but unfortunately there are also healthy one that does the same, such as bone narrow cells. Bone marrow toxicity is a common side effect encountered after chemotherapeutic treatments, which results in a weakening of the immune and a higher probability to get secondary infections.[2,5]

For these reasons, chemotherapeutic treatments are commonly scheduled as multiple cycles spaced out by rest periods to allow the patient to recover. In addition, each drug (or drug combinations) dose never reaches the ideal value, determined from *in-vitro* or *in-vivo* studies.

Anticancer chemotherapeutics can be classified according to many features, such as the chemical structure, the molecular target (e.g., DNA, enzymes) and the mechanism of interaction towards it (DNA intercalators, DNA alkylators, DNA topoisomerase inhibitors, etc.), their selectivity towards certain cell cycle phases (specific and non-specific cell cycle drugs).

Cisplatin (*cis*-diamminedichloroplatinum(II)) is the first example of anticancer chemotherapeutic coordination compound, whose biological properties were fortuitously discovered by *Rosemberg et al.* in 1965.[6] The introduction of cisplatin in the clinical practice

(1978) represented a milestone in cancer treatment, thanks to its broad spectrum of applications and high anticancer potency. Cisplatin is administered intravenously, due to its low biological stability, while its distribution through the bloodstream is guaranteed by thiol-containing plasma proteins.[7,8] Cellular uptake of cisplatin occurs via passive diffusion or thanks to active transporters, such as the human copper transport proteins (hctr1).[9] In cytoplasm cisplatin undergoes to substitution of one of the chloride ligands with a water molecule, forming the species $[Pt(Cl)(OH_2)(NH_3)_2]^+$, which metalates DNA (by attacking at N7 position of adenine and guanine or N3 of cytosine) forming the monofunctional adduct $[Pt(Cl)(DNA)(NH_3)_2]^+$. This intermediate can form the bifunctional adducts $[Pt(DNA)(NH_3)_2]^+$ by direct substitution of the second chloride ligand or through hydrolysis to afford the species $[Pt(OH_2)(DNA)(NH_3)_2]^+$. Cisplatin can form bifunctional adducts with DNA in several ways, such as by 1,2- intrastrand with two adjacent guanines (1,2-d(GpG)), 1,2-intrastrand with a guanine and an adjacent adenine (1,2-d(ApG)), 1,3-intrastrand adducts with two non-adjacent guanines, and by interstrand adducts (**Figure 1**). These species are not recognized by the DNA repairing systems, thus forcing the cells affected to undergo apoptosis.[10–12]
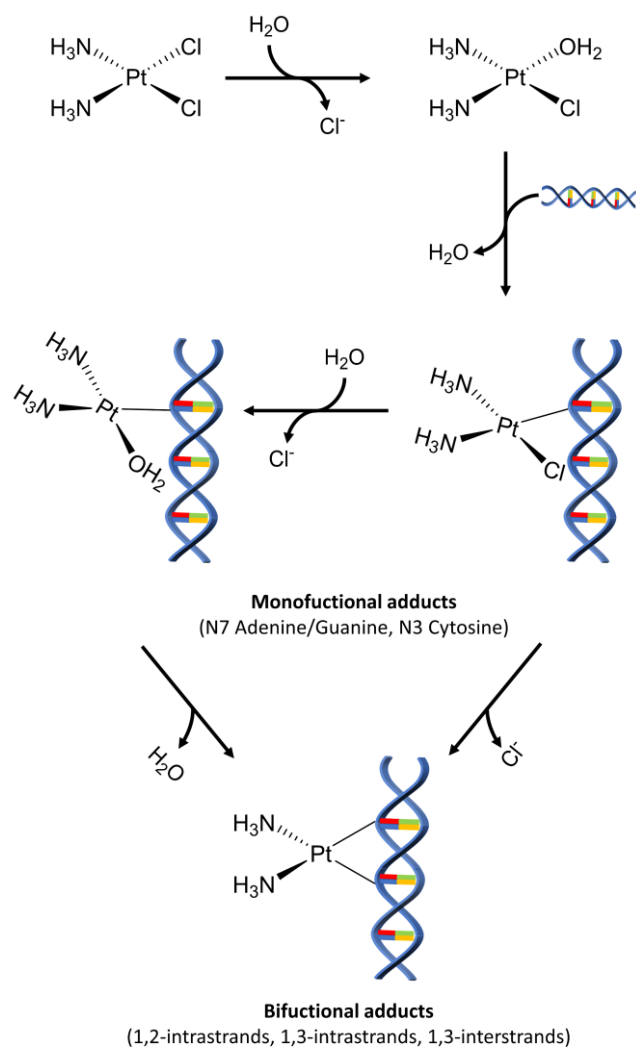
Figure 1. Molecular mechanism of cisplatin. Adapted from Ref.[1]

Despite its advantages, cisplatin shows low selectivity towards healthy cells. That's why patients treated with this drug often experience side effects, such as nausea and vomiting as the less acute, and nephrotoxicity among the most severe. Moreover, cisplatin efficacy is often decreased by the development of drug-resistant cancer cells.[13]

In the design of novel anticancer coordination compounds, a commonly exploited approach is to substitute Pt(II) with endogenous metal ions. The rationale behind this choice is that complexes of such metal ions could target cancer cell by interfering at alternative molecular

targets and pathways compared to cisplatin. In addition, the systemic toxicity of these compounds could be alleviated thanks to the molecular machinery in charge of the transport and homeostasis of endogenous metal ions in biological systems.[1]

Copper constitutes a typical example of endogenous metal ions that has been studied under this perspective, since its presence as cofactor in many biochemically relevant enzymes (e.g., cytochrome-c oxidase, superoxide dismutase, tyrosinase, etc.). After being reduced as Cu(I) by cellular metalloreductases and endogenous ascorbate, Copper is absorbed in the stomach and small intestine, while its transport through the bloodstream is guaranteed by albumin, ceruloplasmin and transcuprein.[14,15] In analogy with cisplatin, cellular uptake mainly takes place through by the hCtr1 active transporter.[11] Cellular Copper homeostasis through its transporters and molecular chaperones (e.g., GSH, ATOX-1, COX17 and CCS1), since an excess concentration of this essential metal ion could be dangerous for human organisms.

 It is known that the toxicity of free Copper derives from its involvement in the production of Reactive Oxygen Species (ROS), which is related to the accessibility of both Cu(II) and Cu(I) redox states under biological conditions.[16] Free Copper in excess is associated with the pathogenesis of Wilson disease, but it is also believed to enhance tumour progression, metastasis, and angiogenesis.[17,18] Moreover, high concentrations of Copper were evidenced in serum and tissues of various human tumours.[19]

Based on these evidences, two different approaches are usually followed when novel anticancer Copper-based drugs are developed: (*i*) sequestration of free Copper ions in excess through the use of selective metal chelators; (*ii*) design and synthesis of Copper complexes

that induce the apoptosis through metal ion accumulation and induction of ROS production.[20]

The second tactic has been extensively followed in the last decades, since the discovery of the artificial nuclease activity of the $[Cu(phen)_2]^+$ complex.[21] The molecular mechanisms of many of these compounds haven't been completely revealed yet. However, based on the information available at present moment, we can conclude that is multi factored a (e.g., proteasome, topo-isomerase inhibition, induction of the apoptosis, etc.) and not necessarily restricted to DNA interaction.[1,22–24] Despite the huge number of Copper complexes screened *in-vitro* as for anticancer activity, only a few number underwent to clinical trials. For instance, compounds Cas-II-gly and Cas-III-ia (**Figure 2**), belonging to the family of the Casiopeinas[®25] (molecular formula $[Cu(N-N)(A-A)](NO_3)$, where N-N is a neutral diimine ligand and A-A an essential amino acid) have been recently selected as candidates for Phase I studies.[26,27]
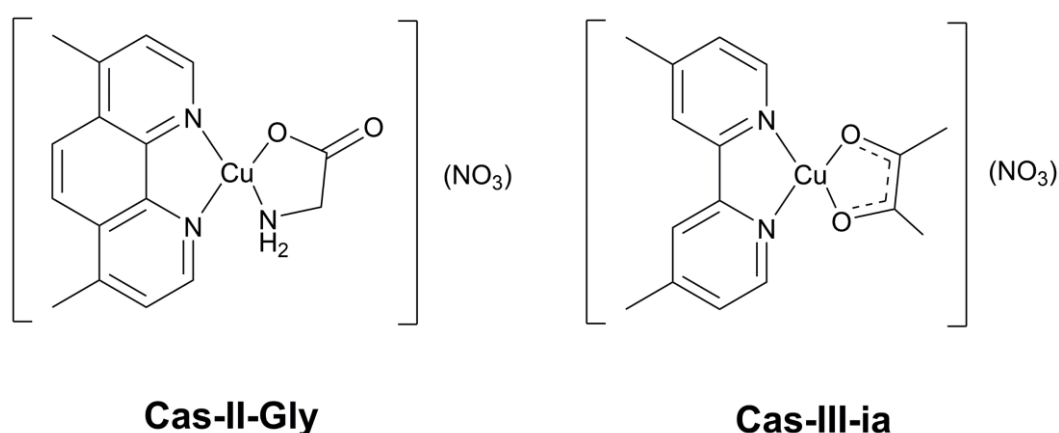

Cas-II-Gly   **Cas-III-ia**

Figure 2. Structures of Cas-II-Gly (left) and Cas-III-ia (right).

References

1   F. Trudu, F. Amato, P. Vaňhara, T. Pivetta, E. M. Peña-Méndez and J. Havel, *J. Appl.*

Biomed., 2015, **13**, 79–103.

2   P. Graham, *An Introduction to Medicinal Chemistry*, Oxford University Press, 5th edn., 2013.

3   X. Wang, X. Huang and Y. Zhang, *Front. Microbiol.*, , DOI:10.3389/fmicb.2018.02896.

4   H. Sung, J. Ferlay, R. L. Siegel, M. Laversanne, I. Soerjomataram, A. Jemal and F. Bray, *CA. Cancer J. Clin.*, 2021, **71**, 209–249.

5   J. N. Barreto, K. B. McCullough, L. L. Ice and J. A. Smith, *J. Pharm. Pract.*, 2014, **27**, 440–446.

6   B. Rosemberg, L. Vancamp, J. E. Trosko and V. H. Mansour, *Nature*, 1969, **222**, 385–386.

7   A. V. Rudnev, S. S. Aleksenko, O. Semenova, C. G. Hartinger, A. R. Timerbaev and B. K. Keppler, *J. Sep. Sci.*, 2005, **28**, 121–127.

8   M. Sooriyaarachchi, A. Narendran and J. Gailer, *Metallomics*, 2011, **3**, 49–55.

9   S. Ishida, J. Lee, D. J. Thiele and I. Herskowitz, *Proc. Natl. Acad. Sci.*, 2002, **99**, 14298–14302.

10   R. A. Alderden, M. D. Hall and T. W. Hambley, *J. Chem. Educ.*, 2006, **83**, 728.

11   S. Dilruba and G. V. Kalayda, *Cancer Chemother. Pharmacol.*, 2016, **77**, 1103–1124.

12   S. Dasari and P. Bernard Tchounwou, *Eur. J. Pharmacol.*, 2014, **740**, 364–378.

13   R. Oun, Y. E. Moussa and N. J. Wheate, *Dalt. Trans.*, 2018, **47**, 6645–6653.

14   M. Bost, S. Houdart, M. Oberli, E. Kalonji, J. F. Huneau and I. Margaritis, *J. Trace Elem. Med. Biol.*, 2016, **35**, 107–115.

15   P. V. E. Van Den Berghe and L. W. J. Klomp, *Nutr. Rev.*, 2009, **67**, 658–672.

16   K. Jomova, S. Baros and M. Valko, *Transit. Met. Chem.*, 2012, **37**, 127–134.

17   K. G. Daniel, H. R. Harbach, W. C. Guida and Q. P. Dou, *Front. Biosci.*, 2004, **9**, 2652.

18   A. De Luca, A. Barile, M. Arciello and L. Rossi, *J. Trace Elem. Med. Biol.*, 2019, **55**, 204–213.

19   M. Díez, M. Arroyo, F. J. Cerdàn, M. Muñoz, M. A. Martin and J. L. Balibrea, *Oncology*, 1989, **46**, 230–234.

20   D. Denoyer, S. Masaldan, S. La Fontaine and M. A. Cater, *Metallomics*, 2015, **7**, 1459–1476.

21   D. S. Sigman, D. R. Graham, V. D. Aurora, A. M. Stern and D. Aurora, *J. Biol. Chem.*, 1979, **254**, 12269–12272.

22   C. Marzano, M. Pellei, F. Tisato and C. Santini, *Anticancer. Agents Med. Chem.*, 2009, **9**, 185–211.

23   C. Santini, M. Pellei, V. Gandin, M. Porchia, F. Tisato and C. Marzano, *Chem. Rev.*, 2014, **114**, 815–862.

24   C. Molinaro, A. Martoriati, L. Pelinski and K. Cailliau, *Cancers (Basel).*, 2020, **12**, 1–26.

25   Eur. Pat. Appl., EP0434445, A2, 1991, Eur. Pat. Appl., EP0434445, 10 pages.

26   2nd March 2017; New Cancer Drug Called Casiopeínas Tested at Phase I Clinical Trials, Source: Information Agency CONACYT -, http://www.salud.carlosslim.org/english2/new-cancer-drug-called-casiopeinas-tested-at-phase-i-clinical-trials/.

27   I. Correia, S. Borovic, I. Cavaco, C. P. Matos, S. Roy, H. M. Santos, L. Fernandes, J. L. Capelo, L. Ruiz-Azuara and J. C. Pessoa, *J. Inorg. Biochem.*, 2017, **175**, 284–297.

Aim of the Work

In the framework of the second research line of this PhD project ("*Bioactive ligands and metal complexes*"), I decided to study different classes of organic molecules and metal complexes with potential biological applications.

In particular, I designed a series of heteroleptic Cu(II)-phenanthroline complexes bearing different types of auxiliary ligands (imidazolidine-2-thiones, ER stress modulators, coumarin-based ligands) with the aim of finding novel potential anticancer metallodrugs that might overcome Pt(II)-based compounds in the future. For each compound, I studied the complex formation process on both solid and solution state and determined their structures my merging different spectroscopic and computational data. The anticancer activity *in-vitro* and the biochemical molecular mechanisms were also preliminary assessed.

I have also evaluated the possible biological mechanisms of action of Cu(II) phen-based complexes reported in the literature in the recent years, and I have prepared a review for the special issue "Coordination Chemistry in Cancer Therapy" of the journal Molecules.

Considering the involvement of oxidoreductases like lipoxygenase and tyrosinase in the pathogenesis of several disease (e.g., cancer, inflammatory and skin-related disorders), I focused my attention on the preparation of novel potential coumarin-based inhibitors of such enzymes.

In particular, I prepared a series of hydroxylated derivatives of 3-(pyridin-2-yl)-2-*H*-chromen-2-one and evaluated their antioxidant and soybean lipoxygenase inhibitory properties by combining different experimental and theoretical results. Considering the importance of the protonation state of a molecule in understanding the potential absorption

and biological properties, I evaluated the protonation constants and sequencies of the studied molecules by combining experimental (potentiometry and spectroscopy) with computational (DFT) data.

Finally, I'll show the preliminary results on the antioxidant and mushroom tyrosinase inhibitory activities of a panel of hydroxylated thiosemicarbazones of 3-acetylcoumarin that I've prepared and characterized.

Results and discussion

Article 2.

Mixed copper(II)–phenanthroline complexes induce cell death of ovarian cancer cells by evoking the unfolded protein response.

Mixed copper(II)−phenanthroline complexes induce cell death of ovarian cancer cells by evoking the unfolded protein response†

Lukáš Moráň,[a] Tiziana Pivetta,[b] Sebastiano Masuri,[b] Kateřina Vašíčková,[a] Franziska Walter,[c] Jochen Prehn,[c] Moustafa Elkalaf,[de] Jan Trnka,[de] Josef Havel[fg] and Petr Vaňhara[*ag]

There is an ongoing need for the development of new cancer therapeutics that combine high cytotoxic efficiency with low side effects, and also override resistance to the first-line chemotherapeutics. Copper(II)−phenanthroline complexes are promising compounds that were shown previously to induce an immediate cytotoxic response over a panel of tumor cell lines *in vitro*. The molecular mechanism, however, remained unresolved. In this work we performed a thorough study of the copper(II)−phenanthroline complexes containing different imidazolidine-2-thione ligands in ovarian cancer cells, and revealed that these complexes induce endoplasmic reticulum (ER) stress and subsequently cell death mediated by the unfolded protein response. Alleviation of the ER-stress by tauroursodeoxycholic acid (TUDCA) attenuated the cytotoxic effects. In summary, we have identified a novel, ER-dependent, molecular mechanism mediating cytotoxic effects of copper(II)−phenanthroline complexes.

Significance to metallomics

Mixed copper(II)–phenanthroline complexes represent a class of metal coordination compounds with promising anti-proliferative effects on various cancer cells. Here we revealed that copper(II)–phenanthroline complexes **C0–C3** containing imidazolidine-2-thione ligands specifically target the endoplasmic reticulum (ER) and evoke rapid cell death by eliciting the unfolded protein response (UPR) in ovarian cancer cells. Targeting ER homeostasis by copper(II)–phenanthroline complexes may represent an alternative strategy to current cytotoxic drugs.

Introduction

Ovarian cancer (OC) is one of the most lethal gyneco-oncological diseases[1,2] with rather limited therapeutic options in advanced stages. Cisplatin stays in the midpoint of the first line therapy of OC with a significant therapeutic response; however, the majority of patients finally develop resistance and relapse. Thus, there is a necessity of novel cytotoxic compounds that would complement a portfolio of available pharmacological solutions and offer molecular mechanisms of cytotoxicity different to those evoked by standard therapy, including cisplatin. Since the breakthrough discovery of cisplatin in 1965, numerous compounds were designed and synthesized in order to reduce unwanted side effects, enhance cytotoxicity and override acquired drug resistance of cancer cells. Among them, metal coordination compounds appeared as the most promising chemical entities inducing cell death,[3] also in drug-resistant cell lines.[4,5] There have been a variety of cytotoxic copper compounds complexed with different cores, including phenanthroline, synthesized so far, targeting mostly DNA and DNA-repair machinery.[6–9]

Mixed copper Cu(II)−phenanthroline complexes assigned **C1–C3** differing in imidazolidinethione ligand moiety (Fig. 1) were synthesized from the parent complex (**C0**) [Cu(phen)₂(OH₂)](ClO₄)₂ by T. Pivetta previously, and were shown to induce massive cell

[a] *Department of Histology and Embryology, Faculty of Medicine, Masaryk University, Kamenice 3, CZ-62500, Brno, Czech Republic.*
E-mail: pvanhara@med.muni.cz; Fax: +420 54949 1320; Tel: +420 54949 7780
[b] *Department of Chemical and Geological Sciences, University of Cagliari, Monserrato, CA, Italy*
[c] *Centre for Systems Medicine and Department of Physiology and Medical Physics, Royal College of Surgeons in Ireland, Dublin, Ireland*
[d] *Laboratory for Metabolism and Bioenergetics, Department of Biochemistry, Cell and Molecular Biology, Third Faculty of Medicine, Charles University, Prague, Czech Republic*
[e] *Centre for Research on Nutrition, Metabolism and Diabetes, Third Faculty of Medicine, Charles University, Prague, Czech Republic*
[f] *Department of Chemistry, Faculty of Science, Masaryk University, Brno, Czech Republic*
[g] *International Clinical Research Center, St. Anne's University Hospital, Brno, Czech Republic*
† Electronic supplementary information (ESI) available. See DOI: 10.1039/c9mt00055k

Abstract

In this study, the molecular mechanism of the mixed Cu(II) complexes **C0** (molecular formula: [Cu(phen)$_2$(OH$_2$)](ClO$_4$)$_2$, **Figure 3**) and **C1-3** (molecular formula: [Cu(phen)$_2$(L)](ClO$_4$)$_2$, where L are imidazolidine-2-thione and its N-alkylated derivatives, **Figure 3**) have been partially unveiled on ovarian (A-2780, SKOV-3) and kidney (HEK-293) cancer cell lines[1].
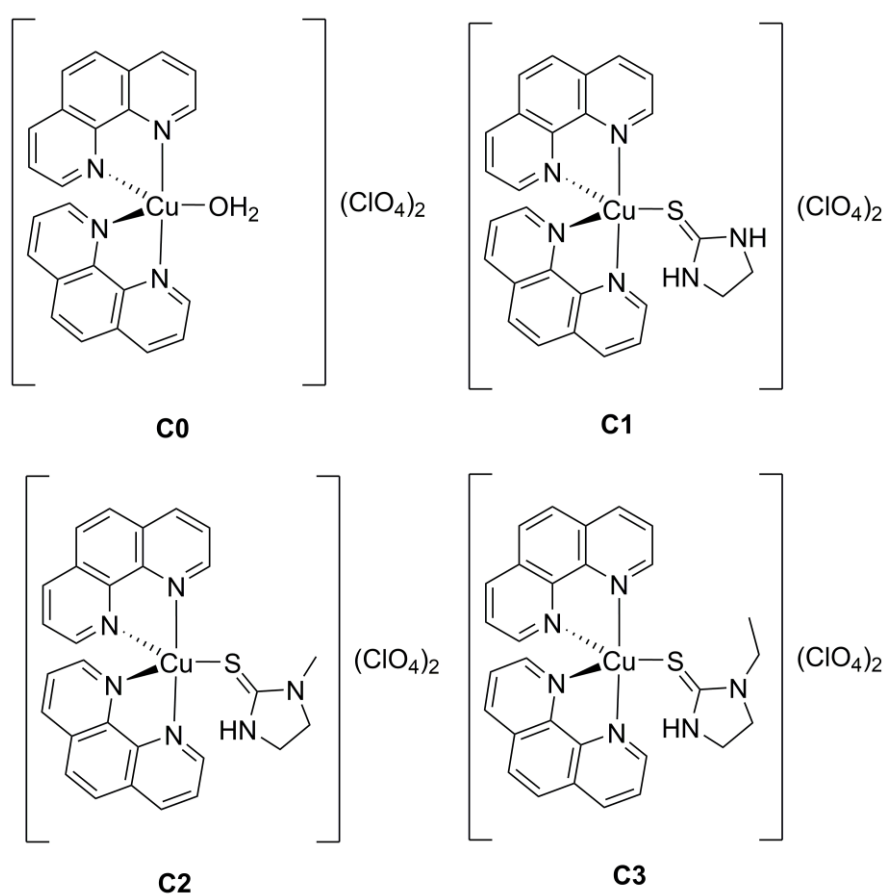
Figure 3. Molecular structures of **C0** and **C1-3** complexes

These compounds interfere at the Endoplasmic Reticulum (ER) level activating the pro-apoptotic branch of the Unfolded Protein Response (UPR). UPR is a coordinating adaptive program that is activated by cells that undergoes to a condition of ER stress due to the accumulation of incorrectly processed proteins in this organelle. The final cell response

depends on the specific pathways that are activated under UPR and can lead to adaptation or apoptosis, especially in a condition of prolonged and severe ER stress condition.

The studied compounds alter the cell morphology even at sublethal concentrations, interfering with the expressions of typical biomarkers of the UPR, such as BiP, CHOP, IRE1 and PERK, whose expression has been evaluated by means of microscopical and electrophoretic methods.

Interestingly, the activity of the reported molecules is partially reverted (**Figure 4**) when the studied cells are co-treated with the ER-modulator Taursodeoxycholic Acid (**TUDCA**).[*]
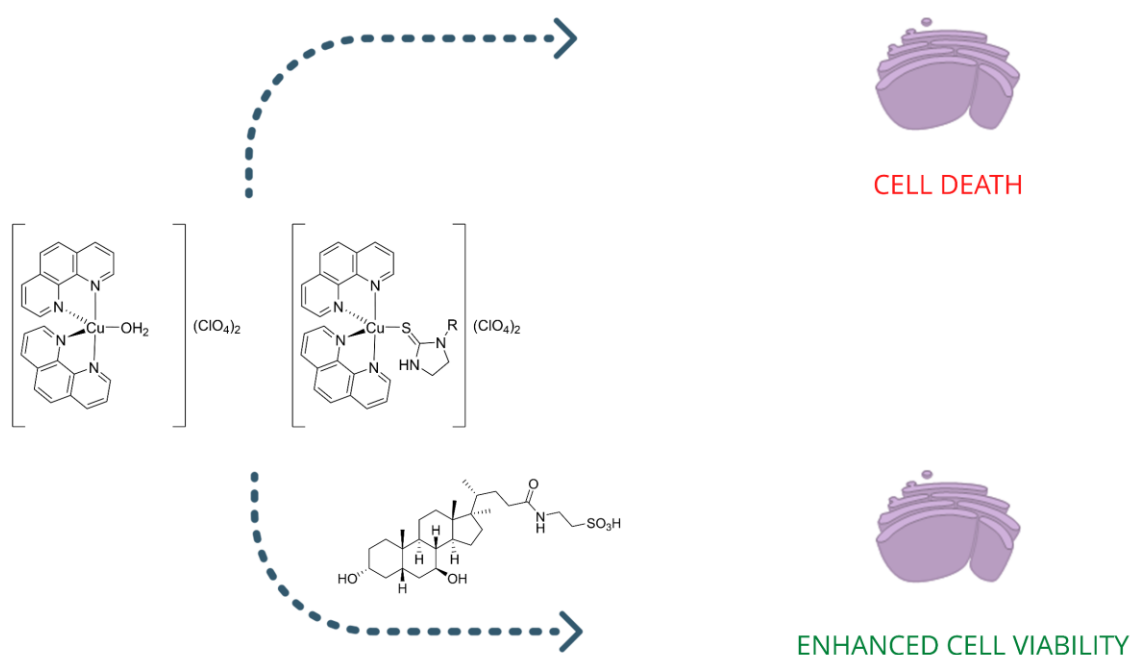
Figure 4. Schematic representation of the cytoprotective effect of TUDCA in co-treatment with the studied compounds

These results could provide a better understanding of the molecular mechanism of Cu(II) phenanthroline-based complexes and might constitute a novel strategy to currently approved anticancer metallodrugs.

Mixed copper(II)–phenanthroline complexes induce cell death of ovarian cancer cells by evoking the unfolded protein response.

Lukáš Moráň[1], Tiziana Pivetta[2], Sebastiano Masuri[2], Kateřina Vašíčková[1], Franziska Walter[3], Jochen Prehn[3], Moustafa Elkalaf[4,5], Jan Trnka[4,5], Josef Havel[6,7], Petr Vaňhara[1,7,]*

[1]Department of Histology and Embryology, Faculty of Medicine, Masaryk University, Brno, Czech Republic.

[2]Department of Chemical and Geological Sciences, University of Cagliari, Cittadella Universitaria, Monserrato, Cagliari, Italy.

[3]Centre for Systems Medicine and Department of Physiology and Medical Physics, Royal College of Surgeons in Ireland, Dublin, Ireland.

[4]Laboratory for Metabolism and Bioenergetics, Department of Biochemistry, Cell and Molecular Biology, Third Faculty of Medicine, Charles University, Prague, Czech Republic;

[5]Centre for Research on Nutrition, Metabolism and Diabetes, Third Faculty of Medicine, Charles University, Prague, Czech Republic.

[6]Department of Chemistry, Faculty of Science, Masaryk University, Brno, Czech Republic.

[7]International Clinical Research Center, St. Anne's University Hospital, Brno, Czech Republic.

* Corresponding author: pvanhara@med.muni.cz

Metallomics

Check for updates

Mixed copper(II)–phenanthroline complexes induce cell death of ovarian cancer cells by evoking the unfolded protein response†

Lukáš Moráň,[a] Tiziana Pivetta, [b] Sebastiano Masuri, [b] Kateřina Vašíčková, [a] Franziska Walter,[c] Jochen Prehn,[c] Moustafa Elkalaf,[de] Jan Trnka, [de] Josef Havel [fg] and Petr Vaňhara [★ag]

There is an ongoing need for the development of new cancer therapeutics that combine high cytotoxic efficiency with low side effects, and also override resistance to the first-line chemotherapeutics. Copper(II)–phenanthroline complexes are promising compounds that were shown previously to induce an immediate cytotoxic response over a panel of tumor cell lines *in vitro*. The molecular mechanism, however, remained unresolved. In this work we performed a thorough study of the copper(II)–phenanthroline complexes containing different imidazolidine-2-thione ligands in ovarian cancer cells, and revealed that these complexes induce endoplasmic reticulum (ER) stress and subsequently cell death mediated by the unfolded protein response. Alleviation of the ER-stress by tauroursodeoxycholic acid (TUDCA) attenuated the cytotoxic effects. In summary, we have identified a novel, ER-dependent, molecular mechanism mediating cytotoxic effects of copper(II)–phenanthroline complexes.

Significance to metallomics

Mixed copper(II)–phenanthroline complexes represent a class of metal coordination compounds with promising anti-proliferative effects on various cancer cells. Here we revealed that copper(II)–phenanthroline complexes **C0–C3** containing imidazolidine-2-thione ligands specifically target the endoplasmic reticulum (ER) and evoke rapid cell death by eliciting the unfolded protein response (UPR) in ovarian cancer cells. Targeting ER homeostasis by copper(II)–phenanthroline complexes may represent an alternative strategy to current cytotoxic drugs.

Introduction

Ovarian cancer (OC) is one of the most lethal gyneco-oncological diseases[1,2] with rather limited therapeutic options in advanced

[a] *Department of Histology and Embryology, Faculty of Medicine, Masaryk University, Kamenice 3, CZ-62500, Brno, Czech Republic.*
 E-mail: pvanhara@med.muni.cz; Fax: +420 54949 1320; Tel: +420 54949 7780
[b] *Department of Chemical and Geological Sciences, University of Cagliari, Monserrato, CA, Italy*
[c] *Centre for Systems Medicine and Department of Physiology and Medical Physics, Royal College of Surgeons in Ireland, Dublin, Ireland*
[d] *Laboratory for Metabolism and Bioenergetics, Department of Biochemistry, Cell and Molecular Biology, Third Faculty of Medicine, Charles University, Prague, Czech Republic*
[e] *Centre for Research on Nutrition, Metabolism and Diabetes, Third Faculty of Medicine, Charles University, Prague, Czech Republic*
[f] *Department of Chemistry, Faculty of Science, Masaryk University, Brno, Czech Republic*
[g] *International Clinical Research Center, St. Anne's University Hospital, Brno, Czech Republic*
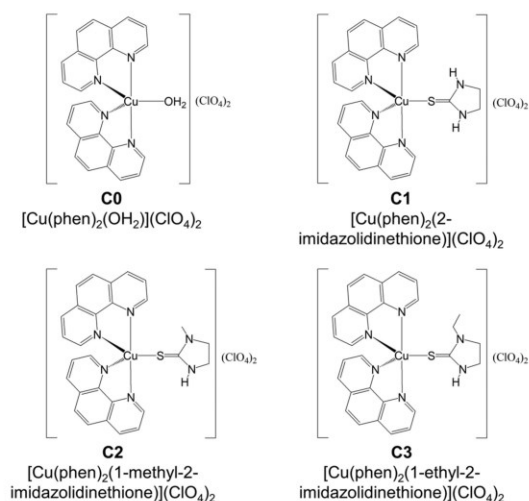† Electronic supplementary information (ESI) available. See DOI: 10.1039/c9mt00055k

stages. Cisplatin stays in the midpoint of the first line therapy of OC with a significant therapeutic response; however, the majority of patients finally develop resistance and relapse. Thus, there is a necessity of novel cytotoxic compounds that would complement a portfolio of available pharmacological solutions and offer molecular mechanisms of cytotoxicity different to those evoked by standard therapy, including cisplatin. Since the breakthrough discovery of cisplatin in 1965, numerous compounds were designed and synthesized in order to reduce unwanted side effects, enhance cytotoxicity and override acquired drug resistance of cancer cells. Among them, metal coordination compounds appeared as the most promising chemical entities inducing cell death,[3] also in drug-resistant cell lines.[4,5] There have been a variety of cytotoxic copper compounds complexed with different cores, including phenanthroline, synthesized so far, targeting mostly DNA and DNA-repair machinery.[6–9]

Mixed copper Cu(II)–phenanthroline complexes assigned **C1–C3** differing in imidazolidinethione ligand moiety (Fig. 1) were synthesized from the parent complex (**C0**) [Cu(phen)₂(OH₂)](ClO₄)₂ by T. Pivetta previously, and were shown to induce massive cell

Fig. 1   Molecular structure of the Cu(II)–phenanthroline complexes **C0–C3**.

death over a panel of cancer cell lines.[10] Similarly to previous reports,[11,12] Cu(II)–phenanthroline complexes possess a strong affinity to DNA *in vitro*; however, a precise mechanism of action has remained unclear so far. In this work, we report a novel mechanism of cell death induced by **C0–C3** through evoking ER-stress followed by the pro-apoptotic unfolded protein response (UPR) in ovarian cancer cells.

UPR represents a molecular series of signaling events that respond to misfolded, under-glycosylated or defective proteins in the ER.[13,14] Abnormal proteins in the ER lumen sequester the ER-chaperone GRP-78 (BiP, HSPA5) and dissociate it from the ER-membrane sensors and initiate two principal kinase pathways. Protein kinase R (PKR)-like endoplasmic reticulum kinase (PERK) phosphorylates the translation initiation factor eIF2α, attenuates proteosynthesis and activates ATF4-driven transcription. Inositol-requiring enzyme 1 (IRE1) alternatively splices the mRNA of Xbp-1 transcription factor and induces expression from promoters containing ER-stress elements (ER SE). Additional transcriptional response is driven by ATF6p90 that is cleaved by Golgi proteases into transcriptionally active form ATF6p50 regulating expression of pro-apoptotic proteins, *e.g.* DDIT3 (GADD153, CHOP).[15] Crosstalk of these prototypical signaling pathways then elicits the variable transcriptional and translational output determining the cell fate. Here we report that Cu(II)–phenanthroline complexes induce rapid cell death of ovarian cancer cells by the UPR-linked mechanism.

Materials and methods

Synthesis of Cu(II) phenanthroline complexes

C0–C3 were synthesized according to previously reported procedures.[10,16] In brief, for **C0** synthesis, concentrated perchloric acid was added to an ethanolic suspension of $Cu_2(CO_3)(OH)_2$,

the resulting solution was cooled and an ethanolic solution of 1,10-phenanthroline was added, and the precipitate was filtered off, washed with ethanol and dried at room temperature; for synthesis of **C1–C3**, the **C0** and the proper imidazolidine-2-thione were suspended in distilled water in 1 : 1 molar ratio. The suspension was stirred for 12 h at room temperature, after which a green powder was recovered by filtration under vacuum. The product was washed with water and dried at room temperature. The authenticity and purity of the reaction product was validated by mass spectrometry, elemental analysis and UV-vis spectrophotometry. For further experiments, **C0–C3** were dissolved in dimethyl sulfoxide (DMSO) to the stock concentration of 4 mM, and used at the indicated concentrations. The stock solution of **C0** in DMSO is stable for 4–6 months at 4 °C, and stock solutions of **C1–C3** in DMSO are stable for more than one month at 4 °C. Stock solutions of **C0–C3** in DMSO diluted by water (0.5 : 99.5 ratio) are stable at 4 °C for one month (**C0**) or 2–3 weeks (**C1–C3**) without significantly compromising the compound stability. In this study, stock solutions of **C0–C3** in DMSO were diluted by serum free culture medium and immediately used for treatment of cells. For details, see ESI.†

Cell culture conditions and treatments

Ovarian cancer cell lines A2780 and SKOV-3, and human embryonic kidney cell line HEK293, were obtained from the American Type Culture Collection (ATTC). Prior to use, the cell lines were authenticated *via* short tandem repeat (STR) profiling, which confirmed the cell identity. Mycoplasma contamination was investigated on a routine basis using PCR.[17,18] All cell lines were cultured in high glucose (4.5 g l^{-1}) Dulbecco's Modified Eagle Medium (DMEM) enriched with 10% fetal calf serum (FCS) (Invitrogen, Life Technologies, Czech Republic), 50 U ml^{-1} penicillin G, and 50 μg ml^{-1} streptomycin sulfate (PAA, GE Healthcare, Austria) at 37 °C in a humidified atmosphere with 5% CO_2. To specifically induce ER-stress by disruption of *N*-glycosylation, 1 mg ml^{-1} tunicamycin stock solution in DMSO (Sigma Aldrich, Czech Republic) was used at the indicated concentrations. ER-stress signaling was modulated by TUDCA (tauroursodeoxycholic acid, 2-[[(4*R*)-4-[(3*R*,5*S*,7*S*,8*R*,9*S*,10*S*,13*R*,14*S*,17*R*)-3,7-dihydroxy-10,13-dimethyl-2,3,4,5,6,7,8,9,11,12,14,15,16,17-tetradecahydro-1*H*-cyclopenta[*a*]phenanthren-17-yl]pentanoyl]amino]ethanesulfonic acid) dissolved in water to make 100 mg ml^{-1} stock solution (Sigma Aldrich, Czech Republic) and used at the indicated concentrations. $CuSO_4$ (Sigma Aldrich, Czech Republic) was diluted in water and used at the indicated concentrations.

Cell viability assay

Cells were cultured for 24 h on a 96-well plate at a density of 10 000 cells per well in medium containing **C0–C3** either alone or co-treated with TUDCA at the indicated concentrations. The respective solvents were used as controls. Then, the MTT reagent (3-(4,5-dimethylthiazol-2-yl)-2,5-diphenyltetrazolium bromide) (Sigma-Aldrich, Czech Republic) was added directly to the culture medium for 4 h. Then, medium including MTT reagent was aspirated, and the cells lysed by addition of 90% isopropanol, 0.04 M HCl and 10% Triton/Tween. Absorbance was recorded at 570 nm by a Synergy HTX multi-mode reader (BioTek Instruments, VT, USA).

All measurements were performed in technical pentaplicates and repeated in three independent experiments.

Transmission electron microscopy (TEM)

Cells were harvested using trypsin–EDTA, washed with $1\times$ PBS, fixed in 3% glutaraldehyde with 0.2% tannin in 0.1 M cacodylate buffer for 1 hour, and postfixed in 1% OsO_4 in the same buffer for 50 min. After post-fixation, cells were washed three times with cacodylate buffer and embedded in small blocks of 1% agar, 1 mm^3 in size. Agar blocks were dehydrated in increasing concentrations of ethanol (50%, 70%, 96%, and 100%), treated 2×10 min with 100% acetone, and embedded in Durcupan resin. Ultrathin sections were prepared on Leica EM UC6 ultramicrotome, stained with uranyl acetate and Reynold's lead citrate, and examined with the FEI Morgagni 286(D) TEM. One hundred cells from each experimental group in two independent experiments were examined. Cytological analysis of TEM images was validated by two independent reviewers (PV, LM).

Analysis of mitochondrial metabolism

Seahorse XFe-24 analyzer (Agilent Technologies, CA, USA) was used to monitor oxygen consumption rate in response to 0.5 μM **C0–C3** added to A2780 cells. The assay medium (XF DMEM, pH 7.4, Agilent Technologies, CA, USA) was supplemented with 4 mM L-glutamine, 1 mM pyruvate, and 4.5 g l^{-1} D-glucose. Cells were seeded at a density of 40 000 cells per well and left overnight to attach. After measuring the basal respiration, **C0–C3** or DMSO were injected and the respiration was followed for 2 hours. Then, the mitochondrial stress test was performed by sequential addition of 1 μM oligomycin, 1 μM carbonyl cyanide-4-(trifluoromethoxy)phenylhydrazone (FCCP), and 1 μM rotenone and antimycin A (all from Sigma-Aldrich, Czech Republic).

SDS-PAGE and western blotting

Trypsinised cells were washed two times with ice-cold $1\times$ PBS and resuspended in NP-40 lysis buffer containing 50 mM Tris–Cl (pH 7.4), 150 mM NaCl, 2 mM EDTA, 1% NP-40, 50 mM NaF supplemented with phosphatase inhibitor cocktail (PhosStop, Roche Applied Science, Czech Republic) and protease inhibitor cocktail (complete, Roche Applied Science, Czech Republic). Protein content in the cell extract was quantified using the Bradford-based BioRad protein Assay Kit (BioRad). Cell extracts were then mixed with $2\times$ Laemmli sample buffer (100 mM Tris pH 6.8, 4% SDS, 200 mM DTT, 20% glycerol, and 0.1% bromophenol blue) and boiled for 3 min. An equivalent of 15 μg proteins was resolved using 10% sodium dodecylsulfate-polyacrylamide gel electrophoresis (SDS-PAGE). Resolved proteins were then electroblotted onto a 0.45 μm polyvinylidene difluoride (PVDF) membrane (Millipore, Czech Republic) and incubated with the indicated primary antibodies diluted 1 : 200–1 : 1000 at 4 °C overnight (Actin cat. no: Ab1801, from Abcam, UK; DDIT3 #2895 and GRP-78 #3177; from Cell Signaling, MA, USA). Blots were developed using horseradish peroxidase (HRP)-conjugated anti-rabbit HRP #7074 or anti-mouse HRP #7076 (both Cell Signaling, USA) secondary antibodies, diluted 1 : 5000, and Immobilon Western HRP Substrate (Millipore, Czech Republic), according to the manufacturer's protocols.

RNA isolation, reverse transcription, and real-time quantitative PCR

Total RNA was extracted using an RNeasy Mini Kit (Qiagen, Germany) and quantified using a NanoDrop (Thermo Scientific, MA, USA). cDNA was synthesized from 1 μg of DNase I-treated total RNA using a First Strand Reverse Transcription Kit (Roche, Switzerland). Real-time qPCR was performed using a Roche LightCycler 480 RT PCR Kit according to the manufacturer's instructions. Relative expression was quantified using a UPL probe (Roche Applied Science, Czech Republic) and primers specific for *GRP-78* and *DDIT3*. Glyceraldehyde 3-phosphate dehydrogenase (*GAPDH*) was used as the housekeeping gene control. Results were expressed as relative ratio units visualized in a log scale. All PCR reactions were performed in triplicate in three independent experiments with reverse transcriptase-negative and template-negative controls included.

Analysis of IRE1 and PERK activity

Vectors harboring IRE1 and PERK reporters were constructed previously by Walter *et al.*[19] Briefly, either IRE1 splicing activity or PERK-mediated ATF4 expression results in generation of YFP-linked fusion proteins and increase of fluorescent signal in cells exposed to ER-stress conditions. The YFP fluorescence was normalized to nuclear staining by Hoechst dye. Approximately 600 cells per each experimental group were analyzed by a Cell Profiler 2.2.[20] A2780 cells carrying IRE1 and PERK vectors were generated using a FuGENE®6 (Promega, CA, USA) according to the manufacturer's instructions.

Spheroid culture and analysis

Formation of cell spheroids was induced by culture of a A2780 single cell suspension (approx. 1000 cells/20 μl) in the hanging-drop setup for 48 h. Spheroids were treated by tunicamycin or **C0–C3** and/or TUDCA, at the indicated concentrations, and cultured for an additional 24 h. Then, the spheroids were collected by gentle centrifugation, washed twice with $1\times$ PBS and fixed using 4% formaldehyde (Sigma-Aldrich, Czech Republic). For immunofluorescent labeling, spheroids were washed with $1\times$ PBS containing 3% BSA and 0.1% Triton X-100 and incubated with DDIT3 (#2895) or GRP-78 (#3177) antibodies (both from Cell Signaling, MA, USA), diluted 1 : 200 at 4 °C overnight. Immunofluorescent signals were obtained by Alexa Fluor conjugated secondary antibodies (AF488, cat. no. A32731 or AF568, cat. no. A11004, both from Life Technologies, USA), diluted 1 : 2000. Cell nuclei were visualized by a Hoechst dye (Life Technologies, USA). Spheroids were scanned by the inverted microscope Zeiss Axio Observer Z1 equipped with a LSM800 confocal unit.

Statistical analysis

Statistical analysis was performed in Statistica 6.0 (StatSoft, Inc., Tulsa, USA). Student's *T*-test was used to confirm statistically significant differences in cell viability assays (MTT).

Results

To address the mechanism of the cytotoxic activity of copper(II)–phenanthroline complexes (**C0–C3**), the A2780 ovarian cancer cell line was used as a pilot cell model. First, we estimated the lethal concentration of individual complexes that effectively induces cell death, by measuring the cell metabolic rate using the MTT assay (Fig. 2). All complexes evoked early cell death in OC cells even with more rapid onset and lower effective doses than cisplatin in the time course of the experiment (Fig. S1A and B, ESI†). In addition, we wanted to reveal whether the cytotoxic effects of **C0–C3** are dependent on their complexation with phenanthroline and the cell death is not induced by free Cu(II) ion in the culture microenvironment. Therefore, we treated the A2780 cells for 24 h with an aqueous solution of $CuSO_4$ in the concentration range equimolar to the concentration of Cu in **C0–C3**, and performed the MTT assay. In agreement with previous reports,[21] the free Cu(II) ions dissociated from the sulfate did not induce cell death at the concentration range used in this study, suggesting that the Cu(II)–phenanthroline complex is indeed essential for the cytotoxicity observed (Fig. S1C, ESI†), possibly through enhanced transport across the plasma membrane.

To elucidate the events preceding ultimate induction of cell death, we treated the cells for 24 h with sub-lethal concentrations of **C0–C3** complexes (0.5 μM) and searched for treatment-associated structural and molecular alterations in A2780 cells. The sub-lethal dose was confirmed by propidium iodide/phosphatidylserine staining followed by flow-cytometry, documenting that the cell death rate did not exceed 20% in any experimental group (Fig. S2A and B, ESI†). Then, we performed a systematic transmission electron microscopy (TEM) screening of major organelles, to reveal the potential abnormalities in the cell ultrastructure (Fig. 3). The control cells treated with DMSO only, contained normal mitochondria and non-dilated, regularly arranged cisterns of ER with attached ribosomes. In all treated variants (**C0–C3**), we observed moderate alterations of mitochondrial ultrastructure, such as abnormal density and thickening of the mitochondrial membrane (Fig. S3A, ESI†). The endoplasmic
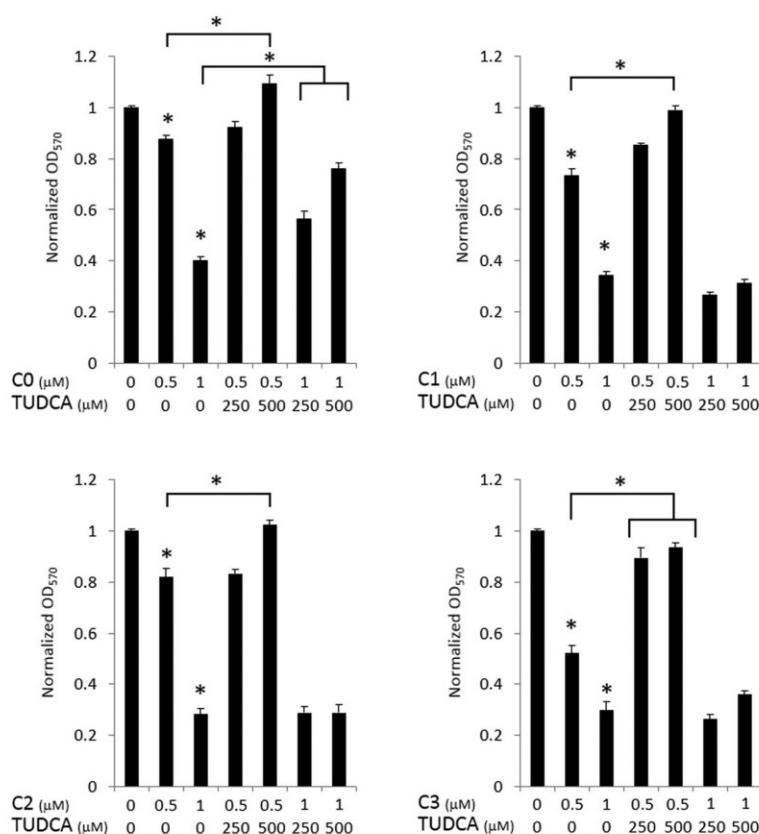
Fig. 2 Cu(II)–phenanthroline complexes **C0–C3** induce cell death that is inhibited by co-treatment with tauroursodeoxycholic acid (TUDCA). A2780 cells were cultured for 24 h in the presence of individual **C0–C3** either in the absence or presence of TUDCA. Then, the cell viability was determined by conversion of the 4-nitro blue tetrazolium chloride to formazan followed by measurement of OD at 570 nm (MTT assay). The plots represent means ± SD from three independent experiments performed in technical pentaplicates. Asterisk indicates statistical significance at $p < 0.05$.
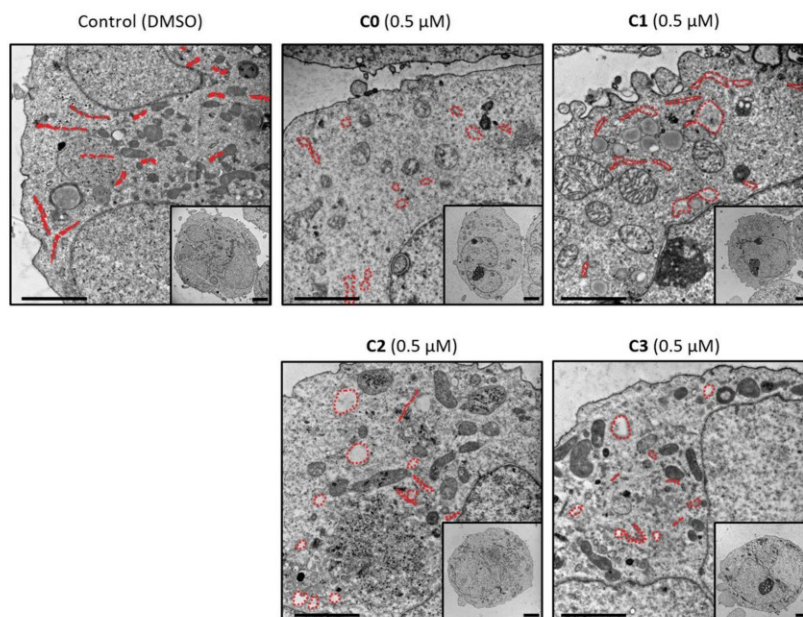
Fig. 3 Transmission electron microscopy (TEM) of A2780 cells treated for 24 h with **C0–C3**, or DMSO as a control, visualizing cell ultrastructure. Red contours indicate ER cisterns. Insets show the overall cell morphology. Scale bars indicate 2 μm.

reticulum (ER) contained apparently dilated cisterns that lacked attached ribosomes. The treated cells also exhibited a large number of vesicular structures similar to apoptotic bodies bulging outwards from a cell. These ultrastructural hallmarks of mitochondrial and ER distortions prompted us to decipher whether the **C0–C3** complexes induce cell death through mitochondrial dysfunction, or induction of ER-stress and the unfolded protein response (UPR). Therefore, we performed the analysis of mitochondrial metabolism by using the Seahorse assay. The A2780 cells were exposed to 0.5 μM **C0–C3** or DMSO only and followed for 3 h. Interestingly, the **C0–C3** treated cells did not show a statistically significant decrease in mitochondrial respiration, suggesting that the mitochondria are not directly involved in the immediate response to **C0–C3** (Fig. S3B, ESI†). This prompted us to pursue further the ER-associated machinery.

To reverse, or specifically induce, the state of ER-stress in A2780 cells, we used tauroursodeoxycholic acid (TUDCA), a chemical chaperone attenuating general ER-stress, or tunicamycin, an established inducer of ER-stress inhibiting the N-glycosylation machinery, respectively. Both TUDCA and tunicamycin are well established ER stress modulators in an ovarian context and other models.[22] To link the pilot observations with underlying molecular mechanisms, we performed immunoblotting to visualize levels of major ER-stress associated proteins. We showed that GRP-78 is downregulated while DDIT3 is upregulated; however, the extent of GRP-78/DDIT3 alteration differed among individual experimental groups treated by **C0–C3** complexes and may depend on the auxiliary ligand moiety. The Cu(II)–phenanthroline complex carrying the methylated imidazolidine-2-thione ligand (**C2**) demonstrated

the strongest effect on GRP-78 and DDIT3 expression. Interestingly, concomitant treatment by **C0–C3** and TUDCA reduced the cytotoxic activity of **C0–C3** complexes (Fig. 2). TUDCA also partially reversed the upregulation of GRP-78 and DDIT3 proteins, suggesting that alleviation of ER-stress may be responsible for cell survival (Fig. 4A). The data from immunoblotting were confirmed by quantitative real time PCR specific to GRP-78 and DDIT3 (Fig. S4A, ESI†). Principally the same trends were observed in another ovarian cancer cell line SKOV-3 at both the mRNA and protein levels (Fig. S4B and S5, ESI†), and in a human immortalized line of embryonic kidney cells (HEK293) on the mRNA level (Fig. S4C, ESI†).

To mimic culture conditions in a scenario close to real tissues, we generated 3D cell spheroids and cultured them under low adhesion conditions either in the presence or absence of **C0–C3** complexes. Cell spheroids derived from approx. 1000 cells were then stained for GRP-78 and DDIT3 and analyzed by confocal microscopy. Similarly to standard culture conditions, UPR was evoked in **C0–C3**-treated A2780 cells and attenuated when treated simultaneously by TUDCA (Fig. 4B and C). Specificity of UPR induction in 3D cell spheroids was validated by tunicamycin (Fig. S6A, ESI†).

Then we were curious whether the upstream UPR signaling is indeed involved in deregulation of GRP-78 and DDIT3 levels. We used fluorescent reporters constructed previously by the J. Prehn group that express YFP-fusion protein reporters upon PERK or IRE1 activation.[19] The sensitivity of the reporter system was validated using tunicamycin treatment (Fig. S6B, ESI†). Both PERK and IRE1 were activated upon treatment with **C0–C3** complexes. Interestingly, TUDCA reverted the activity of PERK
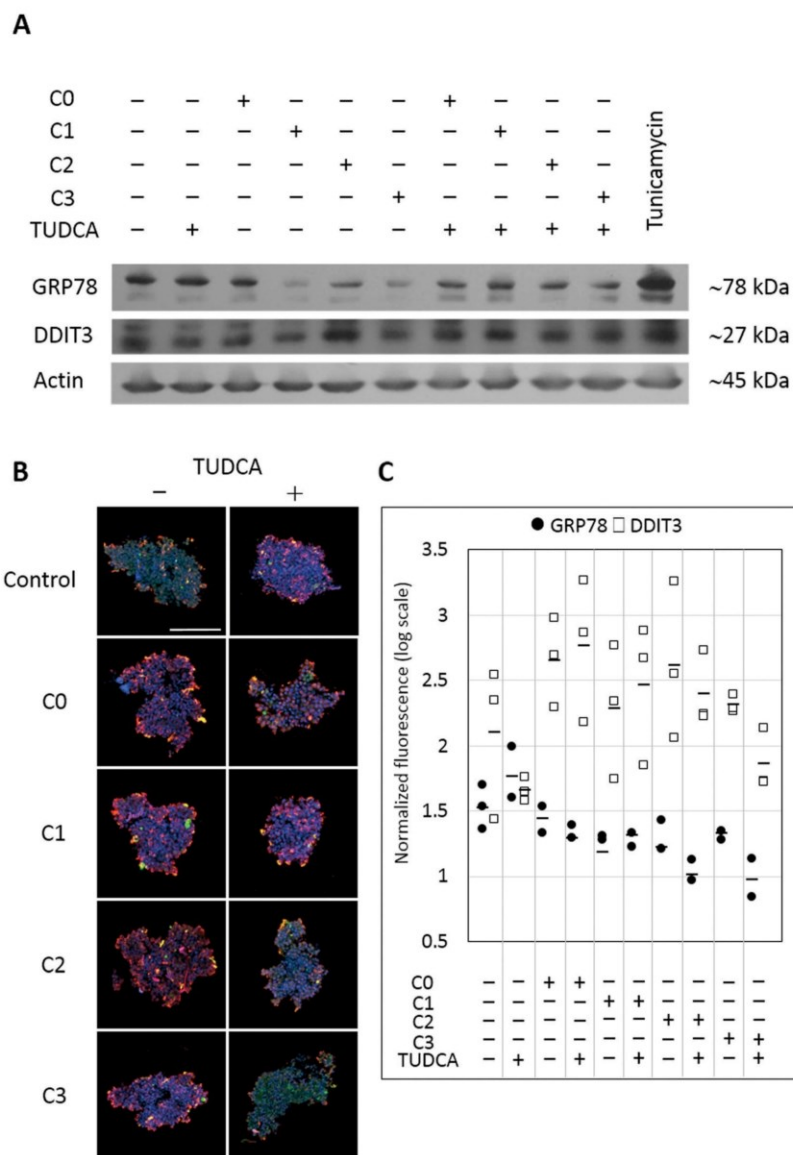
A

B

C

Fig. 4 (A) Protein levels of GRP-78 and DDIT3 in A2780 cells treated for 24 h with **C0–C3** or TUDCA as documented by immunoblotting. Actin was used as a control of equal loading. (B) 3D spheroids derived from A2780 cells were treated with **C0–C3** and/or TUDCA and analyzed by immunofluorescent microscopy for expression of GRP-78 and DDIT3 proteins. GRP-78 and DDIT3 are visualized by the green and red signal, respectively. Nuclei (blue) are visualized by Hoechst staining. The scale bars indicate 200 μm. (C) Intensity of fluorescent signals of GRP-78 and DDIT3 was normalized to nuclear fluorescence. Results visualize GRP-78 and DDIT3 expression within three different spheroids. Line represents a mean value.

and IRE1 even in the presence of **C0–C3** complexes (Fig. 5A and B). This indicates that the UPR is the effective pathway leading to cell death evoked upon generalized ER-stress. In summary, our data clearly demonstrated that the cytotoxic activity of copper(II)–phenanthroline **C0–C3** complexes is dependent on ER-stress induction and UPR signaling in ovarian cancer cells.

Discussion

In ovarian cancer, debulking surgery followed by cisplatin chemotherapy is still at the core of the initial treatment. However, most of the patients acquire resistance to cisplatin and eventually relapse. Resistance to antitumor therapy thus
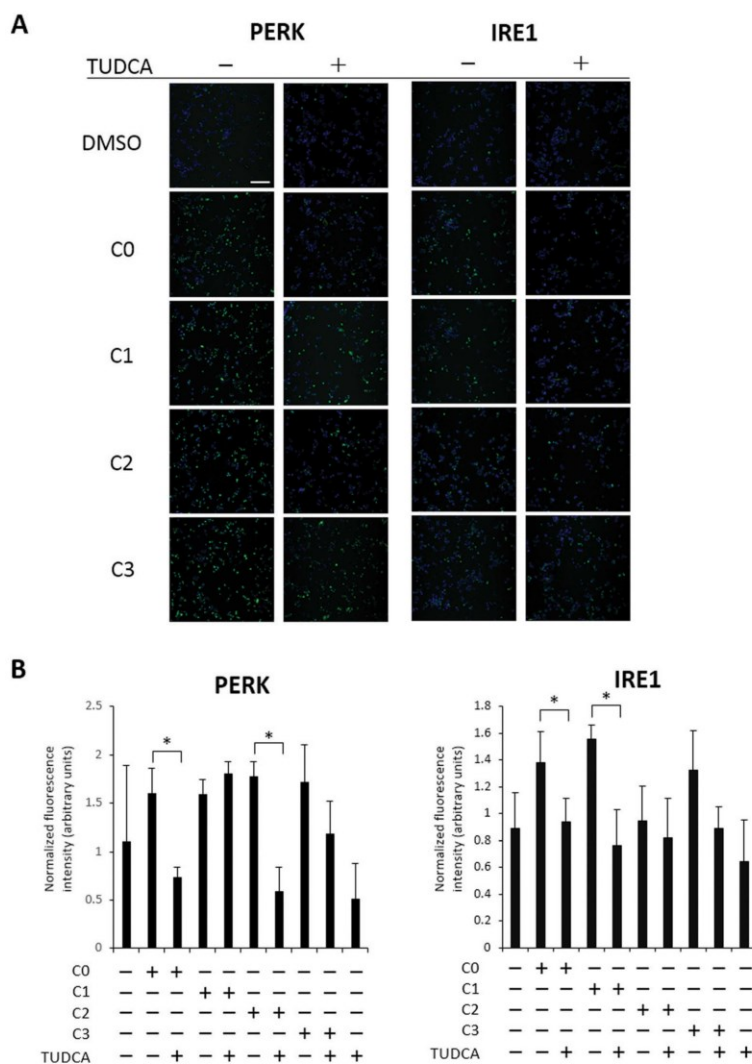
Fig. 5 (A) Representative images revealing activity of PERK and IRE1 in A2780 cells treated with **C0–C3** or TUDCA for 24 h. Green signal corresponds to cells with activated PERK or IRE1 YFP reporters. (B) Quantitative representation of immunofluorescent data. The plots represent means ± SD of the YFP fluorescence, acquired from 600 cells and normalized to the nuclear Hoechst signal. An asterisk indicates statistical significance at $p < 0.05$. Scale bars indicate 100 μm.

represents one of the major causes of cancer-associated deaths. Development of cisplatin resistance follows alterations especially in DNA repair machinery (for a review see ref. 23). Therefore, there is a great need for novel therapeutic strategies that would target different molecular entities within cancer cells, preventing the acquisition of the resistant phenotype. Copper and its derivatives were introduced to the portfolio of candidate cytotoxic drugs due to a promising balance between direct cytotoxicity and reduced side effects. Various Cu(II) complexes, such as pyridine-2-carbohidrazides, pyrrolidine dithiocarbamate, and salicylaldoxime, were shown to interfere with the crucial

enzymatic machinery involved in reactive oxygen species production, DNA damage repair or protein degradation through the proteasome (for review see ref. 3). So far, only a few copper compounds were reported to target directly the ER. A phosphine Cu(I) complex evoked the UPR and apoptosis in B-cell leukemia.[24] Similarly, thioxotriazole Cu(II) complex A0 evoked paraptotic cell death associated with ER abnormalities in a panel of cancer cell lines.[25] Interestingly, Cu(II) ions may regulate the cytotoxicity of other drugs, such as disulfiram in chronic myeloid leukemia,[26] or target global metabolic machinery, e.g. protein degradation in the proteasome.[27] Concordantly, 1,10-phenanthroline complexed with

indole-3-acetic acid and indole-3-propionic acid and copper, induced cell death of prostate (PC-3) and breast (MDA-MB-231) cancer cells through inhibition of the proteasome in a dose dependent manner.[28] When the proteasome is pharmacologically inhibited, *e.g.* in multiple myeloma, the pro-apoptotic branch UPR is preferentially elicited, leading to programmed cell death of cancer cells.[29,30]

The UPR represents a generalized response to stress within the ER, evoked mostly by abnormally folded proteins in the ER lumen. Signaling from the ER through PERK, IRE1 and ATF6 can attenuate the load on the ER by downregulation of translation; however, in the case of sustained stress, the ER signaling switches towards cell death induction. The balance between pro-survival and pro-apoptotic ER signaling, represented by ratio of GRP78 to DDIT3, can represent relevant phenomenon in cell life[31] as well as in ovarian cancer and aging of normal ovarian epithelium.[22,32] Treatment using chemical chaperones acting within the ER, such as TUDCA improves the ER homeostasis. We have observed previously, that alleviation of ER-stress by TUDCA leads to restoration of normal ER architecture as well as the molecular signaling initiated in the ER.[22] However, the effect of TUDCA can be cumulative because of its effects on mitochondrial respiration and regulation of apoptosis.[33]

The Cu(II) phenanthroline complexes **C0–C3** were originally synthesized by Pivetta *et al.* and their cytotoxic activity has been demonstrated in a panel of cell lines.[34] Depending of the ligand carried on the Cu(II) phenanthroline core, these compounds showed differential DNA-binding activity *in vitro*.[10] However, the molecular targets remained mostly unknown. Interestingly, treatment by using copper–platinum complex derived from Cu(II) phenanthroline complexes and cisplatin, showed a synergistic anti-proliferative effect in human acute T-lymphoblastic leukaemia cells.[4,35] In this work, we localized the activity of **C0–C3** complexes primarily to the endoplasmic reticulum and documented that cell death evoked by **C0–C3** is dependent on UPR induction. Concomitant treatment with chemical chaperones acting within the ER, such as TUDCA, showed interestingly a significant antagonistic effect to **C0–C3** complexes on viability of ovarian cancer cells, most likely by activation of the pro-survival branch of the UPR. Interestingly, the specific ligand bonded to the Cu(II) phenanthroline core, *e.g.* methylated imidazolidine-2-thione, can enhance the molecular response, suggesting a possible course of the compound modification towards increased efficacy.

In summary, targeting the ER by using copper ions coordinated with specific nitrogen ligands, such as phenanthroline, can represent an alternative strategy to override the acquired resistance of cancer cells to chemotherapy.

Conflicts of interest

There are no conflicts to declare.

Acknowledgements

References

1 L. A. Torre, B. Trabert, C. E. DeSantis, K. D. Miller, G. Samimi, C. D. Runowicz, M. M. Gaudet, A. Jemal and R. L. Siegel, Ovarian cancer statistics, 2018, *Ca-Cancer J. Clin.*, 2018, **68**, 284–296.

2 R. L. Siegel, K. D. Miller and A. Jemal, Cancer statistics, 2018, *Ca-Cancer J. Clin.*, 2018, **68**, 7–30.

3 F. Trudu, F. Amato, P. Vanhara, T. Pivetta, E. M. Pena-Mendez and J. Havel, Coordination compounds in cancer: Past, present and perspectives, *J. Appl. Biomed.*, 2015, **13**, 79–103.

4 S. Vascellari, E. Valletta, D. Perra, E. Pinna, A. Serra, F. Isaia, A. Pani and T. Pivetta, Cisplatin, glutathione and the third wheel: a copper-(1,10-phenanthroline) complex modulates cisplatin–GSH interactions from antagonism to synergism in cancer cells resistant to cisplatin, *RSC Adv.*, 2019, **9**, 5362–5376.

5 E. Cadoni, E. Valletta, G. Caddeo, F. Isaia, M. G. Cabiddu, S. Vascellari and T. Pivetta, Competitive reactions among glutathione, cisplatin and copper–phenanthroline complexes, *J. Inorg. Biochem.*, 2017, **173**, 126–133.

6 I. Naletova, C. Satriano, A. Curci, N. Margiotta, G. Natile, G. Arena, D. La Mendola, V. G. Nicoletti and E. Rizzarelli, Cytotoxic phenanthroline derivatives alter metallostasis and redox homeostasis in neuroblastoma cells, *Oncotarget*, 2018, **9**, 36289–36316.

7 B. Selvakumar, V. Rajendiran, P. Uma Maheswari, H. Stoeckli-Evans and M. Palaniandavar, Structures, spectra, and DNA-binding properties of mixed ligand copper(II) complexes of iminodiacetic acid: the novel role of diimine co-ligands on DNA conformation and hydrolytic and oxidative double strand DNA cleavage, *J. Inorg. Biochem.*, 2006, **100**, 316–330.

8 J. M. Veal, K. Merchant and R. L. Rill, The influence of reducing agent and 1,10-phenanthroline concentration on DNA cleavage by phenanthroline + copper, *Nucleic Acids Res.*, 1991, **19**, 3383–3388.

9 Y. Xiao, Q. Wang, Y. Huang, X. Ma, X. Xiong and H. Li, Synthesis, structure, and biological evaluation of a copper(II) complex with fleroxacin and 1,10-phenanthroline, *Dalton Trans.*, 2016, **45**, 10928–10935.

10 T. Pivetta, M. D. Cannas, F. Demartin, C. Castellano, S. Vascellari, G. Verani and F. Isaia, Synthesis, structural characterization, formation constants and in vitro cytotoxicity of

phenanthroline and imidazolidine-2-thione copper(ii) complexes, *J. Inorg. Biochem.*, 2011, **105**, 329–338.

11 B. C. Bales, T. Kodama, Y. N. Weledji, M. Pitie, B. Meunier and M. M. Greenberg, Mechanistic studies on DNA damage by minor groove binding copper–phenanthroline conjugates, *Nucleic Acids Res.*, 2005, **33**, 5371–5379.

12 C. Rajarajeswari, M. Ganeshpandian, M. Palaniandavar, A. Riyasdeen and M. A. Akbarsha, Mixed ligand copper(ii) complexes of 1,10-phenanthroline with tridentate pheno-late/pyridyl/(benz)imidazolyl Schiff base ligands: covalent vs non-covalent DNA binding, DNA cleavage and cytotoxicity, *J. Inorg. Biochem.*, 2014, **140**, 255–268.

13 K. Kratochvilova, L. Moran, S. Padourova, S. Stejskal, L. Tesarova, P. Simara, A. Hampl, I. Koutna and P. Vanhara, The role of the endoplasmic reticulum stress in stemness, pluripotency and development, *Eur. J. Cell Biol.*, 2016, 9, DOI: 10.1016/j.ejcb.2016.02.002.

14 M. Wang and R. J. Kaufman, The impact of the endoplasmic reticulum protein-folding environment on cancer development, *Nat. Rev. Cancer*, 2014, **14**, 581–597.

15 N. Sovolyova, S. Healy, A. Samali and S. E. Logue, Stressed to death – mechanisms of ER stress-induced cell death, *Biol. Chem.*, 2014, **395**, 1–13.

16 T. Pivetta, F. Isaia, G. Verani, C. Cannas, L. Serra, C. Castellano, F. Demartin, F. Pilla, M. Manca and A. Pani, Mixed-1,10-phenanthroline–Cu(ii) complexes: synthesis, cytotoxic activity versus hematological and solid tumor cells and complex formation equilibria with glutathione, *J. Inorg. Biochem.*, 2012, **114**, 28–37.

17 C. C. Uphoff and H. G. Drexler, Detection of mycoplasma in leukemia-lymphoma cell lines using polymerase chain reaction, *Leukemia*, 2002, **16**, 289–293.

18 C. C. Uphoff and H. G. Drexler, Comparative antibiotic eradication of mycoplasma infections from continuous cell lines, *In Vitro Cell. Dev. Biol.: Anim.*, 2002, **38**, 86–89.

19 F. Walter, J. Schmid, H. Dussmann, C. G. Concannon and J. H. M. Prehn, Imaging of single cell responses to ER stress indicates that the relative dynamics of IRE1/XBP1 and PERK/ATF4 signalling rather than a switch between signalling branches determine cell survival, *Cell Death Differ.*, 2015, **22**, 1502–1516.

20 A. E. Carpenter, T. R. Jones, M. R. Lamprecht, C. Clarke, I. H. Kang, O. Friman, D. A. Guertin, J. H. Chang, R. A. Lindquist, J. Moffat, P. Golland and D. M. Sabatini, CellProfiler: image analysis software for identifying and quantifying cell phenotypes, *Genome Biol.*, 2006, **7**, R100.

21 A. K. Holzer, G. Samimi, K. Katano, W. Naerdemann, X. Lin, R. Safaei and S. B. Howell, The copper influx transporter human copper transport protein 1 regulates the uptake of cisplatin in human ovarian carcinoma cells, *Mol. Pharmacol.*, 2004, **66**, 817–823.

22 K. Vasickova, L. Moran, D. Gurin and P. Vanhara, Alleviation of endoplasmic reticulum stress by tauroursodeoxycholic acid delays senescence of mouse ovarian surface epithelium, *Cell Tissue Res.*, 2018, **374**, 643–652.

23 G. Damia and M. Broggini, Platinum Resistance in Ovarian Cancer: Role of DNA Repair, *Cancers*, 2019, **11**, 119.

24 R. Bortolozzi, G. Viola, E. Porcu, F. Consolaro, C. Marzano, M. Pellei, V. Gandin and G. Basso, A novel copper(i) complex induces ER-stress-mediated apoptosis and sensitizes B-acute lymphoblastic leukemia cells to chemotherapeutic agents, *Oncotarget*, 2014, **5**, 5978–5991.

25 S. Tardito, C. Isella, E. Medico, L. Marchio, E. Bevilacqua, M. Hatzoglou, O. Bussolati and R. Franchi-Gazzola, The thioxotriazole copper(ii) complex A0 induces endoplasmic reticulum stress and paraptotic death in human cancer cells, *J. Biol. Chem.*, 2009, **284**, 24306–24319.

26 J. Navratilova, P. Jungova, P. Vanhara, J. Preisler, V. Kanicky and J. Smarda, Copper ions regulate cytotoxicity of disulfiram to myeloid leukemia cells, *Int. J. Mol. Med.*, 2009, **24**, 661–670.

27 X. Zhang, C. F. Bi, Y. H. Fan, Q. Z. Cui, D. Chen, Y. Xiao and Q. P. Dou, Induction of tumor cell apoptosis by taurine Schiff base copper complex is associated with the inhibition of proteasomal activity, *Int. J. Mol. Med.*, 2008, **22**, 677–682.

28 Z. Zhang, C. F. Bi, S. M. Schmitt, Y. H. Fan, L. L. Dong, J. Zuo and Q. P. Dou, 1,10-Phenanthroline promotes copper complexes into tumor cells and induces apoptosis by inhibiting the proteasome activity, *J. Biol. Inorg. Chem.*, 2012, **17**, 1257–1267.

29 A. H. Lee, N. N. Iwakoshi, K. C. Anderson and L. H. Glimcher, Proteasome inhibitors disrupt the unfolded protein response in myeloma cells, *Proc. Natl. Acad. Sci. U. S. A.*, 2003, **100**, 9946–9951.

30 E. A. Obeng, L. M. Carlson, D. M. Gutman, W. J. Harrington, K. P. Lee and L. H. Boise, Proteasome inhibitors induce a terminal unfolded protein response in multiple myeloma cells, *Blood*, 2006, **107**, 4907–4916.

31 C. Hetz, The unfolded protein response: controlling cell fate decisions under ER stress and beyond, *Nat. Rev. Mol. Cell Biol.*, 2012, **13**, 89–102.

32 K. Kratochvilova, P. Horak, M. Esner, K. Soucek, D. Pils, M. Anees, E. Tomasich, F. Drafi, V. Jurtikova, A. Hampl, M. Krainer and P. Vanhara, Tumor suppressor candidate 3 (TUSC3) prevents the epithelial-to-mesenchymal transition and inhibits tumor growth by modulating the endoplasmic reticulum stress response in ovarian cancer cells, *Int. J. Cancer*, 2015, **137**, 1330–1340.

33 I. Fonseca, G. Gordino, S. Moreira, M. J. Nunes, C. Azevedo, M. J. Gama, E. Rodrigues, C. M. P. Rodrigues and M. Castro-Caldas, Tauroursodeoxycholic Acid Protects Against Mitochondrial Dysfunction and Cell Death *via* Mitophagy in Human Neuro-blastoma Cells, *Mol. Neurobiol.*, 2017, **54**, 6107–6119.

34 T. Pivetta, F. Trudu, E. Valletta, F. Isaia, C. Castellano, F. Demartin, R. Tuveri, S. Vascellari and A. Pani, Novel copper(ii) complexes as new promising antitumour agents. A crystal structure of [Cu(1,10-phenanthroline-5,6-dione)$_2$(OH$_2$)(OClO$_3$)](ClO$_4$), *J. Inorg. Biochem.*, 2014, **141**, 103–113.

35 T. Pivetta, V. Lallai, E. Valletta, F. Trudu, F. Isaia, D. Perra, E. Pinna and A. Pani, Mixed copper-platinum complex formation could explain synergistic antiproliferative effect exhibited by binary mixtures of cisplatin and copper-1,10-phenanthroline compounds: An ESI-MS study, *J. Inorg. Biochem.*, 2015, **151**, 107–114.

Mixed copper (II)-phenanthroline complexes induce cell death of ovarian cancer cells by evoking unfolded protein response

Supplementary methods

Lukáš Moráň[1], Tiziana Pivetta[2], Sebastiano Masuri[2], Kateřina Vašíčková[1], Franziska Walter[3], Jochen Prehn[3], Moustafa Elkalaf[4], Jan Trnka[4], Josef Havel[5,6], Petr Vaňhara[1,6#]

[1]Department of Histology and Embryology, Faculty of Medicine, Masaryk University, Brno, Czech Republic
[2]Department of Chemical and Geological Sciences, University of Cagliari, Monserrato (CA), Italy
[3]Centre for Systems Medicine and Department of Physiology and Medical Physics, Royal College of Surgeons in Ireland, 123 St Stephen's Green, Dublin 2, Ireland
[4]Laboratory for Metabolism and Bioenergetics, Department of Biochemistry, Cell and Molecular Biology, Third Faculty of Medicine, Charles University, Prague, Czech Republic
[5]Department of Chemistry, Faculty of Science, Masaryk University, Brno, Czech Republic
[6]International Clinical Research Center, St. Anne's University Hospital, Brno, Czech Republic
[#]Author for correspondence

Synthesis of Cu(II) phenanthroline complexes

C0-C3 were synthesized according to previously reported procedures [10, 15]. For **C0**, a one-pot synthesis was chosen so as not to isolate the copper perchlorate, hygroscopic and explosive if dried out. In brief, concentrated perchloric acid was added to a warmed (60°C) ethanolic suspension of $Cu_2(CO_3)(OH)_2$ (involved reaction is $Cu_2(CO_3)(OH)_2 + 4HClO_4 \rightarrow 2Cu^{+2} + 4ClO_4^- + CO_2 + 3H_2O$), the resulting solution was cooled and an ethanolic solution of 1,10- phenanthroline (phen) was added (involved reaction is $2Cu^{+2} + 4ClO_4^- + 2H_2O + 4phen \rightarrow 2[Cu(phen)_2(OH_2)](ClO_4)_2)$, the formed precipitate $Cu(phen)_2(OH_2)](ClO_4)_2$ (**C0**) was filtered off, washed with ethanol and dried at room temperature. This compound is stable at room temperature, is soluble in DMSO at 0.1 M concentration level, in CH_3CN at 0.01M, and in pure water at 5 microM. Millimolar concentration of **C0** in water could be reached by dissolving the product in few μl of DMSO and then diluting with water, warming at 40 °C and gently mixing (avoid sonication to prevent the formation of emulsions). Stock solutions of **C0** in DMSO and CH_3CN are stable at 4°C for 4-6 months, stock solutions in DMSO:water (0.5:99.5) prepared as described before are stable at 4°C for max 1 month.

As regards **C1-C3**, an heterogenous phase reaction was used exploiting the different solubility in water of **C0** and the products (approx. 1 μM). **C0** and the proper imidazolidine-2-thione were suspended in distilled water in 1:1 molar ratio and the suspension was stirred for 12 h at room

temperature, after which a green powder was recovered by filtration under vacuum. This reaction ($[Cu(phen)_2(OH_2)](ClO_4)_2 + L \rightarrow [Cu(phen)_2(L)](ClO_4)_2 + H_2O$) occurs faster (2 h) under sonication, however the obtained precipitate is finely dispersed and should be recovered by centrifuge. The final product was washed with water and dried at room temperature. The **C1-C3** complexes, as **C0**, are soluble in DMSO (0.1 M) and in CH_3CN (0.01M). Water solutions at 1 mM could be prepared as described before for **C0**. Stock solutions of **C1-C3** in DMSO or CH_3CN should be stored in the darkness at 4°C and are stable for 1 month. DMSO:water (0.5:99.5) solutions, stored in the darkness at 4°C, are stable for 2/3 weeks.

The authenticity and purity of reaction products were validated by mass spectrometry, elemental analysis and UV/VIS spectrophotometry.

Fig. S1
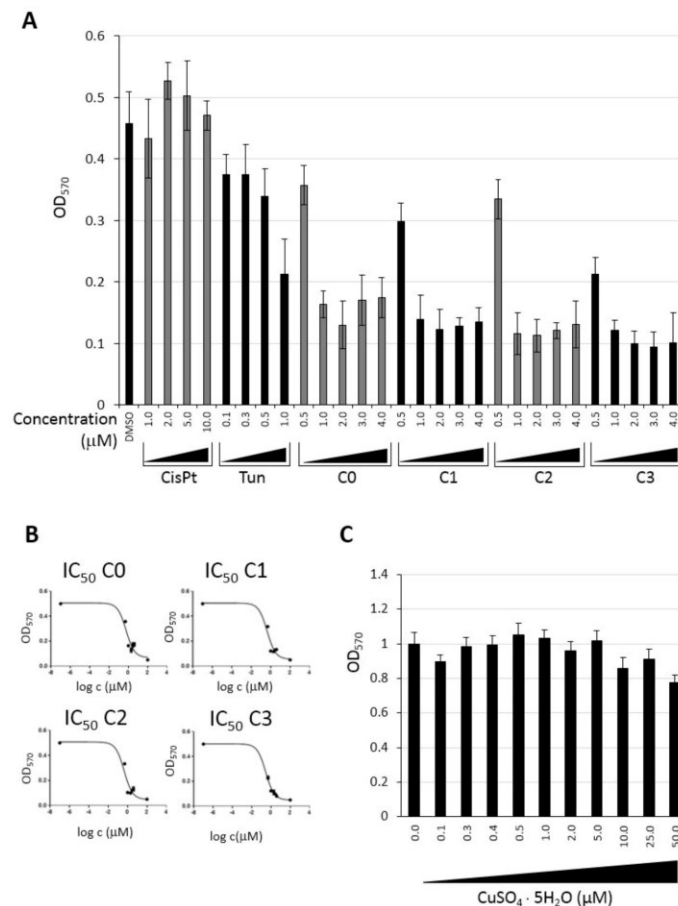
Fig. S1. (A) Viability of A2780 cells cultured for 24 hrs. in presence of individual **C0-C3**, cisplatin and tunicamycin at different concentrations, or DMSO as a control. Then, the cell viability was determined by conversion of the 4-nitro blue tetrazolium chloride to formazan followed by measurement of OD at 570nm (MTT assay). The plots represent means ± SD from three independent experiments performed in technical pentaplicates. Asterisk indicates statistical significance at $p < 0.05$. **(B)** IC50 dose of **C0-C3** on A2780 as determined by the MTT assay. **(C)** Viability of A2780 cells cultured in presence of $CuSO_4 \cdot 5H_2O$ for 24 hrs. as determined by the MTT assay.

Fig. S2

A

B
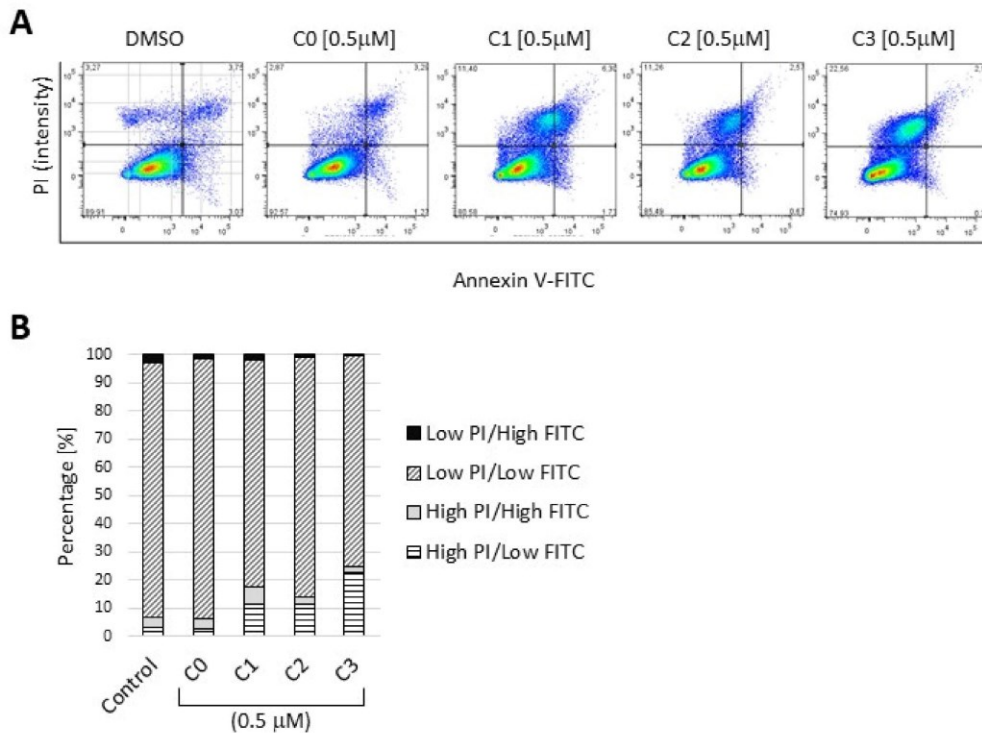
Fig. S2. (**A**) Viability of A2780 cells determined by propidium iodide (PI) and annexin V staining and FACS analysis. Quadrant 1 (Q1) represents PI positive, annexin V negative cells (necrosis); Q2 PI positive, annexin V positive cells (late apoptosis/secondary necrosis); Q3 PI negative, annexin V positive cells (early apoptosis); and Q4 PI negative, annexin V negative cells (viable). (**B**) Quantification of cell death analyzed by propidium iodide (PI) /annexin V staining. Bars represent the percentage of PI/ annexin V negative cells (viable), PI positive (necrosis), annexin V positive (early apoptosis), and PI/ annexin V positive cells (late apoptosis/secondary necrosis).

Fig. S3

A

B
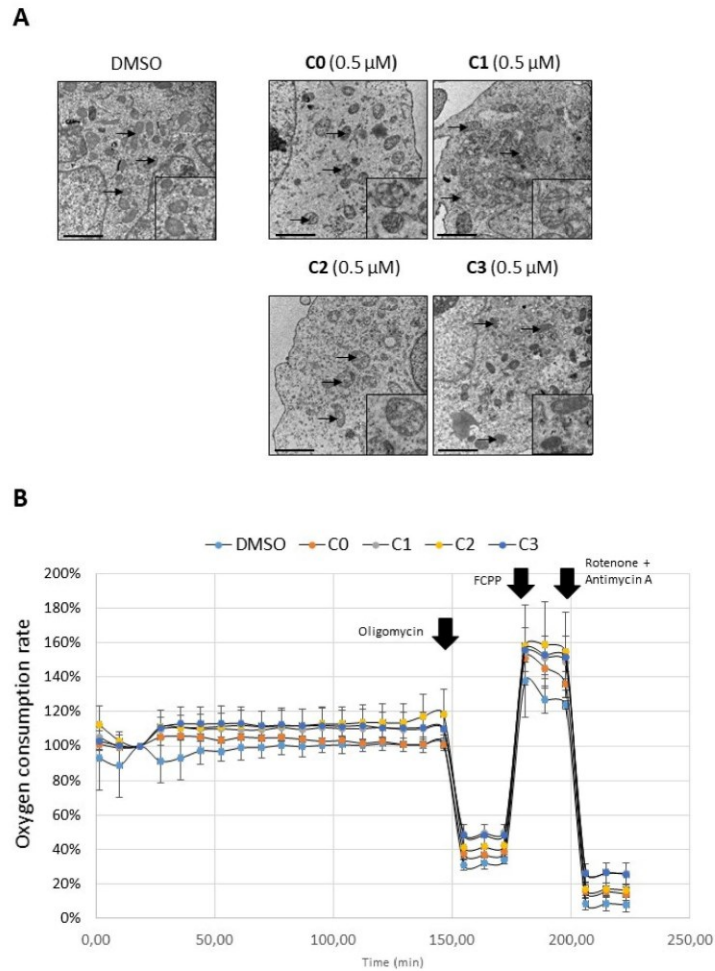
Fig. S3. (**A**) Transmission electron microscopy (TEM) of A2780 cells treated for 24 hrs. with **C0**-**C3** or DMSO as a control, revealing mitochondria (arrows). Insets show details of mitochondrial structure. Scale bars indicate 2 μm. (**B**) Representative plot (means ± SDs) of four independent measurements in technical tetraplicates documenting mitochondrial respiration of A2780 cells expressed as oxygen consumption rate (%). First the basal respiration of A2780 adhering overnight was measured, then **C0**-**C3** or DMSO were injected and the respiration was followed for 2 hours Then mitochondrial stress was induced by sequential addition of 1 μM oligomycin, 1 μM carbonyl cyanide-4-(trifluoromethoxy)phenylhydrazone (FCCP) and 1 μM rotenone and antimycin A.
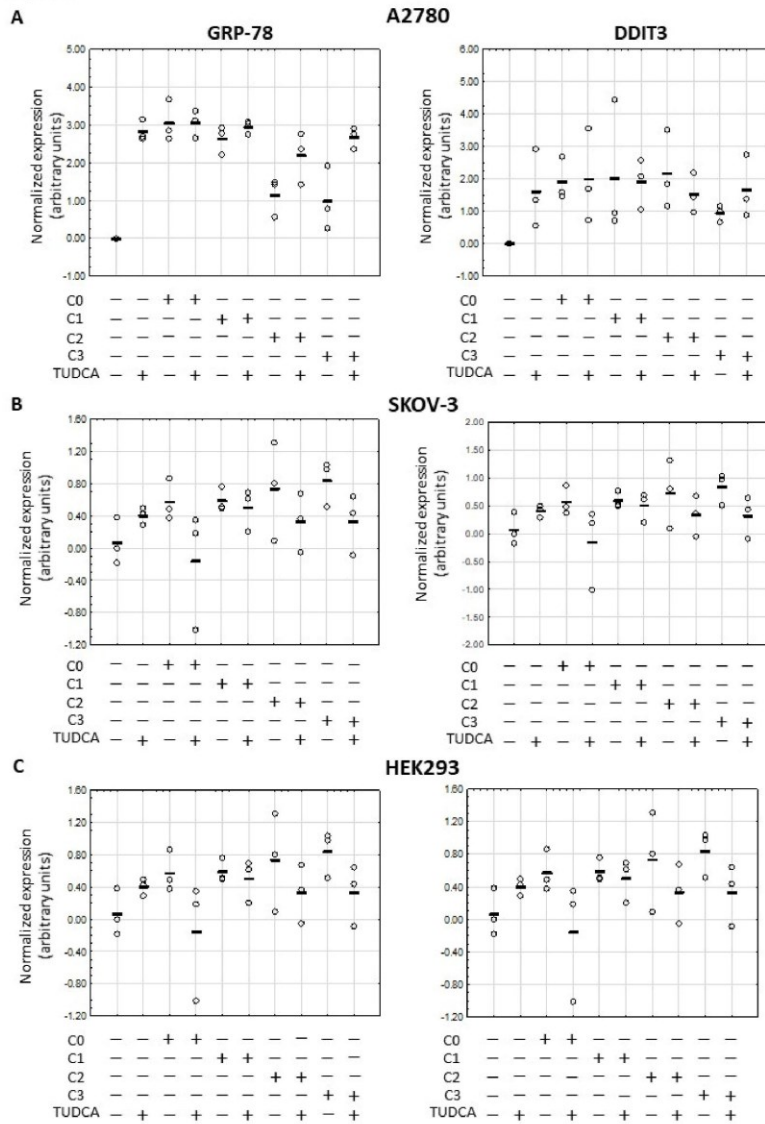
Fig. S4. Expression of GRP-78 and DDIT3 in (**A**) A2780, (**B**) SKOV-3 and (**C**) HEK293 cells. Briefly, cells were treated with **C0-C3** or DMSO and/or TUDCA for 24 hrs. The RNA was extracted, reversely transcribed and used as template for GRP-78 and DDIT3-specific qPCR. Glyceraldehyde 3-phosphate dehydrogenase (GAPDH) was used as housekeeping gene control. GAPDH-normalized expression from three independent experiments (open circles) is expressed in log scale. Line represents a mean value.

Fig. S5
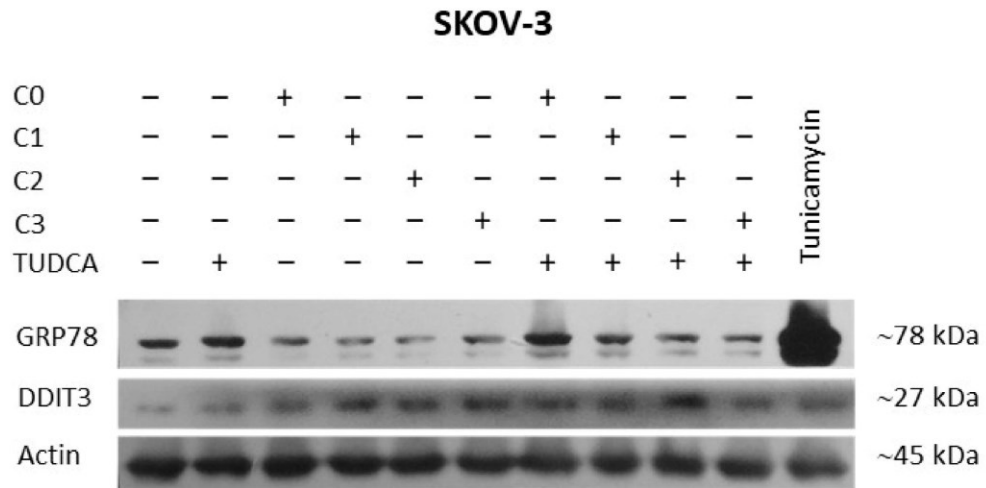
Fig. S5. Protein levels of GRP-78 and DDIT3 in SKOV-3 cells treated for 24 hrs. by **C0-C3** or TUDCA as documented by immunoblotting. Actin was used as a control of equal loading.

Fig. S6.

A

B
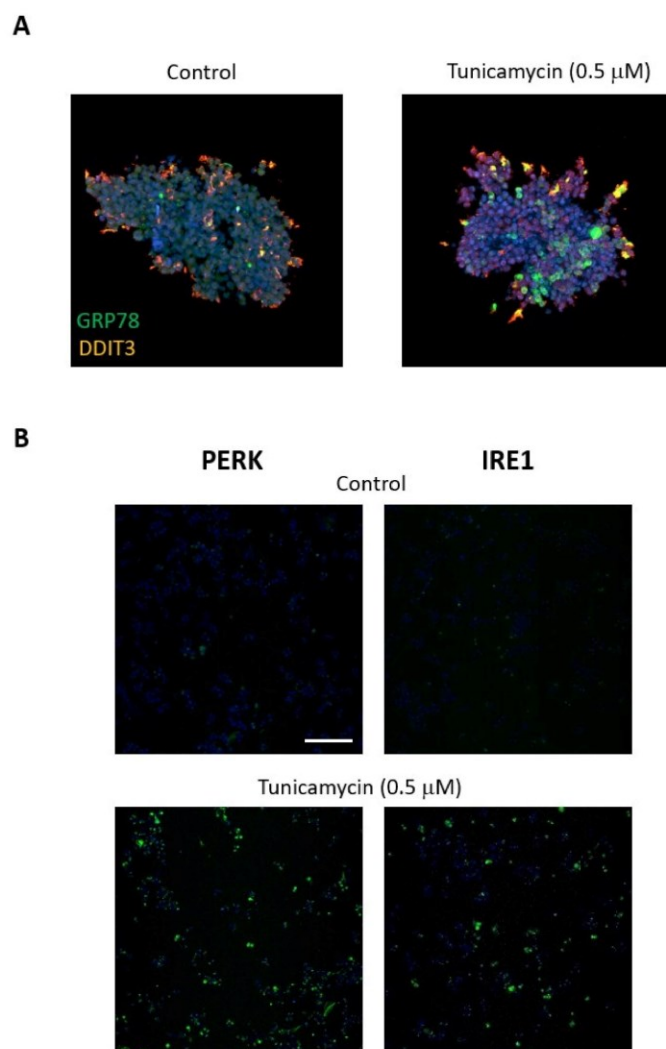
Fig. S6. (**A**) Upregulation of PERK and IRE1 activities in A2780 transfected with PERK and IRE1 fluorescent reporters upon treatment by 0.5μM tunicamycin as documented by fluorescent microscopy. (**B**) 3D spheroids were derived from A2780 cell, treated with 0.5 μM tunicamycin and analyzed by immunofluorescent microscopy for expression of GRP-78 and DDIT3 proteins. GRP-78 and DDIT3 are visualized by the green and red signal, respectively. Nuclei (blue) are visualized by Hoechst staining. The scale bars indicate 200 μm.

Results and discussion

Article 3.

The first copper(II) complex with 1,10-phenanthroline and salubrinal with interesting biochemical properties

Check for updates

The first copper(II) complex with 1,10-phenanthroline and salubrinal with interesting biochemical properties†

Sebastiano Masuri, [a] Enzo Cadoni, [a] Maria Grazia Cabiddu, [a] Francesco Isaia, [a] Maria Giovanna Demuru, [a] Lukáš Moráň, [bc] David Buček, [b] Petr Vaňhara, [bc] Josef Havel [cd] and Tiziana Pivetta ★[a]

The novel copper complex [Cu(phen)₂(salubrinal)](ClO₄)₂ (**C0SAL**) has been synthesised and characterised. Copper(II) is coordinated by salubrinal through the thionic group, as shown by the UV-Vis, IR, ESI-MS and tandem mass results, together with the theoretical calculations. The formed complex showed a DPPH radical scavenging ability higher than that of salubrinal alone. Studies on lipid oxidation inhibition showed that the **C0SAL** concentration, required to inhibit the enzyme, was lower than that of salubrinal. The inhibition of the enzyme could take place *via* allosteric modulation, as suggested by docking calculations. **C0SAL** showed a good cytotoxic activity on A2780 cells, 82 fold higher than that of the precursor salubrinal and 1.4 fold higher than that of [Cu(phen)₂(H₂O)](ClO₄)₂. Treatment with **C0SAL** in SKOV3 ovarian cancer cells induced expression of GRP-78 and DDIT3 regulators of ER-stress response. The cytotoxic effect of **C0SAL** was reverted in the presence of TUDCA, suggesting that **C0SAL** induces cell death through ER-stress. In A2780 cells treated with **C0SAL** γ-H2AX was accumulated, suggesting that DNA damage was also involved.

Significance to metallomics

Copper compounds, alone or in combination with other drugs, are promising anticancer agents. In a test on cancer cells treated with combinations of the ER stress antioxidative agent salubrinal and Cu(phen)₂(H₂O)(ClO₄)₂, we observed a modulatory effect that pushed us to verify a possible chemical interaction between the two molecules. A new compound was hypothesized and prepared showing that the introduction of the antioxidant salubrinal in the [Cu(phen)₂] core leads to a new molecule with high free radical scavenging activity and with the ability to attenuate *in vitro* lipid peroxidation. The new compound was tested on A2780 and SKOV3 cells and the results may be exploited to enlarge the therapeutical portfolio of metal complexes as antitumoral drugs. This research is a cross-disciplinary study involving metallobiochemistry, pharmacology, medicine, and toxicology, and can provide a better understanding of the mechanisms of action of potential copper anticancer drugs, giving useful insights into the design of new active species.

Introduction

At present days cancer represents one of the main causes of death in industrialized society. With the term "cancer", we refer to a wide range of diseases that share some common traits, such as the abnormal proliferation of cells resulting in the growth of tissue masses, known as tumours. Since the

[a] Dipartimento di Scienze Chimiche e Geologiche, Università degli Studi di Cagliari, Cittadella Universitaria, 09042 Monserrato, CA, Italy. E-mail: tpivetta@unica.it
[b] Department of Histology and Embryology, Faculty of Medicine, Masaryk University, Brno, Czech Republic
[c] International Clinical Research Centre, St. Anne's University Hospital, Brno, Czech Republic
[d] Department of Chemistry, Faculty of Science, Masaryk University, Brno, Czech Republic
† Electronic supplementary information (ESI) available. See DOI: 10.1039/d0mt00006j

discovery of the cytotoxic activity of cisplatin, several metal complexes have been proposed as antitumor agents with good potential biological activity and less side effects. Copper(II) has attracted much attention because of its ubiquity as a cofactor of several enzymes and proteins,[1] and, since copper complexes with 1,10-phenanthroline (phen) were able to cleave DNA acting as chemical nucleases,[2] several complexes containing nitrogen donor ligands have been designed and evaluated as anticancer agents. Previous studies evidenced how copper(II)-phenanthroline based complexes and in particular [Cu(phen)₂(H₂O)](ClO₄)₂ (**C0**, Fig. 1) induce massive cell death in both solid and haematological human tumour cells.[3–8] The involved molecular mechanism has been partially unveiled in a recent study where it has been evidenced how these compounds induce the pro-apoptotic branch of Unfolded Protein Response (UPR).[9] UPR is a coordinating adaptive program that responds to accumulation of incorrectly

Abstract

Preliminary *in-vitro* results on **C0** with ER-stress modulator Salubrinal (**SAL**, **Figure 5A**) have shown how the anticancer potency of this Cu(II) complex is tuneable according to the concentrations of both compounds. Considering that Salubrinal shares with imidazolidine-2-thione a thioamide moiety, I deemed interesting to investigate on the reactivity between these two compounds. As a results, a novel ternary Cu(II) complex named **C0SAL** (molecular formula: $[Cu(phen)_2(SAL)](ClO_4)_2$, **Figure 5B**) has been isolated at solid state, and its structure has been hypothesized by merging results from different experimental (Vis-NIR, FT-IR, MS) and computational (DFT) techniques.
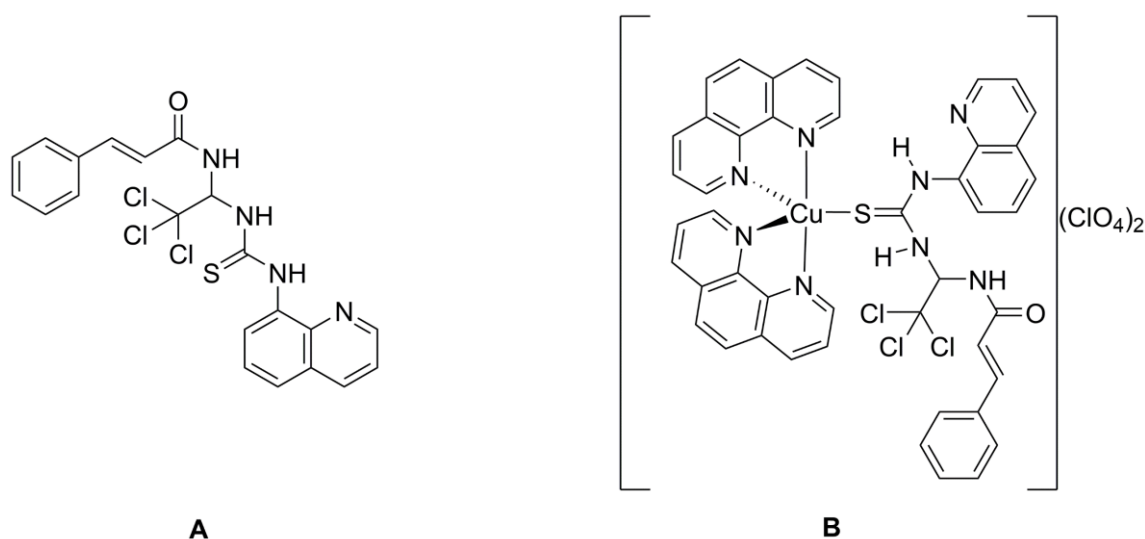
Figure 5. Molecular structures of **SAL** (**A**) and **C0SAL** (**B**)

Interestingly, the cytoprotective ability of **SAL** on ovarian (A-2780, SKOV-3) cancer cells is reverted when complexed to the $[Cu(phen)_2]^{2+}$ core, as in **C0SAL**, which is more potent (1.4-fold more) than parent compound **C0**. The cytotoxicity of **C0SAL** is alleviated in co-presence of TUDCA, thus suggesting that cell death undergoes though UPR activation, as further confirmed by the expression of typical markers such as BiP and CHOP. Moreover, cellular

DNA damage was observed, in different extent according to the cell line considered, by the accumulation of the phosphorylated histone γ-H2AX (**Figure 6**).[*]
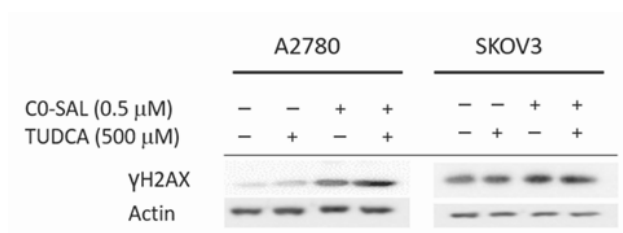
Figure 6. Intracellular levels of phosphorylated histone γ-H2AX after **C0SAL** treatment on A-2780 and SKOV-3 cells

The novel Cu(II) complex possess also higher antioxidant and lipoxygenase inhibitory potencies compared to the parent compounds **C0** and **SAL**.

---

[*] These studies were performed in collaboration with the research group of Prof. Petr Vaňhara, Masaryk University (MUNI).

The first copper(II) complex with 1,10-phenanthroline and salubrinal with interesting biochemical properties

Sebastiano Masuri[1], Enzo Cadoni[1], Maria Grazia Cabiddu[1], Francesco Isaia[1], Maria Giovanna Demuru[1], Lukáš Moráň[2,3], David Buček[2], Petr Vaňhara[2,3], Josef Havel[3,4], Tiziana Pivetta[1, *]

[1]Department of Chemical and Geological Sciences, University of Cagliari, Cittadella Universitaria, Monserrato, Cagliari, Italy.

[2]Department of Histology and Embryology, Faculty of Medicine, Masaryk University, 62500, Brno, Czech Republic.

[3]International Clinical Research Center, St. Anne's University Hospital, 65691, Brno, Czech Republic.

[4]Department of Chemistry, Faculty of Science, Masaryk University, 62500, Brno, Czech Republic.

* Corresponding author: tpivetta@unica.it

The first copper(II) complex with 1,10-phenanthroline and salubrinal with interesting biochemical properties†

Sebastiano Masuri, [a] Enzo Cadoni, [a] Maria Grazia Cabiddu, [a] Francesco Isaia, [a] Maria Giovanna Demuru, [a] Lukáš Moráň, [bc] David Buček, [b] Petr Vaňhara, [bc] Josef Havel [cd] and Tiziana Pivetta [*a]

The novel copper complex [Cu(phen)$_2$(salubrinal)](ClO$_4$)$_2$ (**C0SAL**) has been synthesised and characterised. Copper(II) is coordinated by salubrinal through the thionic group, as shown by the UV-Vis, IR, ESI-MS and tandem mass results, together with the theoretical calculations. The formed complex showed a DPPH radical scavenging ability higher than that of salubrinal alone. Studies on lipid oxidation inhibition showed that the **C0SAL** concentration, required to inhibit the enzyme, was lower than that of salubrinal. The inhibition of the enzyme could take place via allosteric modulation, as suggested by docking calculations. **C0SAL** showed a good cytotoxic activity on A2780 cells, 82 fold higher than that of the precursor salubrinal and 1.4 fold higher than that of [Cu(phen)$_2$(H$_2$O)](ClO$_4$)$_2$. Treatment with **C0SAL** in SKOV3 ovarian cancer cells induced expression of GRP-78 and DDIT3 regulators of ER-stress response. The cytotoxic effect of **C0SAL** was reverted in the presence of TUDCA, suggesting that **C0SAL** induces cell death through ER-stress. In A2780 cells treated with **C0SAL** γ-H2AX was accumulated, suggesting that DNA damage was also involved.

Significance to metallomics

Copper compounds, alone or in combination with other drugs, are promising anticancer agents. In a test on cancer cells treated with combinations of the ER stress antioxidative agent salubrinal and Cu(phen)$_2$(H$_2$O)(ClO$_4$)$_2$, we observed a modulatory effect that pushed us to verify a possible chemical interaction between the two molecules. A new compound was hypothesized and prepared showing that the introduction of the antioxidant salubrinal in the [Cu(phen)$_2$] core leads to a new molecule with high free radical scavenging activity and with the ability to attenuate in vitro lipid peroxidation. The new compound was tested on A2780 and SKOV3 cells and the results may be exploited to enlarge the therapeutic portfolio of metal complexes as antitumoral drugs. This research is a cross-disciplinary study involving metallobiochemistry, pharmacology, medicine, and toxicology, and can provide a better understanding of the mechanisms of action of potential copper anticancer drugs, giving useful insights into the design of new active species.

Introduction

At present days cancer represents one of the main causes of death in industrialized society. With the term "cancer", we refer to a wide range of diseases that share some common traits, such as the abnormal proliferation of cells resulting in the growth of tissue masses, known as tumours. Since the discovery of the cytotoxic activity of cisplatin, several metal complexes have been proposed as antitumor agents with good potential biological activity and less side effects. Copper(II) has attracted much attention because of its ubiquity as a cofactor of several enzymes and proteins,[1] and, since copper complexes with 1,10-phenanthroline (phen) were able to cleave DNA acting as chemical nucleases,[2] several complexes containing nitrogen donor ligands have been designed and evaluated as anticancer agents. Previous studies evidenced how copper(II)-phenanthroline based complexes and in particular [Cu(phen)$_2$(H$_2$O)](ClO$_4$)$_2$ (**C0**, Fig. 1) induce massive cell death in both solid and haematological human tumour cells.[3–8] The involved molecular mechanism has been partially unveiled in a recent study where it has been evidenced how these compounds induce the pro-apoptotic branch of Unfolded Protein Response (UPR).[9] UPR is a coordinating adaptive program that responds to accumulation of incorrectly

[a] Dipartimento di Scienze Chimiche e Geologiche, Università degli Studi di Cagliari, Cittadella Universitaria, 09042 Monserrato, CA, Italy. E-mail: tpivetta@unica.it

[b] Department of Histology and Embryology, Faculty of Medicine, Masaryk University, Brno, Czech Republic

[c] International Clinical Research Centre, St. Anne's University Hospital, Brno, Czech Republic

[d] Department of Chemistry, Faculty of Science, Masaryk University, Brno, Czech Republic

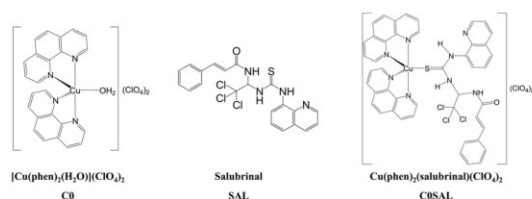† Electronic supplementary information (ESI) available. See DOI: 10.1039/d0mt00006j

Fig. 1 Molecular structures and acronyms of the studied compounds.

processed proteins in the endoplasmic reticulum (ER), a condition known as ER stress. The final cell response is dependent on a specific activity of individual pathways and can lead to adaptation or apoptosis, especially when ER stress is prolonged or severe. Many pieces of evidence indicate that ER stress is involved also in the pathogenesis of misfolded protein diseases and in the cytotoxicity of environmental pollutants and industrial chemicals.[10,11]

Salubrinal ((2E)-3-phenyl-N-[2,2,2-trichloro-1-[[(8-quinolinyl-amino)thioxomethyl]amino]ethyl]2-propenamide, **SAL**, Fig. 1) was discovered in an attempt to identify novel cytoprotective compounds that protect PC12 rat pheochromocytoma cells from ER stress-mediated apoptosis, induced by the N-glycosylation inhibitor Tunicamycin.[12] During UPR, dissociation of BiP (GRP 78) activates PERK (protein kinase RNA (PKR)-like ER kinase), an ER-resident transmembrane protein that phosphorylates eIF2α (eukaryotic Initiation Factor 2, subunit α), in order to arrest protein synthesis under ER Stress. **SAL** proved to possess cytoprotective activity preventing eIF2α dephosphorylation. Although the precise molecular mechanism has not been completely clarified yet, **SAL** is thought to interfere with the sequestration of eIF2α by the protein complex GADD34-PP1 (Protein phosphatase 1).[12,13]

Interestingly, studies of **C0** and variously substituted imid-azolidine-2-thione[3] complexes with the general formula [Cu(phen)₂L](ClO₄)₂ revealed a synergistic cytotoxic effect in combination with **SAL**. In particular, an enhanced upregulation in the expression of CHOP (DDIT3) as well as BiP (GRP78) was detected. From these results and considering that **SAL** has a backbone resembling the imidazolidine-2-thione structure, we deemed if **C0** and **SAL** were able to interact from a chemical point of view. The reactivity of the two molecules was studied and the formation of a complex between **C0** and **SAL**, named **C0SAL** (Fig. 1), was observed. The coordination mode, the stability constant, the interaction with specific proteins, and the cytotoxic properties of the formed complex were studied. Moreover, the free radical scavenging activity as well as the in vitro inhibitory activity against soybean lipoxygenase of the new complex was measured and compared with that of the precursors **C0** and **SAL**. Combination studies with tauroursodeoxycholic acid (TUDCA) indicated the induction of ER-stress as the driving mechanism of cell death caused by **C0SAL**.

Materials and methods

Reagents

Acetonitrile, methanol, isopropanol, dimethyl sulfoxide (DMSO), tetrahydrofuran (THF), acetone, absolute ethanol, sodium linoleate, lipoxygenase, butylated hydroxytoluene (BHT) and tris (hydroxy-methyl) aminomethane hydrochloride (TRIS) were purchased from Merck (Milan, Italy). Toluene, potassium thiocyanate, copper(II) carbonate hydroxide and thionyl chloride were purchased from Alfa-Aesar. Trans-Cinnamamide and chloral hydrate were purchased from TCI. 3-(4,5-Dimethylthiazol-2-yl)-2,5-diphenyltetrazolium bromide (MTT) was purchased from Sigma-Aldrich (Czech Republic). The commercial reagents were used as received, without any further purification. Ultrapure water was obtained from MilliQ Millipore. THF was distilled from sodium/benzophenone.

NMR

^{1}H NMR spectra were recorded on a Bruker Advance III HD 600 spectrometer at room temperature with tetramethylsilane (TMS) as the internal standard in DMSO-d₆. Chemical shifts, multiplicity and coupling constants were reported.

Mass spectrometry studies

Mass spectra were recorded using a triple quadrupole QqQ Varian 310-MS mass spectrometer using the atmospheric-pressure ESI technique. The sample solutions were infused directly into the ESI source using a programmable syringe pump at a flow rate of 1.25 mL h⁻¹. A dwell time of 14 s was used, and the spectra were accumulated for at least 10 min in order to increase the signal-to-noise ratio. Mass spectra were recorded in the m/z 100–1200 range. The experimental conditions were: needle voltage 3500 V, shield 800 V, source temperature 60 °C, drying gas pressure 20 psi, nebulizing gas pressure 20 psi, detector voltage 1450 V. Tandem MS experiments were performed using argon as the collision gas (1.8 psi). The collision energy was varied from 5 to 40 V. The isotopic patterns of the measured peaks in the mass spectra were analysed using the mMass 5.5.0 software package.[14,15] High resolution mass spectra were recorded on a Thermofisher ESI-MS/MS-ORBITRAP-ELITE and Velos PRO. The sample solutions were infused directly into the ESI source using a programmable syringe pump at a flow rate of 5 μL min⁻¹. Mass spectra were recorded in the m/z 700–950 range. The experimental conditions were: needle voltage 2.5 kV, shield 0.8 kV, source temperature 50 °C, drying gas pressure 20 psi, nebulizing gas pressure 20 psi, detector voltage 1.3 kV.

Spectrophotometric studies

UV-Visible spectrophotometric measurements were performed in the 200–1100 nm range on an Agilent Cary 60 spectro-photometer, using a 1 cm quartz cell at 25 °C. The formation constant for the complex formed between **C0** and **SAL** was determined at 25 °C by spectrophotometric titration in aceto-nitrile solution in 0.05 M NaClO₄ ionic buffer. The number of linearly independent absorbing species was obtained by applying eigenvalue analysis on the absorbance data matrix. The complex formation constant, expressed as the overall association constant, was calculated using the Hyperquad 2006 program.[16] The stoichio-metry of the formed complex was also studied by the continuous variation method (Job's plot).[17,18] IR spectra were acquired using a Bruker Vector 22 spectrophotometer, preparing the samples as KBr pellets.
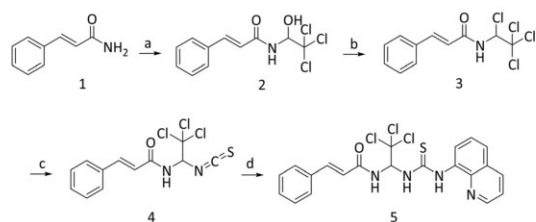
Scheme 1 *Reagents and conditions*: (a) chloral hydrate, toluene, r.f. 4 h; (b) SOCl₂, dry THF, r.f. 2 h; (c) KSCN, acetone, r.f. 2 h; (d) quinolin-8-amine, dry THF, r.f. 2 h.

Synthesis of salubrinal (SAL)

SAL was synthesized according to a reported method[19] with modifications required to increase the purity of the final product. The synthetic pathway is reported in Scheme 1.

In brief, toluene (136 mL) was added to the mixture of cinnamamide (**1**, 6.8 mmol) and chloral hydrate (6.8 mmol). The mixture was left under reflux for 4 h. After cooling, the white crystalline solid **2** was precipitated, filtered and dried. The solid (**2**) was dissolved in dry THF (20 mL) and chlorinated by reflux with SOCl₂ (25.8 mmol) for 2 h. The yellow solid (**3**) was obtained by evaporating the solvent and washing with cold petroleum ether. By refluxing with potassium thiocyanate (8.4 mmol) in acetone (18 mL) for 2 h, it was transformed to isothiocyanate (**4**). The title compound was used as crude and refluxed in dry THF (8.4 mL) with quinolin-8-amine (4.2 mmol) for 2 h. After solvent evaporation the residue was washed with dichloromethane to obtain **5** as a white powder. This last product was then suspended and stirred in distilled water to dissolve the soluble thiocyanate. The white solid was recovered by filtration under vacuum and Fe(III) solution (1 mM) was added to the supernatant to check the formation of the red compound $[Fe(SCN)_6]^{3+}$. The washing procedure was repeated until the supernatant solution stayed colourless upon the addition of the iron solution. The recovered solid was washed with ethyl ether and dried. The yield was 75%.

(2*E*)-3-Phenyl-*N*-[2,2,2-trichloro-1-[[(8-quinolinylamino)thioxomethyl]amino]ethyl]-2-propenamide, SAL (5). Spectroscopic data were consistent with those reported in the literature.[19] ESI-MS, *m/z* found: 479.3 (calc. 479.0), $[M + H]^+$, with the expected isotopic pattern. ¹H-NMR (Fig. S1, ESI†) (600 MHz, DMSO d₆, δ, ppm): 11.03 (s, 1H), 9.58 (s, 1H), 9.04 (d, 2H, *J* = 7.76 Hz), 8.96 (dd, 1H, *J* = 4.40 Hz, *J* = 1.28 Hz), 8.43 (d, 1H, *J* = 8.14 Hz), 7.72 (d, 1H, *J* = 7.02 Hz), 7.66 (q, 1H, *J* = 4.05 Hz), 7.56–7.61 (m, 5H), 7.39–7.45 (m, 3H), 6.91 (d, 1H, *J* = 15.70 Hz). Elemental analysis: expected C 52.57, H 3.57, N 11.68, found C 52.53, H 3.61, N 11.70.

Synthesis of Cu(II)-phenanthroline complexes

C0. The precursor $[Cu(phen)_2(OH_2)](ClO_4)_2$ (**C0**) was prepared as previously described.[3] In brief, perchloric acid was added to an ethanolic suspension of $Cu_2(CO_3)(OH)_2$. The resulting solution was cooled and an ethanolic solution of 1,10-phenanthroline (1:2 Cu:phen molar ratio) was added. The formed blue-green

precipitate was filtered off, washed with ethanol and dried at room temperature (yield 85%). **C0SAL:** $[Cu(phen)_2(SAL)](ClO_4)_2$ was prepared as follows: **SAL** (white in colour, 0.067 mmol) was suspended in 4.0 mL of 2-propanol and slowly added to a suspension of **C0** (blue in color, 1 eq.) in 4.0 mL of 2-propanol. The reaction mixture was stirred at room temperature for 24 hours to obtain a green powder. The desired product (**C0SAL**, 0.0490 g) was recovered by filtration in vacuum, washed with diethyl ether and dried. The yield was 66%. Elemental analysis: expected C 49.02, H 3.02, N 10.16, found C 49.12, H 3.00, N 10.12. ESI-MS. *m/z*, found (calc.): 1000.0 (1000.0) $[Cu(phen)_2(SAL)(ClO_4)]^+$, with the expected isotopic pattern. FT-IR (KBr), cm^{-1}: 1661 (C=O). UV-Vis (CH₃CN, NaClO₄ 0.05 M) log ε (λ, nm): 5.22 (268), 3.82 (289, sh).

Determination of the reducing activity of the stable radical 1,1-diphenyl-picrylhydrazyl (DPPH)

Each test compound was dissolved in DMSO at 1.0 mM concentration, and then a 1:10 dilution was performed with absolute ethanol. DPPH solution (0.1 mM, absolute ethanol) was prepared freshly, stored in the dark and used in a few hours. The test solution (1500 μL) was added to an equal volume of DPPH inside the cuvette and the absorbance in the 200–650 nm range was recorded at room temperature for 70 minutes. The absorbance at 517 nm was evaluated to examine the time-dependence of the radical scavenging activity (RA).[20,21] The RA of each compound was expressed as the percentage inhibition of the absorbance of the initial DPPH solution (RA%). BHT (butylated hydroxytoluene) was used as the reference compound.

Soybean lipoxygenase inhibition study *in vitro*

Stock solutions of **C0**, **SAL** and **C0SAL** were dissolved in DMSO at ≈0.1 mM concentration, and then a proper dilution was performed with Tris buffer at pH 7.4. Sodium linoleate (0.00200 g, *V* 10.0 mL, ≈0.65 mM) and soybean lipoxygenase (0.00200 g, *V* 10.0 mL, ≈2×10^{-6} M) were dissolved in Tris buffer at pH 7.4, and the required dilutions were performed with Tris buffer at pH 7.4. Solutions of sodium linoleate, soybean lipoxygenase and **SAL** were prepared daily and kept in the dark at 5 °C. The conversion of sodium linoleate to 13-hydroperoxylinoleic acid was monitored by recording the absorbance at 243 nm. The absorbance at 243 nm and not at 234 nm (maximum) was chosen since at 234 nm the contribution of **C0** or **C0SAL** absorbance was too relevant.

DFT calculations

The geometry optimization of **SAL** and the copper complexes $[Cu(phen)_2(H_2O)]^{2+}$ and $[Cu(phen)_2(SAL)]^{2+}$ was performed on an Intel-i7 based system using the release 4.2 of ORCA.[22] Input files for DFT calculations were prepared using Avogadro 1.2.0.[23] Geometry optimizations were performed at the DFT level, using the hybrid PBE0 functional[24] and def-2 TZVP basis set.[25] The molecular geometry optimizations were performed starting from structural data, when available. IR frequency calculations were carried out to verify the nature of the minima of each

optimization by assessing the absence of calculated negative frequencies. Atomic charges at the natural population analysis (NPA) level were calculated by means of the JANPA software package.[26] Molecular orbital shapes and energies were investigated using Chemcraft v1.8.[27]

Docking calculations

Molecular docking calculations were performed using Autodock Vina software.[28] DFT optimized ligands and Cu(II) complexes were exported as PDB files. The X-ray structure of the complex between soybean lipoxygenase LOX-3 and 3,4-dihydroxybenzoic acid (PDB:1N8Q) was chosen as the receptor.[29] Prior to docking, both ligands and receptor were processed using MG Labs Autodock Tools.[30] In the receptor crystal, water molecules and 3,4-dihydroxybenzoic acid (dhb) were removed, while polar hydrogens and Gasteiger charges were added. The atomic charge for the Fe2858 cofactor was manually adjusted in the generated pdbqt file. For all the ligands, polar hydrogens and Gasteiger charges were added, while no rotational constraints were applied. Atomic charges for copper were manually adjusted in the generated pdbqt files. Validation of the docking protocol was performed by docking ligand dhb into its binding pocket. A grid cube of $20 \times 20 \times 20$ points centred at coordinates $x = 21.287$, $y = 1.743$, $z = 19.171$ with a spacing of 1.0 Å was chosen for this purpose. All the tested compounds were docked as competitive inhibitors or allosteric modulators. In the first case, docking calculations were performed using the parameters reported above. In the second case, a grid box of $30 \times 25 \times 20$ points centred at coordinates $x = 24.970$, $y = 11.444$, $z = -0.396$ with a spacing of 1.0 Å was chosen. Molecular interactions and docked poses were evaluated using Biovia Discovery Studio Viewer v19 (free version).[31]

Viability assay

Cells were cultured for 24 h on a 96-well plate at a density of 10 000 cells per well in medium containing **C0** and **SAL** either alone or in combination, or **C0SAL**, at the indicated concentrations. The respective solvents were used as controls. Then, the MTT reagent was added directly to the culture medium for 4 h. The medium, including the MTT reagent, was aspirated and the cells were lysed by the addition of 90% isopropanol, 0.04 M HCl and 10% Triton/Tween. Absorbance was recorded at 570 nm by using a Synergy HTX multi-mode reader (BioTek Instruments, VT, USA). All the measurements were repeated five times and in three independent experiments.

Transmission electron microscopy (TEM)

Cells treated by **SAL** were harvested using trypsin–EDTA, washed with PBS, fixed in 3% glutaraldehyde with 0.2% tannin in 0.1 M cacodylate buffer for 1 hour, and postfixed in 1% OsO_4 in the same buffer for 50 min. After post-fixation, cells were washed three times with cacodylate buffer and embedded in small blocks of 1% agar, 1 mm³ in size. Agar blocks were dehydrated in increasing concentrations of ethanol (50%, 70%, 96%, and 100%), treated 2×10 min with 100% acetone, and embedded in Durcupan resin. Ultrathin sections were prepared on a Leica EM UC6 ultramicrotome, stained with uranyl acetate and Reynold's lead citrate, and examined with a FEI Morgagni 286(D) TEM. One hundred cells from each experimental group were examined. Cytological analysis of TEM images was performed by two independent reviewers (PV, LM).

Immunofluorescence measurements

Cells were washed three times in $1 \times$ PBS (pH 7.4), fixed in 4% paraformaldehyde for 15 min at room temperature, washed with $1 \times$ PBS containing 3% BSA and 0.1% Triton X-100 and incubated with DDIT3 (#2895) or GRP-78 (#3177) antibodies (both from Cell Signaling, MA, USA), diluted 1 : 200 at 4 °C overnight. Immunofluorescence signals were obtained using Alexa Fluor conjugated secondary antibodies (AF488, cat. no. A32731 or AF568, cat. no. A11004, both from Life Technologies, USA), diluted 1 : 2000. Cell nuclei were visualized by DAPI staining (Life Technologies, USA). Immunofluorescence was recorded using Zeiss Axio Observer Z1 microscope equipped with a LSM800 confocal unit.

SDS-PAGE and western blotting

Trypsinised cells were washed two times with ice-cold $1 \times$ PBS and resuspended in NP-40 lysis buffer containing 50 mM Tris–Cl (pH 7.4), 150 mM NaCl, 2 mM EDTA, 1% NP-40, 50 mM NaF supplemented with phosphatase inhibitor cocktail (PhosStop, Roche Applied Science, Czech Republic) and protease inhibitor cocktail (complete, Roche Applied Science, Czech Republic). The protein content in the cell extract was quantified using the Bradford-based BioRad protein Assay Kit (BioRad). Cell extracts were then mixed with $2 \times$ Laemmli sample buffer (100 mM Tris pH 6.8, 4% SDS, 200 mM DTT, 20% glycerol, and 0.1% bromophenol blue) and boiled for 3 min. An equivalent of 15 mg proteins was resolved using 10% sodium dodecyl sulfate polyacrylamide gel electrophoresis (SDS-PAGE). Resolved proteins were then electroblotted onto a 0.45 mm polyvinylidene difluoride (PVDF) membrane (Millipore, Czech Republic) and incubated with the indicated primary antibodies diluted 1 : 200–1 : 1000 at 4 °C overnight (Actin, cat. no. CST13E5 from Cell Signaling, MA, USA, and γ-H2AX, cat. no. ab81299 from Abcam, UK). Blots were developed using horseradish peroxidase (HRP)-conjugated anti-rabbit HRP #7074 (Cell Signaling, USA) secondary antibody, diluted 1 : 5000, and Immobilon Western HRP Substrate (Millipore, Czech Republic), according to the manufacturer's protocols.

Results and discussion

Synthesis

Salubrinal. SAL was initially synthesized according to the reported method;[19] however unreacted thiocyanate was evidenced in the IR spectrum of the obtained product (see ESI,† Fig. S2). This issue was observed even when changing the reaction conditions such as time and thiocyanate amount. The washing procedure reported in the Experimental section allowed the complete removal of the former impurity, as confirmed by IR spectroscopy (Fig. S3B, ESI†). **SAL** is soluble in DMSO and CH_3CN up to 10^{-1} M

and 4.0 mM concentrations respectively. **SAL** could be also solubilized in $CH_3CN:H_2O$ (1:1 mixture) up to 0.5 mM level. The solubility of **SAL** in H_2O and Tris might be enhanced by dissolving the title compound in DMSO prior to dilution. In this case, sonication and vigorous mixing should be avoided in order to prevent the formation of emulsions. **SAL** solutions prepared in pure DMSO or CH_3CN are stable at r.t. for 48 hours, while $DMSO:H_2O$ and $DMSO:Tris$ solutions are stable at r.t. up to 6 hours. A change of the solution appearance (from colourless to yellow) and the development of sulphurous smell were observed for longer storage periods.

C0SAL copper complex. By the reaction between **C0** and **SAL** in the proper molar ratio, the novel complex $[Cu(phen)_2(SAL)](ClO_4)_2$ (**C0SAL**) was obtained by substitution of the water with a **SAL** molecule into the metal core. The chemical formula of the novel complex has been proposed on the basis of elemental analysis, Job's plot (see the section Spectrophotometric studies) and ESI-MS spectrometry. In the ESI-MS spectrum of $[Cu(phen)_2$-$(SAL)](ClO_4)_2$ (Fig. 2A) a peak at 1000 m/z due to the $[Cu(phen)_2$-$(SAL)(ClO_4)]^+$ species was observed, as a charged fragment of the neutral precursor $[Cu(phen)_2(SAL)](ClO_4)_2$. In addition, a peak at 450.5 m/z due to the doubly charged ion $[Cu(phen)_2(SAL)]^{2+}$ was highlighted. Several fragments containing the deprotonated **SAL**, originated in ESI phase by loss of $HClO_4$, together with Cu(I) complexes, were observed in the mass spectrum (the reduction of Cu(II) to Cu(I) is widely observed in ESI phase, depending on the solvent[32]). The identity of the reported ions was confirmed by matching between calculated and experimental isotopic patterns (Fig. S4, ESI†) and tandem mass experiments (see Mass spectrometry). The mass spectrum was also recorded at high resolution in the 700–950 m/z range (Fig. 2B), to determine the exact masses for the peaks at 720 and 900 m/z and confirm the proposed chemical formula. As can be seen in Fig. 2C, the fitting of the isotopic pattern and the matching of the experimental exact masses with those calculated (720.0096 u *versus* 720.0094 u and 900.0776 u *versus* 900.0781 u) confirm the proposed stoichiometry. The formed copper complex is stable in the solid state at room temperature, without particular precautions. It is soluble in DMSO at the 0.1 M concentration level, in CH_3CN at 0.01 M, and in the $H_2O:CH_3CN$ mixture (1:1) at 0.1 mM. Solubility in water and ethanol might be enhanced by dissolving the title compound in DMSO at 1.0 mM prior to dilution at the desired concentrations.

C0SAL is also soluble in Tris buffer by dissolving it in DMSO at 0.1 mM prior to dilution. In this case, sonication or vigorous mixing should be avoided while performing dilutions, in order to prevent the formation of emulsions. Stock solutions of **C0SAL** in DMSO and CH_3CN are stable at 4 °C up to 6 months. Stock solutions in $H_2O:CH_3CN$, $DMSO:H_2O$, $DMSO:EtOH$ and $DMSO:Tris$ could be stored at r.t. for 48 h, but should be prepared daily and stored in the darkness for enzymatic and antioxidant assays. The absorption spectra of **C0SAL** in DMSO: Tris (0.5:99.5) after 0 and 48 h are shown in the ESI† (Fig. S21). In order to check the stability of **C0SAL** in a medium similar to the aqueous one, the former compound was dissolved in the $H_2O:CH_3CN$ (1:1) mixture at 25 µM concentration and spectral variation in the 200–400 nm range was followed for 24 h by recording 1 spectrum every 60 minutes (Fig S5A, ESI†). No significant variations were observed at both maxima levels (225 and 269 nm respectively).

Spectrophotometric studies

To determine the number and the stoichiometry of the complex formed between **C0** and **SAL**, the method of continuous variation (Job's method) was applied.[17,18] Absorption spectra were collected by varying the ligand molar fraction from 0 to 1 (Fig. S6A, ESI†). Absorbance data at 966 and 722 nm, corrected for the absorbance of the pure reactants, reported as a function of the ligand molar fraction (Fig. S6B, ESI†), clearly indicate a 1:1 ($\chi_L = 0.5$) ligand to metal complex. Once the complexation model was defined, the complex formation constant was determined by spectrophotometric titration. Equilibrium studies of **C0** and **SAL** were carried out in acetonitrile in the 200–400 nm range. In Fig. S7 (ESI†) selected spectra recorded during the titration of **SAL** with **C0** and of **C0** with **SAL** are reported as an example. By adding increasing amounts of **SAL** (Fig. S7A, ESI†) or **C0** (Fig. S7B, ESI†), new absorption bands were evidenced, a feature consistent with an interaction altering the solvated cationic core. Isosbestic points appeared during the titration, providing evidence for at least one equilibrium. From eigenvalue analysis of the spectrophotometric data, three significant eigenvalues were found, indicating three linearly independent absorbing species in solution. By fitting the experimental data considering the species $[Cu(phen)_2]^{2+}$, **SAL** and $[Cu(phen)_2(SAL)]^{2+}$, the complex formation constant expressed as $\log \beta$ was determined (5.10 ± 0.07). As can be seen in Fig. S7 (ESI†),

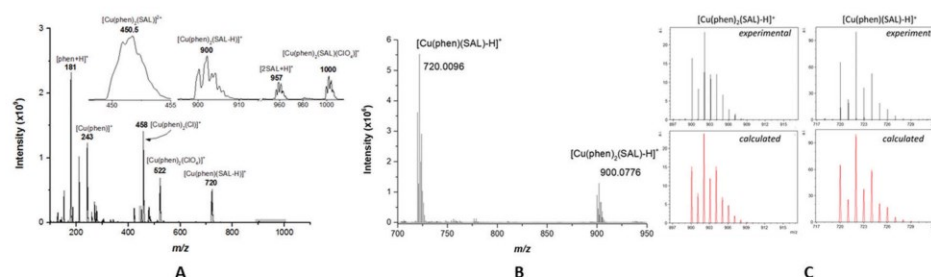Fig. 2 (A) ESI-MS spectrum of **C0SAL** $[Cu(phen)_2(SAL)](ClO_4)_2$, (B) high resolution mass spectrum in the 700–950 m/z range, (C) experimental and calculated isotopic pattern for peaks at 700 and 900 m/z (isopropanol:methanol:water 2:1:1).

the spectral variations are different in the two titrations, but in both the cases they are in agreement with a 1:1 model, *i.e.* with the formation of the complex $[Cu(phen)_2(SAL)]^{2+}$.

Coordination mode in C0SAL

Since any attempt to obtain single crystals suitable for X-ray analysis was unsuccessful, coordination mode around the metal ion for the novel **C0SAL** complex was proposed by combining the experimental data, UV-Vis, IR, ESI-MS and tandem MS spectrometry, with the theoretical calculations.

UV-Vis. The UV-Vis spectrum of **C0SAL** in the region between 400 and 1100 nm (Fig. S5B, ESI†) features a maximum at 714 nm and a shoulder at 914 nm. A penta-coordinated geometry might be proposed also for **C0SAL**, in agreement with the absorption spectra of variously substituted $[Cu(phen)_2(imidazolidine-2-thione)](ClO_4)_2$ complexes.[3] See for comparison the UV-Vis spectrum of **C0** (Fig. S6A, black line, ESI†), where two wide bands with similar heights are present, typical of an octahedral coordination mode around the copper ion[33] (in this case, the sixth position around the metal centre is occupied by a solvent molecule[34]).

IR. From the comparison of the IR spectra of **C0SAL** (Fig. S3C, ESI†) with the parent compounds **C0** (Fig. S3A, ESI†) and **SAL** (Fig. S3B, ESI†), the coordination of the **SAL** carbonyl oxygen to the metal centre might be excluded, since there is no significant shift in its stretching signal (1660 cm^{-1}) upon complexation. Univocal attribution of thiocarbonyl, amidic and thioamidic NH groups of **SAL**, already difficult by the overlapping of skeletal backbone frequencies, becomes more complicated in **C0SAL** by the concomitant presence of the phen signals (1000–500 cm^{-1}). The wide peak at 1100 cm^{-1}, present in **C0** and **C0SAL**, is due to the perchlorate anions.

Mass spectrometry. Tandem MS experiments at different collision energies (CE) were performed to define the identity of all the peaks relative to species containing copper, phenanthroline and **SAL** and to finally hypothesise the structure of the parent compound **C0SAL**. Since **SAL** has several coordinating atoms, all the possible resulting structures for **C0SAL** were considered; however only one could explain the fragmentation pathways observed during the tandem mass experiments. As regards the bi-charged ion $[Cu(phen)_2(SAL)]^{2+}$ (m/z 450.5), at CE 5.0 V two fragments were originated, at 181 m/z ($[phen + H]^+$) and 720 m/z ($[Cu(phen)(SAL-H)]^+$) (Fig. 3), and this fragmentation process might occur under the pathway depicted in Fig. S8A (ESI†): *i.e.* the amidic proton on the **SAL** moiety is transferred to one phen molecule with subsequent nucleophilic attack by the deprotonated nitrogen to the metal centre. The proposed coordination mode for the 720 m/z fragment is well reasonable since (i) the amidic proton of the **SAL** moiety is more acidic than the thioamidic ones and more prone to be transferred to one of the phen molecules, (ii) the former deprotonation brings to a stable 6-membered metal chelated ring (a comparable mechanism was previously proposed for similar copper-phenanthroline complexes[6]). As can be observed in Fig. 3, as CE increased, a gradual decrease in the intensity of the peak at 720 m/z is observed, until its complete disappearance at CE = 20 V. In contrast, an increase in
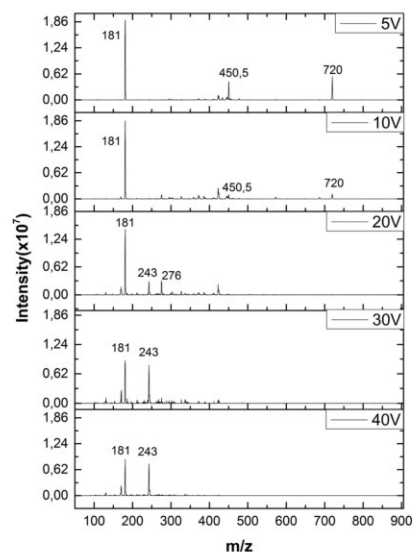
Fig. 3 Tandem MS fragmentation at different collision energies of the peak at 450.5 m/z ($[Cu(phen)_2(SAL)]^{2+}$). All the mass values are indicated as monoisotopic masses, computed as the sum of the masses of the primary isotope of each atom in the molecule (note that the monoisotopic mass may differ from the nominal molecular mass, in particular for big molecules).

intensity for peaks at 276 m/z $[Cu(phen)(SH)]^+$ and 243 m/z $[Cu(phen)]^+$ is observed. This behaviour is consistent with an additional fragmentation of the ion with 720 m/z. The proposed fragmentation patterns are reported in the ESI† (Fig. S8B and C, ESI†). Tandem MS fragmentation of 720 m/z ($[Cu(phen)(SAL-H)]^+$) and that of 900 m/z ($[Cu(phen)_2(SAL-H)]^+$) (Fig. S9, ESI†) follow a similar pattern. In particular, 900 m/z is generated as a rearrangement product in ESI phase, while 720 m/z comes both from 900 m/z by loss of one phen unit (Fig. S10A, ESI†) and from 450.5 m/z as previously shown. Both of them share common product ions, *e.g.* 276 m/z and 243 m/z whose fragmentation mechanism was previously explained, while the formation of 386 m/z might be hypothesized by the migration process shown in Fig. S10B (ESI†). As regards $[Cu(phen)_2(SAL)(ClO_4)]^+$ (m/z 1000), the main product peak at 522 m/z ($[Cu(phen)_2(ClO_4)]^+$) is due to the loss of a neutral **SAL** molecule. A further loss of a phen unit with the generation of a peak at 342 m/z ($[Cu(phen)(ClO_4)]^+$) can be observed at high voltage (Fig S11, ESI†). The absence of ions containing **SAL** fragments bonded to $[Cu(phen)_x]^+$ could be attributed to the steric hindrance of **SAL** itself and supports, in accordance with the findings previously reported, a coordination of **SAL** by a neutral donor group. Considering the strong affinity of copper for sulphur donating groups, and in accordance with the molecular structures of similar mixed Cu(II)-phenanthroline complexes with thioamides,[3,35] a pentacoordinated geometry around the copper ion and a coordination of **SAL** *via* sulphur atom are proposed for $[Cu(phen)_2(SAL)](ClO_4)_2$. More insights about them are provided by DFT calculations.
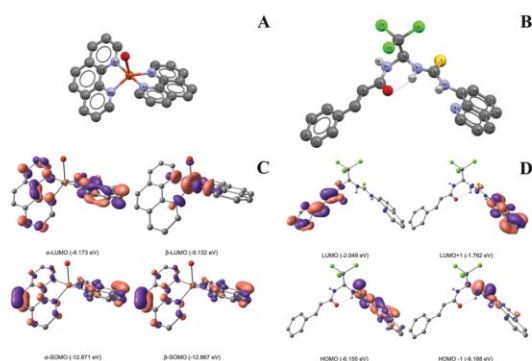
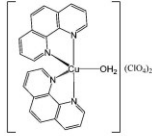**Fig. 4** Molecular drawings and atom labelling schemes for [Cu(phen)$_2$-(H$_2$O)]$^{2+}$ (A) and SAL (B) at the DFT optimized geometry. Isosurface drawings of selected frontier molecular orbitals calculated for (C) [Cu(phen)$_2$(H$_2$O)]$^{2+}$ and (D) SAL (contour value: 0.05). Hydrogen atoms (A and C) and non-polar hydrogen atoms (B and D) are omitted for clarity.

Fig. 5 Molecular drawings and atom labelling schemes for [Cu(phen)$_2$(SAL)]$^{2+}$ (A) at the DFT-optimized geometry. Isosurface drawings of selected frontier molecular orbitals calculated for (B) [Cu(phen)$_2$(SAL)]$^{2+}$ (contour value: 0.05). Non-polar hydrogen atoms are omitted for clarity.

DFT calculations. In order to assess the performance of the DFT protocol employed in this work, theoretical calculations were initially performed on the parent copper complex [Cu(phen)$_2$-(H$_2$O)]$^{2+}$, starting from the **C0** X-ray structural data.[36] The DFT optimized structure of [Cu(phen)$_2$(H$_2$O)]$^{2+}$ is reported in Fig. 4A. As can be seen, a trigonal bipyramidal geometry was predicted in analogy with the experimental data. In Fig. S12 (ESI†) the super-imposition of DFT-optimized and experimental structures is reported (root mean square deviation was 0.0905 Å). In Table S1 (ESI†), selected bond lengths, angles and dihedrals for both X-ray and DFT structures are reported. A very good linear correlation between experimental and theoretical parameters was obtained (Fig. S13, ESI†), especially if we consider that the experimental data are relative to the solid state, while the DFT ones are calculated in gas phase. Atomic charges, computed at the NPA level (Table S2, ESI†), show on the copper ion a significant lower atomic charge when compared with its formal charge +2, suggesting a Ligand to Metal Charge Transfer (LMCT). The former trend is obser-vable also at the molecular orbital level: an analysis of beta occupied frontier MOs shows the highest Singly Occupied Molecular Orbital (SOMO) centred on the phenanthroline ligands, while the Lowest Unoccupied Molecular Orbital (LUMO) is centred mainly on the metal ion (Fig. 4C). DFT optimized geometry for both **SAL** and [Cu(phen)$_2$(SAL)]$^{2+}$ was obtained using the same computational setup as for [Cu(phen)$_2$(H$_2$O)]$^{2+}$. In the case of **SAL** (Fig. 4B), the optimized geometry is stabilized by an intramolecular hydrogen bond between H10 and O forming a pseudo oxadiazine ring with a H10···O length of 1.94 Å and a H10···OC9 angle of 102.37 Å. In Table S3 (ESI†), selected bond lengths, angles and dihedrals are reported. An analysis of the frontier molecular orbitals (Fig. 4D) reveals both HOMO−1 and HOMO highly centred on the sulphur thioamide moiety, sup-porting the hypothesis of a coordinating ability through this donor group. The DFT optimized structure of [Cu(phen)$_2$(SAL)]$^{2+}$ (Fig. 5A) shows an intermediate geometry between trigonal bipyramidal and square pyramidal, as evidenced by the value
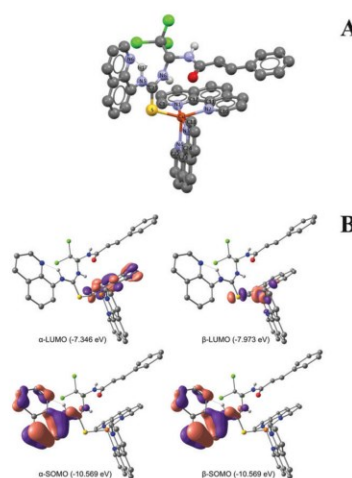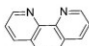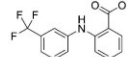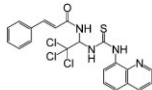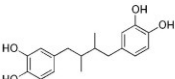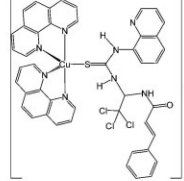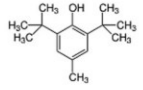
of the geometrical parameter $\tau = \dfrac{\beta - \alpha}{60}$ of 0.42.[37] As expected, a tetragonal distortion due to the Jahn–Teller effect is observed, with the elongation of basal bond lengths (e.g. S–Cu, N2–Cu and N4–Cu equal to 2.379, 2.184 and 2.108 Å respectively) accom-panied by the shortening of the axial ones (e.g. N1–Cu and N3–Cu equal to 2.014 and 2.037 Å respectively). A comparison between C–S bond lengths in **SAL** and in [Cu(phen)$_2$(SAL)]$^{2+}$ shows a significant reduction of the double bond character (1.661 and 1.712 Å, respectively), in agreement with similar systems structurally characterized.[3] The DFT optimized geometry of [Cu(phen)$_2$(SAL)]$^{2+}$ is further stabilized by an intramolecular hydrogen bond between H17 and N6 (1.907 Å). Selected values of calculated bond lengths, angles and dihedrals are reported in Table S4 (ESI†). As observed for [Cu(phen)$_2$(H$_2$O)]$^{2+}$, both atomic charges (Table S5, ESI†) and frontier molecular orbitals (Fig. 5B) suggest a LMCT behaviour.

Determination of the reducing activity of the stable radical 1,1-diphenyl-picrylhydrazyl (DPPH)

Molecules that exhibit a DPPH radical scavenging ability might also show anticancer and anti-inflammatory activities, and, under this light, the model of the scavenging of the stable DPPH radical is widely exploited to evaluate the antioxidant activity of promising compounds. DPPH may accept a radical hydrogen to be converted into a diamagnetic form, whose absorption spectrum differs from the previous one. The DPPH radical has a deep violet colour in solution (λ_{max} = 530 nm), while the diamagnetic form is pale yellow coloured.[38] Following the change in the optical absorption at 520 nm it is possible to monitor the course of the reaction during the time and com-pare the scavenger ability of different compounds. The results

Table 1 Interaction percentage with DPPH (RA%) shown by ligands and copper complexes; phen is 1,10-phenanthroline, bipy is 1,10-bipyridine, fluf is deprotonated flufenamic acid (N-(α,α,α-trifluoro-m-tolyl)anthranilic acid), NDGA is nordihydroguaiaretic acid, BHT is butylated hydroxytoluene (0.05 mM EtOH, 25 °C)

Compound	RA% at 20′	RA% at 60′	Structure	Ref.	Compound	RA% at 20′	RA% at 60′	Structure	Ref.
phen	<1	<1		This work, ref. 39	Hfluf	7.36	9.74		20
Salubrinal **SAL**	82.0	97.0		This work	Cu(fluf)(bipy)Cl	9.48	10.01		20
Cu(phen)₂(OH₂)(ClO₄)₂ **C0**	2.1	4.0		This work	NDGA	81.02	82.60		20
Cu(phen)₂(SAL)(ClO₄)₂ **C0SAL**	96.5	97.0		This work	BHT	31.30	60.00		20
Cu(fluf)(phen)Cl	22.46	26.52		20					

of the DPPH radical scavenging ability measured for **C0**, **SAL** and **C0SAL** are reported in the ESI† (Fig. S14). **C0** did not show any reducing activity in 60 min, as expected since the copper complex does not have any hydrogen to be lost as H•, and the 1,10-phenanthroline does not show reducing activity (6% at 20 min, 8% at 60 min[39]). **SAL**, having three hydrogen atoms to be involved in the redox reaction, exhibited an interesting reducing activity, that is of ≈80% after 20 min and almost quantitative (RA ≈ 100%) after 50 min. This reduction process is even faster than that of BHT (31% at 20 min, 60% at 60 min[20]). As regards **C0SAL**, this mixed complex not only exhibited a reducing activity, but it was almost 100% completed after 3 min, showing that the coordination with the Cu(phen)₂ backbone increases the reducing activity of **SAL** more than 100%. It is interesting to compare the % of RA shown by other copper complexes containing a nitrogen donor chelator and an auxiliary ligand similar to **SAL**. In Table 1 are reported the % of RA for some complexes and the related auxiliary ligand. As can be seen, the novel complex **C0SAL** presents the highest radical scavenging ability.

Soybean lipoxygenase inhibition study *in vitro*

Several experiments were performed keeping constant the concentration of the substrate and enzyme and varying the concentration of **C0** or **SAL** or **C0SAL** to obtain the following results:

(i) in the absence of **C0**, the conversion of sodium linoleate to 13-hydroperoxylinoleic acid is completed in approx. 20–30 min, while in the presence of **C0**, the rate of the reaction is lowered (20–40 min), and the conversion percentage never reaches 100% (Fig. S15A, ESI†);

(ii) in the presence of increasing amounts of **SAL**, the absorbance decreases with time with a trend similar for all the curves. The conversion of sodium linoleate to 13-hydroperoxylinoleic acid ends in approx. 40–60 min in the presence of **SAL** and the conversion percentage never reaches 100% (Fig. S15B, ESI†);

(iii) in the presence of increasing amounts of **C0SAL**, the absorbance decreases with time with a trend similar for all the curves. The conversion of sodium linoleate to 13-hydroperoxylinoleic acid ends in approx. 60–80 min in the presence of **C0SAL** and the conversion percentage never reaches 100% (Fig. S15C, ESI†).

Reporting the inhibition percentage (IP) as a function of the inhibitor concentration (Fig. 6), it was found that IP varies with time for every given concentration. This trend became invariant after 30 min for **C0**, 20 min for **SAL** and 5 min for **C0SAL**. This time was chosen as the reference one to calculate the IC_{50} value, *i.e.* the concentration required to inhibit 50% of enzyme activity. For the three compounds, IC_{50} resulted to be 55 ± 5 μM (**C0**), 4.4 ± 0.6 μM (**SAL**) and 4.2 ± 0.2 μM (**C0SAL**) while the concentration required to inhibit 100% of enzyme activity was 130 μM for **C0**, 20 μM for **SAL** and 10 μM for **C0SAL**. The trends shown in Fig. 6 suggest different mechanisms involved in the reaction with the enzyme.

Molecular docking

Considering the ability of several LOX inhibitors to express their activity by targeting the catalytic binding site,[29,40–42] we initially performed simulations considering our test compounds as competitive inhibitors. In order to validate the docking protocol chosen, we decided to dock at first the inhibitor 3,4-dihydroxybenzoic
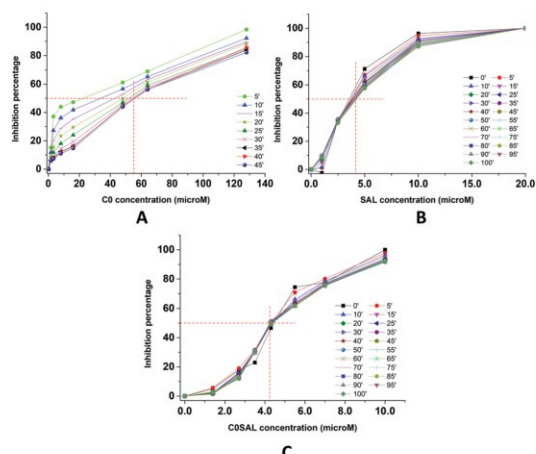
Fig. 6 Inhibition percentage observed at different concentrations of **C0** (A), **SAL** (B) or **C0SAL** (C) at different times after the mixing of the reactants; linoleic acid 32 μM, lipoxygenase 0.88 nM, pH 7.4 Tris buffer, *T* 25 °C.
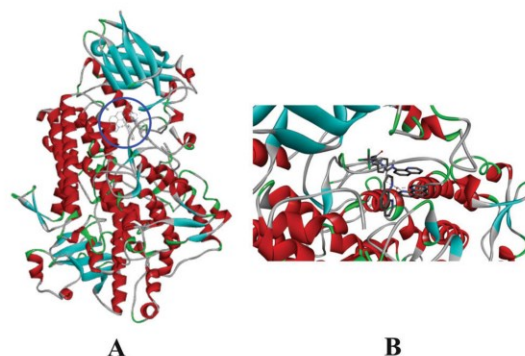

Fig. 8 Full view of the complex between the highest-ranking score of $[Cu(phen)_2(SAL)]^{2+}$ and soybean LOX (A); zoom of the binding pocket occupied by the highest-ranking score of $[Cu(phen)_2(SAL)]^{2+}$ within soybean LOX (B).

acid (dhb), obtained as the oxidation product of quercetin by LOX-3,[29] in its binding site. A satisfactory overlapping of the docked pose with the crystallized one was obtained, as shown in Fig. S16 (ESI†), with a RMSD of 0.6176 Å and a scoring function (expressed as binding affinity) of −5.5 kcal mol^{-1}. A closer view of intermolecular interactions between the docked pose of dhb and LOX residues (Fig. 7A) shows a series of π interactions, *e.g.* T-shaped with HIS518 and π-alkyl with LEU565 and ALA561. In the same way, the docking protocol was applied to $[Cu(phen)_2(H_2O)]^{2+}$, **SAL** and $[Cu(phen)_2(SAL)]^{2+}$, obtaining in each case high positive scoring functions (7.7, 38.5, and 69.2 kcal mol^{-1} for **SAL**, $[Cu(phen)_2(H_2O)]^{2+}$ and $[Cu(phen)_2(SAL)]^{2+}$, respectively) due to hindering shape effects related to the bulky nature of the ligands. These results,

Fig. 7 Docked poses of dhb (A), **SAL** (B), $[Cu(phen)_2(H_2O)]^{2+}$ (C), $[Cu(phen)_2(SAL)]^{2+}$ (D) and intermolecular interactions with the surrounding residues of soybean LOX.

in analogy with previous docking studies performed on similar Cu(II) mixed complexes,[39,43] prompted us to explore the possibility that their inhibitory activity was a result of allostery. A cavity previously identified and located between the C-terminus and N-terminus domains of LOX-3 was chosen as the potential binding site for the tested compounds. In this case, scoring functions of −9.6, −8.9 and −8.1 kcal mol^{-1} were obtained for **SAL**, $[Cu(phen)_2(H_2O)]^{2+}$ and $[Cu(phen)_2(SAL)]^{2+}$, respectively. The full view and zoom view of the binding cavities determined for the docked compounds are shown in Fig. 8 for $[Cu(phen)_2(SAL)]^{2+}$ and in Fig. S17 and S18 (ESI†) for $[Cu(phen)_2(H_2O)]^{2+}$ and **SAL**. Analysis of the docked pose for **SAL** (Fig. 7B) revealed several π interactions (*e.g.* π–π T-shaped with PRO549, π alkyl with LEU187 and LYS547). A closer inspection of the docked poses revealed for $[Cu(phen)_2(H_2O)]^{2+}$ (Fig. 7C) a series of hydrophobic interactions (mainly π-alkyl, *e.g.* with VAL26, ALA263 and LEU258), while for $[Cu(phen)_2(SAL)]^{2+}$ (Fig. 7D), along with π interactions with MET19 and ARG786, we have in addition a hydrogen bond between the N–H of GLN96 and the carbonyl oxygen of the **SAL** moiety. The docked pose of $[Cu(phen)_2(SAL)]^{2+}$ is further stabilized by several intramolecular non-covalent interactions, *e.g.* π–π stacking between the quinoline fragment of **SAL** and one of the phenanthroline molecules, and a hydrogen bond between one of the thioamidic –NH groups and carbonyl oxygen, both belonging to the **SAL** moiety.

Biological mechanism

First, we were curious if there was any effect on cell ultrastructure induced by **SAL** alone. We employed A2780 and SKOV3 cells and performed transmission electron microscopy analysis. We revealed that cells treated by **SAL** have not suffered from any ultrastructural aberrations (Fig. S19, ESI†). In contrast, treatment by **C0** induced massive alterations of the endoplasmic reticulum (ER) and partially also mitochondria.[9] Then, to assess the cytotoxic properties of the newly synthesized **C0SAL** compound, we performed viability assay based on the activity of cellular NAD(P)H-dependent oxidoreductases (MTT assay). While the treatment by
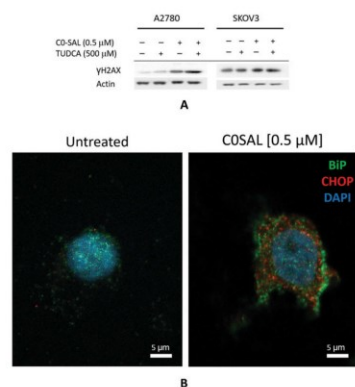
Fig. 9 (A) Intracellular levels of phosphorylated histone γ-H2AX after **C0SAL** treatment on A2780 and SKOV3 cells; (B) expression of GRP-78 and DDIT3 regulators of ER-stress response in SKOV3 ovarian cancer cells treated with **C0SAL**. SKOV3 cells were cultured for 18 h in the presence of **C0SAL** and then analyzed by immunofluorescence microscopy for expression of GRP-78 (green) and DDIT3 proteins (red). Nuclei (blue) were visualized by DAPI staining.

SAL had no significant effect in a wide concentration range (Fig. S20A, ESI†), we revealed massive reduction of cell viability when **SAL** was bound to **C0** (Fig. S20B, ESI†). The cytotoxicity rate was similar to the treatment with individual **C0** or **C0** co-treated with **SAL** (Fig. S20C, ESI†). The EC_{50} of **C0SAL** on A2780 cells was (0.68 ± 0.05) μM, while those of **SAL** and **C0** were (56 ± 4) μM and (0.94 ± 0.04) μM, respectively.

To reveal the possible mechanism of action of the **C0SAL** complex, we first analyzed the intracellular levels of phosphorylated histone γ-H2AX which is recruited in DNA damage. After **C0SAL** treatment on A2780 and SKOV3 cells, γ-H2AX was massively accumulated in A2780 cells, while the SKOV3 cells contained a significant basal expression of γ-H2AX and the relative increase was minor (Fig. 9A).
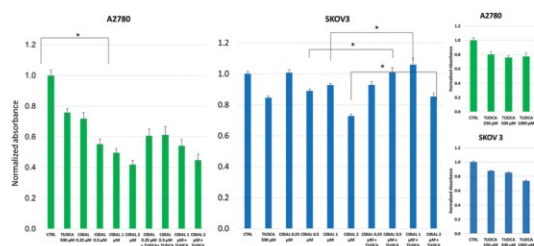
Fig. 10 SKOV3 and A2780 cells were cultured for 18 h either in the presence or absence of **C0SAL** and/or SKOV3 and A2780 cells were cultured for 18 h either in the presence or absence of **C0SAL** and/or tauroursodeoxycholic acid (TUDCA) at indicated concentrations. Then, the cell viability was determined by conversion of the 4-nitro blue tetrazolium chloride to formazan followed by measurement of OD at 570 nm (MTT assay). The plots represent means and SDs from three independent experiments performed in technical pentaplicates. The asterisks indicate statistical significance at $p < 0.05$.

We have recently described that the **C0** complex and its derivatives induce cell death by activation of unfolded protein response. Similarly, treatment by **C0SAL** induces expression of GRP-78 and DDIT3 regulators of ER-stress response in SKOV3 ovarian cancer cells, as can be seen in Fig. 9B. Moreover, to elucidate whether **C0SAL** induced cell death *via* activation of unfolded protein response, A2780 and SKOV3 ovarian cancer cells were treated with either **C0SAL** alone or in combination with tauroursodeoxycholic acid. TUDCA reverted the cytotoxic effect of **C0SAL** in A2780 cells, and this effect was even more pronounced in SKOV3 cells (Fig. 10). This might suggest that induction of ER-stress is the preferred driving mechanism of cell death induced by **C0SAL**.

Conclusions

By the reaction between $[Cu(phen)_2(H_2O)](ClO_4)_2$ (**C0**) and the ER stress modulator salubrinal the novel complex $[Cu(phen)_2(salubrinal)](ClO_4)_2$ (**C0SAL**) was obtained. The chemical formula and the complex formation constant of **C0SAL** were determined by mass spectrometry and spectrophotometric measurements. The experimental results showed the metal ion coordinated by the thionic group of the salubrinal molecule, as confirmed also by theoretical calculations. The DPPH radical scavenging ability of the novel compound and of the precursors **C0** and **SAL** was studied, showing that the coordination with the $Cu(phen)_2$ backbone increases the reducing activity of salubrinal more than 100%. Studies on soybean lipoxygenase inhibition showed that the concentration of **C0SAL** required to inhibit 50% of enzyme activity was lower than that of **C0** (4.2 μM *versus* 55 μM) and comparable to that of salubrinal. However, the concentration required to inhibit 100% enzyme activity was lower than that of **C0** or salubrinal (10 μM *versus* 130 μM or 20 μM). Docking calculations performed on the former enzyme suggest allosteric modulation as a possible mechanism of inhibition by the studied compounds. **C0SAL** was revealed to possess high potency in terms of cytotoxicity on A2780 cells, 82-fold higher than that of Salubrinal and 1.4-fold higher than that of **C0**.

Treatment with **C0SAL** in SKOV3 ovarian cancer cells induces expression of GRP-78 and DDIT3 regulators of ER-stress response. In the presence of TUDCA, the cytotoxic effect of **C0SAL** was reverted, suggesting that the induction of ER-stress is indeed the driving mechanism of cell death caused by **C0SAL**. In A2780 cells treated with **C0SAL** γ-H2AX was accumulated, suggesting that DNA damage was also involved.

In conclusion, this research, being a cross-disciplinary study that involves metallobiochemistry, pharmacology, medicine, and toxicology, might provide a better understanding of the mechanisms of action of potential copper anticancer drugs and give useful insights into the design of new active species.

Conflicts of interest

There are no conflicts to declare.

108

Acknowledgements

Notes and references

1 F. Trudu, F. Amato, P. Vaňhara, T. Pivetta, E. M. Peña-Méndez and J. Havel, *J. Appl. Biomed.*, 2015, **13**, 79–103.
2 D. S. Sigman, D. R. Graham, V. D. Aurora, A. M. Stern and D. Aurora, *J. Biol. Chem.*, 1979, **254**, 12269–12272.
3 T. Pivetta, M. Dolores, F. Demartin, C. Castellano, S. Vascellari, G. Verani and F. Isaia, *J. Inorg. Biochem.*, 2011, **105**, 329–338.
4 T. Pivetta, F. Isaia, G. Verani, C. Cannas, L. Serra, C. Castellano, F. Demartin, F. Pilla, M. Manca and A. Pani, *J. Inorg. Biochem.*, 2012, **114**, 28–37.
5 T. Pivetta, V. Lallai, E. Valletta, F. Trudu, F. Isaia, D. Perra, E. Pinna and A. Pani, *J. Inorg. Biochem.*, 2015, **15**, 107–114.
6 E. Cadoni, E. Valletta, G. Caddeo, F. Isaia, M. G. Cabiddu, S. Vascellari and T. Pivetta, *J. Inorg. Biochem.*, 2017, **173**, 126–133.
7 T. Pivetta, F. Trudu, E. Valletta, F. Isaia, C. Castellano, F. Demartin, R. Tuveri, S. Vascellari and A. Pani, *J. Inorg. Biochem.*, 2014, **141**, 103–113.
8 S. Vascellari, E. Valletta, D. Perra, E. Pinna, A. Serra, F. Isaia, A. Pani and T. Pivetta, *RSC Adv.*, 2019, **9**, 5362–5376.
9 L. Moráň, T. Pivetta, S. Masuri, K. Vašíčková, F. Walter, J. Prehn, M. Elkalaf, J. Trnka, J. Havel and P. Vaňhara, *Metallomics*, 2019, **11**, 1481–1489.
10 S. Wang and R. J. Kaufman, *J. Cell Biol.*, 2012, **197**, 857–867.
11 M. Kitamura, *Semin. Immunopathol.*, 2013, **35**, 259–275.
12 M. Boyce, K. F. Bryant, C. Jousse, K. Long, H. P. Harding, D. Scheuner, R. J. Kaufman, D. Ma, D. M. Coen, D. Ron and J. Yuan, *Science*, 2005, **307**, 935–939.
13 K. Long, M. Boyce, H. Lin, J. Yuan and D. Ma, *Bioorg. Med. Chem. Lett.*, 2005, **15**, 3849–3852.
14 M. Strohalm, D. Kavan, P. Nova and M. Volny, *Anal. Chem.*, 2010, **82**, 4648–4651.
15 T. H. J. Niedermeyer and M. Strohalm, *PLoS One*, 2012, **7**, e44913.
16 P. Gans, A. Sabatini and A. Vacca, *Talanta*, 1996, **43**, 1739–1753.
17 P. Job, *Ann. Chim. Appl.*, 1928, **9**, 113–203.
18 J. S. Renny, L. L. Tomasevich, E. H. Tallmadge and D. B. Collum, *Angew. Chem., Int. Ed.*, 2013, **52**, 11998–12013.

19 J. Liu, K.-L. He, X. Li, R.-J. Li, C.-L. Liu, W. Zhong and S. Li, *Curr. Med. Chem.*, 2012, **19**, 6072–6079.
20 C. Tolia, A. N. Papadopoulos, C. P. Raptopoulou, V. Psycharis, C. Garino, L. Salassa and G. Psomas, *J. Inorg. Biochem.*, 2013, **123**, 53–65.
21 Z. Boulsourani, G. D. Geromichalos, S. Katsamakas, V. Psycharis and C. P. Raptopoulou, *Mater. Sci. Eng., C*, 2019, **94**, 493–508.
22 F. Neese, *Wiley Interdiscip. Rev.: Comput. Mol. Sci.*, 2012, **2**, 73–78.
23 M. D. Hanwell, D. E. Curtis, D. C. Lonie, T. Vandermeersch, E. Zurek and G. R. Hutchison, *J. Cheminf.*, 2012, **4**, 17.
24 C. Adamo and V. Barone, *J. Chem. Phys.*, 1999, **110**, 6158–6170.
25 F. Weigend and R. Ahlrichs, *Phys. Chem. Chem. Phys.*, 2005, **7**, 3297–3305.
26 T. Y. Nikolaienko, L. A. Bulavin and D. M. Hovorun, *Comput. Theor. Chem.*, 2014, **1050**, 15–22.
27 Chemcraft – graphical software for visualization of quantum chemistry computations, https://www.chemcraftprog.com.
28 O. Trott and A. J. Olson, *J. Comput. Chem.*, 2009, 455–461.
29 O. Y. Borbulevych, J. Jankun, S. H. Selman and E. Skrzypczak-Jankun, *Proteins: Struct., Funct., Bioinf.*, 2003, **54**, 13–19.
30 G. M. Morris, H. Ruth, W. Lindstrom, M. F. Sanner, R. K. Belew, D. S. Goodsell and A. J. Olson, *J. Comput. Chem.*, 2009, **30**, 2785–2791.
31 Dassault Systèmes BIOVIA, Discovery Studio Viewer, v19, San Diego, Dassault Systèmes, 2019.
32 C. Hao and R. E. March, *J. Mass Spectrom.*, 2001, **36**, 509–521.
33 J. Foley, D. Kennefick, D. Phelan, S. Tyagi and B. Hathaway, *J. Chem. Soc., Dalton Trans.*, 1983, 2333–2338.
34 T. Pivetta, M. D. Cannas, F. Demartin, C. Castellano, S. Vascellari, G. Verani and F. Isaia, *J. Inorg. Biochem.*, 2011, **105**, 329–338.
35 M. B. Ferrari, G. G. Fava and A. Montenero, *Cryst. Struct. Commun.*, 1975, **4**, 577.
36 G. Murphy, C. Murphy, B. Murphy and B. Hathaway, *J. Chem. Soc., Dalton Trans.*, 1997, **2**, 2653–2660.
37 A. W. Addison, T. N. Rao, J. Reedijk, J. van Rijn and G. C. Verschoor, *J. Chem. Soc., Dalton Trans.*, 1984, 1349–1356.
38 D. Huang, B. Ou and R. L. Prior, *J. Agric. Food Chem.*, 2005, **53**, 1841–1856.
39 Z. Boulsourani, G. D. Geromichalos, S. Katsamakas, V. Psycharis, C. P. Raptopoulou, D. Hadjipavlou-Litina, D. Sahpazidou and C. Dendrinou-Samara, *Mater. Sci. Eng., C*, 2019, **94**, 493–508.
40 E. Skrzypczak-Jankun, K. Zhou, N. McCabe, S. Selman and J. Jankun, *Int. J. Mol. Med.*, 2003, 17–24.
41 E. Skrzypczak-Jankun, K. Zhou and J. Jankun, *Int. J. Mol. Med.*, 2003, 415–420.
42 E. Skrzypczak-Jankun, O. Y. Borbulevych and J. Jankun, *Acta Crystallogr., Sect. D: Biol. Crystallogr.*, 2004, **60**, 613–615.
43 Z. Boulsourani, S. Katsamakas, G. D. Geromichalos, V. Psycharis, C. P. Raptopoulou, D. Hadjipavlou-Litina, E. Yiannaki and C. Dendrinou-Samara, *Mater. Sci. Eng., C*, 2017, **76**, 1026–1040.

The first copper (II) complex with 1,10-phenanthroline and salubrinal with interesting biochemical properties

S. Masuri[1], E. Cadoni[1], M.G. Cabiddu[1], F. Isaia[1], M.G. Demuru[1], L. Moráň[2,3], D. Buček[2,] P. Vaňhara[2,3], J. Havel[3,4], T. Pivetta[*,1]

[1]Dipartimento di Scienze Chimiche e Geologiche, Università degli Studi di Cagliari, Cittadella Universitaria, 09042 Monserrato CA – Italy; [2]Department of Histology and Embryology, Faculty of Medicine, Masaryk University, Brno, Czech Republic; [3]International Clinical Research Center, St. Anne's University Hospital, Brno, Czech Republic; [4]Department of Chemistry, Faculty of Science, Masaryk University, Brno, Czech Republic.

SUPPLEMENTARY INFORMATION
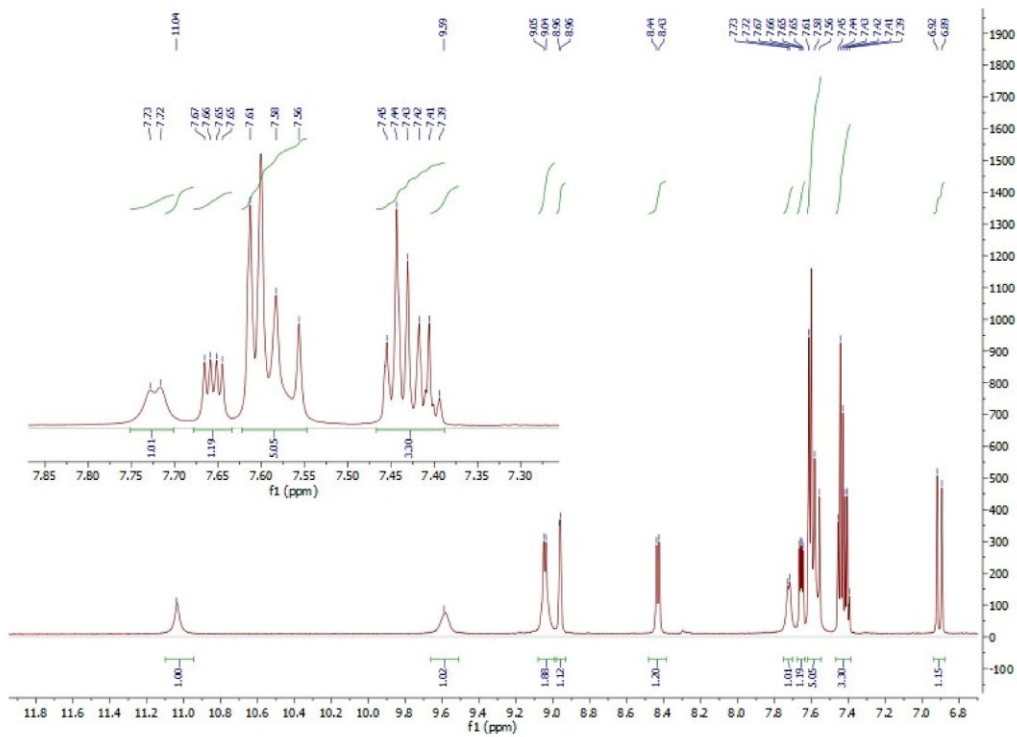
Fig. S1: [^1]H-NMR spectrum of **SAL** (600 MHz, DMSO d-6).
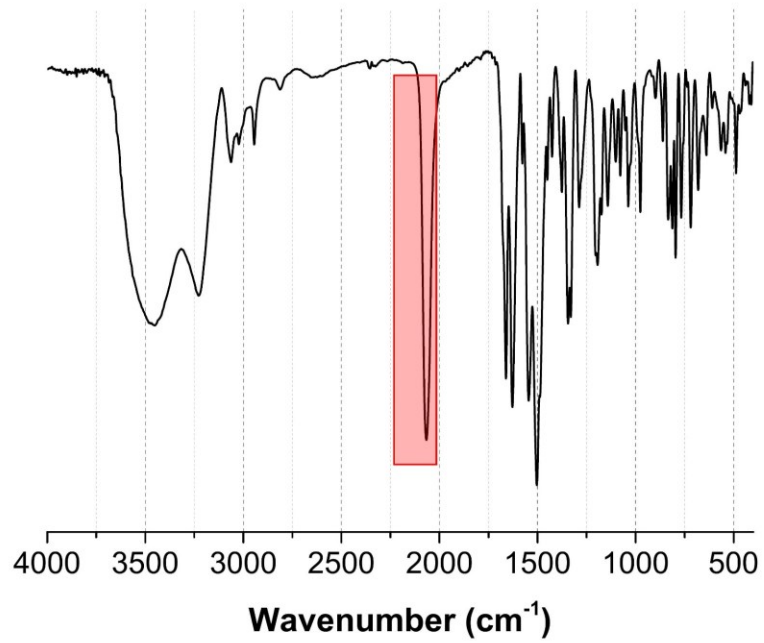
Fig. S2: FT-IR of **SAL** prior to aqueous washing for SCN⁻ removal. The peak relative to SCN⁻ at 2070 cm⁻¹ is evidenced.
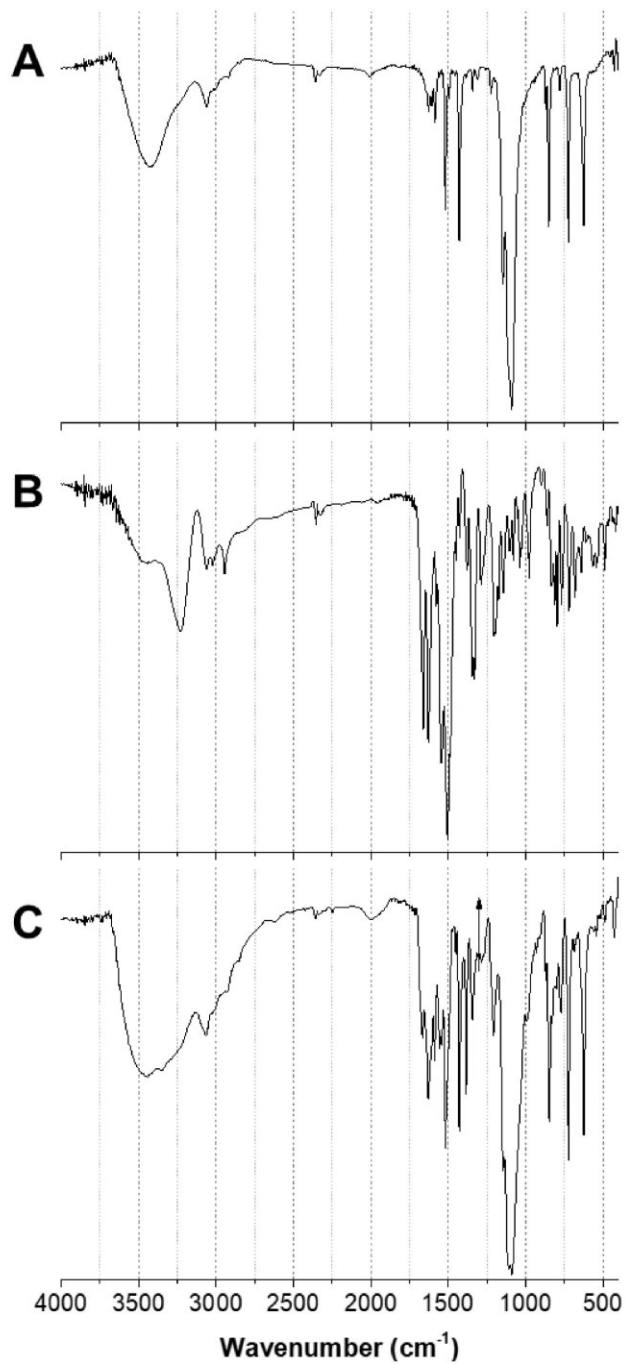
Fig. S3: IR spectra of C0 (**A**), SAL (**B**) and [Cu(phen)$_2$(SAL)](ClO$_4$)$_2$ (**C**)
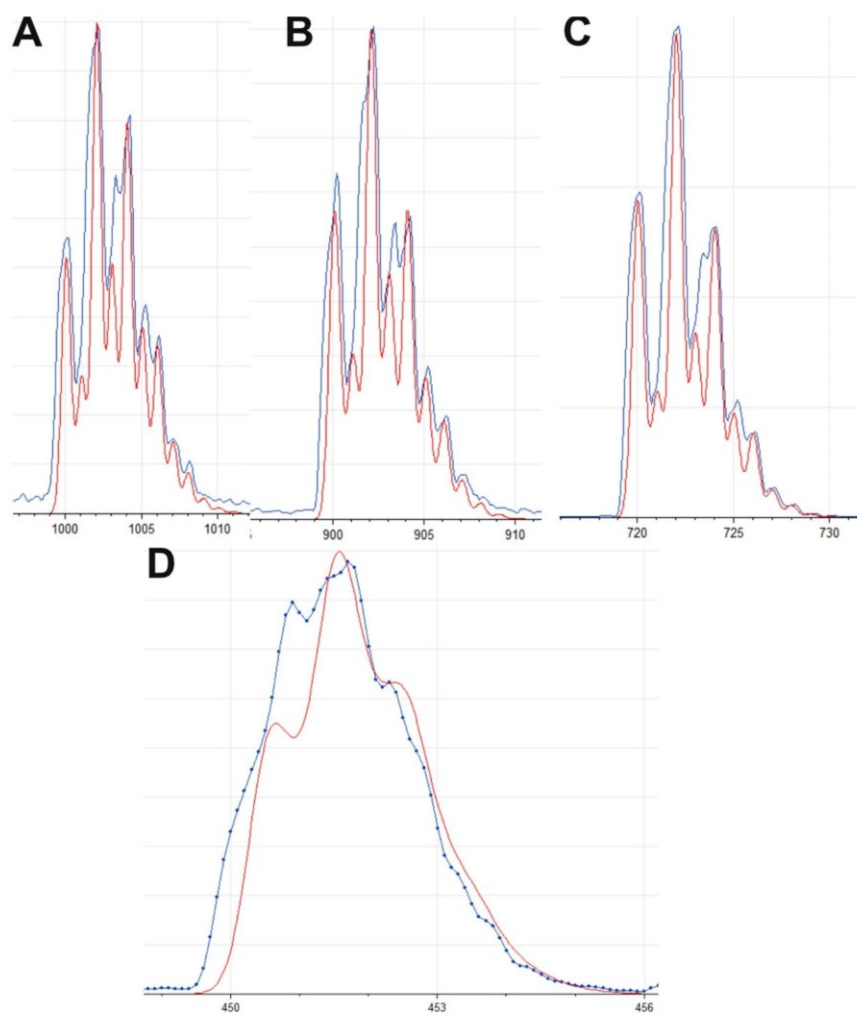
Fig. S4: Experimental (blue line) and calculated (red line) isotopic patterns of the peaks at *m/z* (**A**) 1002-1000 ([Cu(phen)$_2$(SAL)(ClO$_4$)]$^+$), (**B**) 902-900 ([Cu(phen)$_2$(SAL-H)]$^+$), (**C**) 722-720 ([Cu(phen)(SAL-H)]$^+$), (**D**) 450.5 ([Cu(phen)$_2$(SAL)]$^{2+}$).
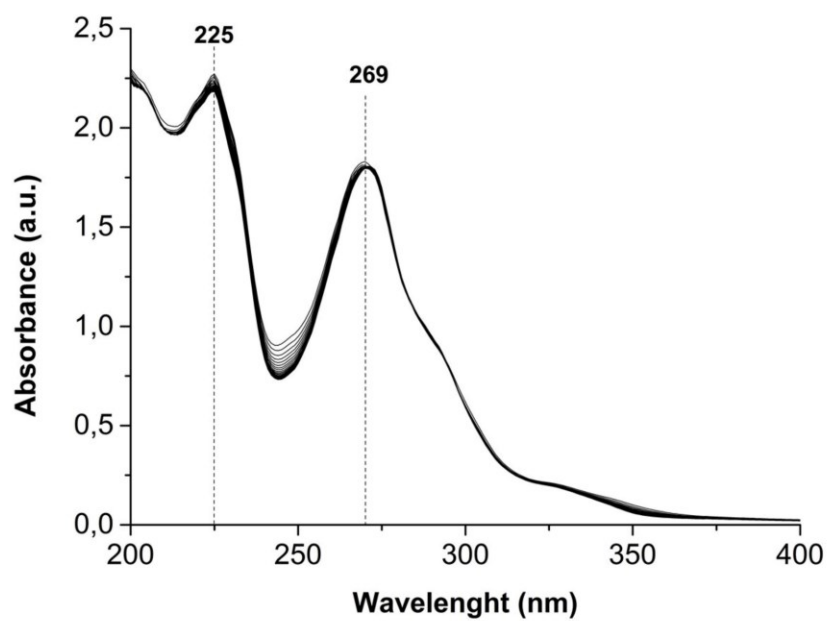
A
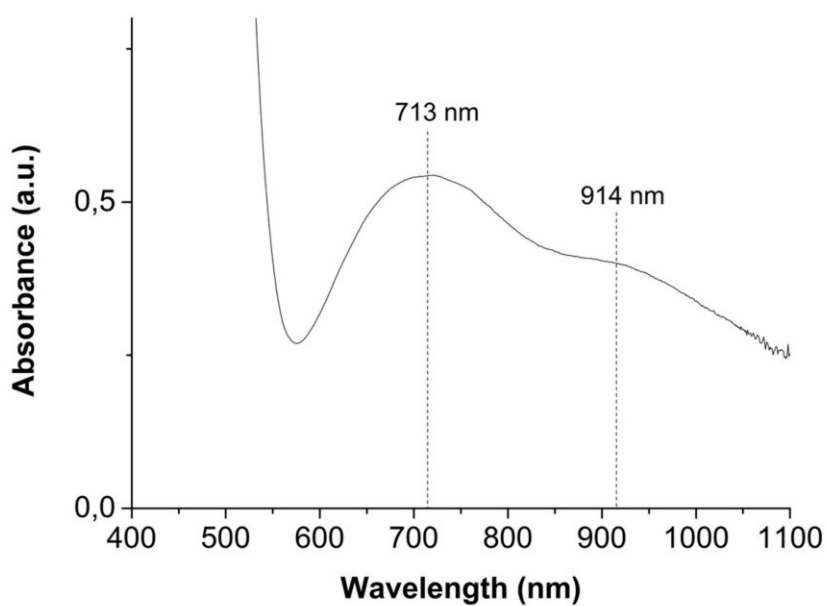
B

Fig. S5: (**A**) UV-Vis spectra of **C0SAL** (2.54 10^{-5} M) in the range 200-400 nm recorded in 24h, each spectrum was acquired every 60 minutes, $CH_3CN:H_2O$ (1:1); (**B**) UV-Vis spectrum of **C0SAL** (6.49·10^{-3} M) in the region 400-1100 nm, CH_3CN; 25°C, 1 cm path length.

A)

450.5   181   720

B)

720

C)

720
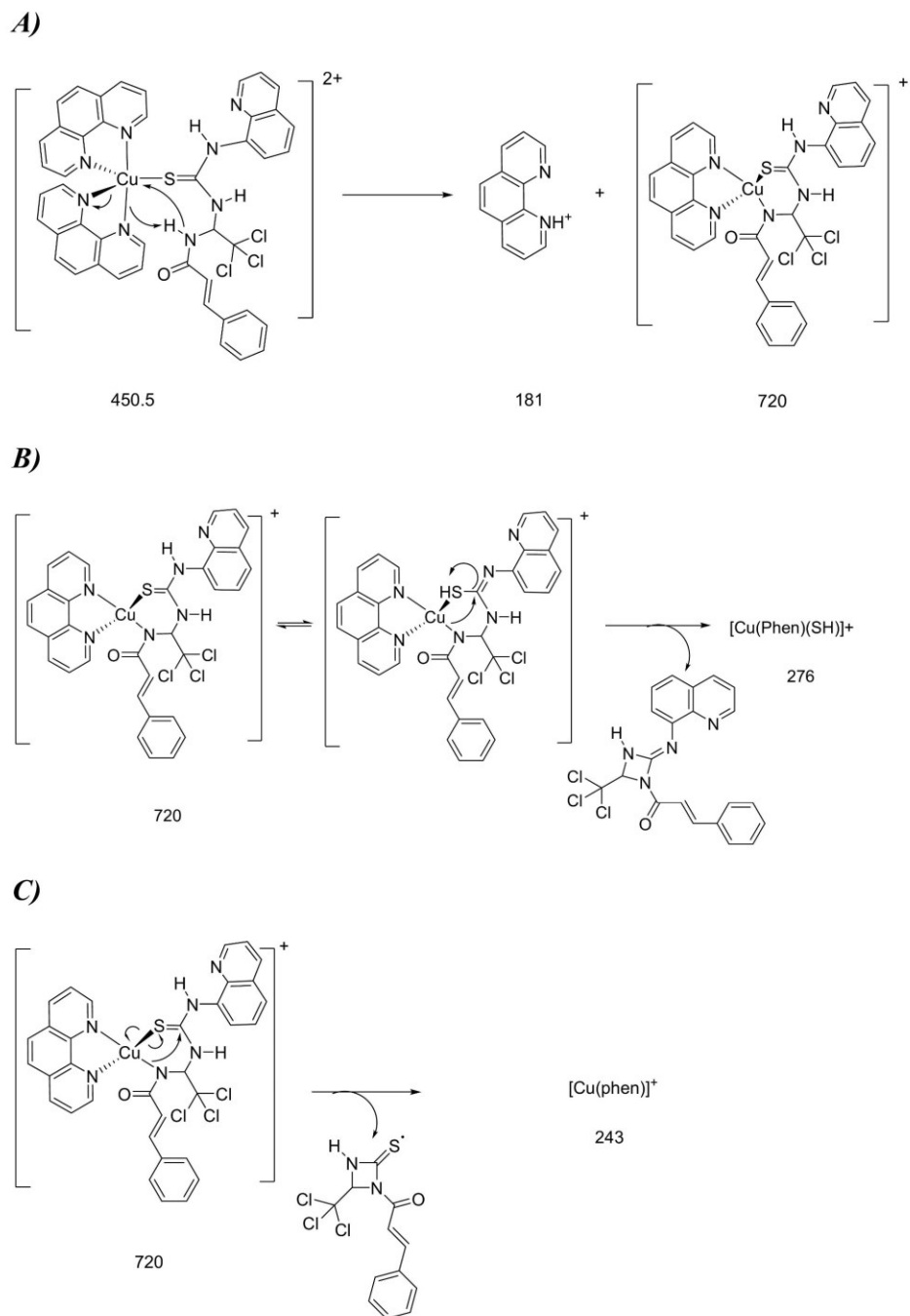
Fig. S8: proposed fragmentation patterns for product ions at 720 (**A**), 276 (**B**), 243 (**C**) *m/z* generated from 450.5 *m/z* under CID conditions.
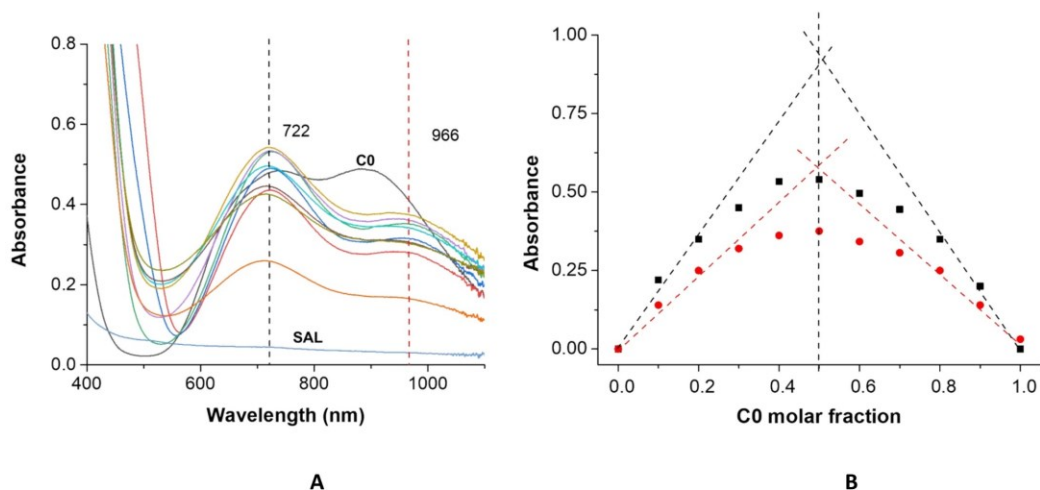
Fig. S6. Absorption spectra collected varying the ligand molar fraction from 0 to 1 for the system between **C0** (1.0 mM) and **SAL** (1.0 mM) in CH_3CN, 0.1 M $NaClO_4$, 25 °C, 1 cm optical path length (**A**). Normalized Job's plot of **C0** and **SAL** at 966 nm (red dots) and 722 nm (black dots).
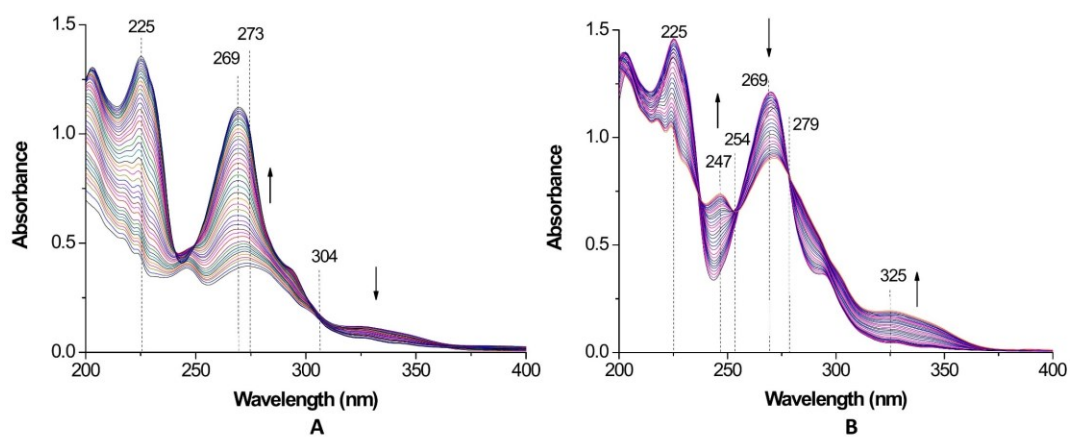
Fig. S7: Selected spectra collected during the titration of $4 \cdot 10^{-5}$ mmoles of **SAL** with **C0** $2 \cdot 10^{-5}$ M (**A**) and of $4 \cdot 10^{-5}$ mmoles of **C0** with **SAL** $4 \cdot 10^{-5}$ M (**B**), CH_3CN, 0.05 M $NaClO_4$ ionic buffer, 25 °C, 1 cm optical path length.
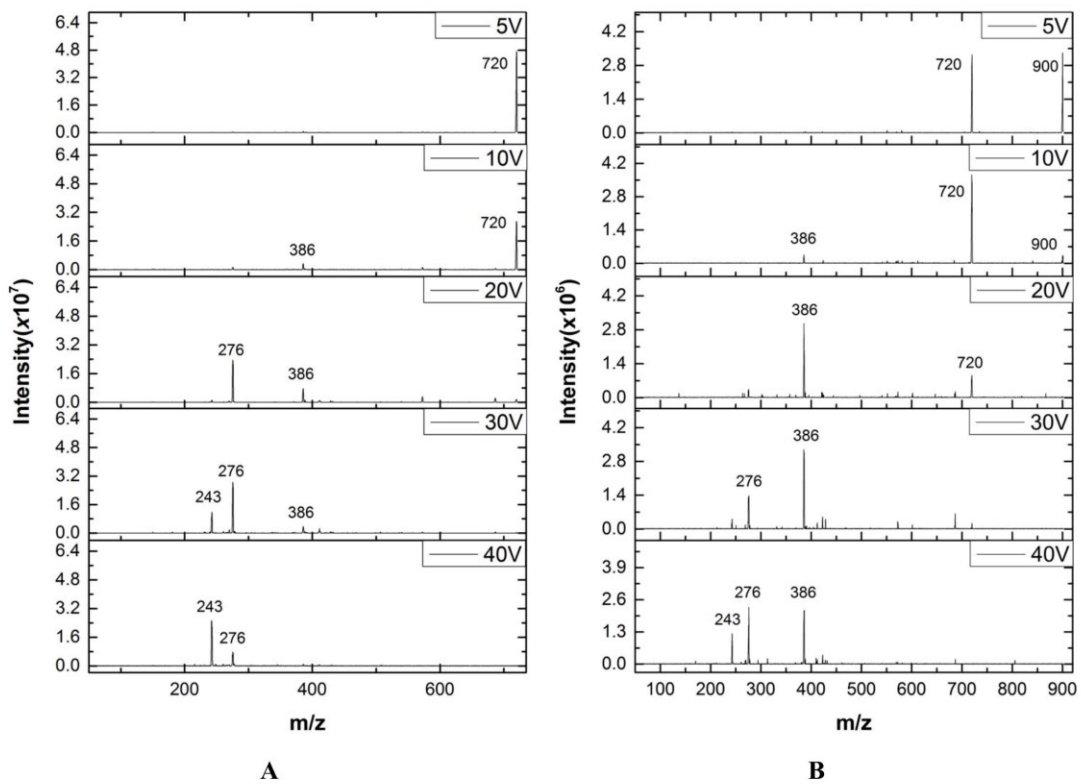
Fig.S9: Tandem mass spectra at different collision energies of (**A**) 720 *m/z* ([Cu(phen)(SAL-H)]$^+$) and (**B**) 900 *m/z* ([Cu(phen)$_2$(SAL-H)]$^+$).

A)

900 → 720

B)

720 → 386
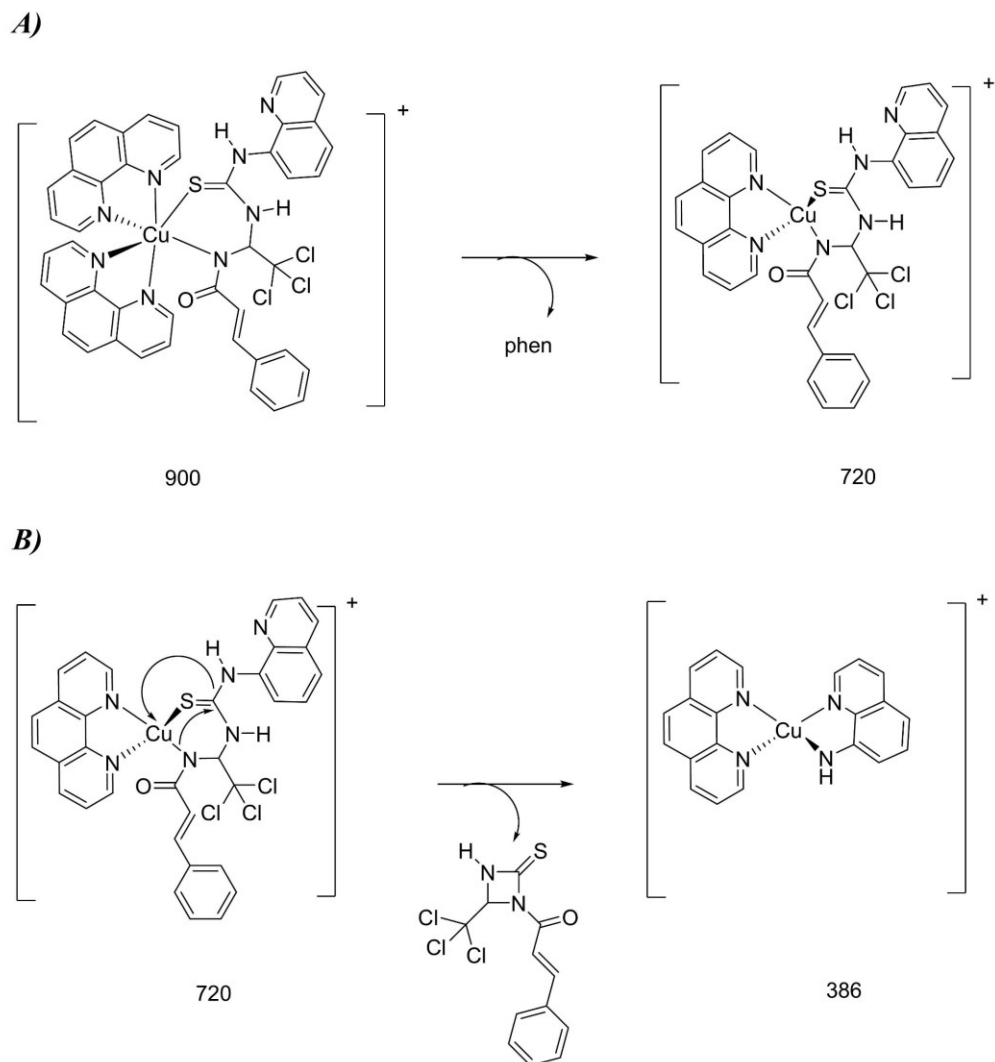
Fig.S10: proposed fragmentation patterns for product ions at 720 (**A**) m/z generated from 900 *m/z*, and for 386 *m/z* (**B**) generated from precursor 720 *m/z* under CID conditions.
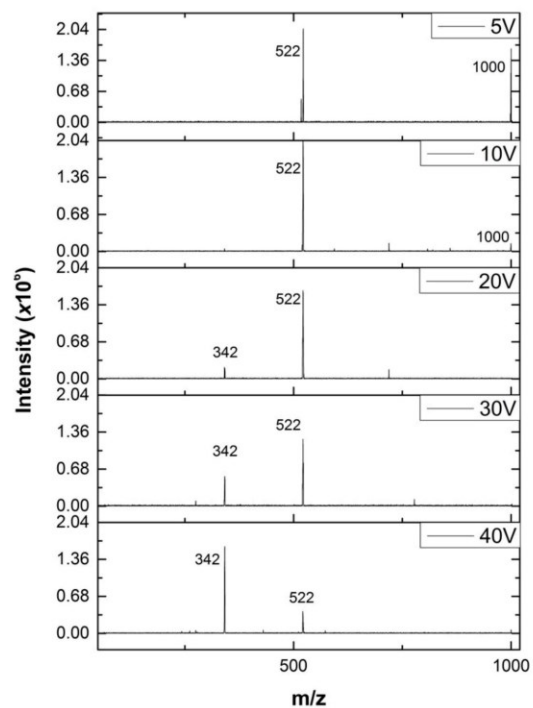
Fig.S11: Tandem mass fragmentation at different collision energies of peak at 1000 *m/z* ([Cu(phen)$_2$(SAL)(ClO$_4$)]$^+$).
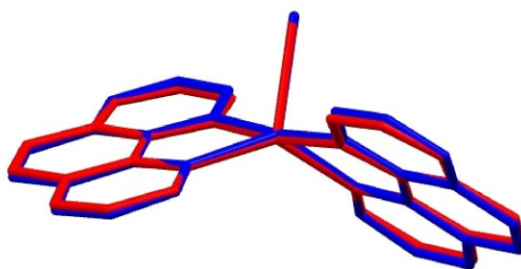
Fig. S12: superimposition of the X-Ray structure (blue coloured) and the DFT optimized structure (red coloured) of [Cu(phen)$_2$(H$_2$O)]$^{2+}$. RMSD value obtained for the optimized structure was 0.0905 Å.

120
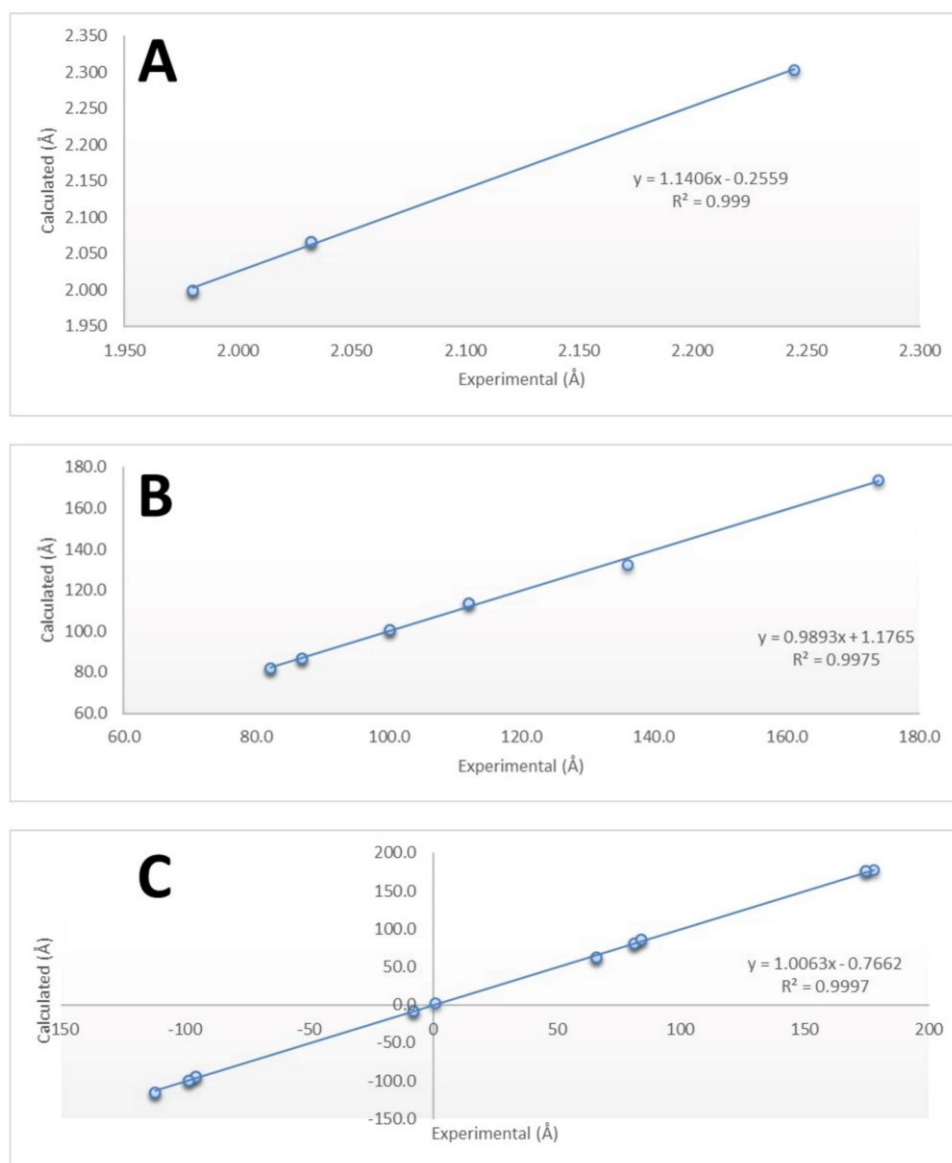
Fig. S13: linear correlation between calculated and experimental bond lengths (**A**), angles (**B**) and dihedrals (**C**) for $[Cu(phen)_2(H_2O)]^{2+}$.
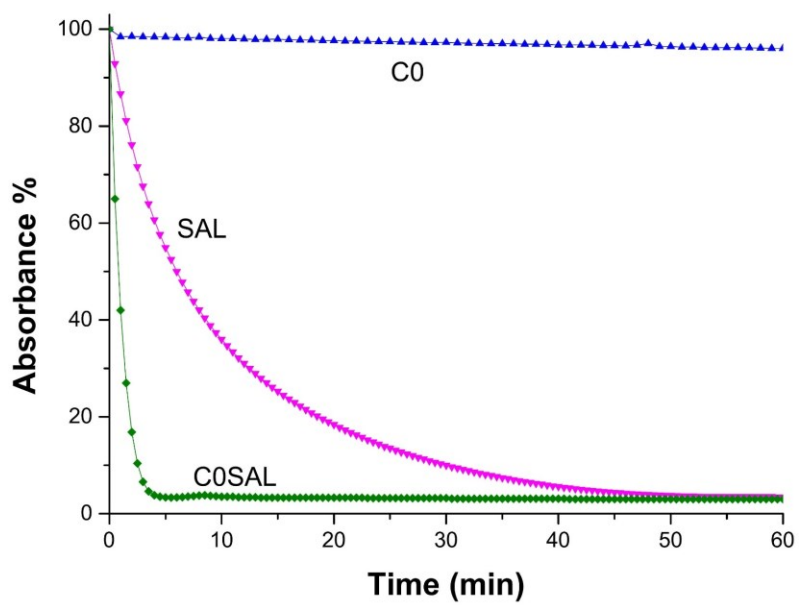
Fig. S14. Reducing activity of DPPH shown by **C0**, **SAL** and **C0SAL** (0.05 mM, absolute ethanol, 25 °C, λ 517 nm).
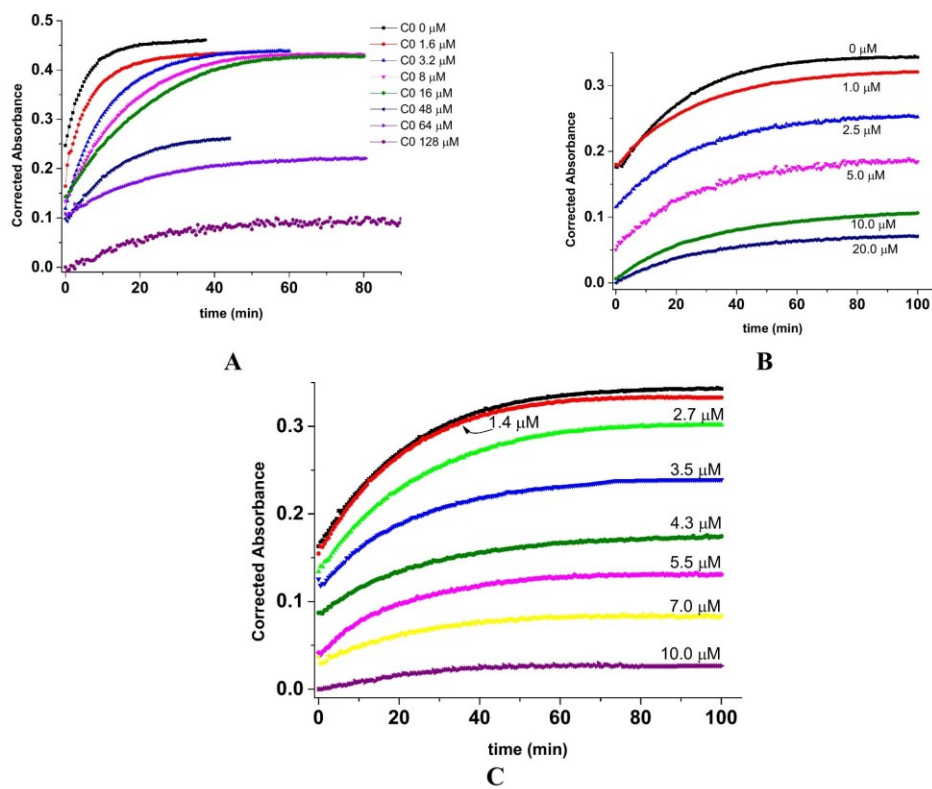
Figure S15. Absorbance at 243 nm of solutions containing linoleic acid, lipoxygenase enzyme and **C0** (**A**) or **SAL** (**B**) or **C0SAL** (**C**) at different molar concentration; linoleic acid 32 μM, lipoxygenase 0.88 nM, pH 7.4 TRIS buffer, T 25°C (values are corrected for the absorbance of **C0SAL**).

Fig. S16: superimposition of the crystallized pose (blue colored) and the docked pose (red colored) of ligand 3,4-dihydroxybenzoic acid (dhb). RMSD value obtained for the docked pose was 0.6176 Å.
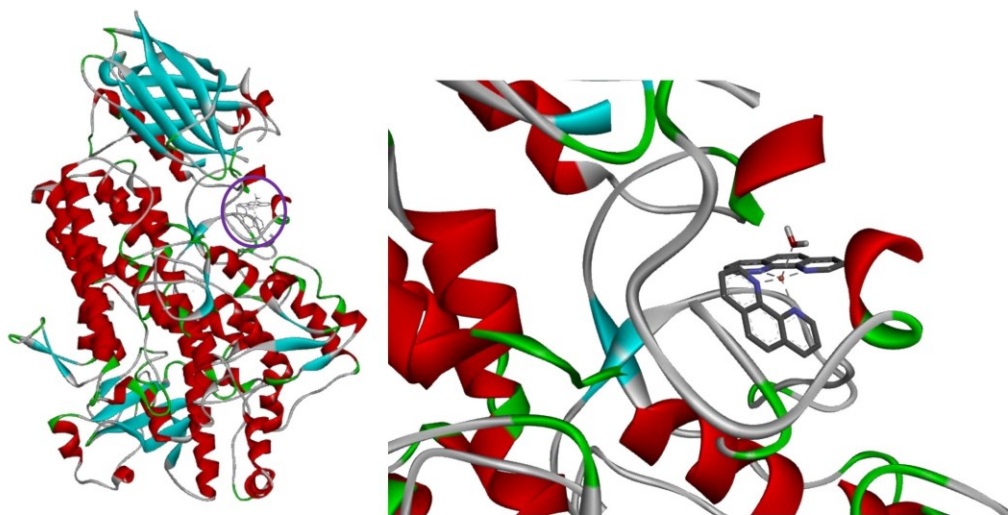
Fig. S17: full view of the complex between the highest-ranking score of $[Cu(phen)_2(H_2O)]^{2+}$ and Soybean LOX (sx); zoom of the binding pocket occupied by the highest ranking score of $[Cu(phen)_2(H_2O)]^{2+}$ and Soybean LOX (dx).
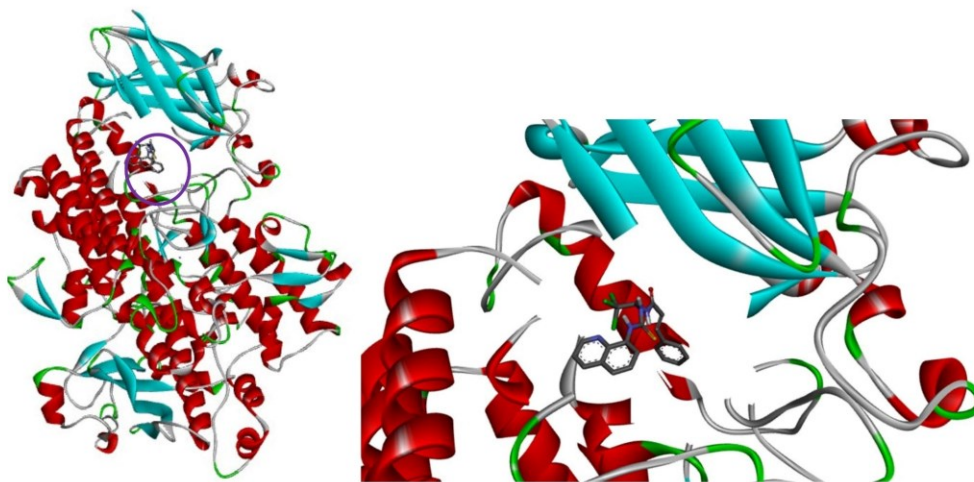
Fig. S18: full view of the complex between the highest-ranking score of SAL and Soybean LOX (sx); zoom of the binding pocket occupied by the highest ranking score of SAL and Soybean LOX (dx).
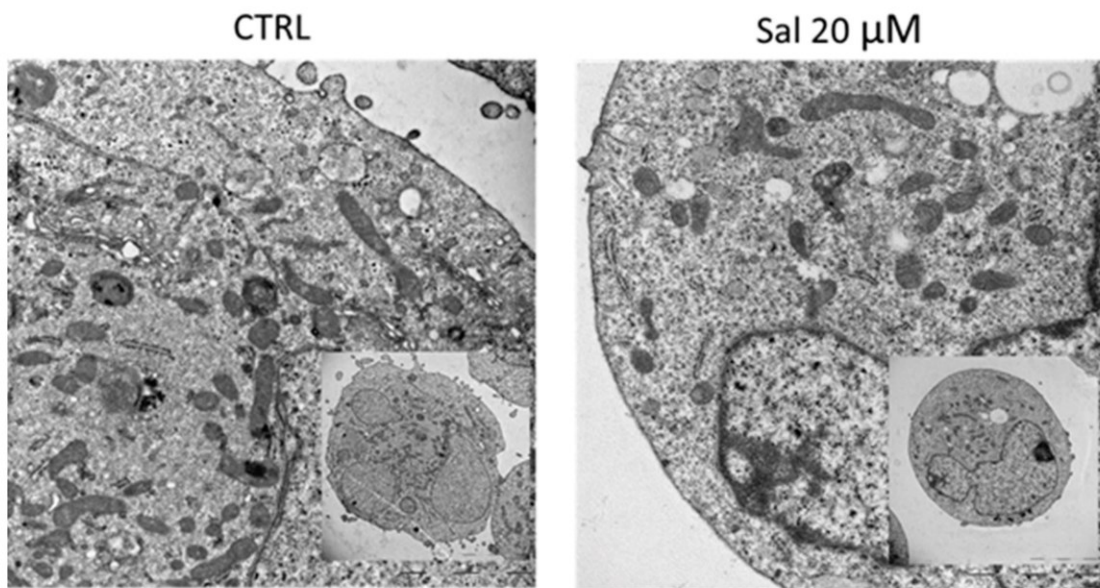
Fig. S19. Transmission electron microscopy (TEM) documenting absence of cytotoxicity in 24 h SAL-treated cells, by visualizing cell ultrastructure. Insets show the overall cell morphology. Scale bars indicate 2 mm.
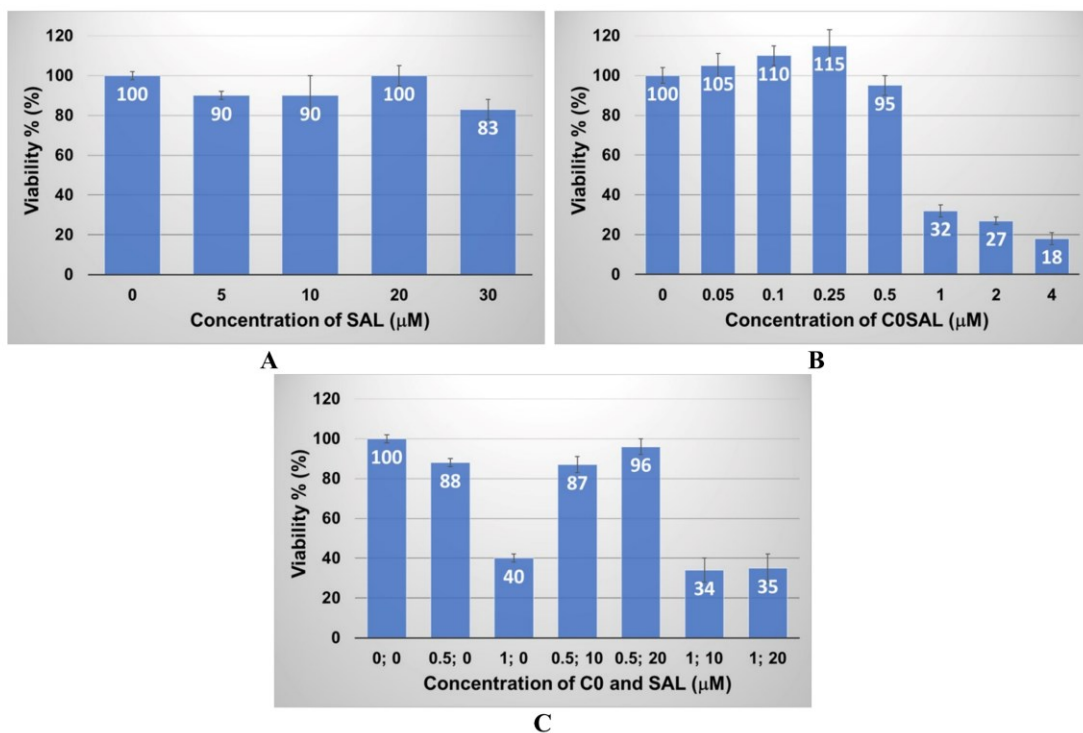
Fig. S20. Viability % of A2780 cells cultured for 24 h in the presence of **SAL** (**A**), **C0** (**B**) and **C0SAL** (**C**). Plots represent means and SD from three independent experiments performed in technical pentaplicates.
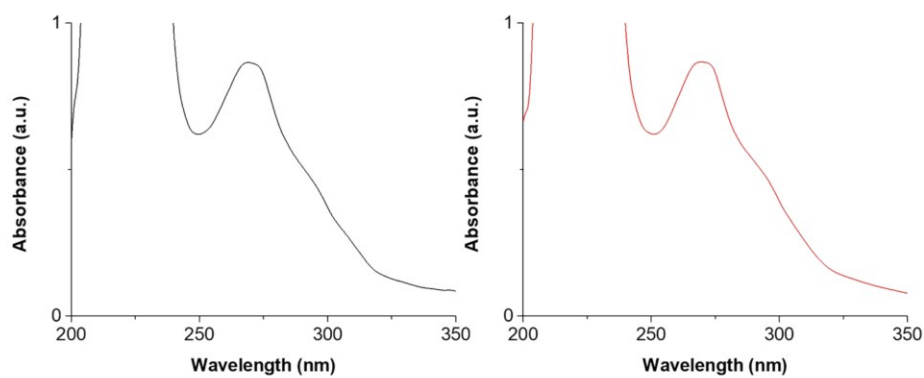

Fig. S21. C0SAL absorption spectrum in DMSO:TRIS (0.5:99.5) freshly prepared (right) and after 48 hrs. (left), C0SAL 10 microM, 1 cm optical path length, 25 °C, pH 7.4 TRIS buffer.

SAL	DFT
C9-O	1.223
C9-N1	1.363
C11-Cl1	1.765
C11-Cl2	1.782
C11-Cl3	1.761
N2-C12	1.371
C12-S	1.661
C12-N4	1.353
H10⋯O	1.938
H10⋯O-C9	102.4
N1-C10-N2	112.5
N2-C12-S	122.9
N4-C12-S	126.3
N2-C12-N4	110.7
Cl1-C11-C10	107.9
H10⋯O-C9-N1	-14.2
C9-N1-C10-C11	-96.4
C9-N1-C10-N2	30.1
Cl1-C11-C10-N2	176.5
C1-C11-C10-N1	-56.6

Table S3: Selected optimized bond distances (Å), angles (°) and dihedrals (°) for the DFT optimized structure of **SAL** and corresponding structural data. Atom labelling scheme as in Figure 4B.

Results and discussion

Article 4.

A novel heteroleptic Cu(II)-phenanthroline complex with the ER-stress modulator Ursodeoxycholic Acid with anticancer properties

Abstract

By reacting the anticancer [Cu(phen)$_2$(OH$_2$)](ClO$_4$)$_2$ (**C0**) with the bile acid Ursodeoxycholic Acid (**UDCA**), the novel heteroleptic [Cu(phen)$_2$(UDCA-H)](ClO$_4$) (**C0UDCA**) complex was obtained. The coordination mode for the novel **C0UDCA** complex has been proposed by merging results from different experimental (MS, UV-Vis, FT-IR) and theoretical (DFT) techniques. This complex inhibits cell growth and affects cell viability of both ovarian (SKOV-3) and pancreatic (PANC-1) cancer cells at micromolar concentration level. Moreover, it interferes at the Endoplasmic Reticulum (ER) level, inducing the Unfolded Protein Response (UPR), as evidenced from Western Blot results.[*] Although being devoid of antioxidant activity, this compound can inhibit soybean lipoxygenase at micromolar level, with an IC$_{50}$ value that is 15.7 and 12.5-fold lower than its synthetic precursors **UDCA** and **C0**, respectively. **C0UDCA** could inhibit this enzyme via allosteric modulation, as indicated from docking calculation results.

---

[*]These studies were performed in collaboration with the research group of Prof. Petr Vaňhara, Masaryk University (MUNI).

A novel heteroleptic Cu(II)-phenanthroline complex with the ER-stress modulator Ursodeoxycholic Acid with anticancer properties

Sebastiano Masuri[1], Lukáš Moráň[2,3], Tereza Vesselá[2], Enzo Cadoni[1], Maria Grazia Cabiddu[1], Francesco Isaia[1], Francesca Simeoni[1], Luca Puddu[1], Josef Havel[4,5], Petr Vaňhara[2,4], Tiziana Pivetta[*,1]

[1] Department of Chemical and Geological Sciences, University of Cagliari, Cittadella Universitaria, 09042, Monserrato, Cagliari, Italy.

[2] Department of Histology and Embryology, Faculty of Medicine, Masaryk University, 62500, Brno, Czech Republic.

[3] Research Centre for Applied Molecular Oncology, Masaryk Memorial Cancer Institute, 65653 Brno, Czech Republic.

[4] International Clinical Research Center, St. Anne's University Hospital, 65691, Brno, Czech Republic.

[5] Department of Chemistry, Faculty of Science, Masaryk University, 62500, Brno, Czech Republic.

*corresponding author: tpivetta@unica.it

To be submitted

Introduction

Bile acids are hydroxylated steroid acids biosynthesized from cholesterol and predominantly found in the bile of mammal and other vertebrates. They are classified in primary (i.e. cholic acid CA, chenodeoxycolic acid CDA), whose biosynthesis take place in liver cells, and secondary (i.e. deoxycholic acid DCA, ursodeoxycholic acid **UDCA**), which are the results of biochemical modifications on the primary ones by intestinal bacteria.[1] Bile acids are involved in cholesterol catabolism and emulsification of lipid in the intestinal tract. In addition, thanks to their steroidal backbone, these compounds work as endocrine mediators activating several receptors (e.g. nuclear farnesoid X receptor (FXR) and pregnane X receptor (PXR), the G-protein coupled receptor TGR5, etc) that are involved in pathways, such as glucose and lipid metabolisms.[2] **UDCA** (**Figure 1A**), currently approved for the treatment of primary biliary cirrhosis and other cholestatic disorders,[3,4] have shown to possess both cytoprotective and cytotoxic activities, as evidenced by several studies. The mechanism of action has proved to be mostly cell-type dependent and multifactored.[1] Studies of **UDCA** in combination with conventional anticancer drugs have pointed out that some common side effects of the former ones are attenuated by the presence of **UDCA**.[5]

Since the discovery of cisplatin cytotoxic properties, and with the perspective of designing novel metal based anticancer compounds with a better toxicological profile, several copper based metallodrugs have been prepared and tested on different cell lines.[6–8] Previous studies carried out in our research group have shown that Cu(II) complexes such as $[Cu(phen)_2(H_2O)](ClO_4)_2$ (**C0**, **Figure 1B**), $[Cu(phen)_2(L)](ClO_4)_2$ (where L are imidazolidine-2-thione and some N-alkylated derivatives) and $[Cu(phen)_2(Salubrinal)](ClO_4)_2$ are able to

induce massive cell death in ovarian cancer cells (A2780, SKOV-3) by activating the pro-apoptotic branch of the Unfolded Protein Response (UPR).[9,10] UPR is a coordinating adaptive program that responds to accumulation of improperly folded proteins in the endoplasmic reticulum (ER), a condition known as ER stress. Initiation of UPR can lead to adaptation or apoptosis, especially in a condition of prolonged or severe ER stress.[11] **UDCA** and its taurine-conjugated derivative (taursodeoxycholic acid, **TUDCA**), have been extensively studied as ER stress modulator, and proved to exert its cytoprotective activity acting as chemical chaperone.[12,13] Previous studies of **TUDCA** in combination with the mixed Cu(II) phenanthroline complexes cited above have evidenced how the cytotoxicity of the former compounds might be tuned by the presence of **TUDCA** itself.[9,10]

Given these premises and considering that **UDCA** comprises a carboxylic group that might interact with Cu(II), we deemed to verify if **C0** and **UDCA** could chemically react to show interesting biological properties. The reactivity of **C0** and **UDCA** (as sodium salt) was studied, and the novel mixed complex **C0UDCA** (**Figure 1C**) was obtained. Coordination around the metal ion was speculated by combining solution and solid-state studies with theoretical calculations. The antioxidant and lipoxygenase inhibition profile of the novel mixed complex were evaluated and compared with its precursors **C0** and **UDCA**. Cytotoxicity of **C0**, **UDCA** and **C0UDCA** against ovarian (SKOV-3) and pancreatic (PANC1) cancer cells was studied.
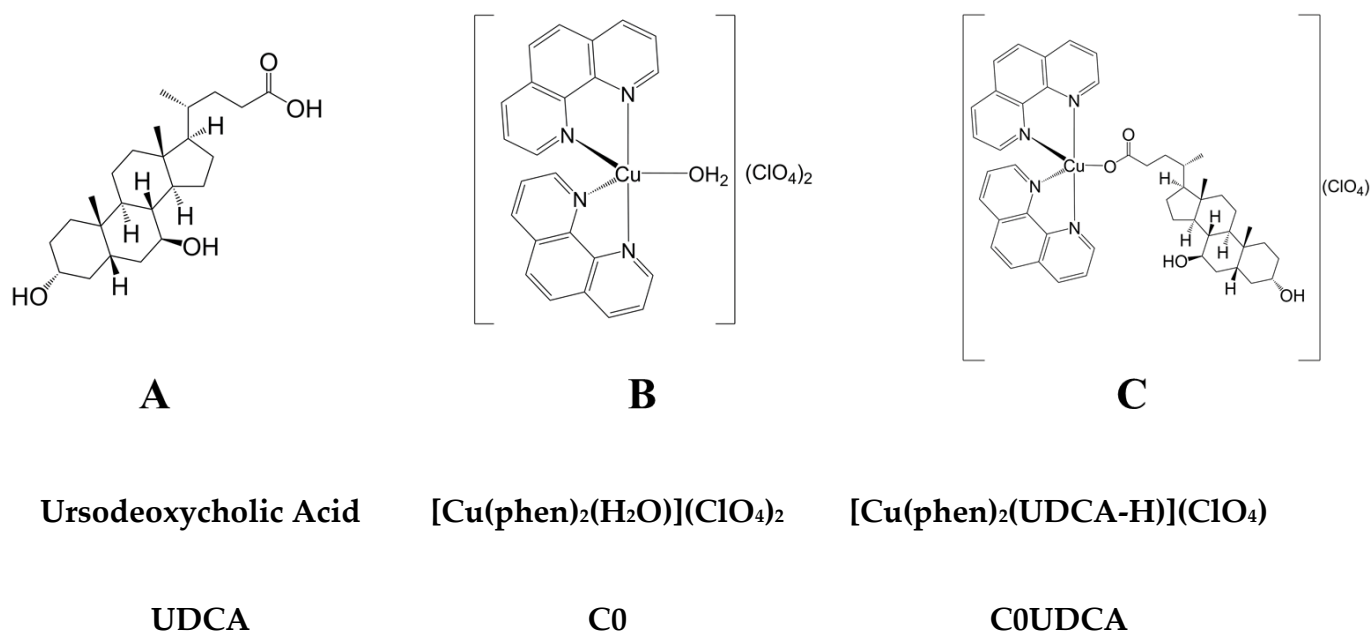
A	B	C
Ursodeoxycholic Acid	**[Cu(phen)₂(H₂O)](ClO₄)₂**	**[Cu(phen)₂(UDCA-H)](ClO₄)**
UDCA	C0	C0UDCA

Figure 1. Molecular structures and acronyms of the studied compounds.

Experimental

Reagents

Acetonitrile, isopropanol, absolute ethanol, sodium linoleate, lipoxygenase, tris(hydroxymethyl)aminomethane hydrochloride (TRIS), dimethyl sulfoxide (DMSO), butylated hydroxytoluene (BHT), were purchased from Merck (Milan, Italy). Basic copper carbonate and ursodeoxycholic acid were purchased from Alfa-Aesar. 3- (4,5-dimethylthiazol-2-yl)-2,5-diphenyltetrazolium bromide (MTT) was purchased from Sigma-Aldrich (Czech Republic). The commercial reagents were used as received, without any further purification. Ultrapure water was obtained with MilliQ Millipore.

Mass spectrometry studies

Mass spectra were recorded using a triple quadrupole QqQ Varian 310-MS mass spectrometer by using the atmospheric-pressure ESI technique. All the sample solutions were infused into the ESI source with a programmable syringe pump (1.25 mL/h constant

flow rate). A dwell time of 14 s was used, and the spectra were accumulated for at least 10 min to increase the signal-to-noise ratio. Mass spectra were recorded in the m/z 100 – 1000 range. The experimental conditions were: needle voltage 3500 V, shield 800 V, source temperature 60 °C, drying gas pressure 20 psi, nebulizing gas pressure 20 psi, detector voltage 1450 V. Tandem MS experiments were performed using argon as the collision gas (1.8 psi). The collision energy was varied from 5 to 50 V. High resolution mass spectra were recorded on a Thermofisher ESI-MS/MS-ORBITRAP-ELITE and Velos PRO. The sample solutions were infused directly into the ESI source using a programmable syringe pump at a flow rate of 5 µL/min. Mass spectra were recorded in the m/z 600 – 850 range. The experimental conditions were needle voltage 2.5 kV, shield 0.8 kV, source temperature 50 °C, drying gas pressure 20 psi, nebulizing gas pressure 20 psi, detector voltage 1.3 kV. The isotopic patterns of the measured peaks in the mass spectra were analysed using the mMass 5.5.0 software package.[14,15] All the mass values are indicated as monoisotopic masses, computed as the sum of the masses of the primary isotope of each atom in the molecule (note that the monoisotopic mass may differ from the nominal molecular mass, in particular for big molecules).

Spectroscopic studies

UV–Visible spectrophotometric measurements were performed with an Agilent Cary 60 spectrophotometer, in the range 200 – 1100 nm, with a 1 cm quartz cell at 25 °C. The complex formation between **C0** and **UDCA** was studied at 25 °C by spectrophotometric titration in phosphate buffer 0.05 M, pH 7.4 The number of linearly independent absorbing species was obtained by applying eigenvalues analysis on the absorbance data matrix. The complex

formation constant was calculated using the Hyperquad 2006 program.[16] The equilibrium constant is expressed as overall association constant. The stoichiometry of the formed complex was studied also by continue variation method (Job's plot).[17,18] IR spectra were acquired with a Bruker Vector 22 spectrophotometer, preparing the samples as KBr pellets.

Synthesis

C0: The precursor $[Cu(phen)_2(OH_2)](ClO_4)_2$ (**C0**) was prepared as previously described.[19] In brief, perchloric acid was added to an ethanolic suspension of $Cu_2(CO_3)(OH)_2$, the resulting blue solution was cooled and an ethanolic solution of 1,10-phenanthroline, at 1:2 metal:ligand molar ratio, was slowly added, the formed blue-green precipitate was filtered off, washed with ethanol and dried at room temperature (Yield 85 %).

Sodium Ursodeoxycholate (prepared for FT-IR measurements): **UDCA** (0.2318 mmol) was suspended in acetonitrile (5.0 mL), then 1 eq of NaOH 1.0 M water solution (232 μL) was added to the suspension. The reaction mixture was left under stirring at r.t. for 1hr. The product was recovered by filtration, washed with acetonitrile, and dried. 0.0411 g (Yield 43%). Elemental analysis % for $C_{24}H_{39}NaO_4$ was expected C 69.53, H 9.48, found C 69.55, H 9.52. FT-IR (KBr), cm^{-1}:1561 $v_{asym}(OCO)$, 1406 $v_{sym}(OCO)$.

C0UDCA: $[Cu(phen)_2(UDCA-H)](ClO_4)$ was prepared as following: UDCA (0.2385 mmol) was treated with 1 eq of NaOH to obtain the corresponding sodium salt. This solution was slowly added to a water suspension of **C0** (1 eq, 10 mL). The progressive formation of a pale blue precipitate was observed. The reaction mixture was stirred at room temperature for 24 hrs. The desired product was recovered by filtration in vacuum, washed with water, diethyl ether and dried. 1.1302 g (Yield 69 %). Elemental analysis % for $C_{48}H_{55}ClCuN_4O_8$ was

expected C 63.01, H 6.06, N 6.12, found C 63.12, H 6.11, N 6.09. ESI-MS. m/z found (calc.): 814.2 (814.3) for [Cu(phen)$_2$(UDCA-H)] $^+$, with the expected isotopic pattern. FT-IR (KBr), cm^{-1}:1565 $v_{asym}(OCO)$, 1375 $v_{sym}(OCO)$. UV-Vis (PB 0.05M, pH 7.4) ε, M^{-1} cm^{-1} (λ, nm): 2.29 10^5 (205), 5.4 ·10^4 (271).

Determination of the reducing activity of the stable radical 1,1-diphenyl-picrylhydrazyl (DPPH)

Test compounds were dissolved in DMSO at 1.0 mM concentration, then a 1:10 dilution was performed with absolute ethanol. DPPH solution (0.1 mM, absolute ethanol) was prepared freshly, stored in the dark and used in a few hours. 1500 µL of the test solutions were added to an equal volume of DPPH, inside the cuvette, and the absorbance in the range 200 - 650 nm was recorded, at room temperature, for 70 minutes. The absorbance at 517 nm was evaluated to examine the time-dependence of the radical scavenging activity(RA).[20,21]

Soybean lipoxygenase inhibition study *in-vitro*

Stock solution of **C0**, **UDCA** and **C0UDCA** were dissolved in DMSO at ≈ 0.1 mM concentration, then the proper dilution was performed with TRIS buffer at pH 7.4. Sodium linoleate (0.00200 g, V 10.0 mL, ≈ 0.65 mM) and soybean lipoxygenase (0.00200 g, V 10.0 mL, ≈ 2·10^{-6} M) were dissolved in TRIS buffer at pH 7.4, then the required dilutions were performed with TRIS buffer at pH 7.4. Solutions of sodium linoleate, soybean lipoxygenase and **UDCA** or **C0UDCA** were prepared daily and kept in the dark at 5°C. The conversion of sodium linoleate to 13-hydroperoxylinoleic acid was monitored recording the absorbance at 243 nm and compared with the appropriate standard inhibitor caffeic acid. The absorbance at 243 nm and not at 234 nm (maximum) was chosen since at 234 nm the contribution of **C0** or **C0UDCA** absorbance was not negligible.

DFT calculations

Geometry optimization of deprotonated **UDCA** (**UDCA-H**) and **[Cu(phen)₂(UDCA-H)]⁺**

were performed on an Intel-i7 based system using the release 4.2.0 of ORCA.[22] Input files

for DFT calculations were prepared using Avogadro 1.2.0.[23] Geometry optimizations were

performed at DFT level, using the hybrid PBE0 functional[24] and def-2 TZVP basis set.[25] The

choice of the computational setup has been made based on the results previously reported

for similar Cu(II)-phenanthroline systems.[26] IR frequency calculations were carried out to

verify the nature of the minima of each optimization by assessing the absence of calculated

negative frequencies. Atomic charges at natural population analysis (NPA) level were

calculated by means of JANPA software package.[27] Molecular orbital shapes and energies

were investigated using Chemcraft v1.8.[28]

Molecular Docking

Molecular docking calculations were performed using Autodock Vina software.[29] DFT-

optimized structure of Ursodeoxycholate and **C0UDCA** were exported as PDB files. The X-

ray structure of soybean lipoxygenase LOX-1 (PDB:3PZW) was chosen as the receptor. Prior

to docking, both ligands and receptor were processed using MG Labs Autodock Tools.[30] In

the receptor structure, water molecules were removed, while polar hydrogens and

Gasteiger charges were added. The atomic charge for the Fe2840 cofactor was manually

adjusted in the generated pdbqt file. For all the ligands, polar hydrogens and Gasteiger

charges were added, while no rotational constraints were applied. Atomic charges for

copper were manually adjusted in the generated pdbqt files. The ligands were docked using

a grid cube of 30 × 30 × 30 points centred at Iron cofactor coordinates (x = 24.527, y = 44.349,

z = 10.587), or using a grid cube of 30 × 25 × 20 points at coordinates x = 24.970, y = 11.444, z = -0.936. A spacing of 1.0 Å and an exhaustiveness value of 100 was chosen in both cases. Molecular interactions and docked poses were evaluated using Biovia Discovery Studio Viewer v19.[31]

Cell viability assay

Cells were cultured for 24 h on a 96-well plate at a density of 10 000 cells per well in medium containing **C0**, **TUDCA** or **C0UDCA** at the indicated concentrations. DMSO was used as a control. Then, the MTT reagent (3- (4,5-dimethylthiazol-2-yl)-2,5-diphenyltetrazolium bromide) (Sigma-Aldrich, Czech Republic) was added directly to the culture medium for 4 h. Then, medium including MTT reagent was aspirated, and the cells lysed by addition of 90% isopropanol, 0.04 M HCl and 10% Triton/Tween. Absorbance was recorded at 570 nm by a Synergy HTX multi-mode reader (BioTek Instruments, VT, USA). All measurements were performed in technical pentaplicates and repeated in three independent experiments.

Cell growth assay

Cells were cultured for 24-72 h on a 6-well plate at a density of 20 000 cells per well in medium containing **C0**, **TUDCA** or **C0UDCA** at the indicated concentrations. DMSO was used as a control. Cells were enzymatically detached, washed in Phosphate Buffer Saline (PBS) and counted using Bürker counting chamber. Growth experiments were repeated in three independent experiments.

Flow cytometry

Vital staining of apoptotic cells was performed using FITC-conjugated annexin V (Roche Diagnostics, Mannheim, Germany) and propidium iodide. The cells were washed twice

with staining buffer (10 mM Hepes, 140 mM NaCl, 10 mM $CaCl_2$, pH 7.4), incubated with annexin V-FITC (0.5 ll/sample) and propidium iodide (5 lg/ml) for 15 min and analysed by flow cytometry (BD FACS Aria™ II Cell Sorter). At least 10,000 viable cells were collected for each sample. Flow cytometric data were analyzed using FlowJoTM 7.2.2. software (Becton– Dickinson). Results were evaluated as a percentage of double-negative cells (intact), annexin V-positive cells (early apoptotic), and double-positive (necrotic or late apoptotic) cells.

SDS-PAGE and western blotting

SKOV-3 Cells were incubated with **C0UDCA** at 2.0 μM concentrations for 24 hrs using DMSO as control. Cells were washed twice with PBS and lysed with SDS lysis buffer (100mM TRIS-HCl pH 7.4, 1% SDS, 10% glycerol). Protein content in the cell extract was quantified using the Bradford-based BioRad protein Assay Kit. Cell extracts were then mixed with 2×Laemmli sample buffer (100 mM Tris pH 6.8, 4% SDS, 200 mM DTT, 20% glycerol, and 0.1% bromophenol blue) and boiled for 5 min. An equivalent of 10 μg proteins was resolved using 10% sodium dodecylsulfate polyacrylamide gel electrophoresis (SDS-PAGE). Resolved proteins were then electroblotted onto a 0.45 mm polyvinylidene difluoride (PVDF) membrane (Millipore, Czech Republic) and incubated with the indicated primary antibodies diluted 1:1000 at 4 °C overnight (Actin cat. no: Ab1801, from Abcam, UK; CHOP #2895 and BiP #3177; from Cell Signaling, MA, USA). Blots were developed using horseradish peroxidase (HRP)-conjugated anti-rabbit HRP #7074 or anti-mouse HRP #7076 (both Cell Signaling, USA) secondary antibodies, diluted 1:7500, and ECL plus (GE

Healthcare) according to manufacturer's protocol. Results were visualized using a ChemiDoc® Touch Imaging System (Bio-Rad).

Results and Discussion

Synthesis

By reaction between **C0** and the sodium salt of **UDCA** ($NaC_{24}H_{39}O_4$), the novel complex $[Cu(phen)_2(C_{24}H_{39}O_4)](ClO_4)$ (**C0UDCA**) was obtained. The stoichiometry of the novel complex has been proposed based on the elemental analysis, Job's plot and ESI-MS spectrometry. The coordination mode around the metal ion in was assessed using UV-Vis, I.R. spectroscopy, MS-MS experiments and theoretical calculations. In the ESI-MS spectrum of **C0UDCA** (**Figure 2**) a peak at 814 m/z due to the species $[Cu(phen)_2(UDCA-H)]^+$ ion was observed, as a charged fragment of the neutral precursor $[Cu(phen)_2(UDCA-H)](ClO_4)$. In addition, a peak at 634 m/z of the ion $[Cu(phen)(UDCA-H)]^+$, originated from 814 m/z by loss of a phenanthroline unit, was highlighted. Some fragments of minor intensity containing Cu(I) complexes were also observed in the mass spectrum (the reduction of Cu(II) to Cu(I) is widely observed in ESI phase, depending on the used solvent).[32] The identity of the reported ions was confirmed by matching between calculated and experimental isotopic patterns (**Figure S1**) and tandem mass experiments (see Mass spectrometry).
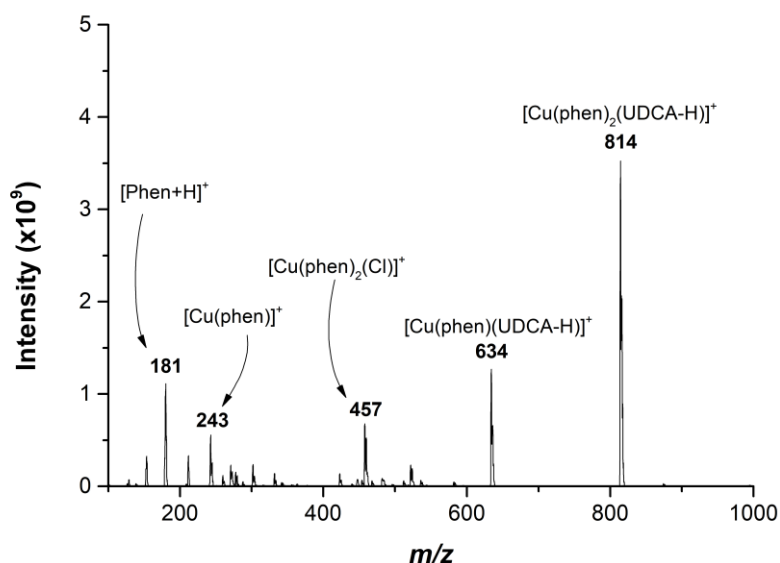
Figure 2: ESI-MS spectrum of [Cu(phen)$_2$(UDCA-H)](ClO$_4$) (methanol:water 1:1). All the mass values are expressed as monoisotopic masses, computed as the sum of the masses of the primary isotope of each atom in the molecule (note that the monoisotopic mass may differ from the nominal molecular mass, especially for big molecules).

High-resolution mass spectrum of **C0UDCA** in the range 600-850 was recorded in order to further confirm the composition of the peaks at 814 and 634 *m/z*, (**Figure 3A**). As can be observed, the fitting of the isotopic pattern (**Figure 3B**) and the matching of the experimental exact masses with the calculated ones (814.3532 u vs 814.3519 u and 634.2844 u vs 634.2832 u) confirm the proposed stoichiometry.
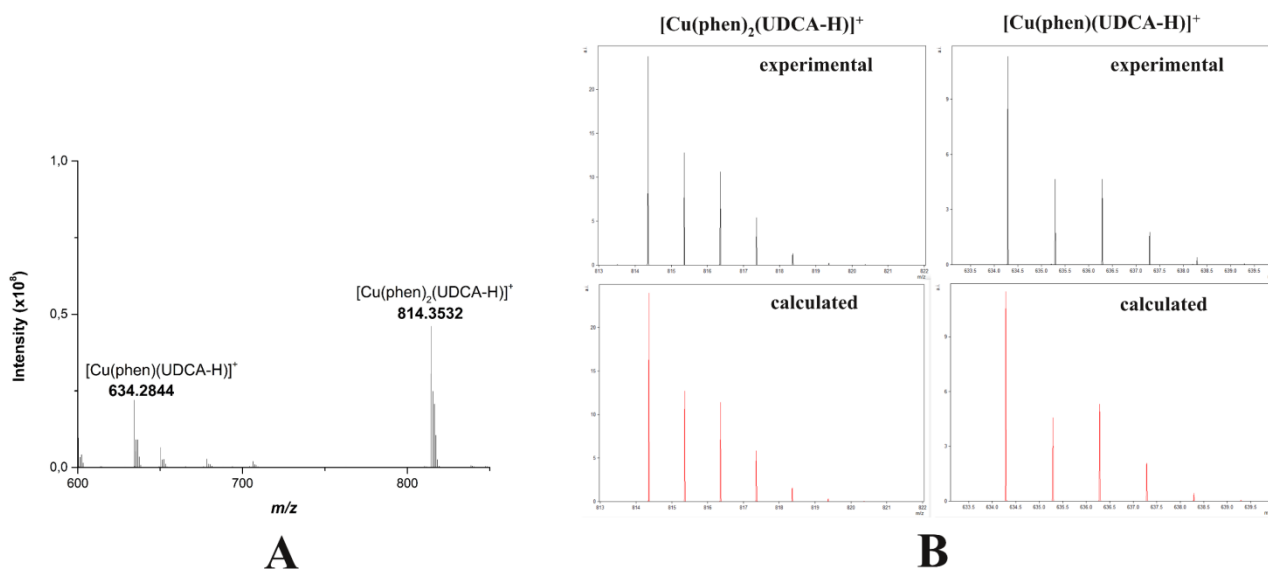
Figure 3: (**A**) High-resolution mass spectrum of **C0UDCA** in the 600-850 *m/z* range, (**B**) experimental and calculated isotopic pattern for peaks at 814 and 634 *m/z*, (methanol:water 1:1). All the mass values are expressed as monoisotopic masses.

The novel copper complex is stable in the solid state at room temperature. It is soluble in DMSO at 0.1 M concentration level, in CH_3CN at 0.01 M, and in the H_2O:CH_3CN mixture (1:1) at 8 mM. Solubility in water could be enhanced by dissolving the title compound in a minimal amount of DMSO at 40 °C prior to water addition. In this case, sonication or vigorous mixing should be avoided to prevent the formation of emulsions. Solubility in aqueous solutions prepared under this experimental setup is up to 0.5 mM. Stock solutions of **C0UDCA** in DMSO and CH_3CN are stable at 4 °C up to 6 months, while stock solutions in H_2O:CH_3CN mixture (1:1) could be stored at r.t. for 2 weeks. In order to check the stability of the novel complex in an aqueous medium that better resemble a biological fluid, **C0UDCA** was dissolved in phosphate buffer (0.05 M pH 7.4) at 4.2 μM and spectral variation in the 200–325 nm range was followed for 24 h by recording 1 spectrum every 60

minutes (**Figure S2**). No significant variations in the shape and intensity of the spectra were observed.

Solution studies

All solution equilibria experiments were performed in phosphate buffer (0.05M, pH 7.4) to study the equilibria involved between **C0** and **UDCA** in an aqueous medium. In this experimental setup **UDCA** will be almost present as monoanionic species due to the proton loss from the carboxylic moiety. The method of continuous variation (Job's method) was initially applied in order to determine the number and stoichiometry of the complexes formed between **C0** and **UDCA**.[17,18] In **Figure 4A** absorption spectra in the 200 – 325 nm range collected varying from 0 to 1 the deprotonated **UDCA** molar fraction, are reported; absorbance data at 207 and 219 nm, corrected for the absorbance of the pure reactants, reported as a function of the deprotonated **UDCA** molar fraction (**Figure 4B**), clearly indicates a 1:1 ($\chi_L = 0.49$) ligand to metal complex. In **Figure S3**, uncorrected absorption data at the same wavelengths are reported.
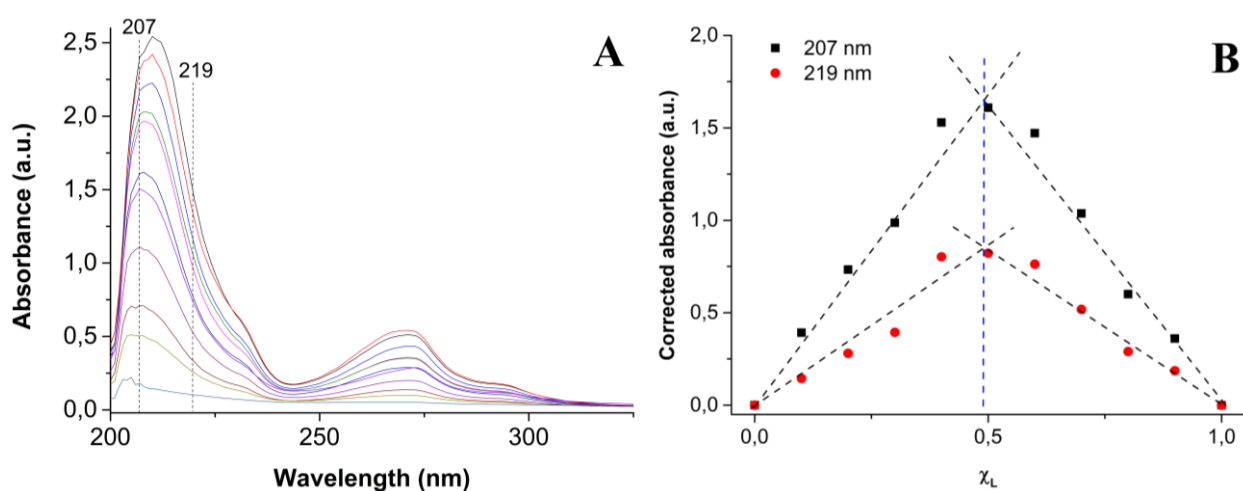
Figure 4. (**A**) Absorption spectra collected varying the deprotonated **UDCA** molar fraction from 0 to 1 for the system **C0** - deprotonated **UDCA** (2.14·10⁻⁵ M, phosphate buffer 0.05 M,

pH 7.4, 25 °C, 1 cm optical path length); (**B**) Normalized Job's plot for **C0** - deprotonated **UDCA**.

Once defined the complexation model, the complex formation constant was determined by spectrophotometric titration. Equilibrium studies of **C0** and deprotonated **UDCA** were carried at 20 μM concentration. In **Figure 5A** selected spectra recorded in the 200 – 325 nm range during the titration of **C0** with deprotonated **UDCA**, are reported. By adding increasing amounts of the ligand, a decrease in absorbance accompanied with a gradual shift at 204 nm of the band initially centred at 208 nm was observed. From eigenvalue analysis of the spectrophotometric data, three significant eigenvalues were found, indicating three linearly independent absorbing species in solution. By fitting the experimental data considering the species $[Cu(phen)_2]^{2+}$, deprotonated **UDCA** and $[Cu(phen)_2(UDCA-H)]^+$, the complex formation constant expressed as log β was determined (5.17 ± 0.19). Calculated pure spectra, expressed as Absorptivity against wavelengths, for all the absorbing species are reported in **Figure 5B.**
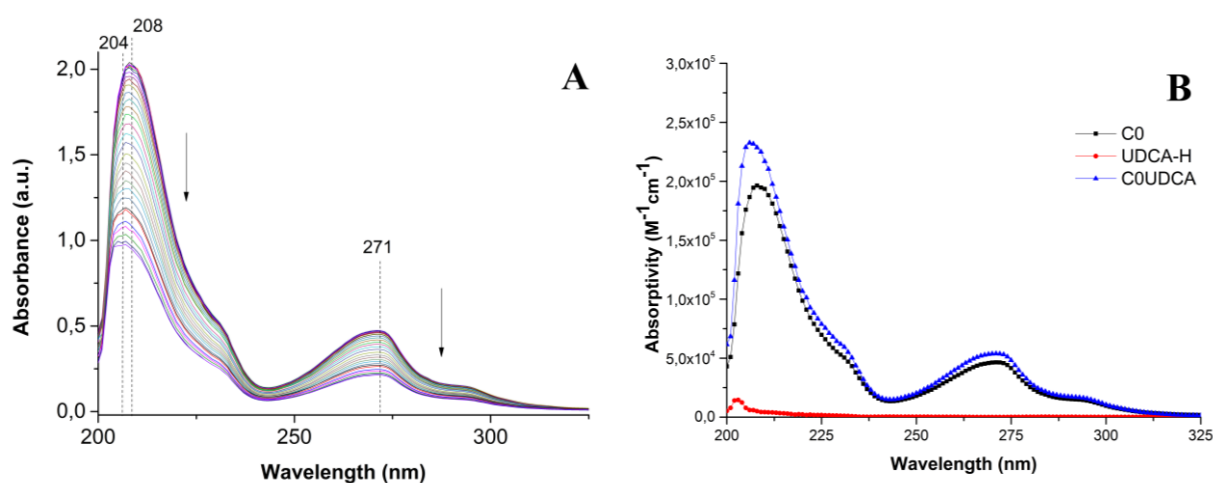
Figure 5: Selected spectra collected during the titration of (**A**) 2.12·10⁻⁵ mmol of **C0** with deprotonated **UDCA** (2.55·10⁻⁵ M) in 200-325 nm range; (**B**) absorptivity spectra of **C0**, deprotonated **UDCA** (**UDCA-H**) and **C0UDCA** in 200 - 325 nm range (phosphate buffer 0.05 M, pH 7.4, 25 °C, 1 cm optical path length).

Coordination mode in C0UDCA

Since any attempt to obtain single crystals suitable for X-ray analysis was unsuccessful, coordination mode around the metal ion for the novel **C0UDCA** complex was proposed by combining the experimental data, Vis-NIR and IR spectroscopy, ESI-MS and tandem MS spectrometry, with the theoretical calculations.

Vis-NIR. Vis-NIR spectrum of **C0UDCA** in the region 450 - 1100 nm is reported in **Figure S4** and features a maximum at 686 nm and a shoulder at 928 nm. A In analogy with the absorption spectra of variously ternary Cu(II) bis-phenanthroline complexes previously characterized,[19] a penta-coordinated geometry might be proposed also for the novel complex **C0UDCA**.

IR. FT-IR spectrum of **C0UDCA** (**Figure S5C**) shows a large and intense band at 3410 cm⁻¹, attributed to the hydroxyl groups of the **UDCA** moiety, while the two peaks at 2933 and 2865 cm⁻¹ are relative to the backbone stretching frequencies of the same ligand. Asymmetric and symmetric stretching peaks of oxygen carboxylate group ($v_{asym}(OCO)$ and $v_{sym}(OCO)$) fall at 1565 and 1375 cm⁻¹ respectively. In the FT-IR spectrum of sodium ursodeoxycholate (**Figure S5A**) the same bands appear at 1561 and 1406 cm⁻¹ respectively. The parameter $\Delta(OCO) = v_{asym}(OCO) - v_{sym}(OCO)$ is commonly used to gain more insights regarding the coordination mode of carboxylate functional groups in metal complexes. In particular, a $\Delta(OCO)complex > \Delta(OCO)ligand$ is indicative of an unidentate coordination mode of the

titled coordinating group.[33,34] Considering that $\Delta(OCO)$ for **C0UDCA** equals to 190 cm^{-1}, which is higher than the same value for sodium ursodeoxycholate (155 cm^{-1}), we can assume that also for **C0UDCA** coordination of carboxylate group to the metal centre takes place in mono-dentate fashion. Signals of the phen moieties are visible at 3068, 1519, 1430, 1386, 851, 724, 624 cm^{-1} (see for comparison IR spectrum of the precursor **C0**, **Figure S5B**), while the wide band in the region 1150-1030 is due to the perchlorate anion.

Mass spectrometry. Tandem MS experiments at different collision energies (CE) were performed to identify the nature of the peaks containing Copper (II), phenanthroline and **UDCA** and give more insights about the structure of the novel **C0UDCA** complex. As regards the ion [Cu(phen)$_2$(UDCA-H)]$^+$ (m/z 814), the formation of a product ion at m/z 634 is evidenced from CE 5V (**Figure 5**). The former ion, whose formula was previously proposed as [Cu(phen)(UDCA-H)]$^+$, is originated from precursor at m/z 814 by loss of one phenanthroline unit (**Figure S6A**). As observed in **Figure 5**, a gradual decrease in intensity for the peak at m/z 634 is observed, as CE is increased, a feature consistent with further fragmentation processes of the former ion. In particular, from CE 35V, two peaks at m/z 260 ([Cu(phen)(OH)]$^+$) and 243 ([Cu(phen)]$^+$) were observed. The first product ion might come from its precursor by the rearrangement showed in **Fig S6B**, i.e. transposition of a Hα from **UDCA** moiety and subsequent closure of a Cα=C$_\text{carbonyl}$ double bond with loss of a neutral ketene. The second fragment is originated instead by the radical process depicted in **Figure S6C**, which brings to a Cu(I) ion with the loss of the **UDCA** moiety as radical. CID experiments performed on the ion at m/z 634 (**Figure S7**) showed the same pattern, thus confirming the fragmentation scheme previously reported.
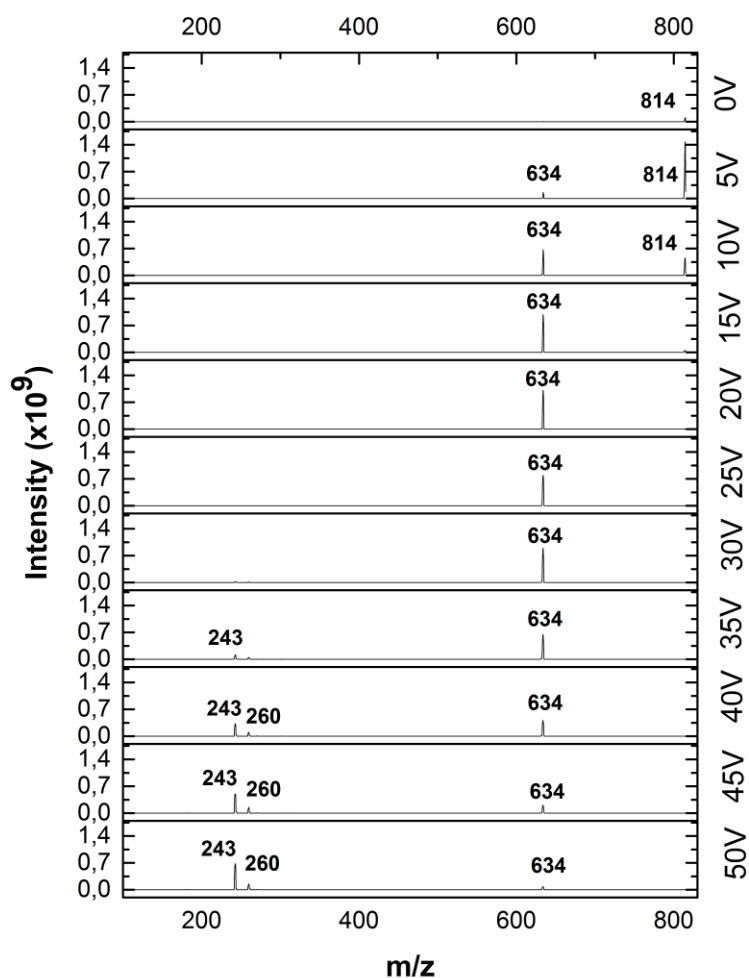
Figure 5: Tandem MS fragmentations at different collision energies of the peak at 450.5 *m/z* ([Cu(phen)₂(UDCA-H)]⁺). All the mass values are expressed as monoisotopic masses

DFT calculations. Geometry optimization for both **UDCA-H** and Cu(II) complex [Cu(phen)₂(UDCA-H)]⁺ were performed using the same computational setup employed for the parent copper complex [Cu(phen)₂(H₂O)]⁺ and other similar Cu(II) complexes, as previously reported.[26] In particular, assessment of the DFT performance for [Cu(phen)₂(H₂O)]⁺ (whose coordinates were taken starting from **C0** single X-Ray structural data) revealed a very good agreement between experimental and calculated data. In **Figure S8A** DFT optimized geometry for **UDCA-H** ligand is reported. As observable from frontier

molecular orbital analysis (**Fig S8B**), HOMO and HOMO-1 molecular orbitals are highly centred on oxygen carboxylate moiety, thus supporting a coordination from this functional group. Selected bonds, angles and dihedrals are reported in **Table S1**. Geometry optimization at DFT level for $[Cu(phen)_2(UDCA-H)]^+$ reveals a geometry closer to a square pyramidal than a trigonal bipyramidal, as suggested by the value of geometrical parameter $\tau = \frac{\beta - \alpha}{60°}$ of 0.22.[35] The former distortion is also evident at bond lengths level, where elongation of Cu-N2 (2.309 Å) is accompanied by shortening of Cu-N3, Cu-N1 and Cu-O1 (2.040, 2.059 and 1.958 Å respectively). These results are in agreement with several mono and binuclear Cu(II) bis-phenanthroline complexes coordinated by carboxylate functional groups.[36–39] Selected bonds, angles and dihedrals are reported in **Table S2**.

Atomic charges, computed at NPA level (**Table S3**), show on copper ion a significant lower atomic charge (1.39) compared with its formal charge +2, while on N1-4 and O1 atoms high negative calculated charges were evidenced. This trend suggests a partial charge transfer to the metal centre from the coordinating atoms of ligands, as evidenced at frontier Molecular Orbital level, where both α and β SOMOs are centred on UDCA moiety, while α and β LUMOs are redistributed among the metal centre and one of the phenanthroline ligands (**Figure 6**).
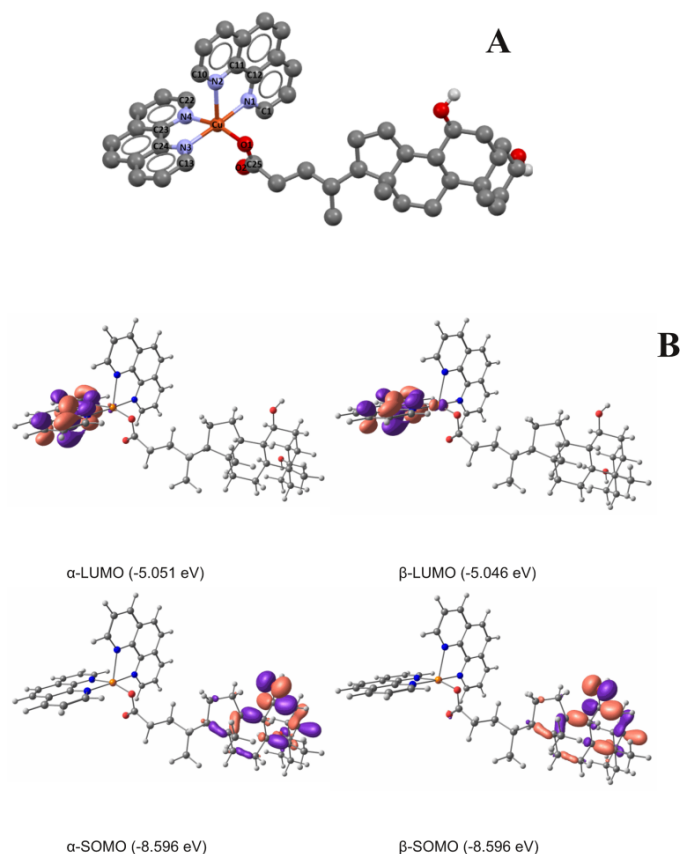
Figure 6. Molecular drawings and atom labelling schemes for [Cu(phen)$_2$(UDCA-H)]$^+$ (**A**) at the DFT-optimized geometry. Isosurface drawings of selected frontier molecular orbitals calculated (**B**) for [Cu(phen)$_2$(UDCA-H)]$^+$ (contour value: 0.05). Non-polar hydrogen atoms in (**A**) are omitted for clarity

Determination of the reducing activity of the stable radical 1,1-diphenyl-picrylhydrazyl (DPPH)

DPPH may accept a radical hydrogen to be converted in a diamagnetic form, which absorption spectrum differs from the previous one. Following the change in the optical absorption at 520 nm it is possible to monitor the course of the reaction during the time and compare the scavenger ability of different compounds.[40] **C0**, **UDCA** and **C0UDCA** did not show any reducing activity, providing evidence to be unable to give a H·.

Soybean lipoxygenase inhibition study in vitro

Lipoxygenases constitute a widespread group of Iron dioxygenases that are involved in the production of leukotrienes through the arachidonic cascade pathway.[41] Increased levels of human lipoxygenases, such as 5-LOX have been observed in several types of cancers, and some 5-LOX inhibitors have shown the ability to arrest the tumour cell proliferation and induce apoptosis.[42]

For this reason, we deemed important to evaluate the inhibition of the studied compounds towards these enzymes using Soybean Lipoxygenase as model. Several experiments were performed keeping constant the concentration of substrate and enzyme and varying that of **UDCA**, or **C0UDCA**. The results obtained were compared with the ones previously reported for **C0**.[26]

i) In presence of increasing amount of **UDCA**, the decrease of absorbance during time is observed, with all the curves following similar trend. The conversion of sodium linoleate to 13-hydroperoxylinoleic acid ends in approx. 60–80 min in the presence of **UDCA** and the conversion percentage never reaches 100 % (**Figure S9A**).

ii) In presence of increasing amount of **C0UDCA**, the absorbance decreases with time following similar trend the curves. The conversion of sodium linoleate to 13-hydroperoxylinoleic acid ends in approx. 60–80 min in the presence of **C0UDCA** and the conversion percentage never reaches 100 % (**Figure S9B**).

Reporting the inhibition percentage (**IP**) as function of the inhibitor concentration (**Figure 7**), it was observed that IP varies with time for every given concentration. This trend became invariant after 35 min for **C0UDCA** and 50 min for **UDCA**. These times were chosen as the reference to calculate the IC_{50} value, i.e., the concentration required to inhibit 50% of enzyme

activity. For the two compounds, IC_{50} resulted to be 69 ± 7 μM (**UDCA**) and 4.4 ± 0.1 μM (**C0UDCA**). The IC_{50} previously reported for **C0** was 55 ± 5 μM,[26] 12.5 higher than **C0UDCA** ones, thus suggesting that the insertion of an auxiliary ligand in the [Cu(phen)2] core will positively affects inhibition ability towards this enzyme. This result is consistent with the ones obtained for the mixed complex [Cu(phen)2(Salubrinal)](ClO4)2.[26] The trends shown in **Figure 7** suggest different mechanisms involved in the reaction with the enzyme.
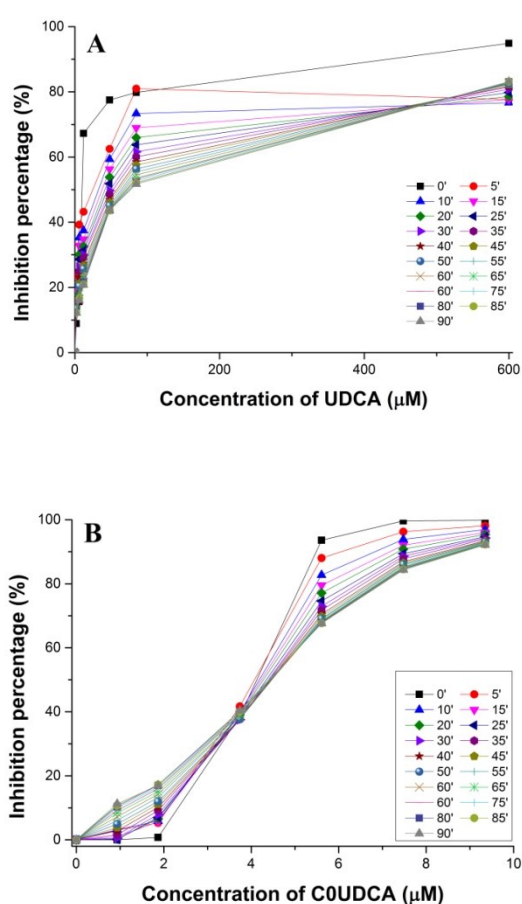
Figure 7. Inhibition percentage observed at different concentrations of **UDCA** (**A**) and **C0UDCA** (**B**) at different times after the mixing of the reactants; linoleic acid 32 μM, lipoxygenase 0.88 nM, pH 7.4 TRIS buffer, 25 °C.

Molecular Docking

Molecular docking calculations were performed for **UDCA-H** and **[Cu(phen)₂(UDCA-H)]⁺**

using the structure of Soybean Lipoxygenase-1 (PDB:3PZW) as receptor model. Both

compounds were initially docked using a grid box centred on the Iron cofactor considering

the ability of various molecules at inhibiting Soybean Lipoxygenase by targeting their

catalytic binding site. Results obtained for **UDCA-H** (**Figure S10**) show that the ligand is

placed in proximity of the catalytic site of the enzyme with a docking score, expressed as

binding affinity, of -7.3 kcal/mol. A closer view of the intermolecular interactions with the

surrounding residues of Soybean Lipoxygenase (**Figure 8A**) reveals mainly alkyl

interactions (e.g. with CYS357 and LEU689) along with hydrogen bonds (e.g. with LEU581

and TRP 684). In the case of **[Cu(phen)₂(UDCA-H)]⁺**, high positive docking score values (17

kcal/mol) were obtained using the same docking protocol. This result come from the

hindering shape effects derived to the bulky nature of the ligands of the mixed Cu(II)

complex. For this reason, docking calculations on the former compound were repeated

using a grid box located between the C-terminus and N-terminus domains of Soybean

Lipoxygenase, as previously reported for similar systems, obtaining a scoring function of -

11.1 kcal/mol (**Figure S11**). A closer inspection of the intermolecular interactions with the

surrounding residues of the receptor (**Figure 8B**) reveals mainly alkyl/π-alkyl interactions

(e.g., with LEU20 and TRP130), along with a π-anion interaction with ASP768 and the

formation of a hydrogen bond with ASN128 residue. These findings a potential allosteric

inhibition mode exerted by the studied compound that might take place, for instance, by
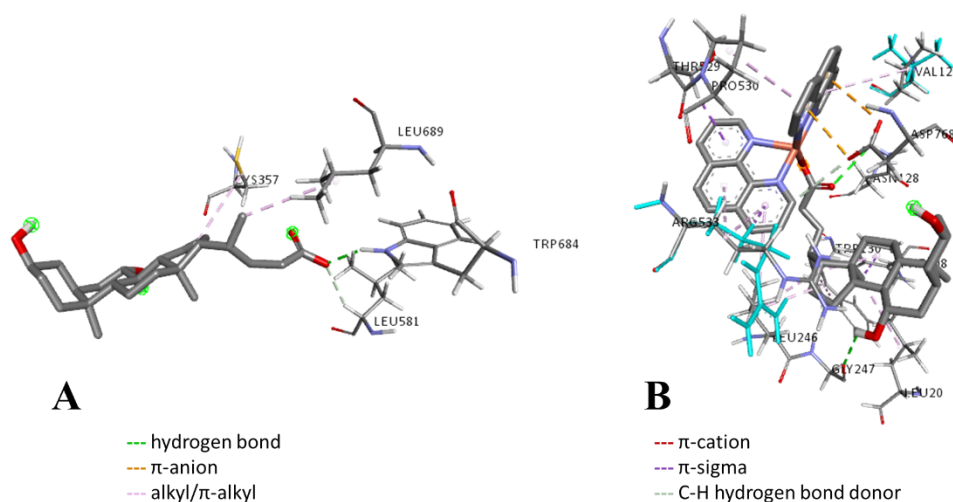
reducing the affinity for the enzyme substrate.

Figure 8. Docked poses of **UDCA-H** (**A**) and **[Cu(phen)₂(UDCA-H)]⁺** (**B**) and intermolecular interactions with the surrounding residues of soybean lipoxygenase.

Biological studies

To reveal whether **C0UDCA** interferes with cell proliferation, the ovarian (SKOV-3) and pancreatic (PANC-1) cancer cells were treated with **C0UDCA**, **C0**, **TUDCA** or left untreated. The cell number was then determined after 48 hrs (**Figure 9A**). The **C0** and **C0UDCA** decrease the proliferation rate of SKOV-3 cells. The same trend, even if it wasn't statistically significant, was observed in PANC-1 cells. Then we were curious whether the drop in cell numbers can be caused by the cytotoxicity of the **C0UDCA**. We stained the intact cells with FITC-conjugated Annexin V (binding to externalized phosphatidylserine of the plasma membrane) and propidium iodide (binding to DNA). Results are shown in **Figure 9B**. **C0UDCA** induced significant cell death as indicated by a decrease of negative (viable) cells. Interestingly, in the SKOV-3 cells, **C0UDCA** preferentially induced the programmed cell death as indicated by increase in Annexin V positive, propidium iodide negative cell. In PANC-1 the propidium iodide positive cells prevailed of over double positive cells, indicating secondary necrosis. Then we performed a metabolic assay, documenting

mitochondrial performance by the MTT assay (**Figure S12**). For each cell line, the IC$_{50}$ values of the studied compounds were determined from MTT results (**Table 1**).
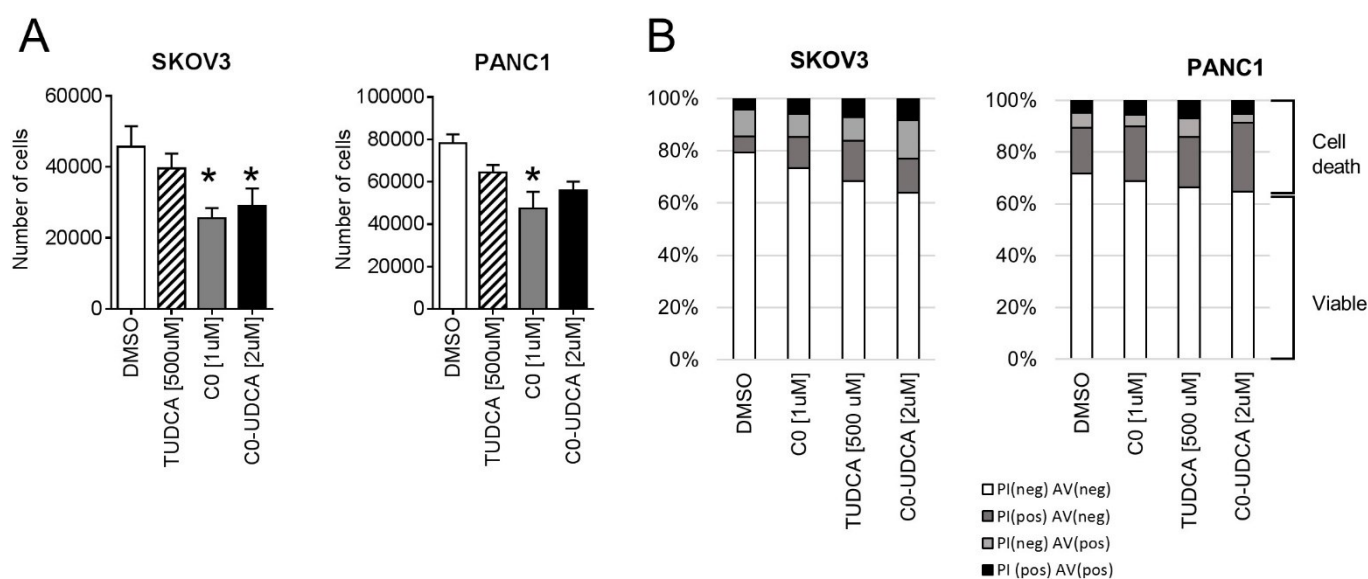

Figure 9. **A**. The cell numbers of SKOV-3 and PANC-1 cells after 48 hrs culture in presence of **C0**, **TUDCA** and **C0UDCA**. The starting number of cells was 20 000. Plot shows means and SDs from three independent experiments. **B**. **C0UDCA** increases externalization of phosphatidylserine in SKOV-3 cells. The cells were cultured as described in (**A**), then the exposure of phosphatidylserine on the cell surface was assessed by FACS using FITC-conjugated Annexin V probe. Cell viability was measured by propidium iodide staining. Typical results of three independent experiments are shown.

Table 1. Anticancer activity of the studied compounds reported as IC$_{50}$ values (concentration of drug able to induce cell death by 50%).

Compound	IC$_{50}$ (μM)	
	SKOV-3	**PANC-1**
C0	7.89	13.04
C0UDCA	6.75	6.96

With the aim of gaining more information regarding the mechanism of action of the novel **C0UDCA** complex and considering that structurally related Cu(II) complexes have already

shown to interfere at UPR level, we decided to evaluate the expression of specific UPR biomarkers (BiP, CHOP, ATF6, XBP-1) by means of Western Blots (**Figure S13**).

Notable, we observe in SKOV-3 cells a significative increase in the expression of CHOP, ATF6 and XBP-1 proteins, while in PANC-1 cell the entity of these variation appear more modest. Considering that both the controls have different levels of expression of the studied biomarkers, as better evidenced from relative densities in **Figure 10**, this behaviour could be indicative of the different origin and features of the cell lines considered.

These evidence are indicative of the involvement of the UPR pathway in exerting the anticancer properties of the novel **C0UDCA** compound.
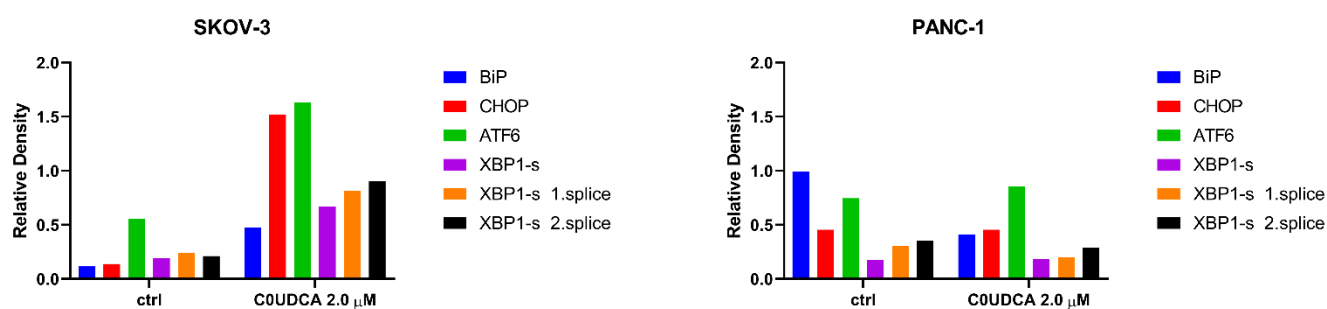
Figure 10. Relative densities calculated from immunoblotting results on SKOV-3 and PANC-1 cells.

Conclusions

The reaction between the anticancer $[Cu(phen)_2(OH_2)](ClO_4)_2$ (**C0**) complex and the bile acid Ursodeoxycholic Acid (**UDCA**) leads to the formation the new heteroleptic complex $[Cu(phen)_2(UDCA-H)](ClO_4)_2$ (**C0UDCA**), whose structure was assessed by merging different experimental and theoretical techniques.

Interestingly, this compound interferes on cell growth and viability at micromolar level on both SKOV-3 and PANC-1 cell lines, as observed from cell growth and MTT studies. Mechanistic studies suggest an involvement of the UPR in exerting the anticancer properties of this novel metal complex.

Studies on soybean lipoxygenase evidence that the concentration of **C0UDCA** required to inhibit the enzymatic activity of 50% was 15.7 and 12.5-fold lower compared to its synthetic precursors **UDCA** and **C0** respectively, thus indicating how presence of an auxiliary ligand in the [Cu(phen)2] core will enhance the lipoxygenase inhibitory activity. Docking results suggest for **C0UDCA** a potential allosteric mechanism in exerting its enzymatic inhibitory abilities.

The results achieved in this work and its interdisciplinary approach might provide novel insights about the mechanism of action of these compounds and will give new hints for the design and synthesis of novel biologically active Cu(II) coordination compounds.

Author contributions

Conceptualization: S.M., P.V., T.P.; Methodology: S.M., P.V., L.M, J.H., E.C., T.P.; Investigation: S.M., M.G.C., L.M., L.P., F.S.; Formal analysis: S.M., M.G.C., L.M., L.P., F.S., T.P.; Validation: S.M., L.M., T.P.; Visualization: S.M., T.P.; Writing – original draft: S.M., T.P.; Writing – review and editing: S.M., T.P., P.V.; Resources: T.P., E.C., J.H., P.V.; Supervision: S.M., T.P., P.V.

Acknowledgments

References

1   J.-F. Goossens and C. Bailly, *Pharmacol. Ther.*, 2019, **203**, 107396.

2   L. Dyakova, D. C. Culita, G. Marinescu, M. Alexandrov, R. Kalfin, L. Patron and R. Alexandrova, *Biotechnol. Biotechnol. Equip.*, 2014, **28**, 543–551.

3   J. Chung, S. H. An, S. W. Kang and K. Kwon, *PLoS One*, 2016, **11**, 1–18.

4   U. Beuers, J. L. Boyer and G. Paumgartner, *Hepatology*, 1998, **28**, 1449–1453.

5   A. L. Cao, L. Wang, X. Chen, Y. M. Wang, H. J. Guo, S. Chu, C. Liu, X. M. Zhang and W. Peng, *Lab. Investig.*, 2016, **96**, 610–622.

6   F. Trudu, F. Amato, P. Vaňhara, T. Pivetta, E. M. Peña-Méndez and J. Havel, *J. Appl. Biomed.*, 2015, **13**, 79–103.

7   C. Santini, M. Pellei, V. Gandin, M. Porchia, F. Tisato and C. Marzano, *Chem. Rev.*, 2014, **114**, 815–862.

8   S. Masuri, P. Vaňhara, M. G. Cabiddu, L. Moráň, J. Havel, E. Cadoni and T. Pivetta, *Molecules*, 2022, **27**, 49.

9   L. Moráň, T. Pivetta, S. Masuri, K. Vašíčková, F. Walter, J. Prehn, M. Elkalaf, J. Trnka, J. Havel and P. Vaňhara, *Metallomics*, 2019, **11**, 1481–1489.

10   S. Masuri, E. Cadoni, M. G. Cabiddu, F. Isaia, M. G. Demuru, L. Moráň, D. Buček, P.

Vaňhara, J. Havel and T. Pivetta, *Metallomics*, 2020, **12**, 891–901.

11 R. Sano and J. C. Reed, *Biochim. Biophys. Acta - Mol. Cell Res.*, 2013, 1833, 3460–3470.

12 S. Munshi and R. Dahl, *Bioorg. Med. Chem.*, 2016, **24**, 2382–2388.

13 U. Ozcan, E. Yilma, L. Özcan, M. Furuhashi, E. Vaillancourt, R. O. Smith, C. Z. Görgün and G. S. Hotamisligil, *Science (80-.).*, 2006, **313**, 1137–1140.

14 M. Strohalm, D. Kavan, P. Nova and M. Volny, *Anal. Chem.*, 2010, **82**, 4648–4651.

15 T. H. J. Niedermeyer and M. Strohalm, *PLoS One*, 2012, **7**, e44913.

16 P. Gans, A. Sabatini and A. Vacca, *Talanta*, 1996, **43**, 1739–1753.

17 J. P., *Ann. Chim. Appl.*, 1928, **9**, 113–203.

18 J. S. Renny, L. L. Tomasevich, E. H. Tallmadge and D. B. Collum, *Angew. Chemie Int. Ed.*, 2013, **52**, 11998–12013.

19 T. Pivetta, M. D. Cannas, F. Demartin, C. Castellano, S. Vascellari, G. Verani and F. Isaia, *J. Inorg. Biochem.*, 2011, **105**, 329–338.

20 C. Tolia, A. N. Papadopoulos, C. P. Raptopoulou, V. Psycharis, C. Garino, L. Salassa and G. Psomas, *J. Inorg. Biochem.*, 2013, **123**, 53–65.

21 Z. Boulsourani, G. D. Geromichalos, S. Katsamakas, V. Psycharis and C. P. Raptopoulou, *Mater. Sci. Eng. C*, 2019, **94**, 493–508.

22 F. Neese, *Wiley Interdiscip. Rev. Comput. Mol. Sci.*, 2012, **2**, 73–78.

23 M. D. Hanwell, D. E. Curtis, D. C. Lonie, T. Vandermeersch, E. Zurek and G. R. Hutchison, *J. Cheminform.*, 2012, **4**, 17.

24 C. Adamo and V. Barone, *J. Chem. Phys.*, 1999, **110**, 6158–6170.

25 F. Weigend and R. Ahlrichs, *Phys. Chem. Chem. Phys.*, 2005, **7**, 3297–3305.

26   S. Masuri, E. Cadoni, M. G. Cabiddu, F. Isaia, M. G. Demuru, L. Morán, L. Morán, D. Bucek, P. Vanhara, P. Vanhara, J. Havel, J. Havel and T. Pivetta, *Metallomics*, 2020, **12**, 891–901.

27   T. Y. Nikolaienko, L. A. Bulavin and D. M. Hovorun, *Comput. Theor. Chem.*, 2014, **1050**, 15–22.

28   Chemcraft - graphical software for visualization of quantum chemistry computations. https://www.chemcraftprog.com.

29   O. Trott and A. J. Olson, *J. Comput. Chem.*, 2009, 455–461.

30   G. M. Morris, H. Ruth, W. Lindstrom, M. F. Sanner, R. K. Belew, D. S. Goodsell and A. J. Olson, *J. Comput. Chem.*, 2009, **30**, 2785–2791.

31   Dassault Systèmes BIOVIA, Discovery Studio Viewer, v19, San Diego: Dassault Systèmes, 2019.

32   C. Hao and R. E. March, *J. Mass Spectrom.*, 2001, **36**, 509–521.

33   G. Deacon and R. J. Phillips, *Coord. Chem. Rev.*, 1980, **33**, 227–250.

34   K. Nakamoto, *Infrared and Raman Spectra of Inorganic and Coordination Compounds*, John Wiley & Sons, Inc., Hoboken, NJ, USA, 2008.

35   A. W. Addison, T. N. Rao, J. Reedijk, J. van Rijn and G. C. Verschoor, *J. Chem. Soc., Dalt. Trans.*, 1984, 1349–1356.

36   M. Devereux, M. McCann, J. F. Cronin, G. Ferguson and V. McKee, *Polyhedron*, 1999, **18**, 2141–2148.

37   F. Clifford, E. Counihan, W. Fitzgerald, K. Seff, C. Simmons, S. Tyagi and B. Hathaway, *J. Chem. Soc. Chem. Commun.*, 1982, 196.

38   M. Barceló-Oliver, Á. García-Raso, Á. Terrón, E. Molins, M. J. Prieto, V. Moreno, J. Martínez, V. Lladó, I. López, A. Gutiérrez and P. V. Escribá, *J. Inorg. Biochem.*, 2007, **101**, 649–659.

39   K. N. Lazarou, S. P. Perlepes, V. Psycharis and C. P. Raptopoulou, *Polyhedron*, 2008, **27**, 2131–2142.

40   D. Huang, B. Ou and R. L. Prior, *J. Agric. Food Chem.*, 2005, **53**, 1841–1856.

41   A. R. Brash, *J. Biol. Chem.*, 1999, **274**, 23679–23682.

42   R. Wisastra and F. Dekker, *Cancers (Basel).*, 2014, **6**, 1500–1521.

A novel heteroleptic Cu(II)-phenanthroline complex with the ER-stress modulator Ursodeoxycholic Acid with anticancer properties

Sebastiano Masuri[1], Lukáš Moráň[2,3], Tereza Vesselá[2], Enzo Cadoni[1], Maria Grazia Cabiddu[1], Francesco Isaia[1], Francesca Simeoni[1], Luca Puddu[1], Josef Havel[4,5], Petr Vaňhara[2,4], Tiziana Pivetta[*,1]

[1] Department of Chemical and Geological Sciences, University of Cagliari, Cittadella Universitaria, 09042, Monserrato, Cagliari, Italy.

[2] Department of Histology and Embryology, Faculty of Medicine, Masaryk University, 62500, Brno, Czech Republic.

[3] Research Centre for Applied Molecular Oncology, Masaryk Memorial Cancer Institute, 65653 Brno, Czech Republic.

[4] International Clinical Research Center, St. Anne's University Hospital, 65691, Brno, Czech Republic.

[5] Department of Chemistry, Faculty of Science, Masaryk University, 62500, Brno, Czech Republic.

SUPPLEMENTARY INFORMATION

Figure S1. Experimental (blue line) and calculated (red line) isotopic patterns of the peaks at m/z (**A**) 814 ([Cu(phen)$_2$(UDCA-H)(ClO$_4$)]$^+$), (**B**) 634 ([Cu(phen)(UDCA-H)]$^+$).
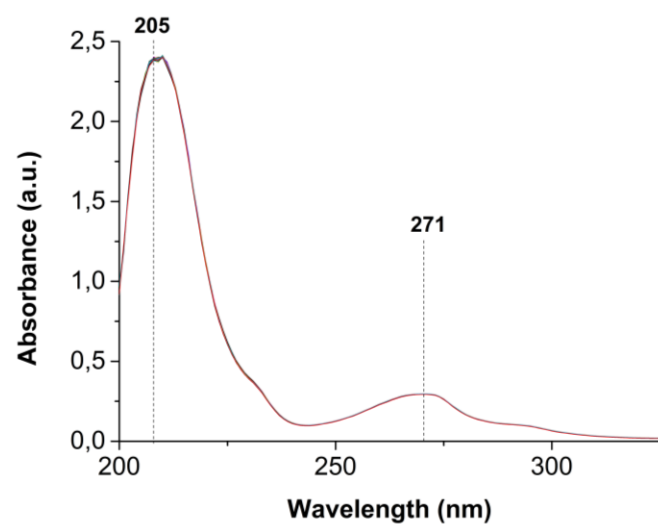
Figure S2. UV-Vis spectra of **C0UDCA** (4.20×10^{-6} M) in the range 200-325 nm recorded in 24h, each spectrum was acquired every 60 minutes.
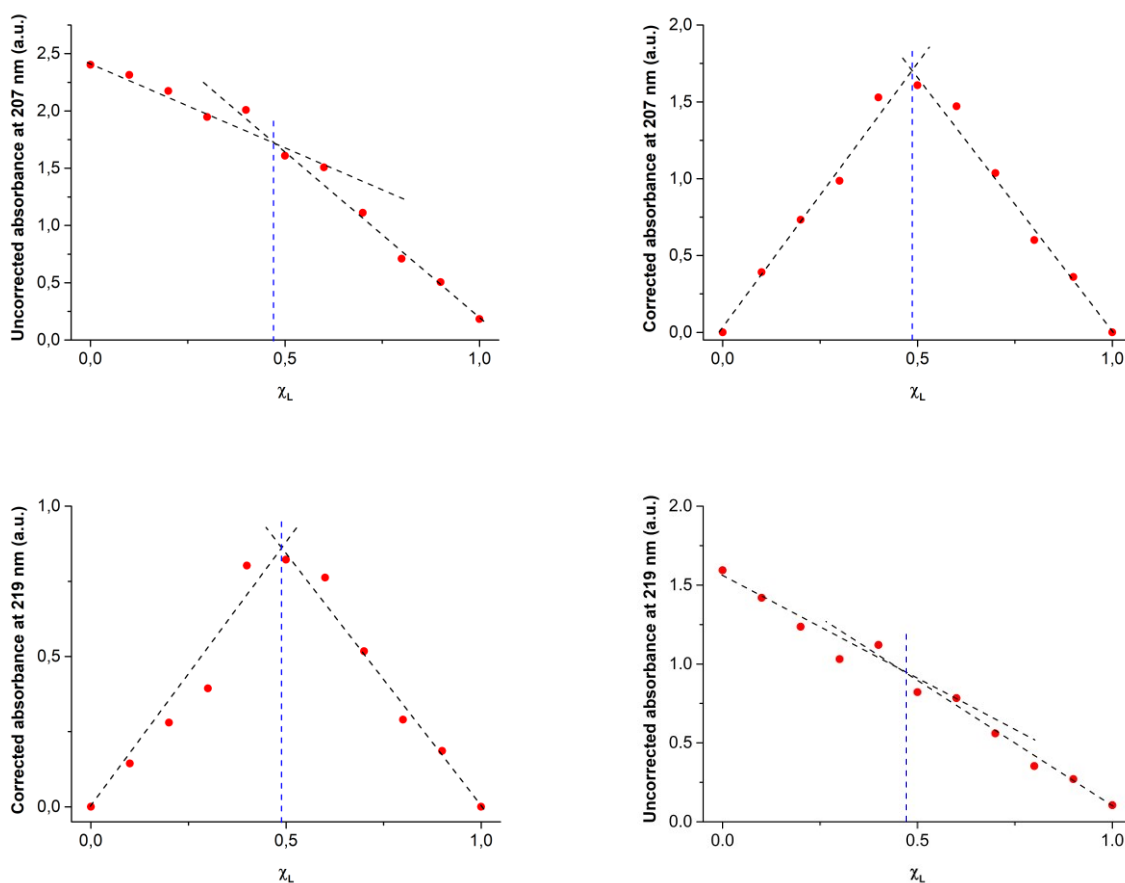
Figure S3. Job's plot for the system **C0** - **deprotonated UDCA**. Uncorrected (left) and corrected (right) absorbances measured at different **C0:deprotonated UDCA** molar ratio at 207 and 219 nm (**C0** $1.07 \cdot 10^{-5}$ M, **UDCA** $1.07 \cdot 10^{-5}$ M, phosphate buffer 0.05 M, pH 7.4, t 25 °C, 1 cm optical path length).
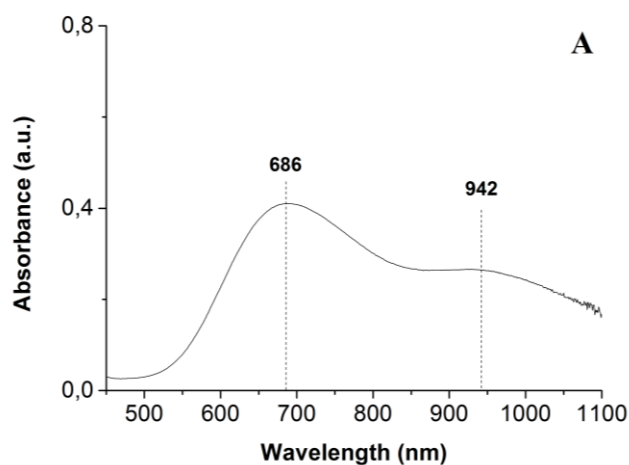
Figure S4. Vis-NIR spectrum of **C0UDCA** ($4.58 \cdot 10^{-3}$ M) in the region 450-1100 nm, CH$_3$CN:H$_2$O (1:1); 25°C, 1 cm path length.
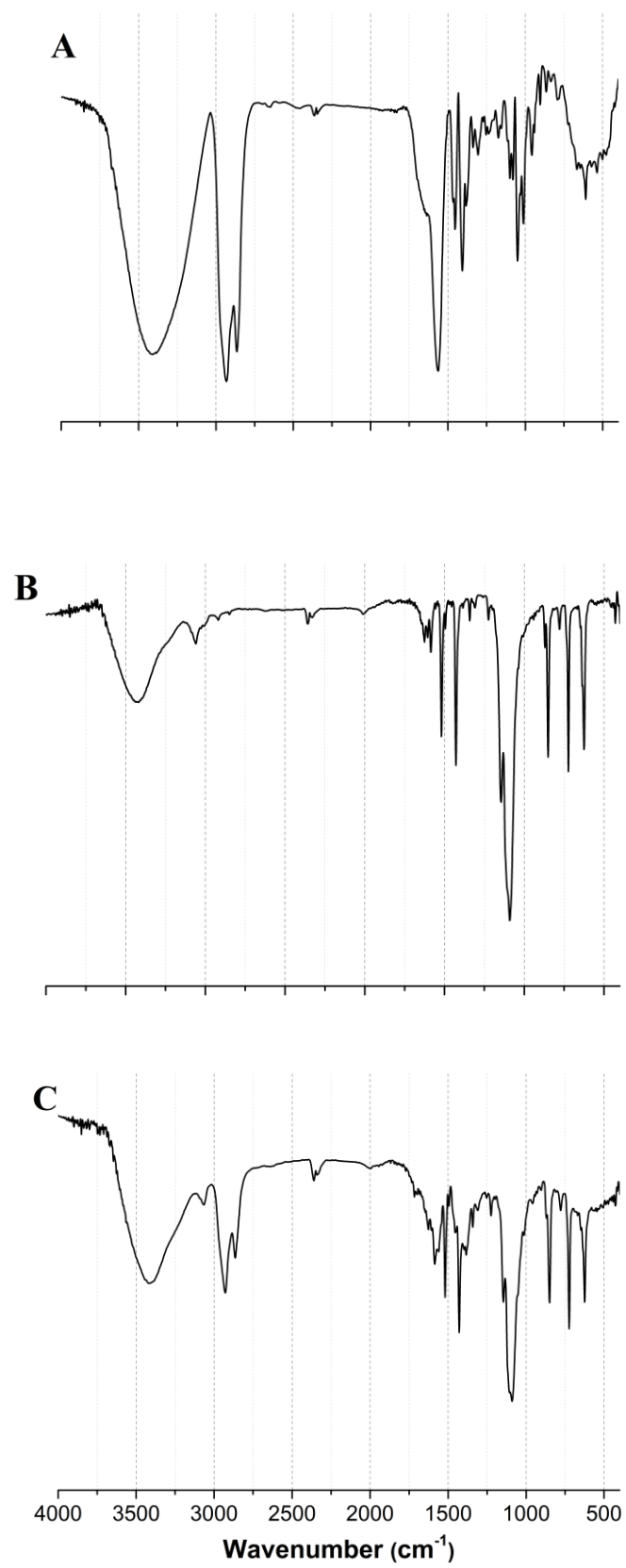
Figure S5. IR spectra of sodium ursodeoxycholate (**A**), **C0** (**B**) and [Cu(phen)$_2$(UDCA-H)](ClO$_4$) (**C**)

A)

814

phen

634

B)

634

[Cu(phen)(OH)]⁺

260

C)

634
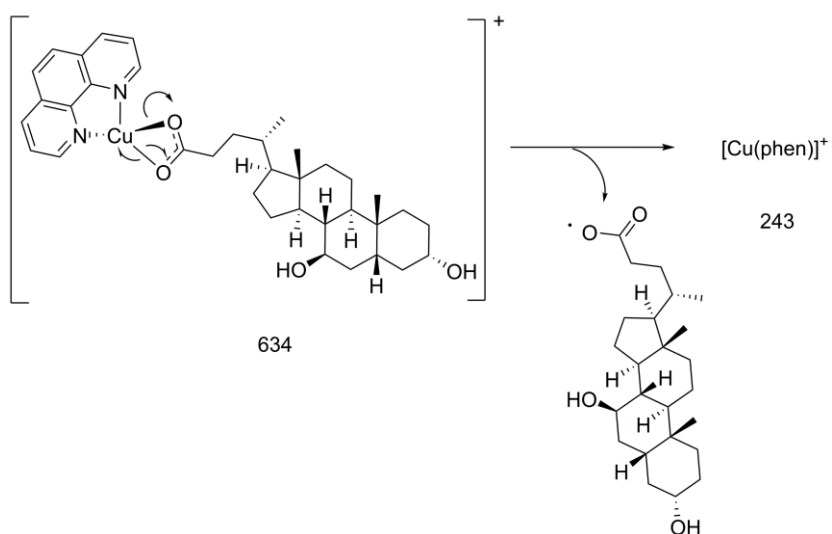
[Cu(phen)]⁺

243
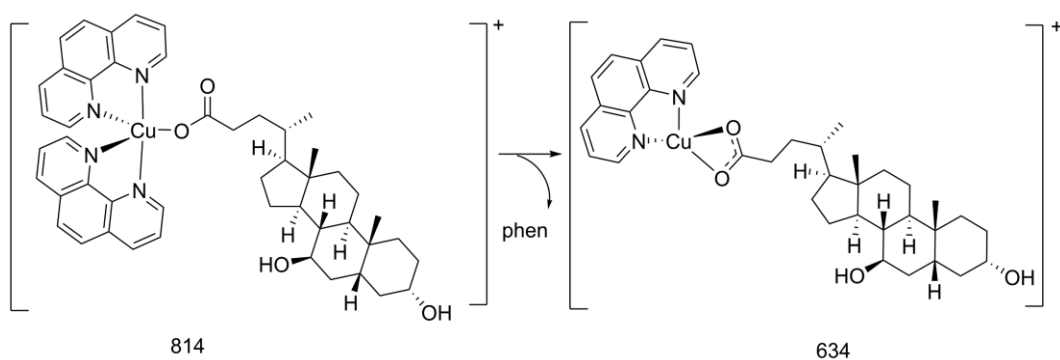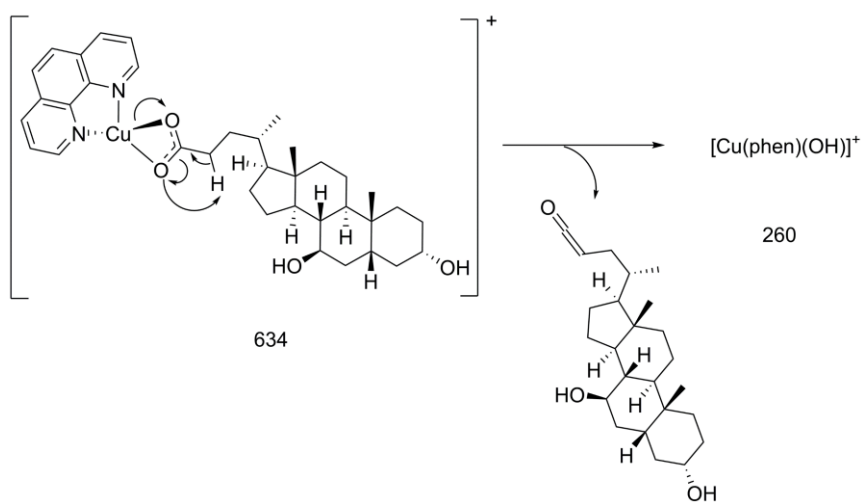
Figure S6. Proposed fragmentation patterns for product ions at 634 (**A**), 260 (**B**), 243 (**C**) *m/z* generated from 814 *m/z* under CID conditions. All masses are referred to the monoisotopic peaks.
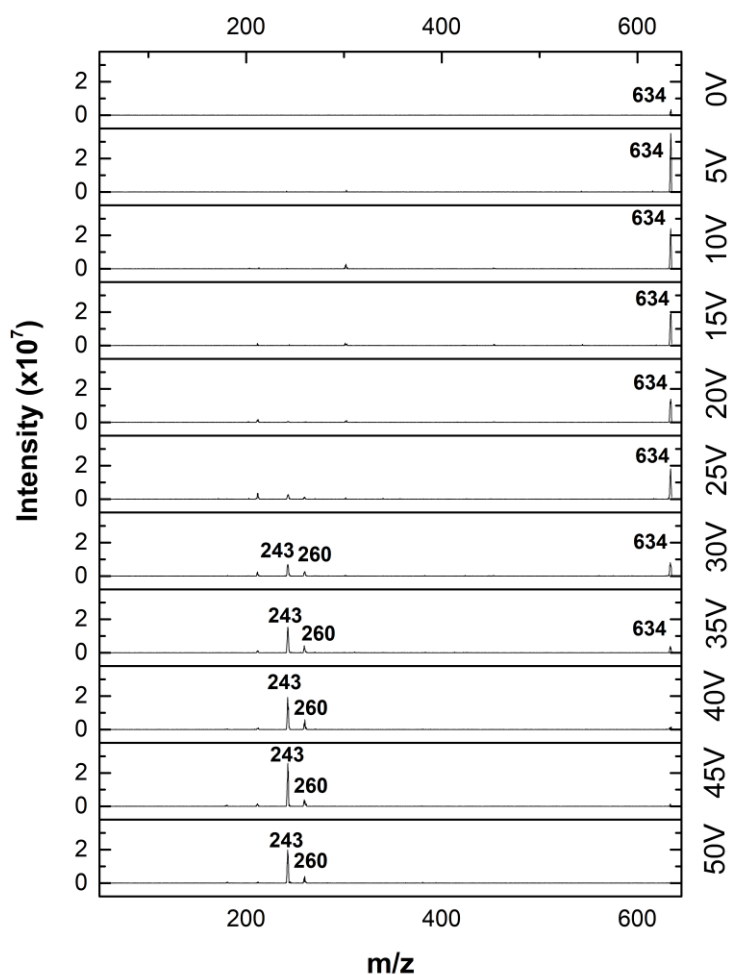

Figure S7. Tandem mass spectra at different collision energies of (**A**) 634 *m/z* ([Cu(phen)(UDCA-H)]⁺) . All masses are referred to the monoisotopic peaks.

A

B

LUMO (2.272 eV)   LUMO +1 (2.529 eV)

HOMO (-1.429 eV)   HOMO -1 (-1.599 eV)

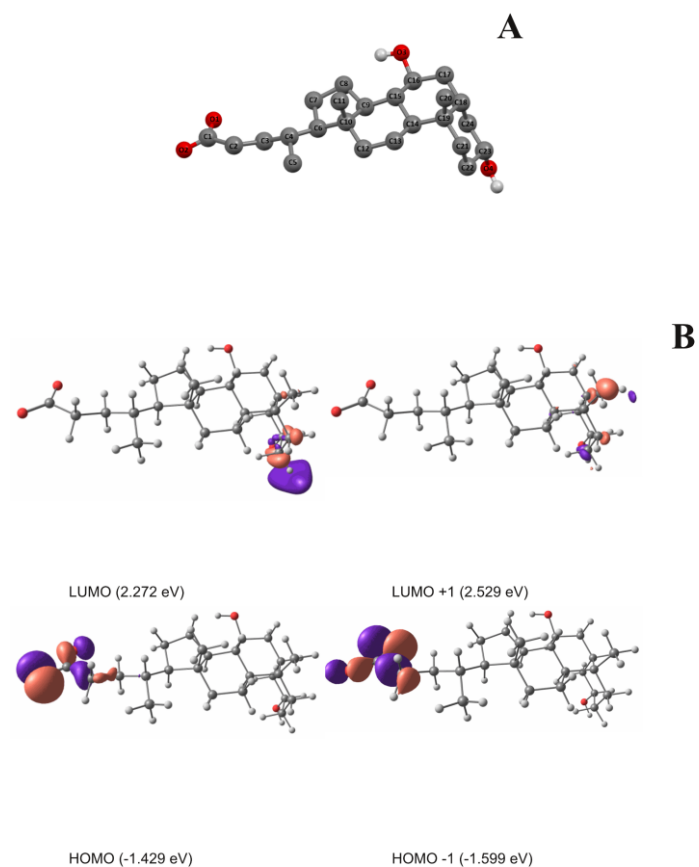**Figure S8**. Molecular drawings and atom labelling schemes for [Cu(phen)$_2$(UDCA-H)]$^+$ (**A**) at the DFT-optimized geometry. Isosurface drawings of selected frontier molecular orbitals calculated (**B**) for [Cu(phen)$_2$(UDCA-H)]$^+$ (contour value: 0.05). Non-polar hydrogen atoms in (**A**) are omitted for clarity
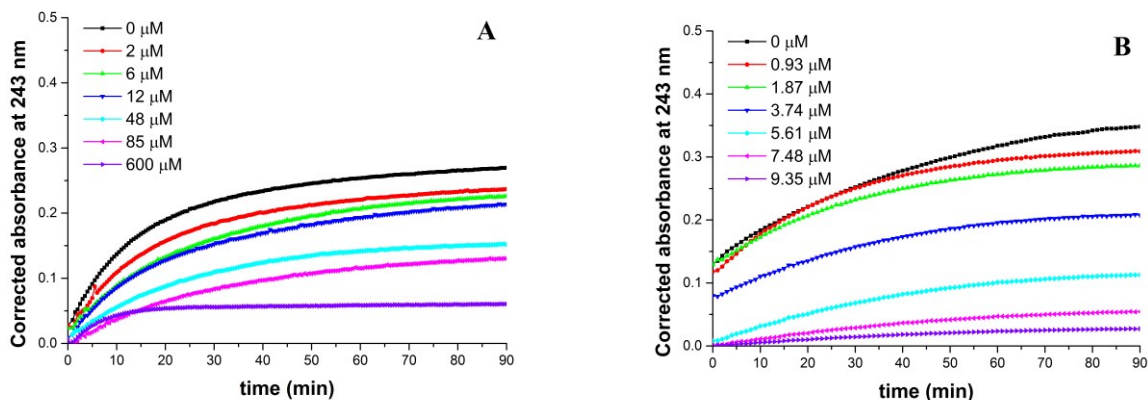
Figure S9. Absorbance at 243 nm of solutions containing sodium linoleate, lipoxygenase enzyme and **UDCA** (**A**) or **C0UDCA** (**B**) at different molar concentration; sodium linoleate 32 μM, lipoxygenase 0.88 nM, pH 7.4 TRIS buffer, T 25°C.
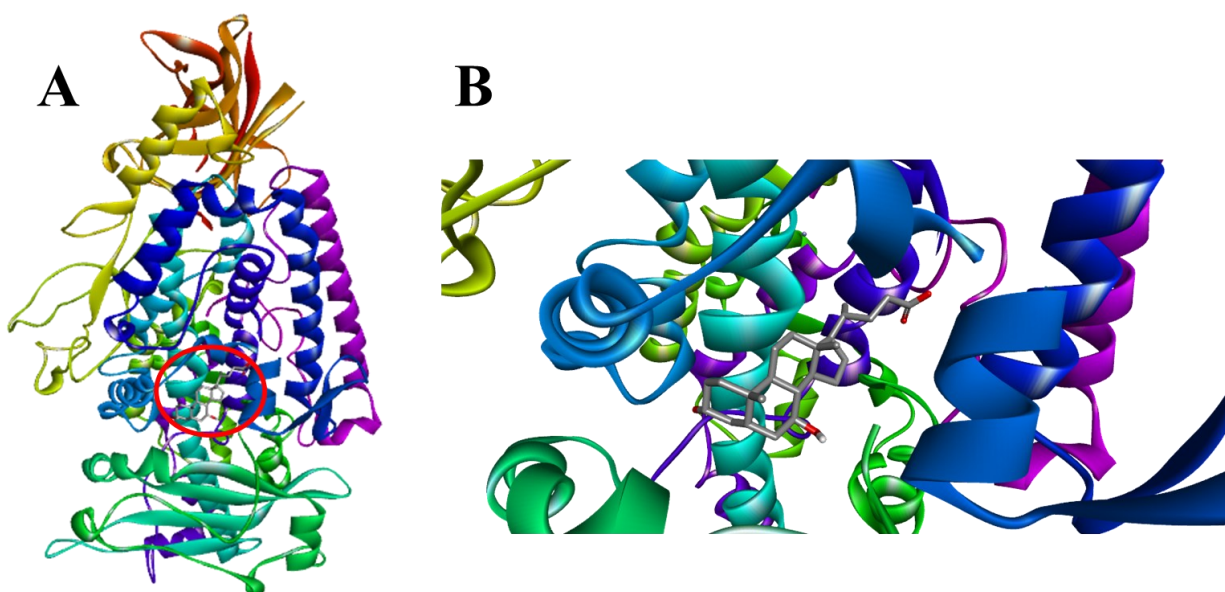

Figure S10. Full view of the complex between the highest-ranking score of **[Cu(phen)₂(UDCA-H)]⁺** and Soybean Lipoxygenase (**A**); zoom of the binding pocket occupied by the highest ranking score of **[Cu(phen)₂(UDCA-H)]⁺** and Soybean Lipoxygenase (**B**).
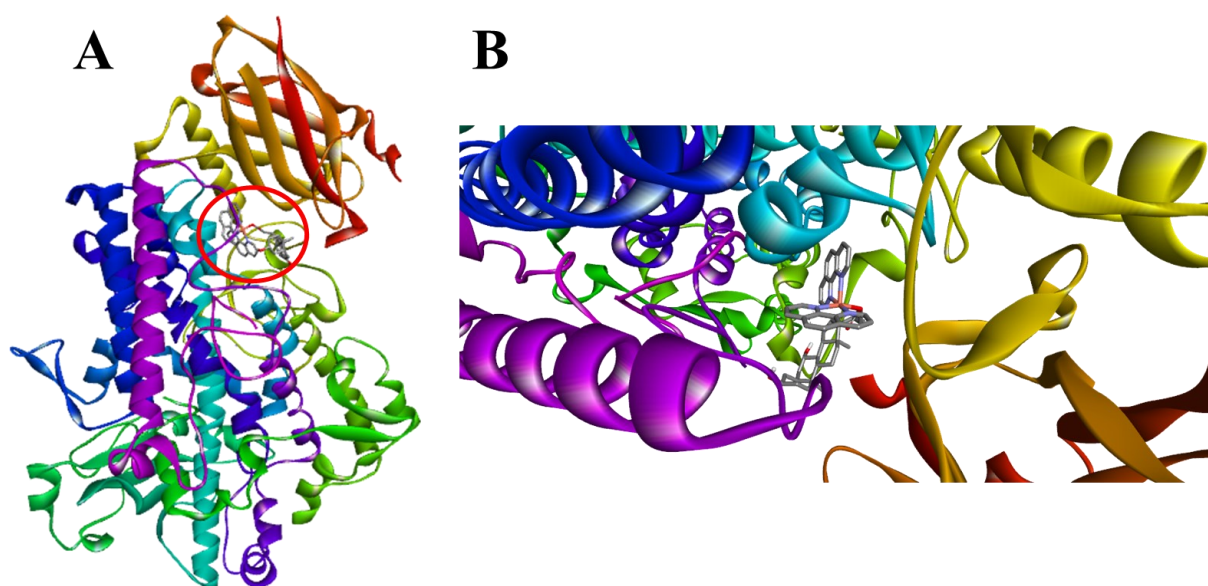
Figure S11. Full view of the complex between the highest-ranking score of **[Cu(phen)₂(UDCA-H)]⁺** and Soybean Lipoxygenase (**A**); zoom of the binding pocket occupied by the highest ranking score of **[Cu(phen)₂(UDCA-H)]⁺** and Soybean Lipoxygenase (**B**).
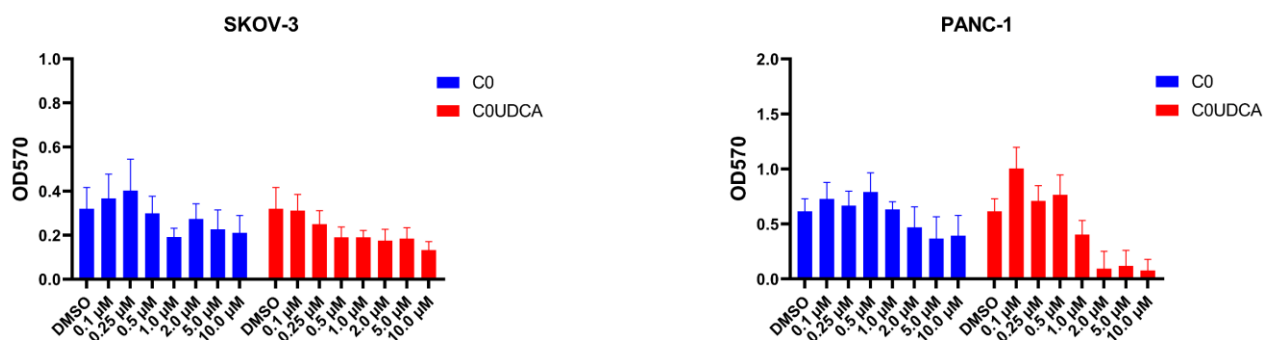

Figure S12. Mitochondrial metabolism as determined by conversion of the 4-nitro blue tetrazolium chloride to formazan followed by measurement of OD at 570 nm (MTT assay). The plots represent means and SEMs from three independent experiments performed in technical pentaplicates.
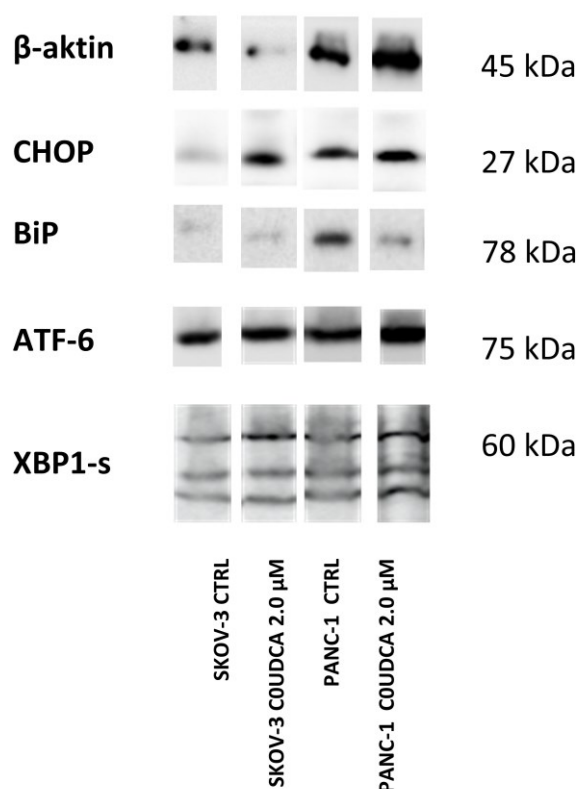
Figure S13. Protein expression of BiP, CHOP, ATF6 and XBP-1 in SKOV-3 and PANC-1cells treated for 24 hrs with **C0UDCA** at 2.0 µM. β-Actin was used as a control of equal loading.

Table S1. Selected optimized bond distances (Å), angles (°) and dihedrals (°) for the DFT optimized structure of UDCA-H and corresponding structural data. Atom labelling scheme as in **Figure S8A**.

UDCA-H	DFT	UDCA-H	DFT
C1-O1	1.248	*O1-C1-C2-C3*	-25.1
C1-O2	1.245	*O2-C1-C2-C3*	156.7
C1-C2	1.565	*C2-C3-C4-C5*	61.7
C2-C3	1.519	*C5-C4-C6-C7*	-178.2
C2-C3-C4	115.8	*C5-C4-C6-C10*	-56.8
O1-C1-O2	129.2	*C7-C6-C10-C12*	-154.5
O1-C1-C2	116.1	*C14-C19-C21-C22*	66.7
O2- C1-C2	114.7	*C16-C17-C18-C24*	72.1
O3-C16-C15	112.8	*O3-C16-C17-C18*	175.3
O3-C16-C17	104.8	*O3-C16-C15-C9*	70.4
O4-C23-C22	112.6	*O4-C23-C24-C18*	179.1
O4-C23-C24	107.7	*O4-C23-C22-C21*	-176.6

Table S2. Selected optimized bond distances (Å), angles (°) and dihedrals (°) for the DFT optimized structure of [Cu(phen)₂(UDCA-H)]⁺ and corresponding structural data. Atom labelling scheme as in **Figure 6**.

[Cu(phen)₂(UDCA-H)]⁺	DFT	[Cu(phen)₂(UDCA-H)]⁺	DFT
Cu-O1	1.958	*N1-Cu-N2*	76.1
Cu-N1	2.059	*N1-Cu-N3*	176.7
Cu-N2	2.309	*N1-Cu-N4*	96.6
Cu-N3	2.040	*N1-Cu-O1-C25*	-84.6
Cu-N4	2.082	*N1-Cu-N3-C13*	-169.0
O1-C25	1.289	*N1-Cu-N3-C24*	13.5
O2- C25	1.238	*N2-Cu-N3-C13*	-84.4
Cu-O1-C25	101.3	*N1-Cu-N3-C24*	98.1
Cu-N1-C1	123.1	*N3-Cu-N1-C1*	-95.7
Cu-N1-C12	117.0	*N3-Cu-N1-C12*	89.9
Cu-N2-C10	131.9	*N3-Cu-N2-C11*	178.8
Cu-N2-C11	109.2	*N3-Cu-N2-C10*	4.4
Cu-N3-C13	127.0	*N4-Cu-N2-C11*	-99.4
Cu-N3-C24	113.6	*N4-Cu-N2-C10*	86.2
Cu-N4-C22	129.4	*N4-Cu-N2-C25*	36.8
Cu-N4-C23	111.9	*N3-Cu-N2-C25*	95.2
N1-Cu-O1	92.0	*N2-Cu-N2-C25*	-161.4
N2-Cu-O1	97.7	*N1-Cu-N2-C25*	-84.6
N3-Cu-O1	91.2	*Cu-O1-C25-O2*	-0.5
N4-Cu-O1	163.4		

Table S3. Selected calculated atomic charges at NPA level for **[Cu(phen)₂(UDCA-H)]⁺**. Atom labelling scheme as in **Figure 6**.

[Cu(phen)₂(UDCA-H)]⁺	Natural Charges
Cu	1.390
N1	-0.498
N2	-0.474
N3	-0.485
N4	-0.487
O1	-0.774

Results and discussion

Article 5.

Ternary Copper (II) complexes of 1,10-phenanthroline and coumarin-based oxylacetates as potential anticancer metallodrugs

Abstract

A panel of novel ternary Cu(II) complexes of general formula $[Cu(phen)_2(Lx)](ClO_4)$ complexes (x: 1 – 6) have been obtained from reaction between the anticancer $[Cu(phen)_2(OH_2)](ClO_4)_2$ with a series of variably substituted coumarin-based oxylacetic acids. The coordination around the metal ion for these new complexes have been assessed by combining results coming from different experimental (MS, UV-Vis, FT-IR) and computational (DFT) techniques. Interestingly, these heteroleptic complexes show high anticancer potency in ovarian (SKOV-3) cancer cells, while the coumarin-based auxiliary ligands are devoid of any cytotoxicity. Mechanistic studies on the most promising compounds of the series have pointed out that these compounds exert their biological activity by inducing the pro-apoptotic branch of the Unfolded Protein Response (UPR). Studies on calf thymus (ct) DNA shows that the studied compounds can interact with this target through electrostatic interactions and groove binding, as evidenced on both experimental (UV-Vis) and theoretical (molecular docking) basis. The electrochemical behaviour of the studied complexes in presence of human DNA was investigated by means of Differential Pulse Voltammetry (DPV), showing how they are more stable in their oxidized form (as Cu(II)).[*]

Ternary Copper (II) complexes of 1,10-phenanthroline and coumarin-based oxylacetates as potential anticancer metallodrugs

Sebastiano Masuri[1], Maria Grazia Cabiddu[1], Lukáš Moráň[2,3], Tereza Vesselá[2], Enzo Cadoni[1], Martin Bartosik[3], Josef Havel[4,5], Petr Vaňhara[2,4], Tiziana Pivetta[*,1]

[1] Department of Chemical and Geological Sciences, University of Cagliari, Cittadella Universitaria, 09042, Monserrato, Cagliari, Italy.

[2] Department of Histology and Embryology, Faculty of Medicine, Masaryk University, 62500, Brno, Czech Republic.

[3] Research Centre for Applied Molecular Oncology, Masaryk Memorial Cancer Institute, 65653 Brno, Czech Republic.

[4] International Clinical Research Center, St. Anne's University Hospital, 65691, Brno, Czech Republic.

[5] Department of Chemistry, Faculty of Science, Masaryk University, 62500, Brno, Czech Republic.

[*]Corresponding author: tpivetta@unica.it

To be submitted

Introduction

The accidental discovery of the antiproliferative activity of cisplatin (*cis*-diaminodichloroplatin (II)) in 1960s has provided a new perspective in terms of application of coordination compounds in medicine.[1] However, if from the one hand cisplatin and derivatives are currently used in the treatment of several types of cancers, from the other hand their efficacy is affected by several dose-dependent side effects, along with a high incidence of developing resistance after some treatment.[2–5] In the design of new potential metal-based drugs that might overcome these limitations, substitution of Pt(II) with endogenous metal ions has been commonly chosen. The rationale behind this approach is that complexes of these ions might interact with DNA differently than Pt(II)-based drugs, or that might trigger cell death by targeting different molecular pathways and biomolecules. In addition, their systemic toxicity might be reduced exploiting the molecular machinery in charge of the transport and homeostasis of endogenous metal ions in biological system.[6] Copper constitutes a typical example of endogenous ion, that shares with cisplatin a common cellular transporter protein (hCtr1).[7] Many nitrogen-based ligands, such as 1,10-phenantroline have been tested for antitumor activity on different human cancer cell lines, both alone or as metal complexes. In the former case, an increase in potency compared to the ligand alone is commonly observed, that might be related to an enhanced ability of crossing biological barrier (due to a modification in the physico-chemical properties compared to the ligand alone) and/or in a different mechanisms of action. Additional modulation in terms of biological properties might also be achieved through the insertion of auxiliary ligands.[8–11]

We have previously synthesized several mixed Cu(II)-phenanthroline complexes bearing different auxiliary ligands, showing that these compounds possess potent anticancer properties in several human cancer cells.[12,13] Recent studies on some of these complexes have pointed out how their molecular mechanism in ovarian (A-2780 and SKOV-3) cancers involves the induction of pro-apoptotic branch of UPR (Unfolded Protein Response), which is activated in condition of prolonged or severe Endoplasmic Reticulum (ER) stress.[14,15]

These remarks have prompted us to further investigate on the cytotoxicity of ternary Cu(II)-phenanthroline complexes having coumarin-based oxylacetates as auxiliary ligands. As commonly known, coumarins comprise a large class of molecules (of both natural and synthetic origin) bearing 2-*H*-cromen-2-one scaffold that have shown high versatility in terms of pharmacological properties (e.g. antimicrobial, anti-inflammatory, antioxidant and anticancer).[16–19] Naturally occurring coumarins, such as coumarin (2-*H*-cromen-2-one) and umbelliferone (7-hydroxy-2-*H*-cromen-2-one), have shown potent cytotoxic and cytostatic activity.[20] Moreover, previous studies on mixed complexes containing a dioxylacetate derivative of aesculetin (6,7-dihyroxy-2-*H*-cromen-2-one) have proved to possess high potency in terms of antiproliferative activity.[21]

In this study, we aimed to prepare a small library of [Cu(phen)$_2$(Lx)](ClO$_4$) complexes (x: 1 – 6) where the auxiliary ligands are coumarin carboxylate derivatives bearing an oxylacetate moiety in the 6th or 7th position and different substituents in the 3rd or 4th position (**Figure 1**). The stoichiometries and coordination modes of the mixed complexes were studied at both solid and solution state by means of different experimental and computational techniques. *In-vitro* anticancer studies on ovarian (SKOV-3) cancer cells show that the ternary complexes

(**D1-6**, **Figure 1**) possess high anticancer potency (in the micromolar order), while the coumarin-based ligands (**HL1-6**, **Figure 1**) are devoid of cytotoxic activity. Mechanistic studies on the most promising compounds of the series have pointed out how they can interfere at ER level inducing the pro-apoptotic branch of the UPR.

Moreover, considering that DNA constitutes a potential target for exerting the biological properties of several anticancer compounds, we decided to preliminary evaluate the affinity towards this biomolecule and the potential mechanism of interaction by combining the results of spectroscopic (UV-Vis, DPV) techniques with molecular docking simulations.
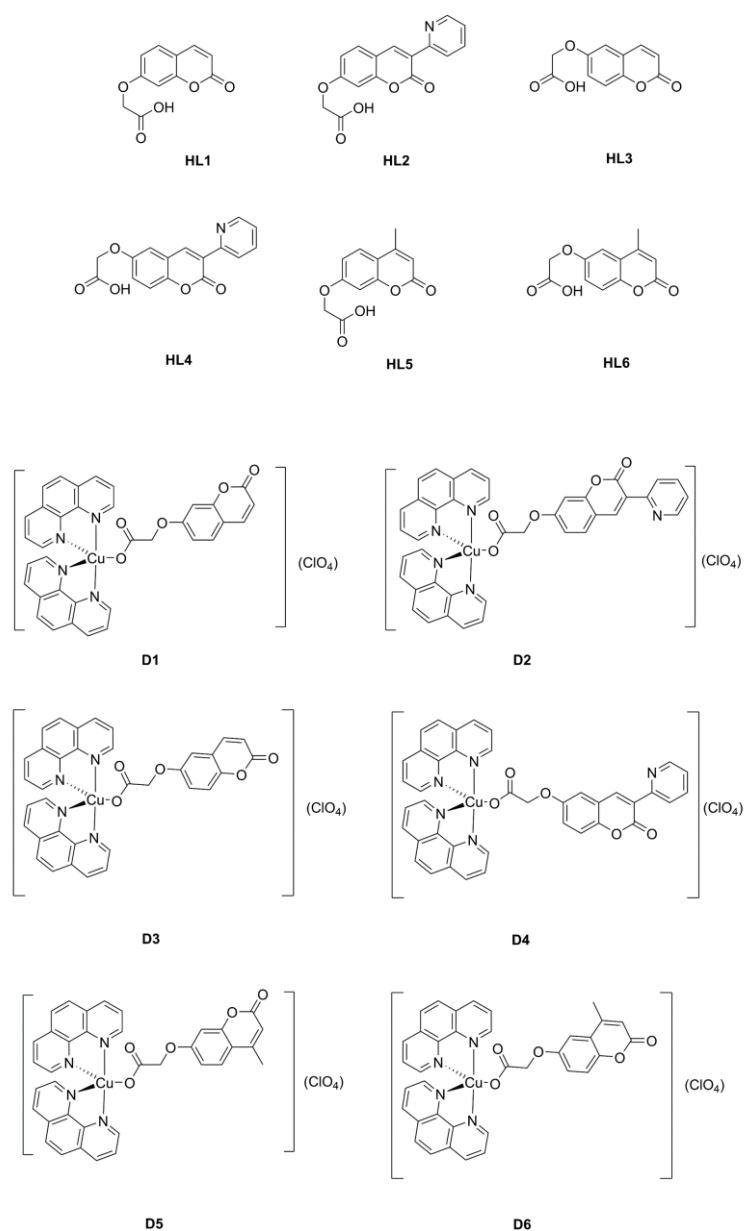
Figure 1. Structure and acronyms of the ligands (**HL1-6**) and Cu(II) complexes (**D1-6**) studied.

Experimental

Materials and methods

Reagents

Acetonitrile, methanol, ethanol, isopropanol, acetone, calf thymus DNA (ct-DNA), tris (hydroxymethyl)aminomethane hydrochloride (TRIS-HCl), sodium chloride, deuterated chloroform, sodium hydroxide, dimethyl sulfoxide and hydrochloric acid were purchased from Merck (Milan, Italy). MTT reagent (3- (4,5-dimethylthiazol-2-yl)-2,5-diphenyltetrazolium bromide) and Tween-20 were purchased from Merck (Czech Republic). Potassium carbonate, copper(II) carbonate hydroxide, ethyl bromoacetate, deuterated dimethyl sulfoxide, 7-hydroxycoumarin, 6-hydroxycoumarin, 7-hydroxy-4-methylcoumarin, 6-hydroxy-4-methylcoumarin 2,4-dihydroxybenzaldehyde, 2,5-dihydroxybenzaldehyde and pyridine 2-acetonitrile were purchased from Alfa-Aesar. The commercial reagents were used as received, without any further purification. Ultrapure water was obtained with a MilliQ Millipore apparatus.

NMR

^{1}H and ^{13}C NMR spectra were recorded on Varian 500 and Bruker Avance III HD 600 spectrometers at room temperature with tetramethylsilane (TMS) as internal standard in DMSO d_6 or CDCl$_3$. Chemical shifts, multiplicity and coupling constants were reported.

FT-IR

Infrared spectra were recorded with a Bruker Vector 22 spectrophotometer, preparing the samples as KBr pellets.

Solution equilibria

UV–Visible spectrophotometric measurements were performed on an Agilent Cary 60 spectrophotometer in the range 200–500 nm using a 1 cm quartz cell at 25 °C. The formation constants of the complexes formed by **C0** with the studied ligands were determined at 25

°C by spectrophotometric titration in phosphate buffer 0.05 M solution. Complex stoichiometries were also evaluated by means of the Job's method.[22,23]

The number of linearly independent absorbing species was obtained by applying eigenvalues analysis on the absorbance data matrix. The complex formation constants (expressed as overall association constants) were calculated using the Hyperquad 2006 program.[24]

The intrinsic binding constants (K_b) between ct-DNA and the studied compounds were determined at 25 °C by spectrophotometric titrations in TRIS-HCl buffer (TRIS-HCl 0.05 M, NaCl 0.05 M) at pH 7.1. Stock solutions of ct-DNA were prepared in TRIS-HCl buffer at pH 7.1 and stored at 4.0 °C within 96 hrs. The concentration of DNA per nucleotide was checked by UV absorption at 260 nm using its molar absorption coefficient (6600 M^{-1} cm^{-1}). DNA purity was verified by determining the A_{280nm}/A_{260nm} ratio: a value ≥ 1.8 is indicative of a sufficiently protein-free DNA.[25,26] Solutions having a fixed amount of ligand/metal complex ($9.78 \cdot 10^{-6}$ M to $1.24 \cdot 10^{-5}$ M according to compounds solubility and absorptivity) were titrated at 25 °C by adding increasing volumes of ct-DNA ($2.27 \cdot 10^{-4}$ M) and recording the UV-Vis spectrum. The K_b values were determined by applying the modified version of the Benesi-Hildebrand equation reported down below.[27]

$$\frac{A_0}{A - A_0} = \frac{\varepsilon_f}{\varepsilon_b - \varepsilon_f} + \frac{\varepsilon_f}{\varepsilon_b - \varepsilon_f} \cdot \frac{1}{K_b \cdot [DNA]} \ Equation \ (1)$$

Where A_0 and A are the absorbances in absence and presence of ct-DNA respectively, while ε_f and ε_b are the molar absorptivity values in absence and presence of ct-DNA respectively. Reporting in graph $\frac{A_0}{A-A_0}$ values ($\lambda = 260 \ nm$) versus $\frac{1}{[DNA]}$ ones, the intrinsic binding

constants were calculated as the ratio between the intercepts and the slopes coefficients determined from linear regression analysis.

Mass spectrometry

Mass spectra were recorded using a triple quadrupole QqQ Varian 310-MS mass spectrometer using the atmospheric pressure ESI technique. The sample solutions were infused directly into the ESI source using a programmable syringe pump at a flow rate of 1.25 mL/h. A dwell time of 14 s was used, and the spectra were accumulated for 5 min to increase the signal-to-noise ratio. Mass spectra were recorded in the m/z 100–1000 range. The experimental conditions for positive and negative ion mode were needle voltage ±3500 V, shield ±800 V, source temperature 100 °C, drying gas pressure 20 psi, nebulizing gas pressure 20 psi. Tandem MS experiments were performed using argon as the collision gas (1.8 psi). The isotopic patterns of the measured peaks in the mass spectra were analysed using the mMass 5.5.0 software package.[28,29]

Electrochemical measurements

Electrochemical measurements were carried out with an Autolab PGSTAT101 potentiostat/galvanostat, equipped with a glassy carbon electrode (GCE) as working electrode, Ag/AgCl/ KCl 3.0 M as reference electrode and a carbon wire as auxiliary electrode. All measurements were performed at 25 °C, using TRIS-HCl buffer (TRIS-HCl 0.05 M, NaCl 0.05 M, pH 7.1) as supporting electrolyte. All solutions were deoxygenated by purging Argon prior to each measurements. GCE surface was regenerated after each measurement by mechanical polishing using 1 µm, 0.3 µm and 0.05 µm alumina slurry, respectively.

The interaction between redox-active compounds **C0** and **D1-6** with genomic DNA was evaluated by means of Differential Pulse Voltammetry (DPV). The following equation has been applied to determine in which redox state the studied complexes are more stable upon interaction with this biomolecule.[30]

$$E_b^{0'} - E_f^{0'} = 59.1 \cdot Log\left(\frac{K^+}{K^{2+}}\right) [mV] \ Equation \ (2)$$

Where $E_b^{0'}$ and $E_f^{0'}$ are the standard redox potentials of the Cu(II)/Cu(I) couple in the bound and free forms respectively, while K^+ and K^{2+} are the equilibrium DNA-binding constants for the Cu(I) and Cu(II) forms respectively. When a K^+/K^{2+} ratio lower than 1 is observed upon increasing additions of DNA, then the studied Copper complexes will be more stable in their oxidized form (as Cu(II)), otherwise they will interact more likely with this biomolecule in their reduced form (as Cu(I)).

Theoretical calculations

DFT calculations were performed using the release 4.2.0 of the ORCA software package.[31] Input files for DFT calculations were prepared using Avogadro 1.2.0.[32] Geometry optimizations were performed using the hybrid PBE0 functional[33] and def-2 TZVP basis set,[34] as previously reported for similar systems.[15] The nature of the minima in each optimization was evaluated by assessing the absence of negative frequencies in calculated IR spectra. Atomic charges at natural population analysis (NPA) level were calculated by means of JANPA software package.[35] Molecular orbital shapes and energies were investigated using Chemcraft v1.8.[36]

Molecular docking calculations were performed using the Autodock Vina software,[37] The X-Ray structure of BNA (PDB: 1BNA) was chosen as receptor. Both ligands and receptor were prepared using MG Labs Autodock Tools before docking.[38] In the receptor water molecules were removed, while polar hydrogens and Gasteiger charges were added. For all the ligands, non-polar hydrogens were removed, Gasteiger charges were added while no rotational constraints were applied. In the complexes, the atomic charges for copper were manually adjusted in the generated pdbqt files. All the tested compounds were docked using a grid cube of $30 \times 30 \times 42$ points, centred at coordinates x = 14.780, y = 20.976, z = 8.807, with a spacing of 1.0 Å and an exhaustiveness value of 100. Molecular interactions and docked poses were evaluated using USCF Chimera 1.15.[39]

Synthesis

Ligands

Synthesis of hydroxy-3-(pyridin-2-yl)coumarin derivatives **1b** *and* **1d**.

Both compounds were prepared as previously reported.[40,41]

Synthesis of coumarin oxyacetic ethylic esters derivatives **2a-f**

K_2CO_3 (5.83 mmol, 1.5 eq.) was added in one portion at r.t. to a suspension of hydroxylated coumarin **1a-f** (3.89 mmol) in acetone (20 mL). After ca 15 minutes under stirring, ethyl bromoacetate (0.65 mL, 5.83 mmol, 1.0 eq.) was added to the reaction mixture. The former one was refluxed for 24 hours. The solution was filtered while hot and the solvent evaporated under reduced pressure, affording a solid that was recrystallized from ethanol.

Ethyl 2-((2-oxo-2*H*-chromen-7-yl)oxy)acetate (2a). White solid. Yield was 67%. Spectral data are consistent with those reported in literature.[42] ^{1}H-NMR (600 MHz, CDCl$_3$, δ, ppm, **Figure**

S1): 7.64 (d, J = 9.5 Hz, 1H), 7.40 (d, J = 8.6 Hz, 1H), 6.90 (dd, J = 8.6, 2.5 Hz, 1H), 6.78 (d, J = 2.5 Hz, 1H), 6.28 (d, J = 9.5 Hz, 1H), 4.68 (s, 2H), 4.29 (q, J = 7.1 Hz, 2H), 1.32 (td, J = 7.1, 0.8 Hz, 3H). ESI-MS, *m/z*, found (calcd) 249.0 (249.1) [M+H]+.

Ethyl 2-((2-oxo-3-(pyridin-2-yl)-2*H*-chromen-7-yl)oxy)acetate (2b). White solid. Yield was 44%. ^{1}H-NMR (500 MHz, DMSO d6, δ, ppm, **Figure S2**): 8.86 (s, 1H), 8.69 (ddd, J = 4.8, 1.9, 1.0 Hz, 1H), 8.27 (dt, J = 8.1, 1.1 Hz, 1H), 7.93 – 7.85 (m, 2H), 7.41 (ddd, J = 7.5, 4.7, 1.2 Hz, 1H), 7.08 (d, J = 2.5 Hz, 1H), 7.04 (dd, J = 8.6, 2.5 Hz, 1H), 4.97 (s, 2H), 4.21 (q, J = 7.1 Hz, 2H), 1.24 (t, J = 7.1 Hz, 3H). ESI-MS, *m/z*, found (calcd): 326.2 (326.1) [M+H]+.

Ethyl 2-((2-oxo-2*H*-chromen-6-yl)oxy)acetate (2c). Beige solid. Yield was 67%. Spectral data are consistent with those reported in literature.[43] ^{1}H-NMR (600 MHz, CDCl3, δ, ppm, **Figure S3**): 7.64 (d, J = 9.5 Hz, 1H), 7.28 (d, J = 9.0 Hz, 1H), 7.15 (dd, J = 9.0, 3.0 Hz, 1H), 6.94 (d, J = 3.0 Hz, 1H), 6.44 (d, J = 9.5 Hz, 1H), 4.66 (s, 2H), 4.29 (q, J = 7.1 Hz, 2H), 1.31 (t, J = 7.2 Hz, 3H). ESI-MS, *m/z*, found (calcd) 249.1 (249.1) [M+H]+.

Ethyl 2-((2-oxo-3-(pyridin-2-yl)-2*H*-chromen-6-yl)oxy)acetate (2d). Beige solid. Yield was 45%. ^{1}H-NMR (600 MHz, CDCl3, δ, ppm, **Figure S4**): 8.71 (s, 1H), 8.68 (ddd, J = 4.7, 1.9, 1.0 Hz, 1H), 8.43 (dt, J = 8.1, 1.1 Hz, 1H), 7.82 – 7.77 (m, 1H), 7.34 (d, J = 9.0 Hz, 1H), 7.31 (ddt, J = 6.8, 4.8, 1.0 Hz, 1H), 7.20 (ddd, J = 9.0, 2.9, 0.8 Hz, 1H), 7.06 (d, J = 3.0 Hz, 1H), 4.67 (s, 2H), 4.32 – 4.27 (m, 2H), 1.32 (td, J = 7.1, 0.8 Hz, 3H). ESI-MS, *m/z*, (calcd): 326.2 (326.1) [M+H]+.

Ethyl 2-((4-methyl-2-oxo-2*H*-chromen-7-yl)oxy)acetate (2e). White solid. Yield was 84%. Spectral data are consistent with those reported in literature.[44] ^{1}H-NMR (600 MHz, CDCl3, δ, ppm): 7.53 (d, J = 8.8 Hz, 1H, **Figure S5**), 6.92 (dd, J = 8.8, 2.6 Hz, 1H), 6.78 (d, J = 2.6 Hz,

1H), 6.16 (q, J = 1.3 Hz, 1H), 4.68 (s, 2H), 4.29 (q, J = 7.1 Hz, 2H), 2.40 (d, J = 1.2 Hz, 3H), 1.32

(t, J = 7.1 Hz, 3H). ESI-MS, *m/z*, found (calcd): 262.2 (262.1) [M+H]⁺.

Ethyl 2-((4-methyl-2-oxo-2*H*-chromen-6-yl)oxy)acetate (2f). White solid. Yield was 88%.

Spectral data are consistent with those reported in literature.[44] ¹H-NMR (600 MHz, CDCl₃,

δ, ppm, **Figure S6**): 7.29 (d, J = 8.9 Hz, 1H), 7.12 (dd, J = 8.9, 3.0 Hz, 1H), 7.10 (d, J = 2.9 Hz,

1H), 6.31 (d, J = 1.5 Hz, 1H), 4.67 (s, 2H), 4.29 (q, J = 7.2 Hz, 2H), 2.41 (d, J = 1.3 Hz, 3H), 1.31

(t, J = 7.1 Hz, 3H). ESI-MS, *m/z*, found (calcd): 262.1 (262.1) [M+H]⁺.

*Synthesis of coumarin oxyacetic acid derivatives (**HL1-6**).*

Compound **2a-f** (1.60 mmol) was dissolved in 7.0 mL of ethanol. 4.0 mL (3 eq.) of NaOH 5%

solution were added in one portion at r.t. and the reaction mixture was refluxed for 24 hours.

The solution was concentrated under reduced pressure to ca half the volume, then 6.0 mL

of distilled water were poured and HCl 2.0 N were added drop by drop until acidic pH was

reached. A solid slowly precipitated from the solution that was filtered under vacuum. The

former one was recrystallized from ethanol.

2-((2-oxo-2*H*-chromen-7-yl)oxy)acetic acid (HL1). White solid. Yield was 58%. Spectral data

are consistent with those reported in literature.[45] ¹H-NMR (600 MHz, DMSO d₆, δ, ppm,

Figure S7): 1H NMR (600 MHz, DMSO-d6) δ 13.09 (s, 1H), 8.00 (d, J = 9.5 Hz, 1H), 7.65 (dd,

J = 9.0, 2.0 Hz, 1H), 6.97 – 6.95 (m, 2H), 6.31 (d, J = 9.4 Hz, 1H), 4.82 (s, 2H). ESI-MS, *m/z*,

found (calcd) 218.5 (219.0) [M+H]⁺, 438.5 (439.0) [2M+H]⁺.

2-((2-oxo-3-(pyridin-2-yl)-2*H*-chromen-7-yl)oxy)acetic acid (HL2). Light yellow solid**.** Yield

was 48%. ¹H-NMR (600 MHz, DMSO d₆, δ, ppm, **Figure S8**) 12.98 (s, 1H), 8.76 (s, 1H), 8.63

(ddd, J = 4.7, 1.8, 0.9 Hz, 1H), 8.21 (dd, J = 8.1, 1.1 Hz, 1H), 7.84 (td, J = 7.8, 1.9 Hz, 1H), 7.44

(d, J = 3.0 Hz, 1H), 7.38 – 7.36 (m, 1H), 7.35 (d, J = 9.0 Hz, 1H), 7.21 (dd, J = 9.0, 3.0 Hz, 1H), 4.69 (s, 2H). ^{13}C-NMR (151 MHz, DMSO d6, δ, ppm, **Figure S9**): 170.35, 160.01, 154.72, 151.45, 149.94, 148.52, 142.72, 137.24, 125.45, 124.17, 123.98, 120.81, 120.04, 117.41, 113.01, 65.42. ESI-MS, *m*/*z*, found (calcd): 298.0 (298.1) [M+H]$^+$, 320.2 (320.1) [M+Na]$^+$.

2-((2-oxo-2*H*-chromen-6-yl)oxy)acetic acid (HL3). Light pink solid. Yield was 65%. Spectral data are consistent with those reported in literature.[43] ^{1}H-NMR (600 MHz, DMSO d$_6$, δ, ppm, **Figure S10**): ^{1}H-NMR (600 MHz, DMSO d$_6$, δ, ppm): 13.15 (s, 1H), 8.01 (d, J = 9.6 Hz, 1H), 7.35 (d, J = 9.0 Hz, 1H), 7.27 (d, J = 3.0 Hz, 1H), 7.22 (dd, J = 9.0, 3.0 Hz, 1H), 6.49 (d, J = 9.6 Hz, 1H), 4.73 (s, 2H). ESI-MS, *m*/*z*, found (calcd) 218.5 (219.0) [M+H]$^+$, 438.5 (439.0) [2M+H]$^+$.

2-((2-oxo-3-(pyridin-2-yl)-2*H*-chromen-6-yl)oxy)acetic acid (HL4). Brown solid. Yield was 42%. ^{1}H-NMR (600 MHz, DMSO d$_6$, δ, ppm, **Figure S11**): 8.89 (s, 1H), 8.73 (ddd, J = 4.8, 1.9, 0.9 Hz, 1H), 8.30 (dt, J = 8.1, 1.1 Hz, 1H), 7.93 (td, J = 7.8, 1.9 Hz, 1H), 7.90 (d, J = 8.5 Hz, 1H), 7.44 (ddd, J = 7.5, 4.7, 1.1 Hz, 1H), 7.09 – 7.03 (m, 2H), 4.88 (s, 2H). ^{13}C-NMR (151 MHz, DMSO d$_6$, δ, ppm, **Figure S12**): 170.05, 162.12, 160.14, 155.61, 151.68, 149.81, 143.04, 137.18, 131.08, 123.69, 123.52, 121.61, 113.62, 113.58, 101.39, 65.64. ESI-MS, *m*/*z*, found (calcd) 298.3 (298.1) [M+H]$^+$, 320.0 (320.1) [M+Na]$^+$, 335.9 (336.0) [M+K]$^+$.

2-((4-methyl-2-oxo-2*H*-chromen-7-yl)oxy)acetic acid (HL5). White solid. Yield was 72%. Spectral data are consistent with those reported in literature.[44] ^{1}H-NMR (600 MHz, DMSO d^6, δ, ppm, **Figure S13**): 13.22 (s, 1H), 7.75 (d, J = 8.7 Hz, 1H), 7.04 (dd, J = 8.7, 2.6 Hz, 1H), 7.02 (d, J = 2.5 Hz, 1H), 6.29 (q, J = 1.3 Hz, 1H), 4.88 (s, 2H), 2.46 (d, J = 1.2 Hz, 3H). ESI-MS, *m*/*z*, found (calcd) 232.9 (233.0) [M-H]$^+$, 467.2 (467.1) [2M-H]$^+$.

2-((4-methyl-2-oxo-2*H*-chromen-6-yl)oxy)acetic acid (HL6). Brown solid. Yield was 62%. Spectral data are consistent with those reported in literature.[44] ^{1}H-NMR (600 MHz, DMSO d[6], δ, ppm, **Figure S14**): 13.09 (s, 1H), 7.37 – 7.33 (m, 1H), 7.24 (dt, J = 4.5, 2.4 Hz, 2H), 6.41 (d, J = 1.4 Hz, 1H), 4.79 (s, 2H), 2.42 (d, J = 1.3 Hz, 3H). ESI-MS, *m/z*, found (calcd) 233.0 (233.0) [M-H][+], 467.0 (467.1) [2M-H][+].

*Synthesis of sodium 2-((2-oxo-2H-chromen-7-yl)oxy)acetate (**NaL1**).*

Compound **HL1** (0.104 mmol) was suspended in 3.0 mL of acetonitrile, then 104 μL of NaOH 1.0 M solution (0.104 mmol, 1.0 eq) were added to the reaction mixture, that was left under stirring at r.t. for 5 hrs. A light brown solid was isolated by filtration, which was washed repeatedly with acetonitrile and dried under vacuum. Yield was 56 %. Elemental analysis, exp (calc.): C 55.19% (54.16%), H 2.98% (2.91%). FT-IR (KBr), cm^{-1}: 1696 ($v(CO)_{ester}$), 1615 ($v(OCO)_{asym}$), 1416 ($v(OCO)_{sym}$).

Synthesis of Cu (II) - phenanthroline complexes

[Cu(phen)[2](OH[2])](ClO[4])[2] (**C0**) was prepared as previously described.[14,46]

[Cu(phen)[2](L1)](ClO[4]) (**D1**) was prepared as follows: **HL1** (0.46 mmol) was treated with 4.6 mL of NaOH 0.1 M solution (0.46 mmol, 1.0 eq.) to obtain the correspondent sodium salt. The former solution was added to a suspension of **C0** (0.46 mmol, 1.0 eq.) in 4.6 mL of methanol. The progressive formation of a pale blue precipitate was observed. Reaction mixture was left under stirring at room temperature for 24 hours. The desired product was recovered by filtration under vacuum, washed with water, ethyl ether and dried. 0.2740 g (81%). Elemental analysis, exp (calc.): C 55.85% (56.61%), H 3.03% (3.12%), N 7.47% (7.55%).

ESI-MS, *m/z*, found (calc.): 641.2 (641.1) [Cu(phen)$_2$(L1)]$^+$ (**Figure S15**). FT-IR (KBr), cm^{-1}: 1728 ($v(CO)_{ester}$), 1611 ($v(OCO)_{asym}$), 1362 ($v(OCO)_{sym}$).

[Cu(phen)$_2$(L2)](ClO$_4$) (**D2**) was prepared as described above starting from 0.22 mmol of **HL2**. The product was obtained as a light green powder 0.1427 g (70%). Elemental analysis, exp (calc.): C 58.35% (58.61%), H 3.11% (3.20%), N 8.46% (8.54%). ESI-MS, *m/z*, found (calc.): 719.1 (719.1) [Cu(phen)$_2$(L2)]$^+$ (**Figure S16**). FT-IR (KBr), cm^{-1}: 1716 ($v(CO)_{ester}$), 1608 ($v(OCO)_{asym}$), 1402 ($v(OCO)_{sym}$).

[Cu(phen)$_2$(L3)](ClO$_4$) (**D3**) was prepared as described above starting from 0.39 mmol of **HL3**. The product was obtained as a light green powder 0.2700 g (93%). Elemental analysis, exp (calc.): C 56.40% (56.61%), H 2.98% (3.12%), N 7.40% (7.55%). ESI-MS, *m/z*, found (calc.): 641.2 (641.1) [Cu(phen)$_2$(L3)]$^+$ (**Figure S17**). FT-IR (KBr), cm^{-1}: 1720 ($v(CO)_{ester}$), 1612 ($v(OCO)_{asym}$), 1366 ($v(OCO)_{sym}$).

[Cu(phen)$_2$(L4)](ClO$_4$) (**D4**) was prepared as described above starting from 0.54 mmol of **HL4**. The product was obtained as an army green powder 0.2814 g (56%). Elemental analysis, exp (calc.): C 58.42 % (58.61%), H 3.08% (3.20%), N 8.49% (8.54%). ESI-MS, *m/z*, found (calc.): 719.2 (719.1) [Cu(phen)$_2$(L4)]$^+$ (**Figure S18**). FT-IR (KBr), cm^{-1}: 1715 ($v(CO)_{ester}$), 1608 ($v(OCO)_{asym}$), 1396 ($v(OCO)_{sym}$).

[Cu(phen)$_2$(L5)](ClO$_4$) (**D5**) was prepared as described above starting from 0.52 mmol of **HL5.** The product was obtained as a pale blue powder. 0.3517 g (90%). Elemental analysis, exp. (calc.): C 57.25 % (57.15%), H 3.13% (3.33%), N 7.29% (7.41%). ESI-MS, *m/z*, found (calc.): 656.1 (656.1) [Cu(phen)$_2$(L5)]$^+$ (**Figure S19**). FT-IR (KBr), cm^{-1}: 1722 ($v(CO)_{ester}$), 1612 ($v(OCO)_{asym}$), 1373 ($v(OCO)_{sym}$).

[Cu(phen)$_2$(L6)](ClO$_4$) (**D6**) was prepared as described above starting from 0.16 mmol of

HL6. The product was obtained as a pale blue powder. 0.1006 g (83%). Elemental analysis, exp. (calc.): C 56.97 % (57.15%), H 3.24% (3.33%), N 7.47% (7.41%). ESI-MS, *m/z*, found (calc.): 656.0 (656.1) [Cu(phen)$_2$(L6)]$^+$ (**Figure S20**). FT-IR (KBr), cm^{-1}: 1714 ($v(CO)_{ester}$), 1608 ($v(OCO)_{asym}$), 1401 ($v(OCO)_{sym}$).

Cell culture conditions

SKOV-3 cells were cultured in in high glucose (4.5 g/L) Dulbecco's Modified Eagle Medium (DMEM) enriched with 10% foetal calf serum (FCS) and 1% of Penicillin/Streptomycin sulphate at 37 °C in humidified atmosphere containing 5% of CO$_2$. Stock solutions of the studied compounds were prepared in DMSO at 2.0 mM concentration.

Cell viability assay

Cells were cultured for 24 hrs on a 96-well plate at a density of 5000 cells per well in medium containing the studied compounds at the indicated concentrations. DMSO was used as a control. Then, the MTT reagent was added directly to the culture medium for 3 hrs. Then, medium including MTT reagent was aspirated, and the cells lysed by addition of 90% isopropanol, 0.04 M HCl and 10% Tween-20. Absorbance was recorded at 570 nm by a Synergy HTX multi-mode reader (BioTek Instruments, VT, USA). All measurements were performed in technical hexaplicates and repeated in three independent experiments. Statistical significance between the treatments and the control was evaluated using Graph Pad Prism 8 using the Student's t-test.
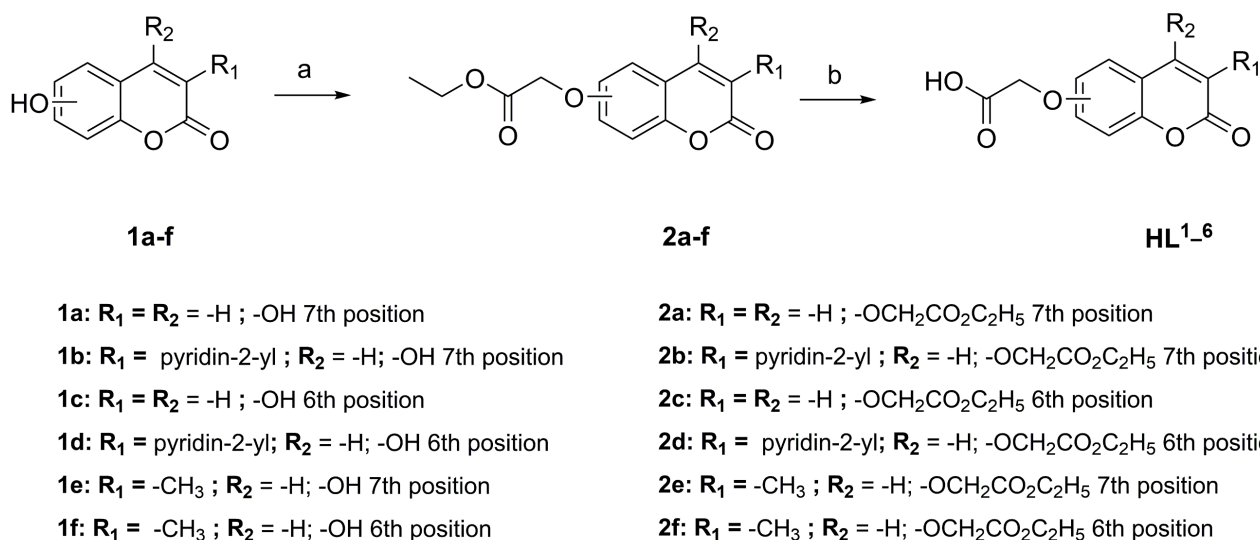
SDS-PAGE and western blotting

SKOV-3 Cells were incubated with the studied compounds at 1.0 and 2.0 μM concentrations for 24 hrs using DMSO as control. Cells were washed twice with PBS and lysed with SDS lysis buffer (100mM TRIS-HCl pH 7.4, 1% SDS, 10% glycerol). Protein content in the cell extract was quantified using the Bradford-based BioRad protein Assay Kit. Cell extracts were then mixed with 2×Laemmli sample buffer (100 mM Tris pH 6.8, 4% SDS, 200 mM DTT, 20% glycerol, and 0.1% bromophenol blue) and boiled for 5 min. An equivalent of 10 μg proteins was resolved using 10% sodium dodecylsulfate polyacrylamide gel electrophoresis (SDS-PAGE). Resolved proteins were then electroblotted onto a 0.45 mm polyvinylidene difluoride (PVDF) membrane (Millipore, Czech Republic) and incubated with the indicated primary antibodies diluted 1:1000 at 4 °C overnight (Actin cat. no: Ab1801, from Abcam, UK; CHOP #2895 and BiP #3177; from Cell Signaling, MA, USA). Blots were developed using horseradish peroxidase (HRP)-conjugated anti-rabbit HRP #7074 or anti-mouse HRP #7076 (both Cell Signaling, USA) secondary antibodies, diluted 1:7500, and ECL plus (GE Healthcare) according to manufacturer's protocol. Results were visualized using a ChemiDoc® Touch Imaging System (Bio-Rad).

Results and Discussion

Synthesis

Target compounds **HL1-6** were obtained starting from hydroxylated derivatives **1a-f** through nucleophilic substitution with ethyl bromoacetate using K_2CO_3 as base. The former ethyl esters **2a-f** were then submitted to basic hydrolysis followed by acidification to obtain the carboxylic acids **HL1-6**. The synthetic pathway is reported in **Scheme 1**.

1a-f   **2a-f**   **HL^{1}–^{6}**

1a: R_1 = R_2 = -H ; -OH 7th position

1b: R_1 = pyridin-2-yl ; R_2 = -H; -OH 7th position

1c: R_1 = R_2 = -H ; -OH 6th position

1d: R_1 = pyridin-2-yl; R_2 = -H; -OH 6th position

1e: R_1 = -CH$_3$; R_2 = -H; -OH 7th position

1f: R_1 = -CH$_3$; R_2 = -H; -OH 6th position

2a: R_1 = R_2 = -H ; -OCH$_2$CO$_2$C$_2$H$_5$ 7th position

2b: R_1 = pyridin-2-yl ; R_2 = -H; -OCH$_2$CO$_2$C$_2$H$_5$ 7th position

2c: R_1 = R_2 = -H ; -OCH$_2$CO$_2$C$_2$H$_5$ 6th position

2d: R_1 = pyridin-2-yl; R_2 = -H; -OCH$_2$CO$_2$C$_2$H$_5$ 6th position

2e: R_1 = -CH$_3$; R_2 = -H; -OCH$_2$CO$_2$C$_2$H$_5$ 7th position

2f: R_1 = -CH$_3$; R_2 = -H; -OCH$_2$CO$_2$C$_2$H$_5$ 6th position

Scheme 1. Reagents and conditions: a) K$_2$CO$_3$, ethyl bromoacetate, acetone rf 24 hrs; b) 5% NaOH (aq), methanol, rf 24 hrs, HCl 2.0 N till pH acid.

The novel mixed mixed coumarin-phenanthroline Cu(II) complexes of general formula [Cu(phen)$_2$(Lx)](ClO$_4$) (where x = 1 - 6) have been obtained by reacting the sodium salts of derivatives **HL1-6** (obtained in-situ) with the precursor [Cu(phen)$_2$(OH$_2$)](ClO$_4$)$_2$ (**C0**). Their stoichiometries have been assessed through UV-Vis (see "Complexes stoichiometries and formation constants" section) and ESI-MS measurements. Picking the spectrum of [Cu(phen)$_2$(L1)](ClO$_4$) (**D1**) as example (**Figure S15**), the most intense peak at *m/z* 642 is due to the ion [Cu(phen)$_2$(L1)]$^+$, derived from ClO$_4^-$ loss of **D1** during the ionization process. The nature of the reported ions was further assessed by comparing calculated and experimental isotopic patterns (**Figure S21**) and Tandem Mass experiments (see "Tandem MS" section).

Both ligands and Cu(II) complexes are stable in the solid state at room temperature. They are soluble in DMSO up to 0.1 M concentration level, in CH$_3$CN at 0.02 M, and in the H$_2$O:CH$_3$CN mixture (1:1) at 0.01 M. Solubility in water is achieved by preparing the studied compounds in DMSO (e.g. 2.0 mM) prior to dilution with distilled water/aqueous buffer (they are soluble at 20 μM concentration 99:1 aqueous buffer:DMSO). In this case, sonication

or vigorous mixing should be avoided to prevent the formation of emulsions. Stock solutions in DMSO and CH₃CN are stable at 4 °C up to 6 months, while stock solutions in H₂O:CH₃CN mixture (1:1) could be stored at r.t. for 2 weeks. The complexes stability in aqueous medium was evaluated by preparing 6.0 μM solutions in phosphate buffer (0.05 M pH 7.4) and following the spectral variation in the 200–450 nm range for 24 hrs by recording 1 spectrum every 60 minutes. No significant variations in the shape and intensity of the spectra were observed for any of the studied complexes. The UV-Vis spectra of **D2**, recorded under this experimental setup, were reported as example in the Supporting (**Figure S22**).

Coordination modes

Since no suitable crystals for structure elucidation were afforded for any of the studied complexes, the coordination around the metal ion was proposed by combining different experimental (Vis-NIR, FT-IR, Tandem MS) and theoretical results.

Vis-NIR. Vis-NIR spectra of **D1-6** in the region 400 - 1100 nm are reported in **Figure S23** and feature a maximum in the 664-696 nm range and a shoulder in the 919-938 nm range. In accordance with the absorption spectra of variously ternary Cu(II) bis-phenanthroline complexes previously characterized,[12] a penta-coordinated geometry might be proposed also for the novel complexes reported in this study.

FT-IR. The coordination mode of the carboxylic group of deprotonated **HL1-6** ligands (**L1-6**, charges are omitted for simplicity) around the metal centre was further investigated by means of FT-IR spectroscopy. As commonly known, carboxylate groups can coordinate metal ions in different manners (unidentate, chelating, bridging modes). The parameter $\Delta(OCO) = v_{asym}(OCO) - v_{sym}(OCO)$ is commonly used to determine the possible

coordination mode adopted by carboxylates upon complexation. Coordination of the carboxylate takes place as unidentate mode when $\Delta(OCO)_{complex} > \Delta(OCO)_{ligand}$, chelating when $\Delta(OCO)_{complex} < \Delta(OCO)_{ligand}$, bridging when $\Delta(OCO)_{complex} \approx \Delta(OCO)_{ligand}$.[47,48] The Cu(II) complex **D1** and the sodium salt of ligand **HL1** (**NaL1**) were taken as example. In the FT-IR spectrum of **NaL1** (**Figure S24A**), asymmetric and symmetric stretching peaks of oxygen carboxylate group ($v_{asym}(OCO)$ and $v_{sym}(OCO)$) fall at 1615 and 1406 cm^{-1} respectively, with a $\Delta(OCO)_{NaL1}$ value of 199 cm^{-1}. In the **D1** complex (**Figure S24B**), the same bands fall at 1611 and 1362 cm^{-1} respectively, with a $\Delta(OCO)_{D1}$ of 249 cm^{-1}. Since $\Delta(OCO)_{D1} > \Delta(OCO)_{NaL1}$, we can conclude that the carboxylic group coordinates the metal centre in **D1** in a monodentate fashion. Considering the structural similarity of the other **HL2-6** auxiliary ligands and the same stoichiometry determined for **D2-6** complexes ([Cu(phen)$_2$(Lx)](ClO$_4$)), we can extend the same considerations to the remaining Cu(II) complexes reported in this work. The signals observed in the FT-IR spectrum of **D1** at 1521, 1429, 851, 724 and 623 cm^{-1} are due to the phenanthroline moieties (see the FT-IR spectrum of **C0** in **Figure S24C** for comparison), while the band centred at around 1100 cm^{-1} derive from the perchlorate anion. The signal observed at 1725 cm^{-1} corresponds to the stretching of the lactonic carbonyl in the 2-*H*-chromen-2-one backbone.

Tandem MS. Collision Induced Dissociation (CID) experiments were performed at different collision energies (CE, 0-50 V) to have more information about the structure of the synthesized complexes. Taking the CID experiments of the **D1's** parent ion at 642 *m/z* ([Cu(phen)$_2$(L1)]$^+$) as example (**Figure 2A**), it is possible to observe the loss of a phenanthroline unit and the formation of a product ion at 462 *m/z* ([Cu(phen)(L1)]$^+$, **Figure**

S25A). A gradual decrease in intensity for the peak at m/z 642 is observed as the CE is increased, a feature consistent with further fragmentation processes of the related ion. For instance, a new peak at m/z 243 ([Cu(phen)]$^+$) is obtained due to the loss of the **L1** moiety as radical (**Figure S25B**), with subsequent reduction of Cu(II) centre, as previously reported.[15,49] This fragmentation scheme is further confirmed by CID experiments of the 462 m/z ion (**Figure 2B**). In addition, minor product ion peaks at intermediate CE (e.g., 15 V **Figure S26**) are observed. For instance, the ion at 418 m/z comes from CO_2 loss from the coumarin moiety (**Figure S27A**), while the one at 390 originates from 418 m/z by loss of CO from the carboxylate coordinating moiety (**Figure S27B**). The product ion at 282 m/z derives from the loss of another phen unit (**Figure S27C**), while the signal at 260 m/z arises from transposition of an Hα from the auxiliary ligand and subsequent closure of a Cα=C$_{carbonyl}$ double bond with loss of a neutral ketene (**Figure S27D**). The same fragmentation patterns were observed with the other complexes here reported.
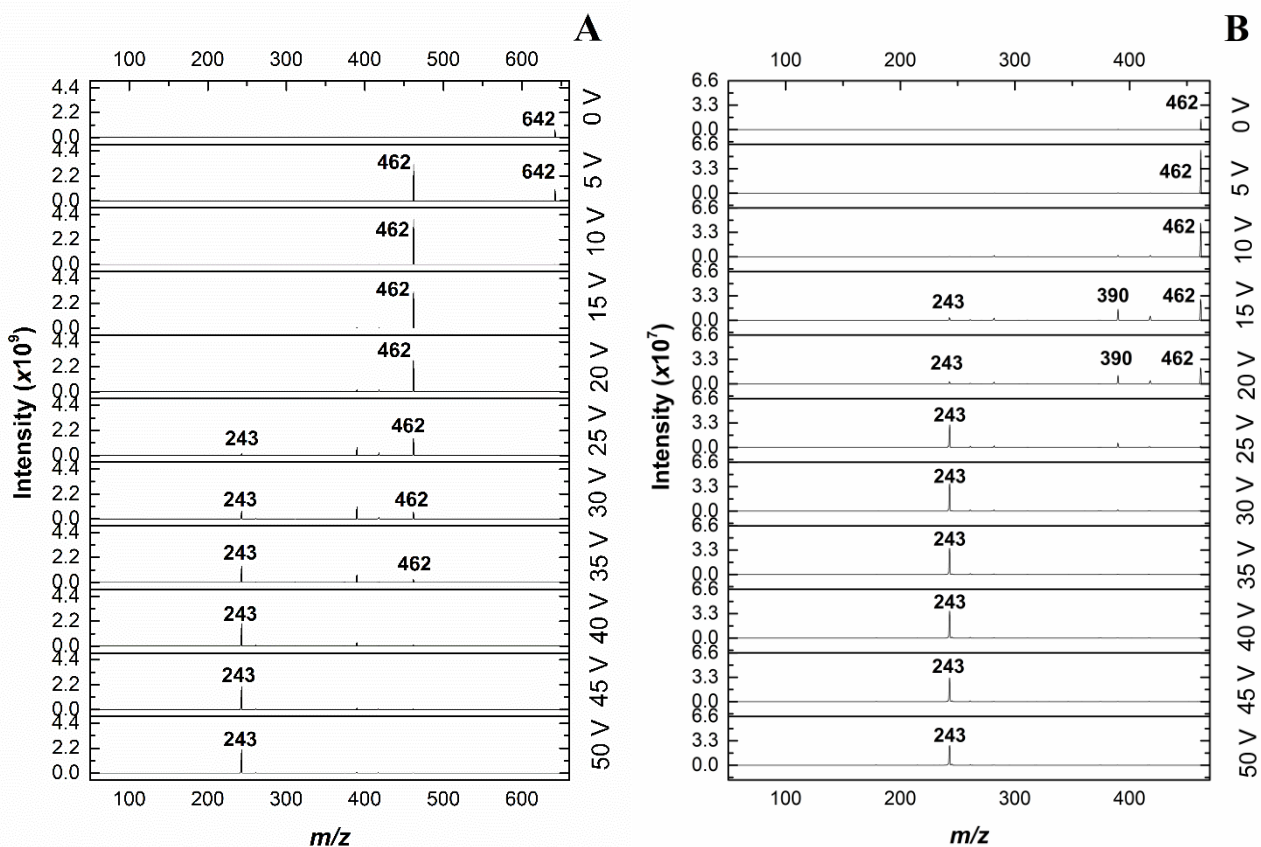
Figure 2. Tandem MS fragmentations at different collision energies of the peaks at (**A**) *m/z* 642 ([Cu(phen)$_2$(L1)]$^+$) and (**B**) 462 ([Cu(phen)(L1)]$^+$). All the mass values are expressed as monoisotopic masses, computed as the sum of the masses of the primary isotope of each atom in the molecule (note that the monoisotopic mass may differ from the nominal molecular mass, especially for big molecules).

DFT calculations. Geometry optimizations for both the deprotonated **HL1-6** ligands (**L1-6**, charges are omitted for simplicity) and **[Cu(phen)$_2$(Lx)]$^+$** (x = 1 – 6) complexes were performed by means of the computational setup used for **[Cu(phen)$_2$(OH$_2$)]$^{2+}$** (whose coordinates were taken from **C0** crystal structure), as previously discussed.[15] In addition, geometry optimization of **L1** was performed starting from the X-Ray crystal structure of dimethylammonium 2-[(2-oxo-2*H*-chromen-7-yl)oxy]acetate previously reported,[50] showing a good agreement between experimental and calculated structural parameters

(**Table S1**). Structures of the DFT-optimized geometries of **L1-6** are shown in **Figure S28**.

Selected bond lengths, angles and dihedrals calculated for **L2–L6** are reported in **Tables S2– S6**. From visual inspection of ligands frontier molecular orbitals (**Figure S29**) it is possible to observe that HOMOs are mainly centred on the carboxylate moiety, thus supporting the hypothesis that these compounds can coordinate a metal ion using this functional group. This assumption finds further confirmation by observing the calculated atomic charges (**Tables S7-8**). Energies of ligands frontier orbitals are reported in **Table S9**. Geometry optimization of the **[Cu(phen)$_2$(Lx)]$^+$** complexes (**Figure 3**) suggest a pentacoordinate geometry closer to a square pyramidal than a trigonal bipyramidal, as indicated by the values of "tau" geometrical parameter ($\tau = (\beta - \alpha)/(60°)$) reported in **Table S16**. The adoption of such geometry is also evident at bond lengths level: taking the structural parameters of **[Cu(phen)$_2$(L1)]$^+$** (**Table S10**) as example, it is possible to observe that the elongation of Cu-N2 (2.285 Å) is accompanied by shortening of Cu-N1, Cu-N3, Cu-N4 and Cu-O1 (2.045, 2.030, 2.087 and 1.986 Å respectively). These results agree with the experimental metrics of several mono and binuclear Cu(II) bis-phenanthroline complexes coordinated by carboxylate functional groups.[51–54] Selected bonds, angles, and dihedrals of **[Cu(phen)$_2$(Ly)]$^+$** (y: 2 - 6) are reported in **Tables S11-S15**. Analysis of atomic charges (NPA level, **Tables S17-18**) show on copper ions a significant lower atomic charge (1.39) compared with its formal charge +2, while on N1-4 and O1 atoms high negative calculated charges were evidenced. This trend might be indicative of a Ligand to Metal Charge Transfer (LMCT), as observed by comparing β-SOMOs, mainly centred on the coumarin-based

moiety, and β-LUMOs, distributed among the metal centre and one of the phenanthrolines (**Figure S30-32**). Energies (in eV) of complexes frontier orbitals are reported in **Table S19**.
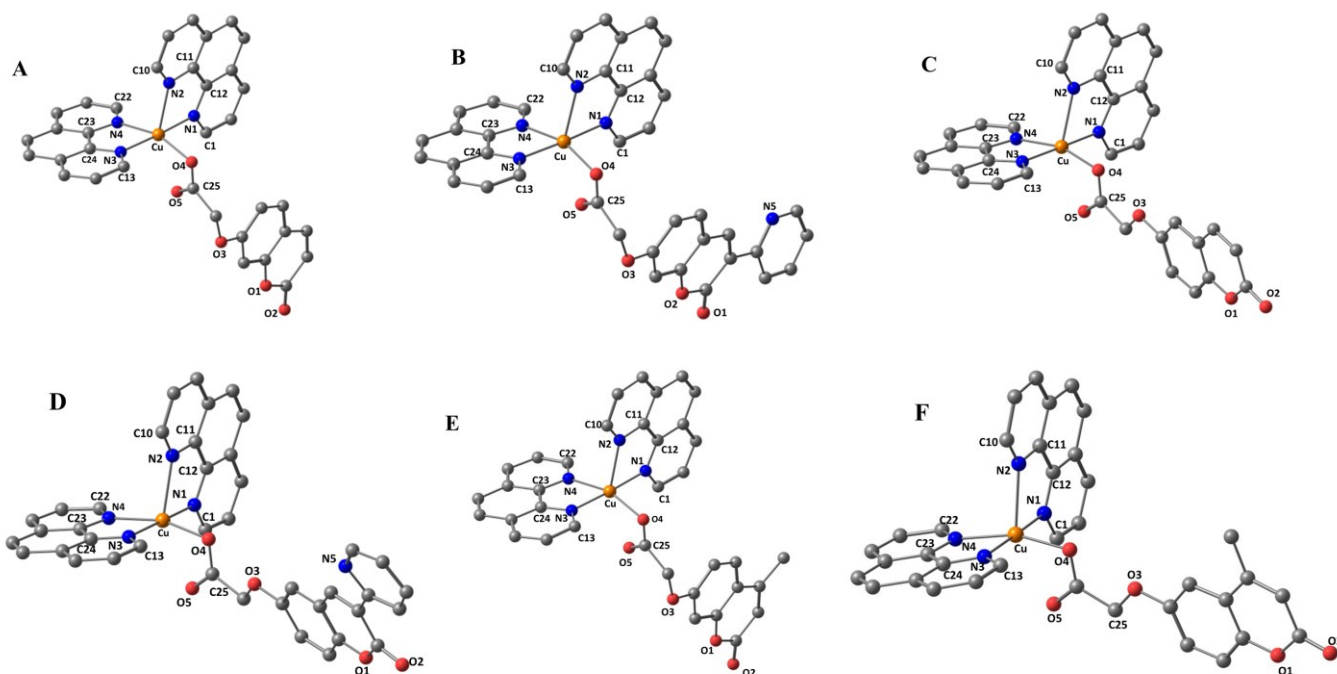
Figure 3. Molecular drawings and atom labelling scheme for **[Cu(phen)₂(L1)]⁺ (A)**, **[Cu(phen)₂(L2)]⁺ (B)**, **[Cu(phen)₂(L3)]⁺ (C)**, **[Cu(phen)₂(L4)]⁺ (D)**, **[Cu(phen)₂(L5)]⁺ (E)**, **[Cu(phen)₂(L6)]⁺ (F)** at the DFT-optimized geometries (gas phase).

Complexes stoichiometries and formation constants

The method of continuous variations (Job's method) was employed with the aim of assessing the number and stoichiometry of the complexes formed between **C0** and the deprotonated ligands **HL1-6**. At the chosen experimental conditions, the studied ligands will predominantly exist as monoanionic species due to the loss of their carboxylic proton. In each case, formation of only one complex with 1:1 molar ratio ($\chi_L = 0.5$) was evidenced. No binuclear complexes were evinced with deprotonated **HL2** and **HL4**, were the nitrogen 3-pyridinyl and coumarin carbonyl could represent a potential chelating site, as previously

observed in different systems.[40,55] In **Figure 4A**, spectra collected varying the ligand molar ratio from 0 to 10 for the system **C0** - deprotonated **HL2** is reported as example. Absorbance data at 344 nm and 292 nm, corrected for the contribution of absorbing reactants, clearly indicate the formation of a 1:1 molar ratio mixed complex (**Figure 4B**). In **Figure S33**, uncorrected absorption data at the same wavelengths are reported.
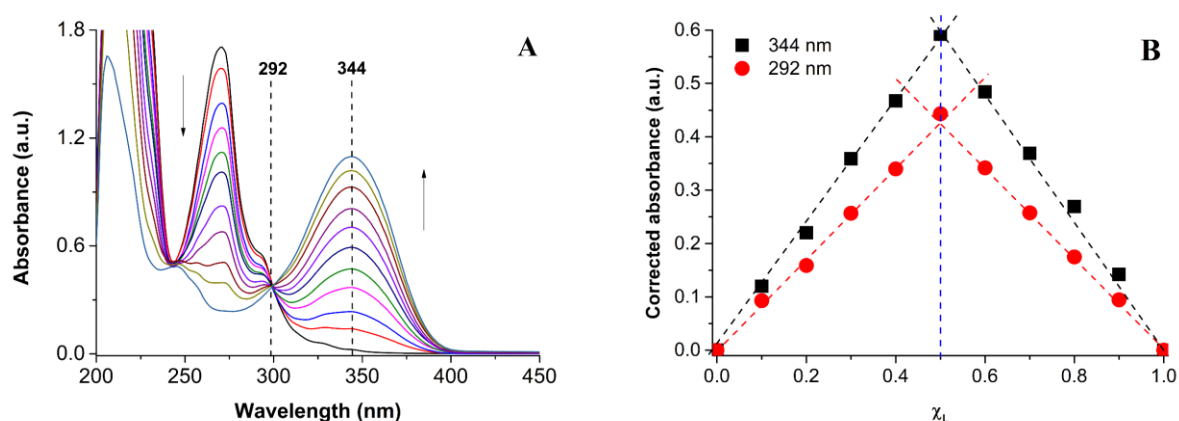
Figure 4. Absorption spectra collected varying the ligand molar fraction from 0 to 1 for the system between **C0** ($4.37 \cdot 10^{-5}$ M) and **HL2** ($4.37 \cdot 10^{-5}$ M) in PB 0.05 M, pH 7.4, 25 °C, 1 cm optical path length (**A**). Job's plot of **C0** and **HL2** (**B**) at 292 nm (red dots) and 344 nm (black squares).

The indication of a mononuclear mixed complex was further assessed by spectrophotometric titrations. By adding increasing amounts of the ligands, a decrease in intensity of **C0** band at 270 nm was observed, along with the formation of a new band in the range 320-340 nm and of an isosbestic point around 300 nm, indicating the presence of at least one equilibrium in solution. From eigenvalue analysis of the spectrophotometric data in the 225–400 nm range, three significant eigenvalues were found, indicating three linearly independent absorbing species in solution. By fitting the experimental data considering the species $[Cu(phen)_2]^{2+}_{free}$, $[Cu(phen)_2L]^+$, and $[L]^-_{free,exc}$ the complex formation constants were

calculated (**Table 1**). Selected spectra recorded during the titrations are reported in **Figure S34**.

Table 1. Complex formation constants and calculated spectral properties for the studied complexes (25 °C, PB 0.05 M, pH 7.4). The standard deviation to the last significant figure is reported in parentheses.

Species	Logβ	Absorption maxima (nm)	Calculated extinction coefficients (10^4 $M^{-1}cm^{-1}$)
[Cu(phen)₂(L1)]⁺	5.03(2)	272, 321 (sh)	5.11, 1.72
[Cu(phen)₂(L2)]⁺	5.1(1)	272, 344	5.23, 2.44
[Cu(phen)₂(L3)]⁺	4.3(1)	272, 321 (sh)	5.70, 0.75
[Cu(phen)₂(L4)]⁺	4.7(1)	272, 344	5.82, 0.60
[Cu(phen)₂(L5)]⁺	5.85(7)	271, 318 (sh)	5.65, 1.36
[Cu(phen)₂(L6)]⁺	6.0 (1)	272, 322 (sh)	6.36, 0.61

Electrochemical behaviour of Cu(II) complexes

The electrochemical behaviour of the redox active compounds **D1-6** and **C0** were evaluated by means of Cyclic Voltammetry (CV). By examining the electrochemical results (**Table S20**), derived from the cyclic voltammograms (**Figure S35**) it is possible to assess how the studied compounds exhibit a quasi-reversible one electron transfer involving the Cu(II)/Cu(I) couple, as evidenced by the ratios between cathodic and anodic current intensities (I_{pc}/I_{pa}) in the 0.8 – 0.9 range (I_{pc}/I_{pa} ideally should be 1 for complete reversibility), and the peak separation (ΔE) values between -51.62 and -77.68 mV (ideally should be -59.1 mV for a single electron transfer).

Taking **D1** as example, the relationship between the current intensity and the square root of the scan rate was evaluated by acquiring the cyclic voltammograms of the studied compound at different scan rates. Results reported in **Figure S36** show a linear relationship

between the two variables, thus supporting how the electron transfer process is diffusion controlled.[56]

DNA interaction studies

Interaction with ct-DNA

The affinity of the studied compounds towards ct-DNA was assessed through Electronic Absorption Spectroscopy. Selected spectra of **HL1-6** in presence of increasing amounts of ct-DNA are reported in **Figure S37**, while the analogous spectra regarding **C0** and **D1-D6** complexes are shown in **Figure S38**. As evident, a general increase in absorbance is observed in the 240-285 nm region for all compounds. In some of cases (e.g., **HL1** and **D2**) a decrease (moderate to low, according to the compound considered) in absorbance in the 305-400 nm region with the appearance of an isosbestic point in the 295-303 nm region is evidenced. The intrinsic binding constants between the studied compounds and ct-DNA were calculated from absorbance data applying the *Equation (1)*, as explained in the Experimental. Results are summarized in **Table 2**. The order of magnitude of these binding constants, along with the changes in the absorption profile during the titration, are indicative of the interaction mode with this biological target.[27] Absorption spectra of small molecules that intercalate DNA generally show hypochromism and bathochromic shift. In particular, DNA intercalators show % of Hypochromism > 35%, batochromic shift > 15 nm and high association constants (> 10^5 M^{-1}).[57,58] Compounds that act as groove binders and/or interact through electrostatic interaction generally results in hyperchromism and show lower binding constants. Based on these findings, we can conclude that the studied compounds will target ct-DNA predominantly through electrostatic interactions and groove binding.

The possibility of a partial intercalative mode for those compounds that showed some hypochromic effect in the 305-400 nm (**HL1**, **D1**, **HL2**, **D2**, **HL4**, **D4**, **HL5**) can be ruled out since the % of Hypochromism, calculated at λ_{max}, considering an excess of ct-DNA (R = [DNA]/[compound] = 4) appears to be quite low (from 2 to 14 %, **Table 2**).

Table 2. DNA-binding constants (K_b) for the studied compounds and % Hypochromism (at λ_{max}, for R = [DNA]/[compound] = 4) for selected ones (25 °C, TRIS-HCl buffer, pH 7.1).

Species	K_b (M^{-1})	% Hypochromism (λ_{max}, nm)*
C0	$8.18 \cdot 10^3$	-
HL1	$2.29 \cdot 10^4$	13.2 (324)
D1	$1.57 \cdot 10^3$	8.4 (324)
HL2	$1.86 \cdot 10^4$	14.1 (344)
D2	$3.30 \cdot 10^4$	9.7 (364)
HL3	$3.75 \cdot 10^4$	-
D3	$2.65 \cdot 10^4$	-
HL4	$6.97 \cdot 10^3$	11.9 (354)
D4	$2.05 \cdot 10^4$	2.0 (355)
HL5	$3.57 \cdot 10^4$	10.7 (319)
D5	$1.77 \cdot 10^3$	3.7 (322)
HL6	$3.42 \cdot 10^3$	-
D6	$2.12 \cdot 10^4$	-

*calculated as $(A_f - A_b/A_f) \cdot 100$, A_f and A_b are the absorbance in absence and presence of ct-DNA respectively.

Interaction with genomic DNA

Interaction of redox-active **C0** and **D1-6** complexes with genomic DNA was evaluated by means of Differential Pulse Voltammetry (DPV). Results are shown in **Figure S39**. As can be seen, by adding increasing amounts of genomic DNA, a decrease in current intensity along with a slight shift towards lower potentials are observed. This feature, indicative of an interaction between the biomolecule and the studied compounds, is further confirmed from a quantitative point of view by calculating the $E_{1/2}$ values in absence and presence of increasing amounts of genomic DNA (**Tables S21-27**). In addition, this shifts suggest that

both Cu(I) and Cu(II) forms of the studied complexes could interact with human DNA, but the Cu(II) form will display higher affinity rather than the Cu(I). This is further assessed on a quantitative basis by calculating the ratio of the K^+/K^{2+} using the *Equation (2)* reported in the Experimental Section. As can be seen from results in **Tables S21-27**, a K^+/K^{2+} ratio lower than 1 is observed for each studied compound by increasing DNA amounts, which is indicative of a higher stability of the reported complexes in their oxidized form upon interaction with this biological target.

Molecular docking

Docking simulations were performed to better clarify the binding mechanism between deprotonated **HL1-6** (**L1-6**, charges re omitted for simplicity), **[Cu(phen)₂(Lx)]⁺** and BDNA. As regards the ligands, they interact at the minor groove of the DNA double helix (**Figure S40**), in agreement with the experimental results from UV-Vis spectroscopy. Compounds **L1**, **L2** and **L5** possess a similar not-covalent interactions profile: they form a hydrogen bond with G10 base using their lactonic oxygen atoms (**Figure S41**) . On the contrary, a different hydrogen bonding profile is observed for **L4** and **L6** with respect to **L3**, where the oxylacetic group is in the 6th position: the introduction of substituents in the coumarinic structure (a pyridyl ring in **L4**, a methyl in **L6**) induces a 180° twist in the conformation orientation (compared to **L3**), determining a different hydrogen bonding profile (**Figure S42**).

As regards the complexes, all of them are positioned in proximity of one of the minor grooves (**Figure 5**), in agreement with the experimental findings from UV-Vis. As expected, the bulky [Cu(phen)₂] moiety is in proximity of the phosphate backbone, thus supporting the possibility of establishing electrostatic interactions, while the interactions with DNA

base pairs are guaranteed by the auxiliary ligands for (the coumarin-based molecules for

[Cu(phen)$_2$(Lx)]$^+$ species, the water molecule for [Cu(phen)$_2$(OH$_2$)]$^{2+}$). The hydrogen

bonding profile for the studied complexes are shown in **Figure S43**.

A   **B**   **C**   **D**   **E**   **F**   **G**
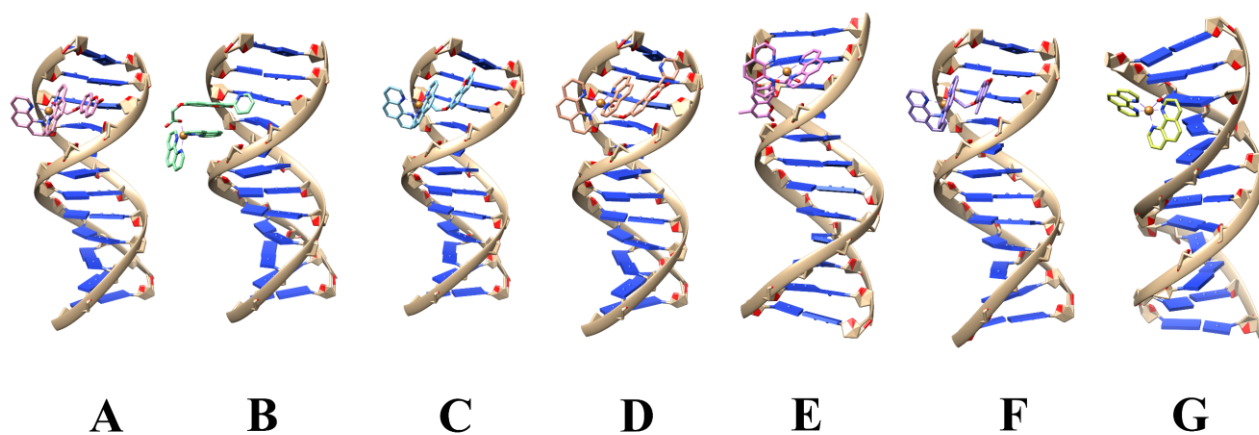
Figure 5. Full view of the complex between the highest-ranking score of **[Cu(phen)$_2$(Lx)]$^+$** (x = 1 – 6) and BDNA (**A-F**). Full view of the complex between the highest-ranking score of **[Cu(phen)$_2$(OH$_2$)]$^{2+}$** and BDNA (**G**).

Cytotoxicity

The anticancer potency *in-vitro* of the studied compounds was evaluated on ovarian (SKOV-3) cancer cells by means of the MTT assay. Results, expressed as IC$_{50}$ values (concentration of drug able to induce cell death by 50%), are summarized in **Table 3**. As observed, the heteroleptic Cu(II) complexes **D1-6** shows anticancer activity in the micromolar concentration range, while the corresponding coumarin-based oxylacetatic acids are devoid of any activity in the concentration range explored. These results confirm the importance of the metal complex structure in exerting the anticancer potency and are not attributable to the only Cu^{2+} ion, as previously demonstrated.[14] Although there are not such big differences in terms of IC$_{50}$ values, compounds **D2** and **D5** (differently substituted in the 3rd and 4th positions, both bearing an oxylacetate in the 7th position) seems to be the most promising

compounds of the series. Viability % of the **D1-6** compounds (from MTT data) at different treatments were reported in **Figure S44**.

Table 3. Anticancer potency of the studied compounds reported as IC_{50} values from MTT data after 24 hrs treatment. Results were obtained from technical hexaplicates in 3 independent experiments.

Compound	$IC_{50} \pm SD$ (μM)
D1	3.0 ± 0.6
D2	2.1 ± 0.1
D3	2.6 ± 0.2
D4	5 ± 2
D5	2.0 ± 0.7
D6	3.4 ± 0.3
HL1-6	>5.0

Mechanistic studies

Considering the ability of similar mixed Cu(II) bis-phenanthroline complexes in inducing the pro-apoptotic branch of UPR,[11,14,15] we deemed interesting to evaluate the role of the studied compounds in alteration of ER homeostasis. For this purpose, we chose the most promising compounds of the series (**D2** and **D5**) and included **D1** and **C0** for structural comparisons. From Western Blots results (**Figure S45**) it is possible to observe how the novel compounds **D1**, **D2** and **D5** induce a decrease of the ER chaperone BiP levels and an increase of the pro-apoptotic transcription factor CHOP, in agreement with results reported on similar systems.[14,15] It is interesting to point out how the entity of these variations are dose-dependent and more pronounced on the novel compounds compared to **C0**. In particular, the presence of a methyl group in the 4th position of the coumarinic backbone (as in **D5**) seems to heavily influence the expression level of these markers even at sub-lethal

concentration level (1.0 μM), as evidenced on a quantitative basis from the relative densities reported in **Figure 6**.
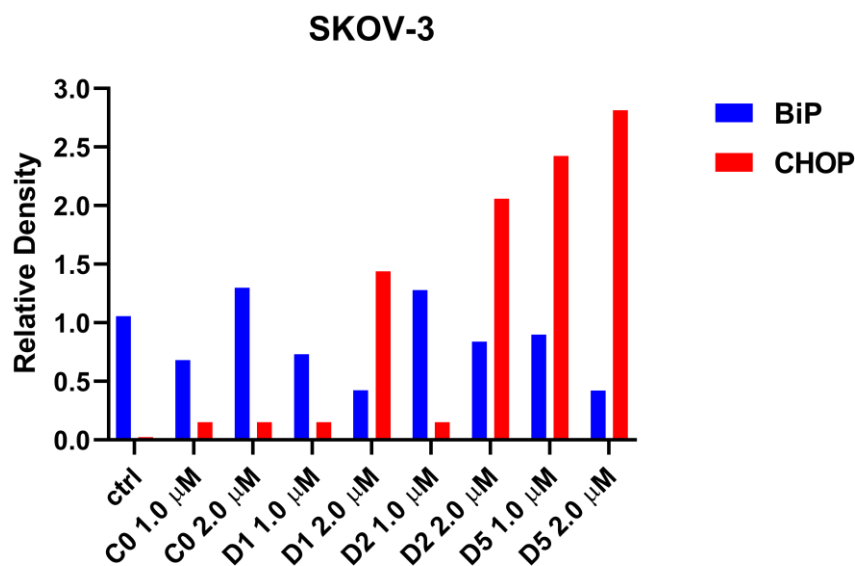
Figure 6. Relative densities for BiP and CHOP calculated from immunoblotting results on SKOV-3 cells.

Conclusions

By reacting the anticancer anticancer compound $[Cu(phen)_2(OH_2)](ClO_4)_2$ (**C0**) with a series of coumarin-based oxylacetic acids (**HL1-6**), a panel of novel heteroleptic Cu(II) complexes having general formula $[Cu(phen)_2(Lx)](ClO_4)$ (**D1-6**) has been obtained. The structure of these compounds has been assessed by merging results coming from different spectroscopic and computational techniques.

Interestingly, these compounds show high anticancer potency (at micromolar level) in ovarian (SKOV-3) cancer cells, as observed from MTT assay results. According to mechanistic studies, these compounds induce cell death activating the pro-apoptotic branch of the UPR.

Studies on both calf thymus and human DNA have evidenced how these complexes can interact with this biological target. Using ct-DNA as study model, we pointed out how these complexes and the related coumarin-based ligands interact with this biomolecule through electrostatic interactions and groove binding, as evidenced by combining the results coming from spectroscopic (UV-Vis) and computational (molecular docking) techniques.

The cross-disciplinarity (chemistry, biochemistry, molecular biology, medicine) of this study and the results achieved in this study could be extremely useful in the design and synthesis of novel potential anticancer metal-based drugs that could target alternative pathways than currently approved Pt(II)-based chemotherapeutics.

Author contributions

Conceptualization: S.M., M.G.C., P.V., T.P.; Methodology: S.M., M.G.C., P.V., L.M, M.B., J.H., E.C., T.P.; Investigation: S.M., M.G.C., L.M., T.V.; Formal analysis: S.M., M.G.C., L.M., T.V.; Validation: S.M., M.G.C., L.M., M.B., T.V.; Visualization: S.M.; Writing – original draft: S.M.; Writing – review and editing: S.M., T.P.; Resources: T.P., M.G.C., E.C., M.B., J.H., P.V.; Supervision: S.M., T.P., P.V.

Acknowledgements

References

1   B. Rosemberg, L. Vancamp, J. E. Trosko and V. H. Mansour, *Nature*, 1969, **222**, 385–386.

2   P. J. Loehrer, *Ann. Intern. Med.*, 1984, **100**, 704.

3   N. Eckstein, *J. Exp. Clin. Cancer Res.*, 2011, **30**, 91.

4   S. Dhar, F. X. Gu, R. Langer, O. C. Farokhzad and S. J. Lippard, *Proc. Natl. Acad. Sci.*, 2008, **105**, 17356–17361.

5   J. Michels, I. Vitale, L. Galluzzi, J. Adam, K. A. Olaussen, O. Kepp, L. Senovilla, I. Talhaoui, J. Guegan, D. P. Enot, M. Talbot, A. Robin, P. Girard, C. Orear, D. Lissa, A. Q. Sukkurwala, P. Garcia, P. Behnam-Motlagh, K. Kohno, G. S. Wu, C. Brenner, P. Dessen, M. Saparbaev, J.-C. Soria, M. Castedo and G. Kroemer, *Cancer Res.*, 2013, **73**, 2271–2280.

6   F. Trudu, F. Amato, P. Vaňhara, T. Pivetta, E. M. Peña-Méndez and J. Havel, *J. Appl. Biomed.*, 2015, **13**, 79–103.

7   S. Dilruba and G. V. Kalayda, *Cancer Chemother. Pharmacol.*, 2016, **77**, 1103–1124.

8   T. J. P. McGivern, S. Afsharpour and C. J. Marmion, *Inorganica Chim. Acta*, 2018, **472**, 12–39.

9   C. Marzano, M. Pellei, F. Tisato and C. Santini, *Anticancer. Agents Med. Chem.*, 2009, **9**, 185–211.

10 C. Santini, M. Pellei, V. Gandin, M. Porchia, F. Tisato and C. Marzano, *Chem. Rev.*, 2014, **114**, 815–862.

11 S. Masuri, P. Vaňhara, M. G. Cabiddu, L. Moráň, J. Havel, E. Cadoni and T. Pivetta, *Molecules*, 2022, **27**, 49.

12 T. Pivetta, F. Isaia, G. Verani, C. Cannas, L. Serra, C. Castellano, F. Demartin, F. Pilla, M. Manca and A. Pani, *J. Inorg. Biochem.*, 2012, **114**, 28–37.

13 T. Pivetta, F. Trudu, E. Valletta, F. Isaia, C. Castellano, F. Demartin, R. Tuveri, S. Vascellari and A. Pani, *J. Inorg. Biochem.*, 2014, **141**, 103–113.

14 L. Moráň, T. Pivetta, S. Masuri, K. Vašíčková, F. Walter, J. Prehn, M. Elkalaf, J. Trnka, J. Havel and P. Vaňhara, *Metallomics*, 2019, **11**, 1481–1489.

15 S. Masuri, E. Cadoni, M. G. Cabiddu, F. Isaia, M. G. Demuru, L. Moráň, D. Buček, P. Vaňhara, J. Havel and T. Pivetta, *Metallomics*, 2020, **12**, 891–901.

16 I. Kostova, S. Bhatia, P. Grigorov, S. Balkansky, V. S. Parmar, A. K. Prasad and L. Saso, *Curr. Med. Chem.*, 2011, **18**, 3929–3951.

17 S. Emami and S. Dadashpour, *Eur. J. Med. Chem.*, 2015, **102**, 611–630.

18   Y. Bansal, P. Sethi and G. Bansal, *Med. Chem. Res.*, 2013, **22**, 3049–3060.

19   O. Kayser and H. Kolodziej, *Zeitschrift fur Naturforsch. - Sect. C J. Biosci.*, 1999, **54**, 169–174.

20   M. E. Marshall, J. L. Mohler, K. Edmonds, B. Williams, K. Butler, M. Ryles, L. Weiss, D. Urban, A. Bueschen, M. Markiewicz and G. Cloud, *J. Cancer Res. Clin. Oncol.*, 1994, **120**, S39–S42.

21   B. Thati, A. Noble, B. S. Creaven, M. Walsh, K. Kavanagh and D. A. Egan, *Eur. J. Pharmacol.*, 2007, **569**, 16–28.

22   J. P., *Ann. Chim. Appl.*, 1928, **9**, 113–203.

23   J. S. Renny, L. L. Tomasevich, E. H. Tallmadge and D. B. Collum, *Angew. Chemie Int. Ed.*, 2013, **52**, 11998–12013.

24   P. Gans, A. Sabatini and A. Vacca, *Talanta*, 1996, 1739–1753.

25   J. Marmur, *J. Mol. Biol.*, 1961, **3**, 208-IN1.

26   N. Raman, K. Pothiraj and T. Baskaran, *J. Mol. Struct.*, 2011, **1000**, 135–144.

27   M. Sirajuddin, S. Ali and A. Badshah, *J. Photochem. Photobiol. B Biol.*, 2013, **124**, 1–19.

28   T. H. J. Niedermeyer and M. Strohalm, *PLoS One*, 2012, **7**, e44913.

29   M. Strohalm, D. Kavan, P. Nova and M. Volny, *Anal. Chem.*, 2010, **82**, 4648–4651.

30   T. Hirohama, Y. Kuranuki, E. Ebina, T. Sugizaki, H. Arii, M. Chikira, P. T. Selvi and M. Palaniandavar, *J. Inorg. Biochem.*, 2005, **99**, 1205–1219.

31   F. Neese, *Wiley Interdiscip. Rev. Comput. Mol. Sci.*, 2012, **2**, 73–78.

32   M. D. Hanwell, D. E. Curtis, D. C. Lonie, T. Vandermeersch, E. Zurek and G. R. Hutchison, *J. Cheminform.*, 2012, **4**, 17.

33   C. Adamo and V. Barone, *J. Chem. Phys.*, 1999, **110**, 6158–6170.

34   F. Weigend and R. Ahlrichs, *Phys. Chem. Chem. Phys.*, 2005, **7**, 3297.

35   T. Y. Nikolaienko, L. A. Bulavin and D. M. Hovorun, *Comput. Theor. Chem.*, 2014, **1050**, 15–22.

36   Chemcraft - graphical software for visualization of quantum chemistry computations. https://www.chemcraftprog.com.

37   O. Trott and A. J. Olson, *J. Comput. Chem.*, 2009, 455–461.

38   G. M. Morris, H. Ruth, W. Lindstrom, M. F. Sanner, R. K. Belew, D. S. Goodsell and A. J. Olson, *J. Comput. Chem.*, 2009, **30**, 2785–2791.

39   E. F. Pettersen, T. D. Goddard, C. C. Huang, G. S. Couch, D. M. Greenblatt, E. C. Meng and T. E. Ferrin, *J. Comput. Chem.*, 2004, **25**, 1605–1612.

40   T. Pivetta, S. Masuri, M. G. Cabiddu, C. Caltagirone, A. Pintus, M. Massa, F. Isaia and E. Cadoni, *New J. Chem.*, 2019, **43**, 12032–12041.

41   S. Masuri, M. G. Cabiddu, E. Cadoni and T. Pivetta, *New J. Chem.*, 2021, **45**, 10749–10760.

42   Z. Gao, D. J. Maloney, L. M. Dedkova and S. M. Hecht, *Bioorganic Med. Chem.*, 2008, **16**, 4331–4340.

43   A. Peperidou, S. Bua, M. Bozdag, D. Hadjipavlou-Litina and C. Supuran, *Molecules*, 2018, **23**, 153.

44   M. Mujahid, N. Trendafilova, A. F. Arfa-Kia, G. Rosair, K. Kavanagh, M. Devereux, M. Walsh, S. McClean, B. S. Creaven and I. Georgieva, *J. Inorg. Biochem.*, 2016, **163**, 53–67.

45   Z. Gao, D. J. Maloney, L. M. Dedkova and S. M. Hecht, *Bioorg. Med. Chem.*, 2008, **16**, 4331–4340.

46   T. Pivetta, V. Lallai, E. Valletta, F. Trudu, F. Isaia, D. Perra, E. Pinna and A. Pani, *J. Inorg. Biochem.*, 2015, **151**, 107–114.

47   G. Deacon and R. J. Phillips, *Coord. Chem. Rev.*, 1980, **33**, 227–250.

48   K. Nakamoto, *Infrared and Raman Spectra of Inorganic and Coordination Compounds*, John Wiley & Sons, Inc., Hoboken, NJ, USA, 2008.

49   E. Cadoni, E. Valletta, G. Caddeo, F. Isaia, M. G. Cabiddu, S. Vascellari and T. Pivetta, *J. Inorg. Biochem.*, 2017, **173**, 126–133.

50   F.-X. Dong, *Acta Crystallogr. Sect. E Struct. Reports Online*, 2011, **67**, o1105–o1105.

51   M. Devereux, M. McCann, J. F. Cronin, G. Ferguson and V. McKee, *Polyhedron*, 1999, **18**, 2141–2148.

52   F. Clifford, E. Counihan, W. Fitzgerald, K. Seff, C. Simmons, S. Tyagi and B. Hathaway, *J. Chem. Soc. Chem. Commun.*, 1982, 196.

53   M. Barceló-Oliver, Á. García-Raso, Á. Terrón, E. Molins, M. J. Prieto, V. Moreno, J. Martínez, V. Lladó, I. López, A. Gutiérrez and P. V. Escribá, *J. Inorg. Biochem.*, 2007, **101**, 649–659.

54   K. N. Lazarou, S. P. Perlepes, V. Psycharis and C. P. Raptopoulou, *Polyhedron*, 2008, **27**, 2131–2142.

55   T. Pivetta, E. Valletta, G. Ferino, F. Isaia, A. Pani, S. Vascellari, C. Castellano, F. Demartin, M. G. Cabiddu and E. Cadoni, *J. Inorg. Biochem.*, 2017, **177**, 101–109.

56   N. Elgrishi, K. J. Rountree, B. D. McCarthy, E. S. Rountree, T. T. Eisenhart and J. L. Dempsey, *J. Chem. Educ.*, 2018, **95**, 197–206.

57   S. U. Rehman, T. Sarwar, M. A. Husain, H. M. Ishqi and M. Tabish, *Arch. Biochem.*

Biophys., 2015, **576**, 49–60.

58   T. Topală, A. Bodoki, L. Oprean and R. Oprean, *Farmacia*, 2014, **62**, 1049–1061.

Ternary Copper (II) complexes of 1,10-phenanthroline and coumarin-based oxylacetates as potential anticancer metallodrugs

Sebastiano Masuri[1], Maria Grazia Cabiddu[1], Lukáš Moráň[2,3], Tereza Vesselá[2], Enzo Cadoni[1], Martin Bartosik[3], Josef Havel[4,5], Petr Vaňhara[2,4], Tiziana Pivetta[*,1]

[1] Department of Chemical and Geological Sciences, University of Cagliari, Cittadella Universitaria, 09042, Monserrato, Cagliari, Italy.

[2] Department of Histology and Embryology, Faculty of Medicine, Masaryk University, 62500, Brno, Czech Republic.

[3] Research Centre for Applied Molecular Oncology, Masaryk Memorial Cancer Institute, 65653 Brno, Czech Republic.

[4] International Clinical Research Center, **St. Anne's University Hospital, 65691, Brno,** Czech Republic.

[5] Department of Chemistry, Faculty of Science, Masaryk University, 62500, Brno, Czech Republic.

SUPPLEMENTARY INFORMATION

Figure S1. ¹H-NMR of **2a**, Ethyl 2-((2-oxo-2*H*-chromen-7-yl)oxy)acetate (600 MHz, CDCl₃).
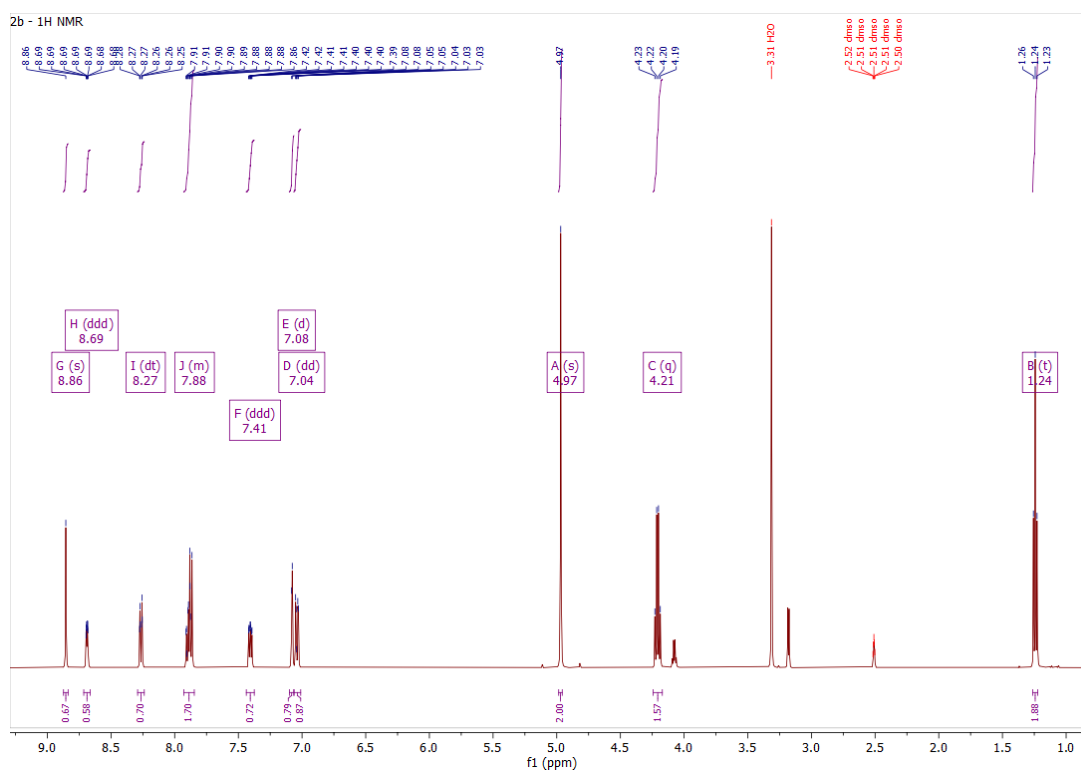
Figure S2. ¹H-NMR of **2b**, Ethyl 2-((2-oxo-3-(pyridin-2-yl)-2*H*-chromen-7-yl)oxy)acetate (500 MHz, DMSO d6).
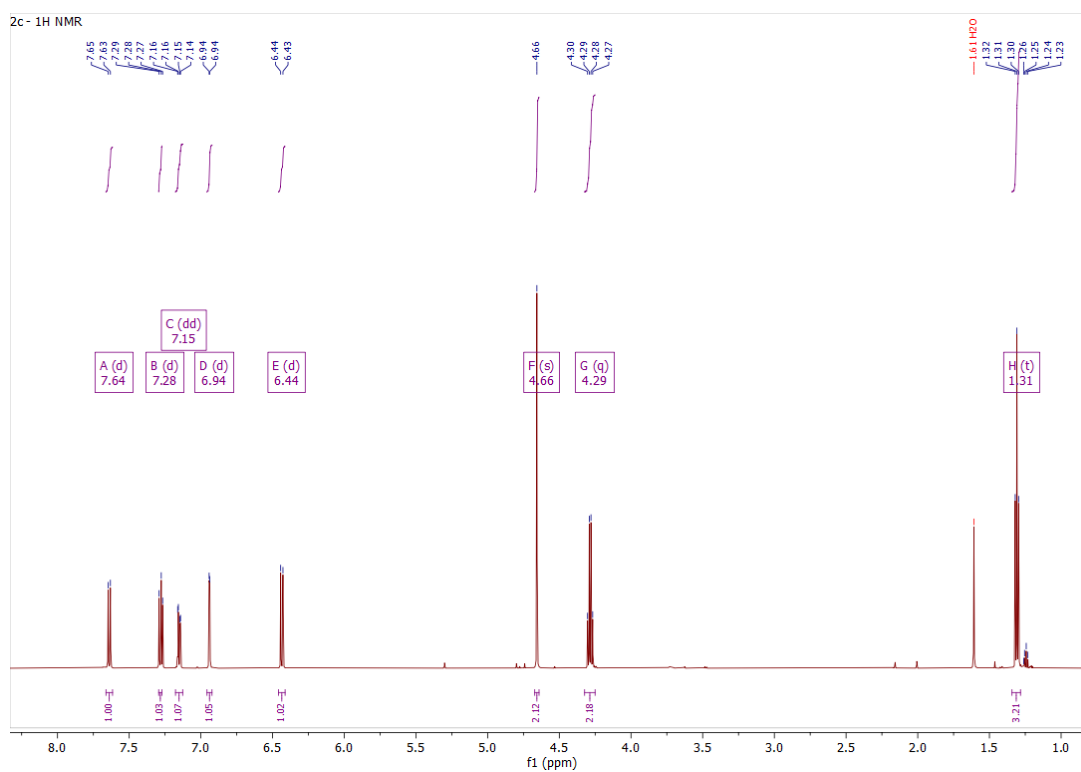
Figure S3. ¹H-NMR of **2c**, Ethyl 2-((2-oxo-2*H*-chromen-6-yl)oxy)acetate (600 MHz, CDCl₃).
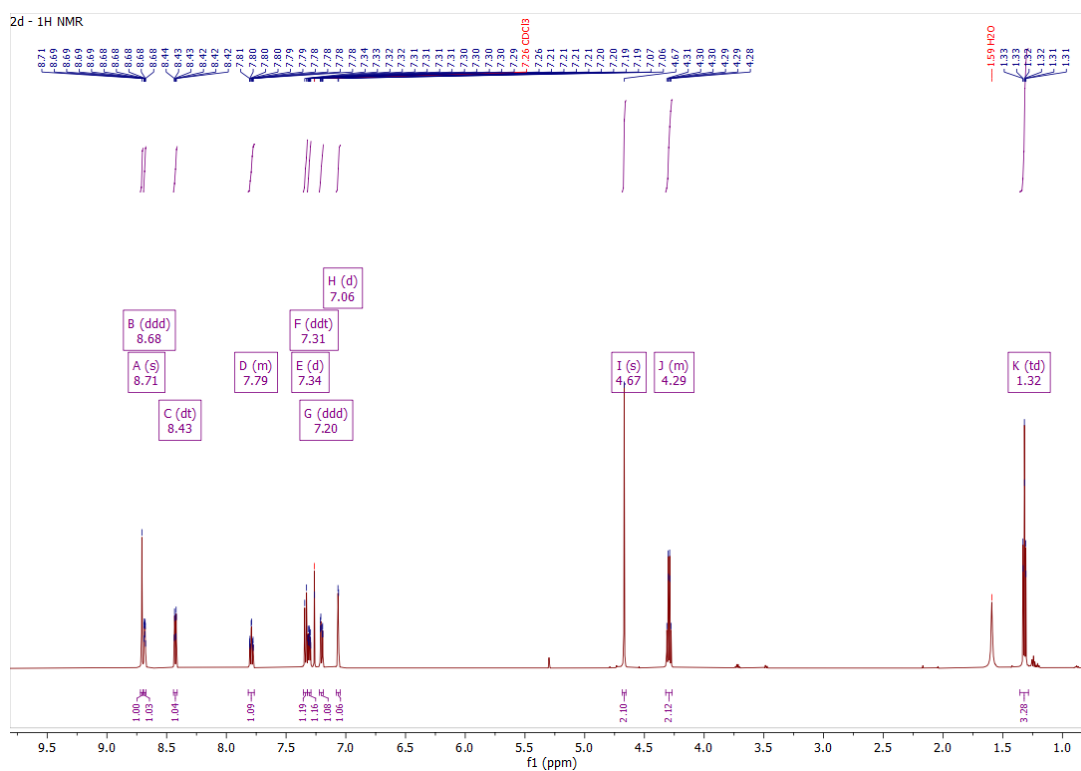
Figure S4. ¹H-NMR of **2d,** Ethyl 2-((2-oxo-3-(pyridin-2-yl)-2*H*-chromen-6-yl)oxy)acetate (600 MHz, CDCl₃).
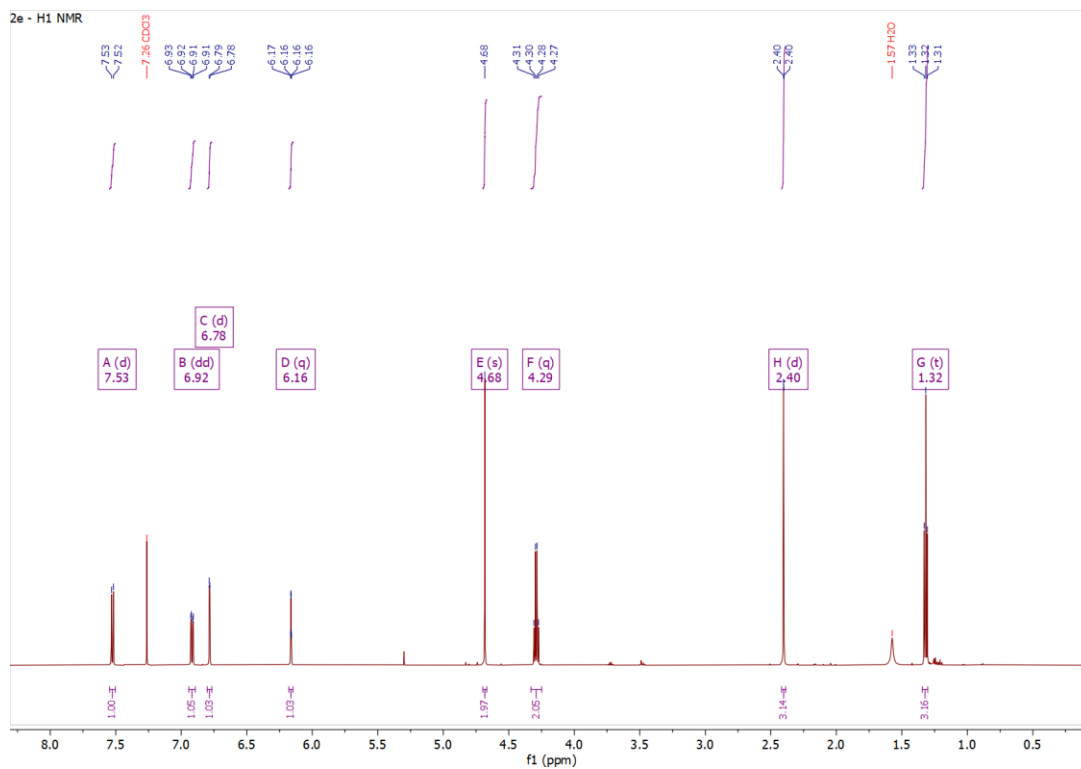
Figure S5. ¹H-NMR of **2e,** Ethyl 2-(4-methyl-2-oxo-2*H*-chromen-7-yl)oxy)acetate (600 MHz, CDCl₃).
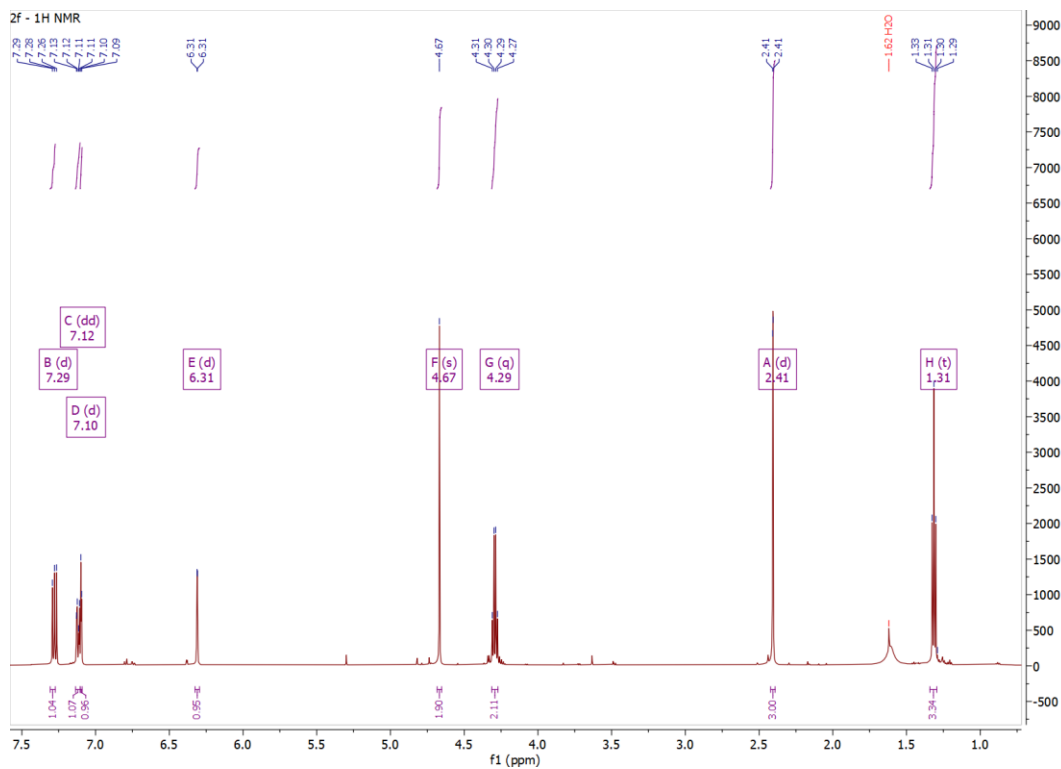
Figure S6. ¹H-NMR of **2f,** Ethyl 2-(4-methyl-2-oxo-2*H*-chromen-6-yl)oxy)acetate (600 MHz, CDCl₃).
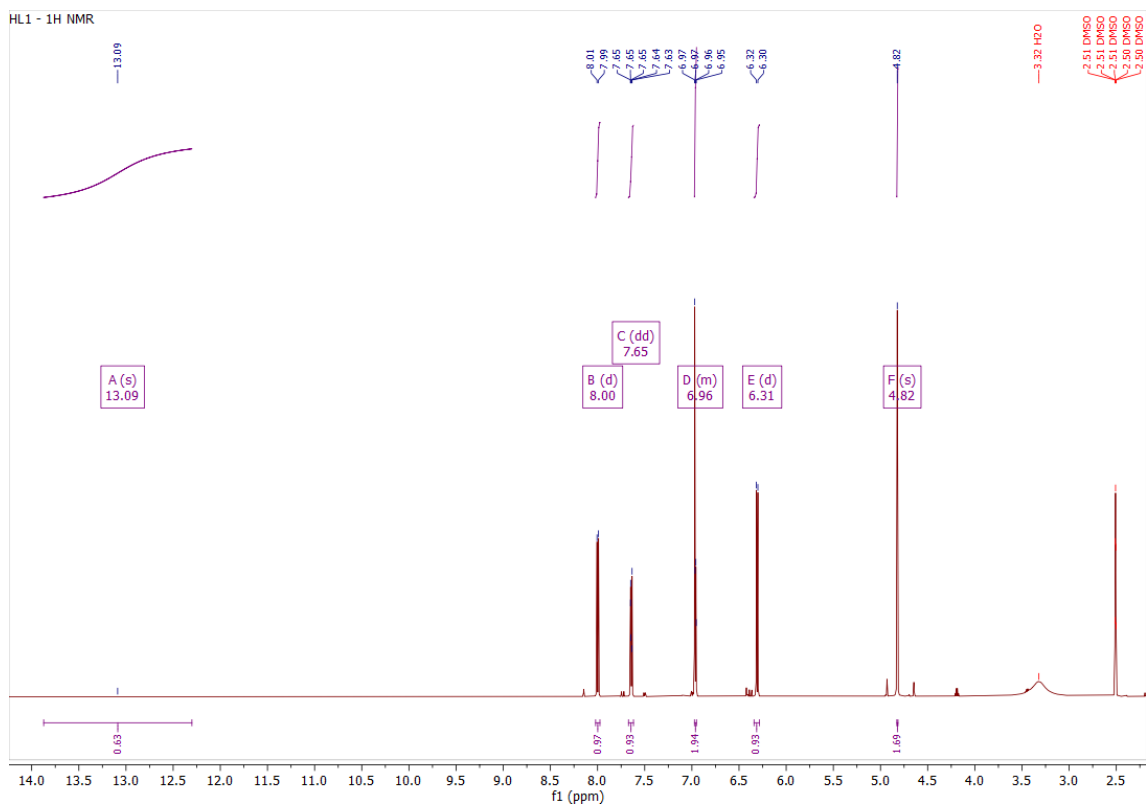
Figure S7. ^{1}H-NMR of **HL1,** 2-((2-oxo-2*H*-chromen-7-yl)oxy)acetic acid (600 MHz, DMSO d6).
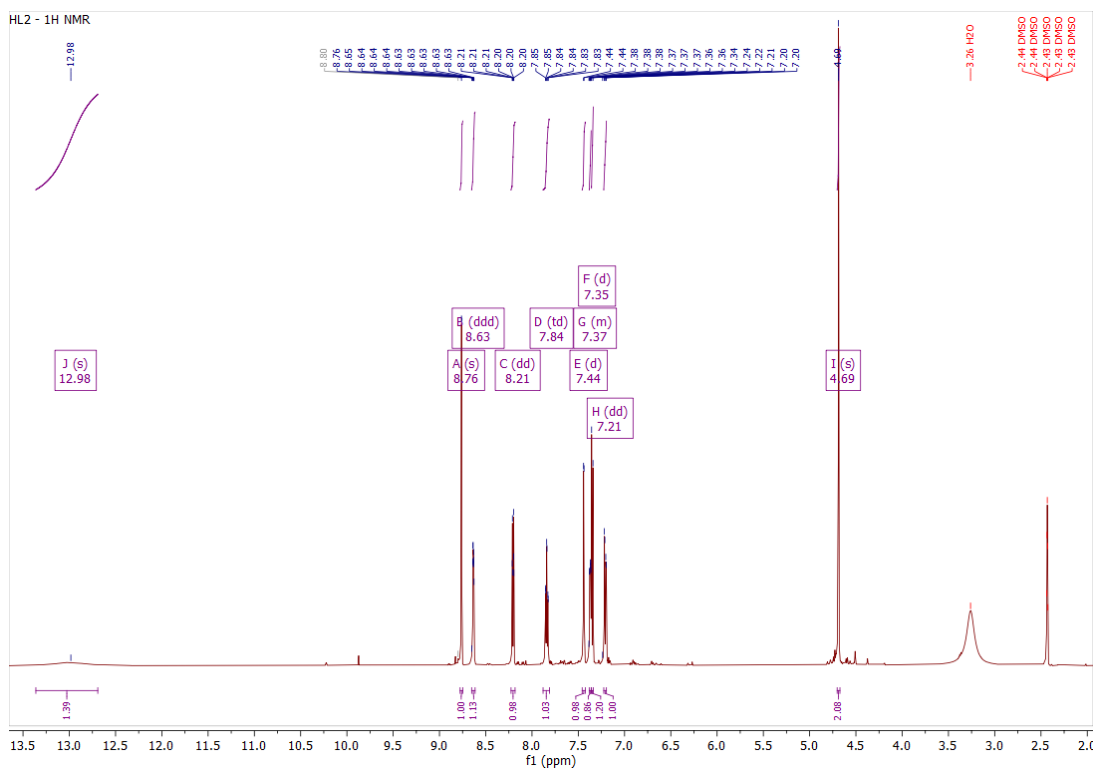
Figure S8. ^{1}H-NMR of **HL2,** 2-((2-oxo-3-(pyridin-2-yl)-2*H*-chromen-7-yl)oxy)acetic acid (600 MHz, DMSO d6).
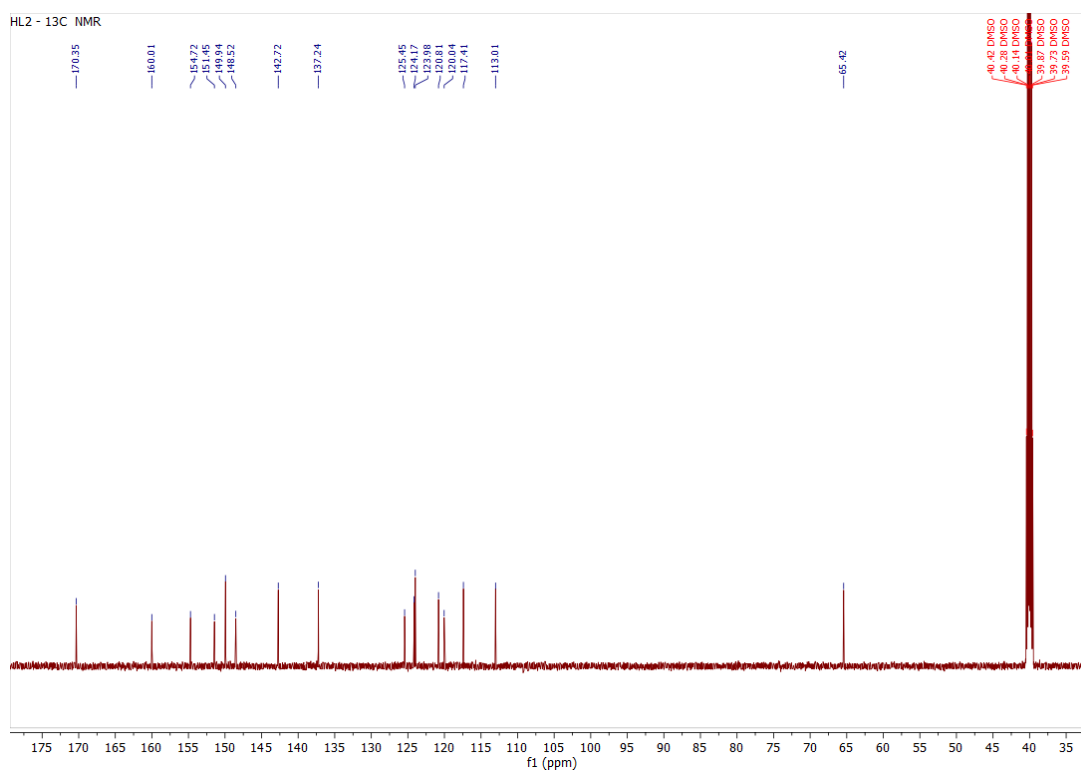
Figure S9. ^{13}C-NMR of **HL2,** 2-((2-oxo-3-(pyridin-2-yl)-2*H*-chromen-7-yl)oxy)acetic acid (151 MHz, DMSO d6).
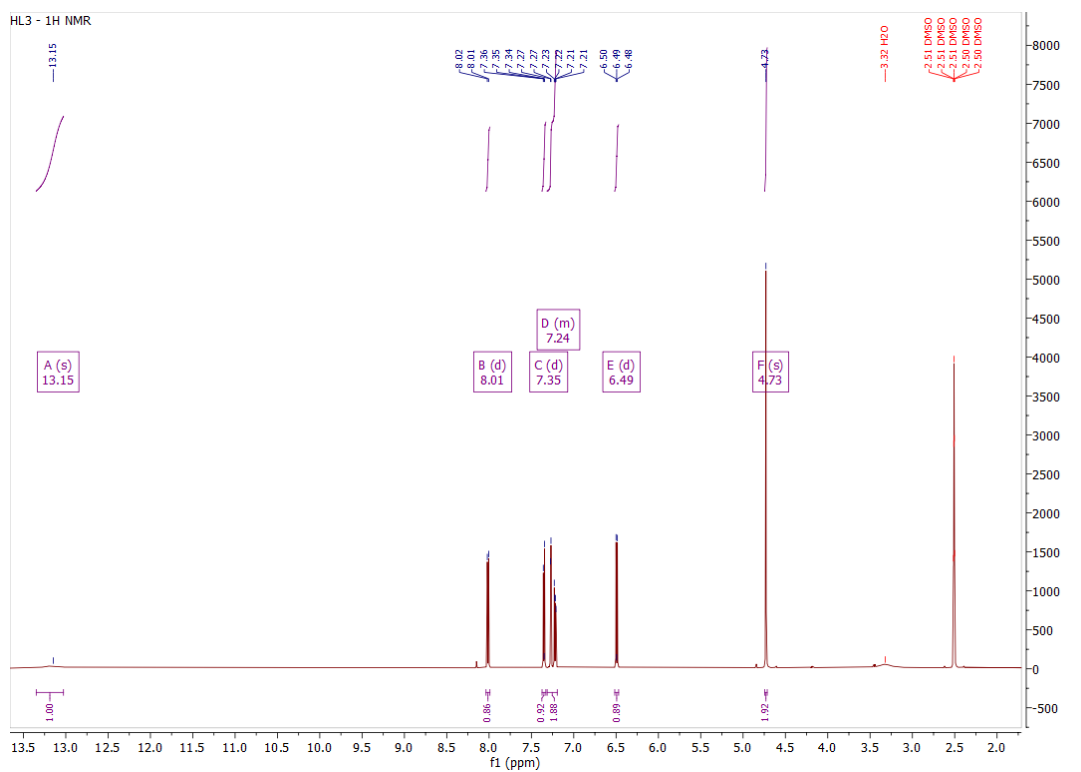
Figure S10. ^{1}H-NMR of **HL3,** 2-((2-oxo-2*H*-chromen-6-yl)oxy)acetic acid (600 MHz, DMSO d6).
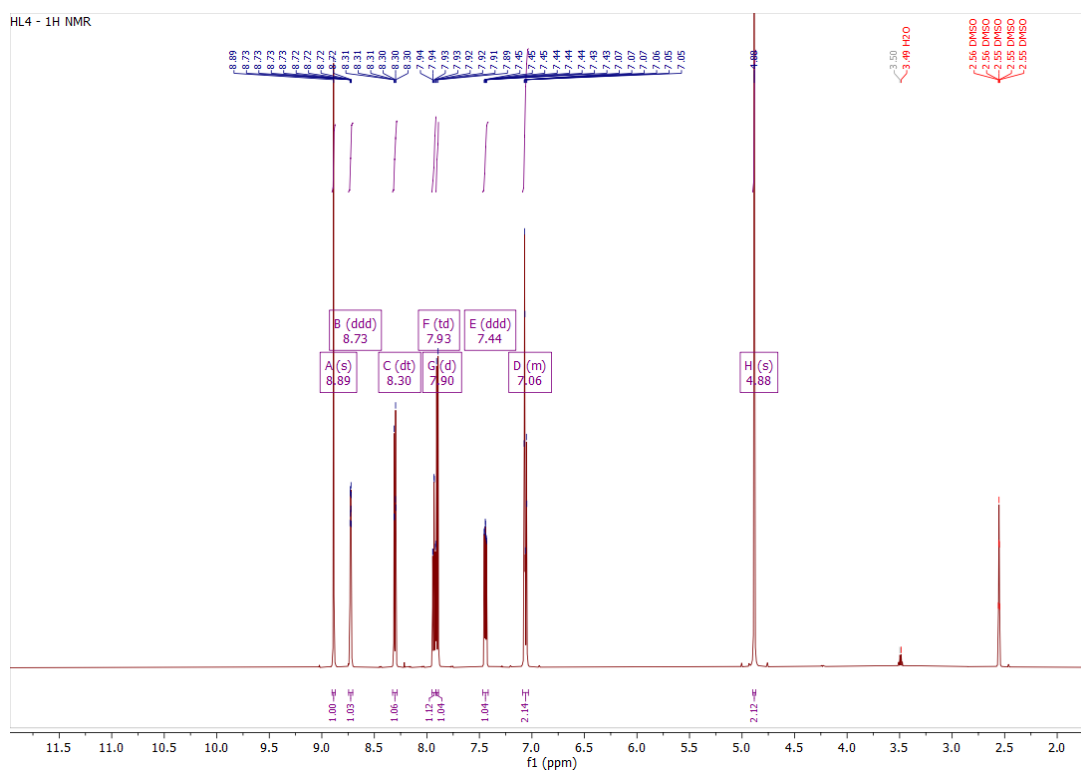
Figure S11. ¹H-NMR of **HL4,** 2-((2-oxo-3-(pyridin-2-yl)-2*H*-chromen-6-yl)oxy)acetic acid (600 MHz, DMSO d6).
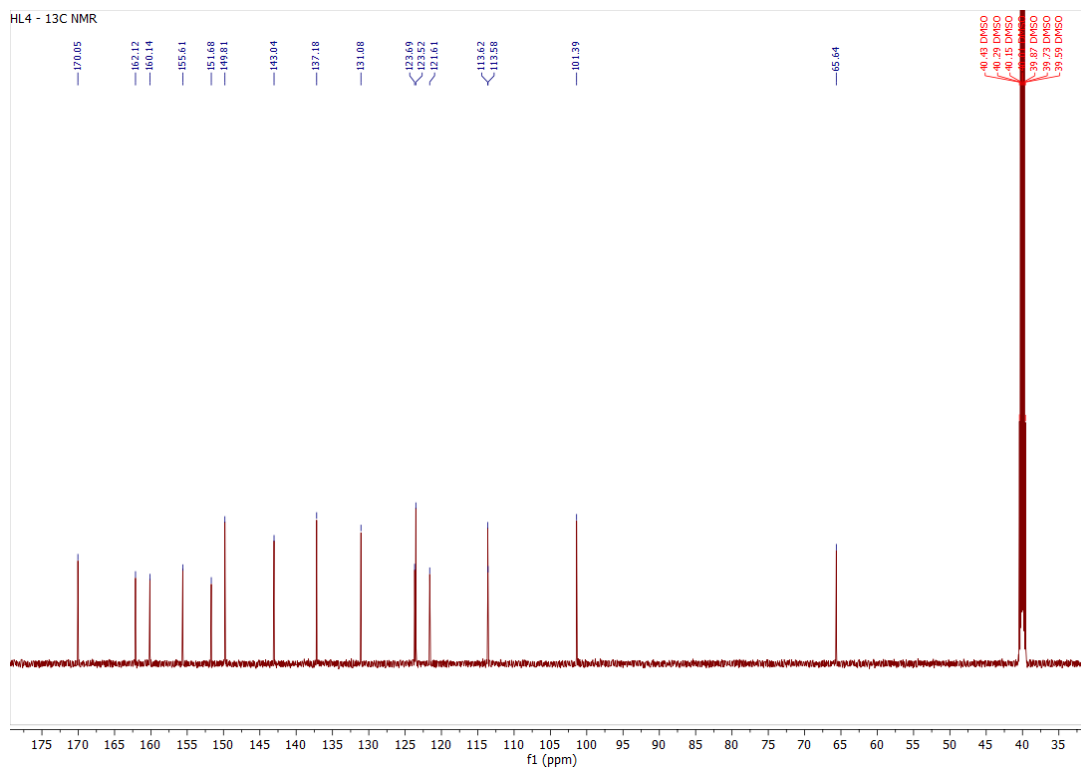
Figure S12. ¹³C-NMR of **HL4,** 2-((2-oxo-3-(pyridin-2-yl)-2*H*-chromen-6-yl)oxy)acetic acid (151 MHz, DMSO d6).
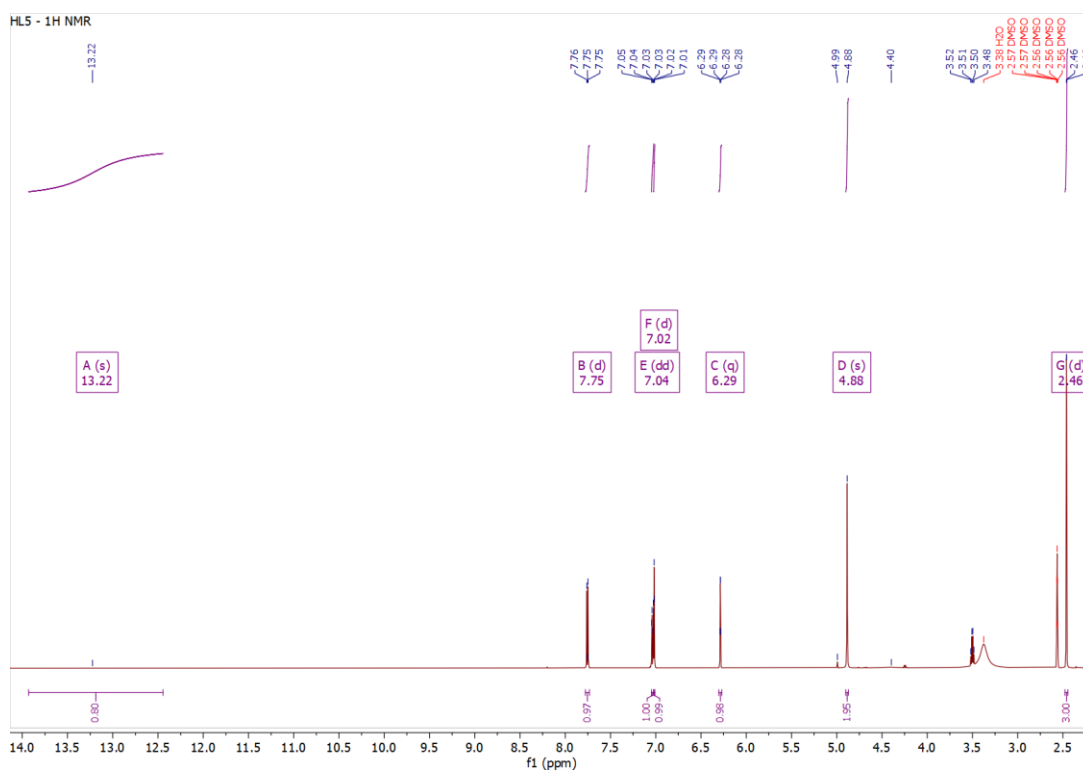
Figure S13. ¹H-NMR of **HL5,** 2-((4-methyl-2-oxo-2*H*-chromen-7-yl)oxy)acetic acid (600 MHz, DMSO d6).
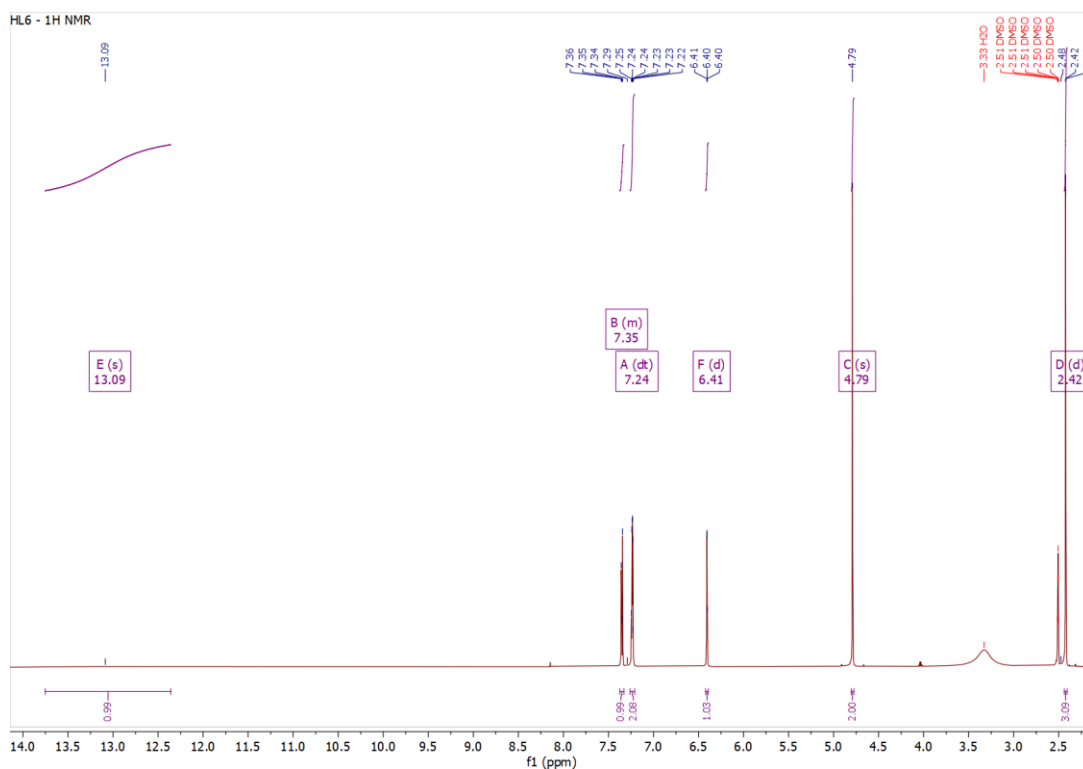
Figure S14. ¹H-NMR of **HL5,** 2-((4-methyl-2-oxo-2*H*-chromen-6-yl)oxy)acetic acid (600 MHz, DMSO d6).
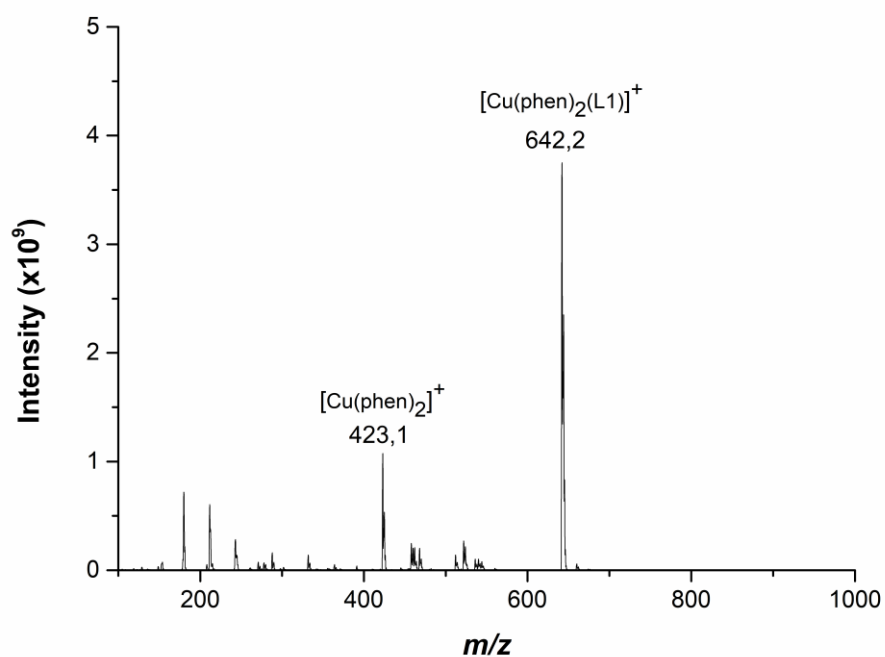
Figure S15. ESI mass spectrum of **D1**, [Cu(phen)$_2$(L1)](ClO$_4$).
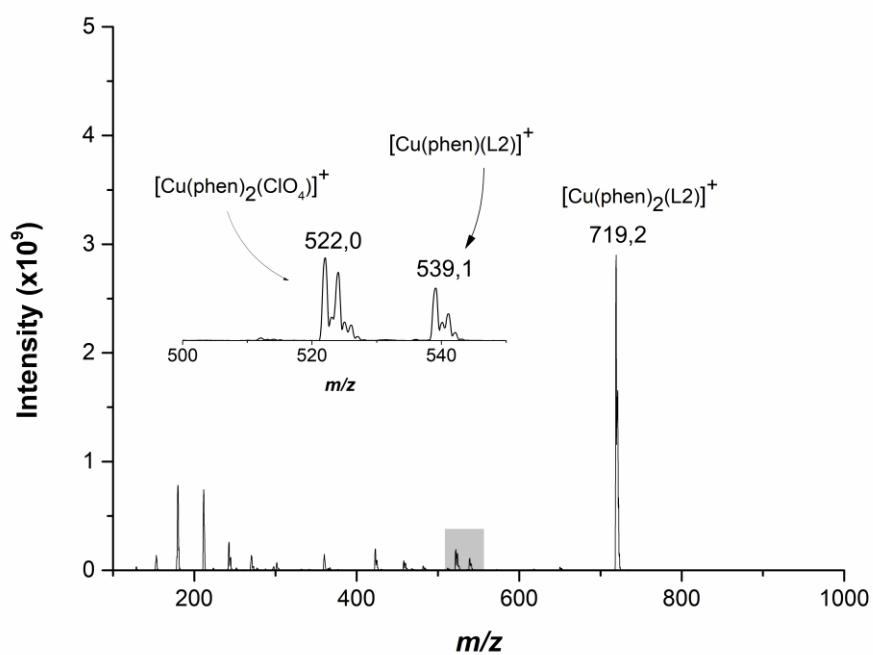
Figure S16. ESI mass spectrum of **D2**, [Cu(phen)$_2$(L2)](ClO$_4$).
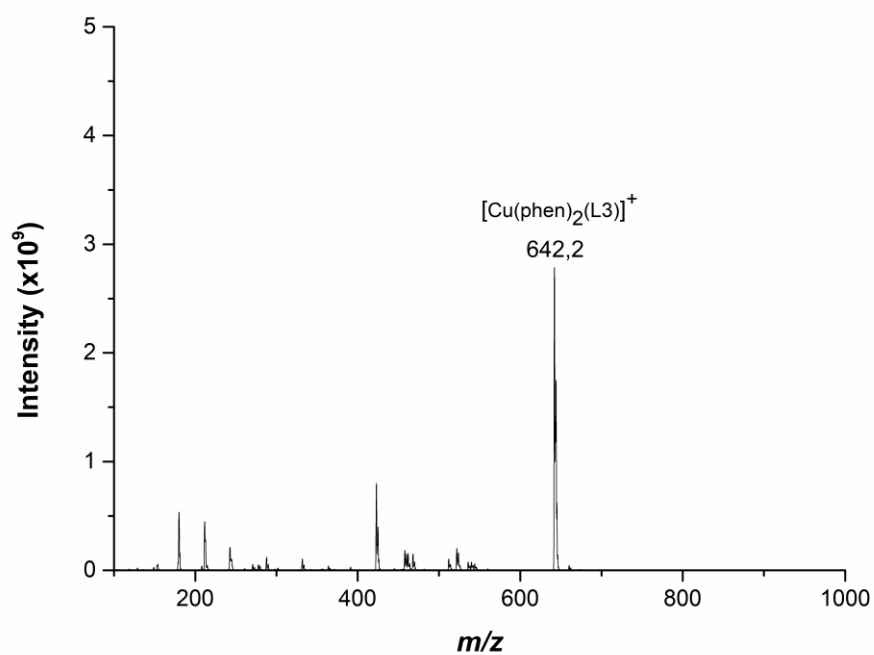
Figure S17. ESI mass spectrum of **D3**, [Cu(phen)₂(L3)](ClO₄).
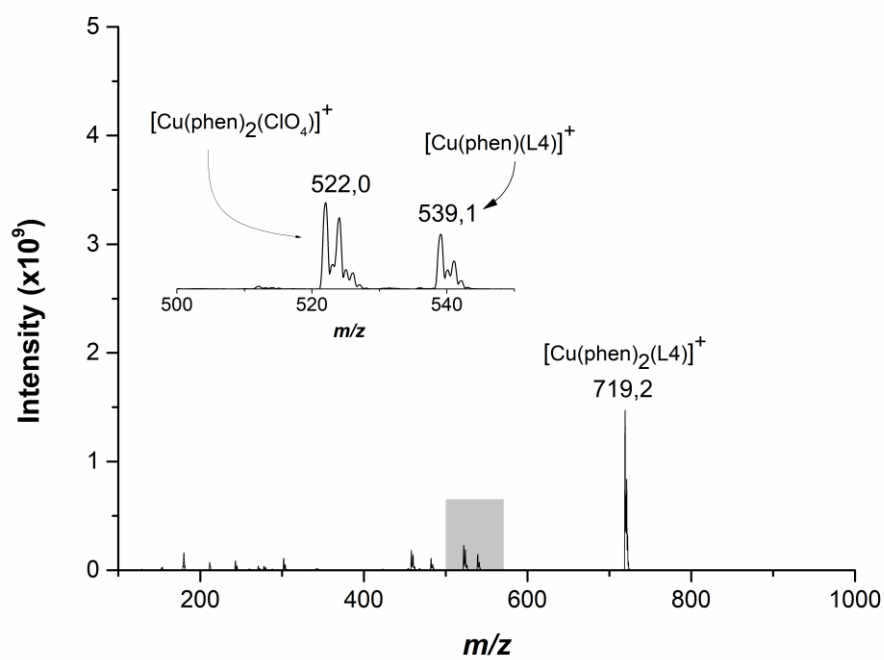
Figure S18. ESI mass spectrum of **D4**, [Cu(phen)₂(L4)](ClO₄).
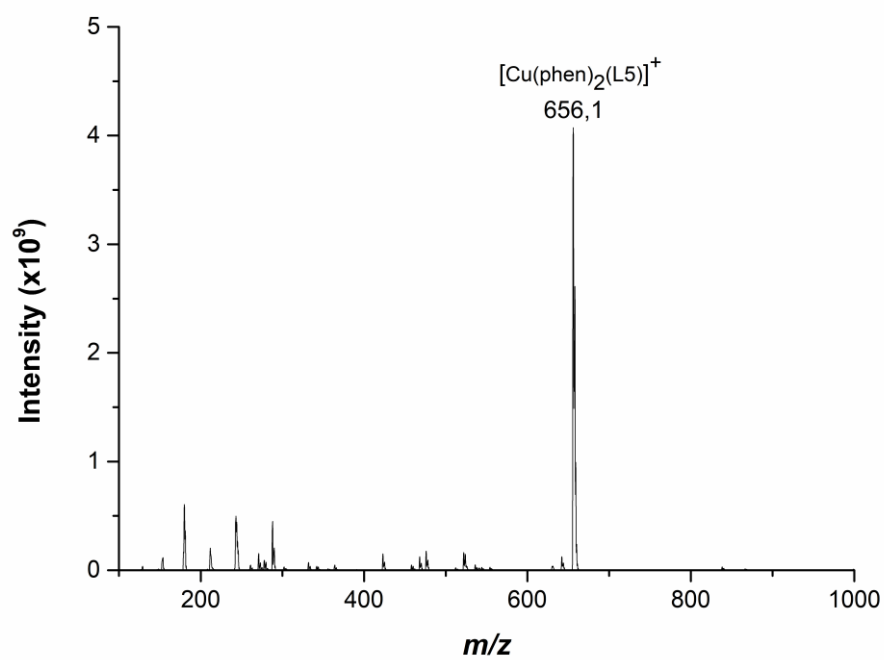
Figure S19. ESI mass spectrum of **D5**, [Cu(phen)₂(L5)](ClO₄).
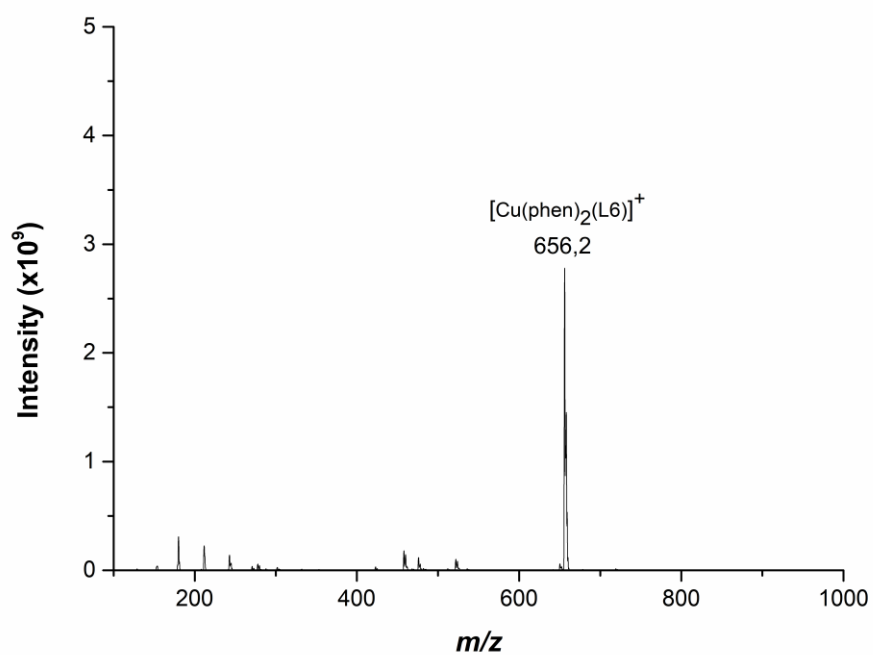
Figure S20. ESI mass spectrum of **D6**, [Cu(phen)₂(L6)](ClO₄).
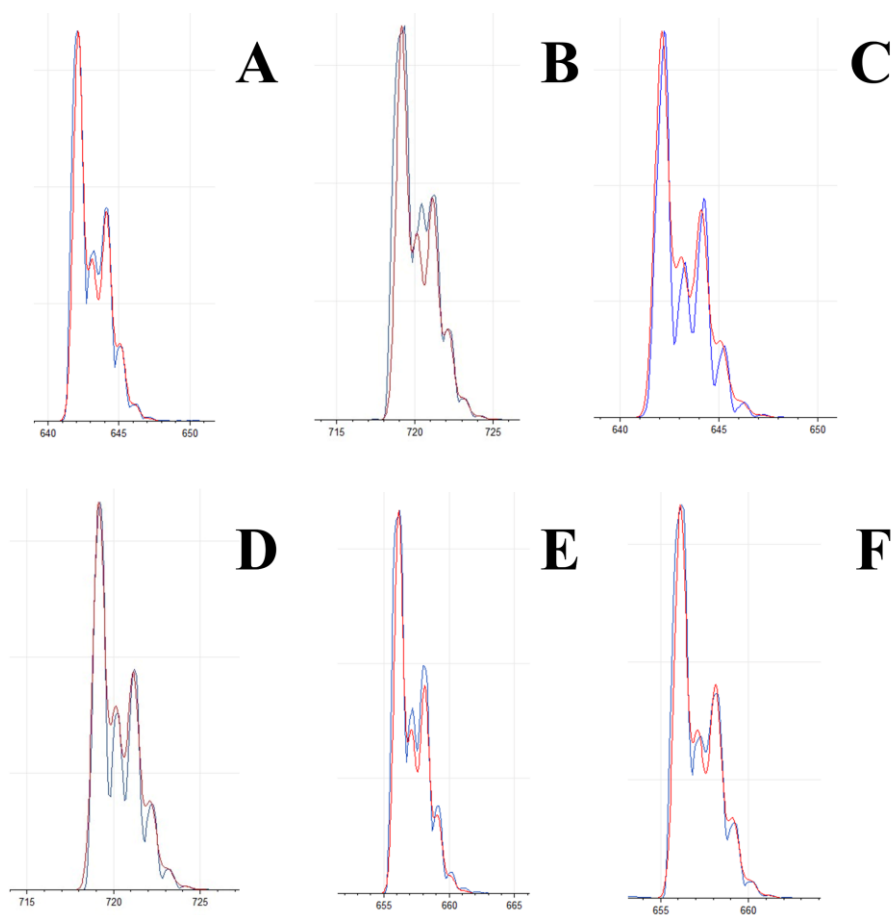
Figure S21. Experimental (blue line) and calculated (red line) isotopic patterns of *m/z* (**A**) 642 [Cu(phen)$_2$(L1)]$^+$, (**B**) 719 [Cu(phen)$_2$(L2)]$^+$, (**C**) 642 [Cu(phen)$_2$(L3)]$^+$ (**D**) 642 [Cu(phen)$_2$(L4)]$^+$, (**E**) 656 [Cu(phen)$_2$(L5)]$^+$, (**F**) 656 [Cu(phen)$_2$(L6)]$^+$.
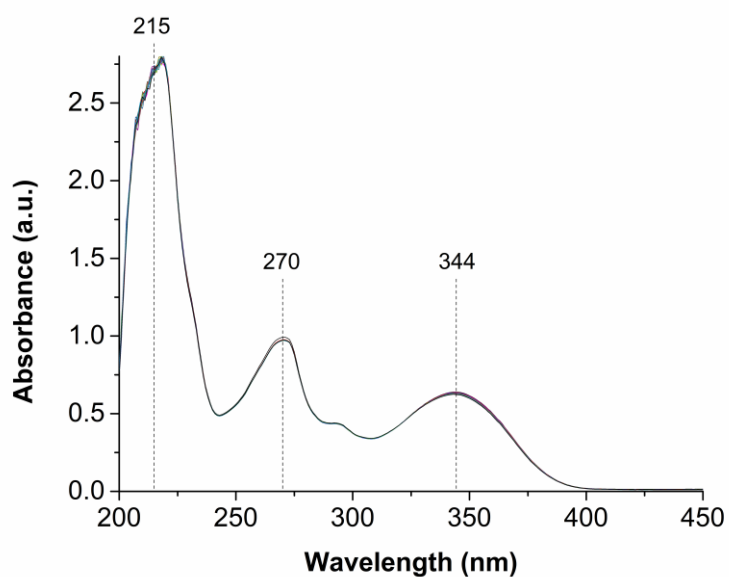
Figure S22. UV-Vis spectra of **D2** ($6.00 \cdot 10^{-6}$ M), in the 200-450 nm range, recorded in 24 hrs. Each spectrum was acquired every 60 minutes, PB 0.05 M, pH 7.4, 25°C, 1 cm optical path length.
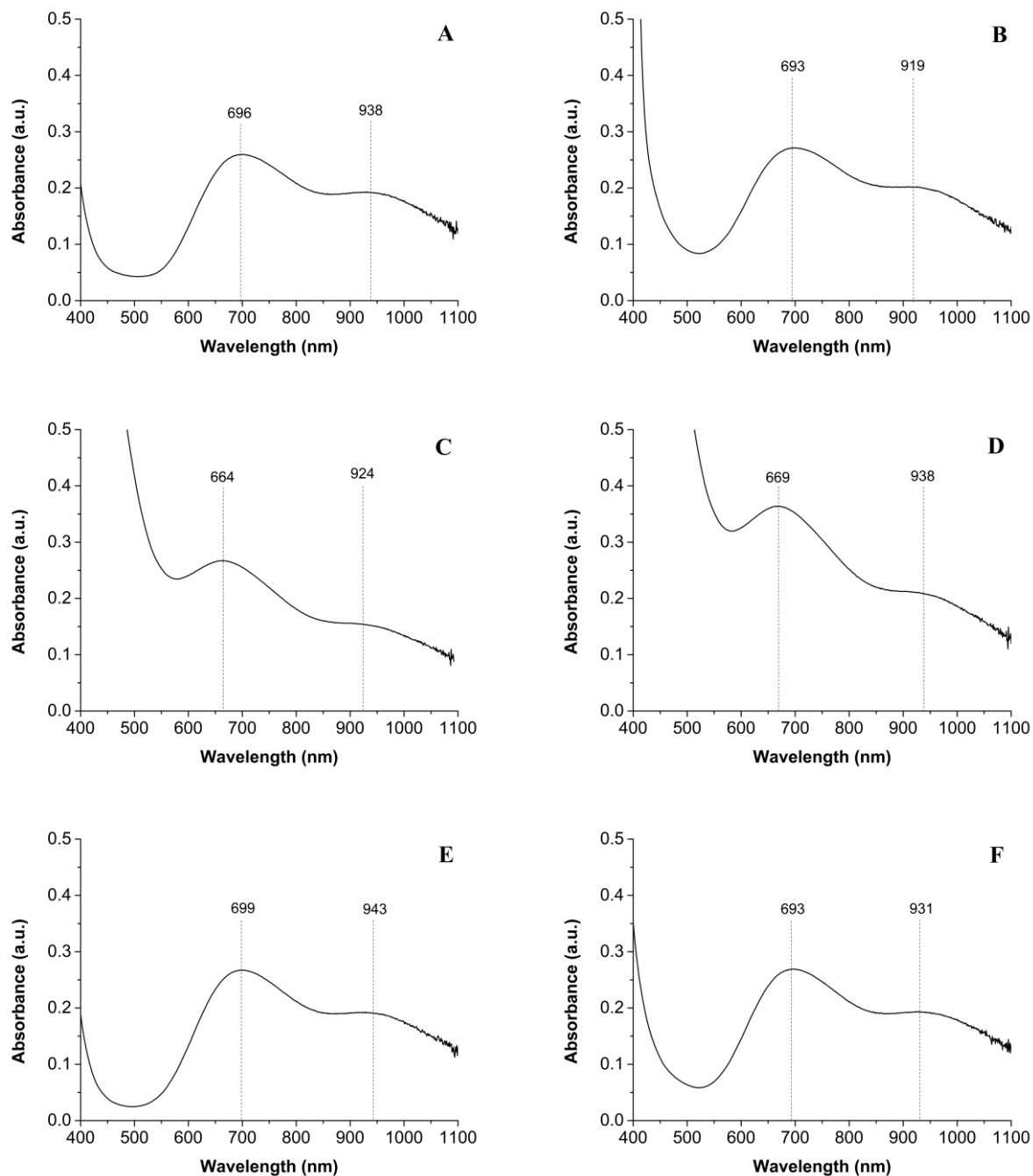

Figure S23. Vis-NIR spectra of (**A**) **D1** ($7.14 \cdot 10^{-3}$ M), (**B**) **D2** ($5.93 \cdot 10^{-3}$ M), (**C**) **D3** ($7.00 \cdot 10^{-3}$ M), (**D**) **D4** ($6.19 \cdot 10^{-3}$ M), (**E**) **D5** ($6.40 \cdot 10^{-3}$ M), (**F**) **D6** ($6.05 \cdot 10^{-3}$ M), CH$_3$CN:H$_2$O (1:1), 25 °C, 1 cm optical path length.

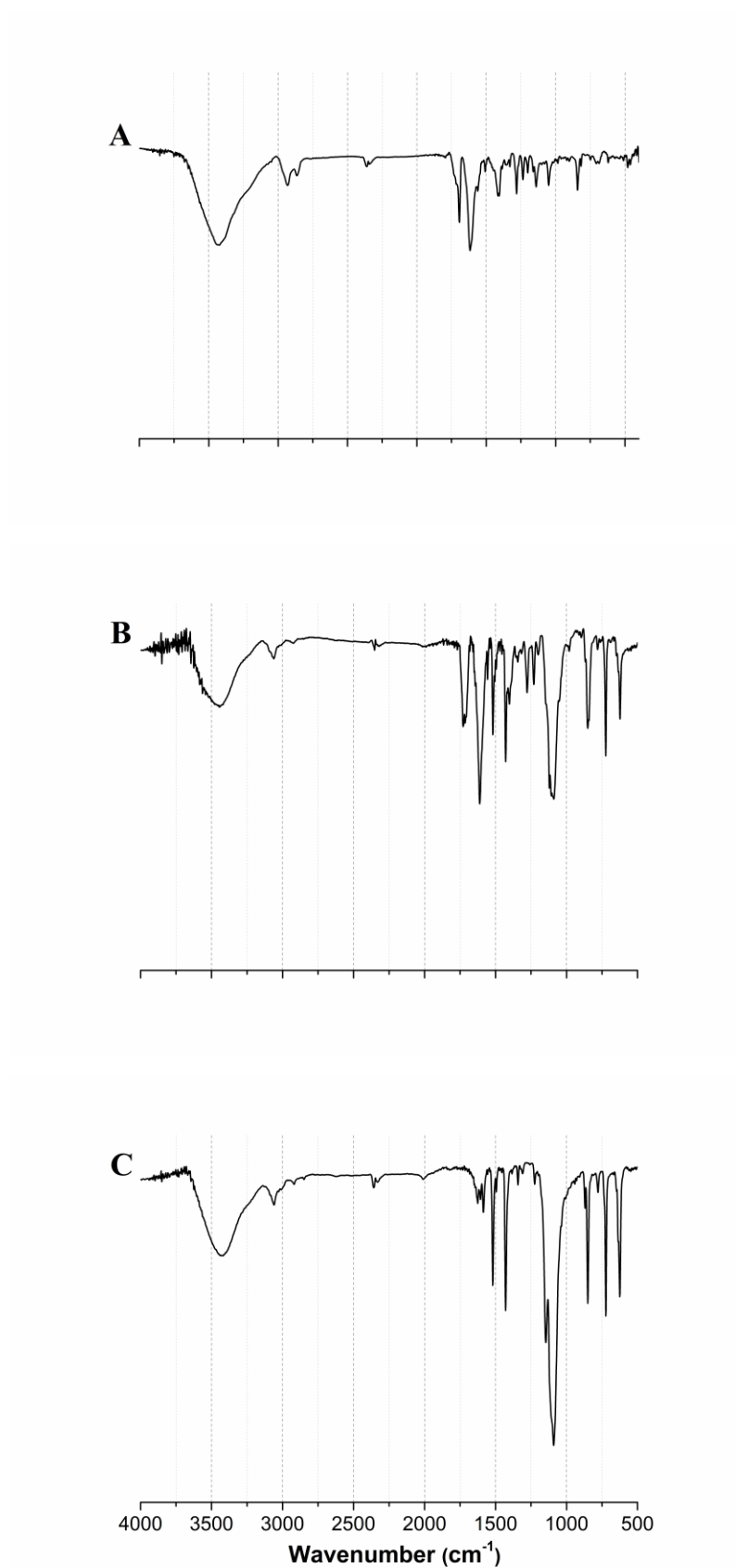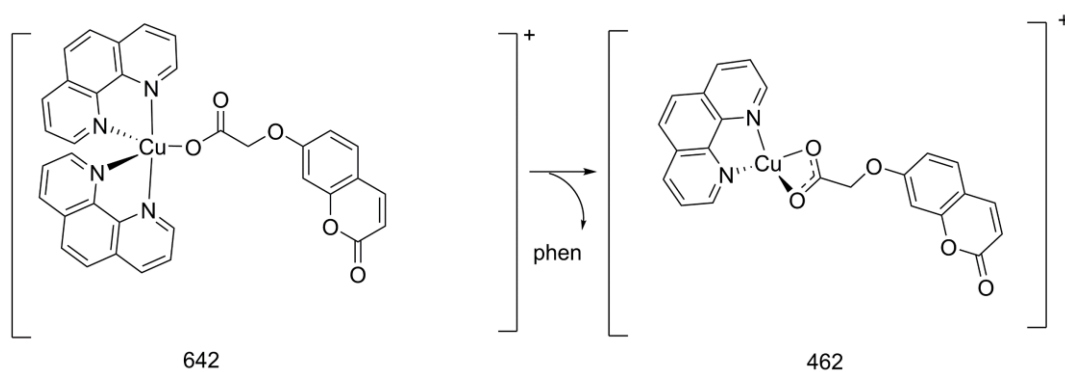**Figure S24.** FT-IR spectrum of **NaL1** (**A**), **D1** (**B**) and **C0** (**C**).

A)

642 → 462

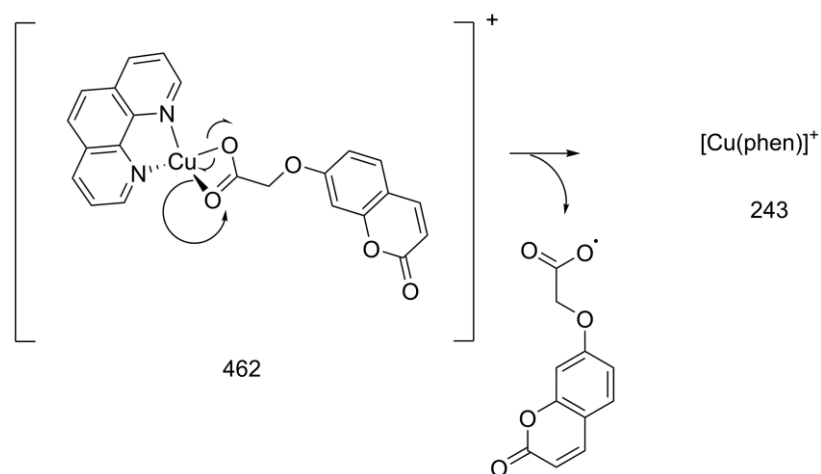**B)**

462 → [Cu(phen)]⁺ 243

Figure S25. proposed fragmentation patterns for product ions at 462 (**A**), 243 (**B**) *m/z* generated from 642 *m/z* under CID conditions. All the mass values are expressed as monoisotopic masses.
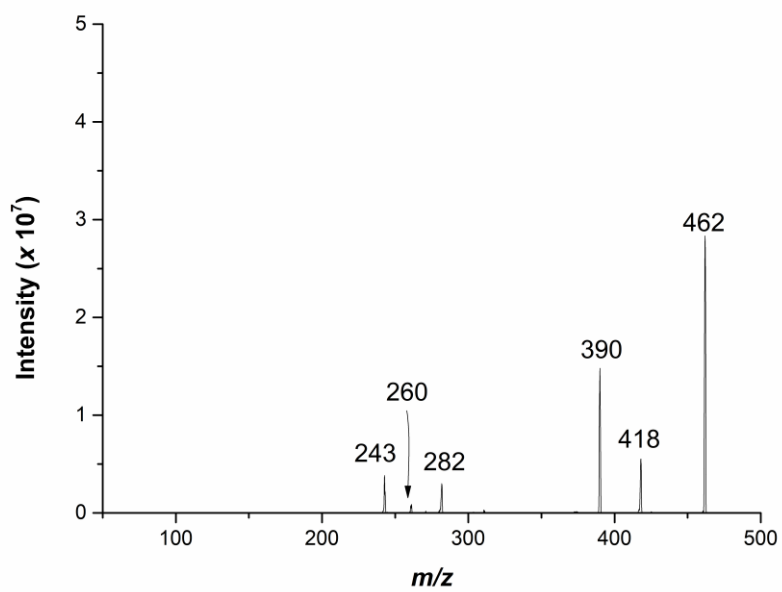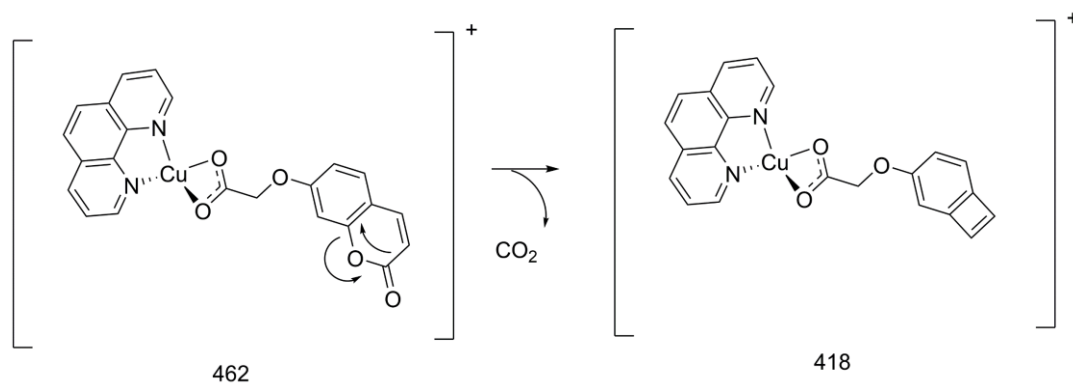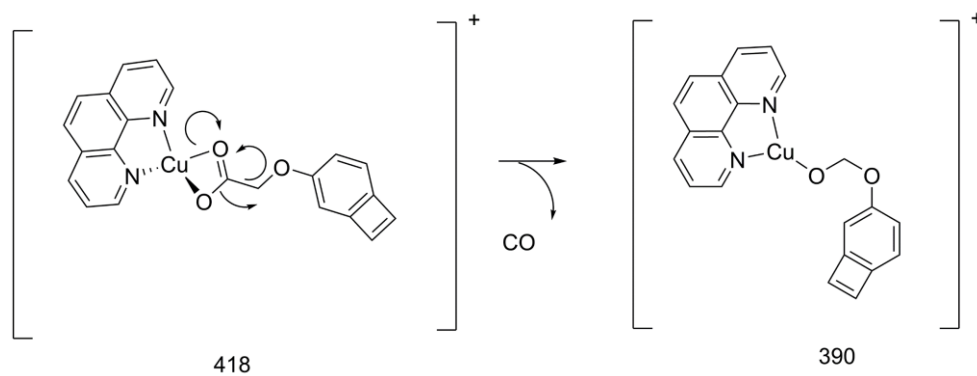
Figure S26. CID experiment on the peak at 462 *m/z* (CE 15 V, Ar 1.8 psi).

A)
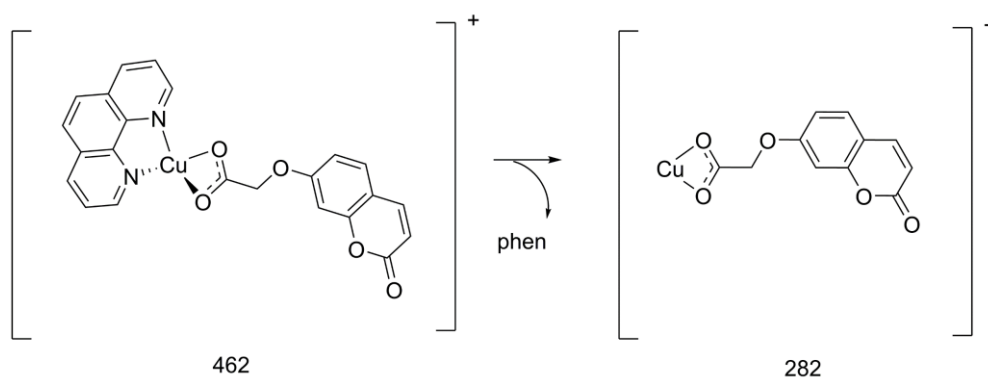

B)

C)

462 → 282

D)

462

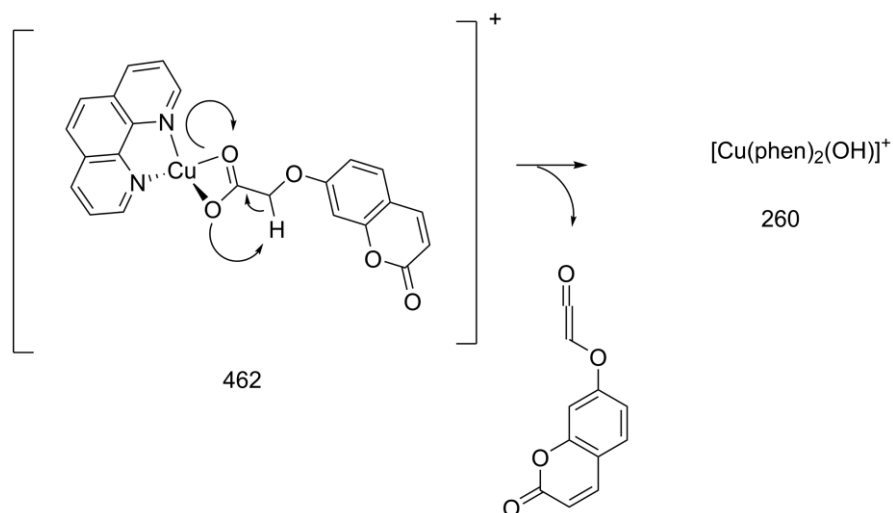[Cu(phen)₂(OH)]⁺

260

Figure S27. proposed fragmentation patterns for product ions at 418 (**A**), 390 (**B**), 282 (**C**), 260 (**D**) *m/z* generated from 462 *m/z* under CID conditions. All the mass values are expressed as monoisotopic masses.
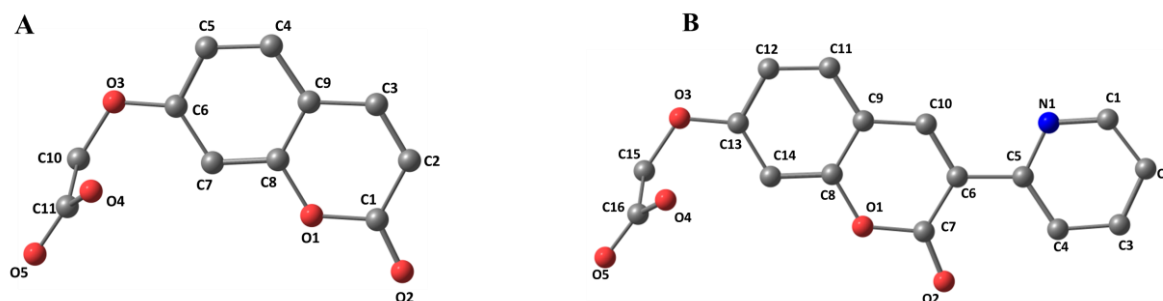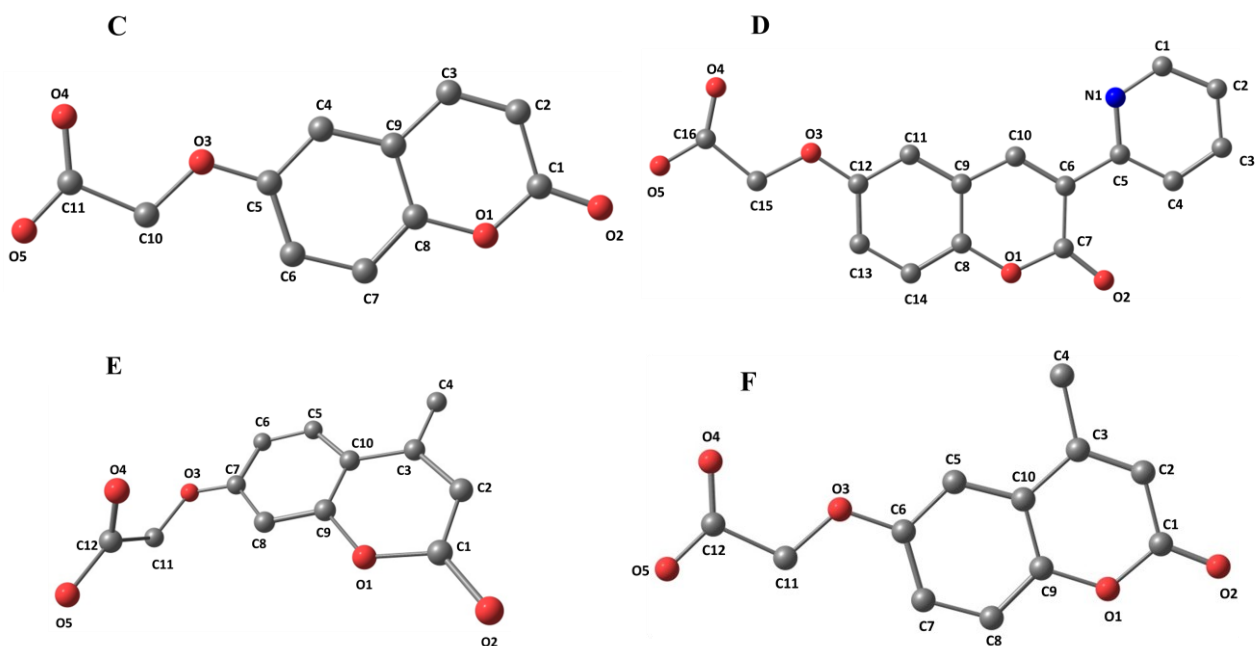
Figure S28. Molecular drawings and atom labelling scheme for **L1** (**A**), **L2** (**B**), **L3** (**C**), **L4** (**D**), **L5** (**E**), **L6** (**F**) at the DFT-optimized geometries (gas phase).
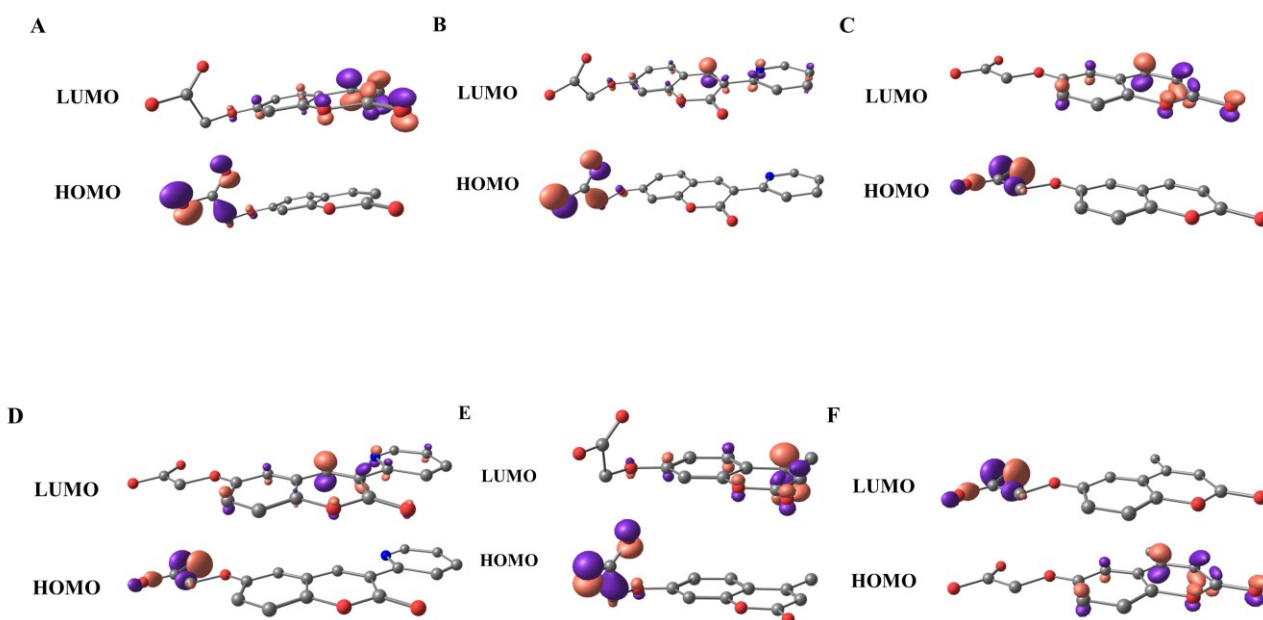
Figure S29. Gas-phase frontier Molecular Orbitals plots (contour value: 0.1) for **L1** (**A**), **L2** (**B**), **L3** (**C**), **L4** (**D**), **L5** (**E**), **L6** (**F**) at the DFT-optimized geometries (gas phase).
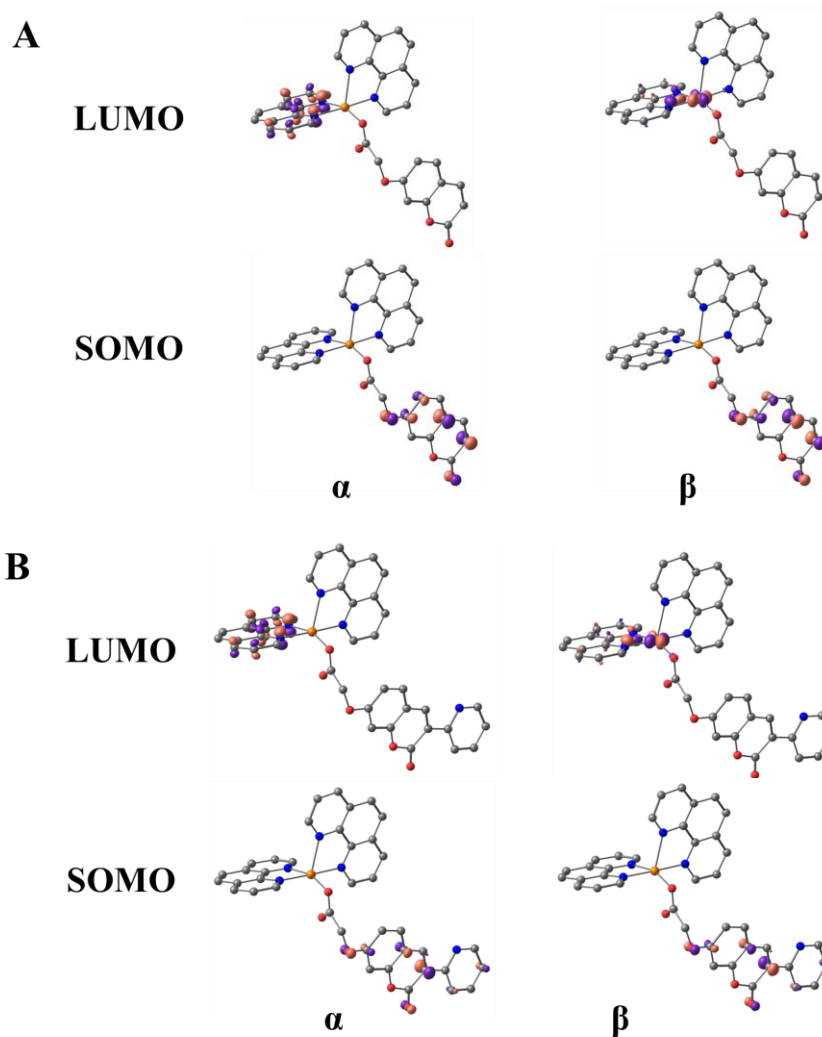
Figure S30. Gas-phase frontier Molecular Orbitals plots (contour value: 0.1) of [Cu(phen)₂(L1)]⁺ (A) and [Cu(phen)₂(L2)]⁺ (B).
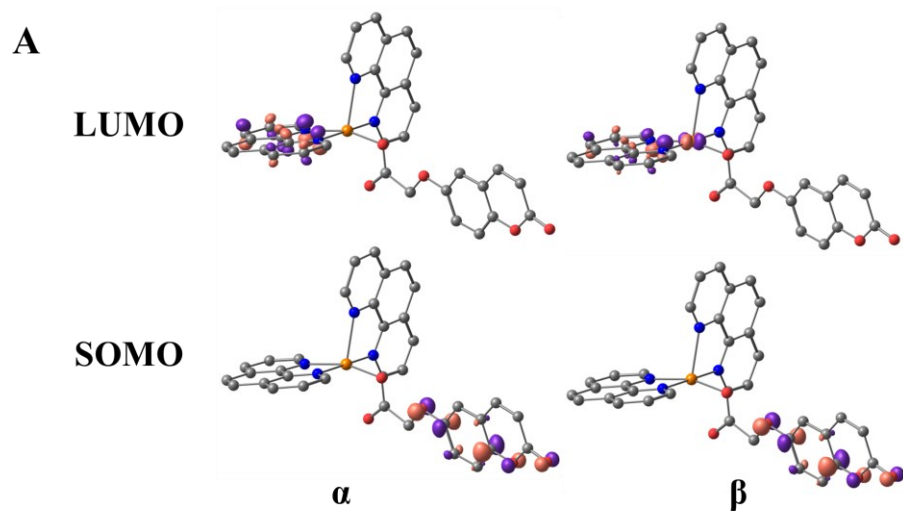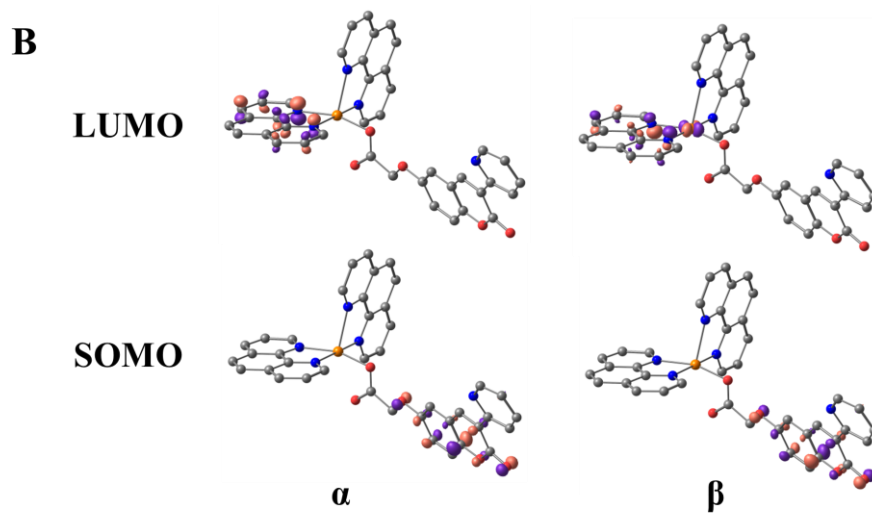
Figure S31. Gas-phase frontier Molecular Orbitals plots (contour value: 0.1) of [Cu(phen)₂(L3)]⁺ (A) and [Cu(phen)₂(L4)]⁺ (B).
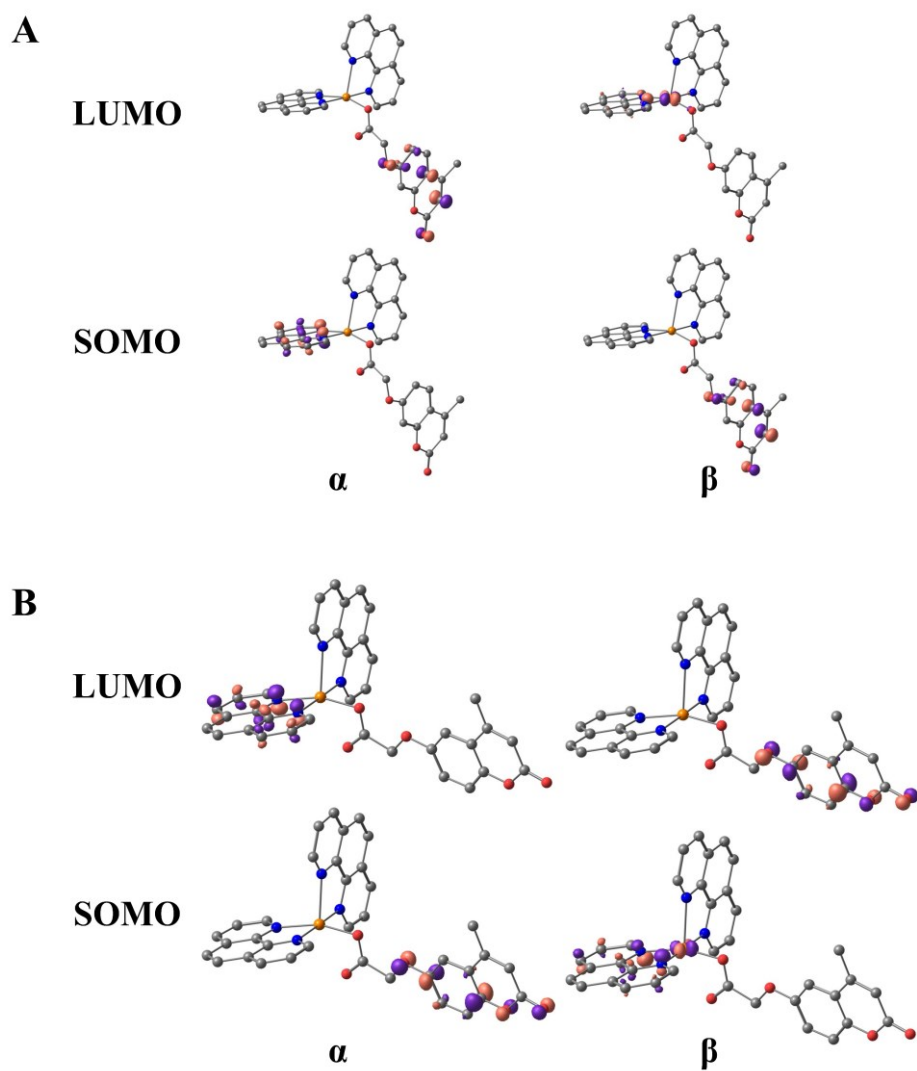
Figure S32. Gas-phase frontier Molecular Orbitals plots (contour value: 0.1) of **[Cu(phen)₂(L5)]⁺ (A)** and **[Cu(phen)₂(L6)]⁺ (B)**.
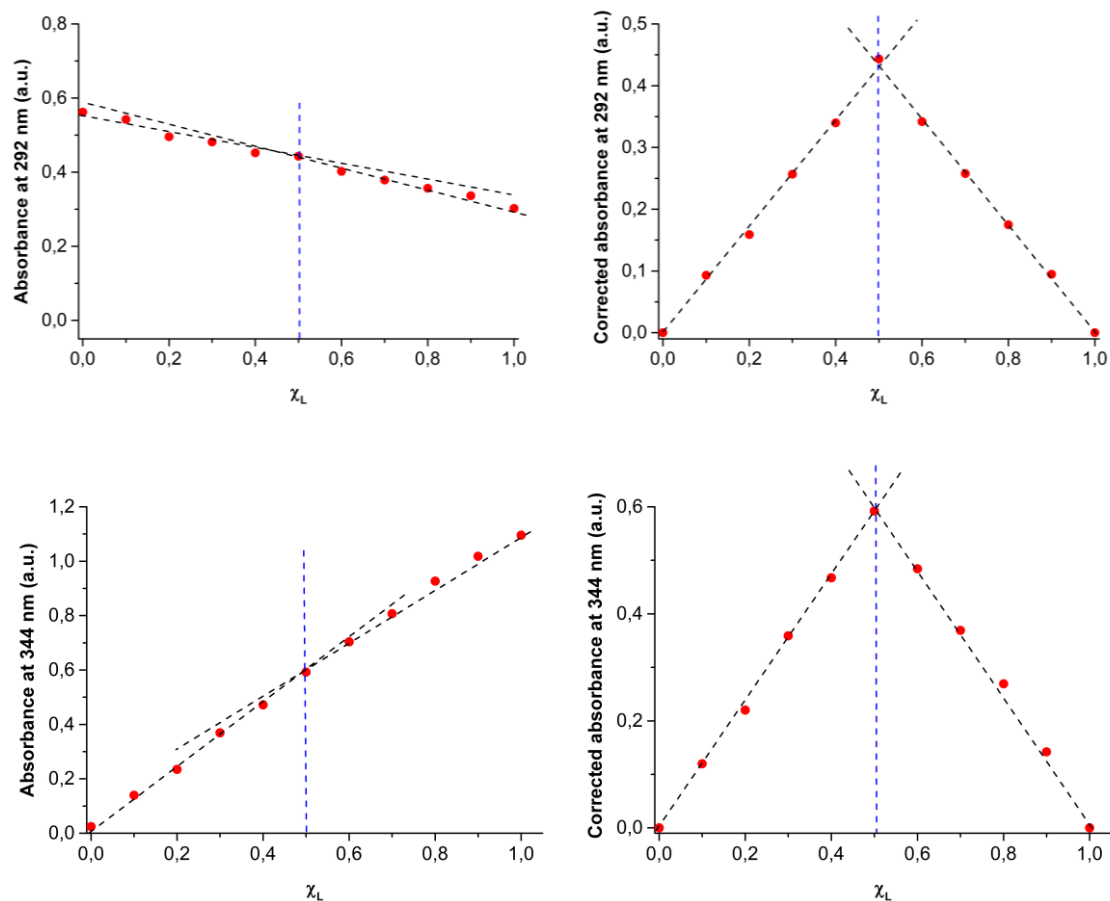
Figure S33. Job's plot for the system **C0** – deprotonated **HL2**. Uncorrected (left) and corrected (right) absorbances measured at different ligand:metal molar ratio at 292 and 344 nm (concentration of **C0** = **HL2** = 4.37·10⁻⁵ M, 0.05 M PB, 25°C, 1 cm optical path length).
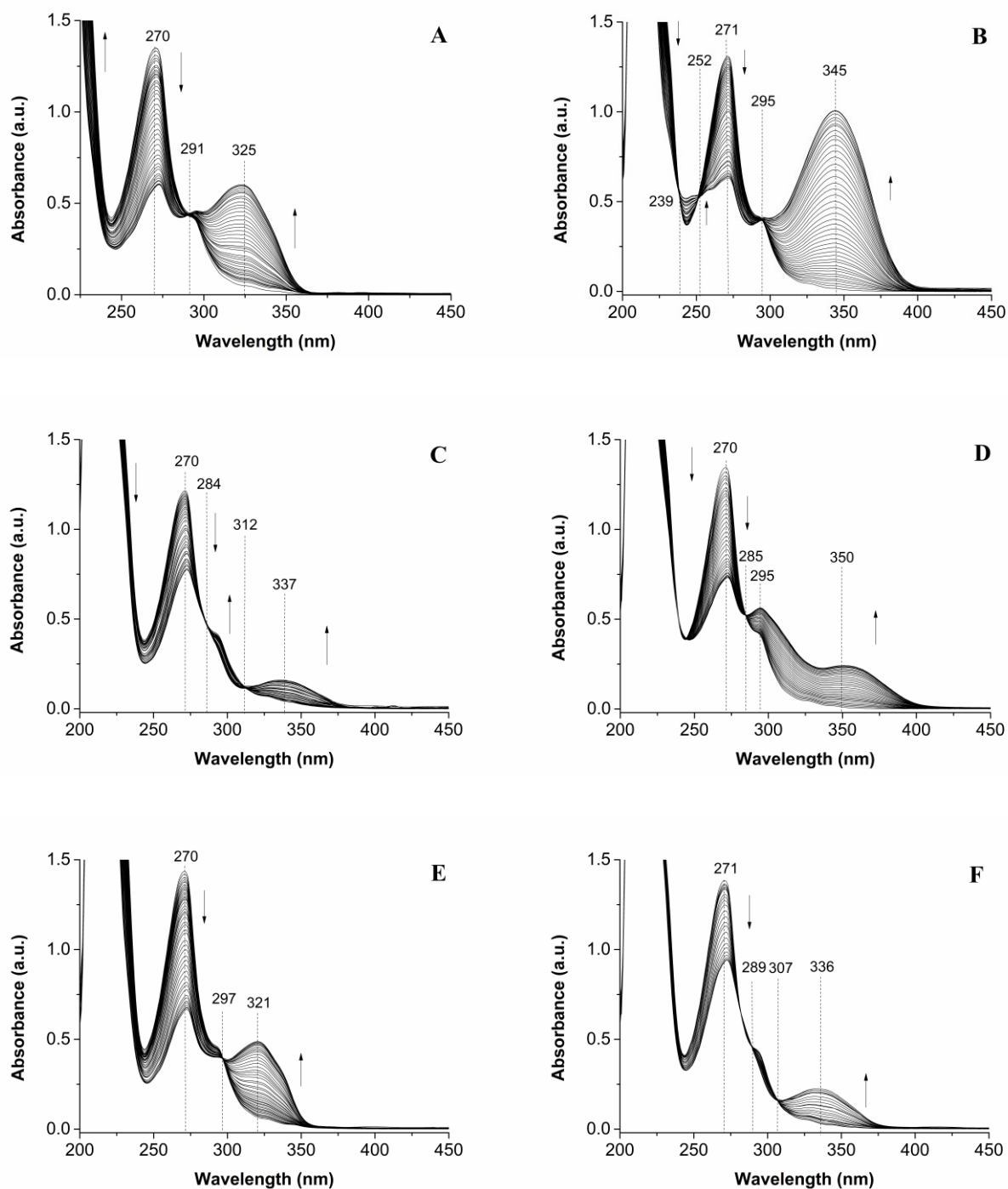
Figure S34. Selected spectra collected during the spectrophotometric titration of **C0** with (**A**) **HL1** (**C0** 5.368·10⁻⁵mmoles, **HL1** 6.177·10⁻⁵ M), (**B**) **HL2** (**C0** 5.304·10⁻⁵mmoles, **HL2** 6.325·10⁻⁵ M), (**C**) **HL3** (**C0** 4.680·10⁻⁵mmoles, **HL3** 5.450·10⁻⁵ M), (**D**) **HL4** (**C0** 5.462·10⁻⁵mmoles, **HL4** 5.046·10⁻⁵ M), (**E**) **HL5** (**C0** 5.368·10⁻⁵mmoles, **HL5** 6.490·10⁻⁵M), (**F**) **HL6** (**C0** 5.304·10⁻⁵mmoles, **HL4** 6.405·10⁻⁵M) ; PB 0.05 M, pH 7.4, 25 °C, 1 cm optical path length.
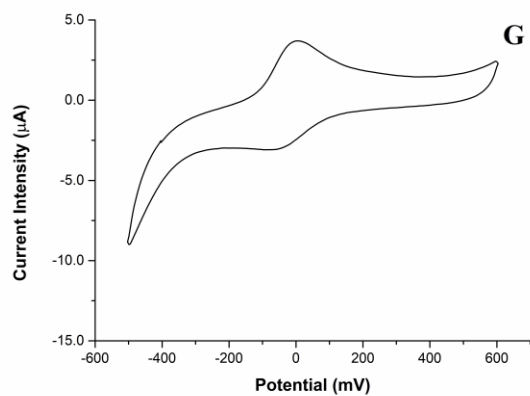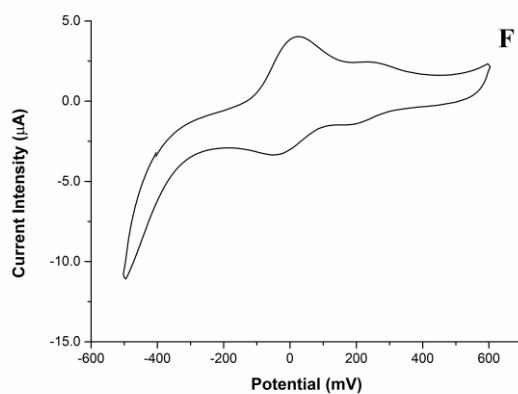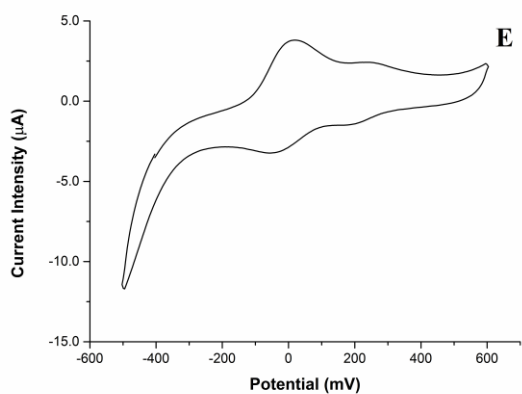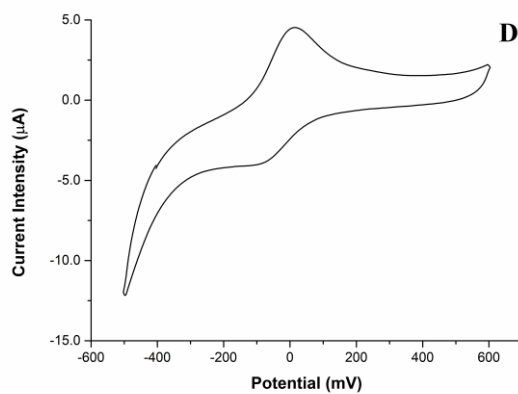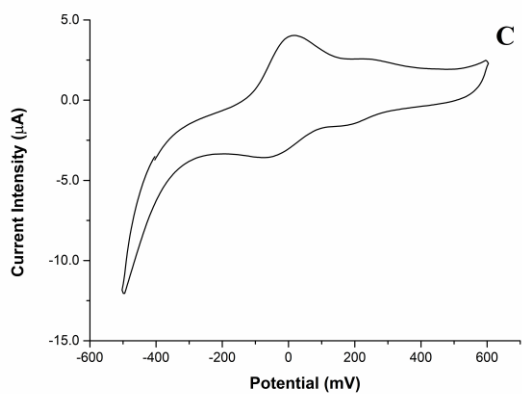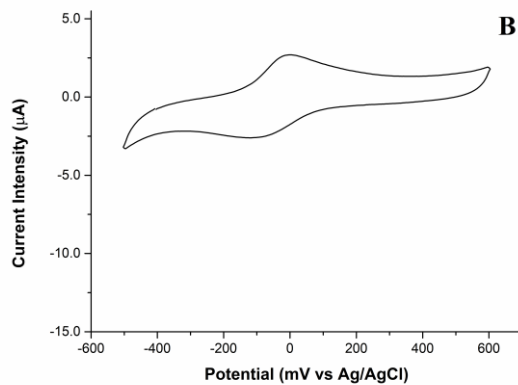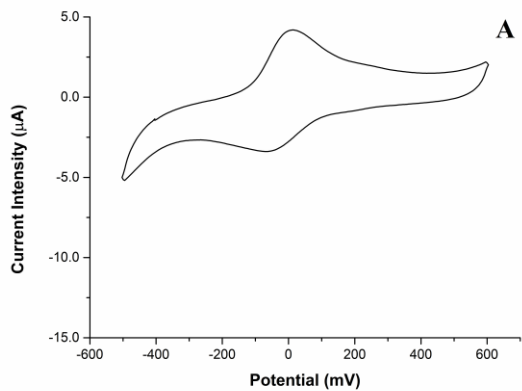
Figure S35. Cyclic voltammograms of (**A**) **D1**, (**B**) **D2**, (**C**) **D3**, (**D**) **D4**, (**E**) **D5**, (**F**) **D6**, (**G**) **C0** at 2.00 10⁻⁵ M, TRIS-HCl buffer (TRIS-HCl 0.05 M, NaCl 0.05 M), pH 7.1, 25 °C, Scan Rate 500 mV/s.
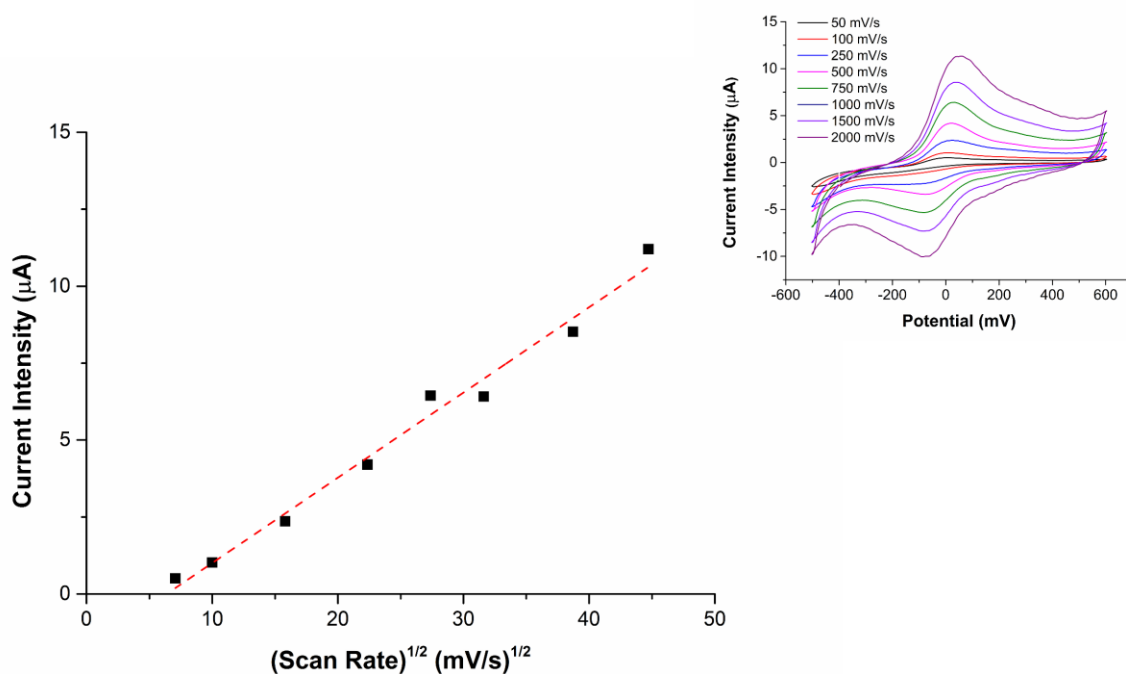
Figure S36. Plot of the dependency of anodic peak current against the square root of the scan rate for compound **D1** (the cyclic voltammograms at different scan rate of **D1** are shown as insert). Linear regression results: $Y = 0.277x - 1.764$, $R = 0.99251$. **D1** 2.00·10⁻⁵ M, TRIS-HCl buffer (TRIS-HCl 0.05 M, NaCl 0.05 M), pH 7.1, t 25 °C.
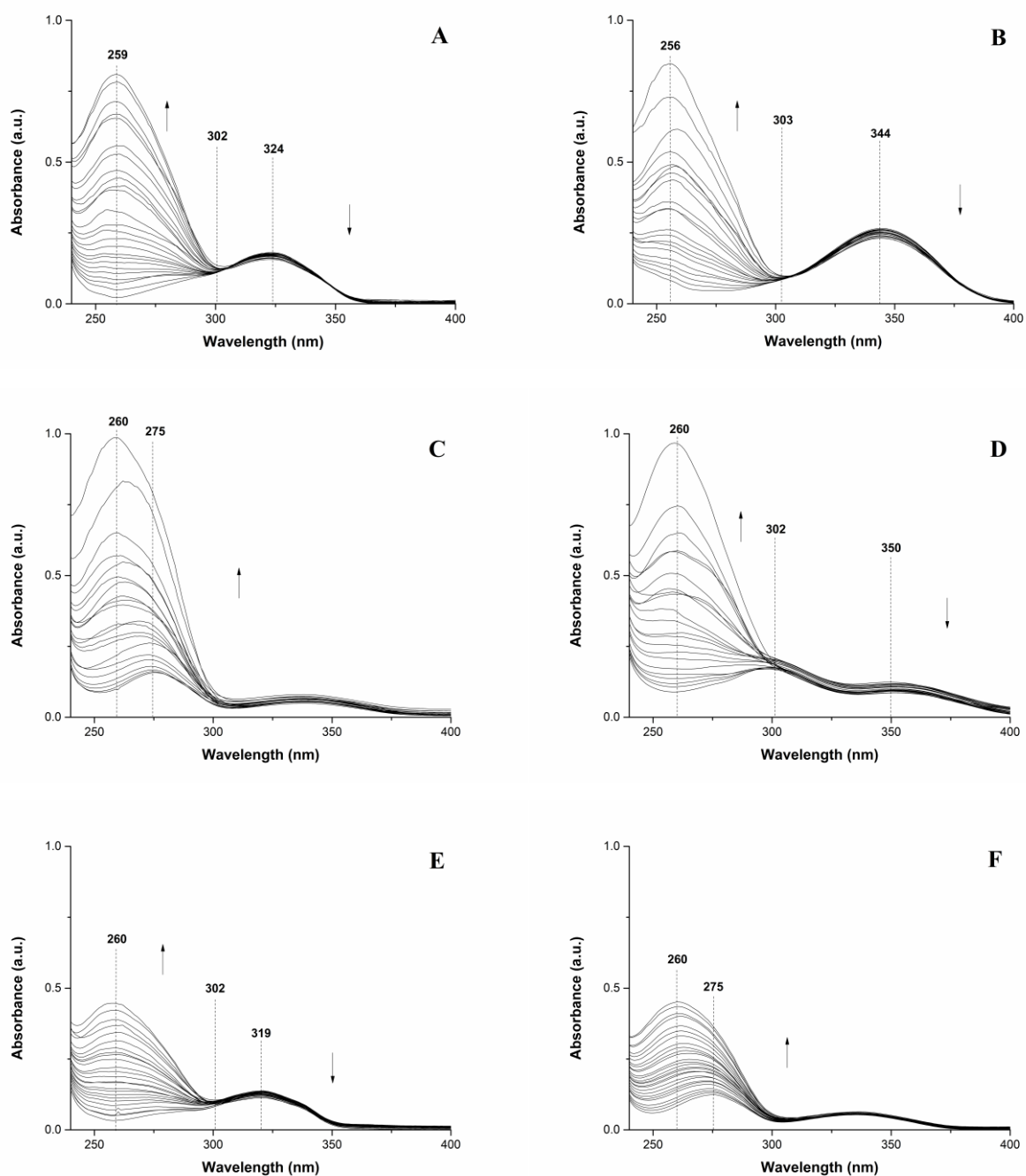
Figure S37. Selected spectra collected during the spectrophotometric titration of (**A**) **HL1** 1.235·10⁻⁵ M, (**B**), **HL2** 1.208·10⁻⁵ M, (**C**), **HL3** 1.042·10⁻⁵ M, (**D**), **HL4** 1.216·10⁻⁵ M, (**E**) **HL5** 9.780·10⁻⁶ M, (**F**) **HL6** 1.121·10⁻⁵ M with ct-DNA 2.270·10⁻⁴ M; TRIS-HCl buffer (TRIS-HCl 0.05 M, NaCl 0.05 M), pH 7.1, 25 °C, 1 cm optical path length.
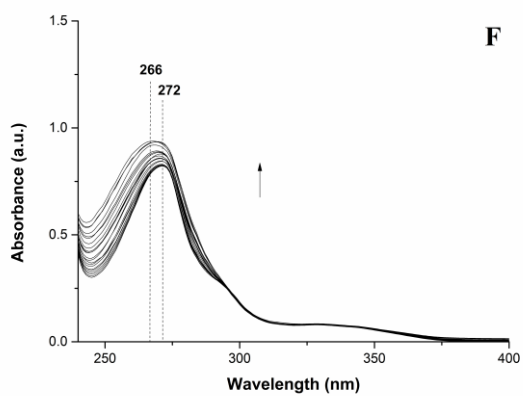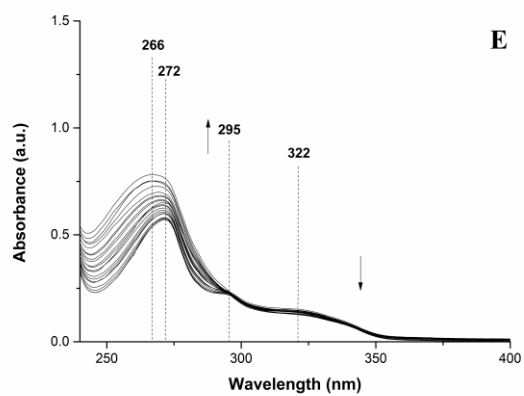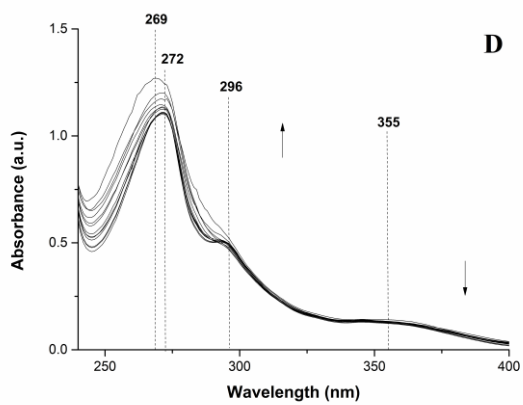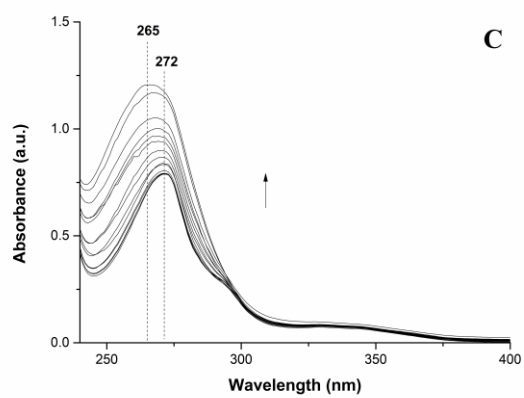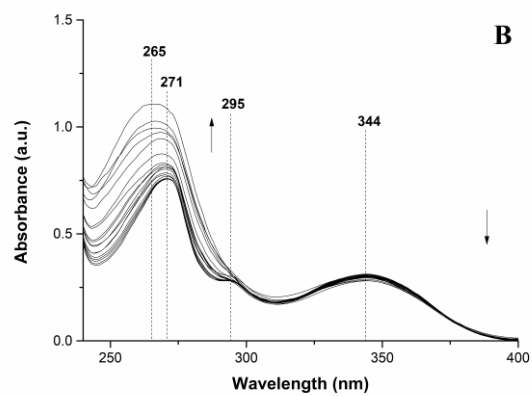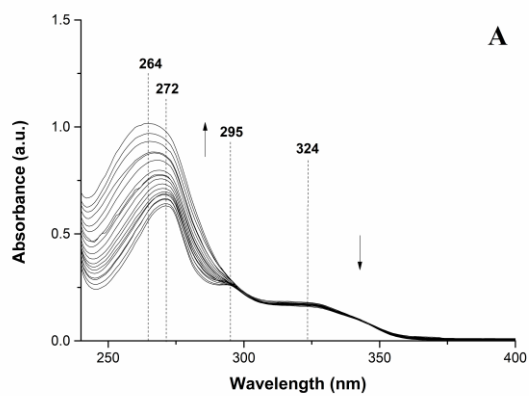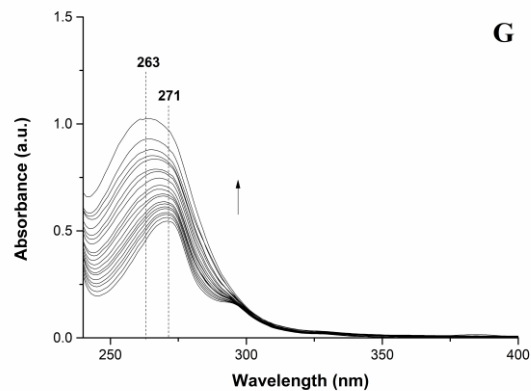
Figure S38. Selected spectra collected during the spectrophotometric titration of (**A**) **D1** 1.144·10⁻⁵ M, (**B**), **D2** 1.031·10⁻⁵ M, (**C**), **D3** 1.105·10⁻⁵ M, (**D**), **D4** 1.213·10⁻⁵ M, (**E**) **D5** 1.002·10⁻⁵ M, (**F**) **D6** 1.244·10⁻⁵ M, (**G**) **C0** 1.061·10⁻⁵ M with ct-DNA 2.270·10⁻⁴ M; TRIS-HCl buffer (TRIS-HCl 0.05 M, NaCl 0.05 M), pH 7.1, 25 °C, 1 cm optical path length.
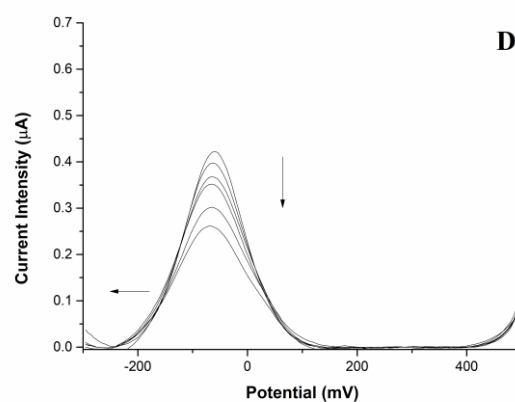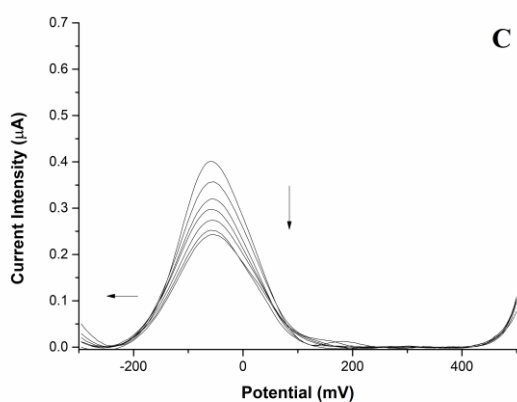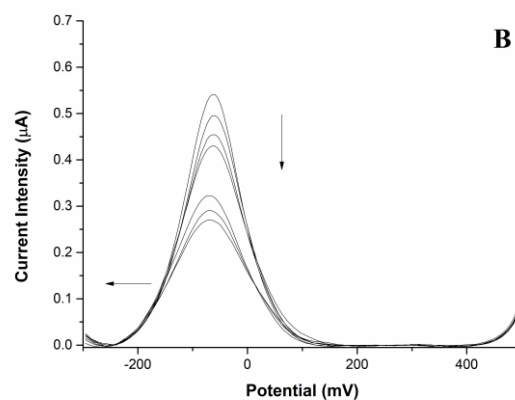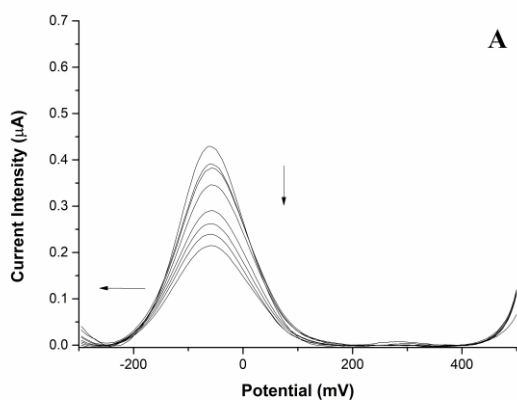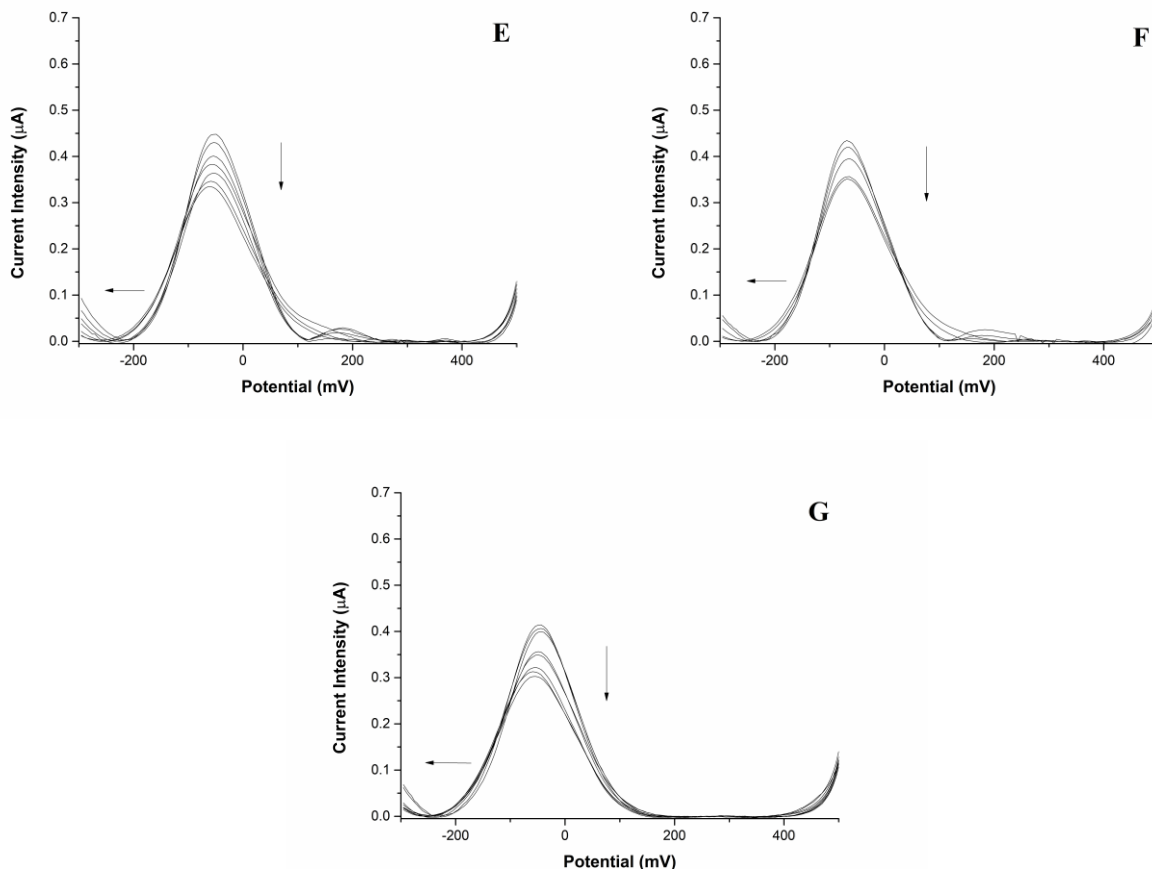
Figure S39. Differential Pulse Voltammograms recorded upon incremental addition of genomic DNA to **D1-6** and **C0** compounds. (**A**) **D1** $2.00 \cdot 10^{-5}$ M, genomic DNA 4428.1 ng/μL, (**B**) **D2** $2.00 \cdot 10^{-5}$ M, genomic DNA 3130.8 ng/μL, (**C**) **D3** $2.00 \cdot 10^{-5}$ M, genomic DNA 4428.1 ng/μL, (**D**) **D4** $2.00 \cdot 10^{-5}$ M, genomic DNA 3340.3 ng/μL, (**E**) **D5** $2.00 \cdot 10^{-5}$ M, genomic DNA 4428.1 ng/μL, (**F**) **D1** $2.00 \cdot 10^{-5}$ M, genomic DNA 3340.3 ng/μL, (**G**) **C0** $2.00 \cdot 10^{-5}$ M, genomic DNA 3340.3 ng/μL; TRIS-HCl buffer (TRIS-HCl 0.05 M, NaCl 0.05 M), pH 7.1, 25 °C, start potential 500 mV, end potential -300 mV, step potential 5 mV, pulse amplitude 25 mV.
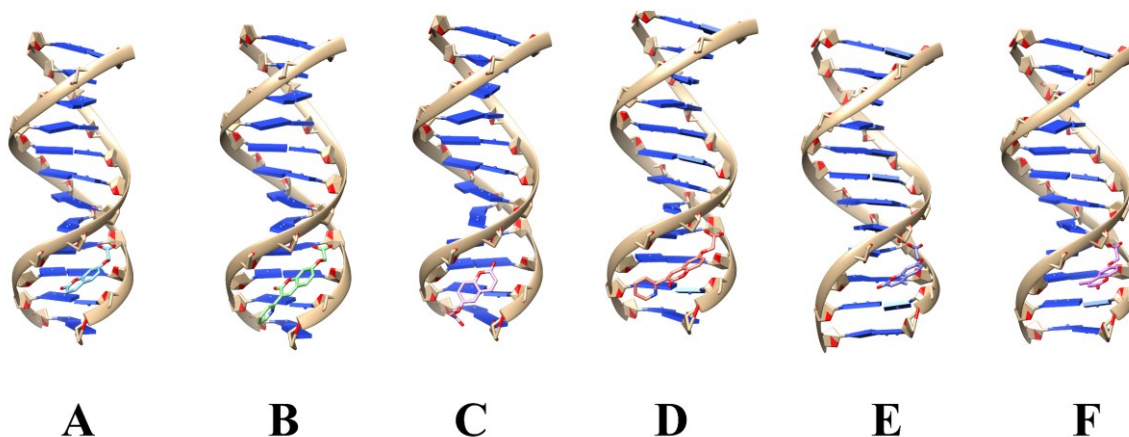
Figure S40. Full view of the complex between the highest-ranking score of deprotonated **HL1-6** (**L1-6**, charges are omitted for simplicity) and BDNA.
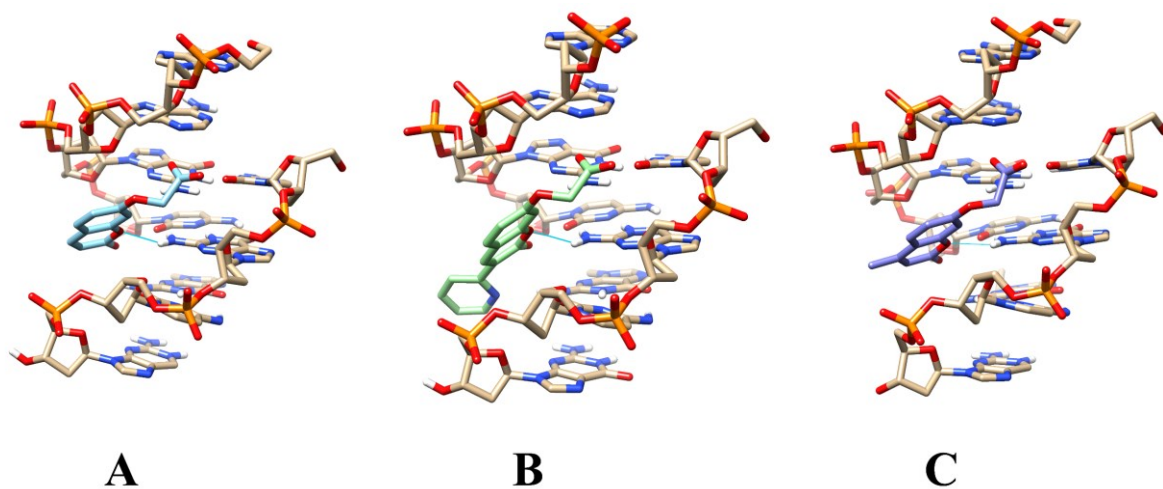
Figure S41. Hydrogen bonding profile between the highest-ranking score of **L1** (**A**), **L2** (**B**), **L5** (**C**) and BDNA.
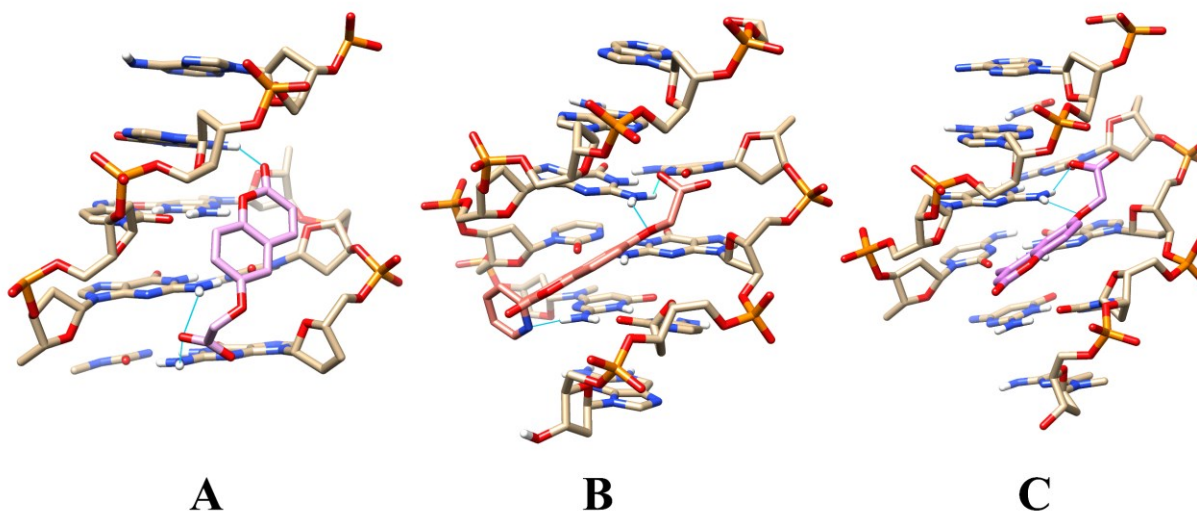
Figure S42. Hydrogen bonding profile between the highest-ranking score of **L3** (**A**), **L4** (**B**), **L6** (**C**) and BDNA.
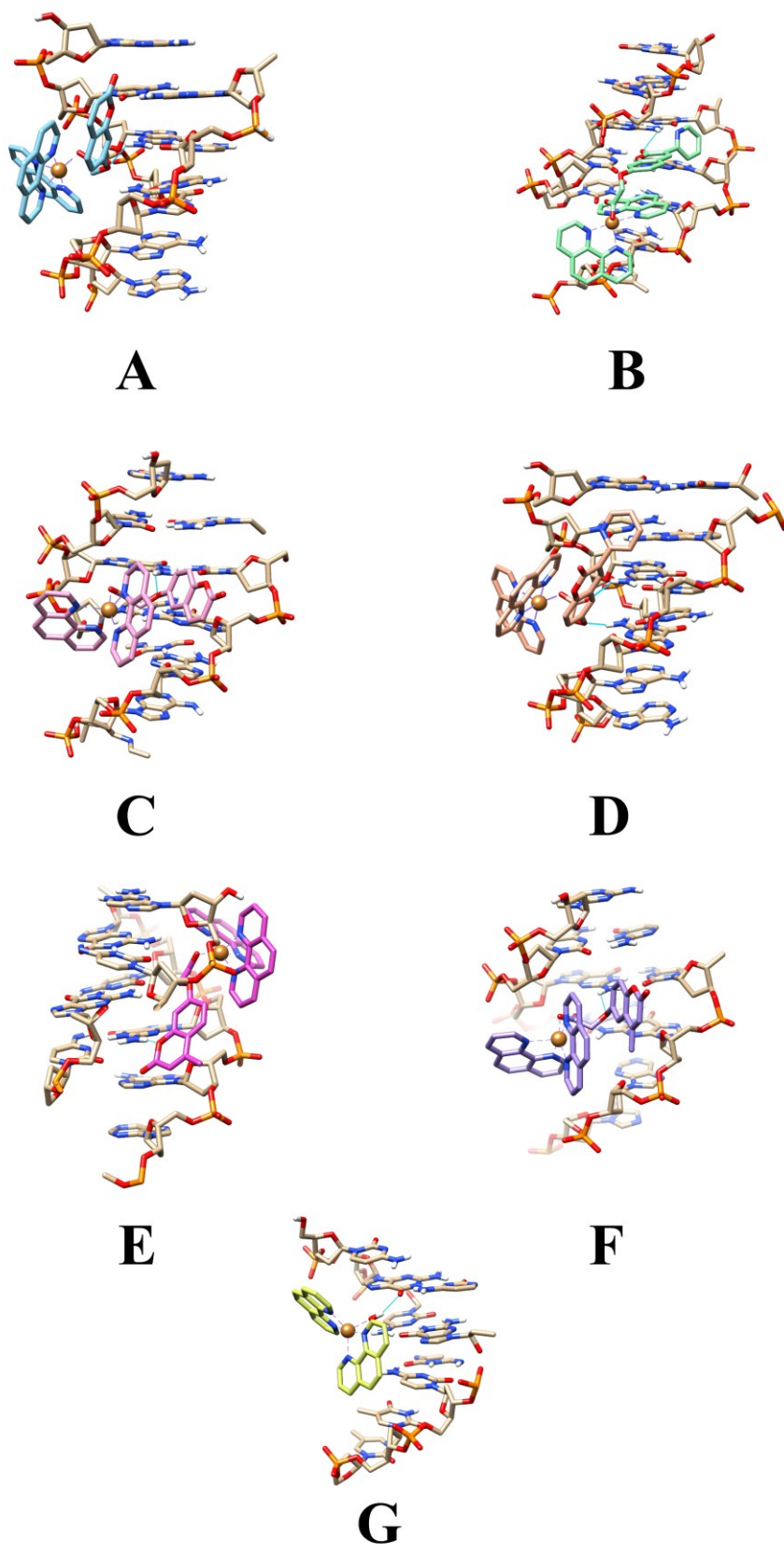
Figure S43. Hydrogen bonding profile between the highest-ranking score of [Cu(phen)₂(L1)]⁺ (A), [Cu(phen)₂(L2)]⁺ (B), [Cu(phen)₂(L3)]⁺ (C), [Cu(phen)₂(L4)]⁺ (D), [Cu(phen)₂(L5)]⁺ (E), [Cu(phen)₂(L6)]⁺ (F), [Cu(phen)₂(OH₂)]²⁺ (g) and BDNA.
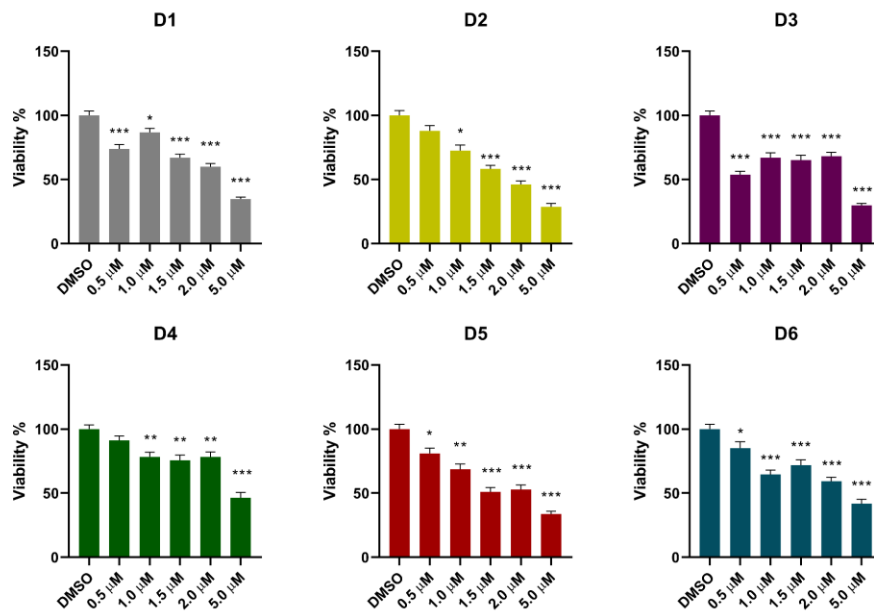
Figure S44. Viability (% compared to the control) of SKOV-3 cells after 24 hrs, in presence of **D1-6** at different concentrations or DMSO (control), determined by means of MTT assay. Results are expressed as Mean ± SEM from 3 independent experiments done in technical hexaplicates. Asterisks indicate statistical significance (with respect to the control) at $p < 0.05$ (*), $p < 0.01$ (**), $p < 0.001$ (***).
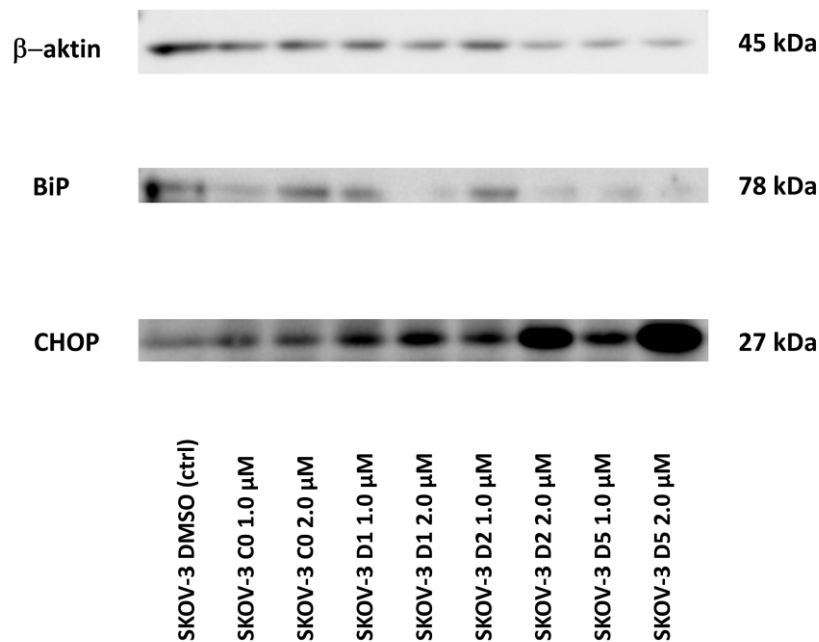
Figure S45. Protein expression of BiP and CHOP in SKOV-3 cells treated for 24 hrs with **C0**, **D1**, **D2** and **D5** at sub-lethal (1.0 μM) and lethal concentrations (2.0 μM). β-Actin was used as a control of equal loading.

Table S1. Selected optimized bond distances (Å) and angles (°) for DFT-optimized structure of **L1** (gas phase) and corresponding X-Ray structural parameters. Atom labelling scheme as in **Figure S27**.

	L1	
	Structural parameters	DFT-optimized
C1-O1	1.378	1.376
O1-C8	1.378	1.359
C1-O2	1.210	1.206
C6-O3	1.361	1.322
O3-C10	1.429	1.430
C11-O4	1.238	1.238
C11-O5	1.249	1.242
O1-C1-C2	117.12	116.38
C8-O1-C1	122.27	123.40
C6-O3-C10	117.88	119.56
C10-C11-O4	119.36	116.70
C10-C11-O5	113.51	111.44
O4-C11-O5	127.03	131.86
C8-O1-C1-C2	3.45	0.98
O3-C10-C11-O4	18.65	1.23
O3-C10-C11-O5	-164.68	-178.76

Table S2. Selected optimized bond distances (Å) and angles (°) for DFT-optimized structure of **L2** (gas phase). Atom labelling scheme as in **Figure S27.**

	L2		
C8-O1	1.353	*C6-C5-N1*	115.87
O1-C7	1.373	*C7-C6-C5*	121.74
C7-O2	1.207	*C5-N1-C1*	119.21
C7-C6	1.456	*O1-C7-C6*	116.80
C6-C5	1.473	*C15-C16-O4*	116.61

C5-N1	1.342	C15-C16-O5	111.37
N1-C1	1.321	O4-C16-O5	132.02
C13-O3	1.319	C7-C6-C5-N1	175.44
O3-C15	1.430	C8-O1-C7-O2	-178.76
C16-O4	1.238	C13-O3-C15-C16	68.61
C16-O5	1.241	O3-C15-C16-O4	2.36
C8-O1-C7	124.49	O3-C15-C16-O5	-177.86

Table S3. Selected optimized bond distances (Å) and angles (°) for DFT-optimized structure of **L3** (gas phase). Atom labelling scheme as in **Figure S27.**

L3			
C1-O1	1.364	C5-O3-C10	119.15
O1-C8	1.366	C10-C11-O4	118.04
C1-O2	1.206	C10-C11-O5	110.38
C5-O3	1.326	O4-C11-O5	131.59
O3-C10	1.431	C8-O1-C1-C2	0.06
C11-O4	1.235	O3-C10-C11-O4	0.63
C11-O5	1.245	O3-C10-C11-O5	-179.41
C8-O1-C1	122.78		

Table S4. Selected optimized bond distances (Å) and angles (°) for DFT-optimized structure of **L4** (gas phase). Atom labelling scheme as in **Figure S27.**

L4			
C8-O1	1.360	C6-C5-N1	115.47
O1-C7	1.362	C7-C6-C5	121.49
C7-O2	1.208	C5-N1-C1	119.24
C7-C6	1.465	O1-C7-C6	116.77
C6-C5	1.480	C15-C16-O4	118.04
C5-N1	1.340	C15-C16-O5	110.31
N1-C1	1.321	O4-C16-O5	131.64
C12-O3	1.326	C7-C6-C5-N1	-178.21
O3-C15	1.432	C8-O1-C7-O2	-179.68
C16-O4	1.235	C12-O3-C15-C16	-179.48
C16-O5	1.245	O3-C15-C16-O4	-0.60
C8-O1-C7	124.01	O3-C15-C16-O5	179.44

Table S5. Selected optimized bond distances (Å) and angles (°) for DFT-optimized structure of **L5** (gas phase). Atom labelling scheme as in **Figure S27.**

L5			
C1-O1	1.371	C7-O3-C11	119.50
O1-C9	1.356	C11-C12-O4	116.74
C1-O2	1.206	C11-C12-O5	111.44
C7-O3	1.322	O4-C12-O5	131.81
O3-C11	1.430	C9-O1-C1-C2	1.14
C12-O4	1.238	O3-C11-C12-O4	-1.04
C12-O5	1.242	O3-C110-C12-O5	178.90
C9-O1-C1	122.86		

Table S6. Selected optimized bond distances (Å) and angles (°) for DFT-optimized structure of **L6** (gas phase). Atom labelling scheme as in **Figure S27.**

L6			
C1-O1	1.363	C6-O3-C11	119.14
O1-C9	1.347	C11-C12-O4	118.03
C1-O2	1.207	C11-C12-O5	110.42
C6-O3	1.327	O4-C12-O5	131.55
O3-C11	1.431	C9-O1-C1-C2	0.02
C12-O4	1.235	O3-C11-C12-O4	0.71
C12-O5	1.246	O3-C110-C12-O5	-179.34
C9-O1-C1	122.23		

Table S7. Selected atomic charges, calculated at NPA level of **L1**, **L3** and **L5**. Atomic scheme as in **Figure 27.**

	L1		L3		L5
	charges		charges		charges
O1	-0.428	O1	-0.576	O1	-0.427
O2	-0.579	O2	-0.724	O2	-0.582
O3	-0.429	O3	-0.421	O3	-0.431
O4	-0.728	O4	-0.724	O4	-0.729
O5	-0.742	O5	-0.757	O5	-0.743

Table S8. Selected atomic charges, calculated at NPA level, of **L2, L4** and **L6**. Atomic scheme as in **Figure S27**.

L2		L4		L6	
	charges		**charges**		**charges**
O1	-0.423	*O1*	-0.422	*O1*	-0.427
O2	-0.591	*O2*	-0.592	*O2*	-0.581
O3	-0.423	*O3*	-0.419	*O3*	-0.422
O4	-0.726	*O4*	-0.723	*O4*	-0.725
O5	-0.738	*O5*	-0.757	*O5*	-0.757
N1	-0.436	*N1*	-0.425		

Table S9. Energy values (eV) of the frontier Molecular Orbitals of **L1-6** in gas phase at the DFT level (PBE0, def-2 TZVP).

compound	HOMO	LUMO
L1	-2.22	1.02
L2	-2.36	0.41
L3	-2.11	0.34
L4	-2.13	-0.17
L5	-2.18	1.08
L6	-2.11	0.47

Table S10. Selected optimized bond distances (Å) and angles (°) for DFT-optimized structure of **[Cu(phen)₂(L1)]⁺** (gas phase). Atom labelling scheme as in **Figure 3.**

[Cu(phen)₂(L1)]⁺			
Cu-N1	2.045	*N3-Cu-O4*	90.76
Cu-N2	2.285	*N4-Cu-O4*	160.08
Cu-N3	2.030	*N1-Cu-N2*	77.41
Cu-N4	2.087	*N1-Cu-N3*	176.12
Cu-O4	1.986	*N1-Cu-N4*	95.79
O4-C25	1.282	*N1-Cu-O4-C25*	-84.24
C25- O5	1.229	*N1-Cu-N3-C13*	-172.01
Cu-O4-C25	100.92	*N1-Cu-N3-C24*	10.36
Cu-N1-C1	123.63	*N2-Cu-N3-C13*	-82.31
Cu-N1-C12	116.68	*N1-Cu-N3-C24*	99.53
Cu-N2-C10	132.01	*N3-Cu-N1-C1*	-90.78

Cu-N2-C11	109.25	N3-Cu-N1-C12	92.08
Cu-N3-C13	126.95	N3-Cu-N2-C11	-178.12
Cu-N3-C24	113.66	N3-Cu-N2-C10	4.87
Cu-N4-C22	129.76	N4-Cu-N2-C11	-96.02
Cu-N4-C23	111.62	N4-Cu-N2-C10	86.97
N1-Cu-O4	93.06	Cu-O4-C25-O5	1.27
N2-Cu-O4	100.12		

Table S11. Selected optimized bond distances (Å) and angles (°) for DFT-optimized structure of **[Cu(phen)₂(L2)]⁺** (gas phase). Atom labelling scheme as in **Figure 3**.

[Cu(phen)₂(L2)]⁺			
Cu-N1	2.043	N3-Cu-O4	90.57
Cu-N2	2.283	N4-Cu-O4	159.62
Cu-N3	2.029	N1-Cu-N2	77.47
Cu-N4	2.089	N1-Cu-N3	175.91
Cu-O4	1.991	N1-Cu-N4	95.58
O4-C25	1.281	N1-Cu-O4-C25	-83.87
C25- O5	1.223	N1-Cu-N3-C13	-175.22
Cu-O4-C25	100.46	N1-Cu-N3-C24	7.33
Cu-N1-C1	123.68	N2-Cu-N3-C13	-82.09
Cu-N1-C12	116.67	N1-Cu-N3-C24	100.46
Cu-N2-C10	132.03	N3-Cu-N1-C1	-86.68
Cu-N2-C11	109.24	N3-Cu-N1-C12	95.71
Cu-N3-C13	126.89	N3-Cu-N2-C11	-177.46
Cu-N3-C24	113.70	N3-Cu-N2-C10	5.20
Cu-N4-C22	129.77	N4-Cu-N2-C11	-95.40
Cu-N4-C23	111.57	N4-Cu-N2-C10	87.44
N1-Cu-O4	93.40	Cu-O4-C25-O5	0.59
N2-Cu-O4	99.93		

Table S12. Selected optimized bond distances (Å) and angles (°) for DFT-optimized structure of **[Cu(phen)₂(L3)]⁺** (gas phase). Atom labelling scheme as in **Figure 3**.

[Cu(phen)₂(L3)]⁺			
Cu-N1	2.045	N3-Cu-O4	90.22
Cu-N2	2.286	N4-Cu-O4	161.64
Cu-N3	2.032	N1-Cu-N2	77.40
Cu-N4	2.080	N1-Cu-N3	177.00
Cu-O4	1.964	N1-Cu-N4	96.65

247

O4-C25	1.276	N1-Cu-O4-C25	-84.90
C25- O5	1.234	N1-Cu-N3-C13	165.29
Cu-O4-C25	103.00	N1-Cu-N3-C24	-12.46
Cu-N1-C1	123.57	N2-Cu-N3-C13	-82.98
Cu-N1-C12	116.59	N1-Cu-N3-C24	-99.27
Cu-N2-C10	132.00	N3-Cu-N1-C1	-68.48
Cu-N2-C11	109.11	N3-Cu-N1-C12	116.72
Cu-N3-C13	127.01	N3-Cu-N2-C11	178.49
Cu-N3-C24	113.55	N3-Cu-N2-C10	4.01
Cu-N4-C22	129.61	N4-Cu-N2-C11	-99.12
Cu-N4-C23	111.75	N4-Cu-N2-C10	86.40
N1-Cu-O4	92.37	Cu-O4-C25-O5	3.43
N2-Cu-O4	97.93		

Table S13. Selected optimized bond distances (Å) and angles (°) for DFT-optimized structure of **[Cu(phen)₂(L4)]⁺** (gas phase). Atom labelling scheme as in **Figure 3.**

[Cu(phen)₂(L4)]⁺			
Cu-N1	2.047	N3-Cu-O4	89.78
Cu-N2	2.285	N4-Cu-O4	162.05
Cu-N3	2.034	N1-Cu-N2	77.35
Cu-N4	2.080	N1-Cu-N3	176.55
Cu-O4	1.959	N1-Cu-N4	96.46
O4-C25	1.277	N1-Cu-O4-C25	-84.93
C25- O5	1.233	N1-Cu-N3-C13	154.56
Cu-O4-C25	103.56	N1-Cu-N3-C24	-23.07
Cu-N1-C1	123.56	N2-Cu-N3-C13	-83.81
Cu-N1-C12	116.63	N1-Cu-N3-C24	-23.07
Cu-N2-C10	131.92	N3-Cu-N1-C1	-58.67
Cu-N2-C11	109.22	N3-Cu-N1-C12	126.18
Cu-N3-C13	127.00	N3-Cu-N2-C11	179.17
Cu-N3-C24	113.55	N3-Cu-N2-C10	4.32
Cu-N4-C22	129.53	N4-Cu-N2-C11	-98.54
Cu-N4-C23	111.84	N4-Cu-N2-C10	86.62
N1-Cu-O4	92.89	Cu-O4-C25-O5	5.74
N2-Cu-O4	98.02		

Table S14. Selected optimized bond distances (Å) and angles (°) for DFT-optimized structure of **[Cu(phen)₂(L5)]⁺** (gas phase). Atom labelling scheme as in **Figure 3.**

[Cu(phen)₂(L5)]⁺			
Cu-N1	2.045	N3-Cu-O4	90.72

Cu-N2	2.284	N4-Cu-O4	159.92
Cu-N3	2.030	N1-Cu-N2	77.42
Cu-N4	2.087	N1-Cu-N3	176.21
CU-O4	1.986	N1-Cu-N4	95.86
O4-C25	1.283	N1-Cu-O4-C25	-84.47
C25- O5	1.229	N1-Cu-N3-C13	-173.38
Cu-O4-C25	100.80	N1-Cu-N3-C24	9.17
Cu-N1-C1	123.62	N2-Cu-N3-C13	-82.85
Cu-N1-C12	116.68	N1-Cu-N3-C24	99.70
Cu-N2-C10	132.01	N3-Cu-N1-C1	-89.55
Cu-N2-C11	109.25	N3-Cu-N1-C12	93.42
Cu-N3-C13	126.95	N3-Cu-N2-C11	-178.18
Cu-N3-C24	113.66	N3-Cu-N2-C10	4.73
Cu-N4-C22	129.76	N4-Cu-N2-C11	-96.07
Cu-N4-C23	111.61	N4-Cu-N2-C10	86.85
N1-Cu-O4	93.00	Cu-O4-C25-O5	1.50
N2-Cu-O4	100.27		

Table S15. Selected optimized bond distances (Å) and angles (°) for DFT-optimized structure of **[Cu(phen)₂(L6)]⁺** (gas phase). Atom labelling scheme as in **Figure 3**.

$[Cu(phen)_2(L6)]^+$			
Cu-N1	2.046	N3-Cu-O4	90.21
Cu-N2	2.289	N4-Cu-O4	161.75
Cu-N3	2.032	N1-Cu-N2	77.38
Cu-N4	2.080	N1-Cu-N3	176.96
Cu-O4	1.965	N1-Cu-N4	96.61
O4-C25	1.276	N1-Cu-O4-C25	-84.87
C25- O5	1.234	N1-Cu-N3-C13	165.49
Cu-O4-C25	102.91	N1-Cu-N3-C24	-12.24
Cu-N1-C1	123.56	N2-Cu-N3-C13	-83.13
Cu-N1-C12	116.62	N1-Cu-N3-C24	99.13
Cu-N2-C10	132.00	N3-Cu-N1-C1	-68.83
Cu-N2-C11	109.12	N3-Cu-N1-C12	116.26
Cu-N3-C13	127.01	N3-Cu-N2-C11	178.68
Cu-N3-C24	113.55	N3-Cu-N2-C10	4.02
Cu-N4-C22	129.61	N4-Cu-N2-C11	-98.97
Cu-N4-C23	111.76	N4-Cu-N2-C10	86.38
N1-Cu-O4	92.43	Cu-O4-C25-O5	3.49
N2-Cu-O4	98.01		

Table S16. Tau ($\tau = \frac{\beta - \alpha}{60°}$) parameters calculated from the DFT-optimized structures (gas phase) of **[Cu(phen)₂(Lx)]⁺** (x = 1 - 6). Atom labelling scheme as in **Figure 3.**

	β (N1 − Cu − N3)	α (N4 − Cu − O4)	τ
[Cu(phen)₂(L1)]⁺	176.12	160.08	0.27
[Cu(phen)₂(L2)]⁺	175.91	159.62	0.27
[Cu(phen)₂(L3)]⁺	177.00	161.64	0.26
[Cu(phen)₂(L4)]⁺	176.55	162.05	0.24
[Cu(phen)₂(L5)]⁺	177.00	161.64	0.26
[Cu(phen)₂(L6)]⁺	176.97	161.75	0.25

Table S17. Selected atomic charges, calculated at NPA level, of **[Cu(phen)₂(L1)]⁺**, **[Cu(phen)₂(L3)]⁺** and **[Cu(phen)₂(L5)]⁺**. Atomic scheme as in **Figure 3**.

[Cu(phen)₂(L1)]⁺		*[Cu(phen)₂(L3)]⁺*		*[Cu(phen)₂(L5)]⁺*	
	charges		**charges**		**charges**
Cu	1.396	*Cu*	1.394	*Cu*	1.396
N1	-0.501	*N1*	-0.499	*N1*	-0.501
N2	-0.481	*N2*	-0.481	*N2*	-0.486
N3	-0.489	*N3*	-0.484	*N3*	-0.481
N4	-0.489	*N4*	-0.490	*N4*	-0.489
O1	-0.427	*O1*	-0.424	*O1*	-0.427
O2	-0.523	*O2*	-0.525	*O2*	-0.531
O3	-0.424	*O3*	-0.442	*O3*	-0.425
O4	-0.774	*O4*	-0.750	*O4*	-0.774
O5	-0.687	*O5*	-0.705	*O5*	-0.687

Table S18. Selected atomic charges, calculated at NPA level, of **[Cu(phen)₂(L2)]⁺**, **[Cu(phen)₂(L4)]⁺** and **[Cu(phen)₂(L6)]⁺**. Atomic scheme as in **Figure 3**.

[Cu(phen)₂(L2)]⁺		*[Cu(phen)₂(L4)]⁺*		*[Cu(phen)₂(L6)]⁺*	
	charges		**charges**		**charges**
Cu	1.396	*Cu*	1.393	*Cu*	1.394

N1	-0.503	*N1*	-0.490	*N1*	-0.169
N2	-0.482	*N2*	-0.481	*N2*	-0.480
N3	-0.489	*N3*	-0.490	*N3*	-0.489
N4	-0.489	*N4*	-0.490	*N4*	-0.490
N5	-0.432	*N5*	-0.427	*O1*	-0.424
O1	-0.424	*O1*	-0.420	*O2*	-0.531
O2	-0.543	*O2*	-0.547	*O3*	-0.443
O3	-0.424	*O3*	-0.444	*O4*	-0.750
O4	-0.773	*O4*	-0.751	*O5*	-0.705
O5	-0.689	*O5*	-0.701		

Table S19. Energy values (eV) of the frontier Molecular Orbitals of **[Cu(phen)₂(Lx)]⁺** (x = 1 - 6) in gas phase at the DFT level (PBE0, def-2 TZVP).

compound	*α-SOMO*	*α-LUMO*	*β-SOMO*	*β-LUMO*
[Cu(phen)₂(L1)]⁺	-8.78	-8.04	-8.79	-8.05
[Cu(phen)₂(L2)]⁺	-8.04	-5.29	-8.04	-5.32
[Cu(phen)₂(L3)]⁺	-7.88	-5.27	-7.88	-5.28
[Cu(phen)₂(L4)]⁺	-7.71	-5.22	-7.71	-5.23
[Cu(phen)₂(L5)]⁺	-7.94	-5.28	-7.95	-5.31
[Cu(phen)₂(L6)]⁺	-7.80	-5.27	-7.80	-5.28

Table S20. Cyclic Voltammetry parameters for **D1-6** and **C0** complexes. Concentrations $2.00 \cdot 10^{-5}$ M, TRIS-HCl buffer (TRIS-HCl 0.05 M, NaCl 0.05 M), pH 7.1, 25 °C, scan rate 500 mV.

Compound	E_{pc} (mV)	E_{pa} (mV)	$E_{1/2}$ (mV)	ΔE (mV)	$-I_{pc}$ ($10^{-6}A$)	I_{pa} ($10^{-6}A$)	$\dfrac{I_{pc}}{I_{pa}}$
D1	-54.19	8.56	-31.37	-62.75	3.35	4.21	0.79

D2	-69.04	-8.61	-38.82	-77.65	2.45	2.67	0.92
D3	-49.02	8.57	-28.79	-57.59	3.51	4.03	0.87
D4	-68.03	9.65	-38.84	-77.68	3.76	4.52	0.83
D5	-44.14	12.10	-28.12	-56.24	3.19	3.79	0.84
D6	-44.13	13.19	-28.66	-57.32	3.31	3.94	0.84
C0	-51.41	-0.21	-25.81	-51.62	3.04	3.67	0.83

Table S21. Electrochemical parameters derived from DPV measurements on **D1** alone and in presence of increasing amounts of genomic DNA (**Figure S38A**).

E_p (mV)	$E_{1/2}$ (mV)*	$\Delta E_{1/2}$ (mV)	Log (K^+/K^{2+})	(K^+/K^{2+})
-58.40	-45.90			
-59.00	-46.50	-0.60	-0.01	0.98
-59.70	-47.20	-1.30	-0.02	0.95
-60.80	-48.30	-2.40	-0.04	0.91
-62.10	-49.60	-3.70	-0.06	0.87
-62.80	-50.30	-4.40	-0.07	0.84
-63.40	-50.90	-5.00	-0.08	0.82
-64.90	-52.40	-6.50	-0.11	0.78

*Calculated as: $E_{1/2} = E_p + \Delta E/2$, where ΔE is the pulse amplitude.

Table S22. Electrochemical parameters derived from DPV measurements on **D2** alone and in presence of increasing amounts of genomic DNA (**Figure S38B**).

E_p (mV)	$E_{1/2}$ (mV)*	$\Delta E_{1/2}$ (mV)	Log (K^+/K^{2+})	(K^+/K^{2+})
-60.20	-47.70			
-61.10	-48.60	-0.90	-0.02	0.97
-61.90	-49.40	-1.70	-0.03	0.94
-64.00	-51.50	-3.80	-0.06	0.86
-71.20	-58.70	-11.00	-0.19	0.65
-71.30	-58.80	-11.10	-0.19	0.65
-73.40	-60.90	-13.20	-0.22	0.60

*Calculated as: $E_{1/2} = E_p + \Delta E/2$, where ΔE is the pulse amplitude.

Table S23. Electrochemical parameters derived from DPV measurements on **D3** alone and in presence of increasing amounts of genomic DNA (**Figure S38C**).

E_p (mV)	$E_{1/2}$ (mV)*	$\Delta E_{1/2}$ (mV)	Log (K^+/K^{2+})	(K^+/K^{2+})
-59.00	-46.50			
-59.70	-47.20	-0.70	-0.01	0.97
-60.40	-47.90	-1.40	-0.02	0.95
-60.60	-48.10	-1.60	-0.03	0.94
-61.20	-48.70	-2.20	-0.04	0.92
-61.90	-49.40	-2.90	-0.05	0.89
-62.00	-49.50	-3.00	-0.05	0.89

*Calculated as: $E_{1/2} = E_p + \Delta E/2$, where ΔE is the pulse amplitude.

Table S24. Electrochemical parameters derived from DPV measurements on **D4** alone and in presence of increasing amounts of genomic DNA (**Figure S38D**).

E_p (mV)	$E_{1/2}$ (mV)*	$\Delta E_{1/2}$ (mV)	Log (K^+/K^{2+})	(K^+/K^{2+})
-59.30	-46.8			
-61.40	-48.9	-2.10	-0.04	0.92
-63.60	-51.1	-4.30	-0.07	0.85
-65.70	-53.2	-6.40	-0.11	0.78
-66.60	-54.1	-7.30	-0.12	0.75
-67.90	-55.4	-8.60	-0.15	0.71

*Calculated as: $E_{1/2} = E_p + \Delta E/2$, where ΔE is the pulse amplitude.

Table S25. Electrochemical parameters derived from DPV measurements on **D5** alone and in presence of increasing amounts of genomic DNA (**Figure S38E**).

E_p (mV)	$E_{1/2}$ (mV)*	$\Delta E_{1/2}$ (mV)	Log (K^+/K^{2+})	(K^+/K^{2+})
-52.4	-39.9			
-54.9	-42.4	-2.50	-0.04	0.91
-55.6	-43.1	-3.20	-0.05	0.88
-56.8	-44.3	-4.40	-0.07	0.84

E_p (mV)	$E_{1/2}$ (mV)[*]	$\Delta E_{1/2}$ (mV)	$Log\ (K^+/K^{2+})$	(K^+/K^{2+})
-57.1	-44.6	-4.70	-0.08	0.83
-59.5	-48.0	-8.10	-0.14	0.73
-60.5	-48.0	-8.10	-0.14	0.73

[*]Calculated as: $E_{1/2} = E_p + \Delta E/2$, where ΔE is the pulse amplitude.

Table S26. Electrochemical parameters derived from DPV measurements on **D6** alone and in presence of increasing amounts of genomic DNA (**Figure S38F**).

E_p (mV)	$E_{1/2}$ (mV)[*]	$\Delta E_{1/2}$ (mV)	$Log\ (K^+/K^{2+})$	(K^+/K^{2+})
-66.80	-54.30			
-67.10	-54.60	-0.30	-0.01	0.99
-67.40	-54.90	-0.60	-0.01	0.98
-67.90	-55.40	-1.10	-0.02	0.96
-68.40	-55.90	-1.60	-0.03	0.94

[*]Calculated as: $E_{1/2} = E_p + \Delta E/2$, where ΔE is the pulse amplitude.

Table S27. Electrochemical parameters derived from DPV measurements on **C0** alone and in presence of increasing amounts of genomic DNA (**Figure S38G**).

E_p (mV)	$E_{1/2}$ (mV)[*]	$\Delta E_{1/2}$ (mV)	$Log\ (K^+/K^{2+})$	(K^+/K^{2+})
-48.04	-35.54			
-48.21	-35.71	-0.17	0.00	0.99
-49.03	-36.53	-0.99	-0.02	0.96
-49.38	-36.88	-1.34	-0.02	0.95
-51.55	-39.05	-3.51	-0.06	0.87
-55.90	-43.40	-7.86	-0.13	0.74
-58.07	-45.57	-10.03	-0.17	0.68
-59.10	-46.60	-11.06	-0.19	0.65

[*]Calculated as: $E_{1/2} = E_p + \Delta E/2$, where ΔE is the pulse amplitude.

Results and discussion

Article 6.

Copper(II) Phenanthroline-Based Complexes as Potential AntiCancer Drugs: A Walkthrough on the Mechanisms of Action

Review

Copper(II) Phenanthroline-Based Complexes as Potential AntiCancer Drugs: A Walkthrough on the Mechanisms of Action

Sebastiano Masuri [1,*,†], Petr Vaňhara [2,3,*,†], Maria Grazia Cabiddu [1], Lukáš Moráň [2,4], Josef Havel [3,5], Enzo Cadoni [1] and Tiziana Pivetta [1]

1 Department of Chemical and Geological Sciences, University of Cagliari, 09042 Cagliari, Italy; mgcabidd@unica.it (M.G.C.); ecadoni@unica.it (E.C.); tpivetta@unica.it (T.P.)
2 Department of Histology and Embryology, Faculty of Medicine, Masaryk University, 62500 Brno, Czech Republic; 408080@muni.cz
3 International Clinical Research Center, St. Anne's University Hospital, 65691 Brno, Czech Republic; havel@chemi.muni.cz
4 Research Centre for Applied Molecular Oncology, Masaryk Memorial Cancer Institute, 65653 Brno, Czech Republic
5 Department of Chemistry, Faculty of Science, Masaryk University, 62500 Brno, Czech Republic
* Correspondence: sebastiano.masuri@unica.it (S.M.); pvanhara@med.muni.cz (P.V.)
† These authors contributed equally to this work.

Abstract: Copper is an endogenous metal ion that has been studied to prepare a new antitumoral agent with less side-effects. Copper is involved as a cofactor in several enzymes, in ROS production, in the promotion of tumor progression, metastasis, and angiogenesis, and has been found at high levels in serum and tissues of several types of human cancers. Under these circumstances, two strategies are commonly followed in the development of novel anticancer Copper-based drugs: the sequestration of free Copper ions and the synthesis of Copper complexes that trigger cell death. The latter strategy has been followed in the last 40 years and many reviews have covered the anticancer properties of a broad spectrum of Copper complexes, showing that the activity of these compounds is often multi factored. In this work, we would like to focus on the anticancer properties of mixed Cu(II) complexes bearing substituted or unsubstituted 1,10-phenanthroline based ligands and different classes of inorganic and organic auxiliary ligands. For each metal complex, information regarding the tested cell lines and the mechanistic studies will be reported and discussed. The exerted action mechanisms were presented according to the auxiliary ligand/s, the metallic centers, and the increasing complexity of the compound structures.

Keywords: cancer; coordination compounds; copper; 1,10-phenanthroline; anticancer chemotherapy; chemoresistance; cell stress response

1. Introduction

The fortuitous discovery of the anticancer properties of cisplatin (Figure 1a) has represented a milestone in the chemotherapeutic treatment of several types of tumors (ovarian, testicular and lung, among others) [1]. Cisplatin and its derivatives (carboplatin and oxaliplatin, Figure 1b,c) are currently approved for clinical use worldwide, while other Pt(II) anticancer metallodrugs (nedaplatin, heptaplatin, and lobaplatin Figure 1d–f) have been introduced only in a few countries [2].

As commonly known, these compounds exhibit numerous dose-dependent side effects (hepatotoxicity, nephrotoxicity, ototoxicity among the most severe). Moreover, their therapeutic efficacy is limited by pharmacoresistance phenomena that might take place after some treatment cycles [3,4].

255

Abstract

Cancer still constitutes one of the principal causes of death in our society. Many efforts have been made through the years towards the development of novel anticancer compounds with better selectivity and an improved toxicological profile compared to currently approved Pt(II)-based drugs. A strategy commonly followed under this perspective consists of the substitution of Pt(II) with endogenous metal ions. Copper constitutes a typical example thanks to its involvement in many important enzymes as cofactor. In addition, cellular uptake of Copper and cisplatin takes place using the same transporter (hCtr1). Many Copper-based coordination compounds have been prepared and screened for anticancer activity *in-vitro* and *in-vivo* models through the years. In this review, we would like to focus on ternary Cu(II) complexes bearing substituted or unsubstituted 1,10-phenanthroline based molecules and different classes of auxiliary ligands. For each metal complex, information regarding their anticancer potency *in-vitro* and mechanistical studies have been reported and discussed. The compounds have been presented using a "structure-based" approach, according to the features of the auxiliary ligand/s, the number of the metal centres, and the increasing complexity of the compound structures.

Copper(II) Phenanthroline-Based Complexes as Potential AntiCancer Drugs: A Walkthrough on the Mechanisms of Action

Sebastiano Masuri [1,*,†], Petr Vaňhara [2,3,*,†], Maria Grazia Cabiddu [1], Lukáš Moráň [2,4], Josef Havel [3,5], Enzo Cadoni [1,4] and Tiziana Pivetta [1]

[1]Department of Chemical and Geological Sciences, University of Cagliari, 09042, Cittadella Universitaria, Monserrato, Cagliari, Italy.

[2]Department of Histology and Embryology, Faculty of Medicine, Masaryk University, 62500, Brno, Czech Republic.

[3]International Clinical Research Center, St. Anne's University Hospital, 65691, Brno, Czech Republic.

[4]Research Centre for Applied Molecular Oncology, Masaryk Memorial Cancer Institute, 65653, Brno, Czech Republic.

[5]Department of Chemistry, Faculty of Science, Masaryk University, 62500, Brno, Czech Republic

[†]Co-first authors: these authors contributed equally to this work.

* Corresponding authors: sebastiano.masuri@unica.it (S.M), pvanhara@med.muni.cz (P.V.)

Review

Copper(II) Phenanthroline-Based Complexes as Potential AntiCancer Drugs: A Walkthrough on the Mechanisms of Action

Sebastiano Masuri [1,*,†] , Petr Vaňhara [2,3,*,†] , Maria Grazia Cabiddu [1] , Lukáš Moráň [2,4], Josef Havel [3,5], Enzo Cadoni [1] and Tiziana Pivetta [1]

[1] Department of Chemical and Geological Sciences, University of Cagliari, 09042 Cagliari, Italy; mgcabidd@unica.it (M.G.C.); ecadoni@unica.it (E.C.); tpivetta@unica.it (T.P.)
[2] Department of Histology and Embryology, Faculty of Medicine, Masaryk University, 62500 Brno, Czech Republic; 408080@muni.cz
[3] International Clinical Research Center, St. Anne's University Hospital, 65691 Brno, Czech Republic; havel@chemi.muni.cz
[4] Research Centre for Applied Molecular Oncology, Masaryk Memorial Cancer Institute, 65653 Brno, Czech Republic
[5] Department of Chemistry, Faculty of Science, Masaryk University, 62500 Brno, Czech Republic
* Correspondence: sebastiano.masuri@unica.it (S.M.); pvanhara@med.muni.cz (P.V.)
† These authors contributed equally to this work.

Abstract: Copper is an endogenous metal ion that has been studied to prepare a new antitumoral agent with less side-effects. Copper is involved as a cofactor in several enzymes, in ROS production, in the promotion of tumor progression, metastasis, and angiogenesis, and has been found at high levels in serum and tissues of several types of human cancers. Under these circumstances, two strategies are commonly followed in the development of novel anticancer Copper-based drugs: the sequestration of free Copper ions and the synthesis of Copper complexes that trigger cell death. The latter strategy has been followed in the last 40 years and many reviews have covered the anticancer properties of a broad spectrum of Copper complexes, showing that the activity of these compounds is often multi factored. In this work, we would like to focus on the anticancer properties of mixed Cu(II) complexes bearing substituted or unsubstituted 1,10-phenanthroline based ligands and different classes of inorganic and organic auxiliary ligands. For each metal complex, information regarding the tested cell lines and the mechanistic studies will be reported and discussed. The exerted action mechanisms were presented according to the auxiliary ligand/s, the metallic centers, and the increasing complexity of the compound structures.

Keywords: cancer; coordination compounds; copper; 1,10-phenanthroline; anticancer chemotherapy; chemoresistance; cell stress response

1. Introduction

The fortuitous discovery of the anticancer properties of cisplatin (Figure 1a) has represented a milestone in the chemotherapeutic treatment of several types of tumors (ovarian, testicular and lung, among others) [1]. Cisplatin and its derivatives (carboplatin and oxaliplatin, Figure 1b,c) are currently approved for clinical use worldwide, while other Pt(II) anticancer metallodrugs (nedaplatin, heptaplatin, and lobaplatin Figure 1d–f) have been introduced only in a few countries [2].

As commonly known, these compounds exhibit numerous dose-dependent side effects (hepatotoxicity, nephrotoxicity, ototoxicity among the most severe). Moreover, their therapeutic efficacy is limited by pharmacoresistance phenomena that might take place after some treatment cycles [3,4].

Figure 1. Structures of cisplatin (**a**), carboplatin (**b**), oxaliplatin (**c**), nedaplatin (**d**), heptaplatin (**e**), lobaplatin (**f**).

Considering the high incidence of cancer worldwide (19.3 million new cases and 10 million deaths estimated in 2020) [5], the development of novel anticancer chemotherapeutics able to overcome the limitations of Pt(II) compounds, appears extremely important.

A common approach exploited in the design of novel anticancer metallodrugs consists in substituting Pt(II) with endogenous metal ions, with the aim of interfering at DNA level through alternative mechanisms compared to Pt(II)-based drugs (metalation), or by targeting completely different biological molecules and pathways. Moreover, the systemic toxicity of these compounds might be reduced exploiting the molecular machinery in charge of the transport and homeostasis of endogenous metal ions in biological systems [6].

Copper is an example of endogenous metal that have been studied under this perspective. It mainly serves as cofactor in several enzymes involved in different biochemical processes, such as energy production (cytochrome-c oxidase), oxidative damage prevention (superoxide dismutase), melanin production (tyrosinase) and blood coagulation (V and VIII coagulation factors). Copper absorption primarily takes place in the stomach and small intestine after being reduced as Cu(I) by ascorbate and cellular metalloreductases [7]. The distribution through the bloodstream is guaranteed by ceruloplasmin, albumin and transcuprein [8]. Cellular uptake of this metal ion occurs through the hCtr1 transport protein, which is also exploited by Pt(II)-based drugs for the same purpose [2]. Copper homeostasis in cells, tissues and organs is controlled through its blood transporters and cellular chaperones (e.g., GSH, ATOX-1, COX17 and CCS1), since an excess of free Copper ions can be potentially dangerous for human organism. It is believed that the toxicity of free Copper arises from its participation in ROS production, which is related to the accessibility of both Copper oxidation states (Cu(II) and Cu(I)) in biological conditions [9,10]. Excess of free Copper ions are correlated with the pathogenesis of Wilson disease, but it is also believed to promote tumor progression, metastasis, and angiogenesis [11]. In addition, high levels of Copper were found in serum and tissues of several types of human cancers [12,13].

Based on these findings, two different strategies are commonly followed in the development of novel anticancer Copper-based drugs: (1) sequestration of free Copper ions in excess by using metal chelators; (2) synthesis of Copper complexes that trigger cell death through accumulation of the metal ion and induction of ROS production [14].

The second strategy has been extensively followed in the last 40 years, since the discovery of Sigman et al. that the [Cu(phen)$_2$]$^+$ complex is able to damage DNA oxidatively, thus acting as an artificial nuclease [15]. These results have been successfully exploited in

the design of many DNA-targeting metals (e.g., Ruthenium, Rhodium) complexes bearing phen-based ligands [16,17].

Many reviews have covered the anticancer properties of a broad spectrum of Copper complexes, showing how the activity of these compounds is multi factored (e.g., proteasome, topo-isomerase inhibition, induction of the apoptosis, etc.) [6,18–23].

In this work, we would like to focus on the anticancer properties of mixed Cu(II) complexes bearing 1,10-phenanthroline (phen) or substituted phenanthrolines (phen-based ligands) and different classes of inorganic (e.g., Cl-, Br-, H_2O) and organic auxiliary ligands (e.g., carboxylic acids, α-amino acids, imines, etc.). The choice to highlight on Cu(II) complexes comes from the higher solubility, coordination numbers (typically 5 and 6) and geometries (square pyramidal, bipyramid trigonal, octahedral, all of them with different degrees of distortion) that Copper in this oxidation state can offer. The complexes here reported will be presented according to: (1) the auxiliary ligand (e.g., inorganic ligands, organic –S donor ligands, -N donor ligands); (2) number of Cu(II) centers; (3) increasing complexity in the structures of the compounds. For each metal complex, information regarding the tested cell lines and the mechanistic studies will be reported and discussed.

2. Mixed Cu(II) Phen-Based Complexes
2.1. Inorganic Auxiliary Ligands

Mixed Cu(II) phenanthroline-based complexes having general formula $Cu(N-N^1)_x$ $(OH_2)_y(ClO_4)_z$ (Figure 2), where "$N-N^1$" are phen and some 5,6-disubstituted derivatives, were prepared and tested on a panel of solid and haematological cancer cells [24–26].
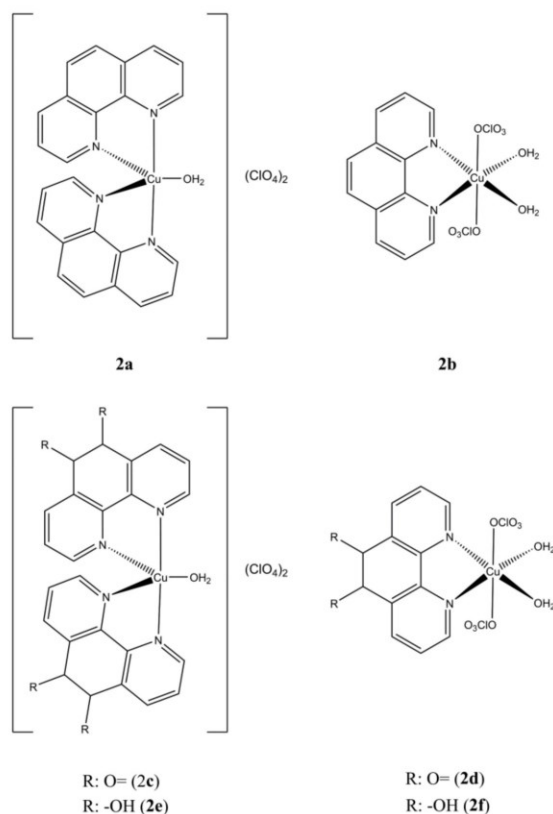
Figure 2. Structures of the $Cu(N-N^1)_x(OH_2)_y(ClO_4)_z$ complexes.

All the studied complexes show IC_{50} in the micro/sub-micromolar range, with complexes having two $N-N^1$ units that appeared more potent compared to complexes having only one $N-N^1$ unit. The potential selectivity, calculated taking the normal fibroblasts as reference, varies from a minimum 0.78 to a maximum of 19.2 according to the type and number of the phen-based moieties and the cancer cell line considered. All the studied compounds can interact with DNA, but the inversely correlated relation between DNA binding constants and anticancer potencies, brings to exclude that the biological properties observed would arise from a direct interaction with this target [25]. Recent results have partially unveiled the biological mechanism in ovarian (A-2780) cells of **2a**, which induces Endoplasmic Reticulum (ER) Stress by activating the pro-apoptotic branch of the Unfolded Protein Response (UPR), as observed by overexpression of typical biomarkers, such as PERK, IRE1 and DDIT3, and alleviation of cytotoxicity in co-administration with ER-stress modulator Taursodeoxycholic Acid (TUDCA) [27].

Shi et al. have synthesized a panel of mixed complexes having general formula $[Cu(LPTn)_x(X)_y](Y)_z$ (Figure 3), where LPTn are phenanthroline derivatives having alkyl chains of different lengths.

3a: n = 1; X = NO$_3$, Cl; Y = NO$_3$
3b: n = 4; X = Cl; Y = Br
3c: n = 6; X = Cl; Y = Br
3d: n = 8; X = Cl; Y = Br
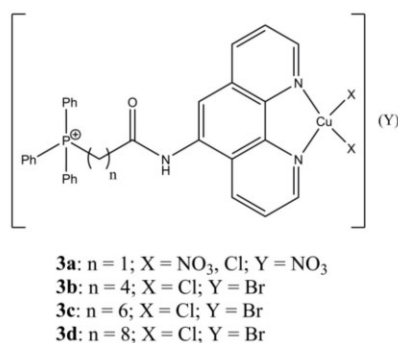
Figure 3. Structures of the $[Cu(LPTn)_x(X)_y](Y)_z$ complexes.

Both cellular uptake and activity on cervical (Hela) and ovarian (SKOV-3) cancer cells appear directly correlated with the lipophilicity of the LPTn ligand, while all of them showed mild toxicity towards healthy HK-2 cells. Intracellular ROS production and lipophilicity show a different correlation depending on the cell line, suggesting that the redox properties are not the determinant factors in the cell death induction. The most promising complex of the series (**3d**) has shown to possess anti metastatic activity, via inhibition of MMP-2 expression, in SKOV-3 cells. In addition, it also possesses antiangiogenic activity, via downregulation of VEGFR-1 expression, blocking of sprouts and tubes formation, in HUV-EC-C cells [28].

Table 1 summarizes the IC_{50} values reported for the compounds so far discussed.

Table 1. IC_{50} values of compounds **2a–3d**.

Compound	Cell Line (IC$_{50}$, μM)	Reference
2a	24 h: CCRF-CEM (1.25 ± 0.2), A-2780 (0.94 ± 0.04), CCRF-SB (0.50 ± 0.5), SKMES-1 (0.93 ± 0.6), DU-145 (1.6 ± 0.2), CRL-7065 (2.20 ± 0.03), HEK-293 (1.098), HEP-G2 (1.05 ± 0.01), A-2780 (0.5916)	[24,27,29]
2b	24 h: CCRF-CEM (3.2 ± 0.1), CCRF-SB (1.4 ± 0.1), SKMES-1 (1.9 ± 0.1), DU-145 (2.6 ± 0.3), CRL-7065 (1.34 ± 0.03), HEP-G2 (2.90 ± 0.03),	[24,25]

Table 1. *Cont.*

Compound	Cell Line (IC$_{50}$, μM)	Reference
2c	24 h: CCRF-CEM (0.80 ± 0.02), CCRF-SB (0.42 ± 0.01), SKMES-1 (1.20 ± 0.01), DU-145 (1.16 ± 0.02), HEP-G2 (0.67 ± 0.02), CRL-7065 (2.47 ± 0.02)	[25]
2d	24 h: CCRF-CEM (3.80 ± 0.02), CCRF-SB (1.21 ± 0.01), SKMES-1 (3.10 ± 0.01), DU-145 (4.10 ± 0.01), HEP-G2 (1.70 ± 0.02), CRL-7065 (6.30 ± 0.01)	[25]
2e	24 h: CCRF-CEM (0.09 ± 0.04), CCRF-SB (0.07 ± 0.03), SKMES-1 (0.54 ± 0.01), DU-145 (0.93 ± 0.01), HEP-G2 (1.20 ± 0.01), CRL-7065 (1.34 ± 0.03)	[25]
2f	24 h: CCRF-CEM (0.18 ± 0.01), CCRF-SB (0.20 ± 0.01), SKMES-1 (2.25 ± 0.02), DU-145 (4.00 ± 0.02), HEP-G2 (3.60 ± 0.01), CRL-7065 (3.10 ± 0.01)	[25]
3a	48 h: HeLa (45.37 ± 1.98), SKOV-3 (32.28 ± 2.43), HK-2 (65.24 ± 2.68)	[28]
3b	48 h: HeLa (33.60 ± 1.53), SKOV-3 (21.81 ± 1.57), HK-2 (57.25 ± 1.43)	[28]
3c	48 h: HeLa (15.97 ± 1.67), SKOV-3 (12.45 ± 1.36), HK-2 (36.18 ± 1.82)	[28]
3d	48 h: HeLa (7.32 ± 1.35), SKOV-3 (6.56 ± 1.28), HK-2 (21.57 ± 1.26)	[28]

2.2. Organic-S Donating Auxiliary Ligands

A series of mixed Cu(II) phenanthroline complexes of general formula [Cu(phen)$_2$ (ITHn)](ClO$_4$)$_2$, where ITHn are imidazolidine-2-thione and some of its *N*-alkylated derivatives (Figure 4a–d), have been prepared and evaluated in vitro [24]. The tested compounds show anticancer potencies in the sub-micromolar range, while the ITHn ligands are inactive (IC$_{50}$ > 100 μM) towards the same cell lines.

4a: R$_1$ = R$_2$ = -H; (ITH1)
4b: R$_1$ = H; R$_2$ = -CH$_3$ (ITH2)
4c: R$_1$ = H; R$_2$ = -CH$_2$CH$_3$ (ITH3)
4d: R$_1$ = R$_2$ = -CH$_3$ (ITH4)

4e
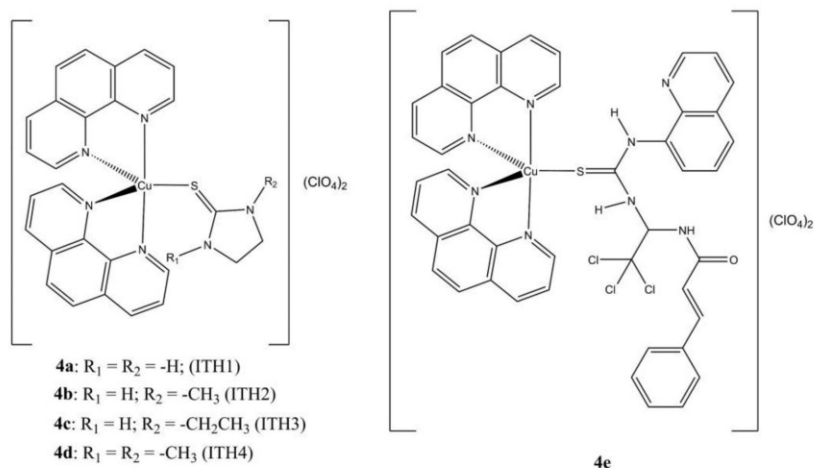
Figure 4. Structures of the [Cu(phen)$_2$(ITHn)](ClO$_4$)$_2$ (**a**–**d**) and [Cu(phen)$_2$(SAL)](ClO$_4$)$_2$ (**e**) complexes.

As shown for **2a**, complexes **4a–c** exert their anticancer properties in A-2780 cells by inducing ER-stress and activating the pro-apoptotic branch of UPR. The cytotoxicity of

these compounds, which differs according to the alkyl groups in the ITHn backbone, can be reduced by co-administration with TUDCA [27].

Since the ITH1 structure resembles the one of ER-stress modulator Salubrinal (SAL), the same authors explored the possibility of a chemical reactivity between SAL and **2a**, obtaining the novel mixed complex **4e** ([Cu(phen)$_2$(SAL)](ClO$_4$)$_2$). In contrast with SAL, this complex shows anticancer potency in the sub-micromolar range (82-fold and 1.4-fold higher than SAL and **2a** in A-2780, respectively), induces ER-stress mediated cell death (BiP, and DDIT3 overexpression) and DNA damage in A-2780 and SKOV-3 cells, as evidenced by the massive intracellular production of the phosphorylated histone γ-H2AX. The cytotoxicity of **4e** can be alleviated by co-administration with TUDCA, as previously seen with **2a** and **4a–c** [30].

IC$_{50}$ values for the selected compounds are reported in Table 2.

Table 2. IC$_{50}$ values of compounds **4a–4e**.

Compound	Cell line (IC$_{50}$, µM)	Reference
4a	24 h: CCRF-CEM (0.8 ± 0.8), CCRF-SB (0.70 ± 0.7), SKMES-1 (0.85 ± 0.04), DU-145 (1.6 ± 0.2), HEK-293 (1.181), A-2780 (0.4342), SKOV-3 (1.524)	[24,27]
4b	24 h: CCRF-CEM (0.8 ± 0.8), CCRF-SB (0.60 ± 0.5), SKMES-1 (0.97 ± 0.7), DU-145 (3.6 ± 0.4), HEK-293 (1.293), A-2780 (0.4385), SKOV-3 (1.381)	[24,27]
4c	24 h: CCRF-CEM (1.1 ± 0.1), CCRF-SB (1.3 ± 0.1), SKMES-1 (0.9 ± 0.1), DU-145 (1.5 ± 0.2), HEK-293 (1.097), A-2780 (0.2865), SKOV-3 (1.524)	[24,27]
4d	24 h: CCRF-CEM (0.90 ± 0.09), CCRF-SB (0.80 ± 0.07), SKMES-1 (0.7 ± 0.1), DU-145 (1.50 ± 0.05)	[24]
4e	24 h: A-2780 (0.68 ± 0.05)	[29]

2.3. Organic-N Donating Auxiliary Ligands

Fantoni et al. have prepared a series of Cu(II)-DPA (DPA is di(2-pycolylamine)) complexes having general formula [Cu(N-N^2)(DPA)](ClO$_4$)$_2$ (Figure 5), where N-N^2 are phen, DPQ and DPPZ [30].
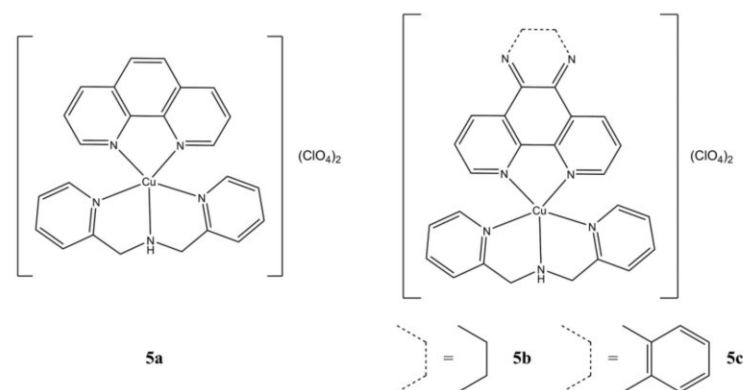
Figure 5. Structures of the [Cu(N-N^2)(DPA)](ClO$_4$)$_2$ complexes.

The studied compounds are active against pancreatic (PIN 127, MIA PaCa-2, Panc-1, HPAC) cancer cells at micromolar concentration range. In particular, **5c** shows higher anticancer potency in PIN 127 (5 times) and Panc-1 (3 times) cells compared to the clinical drug oxaliplatin. Ct-DNA binding experiments suggest that these complexes would

preferentially interact in the G-C rich regions of the minor groove. Oxidative plasmid DNA damage mediated by OH· and $O_2^{-\cdot}$ radicals is also observed. The DNA repairing action mediated by endonucleases (Endo III, IV and V) and glycosylases (Fpg) is differently inhibited according to the type of N-N^2 unit. Interestingly, in association with the repairing hAAG enzyme, the extent of the DNA damage is even increased according to the degree of planarity of the N-N^2 ligand. IC_{50} values from cell viability studies are reported in Table 3.

Table 3. IC_{50} values of compounds **5a–5c**.

Compound	Cell Line (IC_{50}, μM)	Reference
5a	120 h: PIN127 (1.05 ± 0.15), MIA PaCa-2 (2.97 ± 1.27), Panc-1 (1.40 ± 0.33), HPAC (1.27 ± 0.56)	[30]
5b	120 h: PIN127 (0.93 ± 0.02), MIA PaCa-2 (1.06 ± 0.47), Panc-1 (0.57 ± 0.19), HPAC (0.44 ± 0.05)	[30]
5c	120 h: PIN127 (0.20 ± 0.01), Panc-1 (0.48 ± 0.13), HPAC (0.32 ± 0.12)	[30]

2.4. Organic-O Donating Auxiliary Ligands

With the aim of enhancing the target specificity of $[Cu(phen)_2](NO_3)_2$, Prisecaru et al. introduced some simple carboxylic acids in the $[Cu(phen)_2]^{2+}$ core obtaining a small library of mixed Cu(II) complexes having general formula $[Cu(phen)_2(CAn)](NO_3)$ (Figure 6) [31].
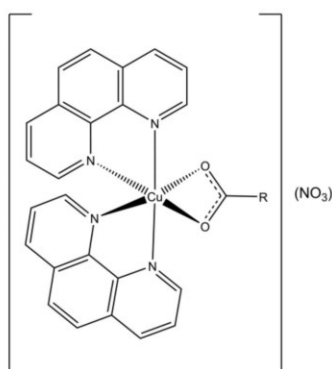
6a: R = -H (CA1)   **6b**: R = -CH$_3$ (CA2)
6c: R = -CH$_2$CH$_3$ (CA3)   **6d**: R = -CH(CH$_3$)$_2$ (CA4)
          6e: R = -C(CH$_3$)$_3$ (CA5)

Figure 6. Structures of the $[Cu(phen)_2(CAn)](NO_3)_2$ complexes.

The introduction of an auxiliary carboxylate moiety allowed to increase the affinity towards ct-DNA while reducing that towards albumin. The studied complexes show DNA cleavage activity upon activation by an exogenous reductant (sodium ascorbate) and oxidant (H_2O_2), which is believed to arise by a combination of a SOD mimetic activity with OH· production by Fenton reaction. DNA damage was also evidenced in SKOV-3 cells by accumulation of phosphorylated γ-H2AX. The studied compounds show IC_{50} values in the sub-micromolar range.

The mixed Cu(II) complex $[Cu(phen)_2(4-Mecdoa)]$ (Figure 7) is active towards kidney (A-498) and liver (Hep-G2) cancer cells compared to cisplatin, while being less sensitive towards non-cancerous CHANG cells [32]. However, the same behaviour was not observed on healthy HK-2 lines, this complex appears to interfere with DNA synthesis without any

264

direct interaction with DNA itself. Cell death induction is switchable from apoptosis to necrosis in a dose-dependent manner.

7
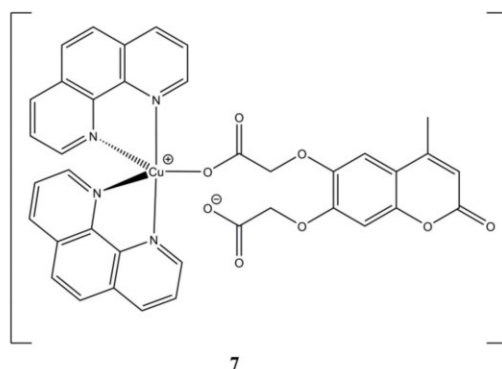
Figure 7. Structures of the [Cu(phen)$_2$(4-Mecdoa)] complex.

Kellet et al. used ftalic acids to prepare the mixed mononuclear [Cu(phen)$_2$(PHTn)] (n = 1,2; Figure 8a,b) and binuclear [Cu$_2$(phen)$_4$(μ-PHT3)](PHT3) (Figure 8c) complexes [33].
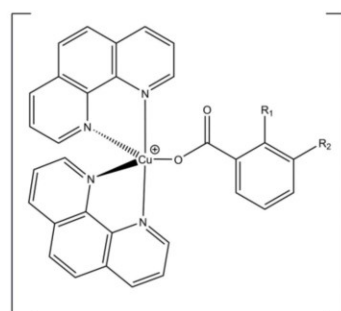
PHT1: R$_1$ = -COO$^-$; R$_2$ = -H (**8a**)
PHT2 :R$_1$ = -H ; R$_2$ = -COO$^-$ (**8b**)

8c
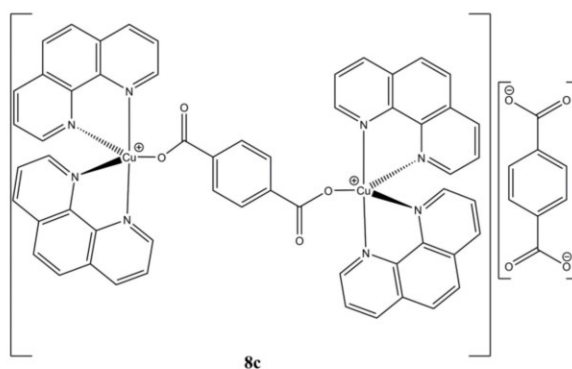
Figure 8. Structures of [Cu(phen)$_2$(PHTn)] (**a**,**b**) and [Cu$_2$(phen)$_4$(μ-PHT3)](PHT3) (**c**) complexes.

These compounds show higher anticancer potencies (at micromolar level) in breast (MCF-7), prostate (DU145) and colon (HT29) cancer cells compared to the approved drugs

265

cisplatin and mitoxantrone, while the Cu(II) complexes of the same PHTn ligands are devoid of any activity. In addition, they can cleave DNA without the presence of exogenous oxidant or reducing agents.

Zhang et al. reported the synthesis and anticancer activity of mixed Cu(II) complexes having general formula [Cu(ICAn)$_2$(phen)], where ICAn are indole 3-carboxylic acids having different alkyl spacers (Figure 9) [34].

ICA1: x = 1 (**9a**)
ICA2: x = 2 (**9b**)
ICA3: x = 3 (**9c**)
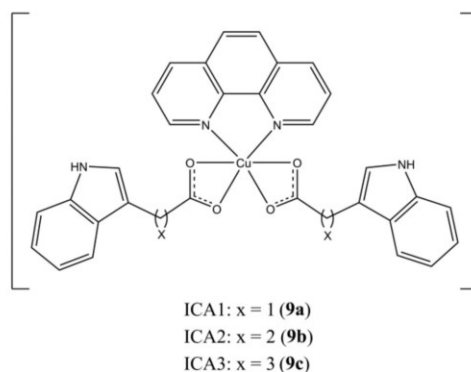
Figure 9. Structures of the [Cu(ICAn)$_2$(phen)] complexes.

These complexes can induce apoptosis in MBA-MDB-231 breast tumours by targeting the Ubiquitin Proteasome Pathway (UPP). It is known that cancer cells are more sensible to UPP inhibition than healthy ones, due to the involvement of this pathway in many carcinogenic processes (e.g., proliferation, apoptosis, and metastasis). In particular, these complexes act at proteasome level by inhibiting the chymotrypsin-like (CT) activity of human 20S proteasome.

Boodram et al. prepared a panel of mixed complexes [Cu(indomethacin)$_2$(5-Rphen)], where the Cu(II) centre is coordinated by the NSAID drug Indomethacin and different 5-substituted phenanthrolines (Figure 10) [35].

R = -H (**10a**)   R = -O(CH$_2$)$_3$N(CH$_3$)$_2$ (**10d**)

R = -CH$_3$ (**10b**)   R = -O(CH$_2$)$_2$N(CH$_2$CH$_3$)$_2$ (**10e**)

R = -O(CH$_2$)$_2$N(CH$_3$)$_2$ (**10c**)
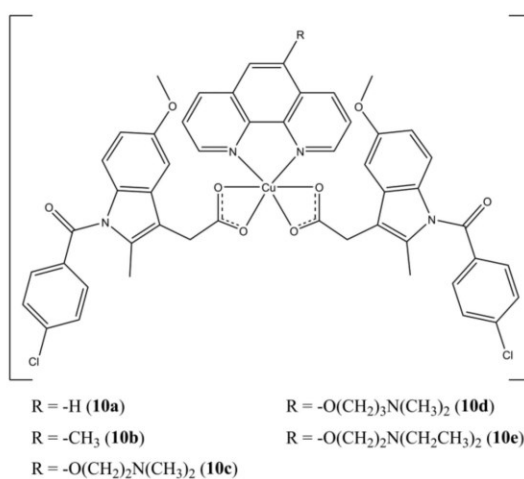
Figure 10. Structures of the [Cu(indomethacin)$_2$(5-Rphen)] complexes.

The studied complexes are active towards HMLER breast cancer cells at micromolar level. Notably, complexes **10c,d** show selectivity for HMLER-shEcad cells, which possess

266

a higher cancer stem cells (CSCs) content (around 90%) over HLMLER ones (5–8%). The ability of targeting breast CSCs is quite important since these sub-populations of cancer cells are often resistant towards conventional clinical treatments (surgical removal followed by chemo or radiotherapy) and are involved in the resurgence of secondary metastatic breast tumours. The studied compounds can induce DNA damage, as shown by self-activating DNA cleavage activity, cellular ROS production (mainly hydroxyl radicals), and accumulation of γ-H2AX. In addition, they are to target cyclooxygenases by selectively inhibiting COX-2, whose expression is enhanced in several mammary carcinomas.

In a series of homo and heteroleptic Cu(II) complexes with 4,5-dichloro-isothiazole 3-carboxylic acid (4,5-dCl-ICA), compounds [Cu(phen)(4,5-dCl-ICA)$_2$] and [Cu(4,7-diMephen)(4,5-dCl-ICA)$_2$] (Figure 11) proved to be the most potent towards Hep-2 (IC$_{50}$ of 3.06 and 0.97 μM, respectively) and MCF-7 (IC$_{50}$ of 4.2 and 1.8 μM, respectively) cells [36].

11a   **11b**
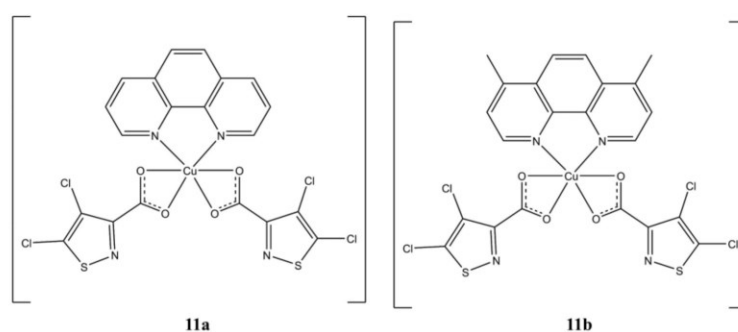
Figure 11. Structures of [Cu(phen)(4,5-dCl-ICA)$_2$] (**a**) and [Cu(4,7-diMephen)(4,5-dCl-ICA)$_2$] (**b**).

The morphological changes observed in cells after treatment with these compounds are indicative of an apoptotic cell death. These complexes can interact with DNA (with K_b in agreement with cytotoxic data) but are also able to inhibit the activity of different Cytochrome P450 families in a dose-dependent manner.

The complex [Cu(phen)(trop)(Cl)], bearing a tropolone molecule as auxiliary ligand (Figure 12a), showed the highest anticancer potency (at micromolar level) among a series of binary and ternary Cu(II) tropolone-based complexes [37]. This compound induces cell death in gastric (MGC80-3) cancer cells mainly through a caspase-regulated apoptotic pathway with the induction of ROS production, alteration of the mitochondrial potential, overexpression of many apoptotic signallers (e.g., Bax, cytochrome C, Bak, apaf1). The induction of autophagy in the same cell lines is also observed.

In a screening of novel M(II) (Cu(II), Ni(II), Co(II)) quercetin-based anticancer complexes, Gençkal et al. identified the compound [Cu(phen)(H$_4$Que)(Cl)] (Figure 12b) as one of the most promising against MCF-7 and MBA-MDB-231 breast cancers. This compound triggers cell death through caspase-mediated apoptosis, with increasing in cellular ROS content and depolarization of the mitochondrial membrane [38].

The IC$_{50}$ for the compounds discussed in this section are summarized in Table 4.
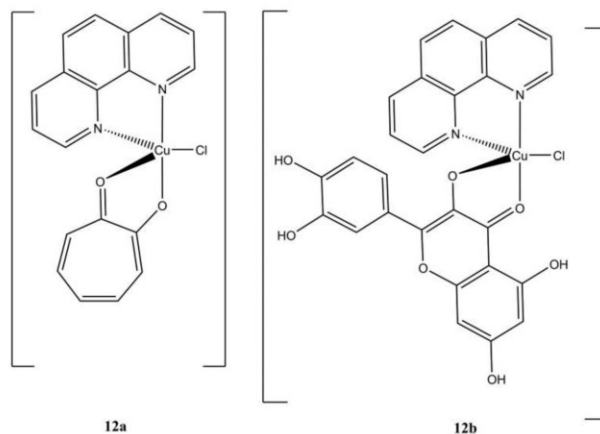
Figure 12. Structures of complexes [Cu(phen)(trop)(Cl)] (**a**) and [Cu(phen)(H$_4$Que)(Cl)] (**b**).

Table 4. IC$_{50}$ values of compounds **6a–12b**.

Compound	Cell Line (IC$_{50}$, μM)	Reference
6a	24 h: PC3 (>200), SKOV-3 (2.28 ± 0.14), PNT1A (52.01 ± 7.02). 96 h: PC3 (4.32 ± 1.14), SKOV-3 (1.41 ± 0.07), PNT1A (1.98 ± 0.23)	[31]
6b	24 h: PC3 (>200), SKOV-3 (3.04 ± 0.19), PNT1A (75.02 ± 30.29). 96 h: PC3 (5.41 ± 3.01), SKOV-3 (2.05 ± 0.14), PNT1A (1.51 ± 0.18)	[31]
6c	24 h: PC3 (26.09 ± 1.56), SKOV-3 (3.02 ± 0.10), PNT1A (27.60 ± 11.37). 96 h: PC3 (2.25 ± 0.22), SKOV-3 (2.07 ± 0.19). 96 h, PNT1A (2.62± 0.66)	[31]
6d	24 h: PC3 (52.00 ± 12.70), SKOV-3 (2.86 ± 1.36), PNT1A (23.89 ± 3.74). 96 h: PC3 (2.31 ± 0.08), SKOV-3 (1.91 ± 0.09), PNT1A (2.05 ± 0.07)	[31]
6e	24 h: PC3 (3.26 ± 4.34), SKOV-3 (3.59 ± 0.10), PNT1A (14.56 ± 2.44). 96 h: PC3 (3.96 ± 1.45), SKOV-3 (1.78 ± 0.05), PNT1A (1.90 ± 0.21)	[31]
7	96 h: CHANG (11 ± 1.8), A-498 (2.0 ± 1.2), HK-2 (2.8 ± 0.8), HEP-G2 (1.3 ± 0.8)	[32]
8a	24 h: MCF-7 (44.9 ± 7.0), DU-145 (11.6 ± 4.5), HT29 (6.0 ± 0.4)	[33]
8b	24 h: MCF-7 (41.2 ± 1.4), DU-145 (10.6 ± 2.2), HT29 (5.8 ± 0.2)	[33]
8c	24 h: MCF-7 (7.9 ± 0.4), DU-145 (5.7 ± 0.2), HT29 (5.4 ± 0.3), SKOV-3 (6.7 ± 0.4), HS-832 (4.5 ± 0.2)	[33,39]
9a	24 h: MDA-MB-231 (4.20), MCF-7 (5.21)	[34]
9b	24 h: MDA-MB-231 (4.71), MCF-7 (6.29)	[34]
9c	24 h: MDA-MB-231 (5.31), MCF-7 (6.82)	[34]
10a	72 h: HMLER (4.4 ± 0.1), HMLER-shEcad (4.3 ± 0.1), 96 h: mammosphere (n.d.)	[35]
10b	72 h: HMLER (2.5 ± 0.2), HMLER-shEcad (2.5 ± 0.1), 96 h: mammosphere (n.d.)	[35]

Table 4. *Cont.*

Compound	Cell Line (IC$_{50}$, µM)	Reference
10c	72 h: HMLER (7.5 ± 1.4), HMLER-shEcad (2.7 ± 0.2), 96 h: mammosphere (16.6 ± 0.6)	[35]
10d	72 h: HMLER (7.4 ± 0.3), HMLER-shEcad (2.2 ± 0.5), 96 h: mammosphere (13.8 ± 0.8)	[35]
10e	72 h: HMLER (6.9 ± 1.4), HMLER-shEcad (4.2 ± 0.6), 96 h: mammosphere (26.3 ± 1.3)	[35]
11a	48 h: Hep2 (3.06 ± 0.07), MC7 (4.2 ± 0.2)	[36]
11b	48 h: Hep2 (0.97 ± 0.03), MC7 (1.8 ± 0.3)	[36]
12a	48 h: A-549 (4.5 + 0.1), Bel-7402 (4.5 ± 0.4), MGC80-3 (3.5 ± 0.9), T24 (4.2 ± 0.1), SKOV-3 (5.3 ± 0.6), NCI-H460 (4.3 ± 1.0), HL-7702 (4.8 ± 0.6)	[37]
12b	24 h: MCF-7 (20.0), MDA-MB-231 (10.2). 48 h: MCF-7 (2.4), MDA-MB-231 (5.4)	[38]

2.5. Organic Mixed Donating Auxiliary Ligands

The mixed Cu(II)-phenanthroline complex "Cas-II Gly" [Cu(4,7-diMephen)(Gly)](NO$_3$) (Figure 13) belongs to the Casiopeinas®, a class of complexes having general formula [Cu(N-N)(A-A)](NO$_3$) (where "N-N" is a neutral di-imine ligand and "A-A" an amino acid) developed by Ruiz-Azuara et al. [40].
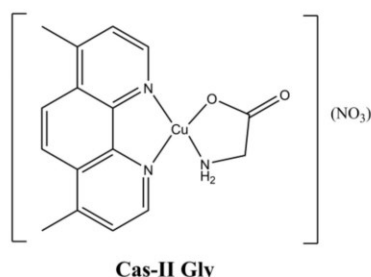
Cas-II Gly

Figure 13. Structure of Cas-II Gly ([Cu(4,7-diMephen)(Gly)](NO$_3$)).

These complexes have been extensively studied on both in vitro and in vivo models, showing that their anticancer activity is exerted through ROS accumulation that causes mitochondrial dysfunction, DNA damage and induces apoptosis [41–47]. Some of these derivatives have been selected as candidates for Phase I clinical trials [48–50].

Based on these results, different Cu(II) complexes bearing phen-based ligands and amino acids have been prepared and assayed for their anticancer properties. For instance, the complex [Cu(5HTP)(phen)(H$_2$O)](NO$_3$) (5HTP is 5-hydroxytryptophan) reported by Naso et al. (Figure 14), shows anticancer activity in the micromolar range (IC$_{50}$ of 3.6 µM) in A-549 cells, while being devoid of any cytotoxic activity in healthy MRC-5 cells.

The authors demonstrated how the anticancer activity of this compound is exerted through cellular ROS production, GSH depletion and alteration of mitochondrial potential. The complex shows also antimetastatic activity on A-549 cells with inhibition of cells adhesion, migration, and invasion [51].

Karpagam et al. prepared a series of Cu(II) Proline-based complexes having general formula [Cu(L-pro)(N-N^3)(H$_2$O)$_n$](ClO$_4$) (n = 0,1) [52]. The insertion of a phenanthroline-based ligand (Figure 15) generally increases the anticancer potency (A-549 cell lines) compared to the bipyridine-based analogues. Compounds **15b** and **15d** proved to be the most promising in terms of potency (IC$_{50}$ of 1.4 and 1.3 µM, respectively), showing the

269

importance of the substitution pattern in the 5th and 6th position of the phenanthroline backbone. Cell death induction mainly take place through apoptosis induction, with cellular overexpression of ROS.
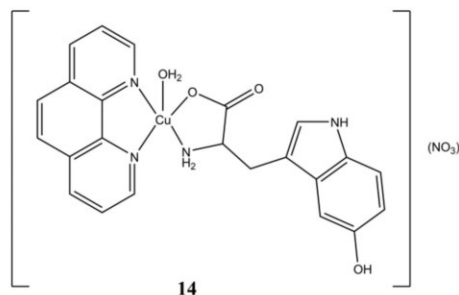
Figure 14. Structure of [Cu(5HTP)(phen)(H$_2$O)](NO$_3$).

R$_1$ = ...= R$_6$ = -H (**15a**)

R$_1$ = R$_2$ = R$_5$ = R$_6$ = -H; R$_3$ = R$_4$ = -CH$_3$ (**15b**)

R$_1$ = R$_2$ = R$_5$ = R$_6$ = -CH$_3$; R$_3$ = R$_4$ = -H (**15c**)
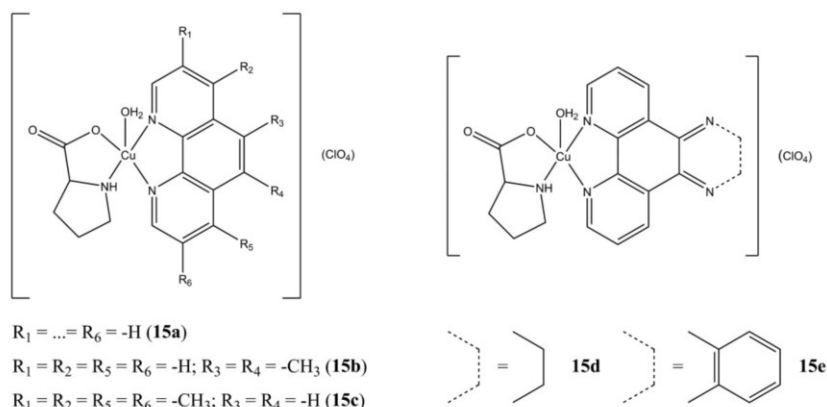
Figure 15. Structures of "phen-based" [Cu(L-pro)(N-N^3)(H$_2$O)$_n$](ClO$_4$) complexes.

The panel of complexes [Cu(phen)(AAn)(H$_2$O)](NO$_3$) ("AAn" are glycine and different methylated glycine derivatives) developed by Seng et al. (Figure 16) show selectivity towards cancerous nasopharyngeal HK1 cells rather than healthy NP69 ones [53]. Derivatives **16c** and **16d** are the most active (IC$_{50}$ of 2.2 µM for both) and selective (Selectivity Index SI > 11.4). The studied compounds show moderate affinity towards ct-DNA, with preferential interaction towards G-C sites. Inhibition towards DNA Topo1 in a dose-dependent manner is also evidenced.

Li et al. prepared a series of heteroleptic Cu(II) complexes having different α-amino acids and the fused phenanthroline derivative OH-PIP (4-(2H-imidazo [4,5-f][1,10]phenanthrolin-2-yl)phenol) as ligands (Figure 17) [54].

These compounds show anticancer potency at micromolar/sub-micromolar concentrations against triple negative (MCF-7, MDA-MB-231, CAL-51) breast cancers. The best activity was observed for CAL-51, with IC$_{50}$ values in the 0.082–0.69 µM range. The complexes here reported show higher potencies compared to clinically approved carboplatin and induces apoptotic cell death by interfering at UPP level (inhibition of CT-like activity of 20S proteasome, PARP cleavage). The most promising complexes of the series (**17c** and **17e**) are also able to significantly reduce the percentage of different triple negative stem cancer sub-populations.

270

R₁ = ...= R₃ = -H (**16a**)   R₁ = -CH₃; R₂ = R₃ = -H (**16b**)

R₁ = R₂ = -CH₃; R₃ = -H (**16c**)   R₁ = R₂ = -H; R₃ = -CH₃ (**16d**)
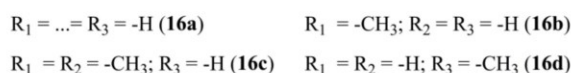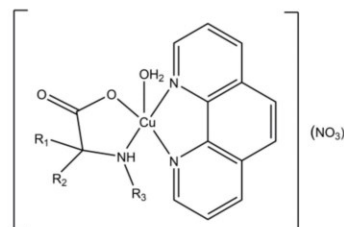
Figure 16. Structures of [Cu(phen)(AAn)(H₂O)](NO₃) complexes.

R = -CH₂(C₆H₅), n = 0 (**17a**)

R = -CH₃, n = 1 (**17b**)

R = -H, Y = NO₃, n = 2 (**17c**)

R = -(CH₂)₂SCH₃, Y = PF₆, n = 2 (**17d**)

R = -(CH₂)₂CONH₂, Y = Cl, n = 3 (**17e**)
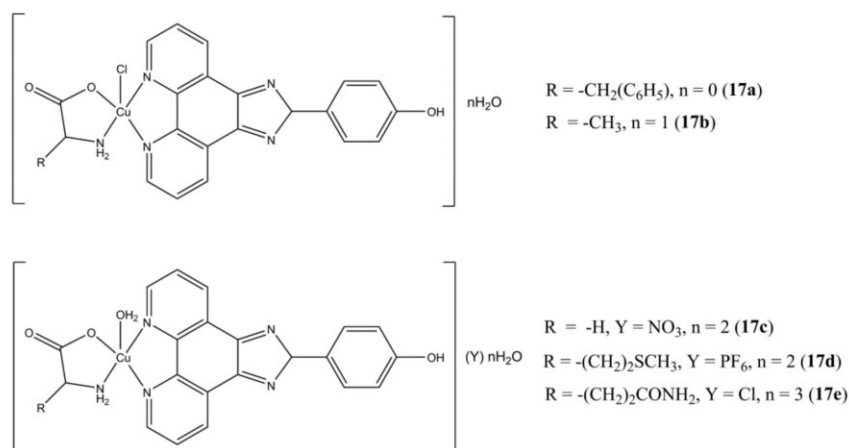
Figure 17. Structures of the Cu(II)–(OH-PIP) based complexes.

Facchin et al. have been focusing on the design and synthesis of ternary Cu(II) complexes bearing phen-based molecules and L-dipeptides [55]. For instance, compounds of general formula [Cu(L-dipeptide)(phen)]·nH₂O (Figure 18) have been screened for anticancer activity in cervical (Hela), breast (MCF-7) and lung (A-549) cancer cells showing anticancer potencies in the micromolar concentration range [56]. Preliminary studies on Albumin and ct-DNA interaction with the studied molecules show low to moderate affinity towards these biomolecules, with ct-DNA binding constants that appear to not be correlated with neither cytotoxicity nor lipophilicity. Interestingly, the author experimentally evaluated the lipophilicity of these molecules, pointing out how this parameter is influenced not only by the number and types of apolar groups (e.g., methylene, phenyl rings), but also on the spatial arrangement of the complexes, as evidenced for compounds **18c** and **18d**, where the auxiliary ligands are the Ala-Phe and Phe-Ala L-dipeptides, respectively.

The chiral Cu(II) complexes [Cu(phen)(L-Val)(OH₂)](NO₃)·2H₂O (Figure 19a) and [Cu(phen)(D-Val)(ONO₂)]·3H₂O (Figure 19b) of Arjmand et al. shows anticancer potency in the micromolar order on breast (MCF-7), pancreatic (BxPC3, AsPC1) and liver (Huh7) cancer cells. Notably, these compounds are able to target G-quadruplex DNA (G4 DNA) by cleaving it at selective sites. In general, compounds that can interfere at G4 DNA level (G4 ligands) are preferred since this interaction will result in telomerase inhibition, whose activity is up regulated in cancer cells while being silent in healthy ones. The inhibition of this enzymatic pathway will result in accumulation of shorter telomers and subsequent induction of apoptosis [57].

271
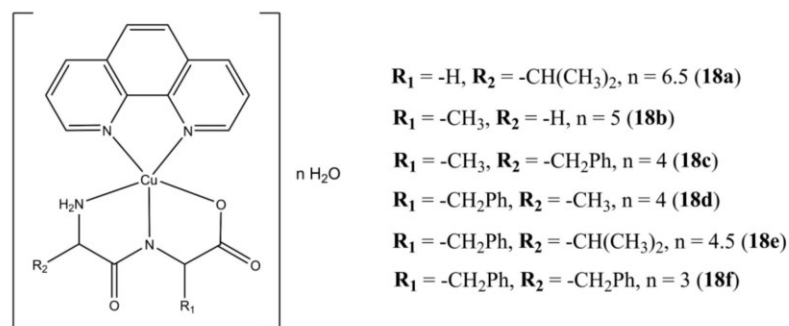
Figure 18. Structure of the [Cu(L-dipeptide)(phen)]·nH_2O complexes.

R_1 = -H, R_2 = -CH(CH$_3$)$_2$, n = 6.5 (**18a**)

R_1 = -CH$_3$, R_2 = -H, n = 5 (**18b**)

R_1 = -CH$_3$, R_2 = -CH$_2$Ph, n = 4 (**18c**)

R_1 = -CH$_2$Ph, R_2 = -CH$_3$, n = 4 (**18d**)

R_1 = -CH$_2$Ph, R_2 = -CH(CH$_3$)$_2$, n = 4.5 (**18e**)

R_1 = -CH$_2$Ph, R_2 = -CH$_2$Ph, n = 3 (**18f**)
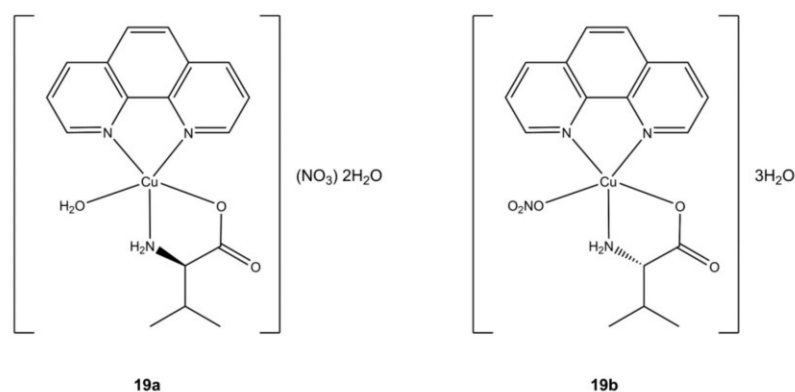
Figure 19. Structure of the [Cu(L-dipeptide)(phen)]·nH_2O complexes.

Acilan et al. prepared a series of [Cu(Sal-Gly)(N-N^4)] complexes (Figure 20), where Sal-Gly is the *O,N,O* Schiff Base obtained from Salicylaldehyde and Glycine, while the N-N^4 ligands are phen, 1,10-phenanthroline-5-amine, 5,6-diepoxy-1,10-phenanthroline [58].

Figure 20. Structures of the [Cu(Sal-Gly)(N-N^4)] complexes.

The complexes show dose and time-dependent micromolar cytotoxicity towards cancerous (A-549, HCT-116, HeLa, MBA-MB-231 and SHSY5Y) cells, while generally being less active against healthy HASMC1 and HASMC2 cells. Compound **20b** appears to be the most promising in terms of both anticancer potency and selectivity. Rapid apoptotic cell death in HCT-116 and HeLa cells was detected with induction of ROS production, depolarization of mitochondrial membrane, depletion of GSH and cellular DNA damage (γ-H2AX expression). Interestingly, gene-knockdown experiments on HeLa cells have

272

shown that apoptotic cell death doesn't rely on p53 status, thus supporting the hypothesis that these complexes might be potent also in p53 deficient cancer cell lines.

Goswami et al. has prepared and studied the photo-toxicity of a series of mixed Cu(II) complexes having neutral N-N^5 ligands (bipy, phen, DPQ, DPPZ), and tryptophan-based (Fc-Trp and Ph-Trp) ligands (Figure 21) [59].

N-N = phen (**21a**) N-N = DPQ (**21b**)   N-N = phen (**21d**) N-N = DPPZ (**21e**)

N-N = DPPZ(**21c**)
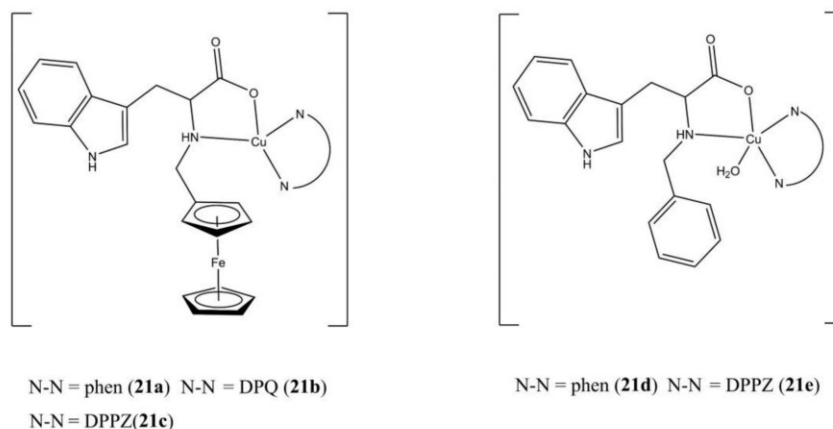
Figure 21. Structures of the phenanthroline-based [Cu(Fc-Trp)(N-N^5)](ClO$_4$) (**a–c**) and [Cu(Ph-Trp)(N-N^5)(OH$_2$)](ClO$_4$) (**d,e**) complexes.

These complexes generally possess enhanced anticancer potencies when exposed to visible light in both He-La (e.g., compound **21c** IC$_{50}$ of 8.95 and 1.29 μM in the dark and under visible light, respectively) and MCF-7 cells (e.g., compound **21c** IC$_{50}$ of 2.99 and 0.65 μM in the dark and under visible light, respectively). Cell death induction takes place through caspase-independent apoptotic mechanism, with higher apoptotic percentage when cells are exposed under visible light. The negligible anticancer activity observed for the [Zn(Fc-Trp)(DPPZ)](ClO$_4$) complex in HeLa cells (IC$_{50}$ > 80 μM) suggest the importance of the Cu(II) centre in exerting the anticancer activity. The studied compounds interact with ct-DNA as groove binders and can induce DNA cleavage through OH· production.

The two [Cu(HMCX)(phen)(OH$_2$)](ClO$_4$) complexes (Figure 22), where the two H$_2$MCX ligands are obtained by coupling L-Valine (X = V) and L-Leucine (X = L) with 7-hydroxy-4-methylcoumarin, intercalates ct-DNA and possess micromolar anticancer activity against human prostate (PC3), liver (L02) and myeloid leukemia (HL-60) cancer cells [60].

R = -CH(CH$_3$)$_2$ (**22a**)   R = -CH$_2$CH(CH$_3$)$_2$ (**22b**)
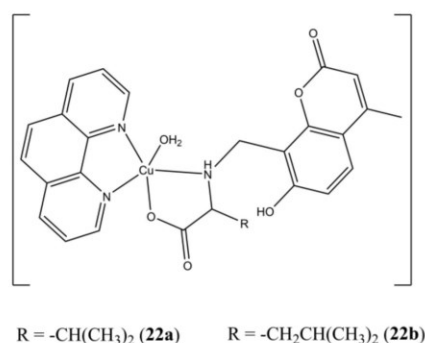
Figure 22. Structures of the [Cu(MCVH)(phen)(OH$_2$)](ClO$_4$) (**a**) and [Cu(MCLH)(phen)(OH$_2$)](ClO$_4$) (**b**) complexes.

The two [Cu(Ly)(bathophen)](PF$_6$) (Figure 23a,b) complexes (Ly are *O/S,N,S* Schiff bases, batophen is 4,7-diphenil-1,10-phenanthroline) show sub-micromolar anticancer potencies (IC$_{50}$ in the 0.21–0.32 µM range) against both HMLER and HMLER-shEcad cells, thus proving to be active against breast CSC subpopulations too. Both complexes show higher anticancer potencies compared to approved drugs cisplatin and salinomycin. Moreover, they can reduce the number and dimensions of 3D HMLER-shEcad mammospheres [61].

X = O ; Ly = L1 (**23a**)   X = S ; Ly = L2 (**23b**)   **23c**
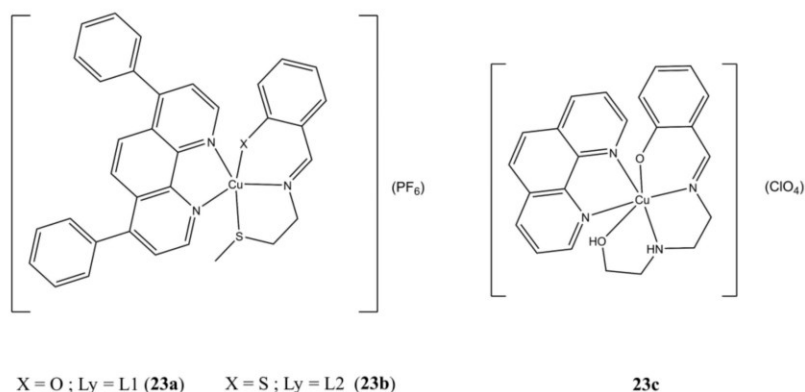
Figure 23. Structures of complexes [Cu(Ly)(bathophen)](PF$_6$) (**a**,**b**) and [Cu(tdp)(phen)](ClO$_4$) (**c**).

The Cu(II) complex [Cu(tdp)(phen)](ClO$_4$) (Figure 23c), where Htdp is 2-[(2-(2-hydroxyethylamino)-ethylimino)methyl]phenol, shows IC$_{50}$ in the micromolar range in both MCF-7 and MDA-MB-231 cancer cells. This compound induces alteration of mitochondrial potential, ROS overexpression, cell-cycle arrest (at S- and G2/M phases) and cellular DNA damage followed by apoptosis, which can turn to necrosis at higher concentrations or longer durations of treatments. Interestingly, the Bax/Bcl-2 expression ratios were differently affected in MCF (p53$^+$, ER$^+$) and MDA-MB-231 (p53$^-$, ER$^-$), thus suggesting a potential genotype-selective mechanism mediated by the p53 protein, which still need to be clarified though [62].

In a series of Cu(II) complexes having 5-(triphenylphosphoniummethyl)-salicylaldehyde benzoylhydrazone] chloride (L3) and *N,N*-diimine ligands, [Cu(phen)(L3)]Cl (Figure 24) proved to be the most promising against A-549 (IC$_{50}$ of 4.2 µM) and PC-3 (IC$_{50}$ of 3.2 µM) cancer cells. The studied complexes are able to interfere at DNA level through inhibition of DNA Topoisomerase-I (Topo-I) [63].

24
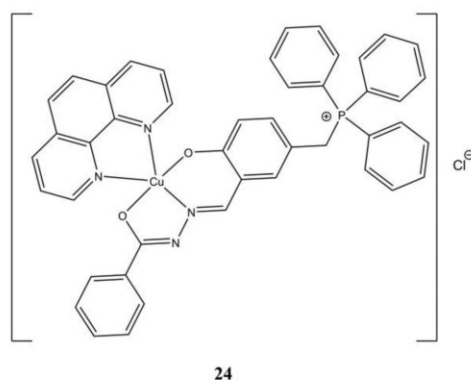
Figure 24. Structure of the [Cu(phen)(L3)]Cl complex.

The complex [Cu(pabt)(phen)](ClO$_4$) (Figure 25), where Hpabt is *N*-(2-mercaptophenyl)-2′-pyridylmethylenimine, shows anticancer activity at micromolar level against A-549 and A-431(IC$_{50}$ of 5.26 and 5.41 μM, respectively) cancer cells, while being less cytotoxic against healthy L132 and HaCaT cells (IC$_{50}$ of 7.47 and >10 μM, respectively). This compound shows intercalates ct-DNA showing good binding affinity and triggers cell death in A-549 through apoptosis [64].

25
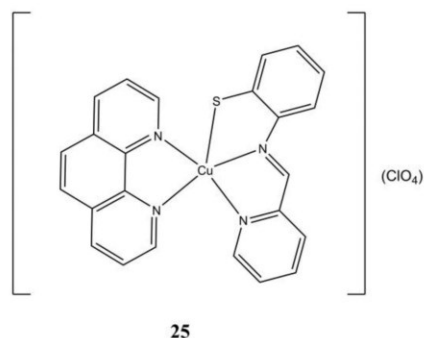
Figure 25. Structure of the [Cu(pabt)(phen)](ClO$_4$) complex.

IC$_{50}$ values for the compounds here reported are shown in Table 5.

Table 5. IC$_{50}$ values of compounds **Cas-II Gly–25**.

Compound	Cell Line (IC$_{50}$, μM)	Reference
Cas-II Gly	24 h: Hela (1.33), HCT-5 (3.7), SKL-U (4.97), MDA-MB-231 (1.55), SK-N-SH (18), MCF-7 (2.1), HCT-15 (2), HeLa (5.5), SiHa (5.5), CHP-212 (31.5), Lymphocytes (1720)	[46,47]
14	24 h: A-549 (3.6), MRC-5 (>100)	[51]
15a	24 h: A-549 (10 ± 0.01)	[52]
15b	24 h: A-549 (1.4 ± 0.20)	[52]
15c	24 h: A-549 (15.5 ± 0.05)	[52]
15d	24 h: A-549 (1.3 ± 0.05)	[52]
15e	24 h: A-549 (9.7 ± 0.20)	[52]
16a	24 h: HK1 (5.2), NP-69 (>25)	[53]
16b	24 h: HK1 (3.9), NP-69 (13.8)	[53]
16c	24 h: HK1 (2.2), NP-69 (>25)	[53]
16d	24 h: HK1 (2.2), NP-69 (>25)	[53]
17a	24 h: CAL-51 (0.52 ± 0.02), MDA-MB-231 (18.89 ± 1.23), MCF-7 (30.88 ± 2.56)	[54]
17b	24 h: CAL-51 (0.080 ± 0.004), MDA-MB-231 (8.35 ± 0.55), MCF-7 (17.08 ± 2.64)	[54]
17c	24 h: CAL-51 (0.37 ± 0.04), MDA-MB-231 (10.98 ± 0.95), MCF-7 (25.59 ± 2.10)	[54]
17d	24 h: CAL-51 (0.69 ± 0.04), MDA-MB-231 (4.92 ± 0.36), MCF-7 (18.99 ± 1.54)	[54]
17e	24 h: CAL-51 (0.27 ± 0.02), MDA-MB-231 (9.33 ± 0.84), MCF-7 (20.32 ± 2.01)	[54]

Table 5. *Cont.*

Compound	Cell Line (IC$_{50}$, μM)	Reference
18a	48 h: HeLa (15), MCF-7(18), A-548 (14)	[56]
18b	48 h: HeLa (7.5), MCF-7(16), A-548 (9.5)	[56]
18c	48 h: HeLa (2.2), MCF-7(1.0), A-548 (1.0)	[56]
18d	48 h: HeLa (7.7), MCF-7(13), A-548 (9.9)	[56]
18e	48 h: HeLa (3.1), MCF-7(7.4), A-548 (7.1)	[56]
18f	48 h: HeLa (5.2), MCF-7(9.6), A-548 (7.8)	[56]
19a	72 h: MCF-7 (2.15 ± 0.04), BxPC3 (2.46 ± 0.22), AsPC1 (2.29 ± 0.19), HuH7 (1.44 ± 0.05)	[57]
19b	72 h: MCF-7 (2.52 ± 0.12), BxPC3 (2.23 ± 0.60), AsPC1 (1.95 ± 0.10), HuH7 (1.43 ± 0.08)	[57]
20a	24 h: A-549 (>12.5), HCT 116 (11.30 ± 0.86), HeLa (7.30 ± 0.59), MDA-MB-231 (8.14 ± 0.02), SHSY5Y (>12.50), HASMC1 (10.81 ± 0.65), HASMC2 (6.31 ± 0.21). 72 h: A-549 (3.58 ± 0.67), HCT 116 (3.02 ± 1.11), HeLa (1.86 ± 1.34), MDA-MB-231 (3.05 ± 0.76), SHSY5Y (0.86 ± 0.99), HASMC1 (7.17 ± 0.13), HASMC2 (2.47 ± 0.32)	[58]
20b	24 h: A-549 (>12.5), HCT 116 (11.87 ± 0.66), HeLa (10.80 ± 1.63), MDA-MB-231 (>12.50), SHSY5Y (>12.50), HASMC1 (>12.5), HASMC2 (>12.5). 72 h: A-549 (1.93 ± 1.56), HCT 116 (1.79 ± 0.43), HeLa (3.13 ± 0.51), MDA-MB-231 (3.60 ± 0.37), SHSY5Y (1.08 ± 0.63), HASMC1 (>12.5), HASMC2 (>12.5)	[58]
20c	24 h: A-549 (>12.5), HCT 116 (>12.5), HeLa (9.16 ± 1.38), MDA-MB-231 (10.19 ± 0.49), SHSY5Y (>12.50), HASMC1 (>12.5), HASMC2 (7.42 ± 0.58). 72 h: A-549 (3.32 ± 0.40), HCT 116 (3.84 ± 0.10), HeLa (3.21 ± 0.53), MDA-MB-231 (3.70 ± 0.37), SHSY5Y (1.66 ± 0.25), HASMC1 (>12.5), HASMC2 (6.18 ± 0.34)	[58]
21a	24 h, dark: HeLa (9.57 ± 0.1), MCF-7 (4.78 ± 0.09). 24 h, visible light: HeLa (4.74 ± 0.1), MCF-7 (2.02 ± 0.07)	[59]
21b	24 h, dark: HeLa (24.45 ± 0.3), MCF-7 (>20). 24 h, visible light: HeLa (10.23 ± 0.3), MCF-7 (14.18 ± 0.1)	[59]
21c	24 h, dark: HeLa (8.95 ± 0.2), MCF-7 (2.99 ± 0.08). 24 h, visible light: HeLa (1.29 ± 0.04), MCF-7 (0.65 ± 0.03)	[59]
21d	24 h, dark: HeLa (8.80 ± 0.3), MCF-7 (8.74 ± 0.1). 24 h, visible light: HeLa (4.79 ± 0.2), MCF-7 (8.26 ± 0.2)	[59]
21e	24 h, dark: HeLa (6.10 ± 0.1), MCF-7 (4.13 ± 0.1). 24 h, visible light: HeLa (4.27 ± 0.1), MCF-7 (2.08 ± 0.09)	[59]
22a	72 h: PC3 (5.4), HL-60 (3.6), L02 (4.8)	[60]
22b	72 h: PC3 (3.1), HL-60 (2.4), L02 (3.4)	[60]
23a	72 h: HMLER (0.21 ± 0.01), HMLER-shEcad (0.32 ± 0.02), MCF10A (0.51 ± 0.01). 120 h: Mammosphere (0.54 ± 0.01)	[61]
23b	72 h: HMLER (0.22 ± 0.01), HMLER-shEcad (0.25 ± 0.01), 120 h: Mammosphere (1.26 ± 0.04)	[61]
23c	24 h: MCF-7 (1.6 ± 0.8), MDA-MB-231 (1.9 ± 1.2). 48 h: MCF-7 (1.2 ± 0.8), MDA-MB-231 (1.0 ± 0.9)	[62]
24	72 h: A-549 (4.2 ± 0.8), PC-3 (3.2 ± 0.2), MRC-5 (5.1 ± 0.3)	[63]
25	24 h: A-549 (5.26), A-431 (5.41), L132 (7.47)	[64]

276

2.6. Polynuclear Complexes

Prisecaru et al. focused their attention on the complex **8c** previously synthesized showing that its ability of cleaving DNA takes place oxidatively and in a non-specific manner. The complex shows comparable potency on both Platinum-resistant SKOV-3 (IC_{50} of 6.7 μM) cells and healthy HS-832 ones (IC_{50} of 4.5 μM) but is also 8 times more active than clinical drug Mitoxantrone on SKOV-3 cells (IC_{50} of 54.5 μM). Cellular ROS production in A-549 cells up to nanomolar concentration level was also observed [39].

The same authors have evaluated the anticancer properties of $[Cu_2(\mu\text{-oda})(phen)_4]$ $(ClO_4)_2$ (Figure 26), where the bridging ligand "oda" is octanedioic acid.

26
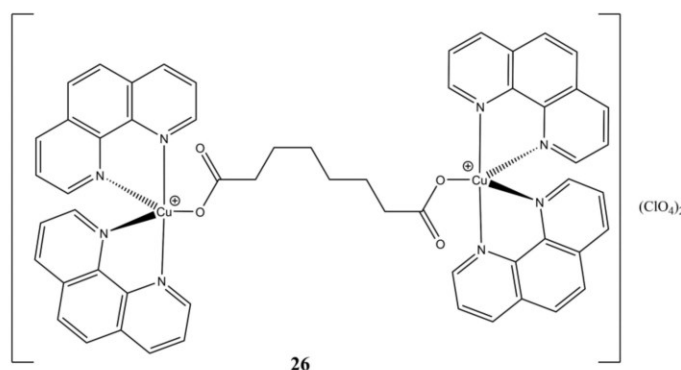
Figure 26. Structure of the $[Cu_2(\mu\text{-oda})(phen)_4](ClO_4)_2$ complex.

This complex shows time and concentration dependent (from low micromolar to nanomolar at 24 and 96 h of treatment, respectively) cytotoxic activity towards colorectal HT29, SW480 and SW620 cancer cells. In vivo drug tolerability studies on *G. Melonella* larvae shows that the complex is better tolerated than cisplatin in the 200–1000 μg/mL concentration range. The reported compound shows good ct-DNA affinity, self-activating DNA cleavage ability in presence of oxygen, along with artificial SOD activity and cellular ROS induction ability. The authors combined these experimental evidence and proposed a model of DNA cleavage based on the formation of reduced $[Cu(phen)_2]^+$ complex and a π carboxylate radical, which can oxidatively damage DNA in multiple ways. For instance, the carboxylate radical and/or its alkyl product of decarboxylation might abstract a hydrogen from the DNA phosphodiester backbone, while the $[Cu(phen)_2]^+$ complex might induce DNA breaks through aerobic-generated oxo and hydroxo complexes [65].

Parsekar et al. obtained the two binuclear Cu(II) complexes [Cu(phen)(SCH)Cu(OAc)] and $[Cu_2(SCH)(phen)_2](OAc)$ by mixing $Cu(OAC)_2$, phen and the SCH ligand (1,5-bis(salicylidene)carbohydrazide) in different molar ratios (Figure 27) [66].

Both complexes are cytotoxic (micromolar level) towards cancerous A-549 and MCF-7 cancer cells and to a lower extent towards healthy HaCaT cells. Cellular growth is arrested mainly at G2/M phase and induction of cell death can switch from early to late apoptosis/necrosis in a dose-dependent manner. Both complexes can intercalate ct-DNA and inducing both hydrolytic and oxidative DNA cleavages. Interestingly, increase in ROS production is evidenced in A-549 while the opposite is observed in MCF-7 lines.

The binuclear $[Cu_2(L4)(phen)](ClO_4)$ complex (Figure 28) can be reduced by GSH, and in turn catalyze the conversion of H_2O_2 to hydroxy radicals, as demonstrated at both spectroscopic and at cellular level. This complex is cytotoxic at micromolar level towards 4T1, A-549, HepG2 and MCF-7 cancer cells and to a lower extent towards healthy COS-7 cells. This compound arrest cell cycle at G0/G1 phase and induces cell death through apoptosis. The dual ability of **26** in depleting the cellular antioxidant GSH and producing ROS through H_2O_2 (often overexpressed in tumorigenic cells) makes this compound a potential candidate for applications in chemo-dynamic therapy [67].
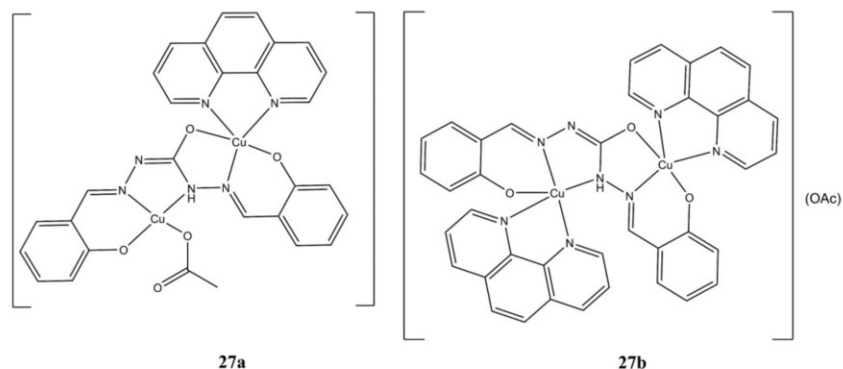
Figure 27. Structure of complexes [Cu(phen)(SCH)Cu(OAc)] (**a**) and [Cu$_2$(SCH)(phen)$_2$](OAc) (**b**).
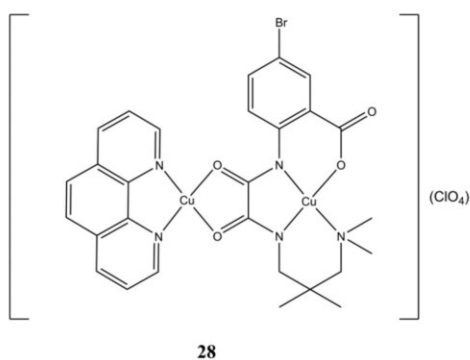
Figure 28. Structure of the [Cu$_2$(L4)(phen)](ClO$_4$) complex.

IC$_{50}$ values for the polynuclear complexes here reported are summarized in Table 6.

Table 6. IC$_{50}$ values of compounds **26–28b**.

Compound	Cell Line (IC$_{50}$, μM)	Reference
26	24 h: HT29 (9.610), SW480 (11.30), SW620 (31.00). 96 h: HT29 (<0.001), SW480 (0.220), SW620 (1.220), HaCaT (0.719)	[65]
27a	24 h: A-549 (4.34), MCF-7 (6.50), HaCaT (11.19)	[66]
27b	24 h: A-549 (8.46), MCF-7 (8.68), HaCaT (16.01)	[66]
28	48 h: MCF-7 (3.227 ± 0.052), HepG2 (3.532 ± 0.055), A-549 (3.984 ± 0.185), 4T1 (3.311 ± 0.100), COS-7 (6.319 ± 0.022)	[67]

3. Conclusions

Mixed Cu(II) complexes bearing phenanthroline-based ligands have potential applications in anticancer chemotherapy, as evidenced by the numerous examples reported in this review. Figure 29 summarizes the principal action mechanisms observed for the copper phen-based complexes so far shown. As can be seen, similar molecules can exert very different biological actions, just as structurally different molecules can act according to the same mechanism of action. In many cases, a molecule can exert its cytotoxic action through multiple mechanisms; the predominance of one or more of them can depend on multiple factors, not always predictable. Comparisons between the different molecules can provide

new druggable cellular targets or contribute to understanding of molecular mechanisms in cell.
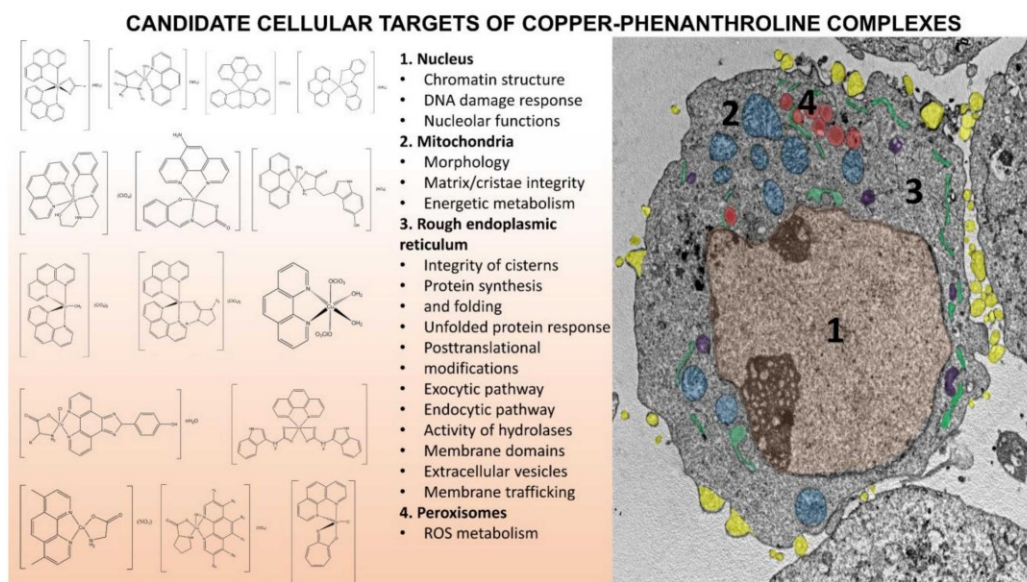
Figure 29. The candidate cellular structures and molecular mechanisms interfering with copper-phen complexes visualized in the A-2780 cancer cell.

The different coordination numbers and geometries adopted by Cu(II) with many classes of ligands has certainly the advantage of extending the number of novel chemical entities that might be screened for their biological activity but also makes more difficult to draw generalized Structure Activity Relationships (SAR). However, some considerations could be made: (i) Cu(II) complexes are generally more potent by the related Cu(II) salts or ligands, thus proving the importance of the complex itself in exerting the anticancer activity; (ii) the Cu(II) centre is fundamental for exerting the desired biochemical properties, due to its involvement in ROS production; (iii) the planarity of the N-N moiety generally increases the anticancer potency (e.g., complexes having phen ligands are more potent than the bipy-based ones).

As regards the auxiliary ligands, their choice is commonly made under two different perspectives, such as their known biochemical properties (e.g., NSAIDs, natural compounds, cytotoxic molecules) or their ability in targeting DNA. However, results achieved from biological assays are not always straightforward, since the activity of the ligand alone could be significantly altered when involved in a metal complex (e.g., Salubrinal is cytoprotective towards ER-stress, while the **4e** complex is cytotoxic).

Rational design of both complexes and biochemical experiments are often performed taking the DNA as the primary (and only) molecular target. As clearly demonstrated in various examples, the way these compounds exert their biochemical properties is not restricted to the binding and/or cleavage of DNA. For this reason, more efforts should be made in evaluating the interactions with other potential biological targets and pathways, in order to better clarify the molecular mechanisms adopted.

Despite the promising in vitro anticancer properties reported there are a few in vivo studies that can confirm the biological activity observed in cellular models and evaluate the ADMET (Absorption, Distribution, Metabolism, Excretion, Toxicity) properties of the studied compounds. More efforts in this direction should be made to evaluate the possible lead compounds that can be further evaluated for pre-clinical studies.

In summary, mixed Cu(II) complexes bearing phenanthroline-based ligands are promising compounds that can be targeted to various molecular pathways and mechanisms in cancer cells.

Author Contributions: Conceptualization, P.V., S.M., T.P. and E.C.; writing—original draft preparation, S.M. and M.G.C.; writing—review and editing, P.V., S.M., T.P., M.G.C. and J.H.; Visualization, S.M., M.G.C., T.P., L.M. and P.V.; Supervision, S.M., P.V., E.C. and T.P. All authors have read and agreed to the published version of the manuscript.

Institutional Review Board Statement: Not applicable.

Informed Consent Statement: Not applicable.

Data Availability Statement: Not applicable.

Conflicts of Interest: The authors declare no conflict of interest.

Sample Availability: Not applicable.

Abbreviations

apaf1	apoptotic protease activating factor-1
ATOX-1	antioxidant 1 copper chaperone
Bak	Bcl-2 homologous antagonist/killer
Bax	Bcl-2 associated X protein
Bip	binding immunoglobulin protein (also known as GRP-78)
CCS1	superoxide dismutase 1 copper chaperone
ct-DNA	calf-thymus DNA
COX17	cytochrome c oxidase copper chaperone
DDIT3	DNA damage inducible transcript 3
DNA Topo1	DNA topoisomerase 1
DPQ	dipyridoquinoxaline
DPPZ	dipyridophenazine
GSH	glutathione
γ-H2AX	phosphorylated H2A histone family member X
hCtr1	human Copper transporter 1
IC50	drug concentration required for 50% inhibition of cell growth
IRE1	inositol-requiring enzyme 1
MMP-2	matrix metalloprotease-2
NSAID	nonsteroidal anti-inflammatory drug
p53	tumour protein p53
PARP	poly (ADP-ribose) polymerase
PERK	protein kinase R (PKR)-like endoplasmic reticulum kinase
SOD	superoxide dismutase
VEGFR-1	vascular endothelial growth factor receptor 1

References

1. Dasari, S.; Bernard Tchounwou, P. Cisplatin in cancer therapy: Molecular mechanisms of action. *Eur. J. Pharmacol.* **2014**, *740*, 364–378. [CrossRef]
2. Dilruba, S.; Kalayda, G.V. Platinum-based drugs: Past, present and future. *Cancer Chemother. Pharmacol.* **2016**, *77*, 1103–1124. [CrossRef]
3. Arnesano, F.; Natile, G. Mechanistic insight into the cellular uptake and processing of cisplatin 30 years after its approval by FDA. *Coord. Chem. Rev.* **2009**, *253*, 2070–2081. [CrossRef]

4. Oun, R.; Moussa, Y.E.; Wheate, N.J. The side effects of platinum-based chemotherapy drugs: A review for chemists. *Dalt. Trans.* **2018**, *47*, 6645–6653. [CrossRef]

5. Sung, H.; Ferlay, J.; Siegel, R.L.; Laversanne, M.; Soerjomataram, I.; Jemal, A.; Bray, F. Global Cancer Statistics 2020: GLOBOCAN Estimates of Incidence and Mortality Worldwide for 36 Cancers in 185 Countries. *CA Cancer J. Clin.* **2021**, *71*, 209–249. [CrossRef]

6. Trudu, F.; Amato, F.; Vaňhara, P.; Pivetta, T.; Peña-Méndez, E.M.; Havel, J. Coordination compounds in cancer: Past, present and perspectives. *J. Appl. Biomed.* **2015**, *13*, 79–103. [CrossRef]

7. Van Den Berghe, P.V.E.; Klomp, L.W.J. New developments in the regulation of intestinal copper absorptionn. *Nutr. Rev.* **2009**, *67*, 658–672. [CrossRef] [PubMed]

8. Bost, M.; Houdart, S.; Oberli, M.; Kalonji, E.; Huneau, J.F.; Margaritis, I. Dietary copper and human health: Current evidence and unresolved issues. *J. Trace Elem. Med. Biol.* **2016**, *35*, 107–115. [CrossRef] [PubMed]

9. Jomova, K.; Baros, S.; Valko, M. Redox active metal-induced oxidative stress in biological systems. *Transit. Met. Chem.* **2012**, *37*, 127–134. [CrossRef]

10. De Luca, A.; Barile, A.; Arciello, M.; Rossi, L. Copper homeostasis as target of both consolidated and innovative strategies of anti-tumor therapy. *J. Trace Elem. Med. Biol.* **2019**, *55*, 204–213. [CrossRef] [PubMed]

11. Daniel, K.G. Copper storage diseases: Menkes, Wilson's, and Cancer. *Front. Biosci.* **2004**, *9*, 2652–2662. [CrossRef]

12. Díez, M.; Arroyo, M.; Cerdàn, F.J.; Muñoz, M.; Martin, M.A.; Balibrea, J.L. Serum and Tissue Trace Metal Levels in Lung Cancer. *Oncology* **1989**, *46*, 230–234. [CrossRef] [PubMed]

13. Geraki, K.; Farquharson, M.J.; Bradley, D.A. Concentrations of Fe, Cu and Zn in breast tissue: A synchrotron XRF study. *Phys. Med. Biol.* **2002**, *47*, 2327–2339. [CrossRef] [PubMed]

14. Denoyer, D.; Masaldan, S.; La Fontaine, S.; Cater, M.A. Targeting copper in cancer therapy: "Copper That Cancer". *Metallomics* **2015**, *7*, 1459–1476. [CrossRef]

15. Sigman, D.S.; Graham, D.R.; D'Aurora, V.; Stern, A.M. Oxygen-dependent cleavage of DNA by the 1,10-phenanthroline cuprous complex. Inhibition of Escherichia coli DNA polymerase I. *J. Biol. Chem.* **1979**, *254*, 12269–12272. [CrossRef]

16. Barton, J.K.; Olmon, E.D.; Sontz, P.A. Metal complexes for DNA-mediated charge transport. *Coord. Chem. Rev.* **2011**, *255*, 619–634. [CrossRef] [PubMed]

17. Nano, A.; Dai, J.; Bailis, J.M.; Barton, J.K. Rhodium Complexes Targeting DNA Mismatches as a Basis for New Therapeutics in Cancers Deficient in Mismatch Repair. *Biochemistry* **2021**, *60*, 2055–2063. [CrossRef] [PubMed]

18. Marzano, C.; Pellei, M.; Tisato, F.; Santini, C. Copper Complexes as Anticancer Agents. *Anticancer Agents Med. Chem.* **2009**, *9*, 185–211. [CrossRef]

19. Santini, C.; Pellei, M.; Gandin, V.; Porchia, M.; Tisato, F.; Marzano, C. Advances in copper complexes as anticancer agents. *Chem. Rev.* **2014**, *114*, 815–862. [CrossRef]

20. Molinaro, C.; Martoriati, A.; Pelinski, L.; Cailliau, K. Copper Complexes as Anticancer Agents Targeting Topoisomerases I and II. *Cancers* **2020**, *12*, 2863. [CrossRef] [PubMed]

21. Zehra, S.; Tabassum, S.; Arjmand, F. Biochemical pathways of copper complexes: Progress over the past 5 years. *Drug Discov. Today* **2021**, *26*, 1086–1096. [CrossRef] [PubMed]

22. Krasnovskaya, O.; Naumov, A.; Guk, D.; Gorelkin, P.; Erofeev, A.; Beloglazkina, E.; Majouga, A. Copper coordination compounds as biologically active agents. *Int. J. Mol. Sci.* **2020**, *21*, 3965. [CrossRef] [PubMed]

23. Park, K.C.; Fouani, L.; Jansson, P.J.; Wooi, D.; Sahni, S.; Lane, D.J.R.; Palanimuthu, D.; Lok, H.C.; Kovačević, Z.; Huang, M.L.H.; et al. Copper and conquer: Copper complexes of di-2-pyridylketone thiosemicarbazones as novel anti-cancer therapeutics. *Metallomics* **2016**, *8*, 874–886. [CrossRef] [PubMed]

24. Pivetta, T.; Isaia, F.; Verani, G.; Cannas, C.; Serra, L.; Castellano, C.; Demartin, F.; Pilla, F.; Manca, M.; Pani, A. Mixed-1,10-phenanthroline–Cu(II) complexes: Synthesis, cytotoxic activity versus hematological and solid tumor cells and complex formation equilibria with glutathione. *J. Inorg. Biochem.* **2012**, *114*, 28–37. [CrossRef] [PubMed]

25. Pivetta, T.; Trudu, F.; Valletta, E.; Isaia, F.; Castellano, C.; Demartin, F.; Tuveri, R.; Vascellari, S.; Pani, A. Novel copper(II) complexes as new promising antitumour agents. A crystal structure of [Cu(1,10-phenanthroline-5,6-dione)$_2$ (OH$_2$)(OClO$_3$)](ClO$_4$). *J. Inorg. Biochem.* **2014**, *141*, 103–113. [CrossRef]

26. Vascellari, S.; Valletta, E.; Perra, D.; Pinna, E.; Serra, A.; Isaia, F.; Pani, A.; Pivetta, T. Cisplatin, glutathione and the third wheel: Acopper-(1,10-phenanthroline) complex modulates cisplatin-GSH interactions from antagonism to synergism in cancer cells resistant to cisplatin. *RSC Adv.* **2019**, *9*, 5362–5376. [CrossRef]

27. Moráň, L.; Pivetta, T.; Masuri, S.; Vašíčková, K.; Walter, F.; Prehn, J.; Elkalaf, M.; Trnka, J.; Havel, J.; Vaňhara, P. Mixed copper(II)–phenanthroline complexes induce cell death of ovarian cancer cells by evoking the unfolded protein response. *Metallomics* **2019**, *11*, 1481–1489. [CrossRef]

28. Shi, X.; Chen, Z.; Wang, Y.; Guo, Z.; Wang, X. Hypotoxic copper complexes with potent anti-metastatic and anti-angiogenic activities against cancer cells. *Dalt. Trans.* **2018**, *47*, 5049–5054. [CrossRef]

29. Masuri, S.; Cadoni, E.; Cabiddu, M.G.; Isaia, F.; Demuru, M.G.; Moráň, L.; Buček, D.; Vaňhara, P.; Havel, J.; Pivetta, T. The first copper(II) complex with 1,10-phenanthroline and salubrinal with interesting biochemical properties. *Metallomics* **2020**, *12*, 891–901. [CrossRef] [PubMed]

30. Fantoni, N.Z.; Molphy, Z.; O'Carroll, S.; Menounou, G.; Mitrikas, G.; Krokidis, M.G.; Chatgilialoglu, C.; Colleran, J.; Banasiak, A.; Clynes, M.; et al. Polypyridyl-Based Copper Phenanthrene Complexes: Combining Stability with Enhanced DNA Recognition. *Chem.-A Eur. J.* **2021**, *27*, 971–983. [CrossRef]

31. Prisecaru, A.; McKee, V.; Howe, O.; Rochford, G.; McCann, M.; Colleran, J.; Pour, M.; Barron, N.; Gathergood, N.; Kellett, A. Regulating bioactivity of Cu^{2+} Bis-1,10-phenanthroline artificial metallonucleases with sterically functionalized pendant carboxylates. *J. Med. Chem.* **2013**, *56*, 8599–8615. [CrossRef] [PubMed]

32. Thati, B.; Noble, A.; Creaven, B.S.; Walsh, M.; Kavanagh, K.; Egan, D.A. Apoptotic cell death: A possible key event in mediating the in vitro anti-proliferative effect of a novel copper(II) complex, [Cu(4-Mecdoa)(phen)$_2$] (phen = phenanthroline, 4-Mecdoa = 4-methylcoumarin-6,7-dioxactetate), in human malignant cancer cells. *Eur. J. Pharmacol.* **2007**, *569*, 16–28. [CrossRef] [PubMed]

33. Kellett, A.; O'Connor, M.; McCann, M.; McNamara, M.; Lynch, P.; Rosair, G.; McKee, V.; Creaven, B.; Walsh, M.; McClean, S.; et al. Bis-phenanthroline copper(II) phthalate complexes are potent in vitro antitumour agents with "self-activating" metallo-nuclease and DNA binding properties. *Dalt. Trans.* **2011**, *40*, 1024–1027. [CrossRef]

34. Zhang, Z.; Wang, H.; Wang, Q.; Yan, M.; Wang, H.; Bi, C.; Sun, S.; Fan, Y. Anticancer activity and computational modeling of ternary copper (II) complexes with 3-indolecarboxylic acid and 1,10-phenanthroline. *Int. J. Oncol.* **2016**, *49*, 691–699. [CrossRef]

35. Boodram, J.N.; Mcgregor, I.J.; Bruno, P.M.; Cressey, P.B.; Hemann, M.T.; Suntharalingam, K. Breast Cancer Stem Cell Potent Copper(II)-Non-Steroidal Anti-Inflammatory Drug Complexes. *Angew. Chem.* **2016**, *128*, 2895–2900. [CrossRef]

36. Eremina, J.A.; Lider, E.V.; Sukhikh, T.S.; Klyushova, L.S.; Perepechaeva, M.L.; Sheven', D.G.; Berezin, A.S.; Grishanova, A.Y.; Potkin, V.I. Water-soluble copper(II) complexes with 4,5-dichloro-isothiazole-3-carboxylic acid and heterocyclic N-donor ligands: Synthesis, crystal structures, cytotoxicity, and DNA binding study. *Inorg. Chim. Acta* **2020**, *510*, 119778. [CrossRef]

37. Mo, X.; Chen, Z.; Chu, B.; Liu, D.; Liang, Y.; Liang, F. Structure and anticancer activities of four Cu(II) complexes bearing tropolone. *Metallomics* **2019**, *11*, 1952–1964. [CrossRef]

38. Mutlu Gençkal, H.; Erkisa, M.; Alper, P.; Sahin, S.; Ulukaya, E.; Ari, F. Mixed ligand complexes of Co(II), Ni(II) and Cu(II) with quercetin and diimine ligands: Synthesis, characterization, anti-cancer and anti-oxidant activity. *J. Biol. Inorg. Chem.* **2020**, *25*, 161–177. [CrossRef]

39. Prisecaru, A.; Devereux, M.; Barron, N.; McCann, M.; Colleran, J.; Casey, A.; McKee, V.; Kellett, A. Potent oxidative DNA cleavage by the di-copper cytotoxin: [Cu$_2$(μ-terephthalate)(1,10-phen)$_4$]$^{2+}$. *Chem. Commun.* **2012**, *48*, 6906–6908. [CrossRef]

40. Ruiz Azuara, L. Process to Obtain New Mixed Copper Aminoacidate Complexes from Phenanthrolines and Their Alkyl Derivatives to be Used as Anticancerigenic Agents. European Patent Application EP0434445A2, 26 June 1991.

41. Kachadourian, R.; Brechbuhl, H.M.; Ruiz-Azuara, L.; Gracia-Mora, I.; Day, B.J. Casiopeína IIgly-induced oxidative stress and mitochondrial dysfunction in human lung cancer A549 and H157 cells. *Toxicology* **2010**, *268*, 176–183. [CrossRef]

42. Marín-Hernández, A.; Gracia-Mora, I.; Ruiz-Ramírez, L.; Moreno-Sánchez, R. Toxic effects of copper-based antineoplastic drugs (Casiopeinas®) on mitochondrial functions. *Biochem. Pharmacol.* **2003**, *65*, 1979–1989. [CrossRef]

43. Rivero-Müller, A.; De Vizcaya-Ruiz, A.; Plant, N.; Ruiz, L.; Dobrota, M. Mixed chelate copper complex, Casiopeina IIgly®, binds and degrades nucleic acids: A mechanism of cytotoxicity. *Chem. Biol. Interact.* **2007**, *165*, 189–199. [CrossRef] [PubMed]

44. Alemón-Medina, R.; Muñoz-Sánchez, J.L.; Ruiz-Azuara, L.; Gracia-Mora, I. Casiopeína IIgly induced cytotoxicity to HeLa cells depletes the levels of reduced glutathione and is prevented by dimethyl sulfoxide. *Toxicol. Vitr.* **2008**, *22*, 710–715. [CrossRef] [PubMed]

45. De Vizcaya-Ruiz, A.; Rivero-Müller, A.; Ruiz-Ramirez, L.; Howarth, J.A.; Dobrota, M. Hematotoxicity response in rats by the novel copper-based anticancer agent: Casiopeina II. *Toxicology* **2003**, *194*, 103–113. [CrossRef]

46. Resendiz-Acevedo, K.; García-Aguilera, M.E.; Esturau-Escofet, N.; Ruiz-Azuara, L. 1H -NMR Metabolomics Study of the Effect of Cisplatin and Casiopeina-II Gly on MDA-MB-231 Breast Tumor Cells. *Front. Mol. Biosci.* **2021**, *8*, 742859. [CrossRef]

47. García-Ramos, J.C.; Gutiérrez, A.G.; Vázquez-Aguirre, A.; Toledano-Magaña, Y.; Alonso-Sáenz, A.L.; Gómez-Vidales, V.; Flores-Alamo, M.; Mejía, C.; Ruiz-Azuara, L. The mitochondrial apoptotic pathway is induced by Cu(II) antineoplastic compounds (Casiopeínas®) in SK-N-SH neuroblastoma cells after short exposure times. *BioMetals* **2017**, *30*, 43–58. [CrossRef] [PubMed]

48. Ruiz-Azuara, L.; Bastian, G.; Bravo-Gómez, M.E.; Cañas, R.C.; Flores-Alamo, M.; Fuentes, I.; Mejia, C.; García-Ramos, J.C.; Serrano, A. Abstract CT408: Phase I study of one mixed chelates copper(II) compound, Casiopeína CasIIIia with antitumor activity and its mechanism of action. In Proceedings of the Clinical Trials; American Association for Cancer Research: Philadelphia, PA, USA, 2014; p. CT408.

49. 2nd March 2017; New Cancer Drug Called Casiopeínas Tested at Phase I Clinical Trials, Source: Information Agency CONACYT. Available online: http://www.salud.carlosslim.org/english2/new-cancer-drug-called-casiopeinas-tested-at-phase-i-clinical-trials/ (accessed on 13 August 2021).

50. Correia, I.; Borovic, S.; Cavaco, I.; Matos, C.P.; Roy, S.; Santos, H.M.; Fernandes, L.; Capelo, J.L.; Ruiz-Azuara, L.; Pessoa, J.C. Evaluation of the binding of four anti-tumor Casiopeínas® to human serum albumin. *J. Inorg. Biochem.* **2017**, *175*, 284–297. [CrossRef]

51. Naso, L.G.; Martínez Medina, J.J.; D'Alessandro, F.; Rey, M.; Rizzi, A.; Piro, O.E.; Echeverría, G.A.; Ferrer, E.G.; Williams, P.A.M. Ternary copper(II) complex of 5-hydroxytryptophan and 1,10-phenanthroline with several pharmacological properties and an adequate safety profile. *J. Inorg. Biochem.* **2020**, *204*, 110933. [CrossRef]

52. Karpagam, S.; Kartikeyan, R.; Paravai Nachiyar, P.; Velusamy, M.; Kannan, M.; Krishnan, M.; Chitgupi, U.; Lovell, J.F.; Abdulkader Akbarsha, M.; Rajendiran, V. ROS-mediated cell death induced by mixed ligand copper(II) complexes of l-proline and diimine: Effect of co-ligand. *J. Coord. Chem.* **2019**, *72*, 3102–3127. [CrossRef]

53. Seng, H.L.; Wang, W.S.; Kong, S.M.; Alan Ong, H.K.; Win, Y.F.; Raja Noor Zaliha, R.N.Z.R.; Chikira, M.; Leong, W.K.; Ahmad, M.; Khoo, A.S.B.; et al. Biological and cytoselective anticancer properties of copper(II)-polypyridyl complexes modulated by auxiliary methylated glycine ligand. *BioMetals* **2012**, *25*, 1061–1081. [CrossRef] [PubMed]

54. Li, D.D.; Yagüe, E.; Wang, L.Y.; Dai, L.L.; Yang, Z.B.; Zhi, S.; Zhang, N.; Zhao, X.M.; Hu, Y.H. Novel Copper Complexes That Inhibit the Proteasome and Trigger Apoptosis in Triple-Negative Breast Cancer Cells. *ACS Med. Chem. Lett.* **2019**, *10*, 1328–1335. [CrossRef] [PubMed]

55. Alvarez, N.; Kramer, M.G.; Ellena, J.; Costa-Filho, A.; Torre, M.H.; Facchin, G. Copper-diimine coordination compounds as potential new tools in the treatment of cancer. *Cancer Reports Rev.* **2018**, *2*, 1–5. [CrossRef]

56. Iglesias, S.; Alvarez, N.; Torre, M.H.; Kremer, E.; Ellena, J.; Ribeiro, R.R.; Barroso, R.P.; Costa-Filho, A.J.; Kramer, G.M.; Facchin, G. Synthesis, structural characterization and cytotoxic activity of ternary copper(II)-dipeptide-phenanthroline complexes. A step towards the development of new copper compounds for the treatment of cancer. *J. Inorg. Biochem.* **2014**, *139*, 117–123. [CrossRef] [PubMed]

57. Arjmand, F.; Sharma, S.; Parveen, S.; Toupet, L.; Yu, Z.; Cowan, J.A. Copper(II) L/D-valine-(1,10-phen) complexes target human telomeric G-quadruplex motifs and promote site-specific DNA cleavage and cellular cytotoxicity. *Dalt. Trans.* **2020**, *49*, 9888–9899. [CrossRef] [PubMed]

58. Acilan, C.; Cevatemre, B.; Adiguzel, Z.; Karakas, D.; Ulukaya, E.; Ribeiro, N.; Correia, I.; Pessoa, J.C. Synthesis, biological characterization and evaluation of molecular mechanisms of novel copper complexes as anticancer agents. *Biochim. Biophys. Acta-Gen. Subj.* **2017**, *1861*, 218–234. [CrossRef] [PubMed]

59. Goswami, T.K.; Chakravarthi, B.V.S.K.; Roy, M.; Karande, A.A.; Chakravarty, A.R. Ferrocene-conjugated l-tryptophan copper(II) complexes of phenanthroline bases showing DNA photocleavage activity and cytotoxicity. *Inorg. Chem.* **2011**, *50*, 8452–8464. [CrossRef]

60. Jia, L.; Xu, X.-M.; Xu, J.; Chen, L.-H.; Jiang, P.; Cheng, F.-X.; Lu, G.-N.; Wang, Q.; Wu, J.-C.; Tang, N. Synthesis, Characterization, Cytotoxic Activities, and DNA-Binding Studies of Ternary Copper(II) Complexes with New Coumarin Derivatives. *Chem. Pharm. Bull.* **2010**, *58*, 1003–1008. [CrossRef]

61. Northcote-Smith, J.; Kaur, P.; Suntharalingam, K. A Cancer Stem Cell Potent Copper(II) Complex with a *S, N, S*-Schiff base Ligand and Bathophenanthroline. *Eur. J. Inorg. Chem.* **2021**, *2021*, 1770–1775. [CrossRef]

62. Periasamy, V.S.; Riyasdeen, A.; Rajendiran, V.; Palaniandavar, M.; Krishnamurthy, H.; Alshatwi, A.A.; Akbarsha, M.A. Induction of Redox-Mediated Cell Death in ER-Positive and ER-Negative Breast Cancer Cells by a Copper(II)-Phenolate Complex: An In Vitro and In Silico Study. *Molecules* **2020**, *25*, 4504. [CrossRef] [PubMed]

63. Chew, S.T.; Lo, K.M.; Lee, S.K.; Heng, M.P.; Teoh, W.Y.; Sim, K.S.; Tan, K.W. Copper complexes with phosphonium containing hydrazone ligand: Topoisomerase inhibition and cytotoxicity study. *Eur. J. Med. Chem.* **2014**, *76*, 397–407. [CrossRef] [PubMed]

64. Kumar, M.; Parsekar, S.U.; Duraipandy, N.; Kiran, M.S.; Koley, A.P. Synthesis, DNA binding and in vitro cytotoxicity studies of a mononuclear copper(II) complex containing N_2S(thiolate)Cu core and 1,10-phenanthroline as a coligand. *Inorg. Chim. Acta* **2019**, *484*, 219–226. [CrossRef]

65. Kellett, A.; O'Connor, M.; McCann, M.; Howe, O.; Casey, A.; McCarron, P.; Kavanagh, K.; McNamara, M.; Kennedy, S.; May, D.D.; et al. Water-soluble bis(1,10-phenanthroline) octanedioate Cu^{2+} and Mn^{2+} complexes with unprecedented nano and picomolar in vitro cytotoxicity: Promising leads for chemotherapeutic drug development. *Med. Chem. Comm.* **2011**, *2*, 579. [CrossRef]

66. Parsekar, S.U.; Singh, M.; Mishra, D.P.; Antharjanam, P.K.S.; Koley, A.P.; Kumar, M. Efficient hydrolytic cleavage of DNA and antiproliferative effect on human cancer cells by two dinuclear Cu(II) complexes containing a carbohydrazone ligand and 1,10-phenanthroline as a coligand. *J. Biol. Inorg. Chem.* **2019**, *24*, 343–363. [CrossRef] [PubMed]

67. Cao, S.; Li, X.; Gao, Y.; Li, F.; Li, K.; Cao, X.; Dai, Y.; Mao, L.; Wang, S.; Tai, X. A simultaneously GSH-depleted bimetallic Cu(II) complex for enhanced chemodynamic cancer therapy. *Dalt. Trans.* **2020**, *49*, 11851–11858. [CrossRef] [PubMed]

Results and discussion

Article 7.

Hydroxylated 3-(pyridin-2-yl)coumarins as radical scavengers with potent lipoxygenase inhibitor activity

Hydroxylated 3-(pyridin-2-yl)coumarins as radical scavengers with potent lipoxygenase inhibitor activity†

Sebastiano Masuri, [ID] Maria Grazia Cabiddu, [ID] Enzo Cadoni [ID] and Tiziana Pivetta [ID] *

Coumarins comprise a large class of natural-based and synthetic compounds containing a 2Hchromen-2-one ring. Derivatives with hydroxy groups are able to donate a $H^•$, exhibiting antioxidant activities similar to phenols and quinones. In this work, 3-(pyridin-2-yl)coumarins with and without hydroxy group/s were prepared and their antioxidant ability and inhibition activity towards lipoxygenase enzymes were studied. The studied derivatives have shown potent lipoxygenase activities with IC_{50} in the μM range, with the radical scavenging properties tuneable according to the number and position of the hydroxy groups. The study of the protonation constants of the 3-(pyridin-2-yl)coumarins, carried out in aqueous solutions, helped in evaluating the absorption and the potential biological properties of the molecules, strongly affected by their protonation state and charge. The antioxidant properties and the way of enzymatic inhibition of the studied 3-(pyridin-2-yl)coumarins are discussed on the basis of the calculated specific thermochemical descriptors and molecular docking.

Introduction

Coumarins have attracted the attention of many scientists for their wide range of biological properties, such as antimicrobial, anti-coagulant, antioxidant, anti-inflammatory and anticancerous,[1–4] all of which are tuneable according to the nature and position of the substituents. In particular, coumarins with hydroxy groups show antioxidant properties similar to potent antioxidant compounds such as phenols and quinones,[5–10] delocalizing the unpaired electron within the π electron systems, also due to the presence of electron-withdrawing functional groups. Additionally, hydroxy-coumarins might interact with enzymes inhibiting their biological functions.

Several pathological conditions, such as cancers, inflammatory diseases, neurological disorders, ageing, asthma, psoriasis, rheumatoid arthritis and allergic phenomena, are related to oxidative stress[11] and enzymatic reactions.[12–14] Oxidative stress arises when the concentration of reactive oxygen species (ROS) increases, leading to the inadequate action of the ubiquitous detoxification system.[15] Hydroxide ($^•OH$), superoxide ($O_2^{-•}$), hydroperoxide ($HOO^•$), peroxides ($ROO^•$), H_2O_2, and singlet oxygen ($^1O_2$) are ROS commonly produced in biological systems as natural by-products of cell metabolism. An important enzyme for human beings is the 5-lipoxygenase (5-LOX). This enzyme, belonging to the lipoxygenases[16] class of non-heme, non-sulphur iron dioxygenases that converts linoleic, arachidonic and other polyunsaturated fatty acids to hydroperoxides, is involved in the arachidonic cascade, which is responsible for the production of leukotrienes that act as chemical mediators of several inflammatory and allergic phenomena. Moreover, increased levels of 5-LOX have also been observed in several types of tumours, and some 5-LOX inhibitors have shown the ability to arrest the tumour cell proliferation, also inducing apoptosis.[17]

In this work, the antioxidant properties and the inhibition activity towards lipoxygenase for 3-(pyridin-2-yl)coumarins (**1–5**, Scheme 1) are discussed. Moreover, since the protonation state and charge could affect the absorption and the potential biological properties of the molecules,[18–23] the protonation constants of **1–5** were also determined. The calculation of specific thermochemical descriptors and molecular docking studies helped in understanding and explaining the antioxidant properties and the enzymatic inhibition shown by **1–5**.

Experimental materials and methods

Sodium chloride, sodium hydroxide, anhydrous ethanol, methanol, piperidine, lipoxygenase, sodium linoleate, 1,1-diphenyl-2-picrylhydrazyl free radical ($DPP^•$), deuterated chloroform and tris (hydroxymethyl)aminomethane hydrochloride (TRIS) were purchased from Merck (Milan, Italy). Pyridine-2-acetonitrile,

Dipartimento di Scienze Chimiche e Geologiche, Università degli Studi di Cagliari, Cittadella Universitaria, 09042 Monserrato CA, Italy. E-mail: tpivetta@unica.it
† Electronic supplementary information (ESI) available. See DOI: 10.1039/d1nj01232k

Abstract

The onset of many pathologies, such as asthma, psoriasis, cancers, and neurological disorders are correlated with an accumulation of ROS and enzymatic reactions. Lipoxygenases are commonly known for their influence in the pathogenesis of many inflammatory and cancerous pathologies. Considering that many natural hydroxycoumarins (e.g., umbelliferone, daphnetin, aesculetin) has shown both antioxidant and lipoxygenase inhibitory activities, I decided to prepare a series of mono and polyhydroxylated derivatives (**2-5**, **Figure 7**) of 3-(pyridin-2-yl)coumarin (1, **Figure 7**).
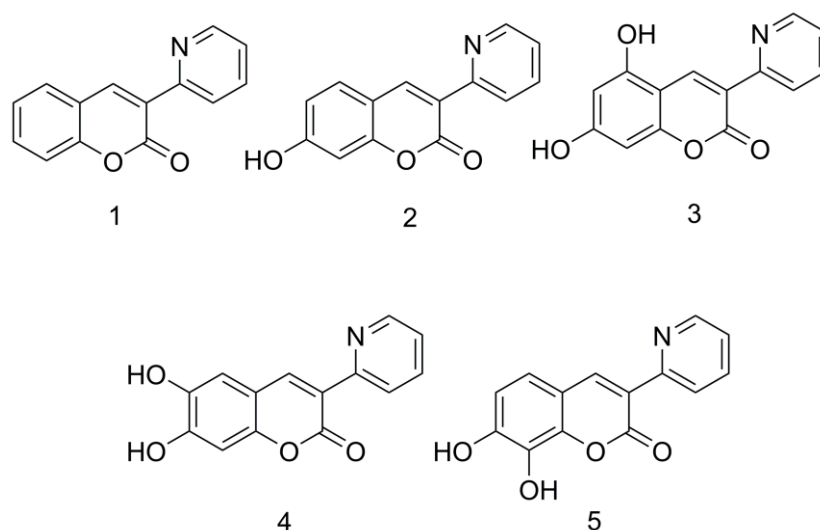
Figure 7. Molecular structures of compounds **1-5**

Interestingly, the insertion of hydroxyl groups in the scaffold of **1** has allowed to obtain novel potent soybean lipoxygenase inhibitors (IC$_{50}$ values in the sub-micromolar range) with tuneable antioxidant activities according to the number and position of the hydroxy groups (**Figure 8**).
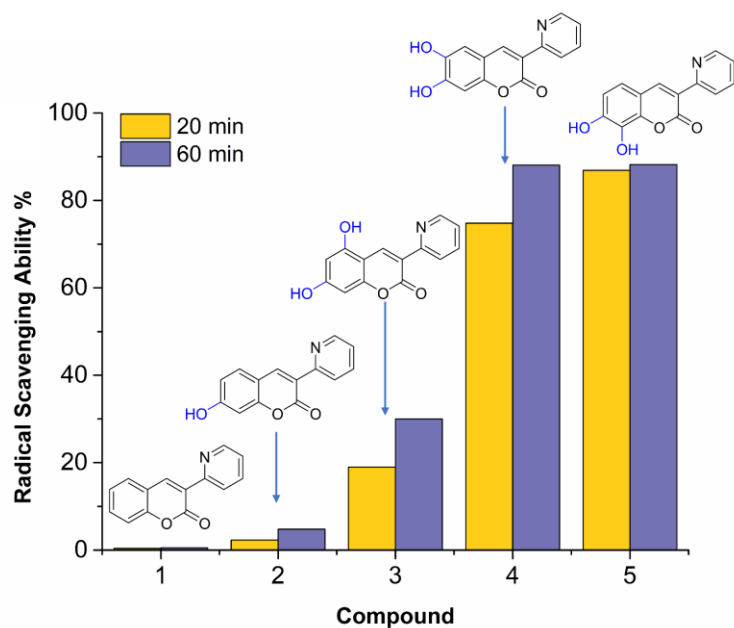
Figure 8. Tuneable antioxidant properties of compounds **1-5**

The antioxidant properties and the way of enzymatic inhibition of the studied compounds have been discussed based on calculated specific thermochemical descriptors and molecular docking.

Moreover, by determining the protonation constants (potentiometric and spectroscopic measurements) with a series of calculated descriptors, it has been possible to speculate about the potential absorption sites of the studied molecules.

Hydroxylated 3-(pyridin-2-yl)coumarins as radical scavengers with potent lipoxygenase inhibitor activity

Sebastiano Masuri[1], Maria Grazia Cabiddu[1], Enzo Cadoni[1], Tiziana Pivetta[1, *]

[1]Department of Chemical and Geological Sciences, University of Cagliari, 09042, Cittadella Universitaria, Monserrato, Cagliari, Italy.

* Corresponding author: tpivetta@unica.it

Check for updates

Hydroxylated 3-(pyridin-2-yl)coumarins as radical scavengers with potent lipoxygenase inhibitor activity†

Sebastiano Masuri, [ID] Maria Grazia Cabiddu, [ID] Enzo Cadoni [ID] and Tiziana Pivetta [ID] *

Coumarins comprise a large class of natural-based and synthetic compounds containing a 2Hchromen-2-one ring. Derivatives with hydroxy groups are able to donate a H[•], exhibiting antioxidant activities similar to phenols and quinones. In this work, 3-(pyridin-2-yl)coumarins with and without hydroxy group/s were prepared and their antioxidant ability and inhibition activity towards lipoxygenase enzymes were studied. The studied derivatives have shown potent lipoxygenase activities with IC_{50} in the μM range, with the radical scavenging properties tuneable according to the number and position of the hydroxy groups. The study of the protonation constants of the 3-(pyridin-2-yl)coumarins, carried out in aqueous solutions, helped in evaluating the absorption and the potential biological properties of the molecules, strongly affected by their protonation state and charge. The antioxidant properties and the way of enzymatic inhibition of the studied 3-(pyridin-2-yl)coumarins are discussed on the basis of the calculated specific thermochemical descriptors and molecular docking.

Introduction

Coumarins have attracted the attention of many scientists for their wide range of biological properties, such as antimicrobial, anti-coagulant, antioxidant, anti-inflammatory and anticancerous,[1–4] all of which are tuneable according to the nature and position of the substituents. In particular, coumarins with hydroxy groups show antioxidant properties similar to potent antioxidant compounds such as phenols and quinones,[5–10] delocalizing the unpaired electron within the π electron systems, also due to the presence of electron-withdrawing functional groups. Additionally, hydroxy-coumarins might interact with enzymes inhibiting their biological functions.

Several pathological conditions, such as cancers, inflammatory diseases, neurological disorders, ageing, asthma, psoriasis, rheumatoid arthritis and allergic phenomena, are related to oxidative stress[11] and enzymatic reactions.[12–14] Oxidative stress arises when the concentration of reactive oxygen species (ROS) increases, leading to the inadequate action of the ubiquitous detoxification system.[15] Hydroxide ($^{•}OH$), superoxide ($O_2{}^{-•}$), hydroperoxide ($HOO^{•}$), peroxides ($ROO^{•}$), H_2O_2, and singlet oxygen ($^1O_2$) are ROS commonly produced in biological systems as natural by-products of cell metabolism. An important enzyme

for human beings is the 5-lipoxygenase (5-LOX). This enzyme, belonging to the lipoxygenases[16] class of non-heme, non-sulphur iron dioxygenases that converts linoleic, arachidonic and other polyunsaturated fatty acids to hydroperoxides, is involved in the arachidonic cascade, which is responsible for the production of leukotrienes that act as chemical mediators of several inflammatory and allergic phenomena. Moreover, increased levels of 5-LOX have also been observed in several types of tumours, and some 5-LOX inhibitors have shown the ability to arrest the tumour cell proliferation, also inducing apoptosis.[17]

In this work, the antioxidant properties and the inhibition activity towards lipoxygenase for 3-(pyridin-2-yl)coumarins (**1–5**, Scheme 1) are discussed. Moreover, since the protonation state and charge could affect the absorption and the potential biological properties of the molecules,[18–23] the protonation constants of **1–5** were also determined. The calculation of specific thermochemical descriptors and molecular docking studies helped in understanding and explaining the antioxidant properties and the enzymatic inhibition shown by **1–5**.

Experimental materials and methods

Sodium chloride, sodium hydroxide, anhydrous ethanol, methanol, piperidine, lipoxygenase, sodium linoleate, 1,1-diphenyl-2-picrylhydrazyl free radical (DPP[•]), deuterated chloroform and tris (hydroxymethyl)aminomethane hydrochloride (TRIS) were purchased from Merck (Milan, Italy). Pyridine-2-acetonitrile,

Dipartimento di Scienze Chimiche e Geologiche, Università degli Studi di Cagliari, Cittadella Universitaria, 09042 Monserrato CA, Italy. E-mail: tpivetta@unica.it

deuterated dimethyl sulfoxide, salicylic aldehyde and its derivatives were purchased from Alfa-Aesar. HCl Normex N/10 was purchased from Carlo Erba Reagents. The commercial reagents were used as received, without any further purification. Ultrapure water was obtained from a MilliQ Millipore system.

NMR measurements

^{1}H and ^{13}C NMR spectra were recorded using a Varian UNITY INOVA 500 and a Bruker Avance III HD 600 spectrometer at room temperature with tetramethylsilane (TMS) as the internal standard in DMSO d6. Chemical shifts, multiplicity and coupling constants were reported.

Mass spectrometry studies

Mass spectra were recorded using a triple quadrupole QqQ Varian 310-MS mass spectrometer using the atmospheric pressure ESI technique. Mass spectra were recorded by direct infusion of the sample solutions. The experimental conditions for positive mode were needle voltage 4500 V, shield 600 V, source temperature 100 °C, drying gas pressure 20 psi, nebulizing gas pressure 20 psi, detector voltage 1450 V, and range 100–500 m/z.

Potentiometric and spectrophotometric titrations

Potentiometric titrations, performed at 25 °C in 0.1 M ionic strength (NaCl) under an Ar atmosphere, were carried out in a thermostatted vessel with a Mettler-Toledo Seven Compact pH/Ion-meter, equipped with a Mettler-Toledo InLab Micro Pro combined glass electrode with an integrated temperature probe. The glass electrode was calibrated daily[24] and checked using the GLEE software package.[25] UV–Visible (UV–Vis) measurements were carried out with an Agilent Cary 60 spectrophotometer using a quartz cuvette with an optical path of 0.5 cm. Protonation constants of the studied compounds were determined by spectrophotometric and potentiometric titrations. Solutions of ligands were prepared daily by dissolving an appropriate amount of the compound in DMSO (concentrations ~ 13 mM) prior to the required dilution in 0.1 M NaCl (final DMSO content $\leq 1\%$ V/V, concentration $\approx 1.2 \times 10^{-4}$ M). Four HCl equivalents for **1** and five HCl equivalents for the other ligands were added before the titration with NaOH standard solution. Potentiometric and spectrophotometric data were analysed using the Hyperquad 2006 suite.[26] Speciation diagrams were obtained using Hyss 2009 software.[27]

Determination of the reducing activity of the stable radical 1,1-diphenyl- picrylhydrazyl (DPP$^\bullet$)

Each test compound was dissolved in DMSO at 1.0 mM concentration, and then a 1:10 dilution was performed with absolute ethanol. DPP$^\bullet$ solution (0.1 mM, absolute ethanol) was prepared freshly, stored in the dark and used in a few hours. The test solution (1500 μL) was added to an equal volume of DPP$^\bullet$ inside the cuvette and the absorbance in the 300–650 nm range was recorded at room temperature for 70 minutes. The final concentrations for both DPP$^\bullet$ and the tested compounds were 50 μM. The absorbance at 517 nm was

evaluated to examine the time-dependence of the radical scavenging activity (RA).[28] The RA of each compound was expressed as the percentage inhibition of the absorbance of the initial DPP$^\bullet$ solution (RA%).

Soybean lipoxygenase inhibition study *in vitro*

Stock solutions of **1–5** were prepared by dissolving an appropriate amount of the compounds in DMSO (≈ 0.1 M) and then diluting with TRIS buffer at pH 7.4 (final concentration 0.2–50 microM depending on the molecule (Fig. S14, ESI†)). Sodium linoleate (0.0013 g, V 10.0 mL, 4.30×10^{-4} M) and soybean lipoxygenase (0.0013 g, V 10.0 mL, 1.24×10^{-6} M) were dissolved in TRIS buffer at pH 7.4 and diluted with TRIS buffer at pH 7.4. Solutions of sodium linoleate, soybean lipoxygenase and **1–5** were prepared daily and kept in the dark at 25 °C. The conversion of sodium linoleate to 13-hydroperoxylinoleic acid was monitored by recording the absorbance at 243 nm, and not at 234 nm (absorption maximum); 243 nm was chosen since at 234 nm the contributions of **1–5** absorbances were not negligible.

DFT calculations

DFT calculations were performed using release 4.2.0 of the ORCA software package.[29] Input files for DFT calculations were prepared using Avogadro 1.2.0.[30] Geometry optimizations were performed using the hybrid PBE0 functional[31] and def-2 TZVP basis set.[32] IR frequency calculations were carried out to verify the nature of the minima of each optimization by evaluating the absence of calculated negative frequencies. DFT calculations were performed both at the gas phase and in the presence of the solvent (ethanol, water). Solvent effects were considered using the conductor-like polarizable continuum model (CPCM).[33] Molecular orbital shapes and energies, and electrostatic potential surfaces were investigated using Chemcraft v1.8.[34] Atomic charges at the natural population analysis (NPA) level were calculated using the JANPA software package.[35]

Several thermochemical parameters were calculated, starting from the appropriate enthalpy values, to give more insights into the preferred pathways chosen by the studied compounds to exert their antioxidant properties. The hydrogen atom transfer (**HAT**), the single electron transfer proton transfer (**SETPT**) and the sequential proton loss electron transfer (**SPLET**) mechanisms, commonly adopted by antioxidant phenolics, were considered.[9,36–39] A brief explanation of these mechanisms for interested readers is provided in the ESI† (Section 5).

The enthalpy for the hydrogen atom was calculated both at the gas phase and in the presence of solvents using the same computational setup. The enthalpies in the gas phase for proton and electron were taken from the literature as 1.481 and 0.752 kcal mol^{-1}, respectively.[40,41] The enthalpies for protons and electrons in the solvent were calculated by assuming the solvation of a proton or an electron with a molecule of solvent using CPCM, as previously reported.[37,41] Both the chemical formalisms and the equations used for the calculation of these enthalpies are reported in the ESI† (Section S5).

Molecular descriptors

Molecular descriptors, such as miLogP (calculated logarithm of the partition coefficient), TPSA (topological polar surface area), number of hydrogen bond donors and acceptors, rotatable bonds, molecular weight, molecular volume and number of violation of the Lipinski's Rule of five were calculated using Molinspiration property software (v2018.10).[42]

Molecular docking

Molecular docking calculations were performed using Autodock Vina software.[43] DFT optimized structures of the ligands were exported as PDB files. The X-ray structure of soybean lipoxygenase LOX-1 (PDB:3PZW) was chosen as the receptor. Prior to docking, both ligands and receptors were processed using MG Labs Autodock Tools.[44] In the receptor structure, water molecules were removed while polar hydrogens and Gasteiger charges were added. The atomic charge for the Fe2840 cofactor was manually adjusted in the generated pdbqt file. For all the ligands, polar hydrogens and Gasteiger charges were added, and no rotational constraints were applied. All the tested compounds were docked using a grid cube of $30 \times 30 \times 30$ points centred at Iron cofactor coordinates ($x = 24.527$, $y = 44.349$, and $z = 10.587$) with a spacing of 1.0 Å and an exhaustiveness value of 100. Molecular interactions and docked poses were evaluated using Biovia Discovery Studio Viewer v19.[45]

Chemistry

General procedure for the preparation of chromene-2-one derivatives[46,47]. Salicylaldehyde derivatives (0.0072 mol) and pyridine-2-acetonitrile (0.76 mL, 0.0072 mol) were dissolved in 14 mL of anhydrous ethanol, and piperidine (0.26 mL) was added dropwise in an ice bath. The mixture was stirred for 20 h at room temperature, treated with HCl (23 mL, 3.5%) and refluxed for 10 h to hydrolyse the iminocoumarin. For compounds **1**, **2**, **3** and **5**, the resulting acidic solution was neutralized with aqueous ammonia until pH 7, affording a precipitate that was recovered by filtration. In the case of **4**, the formed solid product was immediately recovered. The crude products were recrystallized from methanol to yield the desired products. Compounds **1** and **2** were previously prepared and characterized.[46,47]

2 (7-Hydroxy-3-(pyridin-2-yl)-2H-chromen-2-one): yield was 65%. Experimental results are in accordance with those reported in the literature.[48] ^{1}H NMR (500 MHz, DMSO d$_6$, δ, ppm, Fig. S1, ESI†): 8.79 (s, 1H), 8.65 (dt, J = 4.7, 1.4 Hz, 1H), 8.23 (dt, J = 8.1, 1.2 Hz, 1H), 7.85 (td, J = 7.8, 1.9 Hz, 1H), 7.74 (d, J = 8.5 Hz, 1H), 7.36 (ddd, J = 7.5, 4.7, 1.1 Hz, 1H), 6.83 (dd, J = 8.5, 2.3 Hz, 1H), 6.76 (d, J = 2.1 Hz, 1H). ESI-MS (calcd, found, m/z): 240.1, 240.1 [M + H]$^+$ (Fig. S7A, ESI†).

3 (5,7-dihydroxy-3-(pyridin-2-yl)-2H-chromen-2-one): yield was 50%. ^{1}H NMR (600 MHz, DMSO d$_6$, δ, ppm, Fig. S2, ESI†): 8.97 (s, 1H), 8.65 (dd, J = 4.9, 1.8 Hz, 1H), 8.28 (d, J = 8.1 Hz, 1H), 7.85 (td, J = 7.8, 1.9 Hz, 1H), 7.34 (dd, J = 7.5, 4.7 Hz, 1H), 6.33 (d, J = 2.1 Hz, 1H), 6.26 (d, J = 2.1 Hz, 1H). ^{13}C NMR (151 MHz, DMSO d$_6$, δ, ppm, Fig. S3, ESI†): 163.64, 160.54, 157.53, 156.83, 152.13, 149.76,

138.58, 137.12, 123.07, 122.95, 117.96, 102.92, 98.51, 94.17. ESI-MS (calcd, found, m/z): 256.0, 256.1 [M + H]$^+$ (Fig. S7B, ESI†).

4 (6,7-dihydroxy-3-(pyridin-2-yl)-2H-chromen-2-one): yield was 35%. ^{1}H NMR (600 MHz, DMSO d6, δ, ppm, Fig. S4, ESI†): 8.74 (s, 1H), 8.70 (dd, J = 5.4, 1.7 Hz, 1H), 8.31 (d, 8.2 Hz, 1H), 8.18 (t, J = 8.0 Hz, 1H), 7.60 (t, J = 6.5 Hz, 1H), 7.12 (s, 1H), 6.82 (s, 1H). ^{13}C NMR (151 MHz, DMSO d6, δ, ppm, Fig. S5, ESI†) δ 160.24, 153.47, 149.95, 149.83, 145.98, 145.93, 145.60, 144.22, 141.8, 124.94, 124.62, 113.57, 111.42, 102.84. ESI-MS (calcd, found, m/z): 256.0, 256.1 [M + H]$^+$ (Fig. S7C, ESI†).

5 (7,8-dihydroxy-3-(pyridin-2-yl)-2H-chromen-2-one): yield was 52%. Experimental results are in accordance with those reported in literature.[40] ^{1}H NMR (600 MHz, DMSO d6, δ, ppm, Fig. S6, ESI†): 8.77 (s,1H), 8.67 (dt, J = 4.6, 1.5 Hz, 1H), 8.28 (dd, J = 8.1, 1.2 Hz, 1H), 7.88 (td, J = 7.8, 1.9 Hz, 1H), 7.38 (ddd, J = 7.6, 4.8, 1.1 Hz, 1H), 7.25 (d, J = 8.4 Hz, 1H), 6.87 (d, J = 8.4 Hz, 1H). ESI-MS (calcd, found, m/z): 256.0, 256.1 [M + H]$^+$ (Fig. S7D, ESI†).

Results and discussion synthesis

3-(Pyridin-2-yl)coumarin (**1**) and its hydroxylated derivatives (**2–5**) were prepared using appropriate amounts of hydroxylated benzaldehyde and pyridine-2-acetonitrile *via* Knovenagel Condensation and subsequent acidic hydrolysis. This step was required to convert the iminocoumarins obtained *in situ* in the desired products.

The synthetic pathway and the acronyms of the studied compounds are reported in Scheme 1. The novel derivatives **3** and **4** were obtained with 50% and 35% yields, respectively. Structures and purity of the studied compounds were assessed *via* ^{1}H-NMR (Fig. S1, S2, S4 and S6, ESI†) and ESI-MS (Fig. S7, ESI†). ^{13}C-NMR analyses were additionally performed for **3** and **4** in order to provide a complete characterization for these novel compounds (Fig. S3 and S5, ESI†).

The studied compounds have been selected following specific criteria. Considering that natural hydroxycoumarins, such as Umbelliferone (7-hydroxycoumarin), Aesculetin (6,7-dihydroxycoumarin) and Daphnetin (7,8-dihydroxycoumarin), have shown both antioxidant and lipoxygenase inhibitory activities,[49–52] we decided to extend these substitution patterns to the scaffold of **1**. In particular, we first introduced a hydroxy group in the 7th position (**2**), then we added an additional –OH in the 5th, 6th and 8th positions (compounds **3**, **4** and **5**, respectively). The heteroaryl moiety in the 3rd position has been introduced with the aim to enhance the electronic delocalization of the related phenoxide radicals and anions. In addition, the presence of pyridyl nitrogen could be useful in improving the water solubility (as a hydrogen bond acceptor) and could be involved (in conjunction with the carbonyl oxygen) in the chelation of iron(III) metal cofactor of lipoxygenases.

Solution equilibria studies

The protonation constants of the studied compounds were determined by spectrophotometric and potentiometric
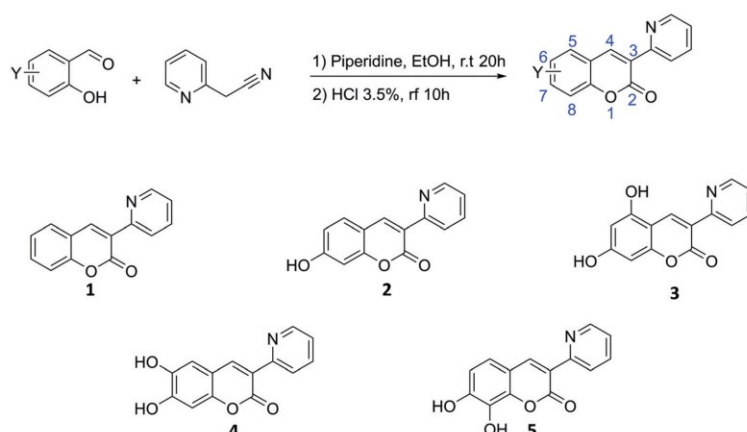
Scheme 1 Reaction scheme and structures of the synthesized compounds.

titrations carried out simultaneously. Titrations were performed in the pH range of 3–11 for ligands **2**–**5** and till pH 10 for **1** since at higher pH the hydrolysis of the 2*H*-pyran-2-one moiety was observed. Hydrolysis of coumarins is a well-known equilibrium,[53,54] which, at basic pH, is shifted towards the opening of the ring with the formation of the phenate and carboxylate ions. This reaction was observed for **1**, specifically, thanks to the spectral variation observed after pH 10 (Fig. S8, ESI†). For the molecules **2**–**5**, this reaction has not been observed, probably because of the presence of one or two OH groups, which at basic pH are deprotonated and show the mesomeric (+M) effect, destabilizing any open anionic form. Selected spectra recorded during the titrations of the studied compounds are shown in Fig. 1, while the spectral variations observed for each ligand during the titrations are detailed in the ESI† (Fig. S9–S13).

From the eigenvalue analysis of the spectrophotometric data, the number of linearly independent absorbing species as the significant eigenvalues was found. In particular, three species were found for **1**, *i.e.* H_2L^{2+}, HL^+ and L, four species for **2**, *i.e.* H_3L^{2+}, H_2L^+, HL, and L^-, and five species for **3**–**5**, *i.e.* H_4L^{2+}, H_3L^+, H_2L, HL^-, and L^{2-}. Potentiometric and spectrophotometric data were simultaneously fitted to obtain the cumulative formation constants (β) expressed as logarithms, and the related p*K* values were calculated (Table 1). Absorptivity values taken at maximum wavelengths for all the absorbing species are summarized in Table 2. The calculated pure spectra are reported in Fig. S14 (ESI†).

Molecular properties

Several molecular descriptors were calculated, as reported in Table 3. All the compounds reported here adhere to Lipinski's rule of five, which states that poor absorption or permeation is more likely observed when there are more than 5 H-bond donors, 10 H-bond acceptors, the molecular weight (MW) is greater than 500 Dalton and the calculated LogP value is greater than 5.[55] The calculated mi Log*P* value ranges from 1.60

(for compound **4**) to 2.59 (for compound **1**), suggesting an acceptable compromise between lipophilicity (for membrane permeability) and hydrophilicity (for oral administration).

The ability of a molecule to cross the cellular membranes and blood–brain barrier (BBB) could also be preliminarily evaluated using TPSA values,[56] which are correlated with the ability of a compound to form hydrogen bonds. For **1**–**5**, the TPSA values range from 43.10 Å^2, for **1**, to 83.56 Å^2, for **3**–**5**. These values are far below the upper limit of 140 Å^2, thus supporting good oral bioavailability. Moreover, for **2**–**5**, the TPSA values, higher than 60 Å^2, suggest a BBB crossing ability from moderate to modest.[57] As shown by solution equilibria experiments, the studied molecules exist in different protonation states according to the medium pH and, as a consequence, can exert different biological activities.[18,58]

From the distribution diagrams obtained from the experimental p*K*s (Fig. 2), some consideration regarding the species potentially present in blood plasma and different compartments of the gastrointestinal (GI) tract could be made. In the blood plasma (pH 7.4), only **1** would be in a neutral state (due to the absence of –OH groups), while the other compounds would be mainly present in their monoanionic forms, *i.e.* L^- for **2** and HL^- for **3**–**5**.

In the GI tract the situation appears more complicated since pH varies among the different regions, and also the regional pH values fluctuate between and within individuals according to factors like the presence of food, GI/systemic diseases, age, circadian rhythms, and concomitant drug administration.[59] In the stomach region, the pH of healthy young Caucasians lies below 3 for 90% of the fasting state, while it could increase till 7 at the fed state, thanks to the buffering effect observed after food ingestion. In the regions of intestines, the pH varies in the range of 4.9–7.4 at the fasting state and between 5.2 and 7.5 at the fed state.[60] By combining these average values with the data available, it is possible to make some hypothesis about the region where these molecules are more likely to be absorbed *via* a passive diffusion mechanism. All the studied
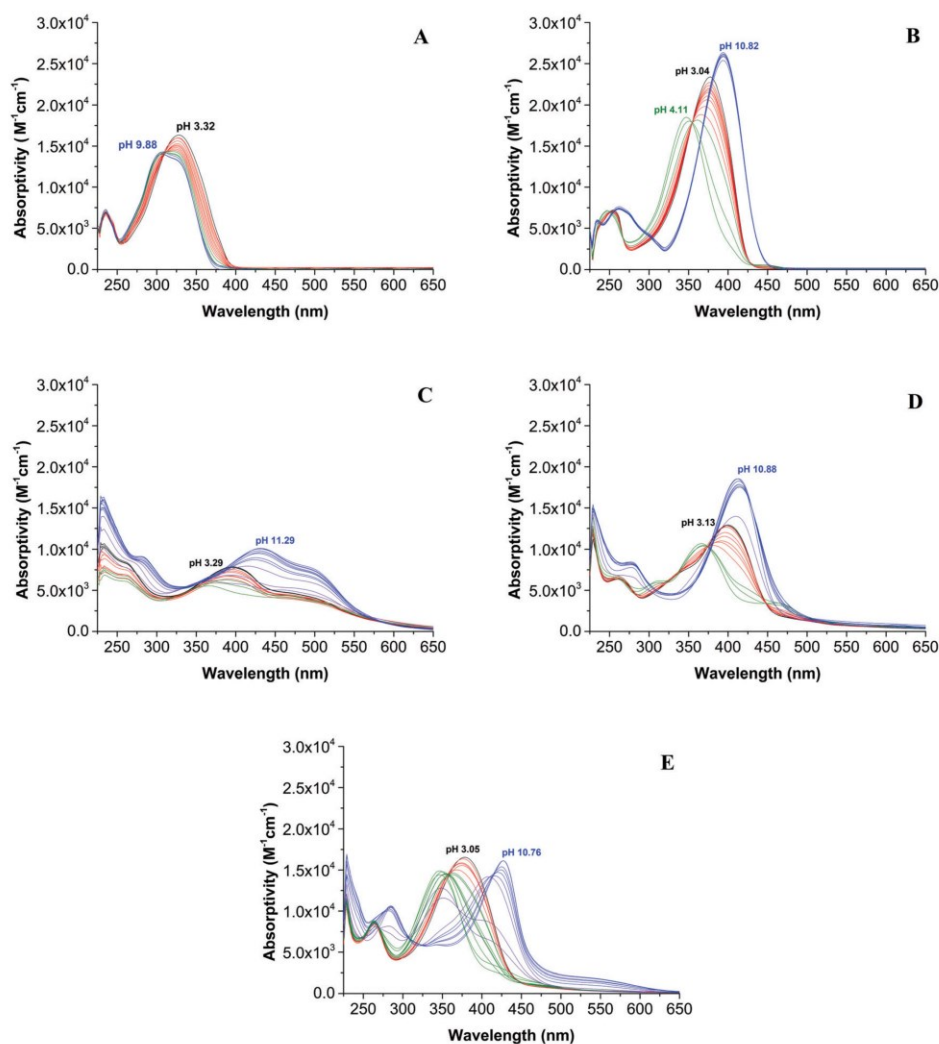
Fig. 1 Selected spectra, reported as absorptivity, collected during the potentiometric and spectrophotometric titrations of **1–5** (A–E) (t 25 °C, NaCl 0.1 M).

compounds appear to be more likely absorbed in the intestines, in particular, at the beginning of the duodenum (pH 4.9 at the fasting state and 5.1 at the fed state), since these molecules are predominantly in a neutral state at these pH values. The same molecules could be absorbed in the stomach at the fed state too, in particular **1,** thanks to the absence of hydroxy groups. This information does not allow excluding the fact that **1–5** could cross the cell membranes in their monoanionic forms using other mechanisms.

Antioxidant assays

Considering the involvement of ROS in the pathogenesis of several inflammatory diseases and neoplasms,[61] and the radical scavenging properties exerted by different non-steroidal anti-inflammatory drugs (NSAIDs),[62,63] the antioxidant activities of **1–5** were evaluated using DPPH assay.

This test, commonly employed to evaluate the antioxidant activity of both synthetic and natural molecules, is based on the ability of the stable radical 1,1-diphenyl-picrylhydrazyl (DPP$^\bullet$) to accept a H$^\bullet$ from the tested compound to be converted into the diamagnetic form (DPPH). The radical DPP$^\bullet$ shows a deep violet colour in absolute ethanol (λ_{max} = 517 nm), while diamagnetic DPPH is pale yellow coloured in the same solvent. The decrease in absorbance at 517 nm due to the radical hydrogen transfer can be followed through time and allows the comparison of the radical scavenging capacity of different compounds. The results for **1–5** are summarized in Fig. 3A and the variation of absorbance (as %) observed during this time is

Table 1 Protonation constants of **1–5** (t 25 °C, NaCl 0.1 M). The standard deviation to the last significant figure is reported in parentheses

Compound	Equilibrium	Log β	pK
1	$L + H^+ \rightleftharpoons HL^+$	4.12 (3)	4.12
	$L + 2H^+ \rightleftharpoons H_2L^{2+}$	7.77 (5)	3.65
2	$L^- + H^+ \rightleftharpoons HL$	6.39 (9)	6.39
	$L^- + 2H^+ \rightleftharpoons H_2L^+$	10.93 (9)	4.54
	$L^- + 3H^+ \rightleftharpoons H_3L^{2+}$	14.94 (5)	4.01
3	$L^{2-} + H^+ \rightleftharpoons HL^-$	9.43 (3)	9.43
	$L^{2-} + 2H^+ \rightleftharpoons H_2L$	15.28 (5)	5.85
	$L^{2-} + 3H^+ \rightleftharpoons H_3L^+$	20.0 (1)	4.72
	$L^{2-} + 4H^+ \rightleftharpoons H_4L^{2+}$	23.5 (1)	3.50
4	$L^{2-} + H^+ \rightleftharpoons HL^-$	9.82 (5)	9.82
	$L^{2-} + 2H^+ \rightleftharpoons H_2L$	16.19 (7)	6.37
	$L^{2-} + 3H^+ \rightleftharpoons H_3L^+$	20.4 (1)	4.21
	$L^{2-} + 4H^+ \rightleftharpoons H_4L^{2+}$	24.7 (1)	3.45
5	$L^{2-} + H^+ \rightleftharpoons HL^-$	9.76 (6)	9.76
	$L^{2-} + 2H^+ \rightleftharpoons H_2L$	15.94 (5)	6.18
	$L^{2-} + 3H^+ \rightleftharpoons H_3L^+$	20.2 (1)	4.26
	$L^{2-} + 4H^+ \rightleftharpoons H_4L^{2+}$	23.4 (1)	3.20

Table 2 Absorptivity values of the various protonated species of **1–5** (t 25 °C, NaCl 0.1 M)

Compound	Species	λ_{max} (nm)	ε ($\times 10^4$ M^{-1} cm^{-1})
1	L	310; 323 (sh)	1.42; 1.36
	HL$^+$	309; 323 (sh)	1.46; 1.43
	H$_2$L^{2+}	343	1.95
2	L$^-$	397	2.62
	HL	351	1.91
	H$_2$L$^+$	382	2.39
	H$_3$L^{2+}	379	2.30
3	L^{2-}	431; 494 (sh)	1.04; 0.78
	HL$^-$	362; 482 (sh)	0.55; 0.31
	H$_2$L	402; 487 (sh)	0.71; 0.47
	H$_3$L$^+$	393; 483 (sh)	0.64; 0.32
	H$_4$L^{2+}	401; 490 (sh)	1.09; 0.69
4	L^{2-}	415	1.98
	HL$^-$	368	1.11
	H$_2$L	405	1.39
	H$_3$L$^+$	376	1.18
	H$_4$L^{2+}	405	1.47
5	L^{2-}	425	1.90
	HL$^-$	348	1.67
	H$_2$L	352	1.40
	H$_3$L$^+$	372	1.61
	H$_4$L^{2+}	390	2.48

Table 3 Calculated molecular descriptors for the studied compounds

	1	2	3	4	5
mi Log P^a	2.59	2.09	1.8	1.6	1.83
TPSA^b (Å^2)	43.10	63.33	83.56	83.56	83.56
n-atoms^c	17	18	19	19	19
MW (Da)	223.23	239.23	255.23	255.23	255.23
n-ON^d	3	4	5	5	5
n-OHNH^e	0	1	2	2	2
n-violations^f	0	0	0	0	0
n-rotb^g	1	1	1	1	1
Volume^h (Å^3)	195.84	203.86	211.87	211.87	211.87

^{a} Calculated logarithm of the partition coefficient between n-octanol and water (mi log P). ^{b} Topological polar surface area (TPSA). ^{c} Number of atoms in the molecule (n-atoms). ^{d} Number of hydrogen bond acceptors (n-ON). ^{e} Number of hydrogen bond donors (n-OHNH). ^{f} Number of violations of the Lipinski's rule of five. ^{g} number of rotatable bonds (n-rotb). ^{h} Molecular volume.

absorbance at 243 nm due to the conversion of linoleic acid to 13-hydroperoxylinoleic acid was followed with time (Fig. S16, ESI†) observing that: (i) in the absence of inhibitors the conversion to 13-hydroperoxylinoleic acid by Soybean Lipoxygenase is completed in approx. 60–70 minutes and (ii) in the presence of **1–5**, the conversion was never quantitative.

The inhibition percentage (IP%) reported as a function of the concentration of the tested inhibitor (Fig. S17, ESI†) shows a trend that is time dependent, preventing an immediate calculation of the inhibitory concentration required to inhibit 50% of the enzyme (IC50). After 80′, the observed trend became invariant, IP % was then mediated in the time interval 80–120′ leading to the calculation of the IC50, that resulted to be <1 µM for all the molecules except **1** (14 ± 4 µM), varying in the order **2** > **5** > **3** > **4** ≫ **1**. These results, reported in Fig. 3B, show how the presence of one or two hydroxy groups increases the inhibition ability of the molecules; however, the less effect shown by the second –OH group could be explained in terms of augmented steric hindrance.

DFT calculations

Structural and electronic properties. DFT-optimized geometries for **1–5** in the gas phase are shown in Fig. 4. It can be observed that the pyridine moiety adopts a distorted antiperiplanar conformation in relation to the coumarin moiety. This feature is consistent with the crystal structure of **1**,[68] whose structural parameters (bond lengths, angles, and dihedrals) are well reproduced by the DFT-optimized structure of the same compound (Table S1, ESI†). Selected bond lengths, angles and dihedrals calculated for **2–5** are reported in Tables S2–S5 (ESI†).

Molecular electrostatic potential (MEP) surfaces help in visualizing the potential regions of different polarities to predict the reactivity with nucleophilic or electrophilic reactants and the presence of hydrogen bonding interactions. For compounds **2–5**, the electropositive regions are localised on the hydrogen atoms of the –OH groups; while for **1** on the aromatic hydrogens of the 2-H-cromen-2-one moiety, the most electronegative regions are detected in the proximity of the heteroatoms (oxygens in particular), as shown in Fig. S18 (ESI†).
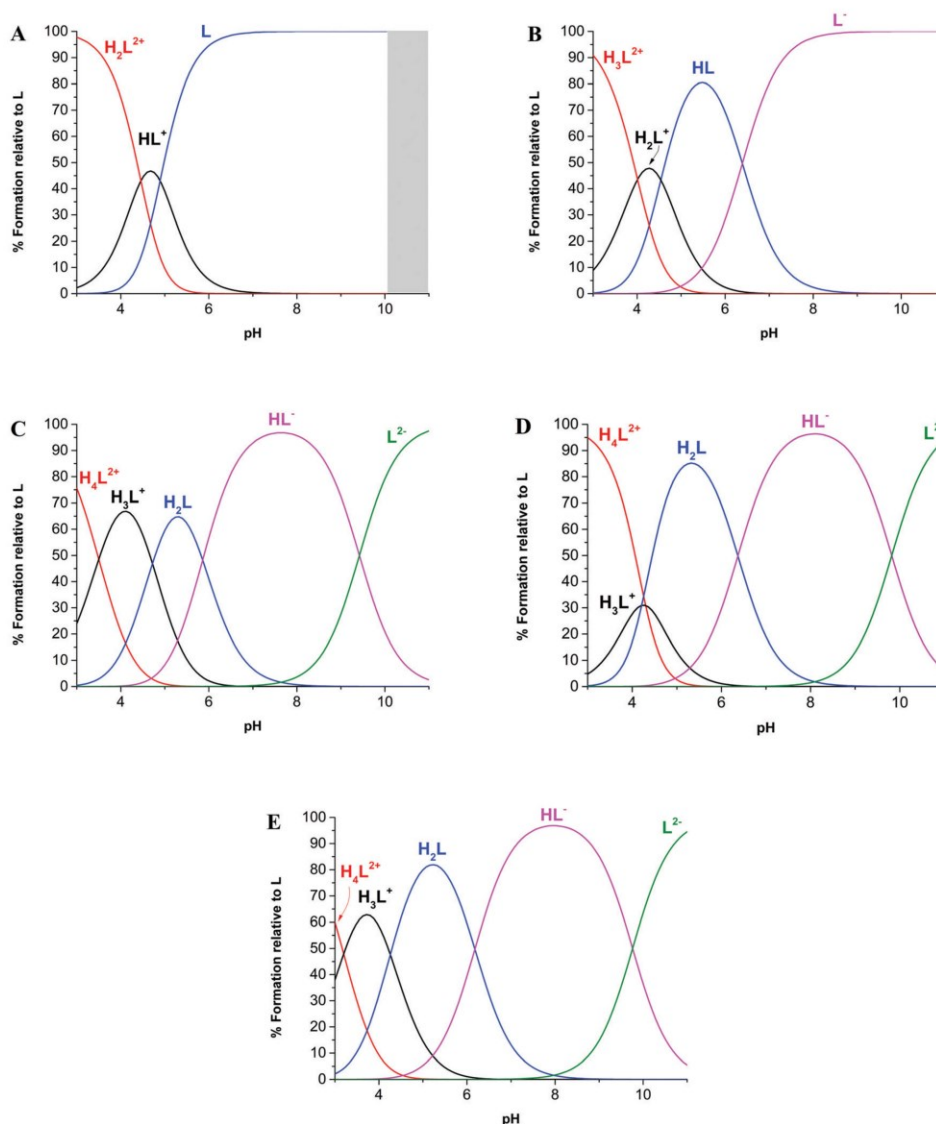
shown in Fig. S15 (ESI†). Compound **1** exhibits negligible DPPH antioxidant activity, lower than 1% at 20′ or 60′. On comparing **1** with the other molecules, we can deduce that the insertion of a hydroxy group in the 7th position of the 2H-cromen-2-one backbone, **2**, determines a modest increase in terms of RA%, while the insertion of a second –OH, **3–5**, causes a significant increment, in particular when the two –OH groups are in the *ortho* position, like in **4** and **5**. This trend is in agreement with the results reported for compounds having a catechol moiety in their backbone.[5,64–66]

Inhibition of soybean lipoxygenase *in vitro*

Soybean lipoxygenase inhibition[67] studies were performed by keeping constant the concentrations of both enzyme and linoleic acid while varying the concentrations of **1–5**. The increase in

293

Fig. 2 pH distribution curves for **1–5 (A–E)**, **1** 1.26×10^{-4} M, **2** 1.24×10^{-4} M, **3** 1.30×10^{-4} M, **4** 1.25×10^{-4} M, and **5** 1.25×10^{-4} M, *t* 25 °C, NaCl 0.1 M.

These results are in accordance with the atomic charges, computed at both Mulliken and NPA levels, reported in Tables S6–S10 (ESI†).

A broad distribution of the frontier molecular orbitals (MOs) (Fig. S19, ESI†) was observed in the 3-(pyridine-2-yl)coumarin system, both at HOMO and LUMO levels, which is consistent with the high degree of delocalization expected from such a conjugated π system. The HOMO energy varies in the order **1** < **2** < **5** < **3** < **4** (Table S11, ESI†), like the ionization potential (IP) values (Table S1, ESI†) calculated for the hydroxylated derivatives **2–5**.

Thermochemical descriptors and antioxidant mechanisms. To give more insights into the preferred pathways used by **1–5** to exert their antioxidant properties, bond dissociation enthalpy (BDE), proton affinity (PA), electron transfer enthalpy (ETE), ionization potential (IP) and proton dissociation enthalpy (PDE) were calculated to quantitatively describe: (i) the tendency of molecules to exert their antioxidant properties by following the HAT pathway, (ii) the tendency of molecules to express their antioxidant properties through the stepwise SPLET mechanism and (iii) the tendency of oxygen-based molecules to express antioxidant properties by the SET-PT
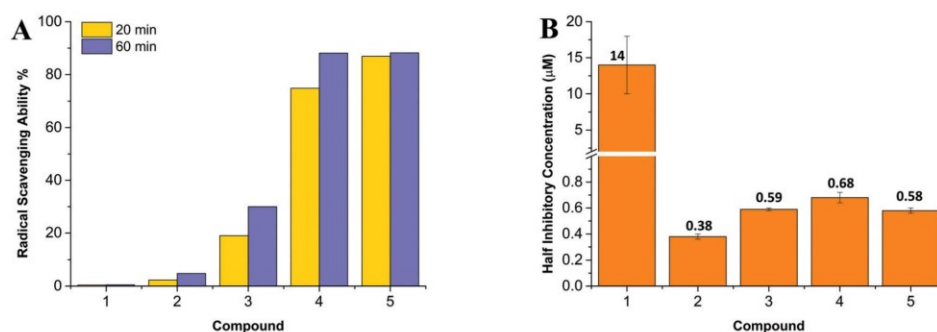
Fig. 3 (A) Radical scavenging activity (as %) of **1–5** on radical 1,1-diphenyl-picrylhydrazyl (DPP•). (B) Half inhibitory concentration of **1–5** towards soybean lipoxygenase.
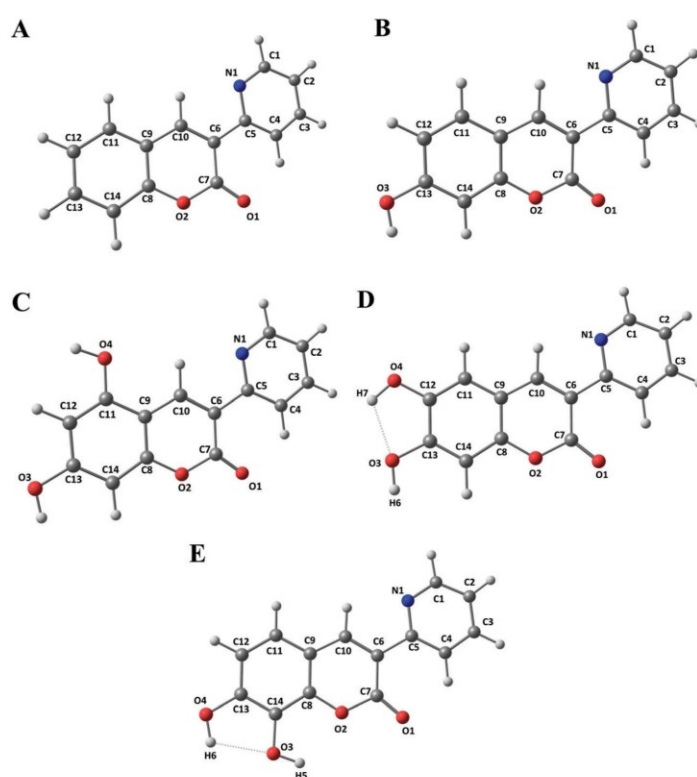

Fig. 4 Molecular drawings and atom labelling scheme for **1–5** (A–E) at the DFT-optimized geometries (gas phase).

mechanism.[9,36,37] The results for all the studied compounds computed for both gas phases and solvents (ethanol and water) are summarized in Table S12 (ESI†).

The calculated BDE values show that the introduction of a second –OH group in the 2-*H*-cromen-2-one backbone generally enhances the antioxidant activity of these molecules *via* the HAT mechanism. The extent of this enhancement differs according to the position of the 2nd-OH group, being poorly influenced by the chosen solvents. For compounds **4** and **5** that have two –OH groups, there is a significant decrease in terms of BDE compared to their parent molecule **2**. In particular, the –OH group in the 7th position for **4** and the –OH group in the 8th position for **5** are more prone to donate the H•. This trend is attributable to the catechol-like motif, present in both
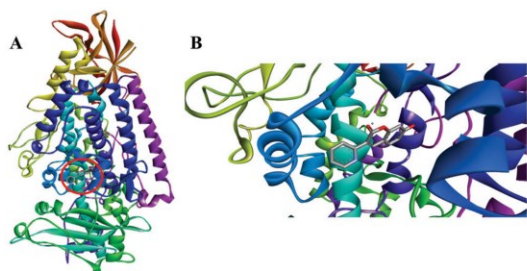
Fig. 5 Full view of the complex between the highest-ranking score of **2** (in its monoanionic form **L⁻**) and soybean lipoxygenase (A); zoom of the binding pocket occupied by the highest-ranking score of **2** (in its mono-anionic form **L⁻**) and soybean lipoxygenase (B).

molecules, that promotes hydrogen transfer due to the H-bonds between the oxygen of the radicalized atom and the hydrogen of the neighbouring –OH group (Fig. S20, ESI†). The same trend is also justified by the presence of a second –OH in *ortho*, due to its electro-releasing effect. With regard to **3**, the BDEs are still lower, if compared to **2**, but not as much as **4** and **5**. This is not only due to the absence of the catecholic structure, but also because of the less significant electron releasing effect of the 2nd-OH group towards the 1st one (and *vice versa*), due to their relative substitution pattern in the 2-*H*-cromen-2-one moiety.

The calculated PAs show a trend similar to the one evidenced for BDEs, with the ligands **4** and **5** being the more inclined ones to release a proton (lower PA values), due to their catechol-like structure (Fig. S21, ESI†). It is interesting to note how the PA values in a polar solvent are significantly lower than those in the gas phase, suggesting a direct role of the solvent in the stabilization of the phenoxide anions, as reported for other

compounds.[6,37] It is also curious to note how the PA values in ethanol and water are significantly lower than the BDEs calculated in the same solvents. However, SPLET is a stepwise process, thus it is necessary to consider the ETE values to determine the preferred antioxidant pathway. For this reason, the global descriptor SPLET, defined as the sum of PA and ETE values, was defined. By comparing the results obtained from the SPLET descriptor with BDEs, we can observe how the BDEs are still lower than SPLETs. For this reason, the SPLET mechanism can be ruled out as a potential antioxidant mechanism for **2–5** in the gas phase and also in polar media like ethanol and water, even if it becomes more competitive towards HAT.

The IP and PDE values show that, for the gas phase and ethanol, the IPs are considerably greater than PDEs, and *vice versa* in water. Thus, IP could be thought as the limiting step in the SET-PT pathway of gas and ethanol, while in water, the same key step is defined by PDE. Anyway, considering the fact that SET-PT is a stepwise process, the cumulative descriptor SET-PT, defined as the sum of IP and PDE values, was preferably considered. BDEs are still lower than the SET-PTs, although in polar media the gap between these two descriptors becomes smaller.

In conclusion, the HAT mechanism is confirmed as the main pathway followed by **2–5** in the gas phase and in the studied polar media. According to the BDEs, the antioxidant properties increase following the same order observed from the experimental DPPH assay (**2** < **3** < **4** ≈ **5**).

Protonation sequences. The protonation sequence and the structures of the different protonated species of **1–5** were evaluated by means of DFT calculations in water, using the same computational setup as previously adopted. For each
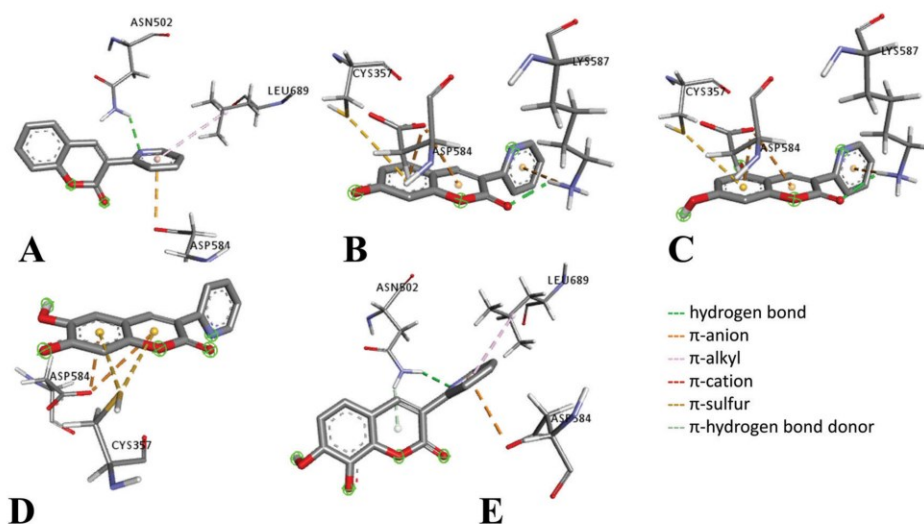

Fig. 6 Docked poses of **1** (A), **2** (as **L⁻**, B), **3** (as **HL⁻**, C), **4** (as **HL⁻**, D), **5** (as **HL⁻**, E) and intermolecular interactions with the surrounding residues of soybean lipoxygenase.

New J. Chem.

calculated structure, the rotational barrier of the pyridine ring was evaluated through a potential energy surface (PES) scan along the dihedral C7–C6–C5–N1 angle ($\tau = 0°$ and $\tau = 180°$ for the periplanar and antiperiplanar conformations, respectively), observing that distorted antiperiplanar conformations were generally adopted by all the species. However, the very modest energy required to switch to the lowest-energy distorted periplanar conformations indicates that both the conformations are expected in solutions. The PES scans and structures of the lowest energy conformers are reported in Fig. S22–S26 (ESI†).

Considering the mono-cationic species $\mathbf{HL^+}$ for **1**, $\mathbf{H_2L^+}$ for **2**, and $\mathbf{H_3L^+}$ for **3–5**, the lowest energy conformer (periplanar) is further stabilized by the pyridinic ring N–H···O intramolecular hydrogen bond (Fig. S19, ESI†). This conformation was observed also in the crystal structure of $\mathbf{1 \cdot HClO_4}$.[47] The species $\mathbf{H_2L}$ of **3** will lose the proton from the –OH group in the 5th position of its backbone, while **4** and **5** from the –OH group in the 7th and 8th position, respectively (see PA values in Table S12, ESI†). By combining all the theoretical data with the experimental ones, the protonation sequences reported in Fig. S27–S31 (ESI†) have been proposed.

Molecular docking

Molecular docking calculations were performed for **1–5** using the structure of soybean lipoxygenase-1 (PDB:3PZW) as a receptor model. At pH 7.4, where the lipoxygenase inhibition was tested, **1** exists mainly in its neutral form, while **2–5** are mostly in their monoanionic form $\mathbf{L^-}$ for **2**, and $\mathbf{HL^-}$ for **3–5**. The highest-ranking score for the most potent molecule of the series **2** (in its mono-anionic form) is reported in Fig. 5, while those for the other compounds are shown in Fig. S32–S35 (ESI†). All the studied ligands interact with the receptor at the same binding site, adopting different orientations and different kinds of non-covalent interactions with the surrounding residues, mainly π interactions (Fig. 6), according to the relative positions of the hydroxy groups in the coumarin backbone. These findings suggest a potential allosteric inhibition mechanism adopted by the studied molecules that might take place in several ways:[69–72] for instance, by decreasing the binding affinity for the enzyme substrate or by acting as scavengers towards the radical intermediates derived from linoleate peroxidation (especially for the hydroxylated derivatives).

Conclusions

The study reported in this manuscript highlighted how the insertion of the hydroxy groups in the structure of 3-(pyridin-2-yl) coumarin increases the lipoxygenase inhibition and the antioxidant activities of these derivatives. Moreover, experimental results show how not only the insertion of a 2nd hydroxy group but also its position in the 3-(pyridin-2-yl)coumarin backbone plays a key role in defining the biological properties of these molecules. A hydrogen atom transfer mechanism was put in place as the preferred way to exert the antioxidant properties of the studied coumarins, whose potential absorption and bioavailability were preliminary evaluated by combining the experimental study of the protonation constants and the *in silico* evaluation of selected descriptors. All these, in terms of results and approach, could be useful in the design and synthesis of novel compounds with potential biological properties.

Author contributions

Conflicts of interest

There are no conflicts to declare.

Acknowledgements

References

1 O. Kayser and H. Kolodziej, *Z. Naturforsch., C: J. Biosci.*, 1999, **54**, 169–174.

2 I. Kostova, S. Bhatia, P. Grigorov, S. Balkansky, V. S. Parmar, A. K. Prasad and L. Saso, *Curr. Med. Chem.*, 2011, **18**, 3929–3951.

3 G. Kirsch, A. Abdelwahab and P. Chaimbault, *Molecules*, 2016, **21**, 1322.

4 S. Emami and S. Dadashpour, *Eur. J. Med. Chem.*, 2015, **102**, 611–630.

5 G. Morabito, D. Trombetta, K. Singh Brajendra, K. Prasad Ashok, S. Parmar Virinder, C. Naccari, F. Mancari, A. Saija, M. Cristani and O. Firuzi, *Biochimie*, 2010, **92**, 1101–1107.

6 J. B. Veselinović, A. M. Veselinović, Ž. J. Vitnik, V. D. Vitnik and G. M. Nikolić, *Chem. – Biol. Interact.*, 2014, **214**, 49–56.

7 T. C. Ngo, T. V. T. Mai, T. T. Pham, S. Jeremic, Z. Markovic, L. K. Huynh and D. Q. Dao, *Chem. Phys. Lett.*, 2020, **746**, 137312.

8 V. D. Kancheva, A. K. Slavova-Kazakova, S. E. Angelova, S. K. Singh, S. Malhotra, B. K. Singh, L. Saso, A. K. Prasad and V. S. Parmar, *Biochimie*, 2017, **140**, 133–145.

9 G. Mazzone, N. Malaj, A. Galano, N. Russo and M. Toscano, *RSC Adv.*, 2015, **5**, 565–575.

10 S. Vazquez-Rodriguez, R. Figueroa-Guíñez, M. J. Matos, L. Santana, E. Uriarte, M. Lapier, J. D. Maya and C. Olea-Azar, *MedChemComm*, 2013, **4**, 993.

11 R. L. Auten and J. M. Davis, *Pediatr. Res.*, 2009, **66**, 121–127.

12 O. Rådmark, O. Werz, D. Steinhilber and B. Samuelsson, *Trends Biochem. Sci.*, 2007, **32**, 332–341.

13 D. A. Yanes and J. L. Mosser-Goldfarb, *J. Am. Acad. Dermatol.*, 2018, **78**, S71–S75.

14 F. Bruno, G. Spaziano, A. Liparulo, F. Roviezzo, S. M. Nabavi, A. Sureda, R. Filosa and B. D'Agostino, *Eur. J. Med. Chem.*, 2018, **153**, 65–72.

15 L. He, T. He, S. Farrar, L. Ji, T. Liu and X. Ma, *Cell. Physiol. Biochem.*, 2017, **44**, 532–553.

16 A. R. Brash, *J. Biol. Chem.*, 1999, **274**, 23679–23682.

17 R. Wisastra and F. Dekker, *Cancers*, 2014, **6**, 1500–1521.

18 D. Sanna, V. Ugone, G. Micera, T. Pivetta, E. Valletta and E. Garribba, *Inorg. Chem.*, 2015, **54**, 8237–8250.

19 F. Gaccioli, R. Franchi-Gazzola, M. Lanfranchi, L. Marchiò, G. Metta, M. A. Pellinghelli, S. Tardito and M. Tegoni, *J. Inorg. Biochem.*, 2005, **99**, 1573–1584.

20 T. Pivetta, F. Trudu, E. Valletta, F. Isaia, C. Castellano, F. Demartin, R. Tuveri, S. Vascellari and A. Pani, *J. Inorg. Biochem.*, 2014, **141**, 103–113.

21 A. A. El-Sherif and T. M. A. Eldebss, *Spectrochim. Acta, Part A*, 2011, **79**, 1803–1814.

22 F. Sabuzi, S. Lentini, F. Sforza, S. Pezzola, S. Fratelli, O. Bortolini, B. Floris, V. Conte and P. Galloni, *J. Org. Chem.*, 2017, **82**, 10129–10138.

23 É. A. Enyedy, N. V. May, V. F. S. Pape, P. Heffeter, G. Szakács, B. K. Keppler and C. R. Kowol, *Dalton Trans.*, 2020, **49**, 16887–16902.

24 A. Albert and E. P. Serjeant, *The Determination of Ionization Constants*, Springer Netherlands, Dordrecht, 1984.

25 P. Gans, *Talanta*, 2000, **51**, 33–37.

26 P. Gans, A. Sabatini and A. Vacca, *Talanta*, 1996, **43**, 1739–1753.

27 L. Alderighi, P. Gans, A. Ienco, D. Peters, A. Sabatini and A. Vacca, *Coord. Chem. Rev.*, 1999, **184**, 311–318.

28 E. Pontiki and D. Hadjipavlou-Litina, *Bioorg. Med. Chem.*, 2007, **15**, 5819–5827.

29 F. Neese, *Wiley Interdiscip. Rev.: Comput. Mol. Sci.*, 2012, **2**, 73–78.

30 M. D. Hanwell, D. E. Curtis, D. C. Lonie, T. Vandermeersch, E. Zurek and G. R. Hutchison, *J. Cheminform.*, 2012, **4**, 17.

31 C. Adamo and V. Barone, *J. Chem. Phys.*, 1999, **110**, 6158–6170.

32 F. Weigend and R. Ahlrichs, *Phys. Chem. Chem. Phys.*, 2005, **7**, 3297.

33 V. Barone and M. Cossi, *J. Phys. Chem. A*, 1998, **102**, 1995–2001.

34 Chemcraft - graphical software for visualization of quantum chemistry computations. https://www.chemcraftprog.com.

35 T. Y. Nikolaienko, L. A. Bulavin and D. M. Hovorun, *Comput. Theor. Chem.*, 2014, **1050**, 15–22.

36 J. S. Wright, E. R. Johnson and G. A. DiLabio, *J. Am. Chem. Soc.*, 2001, **123**, 1173–1183.

37 L. Tabrizi, T. L. A. Nguyen and D. Q. Dao, *RSC Adv.*, 2019, **9**, 17220–17237.

38 C. Y. Lee, A. Sharma, J. Semenya, C. Anamoah, K. N. Chapman and V. Barone, *Antioxidants*, 2020, **9**, 189.

39 J. Kumar, N. Kumar, N. Sati and P. K. Hota, *New J. Chem.*, 2020, **44**, 8960–8970.

40 J. E. Bartmess, *J. Phys. Chem.*, 1994, **98**, 6420–6424.

41 Z. Marković, J. Tošović, D. Milenković and S. Marković, *Comput. Theor. Chem.*, 2016, **1077**, 11–17.

42 Molinspiration Cheminformatics free web services, https://www.molinspiration.com, Slovensky Grob, Slovakia.

43 O. Trott and A. J. Olson, *J. Comput. Chem.*, 2009, 455–461.

44 G. M. Morris, H. Ruth, W. Lindstrom, M. F. Sanner, R. K. Belew, D. S. Goodsell and A. J. Olson, *J. Comput. Chem.*, 2009, **30**, 2785–2791.

45 Dassault Systèmes BIOVIA, Discovery Studio Viewer, v19, San Diego: Dassault Systèmes, 2019.

46 T. Pivetta, S. Masuri, M. G. Cabiddu, C. Caltagirone, A. Pintus, M. Massa, F. Isaia and E. Cadoni, *New J. Chem.*, 2019, **43**, 12032–12041.

47 T. Pivetta, E. Valletta, G. Ferino, F. Isaia, A. Pani, S. Vascellari, C. Castellano, F. Demartin, M. G. Cabiddu and E. Cadoni, *J. Inorg. Biochem.*, 2017, **177**, 101–109.

48 O. V. Khilya, O. V. Shablykina, M. S. Frasinyuk, V. V. Ishchenko and V. P. Khilya, *Chem. Nat. Compd.*, 2005, **41**, 523–528.

49 K. Yoshiyuki, O. Hiromichi, A. Shigeru, B. Kimiye and K. Mitsugi, *Biochim. Biophys. Acta, Lipids Lipid Metab.*, 1985, **834**, 224–229.

50 G. Kanimozhi, N. R. Prasad, S. Ramachandran and K. V. Pugalendi, *Eur. J. Pharmacol.*, 2011, **672**, 20–29.

51 A. Witaicenis, L. N. Seito, A. Da Silveira Chagas, L. D. De Almeida, A. C. Luchini, P. Rodrigues-Orsi, S. H. Cestari and L. C. Di Stasi, *Phytomedicine*, 2014, **21**, 240–246.

52 N. Tomohiro, K. Yasuko and M. Sei-Itsu, *Biochim. Biophys. Acta, Lipids Lipid Metab.*, 1983, **753**, 130–132.

53 B. N. Mattoo, *Trans. Faraday Soc.*, 1957, **53**, 760.

54 I. Yahaya, N. Seferoğlu and Z. Seferoğlu, *Tetrahedron*, 2019, **75**, 2143–2154.

55 C. A. Lipinski, F. Lombardo, B. W. Dominy and P. J. Feeney, *Adv. Drug Delivery Rev.*, 2001, **46**, 3–26.

56 P. Ertl, B. Rohde and P. Selzer, *J. Med. Chem.*, 2000, **43**, 3714–3717.

57 H. Pajouhesh and G. R. Lenz, *NeuroRx*, 2005, **2**, 541–553.

58 C. Fattuoni, S. Vascellari and T. Pivetta, *Amino Acids*, 2020, **52**, 397–407.

59 R. Zhou, P. Moench, C. Heran, X. Lu, N. Mathias, T. N. Faria, D. A. Wall, M. A. Hussain, R. L. Smith and D. Sun, *Pharm. Res.*, 2005, **22**, 188–192.

60 J. B. Dressman, G. L. Amidon, C. Reppas and V. P. Shah, *Pharm. Res.*, 1998, **15**, 11–22.

61 A. Phaniendra, D. B. Jestadi and L. Periyasamy, *Indian J. Clin. Biochem.*, 2015, **30**, 11–26.

62 M. Kataoka, K. Tonooka, T. Ando, K. Imai and T. Aimoto, *Free Radical Res.*, 1997, **27**, 419–427.

63 M. Asanuma, S. Nishibayashi-Asanuma, I. Miyazaki, M. Kohno and N. Ogawa, *J. Neurochem.*, 2001, **76**, 1895–1904.

64 J. Z. Pedersen, C. Oliveira, S. Incerpi, V. Kumar, A. M. Fiore, P. De Vito, A. K. Prasad, S. V. Malhotra, V. S. Parmar and L. Saso, *J. Pharm. Pharmacol.*, 2007, **59**, 1721–1728.

65 D. Hadjipavlou-Litina, T. Garnelis, C. M. Athanassopoulos and D. Papaioannou, *J. Enzyme Inhib. Med. Chem.*, 2009, **24**, 1188–1193.

66 M. Roussaki, K. Zelianaios, E. Kavetsou, S. Hamilakis, D. Hadjipavlou-Litina, C. Kontogiorgis, T. Liargkova and A. Detsi, *Bioorg. Med. Chem.*, 2014, **22**, 6586–6594.

67 S. Masuri, E. Cadoni, M. G. Cabiddu, F. Isaia, M. G. Demuru, L. Moráň, D. Buček, P. Vaňhara, J. Havel and T. Pivetta, *Metallomics*, 2020, **12**, 891–901.

68 Y.-X. Da and Z.-J. Quan, *Acta Crystallogr., Sect. E: Struct. Rep. Online*, 2010, **66**, o2872.

69 V. Sanda and M. Jisak, *Recent Trends for Enhancing the Diversity and Quality of Soybean Products*, InTech, 2011.

70 E. T. Denisov and I. B. Afanas'ev, *Oxidation and Antioxidants in Organic Chemistry and Biology*, CRC Press, 2005, vol. 128.

71 O. Kouzi, E. Pontiki and D. Hadjipavlou-Litina, *Molecules*, 2019, **24**, 1–20.

72 I. Kostopoulou, A. Diassakou, E. Kavetsou, E. Kritsi, P. Zoumpoulakis, E. Pontiki, D. Hadjipavlou-Litina and A. Detsi, *Mol. Divers.*, 2021, **25**, 723–740.

Hydroxylated 3-(pyridin-2-yl)coumarins as radical scavengers with potent lipoxygenase inhibitor activity

Sebastiano Masuri[1], Maria Grazia Cabiddu[1], Enzo Cadoni[1], Tiziana Pivetta[1]*

[1] Dipartimento di Scienze Chimiche e Geologiche, Università degli Studi di Cagliari, Cittadella Universitaria, 09042 Monserrato CA – Italy

SUPPLEMENTARY INFORMATION

Table of contents:

1. Spectral data
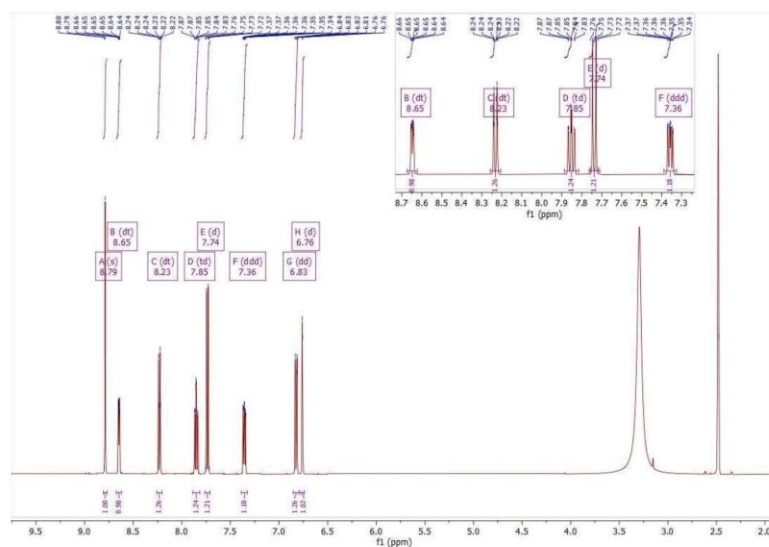
Fig. S1. ^{1}H NMR of ligand **2**, 7-Hydroxy-3-(pyridin-2-yl)-2*H*-chromen-2-one (500 MHz, DMSO-d$_{6}$).
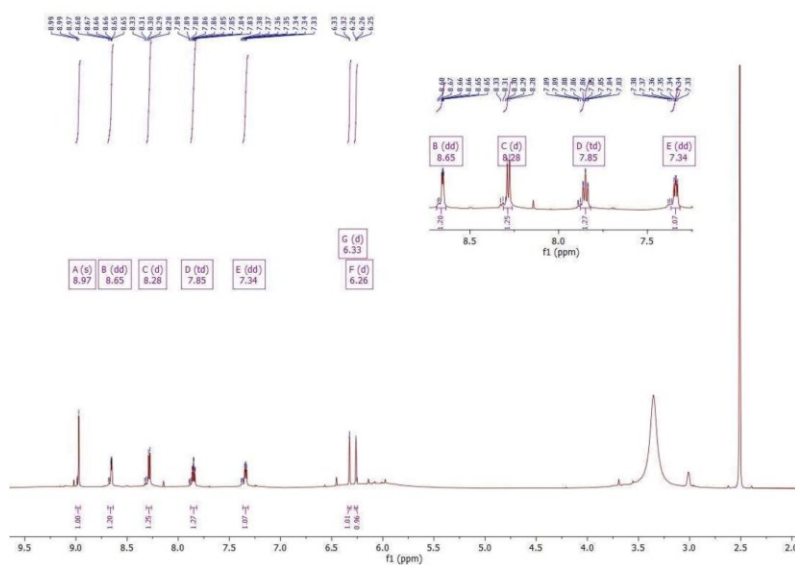
Fig. S2. ^{1}H NMR of ligand **3**, 5,7-dihydroxy-3-(pyridin-2-yl)-2*H*-chromen-2-one (600 MHz, DMSO-d$_{6}$).
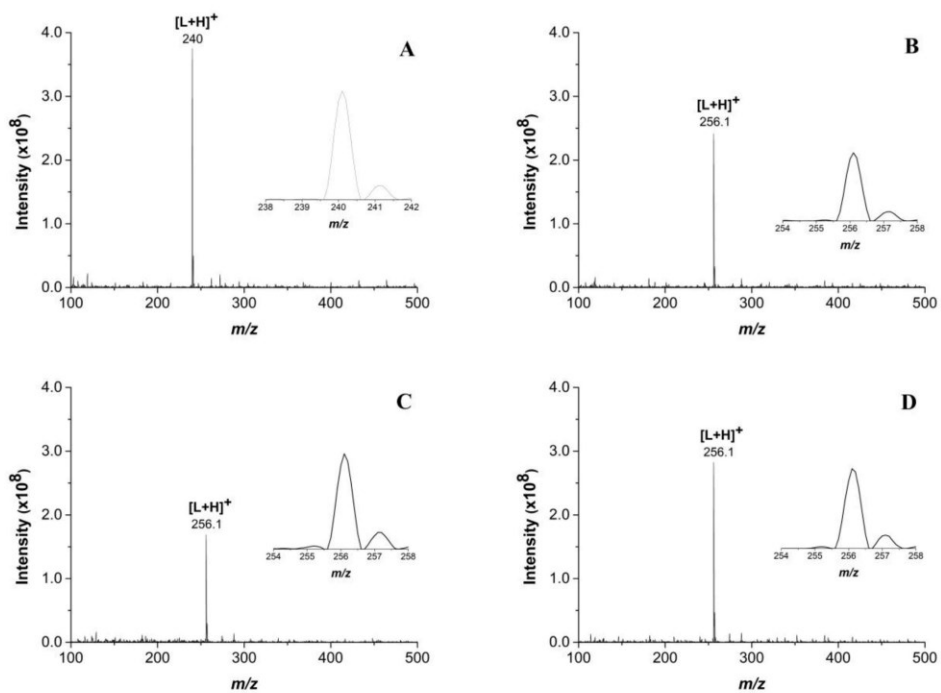
2
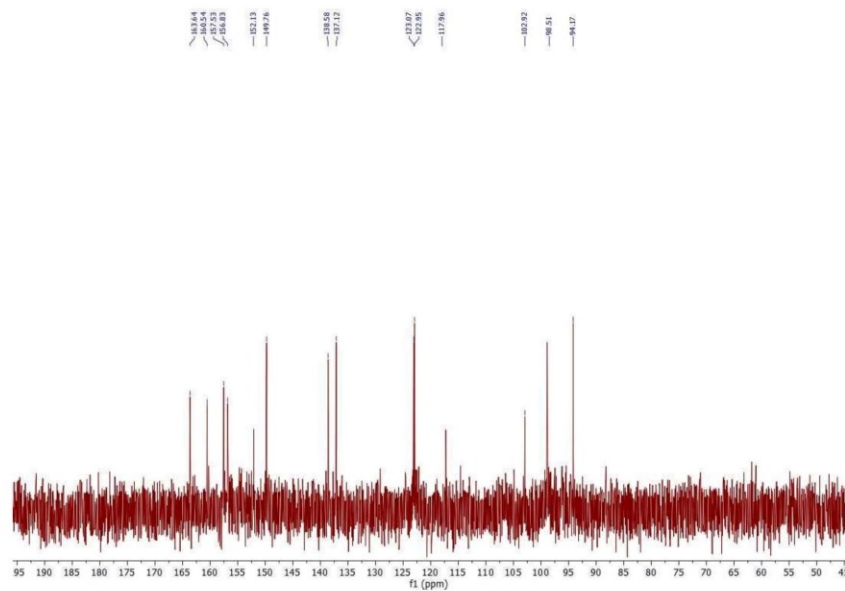
Fig. S3. ¹³C NMR of ligand **3**, 5,7-dihydroxy-3-(pyridin-2-yl)-2*H*-chromen-2-one (158 MHz, DMSO-d₆).
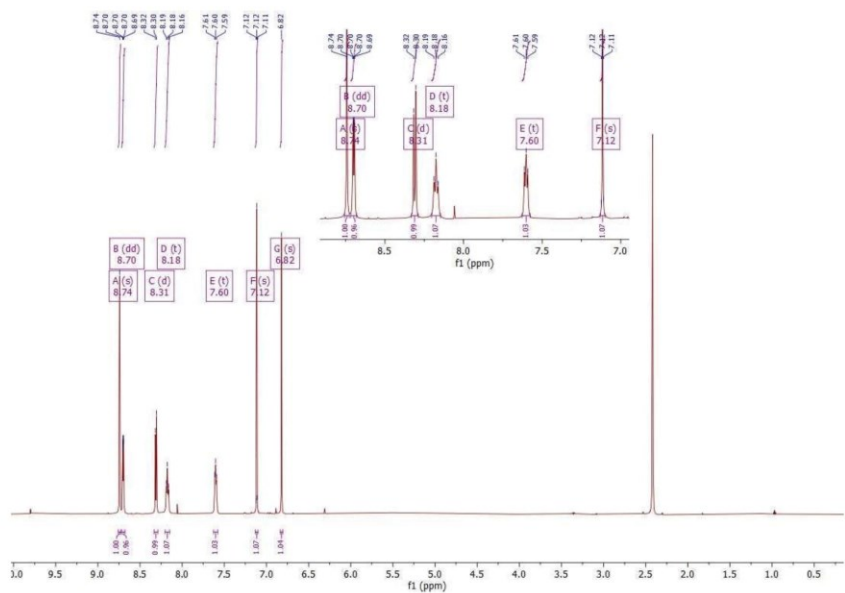
Fig. S4. ¹H NMR of ligand **4**, 6,7-dihydroxy-3-(pyridin-2-yl)-2*H*-chromen-2-one (600 MHz, DMSO-d₆).

Fig. S5. ^{13}C NMR of ligand **4**, 6,7-dihydroxy-3-(pyridin-2-yl)-2*H*-chromen-2-one (158 MHz, DMSO-d$_6$).

Fig. S6. ^{1}H NMR of ligand **5**, 7,8-dihydroxy-3-(pyridin-2-yl)-2*H*-chromen-2-one (600 MHz, DMSO-d$_6$).

4

Fig. S7. ESI-MS spectra of **2** (**A**), **3** (**B**), **4** (**C**), **5** (**D**).
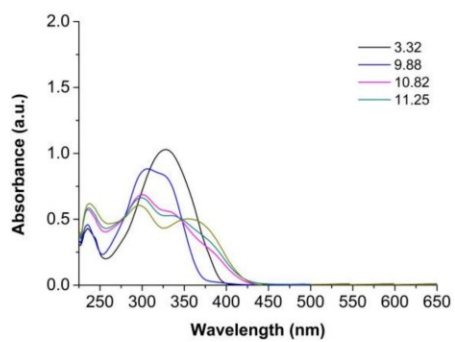
Fig. S8. UV-Vis spectra of **1** at pH > 10 (spectra at pH 3.32 and 9.88 are shown for comparison).

5

2. Spectrophotometric titrations

Spectral variations observed during the titration of 1
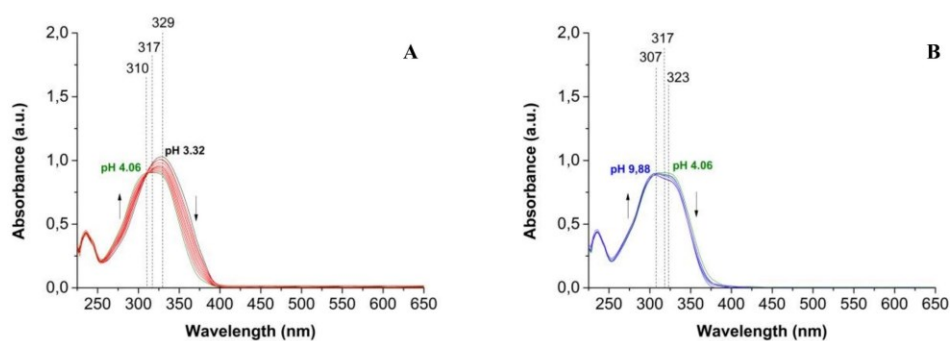
Fig. S9. Selected spectra collected during the potentiometric and spectrophotometric titration of **1** ($1.26{\times}10^{-4}$ M, 0.1 M NaCl, t 25°C, optic path length 0.5 cm) from pH 3.32 to 4.06 (**A**); from pH 4.06 to 9.88 (**B**).

During the titration with NaOH, three equilibria were evidenced in the pH range 3.32-9.88. At pH 3.32 a peak at 329 nm was present, while at increasing pH a decrease of the absorbance, with a blue-shift and the formation of an isosbestic point at 310 nm was observed. At pH 4.06 a larger band at 317 nm was formed (**Fig. S9A**) and further additions of NaOH determined a small decrease in absorbance and a change of the spectral shape (two overlapped peaks at 307 and 323 nm, **Fig. S9B**).

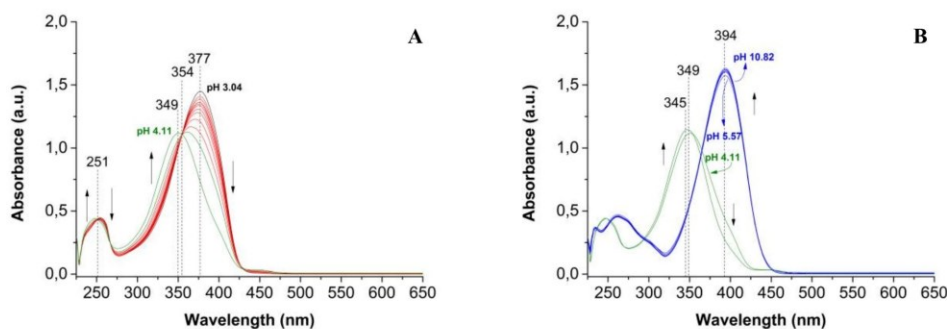**Spectral variations observed during the titration of 2**

Fig. S10. Selected spectra collected during the potentiometric and spectrophotometric titration of **2** (1.24×10^{-4} M, 0.1 M NaCl, *t* 25°C, optic path length 0.5 cm from pH 3.04 to 4.11 (**A**); from pH 4.11 to 10.82 (**B**).

The analysis of the spectra recorded during the titration of **2** (pH range 3.04-10.82) evidenced the presence of four equilibria. At pH 3.04 a peak at 377 nm was observed. At higher pH a gradual decrease in absorbance and the formation of an isosbestic point at 354 nm were observed. Towards pH 4, the formation of a new band centred at 349 nm and the appearance of an additional isosbestic point at 251 nm were put in evidence (**Fig. S10A**). Further additions of NaOH determined an initial blue shift at 345 nm followed by a red shift at 394 nm (see **Fig. S10B**, pH 5.57). In the pH range 5.57 - pH 10.82 a slight increase of absorbance was observed (**Fig. S10B**).

7

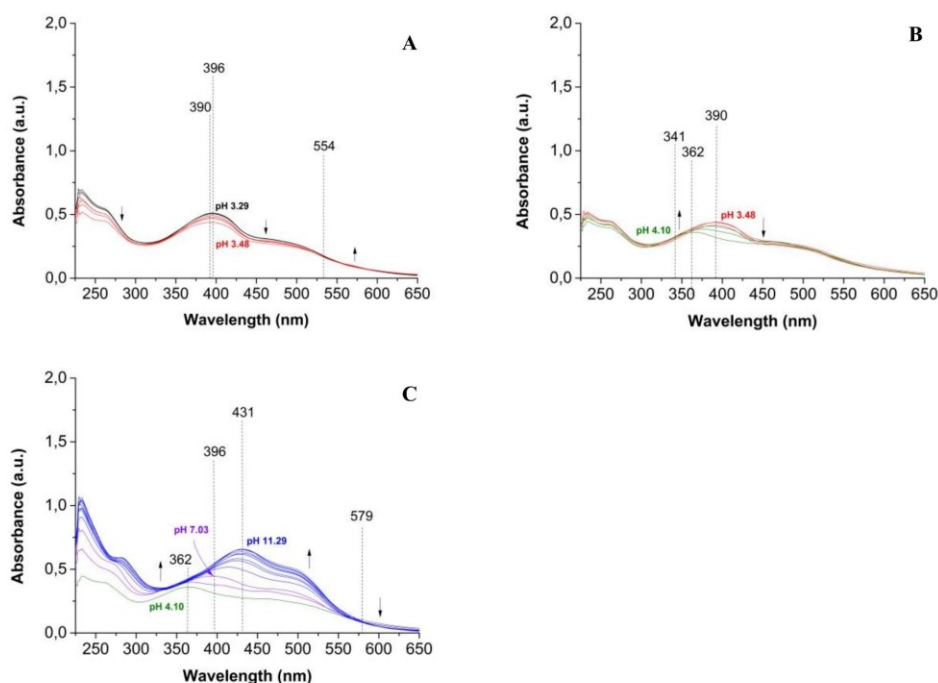**Spectral variations observed during the titration of 3**

Fig. S11. Selected spectra collected during the potentiometric and spectrophotometric titration of **3** (1.30×10^{-4} M, 0.1 M NaCl, t 25°C, optic path length 0.5 cm) from pH 3.29 to 3.48 (**A**); from pH 3.48 to 4.10 (**B**); from pH 4.10 to 11.29 (**C**).

presence of five equilibria. The first spectrum (pH 3.29) shown a peak at 396 nm with a shoulder at 473 nm, and after the firsts NaOH additions, a decrease in terms of absorbance and a slight blue shift at 390 nm together with the formation of an isosbestic point at 554 nm were observed (**Fig. S11A**). Further increases of titrant determined a change of the spectral profile, with the formation of a band at 362 nm and an isosbestic point at 341 nm (**Fig. S11B**). In the pH range 4.10 - 7.03 a red shift towards 396 nm and an increase in absorbance were observed. In the same pH range the solution appeared slightly turbid. With higher NaOH additions, a gradual shift towards wavelengths 431 nm with an increase in absorbance and the formation of an isosbestic point at 597 nm were observed. In this pH range the turbidity previously mentioned completely disappeared (**Fig. S11C**).

8

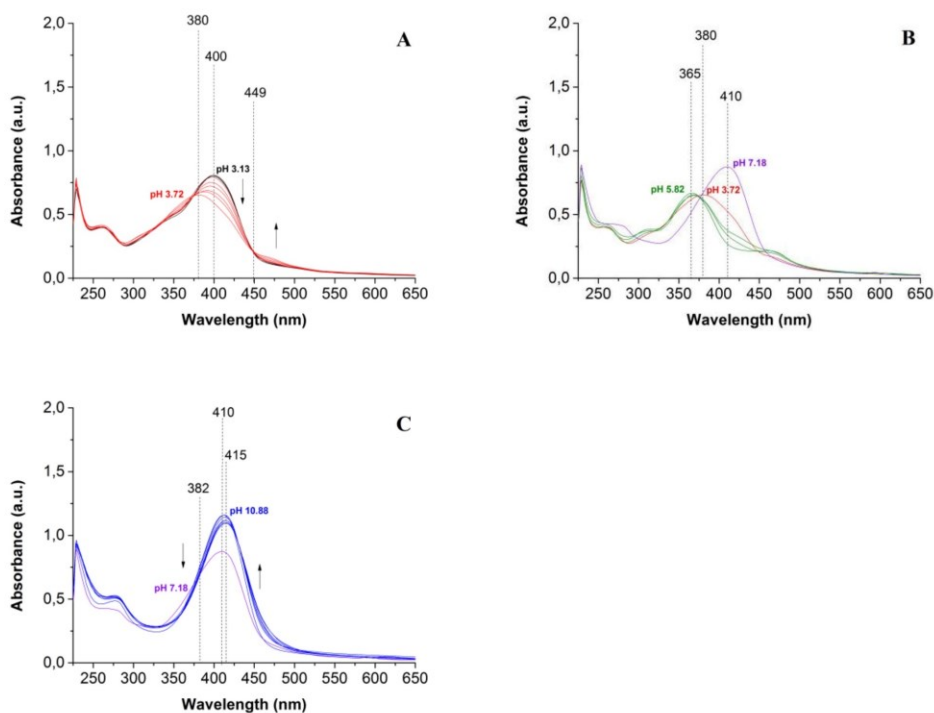**Spectral variations observed during the titration of 4**

Fig. S12. Selected spectra collected during the potentiometric and spectrophotometric titration of **4** (1.25×10^{-4} M, 0.1 M NaCl, t 25°C, optic path length 0.5 cm) from pH 3.13 to 3.72 (**A**); from pH 3.72 to 7.18 (**B**); from pH 7.18 to 10.88 (**C**).

Five chemical equilibria were identified from the analysis of the spectra recorded during the titration of **4** (pH range 3.13-10.88). The first spectrum (pH 3.13) shown a peak at 400 nm, while after the first additions of NaOH, a decrease in terms of absorbance, accompanied by a slight blue shift at 380 nm and the formation of an isosbestic point at 449 nm were observed (**Fig. S12A**). In the pH range 3.72 - 5.82, a band at 365 nm and at pH 7.18 a peak at 410 nm appeared (**Fig. S12B**). In the same pH range the solution was slightly turbid. With further NaOH additions, a gradual shift towards higher wavelengths (415 nm), with an increase of the absorbance and an isosbestic point at 382 nm were observed. In this pH range the turbidity previously mentioned completely disappeared (**Fig. S12C**).

9

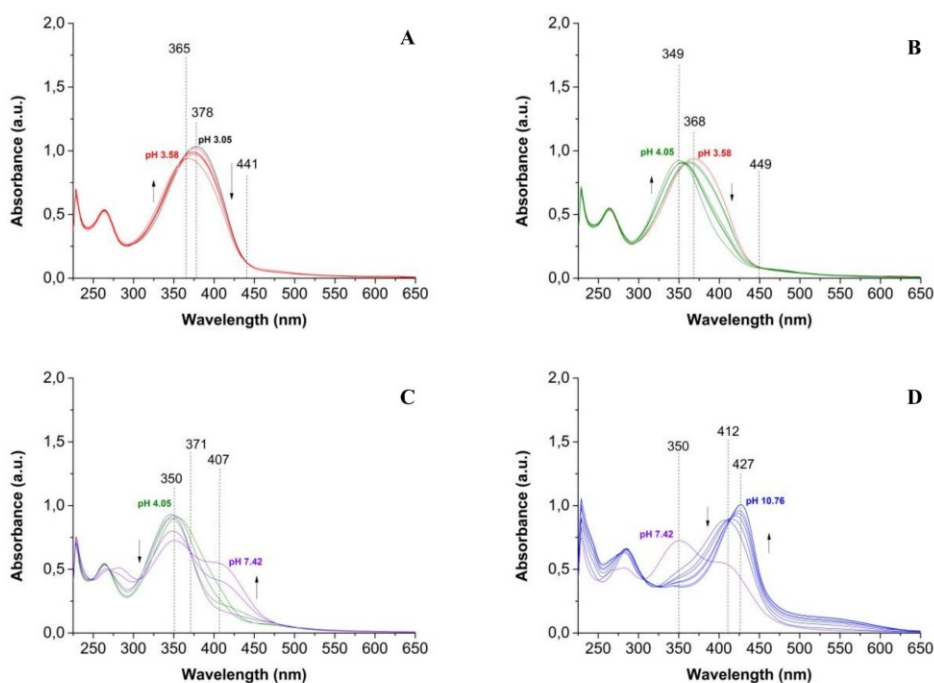**Spectral variations observed during the titration of 5**

Fig. S13. Selected spectra collected during the potentiometric and spectrophotometric titration of **5** (1.24×10^{-4} M, 0.1 M NaCl, t 25°C, optic path length 0.5 cm) from pH 3.05 to 3.58 (**A**); from pH 3.58 to 4.05 (**B**); from pH 4.05 to 7.42(**C**); from pH 7.42 to 10.76 (**D**).

The inspection of the spectra recorded during the titration of **5** (pH range 3.05-10.76) evidenced the presence of five equilibria. The first spectrum (pH 3.05) shown a peak at 378 nm, while after the firsts additions of titrant (pH range 3.05-3.58), a decrease in terms of absorbance and a blue shift at 365 nm together with the formation of an isosbestic point at 441 nm were observed (**Fig. S13A**). Further additions of NaOH (pH 3.58-4.05) determined a change of the spectral profile, with the formation of a new band at 349 nm and an isosbestic point at 449 nm (**Fig. S13B**). In the pH range 4.05 - 7.42 an additional decrease in absorbance with the formation of an overlapped peak at 407 nm and an isosbestic point at 371 nm were also observed (**Fig. S13C**). Further additions of NaOH

(pH range 7.42-10.76), determined a progressive shift towards higher wavelengths (427 nm) and an increase in absorbance and the formation of an isosbestic point at 412 nm (**Fig. S13D**).
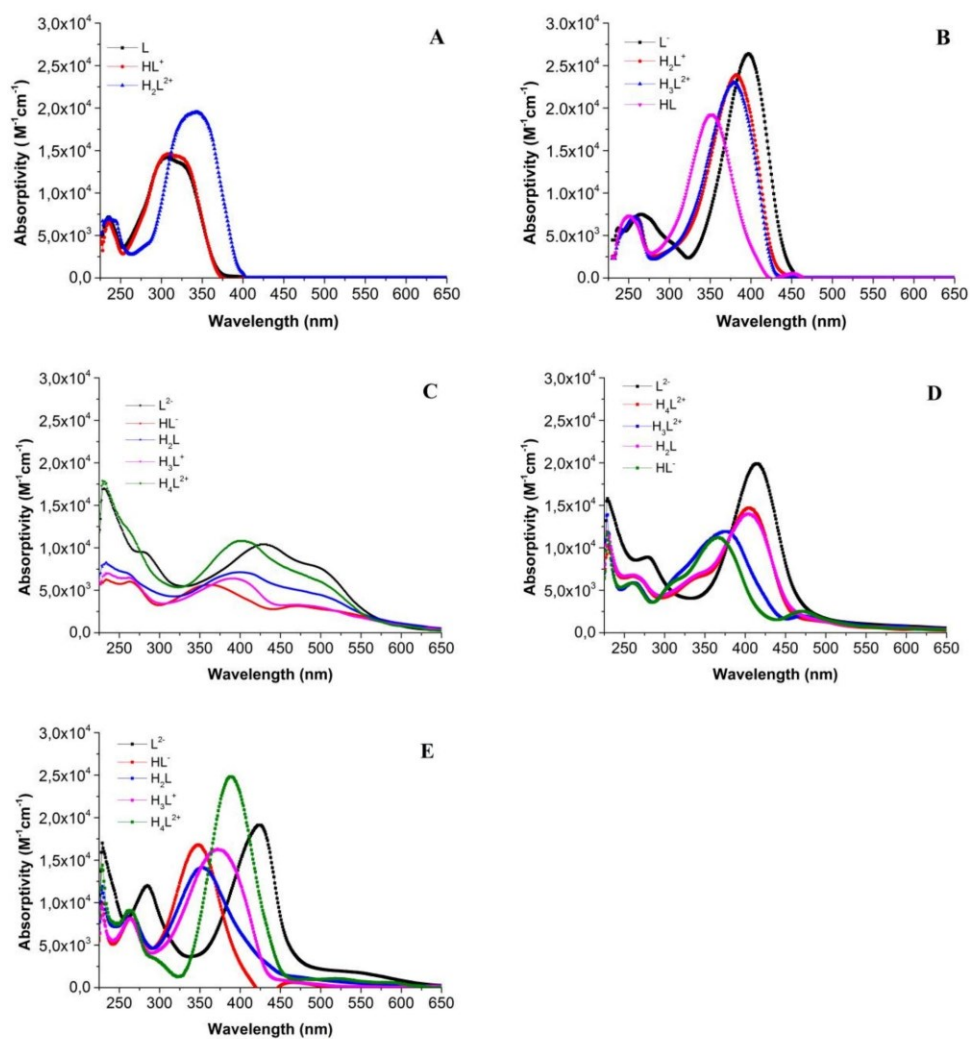

Fig. S14. Calculated pure spectra obtained from the eigenvalue analyses of potentiometric and spectrophotometric titrations of **1-5** (**A-E**).
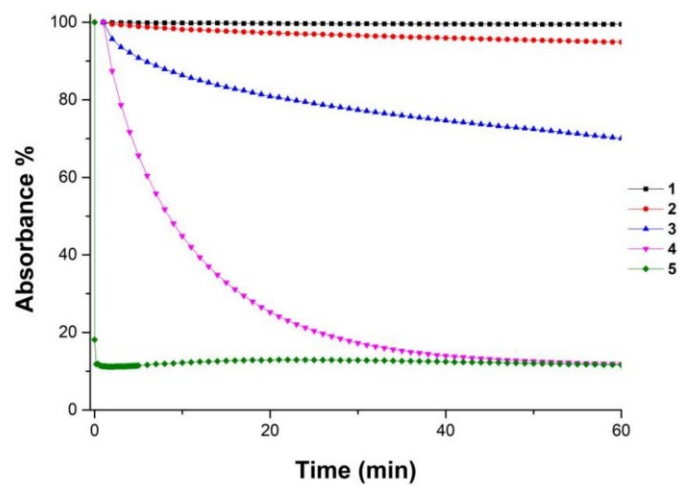
3. Antioxidant tests

Fig. S15. Reducing activity of DPP· shown by the studied compounds (0.05 mM, absolute ethanol, *t* 25 °C, λ 517 nm).

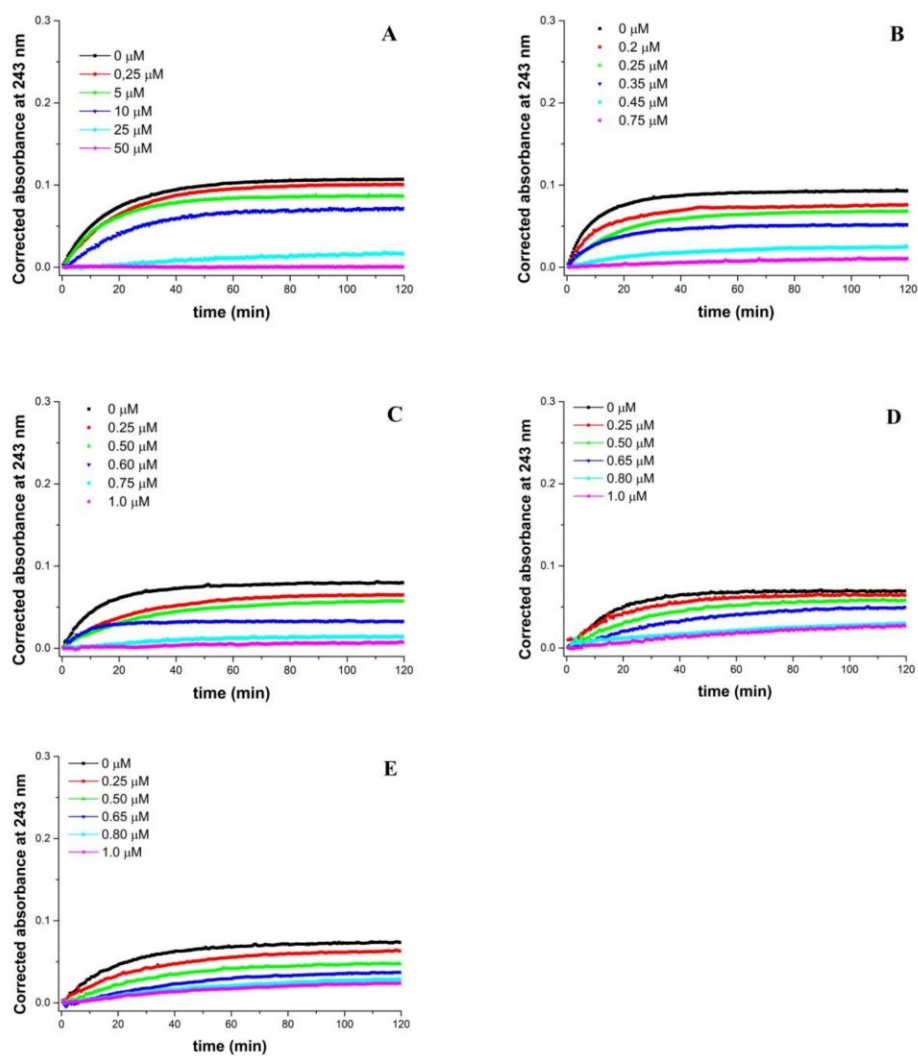## 4. Soybean lipoxygenase inhibition tests

Fig. S16. Absorbance at 243 nm of solutions containing sodium linoleate, lipoxygenase enzyme and **1-5** (**A-E**) at different molar concentration. Sodium linoleate 14 μM, lipoxygenase 0.83 nM, pH 7.4 TRIS buffer, *t* 25°C. Values are corrected for absorbance of ligands.
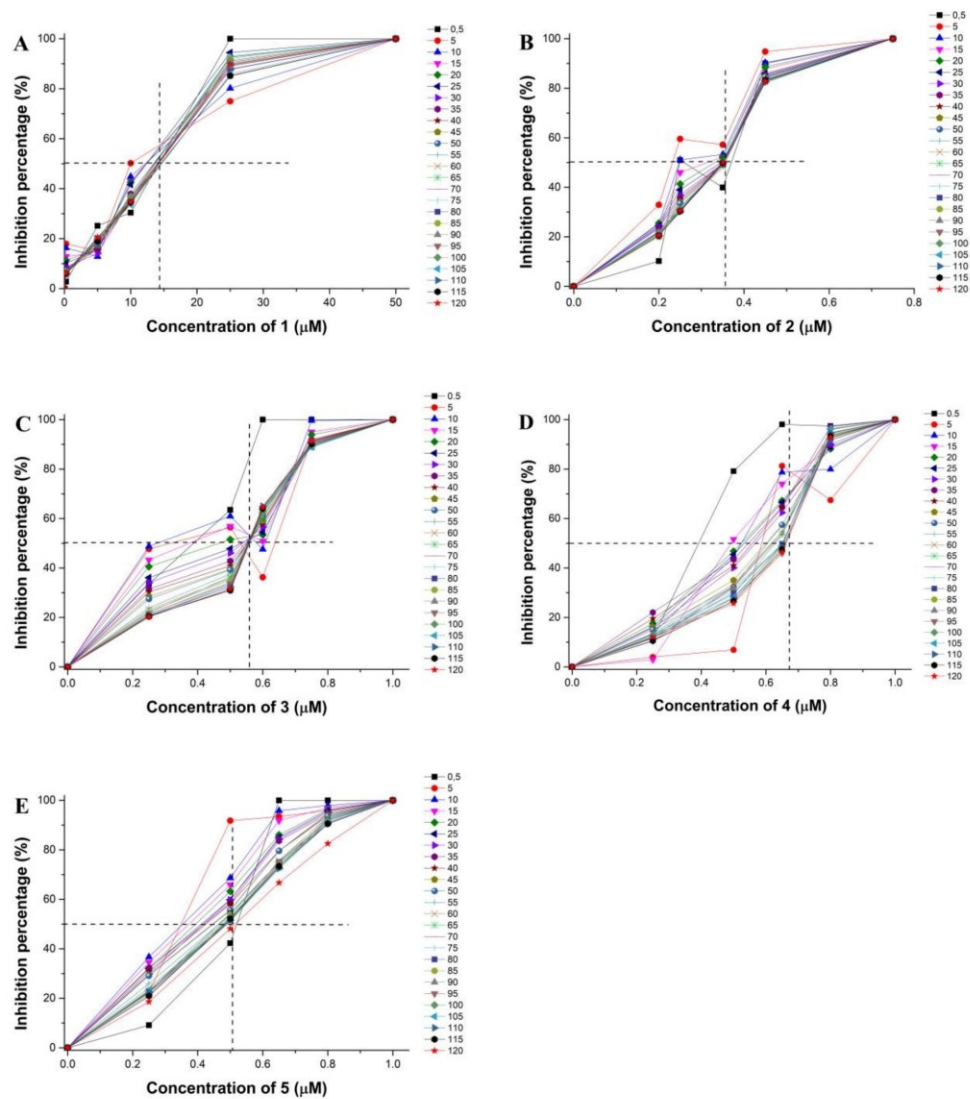
Fig. S17 Inhibition percentages (IP%) observed at different concentrations of solutions containing sodium linoleate, lipoxygenase enzyme and **1-5** (**A-E**). Sodium linoleate 14 μM, lipoxygenase 0.83 nM, pH 7.4 TRIS buffer, t 25°C.
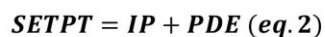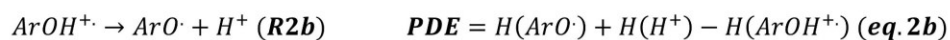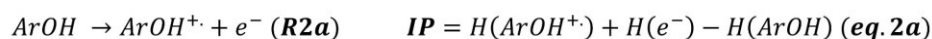
5. Computational details

HAT, SETPT and SPLET description

The Hydrogen Atom Transfer (**HAT**), the Single Electron Transfer Proton Transfer (**SETPT**) and the Sequential Proton Loss Electron Transfer (**SPLET**) mechanisms, commonly adopted by antioxidant phenolics are briefly explained:

1. Hydrogen Atom Transfer (**HAT**), where a radical hydrogen is directly abstracted from the phenolic antioxidant (**R1**). The Bond Dissociation Enthalpy (**BDE, eq.1**) quantitatively describes this reaction path.

$$ArOH \rightarrow ArO^{\cdot} + H^{\cdot} \; (\boldsymbol{R1}) \qquad \boldsymbol{BDE} = H(ArO^{\cdot}) + H(H^{\cdot}) - H(ArOH) \; (\boldsymbol{eq.1})$$
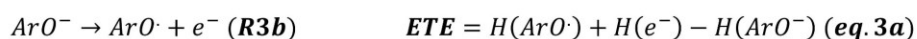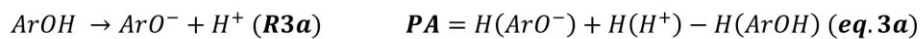
2. Single Electron Transfer Proton Transfer (**SETPT**), where the extraction of an electron from the antioxidant (**R2a**) is followed by proton removal from the subsequent radical cation (**R2b**). Ionization Potential (**IP, eq.2a**) and Proton Dissociation Enthalpy (**PDE, eq.2b**) are commonly exploited to describe the two steps, respectively. The thermochemical parameter **SETPT** (**eq.2**) considers the process in its entirety.

$$ArOH \rightarrow ArOH^{+\cdot} + e^{-} \; (\boldsymbol{R2a}) \qquad \boldsymbol{IP} = H(ArOH^{+\cdot}) + H(e^{-}) - H(ArOH) \; (\boldsymbol{eq.2a})$$

$$ArOH^{+\cdot} \rightarrow ArO^{\cdot} + H^{+} \; (\boldsymbol{R2b}) \qquad \boldsymbol{PDE} = H(ArO^{\cdot}) + H(H^{+}) - H(ArOH^{+\cdot}) \; (\boldsymbol{eq.2b})$$

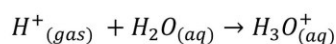$$\boldsymbol{SETPT} = IP + PDE \; (\boldsymbol{eq.2})$$

3. Sequential Proton Loss Electron Transfer (**SPLET**), where the phenolic antioxidant is firstly deprotonated (**R3a**) then converted in its neutral radical by single electron transfer (**R3b**). The first step is described by the Proton Affinity (**PA, eq.3a**), while the second one is

15

314

quantitatively defined by the Electron Transfer Enthalpy (**ETE, eq.3b**). The thermochemical parameter **SPLET (eq.3)** contemplates the process in its entirety.
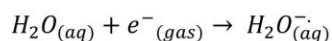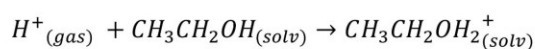
$$ArOH \rightarrow ArO^- + H^+ \; (\textbf{\textit{R3a}}) \qquad \textbf{\textit{PA}} = H(ArO^-) + H(H^+) - H(ArOH) \; (\textbf{\textit{eq. 3a}})$$

$$ArO^- \rightarrow ArO\cdot + e^- \; (\textbf{\textit{R3b}}) \qquad \textbf{\textit{ETE}} = H(ArO\cdot) + H(e^-) - H(ArO^-) \; (\textbf{\textit{eq. 3a}})$$

$$\textbf{\textit{SPLET}} = \textbf{\textit{PA}} + \textbf{\textit{ETE}} \; (\textbf{\textit{eq. 3}})$$

Chemical formalisms and equations used for the calculation of the enthalpies.

$$H^+_{(gas)} + H_2O_{(aq)} \rightarrow H_3O^+_{(aq)}$$

$$\textbf{\textit{H}}\big[\textbf{\textit{H}}^+_{(\textbf{\textit{aq}})}\big] = \textbf{\textit{H}}\big[\textbf{\textit{H}}_3\textbf{\textit{O}}^+_{(\textbf{\textit{aq}})}\big] - \textbf{\textit{H}}\big[\textbf{\textit{H}}_2\textbf{\textit{O}}_{(\textbf{\textit{aq}})}\big] - \textbf{\textit{H}}\big[\textbf{\textit{H}}^+_{(\textbf{\textit{gas}})}\big]$$

$$H_2O_{(aq)} + e^-_{(gas)} \rightarrow H_2O^{\cdot-}_{(aq)}$$

$$\textbf{\textit{H}}\big[\textbf{\textit{e}}^-_{(\textbf{\textit{aq}})}\big] = \textbf{\textit{H}}\big[\textbf{\textit{H}}_2\textbf{\textit{O}}^{\cdot-}_{(\textbf{\textit{aq}})}\big] - \textbf{\textit{H}}\big[\textbf{\textit{H}}_2\textbf{\textit{O}}_{(\textbf{\textit{aq}})}\big] - \textbf{\textit{H}}\big[\textbf{\textit{e}}^-_{(\textbf{\textit{gas}})}\big]$$

$$H^+_{(gas)} + CH_3CH_2OH_{(solv)} \rightarrow CH_3CH_2OH_2^+{}_{(solv)}$$

$$\textbf{\textit{H}}\big[\textbf{\textit{H}}^+_{(\textbf{\textit{solv}})}\big] = \textbf{\textit{H}}\big[\textbf{\textit{CH}}_3\textbf{\textit{CH}}_2\textbf{\textit{OH}}_2^+{}_{(\textbf{\textit{solv}})}\big] - \textbf{\textit{H}}\big[\textbf{\textit{CH}}_3\textbf{\textit{CH}}_2\textbf{\textit{OH}}_{(\textbf{\textit{solv}})}\big] - \textbf{\textit{H}}\big[\textbf{\textit{H}}^+_{(\textbf{\textit{gas}})}\big]$$

$$CH_3CH_2OH_{(solv)} + e^-_{(gas)} \rightarrow CH_3CH_2OH^{\cdot-}_{(solv)}$$
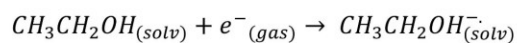
$$\textbf{\textit{H}}\big[\textbf{\textit{e}}^-_{(\textbf{\textit{solv}})}\big] = \textbf{\textit{H}}\big[\textbf{\textit{CH}}_3\textbf{\textit{CH}}_2\textbf{\textit{OH}}^{\cdot-}_{(\textbf{\textit{solv}})}\big] - \textbf{\textit{H}}\big[\textbf{\textit{CH}}_3\textbf{\textit{CH}}_2\textbf{\textit{OH}}_{(\textbf{\textit{solv}})}\big] - \textbf{\textit{H}}\big[\textbf{\textit{e}}^-_{(\textbf{\textit{gas}})}\big]$$
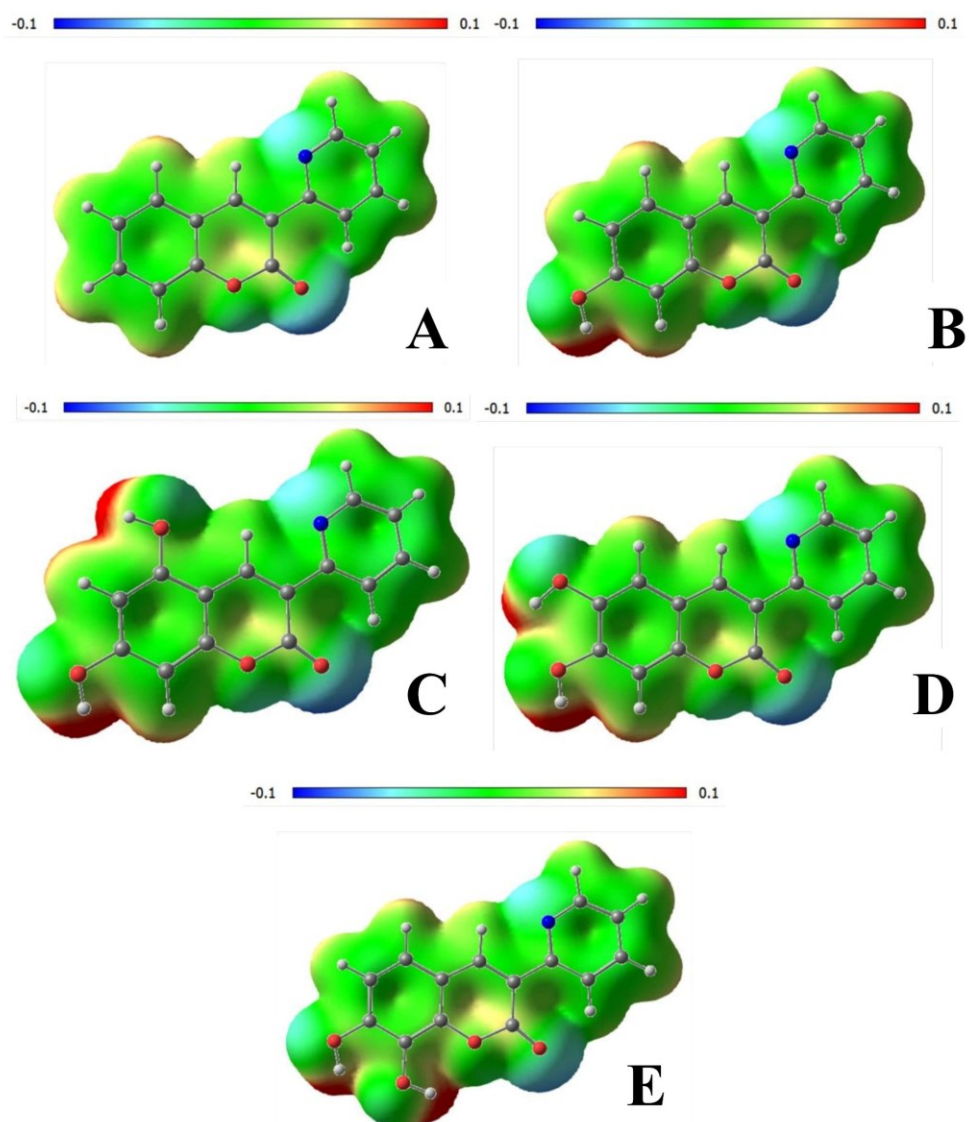
16

Fig. S18. Electrostatic Potential Maps (contour plot: 0.005) for **1-5** (**A-E**) at the DFT-optimized geometries (gas phase).
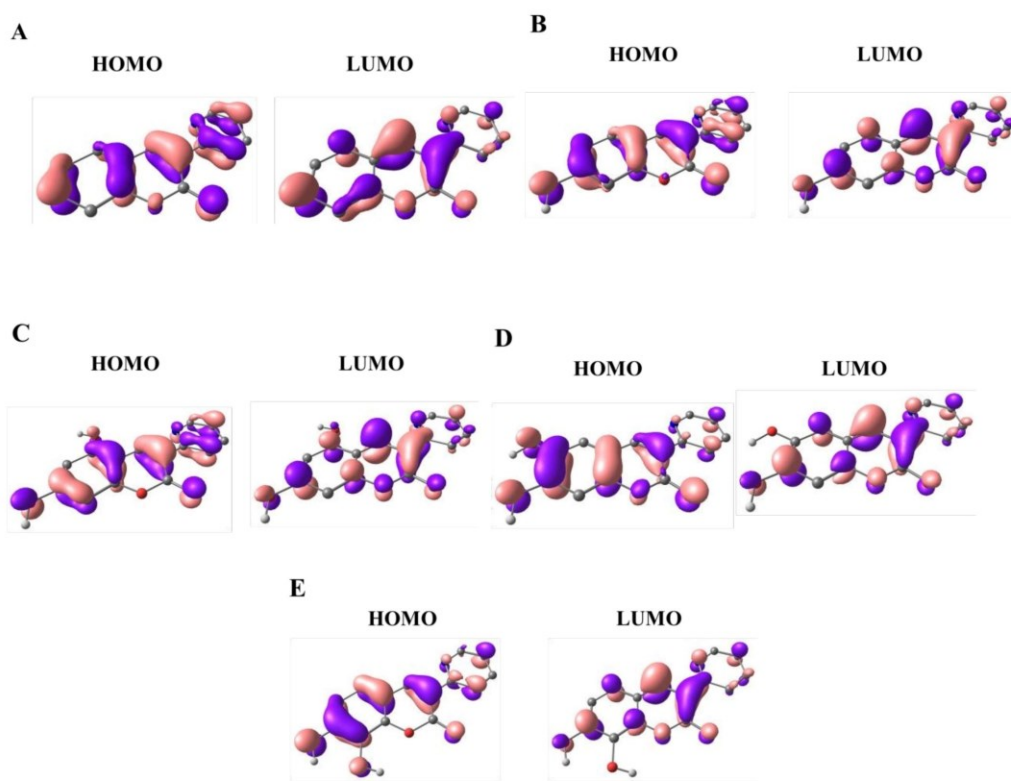
Fig. S19 Gas-phase frontier Molecular Orbitals plots (contour value: 0.005) of **1-5** (**A-E**).
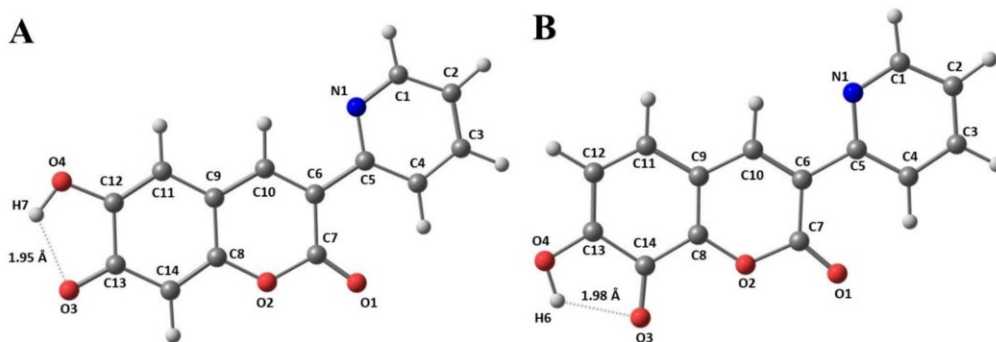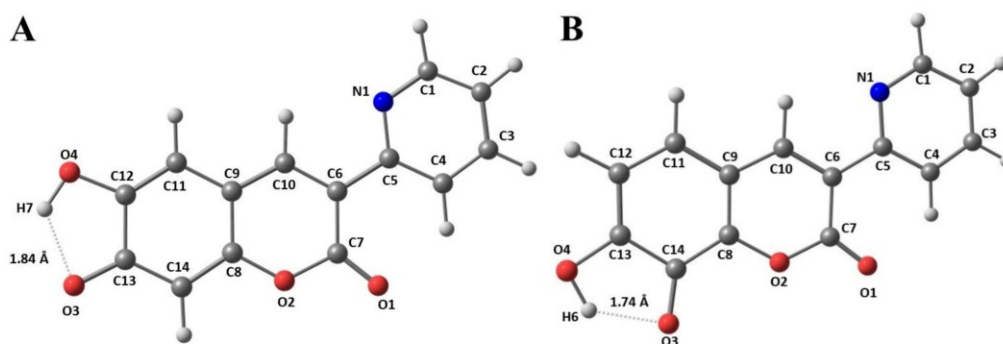
Fig. S20. Molecular drawings and atom labelling scheme for the most stable radical species of **4** (**A**) and **5** (**B**) at the DFT-optimized geometries (gas phase).
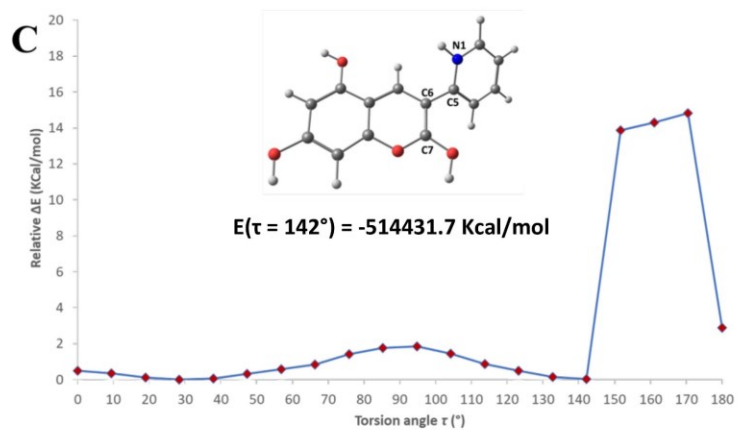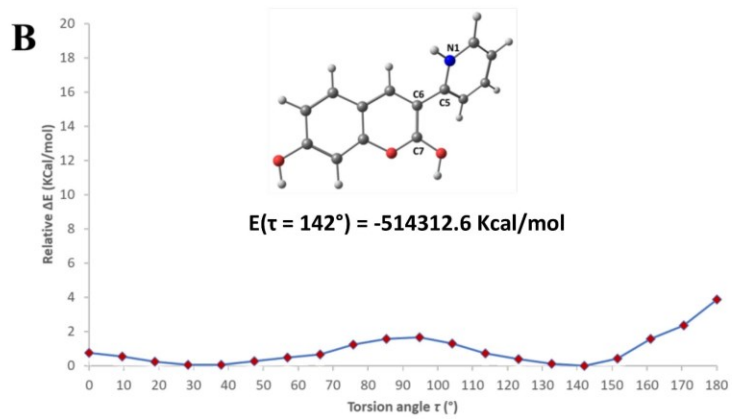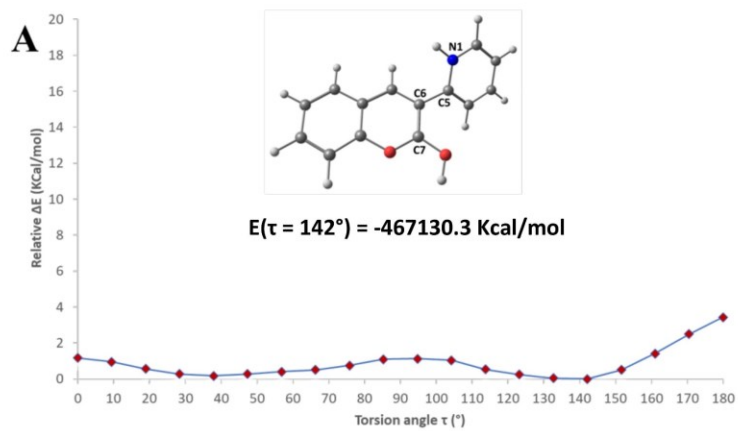

Fig. S21. Molecular drawings and atom labelling scheme for the most stable monoanionic species of **4** (**A**) and **5** (**B**) at the DFT-optimized geometries (gas phase).

A E(τ = 142°) = -467130.3 Kcal/mol

B E(τ = 142°) = -514312.6 Kcal/mol

C E(τ = 142°) = -514431.7 Kcal/mol

D

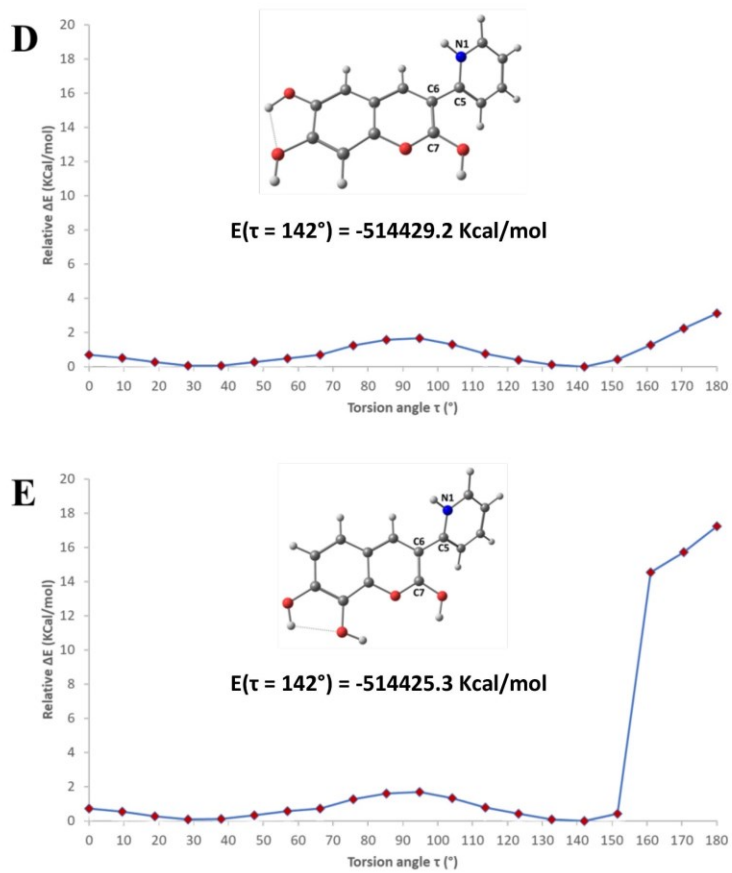E(τ = 142°) = -514429.2 Kcal/mol

E

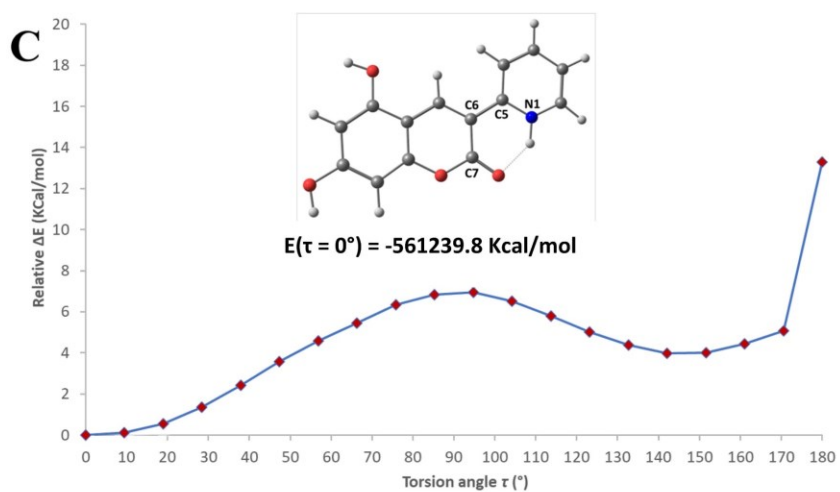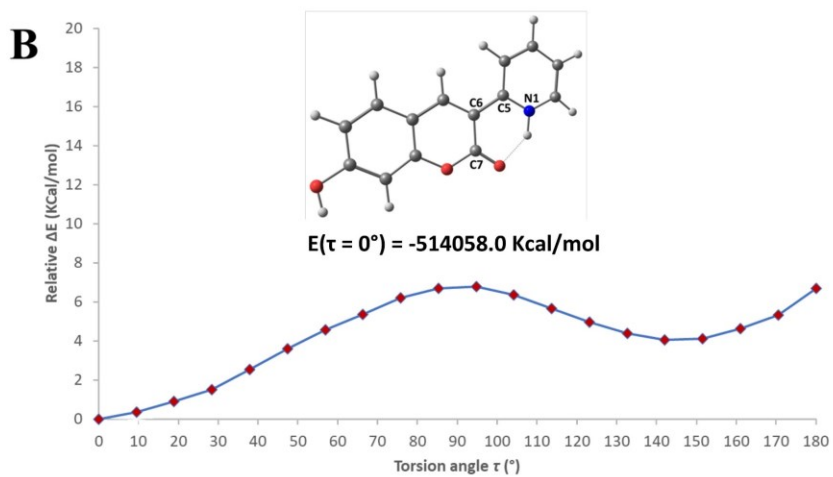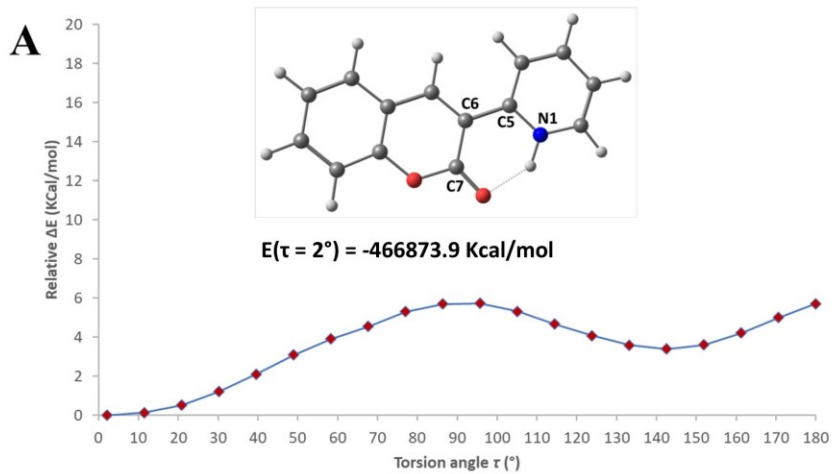
E(τ = 142°) = -514425.3 Kcal/mol

Fig. S22. Relative variation ΔE of the total electronic energy as a function of torsion angle τ (C7–C6–C5–N1 dihedral) calculated for the bis-cationic species of Gas-phase frontier Molecular Orbitals plots (contour value: 0.005) of **1-5** (**A-E**) at the DFT level (PBE0, def-2 TZVP) in water (CPCM).
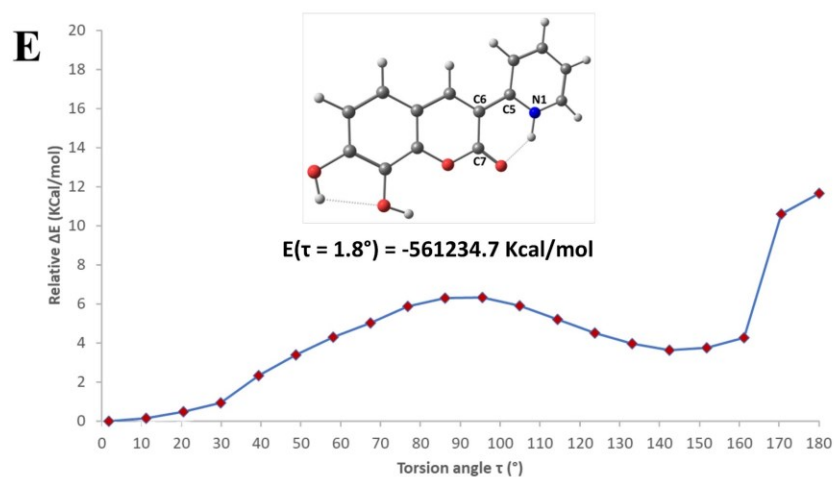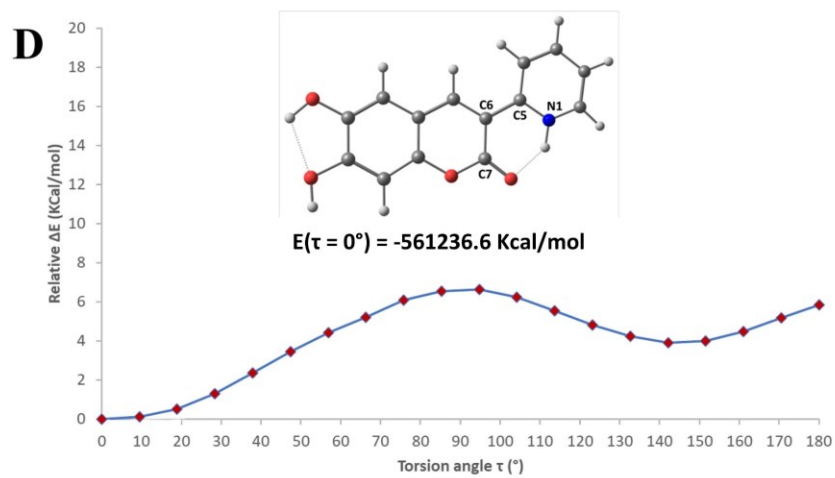
21

A E(τ = 2°) = –466873.9 Kcal/mol

B E(τ = 0°) = –514058.0 Kcal/mol

C E(τ = 0°) = –561239.8 Kcal/mol

22

321

D

E(τ = 0°) = -561236.6 Kcal/mol

E
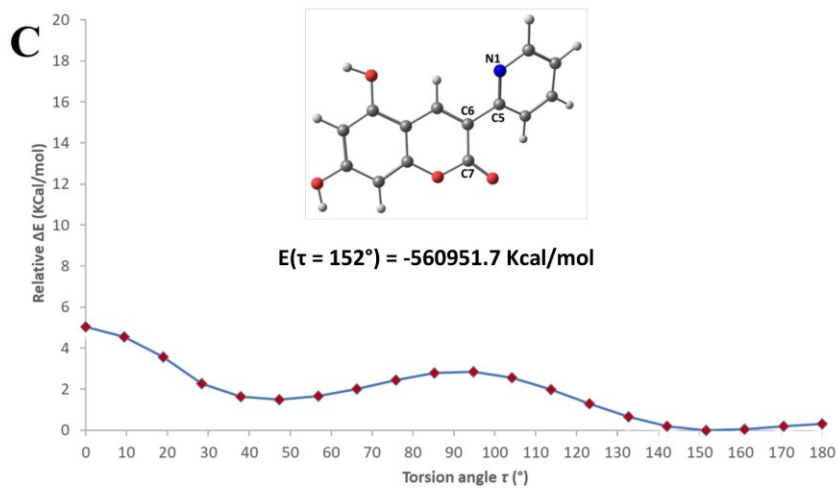
E(τ = 1.8°) = -561234.7 Kcal/mol

Fig. S23. Relative variation ΔE of the total electronic energy as a function of torsion angle τ (C7–C6–C5–N1 dihedral) calculated for the mono-cationic species of **1-5** (**A-E**) at the DFT level (PBE0, def-2 TZVP) in water (CPCM).

A

E(τ = 152°) = –466587.6 Kcal/mol

B

E(τ = 152°) = –513770.3 Kcal/mol

C

E(τ = 152°) = –560951.7 Kcal/mol

24

D

E(τ = 152°) = -560948.9 Kcal/mol

E

E(τ = 152°) = -560947.5 Kcal/mol

Fig. S24. Relative variation ΔE of the total electronic energy as a function of torsion angle τ (C7–C6–C5–N1 dihedral) calculated for **1-5** (**A-E**) at the DFT level (PBE0, def-2 TZVP) in water (CPCM).
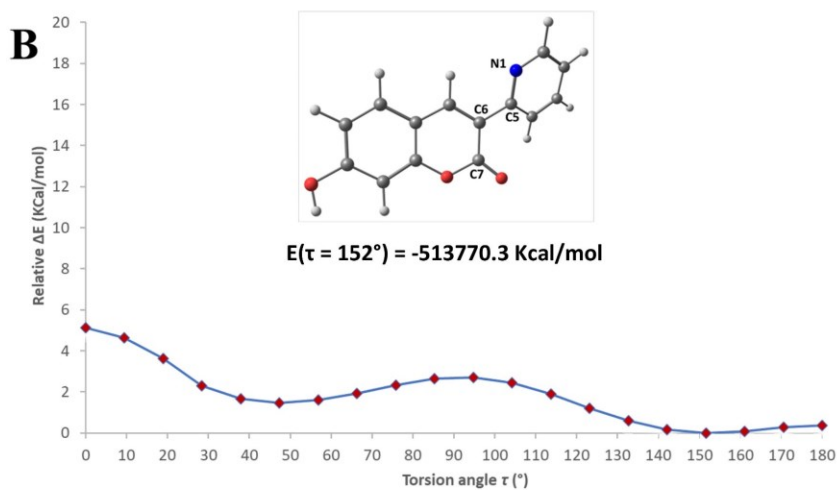
25

A

E(τ = 161°) = −513476.8 Kcal/mol

B

E(τ = 161°) = −560658.6 Kcal/mol

C

E(τ = 161°) = −560660.8 Kcal/mol

26

325

D

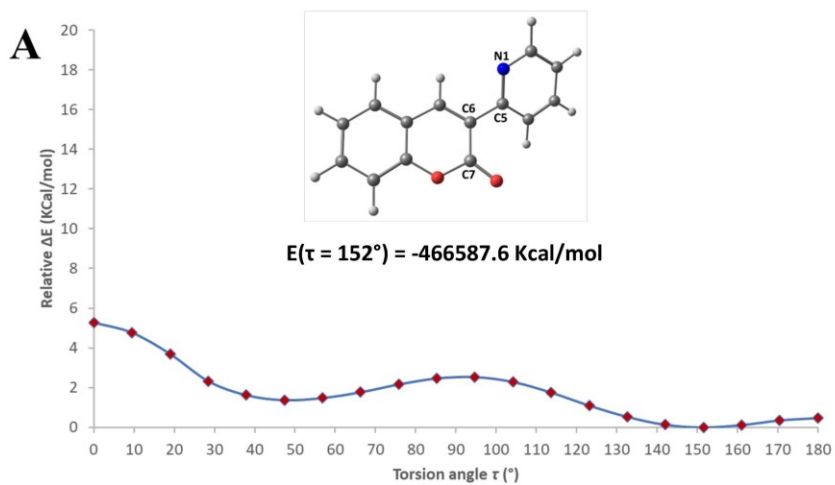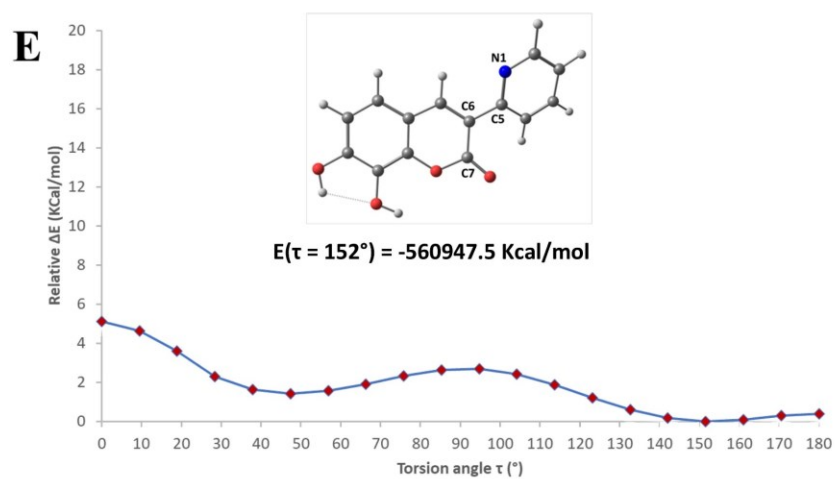E(τ = 152°) = -560654.7 Kcal/mol

Fig. S25. Relative variation ΔE of the total electronic energy as a function of torsion angle τ (C7–C6–C5–N1 dihedral) calculated for the monoanionic species of **2** (**A**), **3** (**B**), **4** (**C**) and **5** (**D**) at the DFT level (PBE0, def-2 TZVP) in water (CPCM).

A

E(τ = 170°) = -560357.9 Kcal/mol

27

B

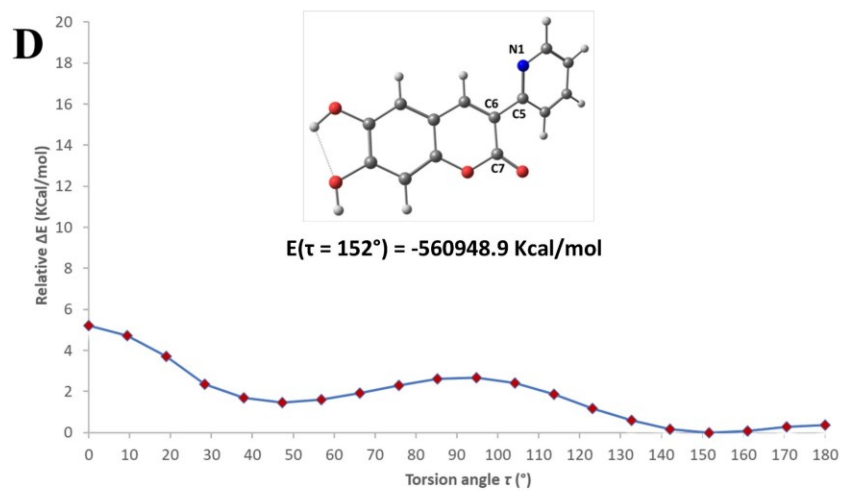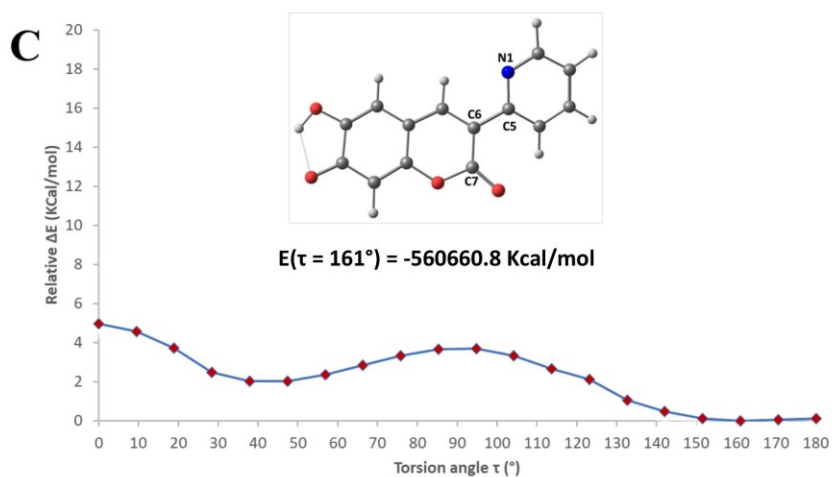E(τ = 170°) = -560349.0 Kcal/mol

C

E(τ = 170°) = -560345.2 Kcal/mol
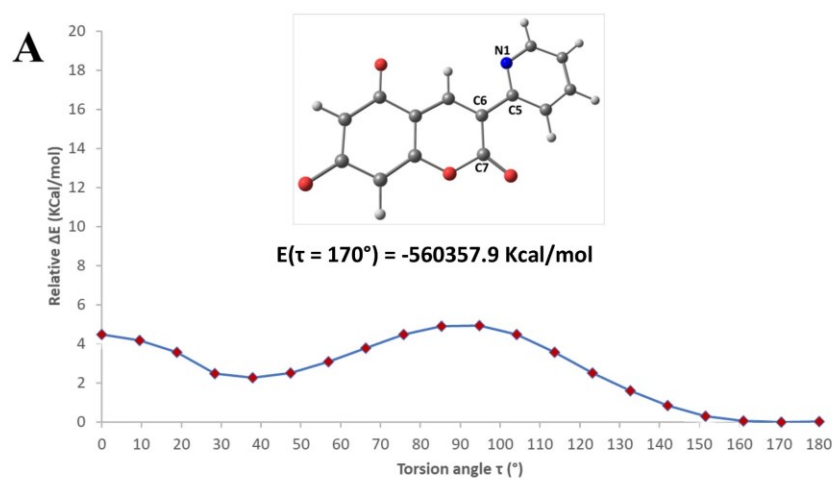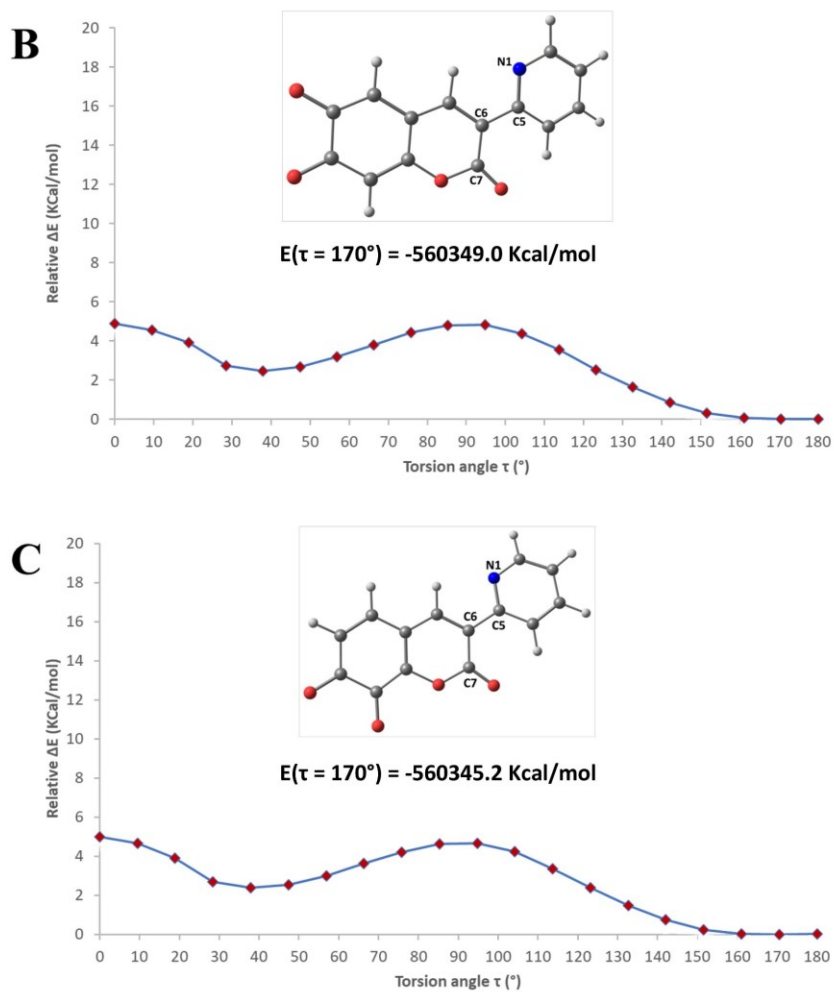
Fig. S26. Relative variation ΔE of the total electronic energy as a function of torsion angle τ (C7–C6–C5–N1 dihedral) calculated for the bis-cationic species of **3** (**A**), **4** (**B**) and **5** (**C**) at the DFT level (PBE0, def-2 TZVP) in water (CPCM).
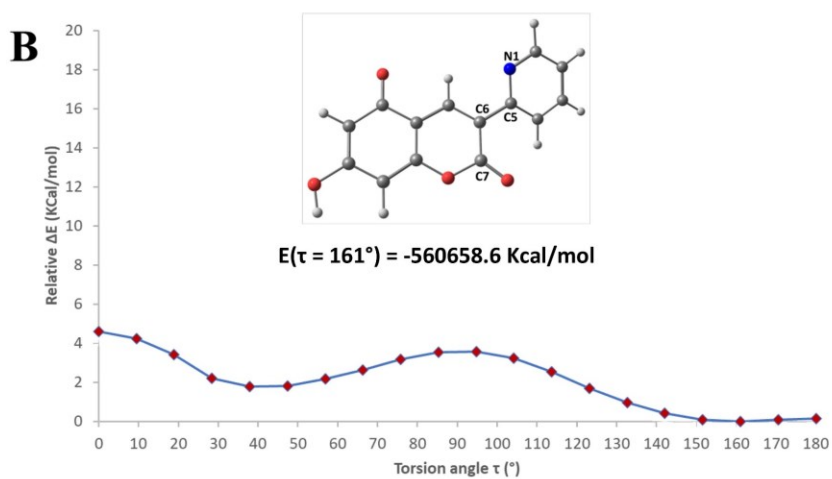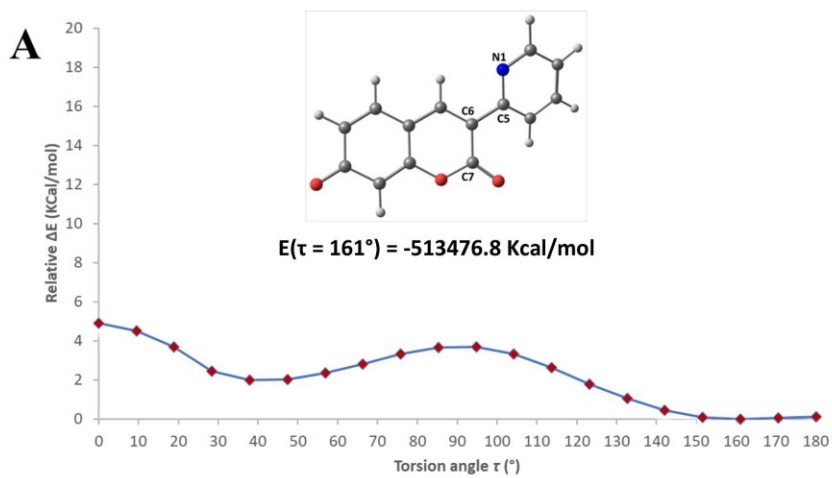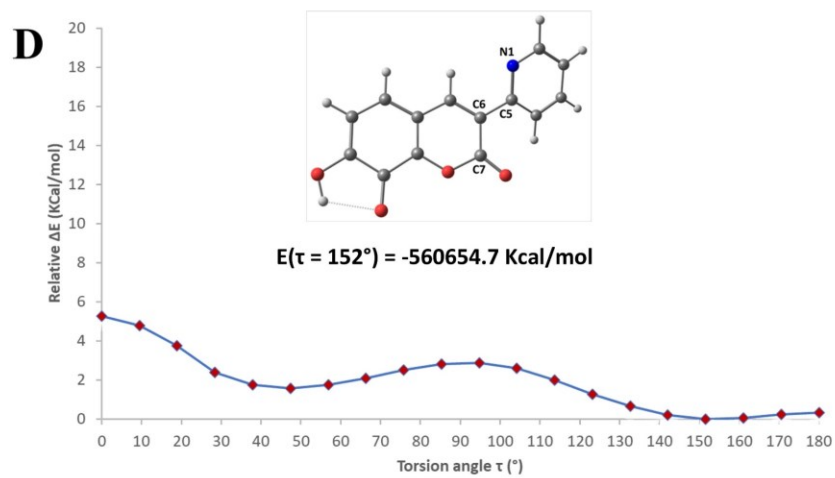
28

Fig. S27. Protonation sequence proposed for compound **1** based on experimental (potentiometric and spectrophotometric titrations) and theoretical data (DFT-PBE0/def-2 TZVP, water CPCM). The lowest-energy conformer for each differently protonated species is reported.
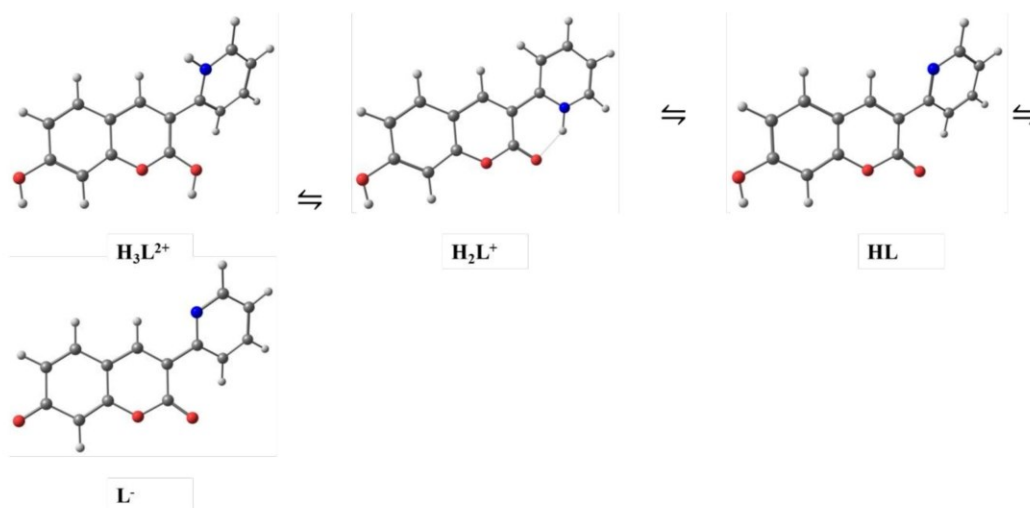
Fig. S28. Protonation sequence proposed for compound **2** based on experimental (potentiometric and spectrophotometric titrations) and theoretical data (DFT-PBE0/def-2 TZVP, water CPCM). The lowest-energy conformer for each differently protonated species is reported.
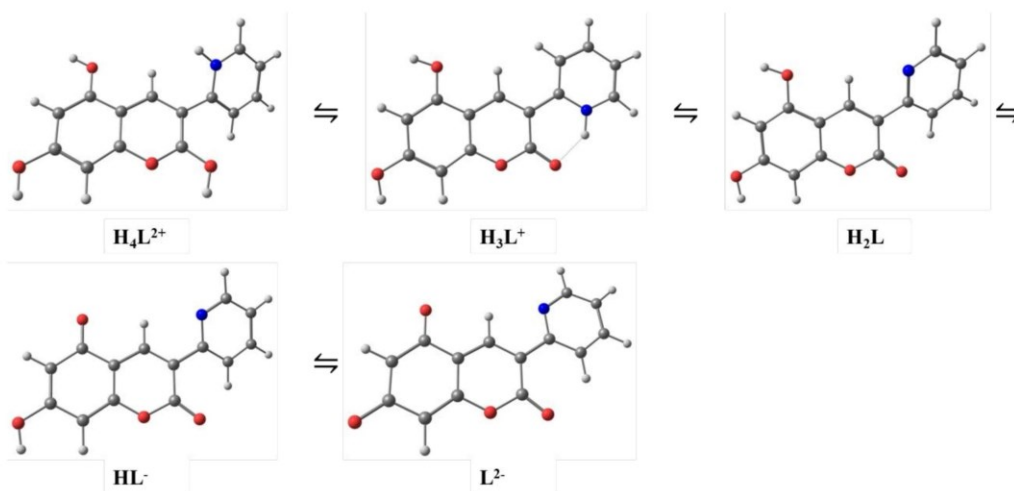
Fig. S29. Protonation sequence proposed for compound **3** based on experimental (potentiometric and spectrophotometric titrations) and theoretical data (DFT-PBE0/def-2 TZVP, water CPCM). The lowest-energy conformer for each differently protonated species is reported.
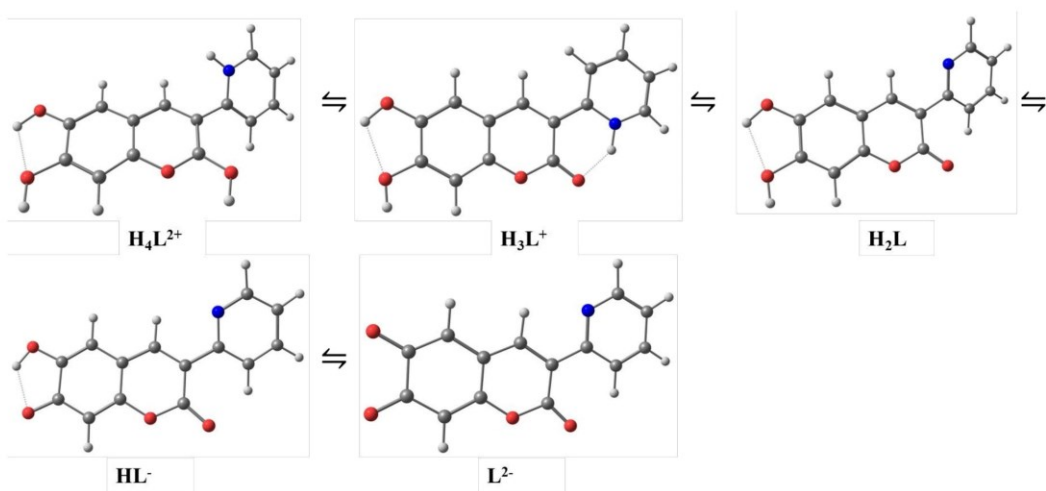
Fig. S30. Protonation sequence proposed for compound **4** based on experimental (potentiometric and spectrophotometric titrations) and theoretical data (DFT-PBE0/def-2 TZVP, water CPCM). The lowest-energy conformer for each differently protonated species is reported.
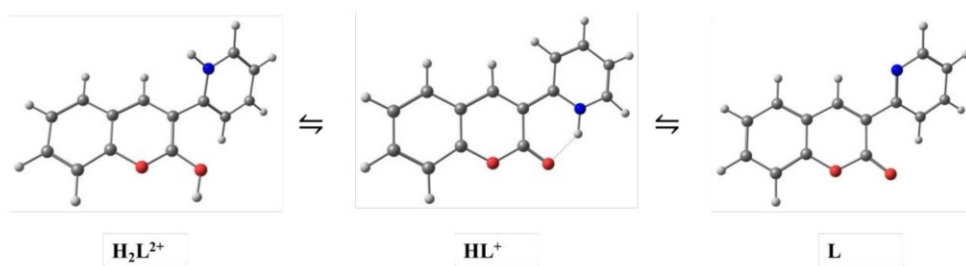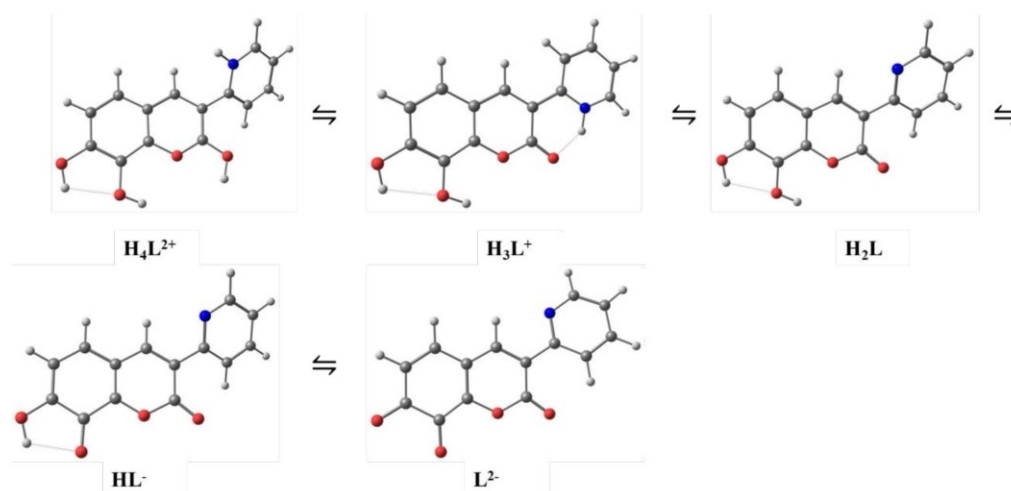
Fig. S31. Protonation sequence proposed for compound **5** based on experimental (potentiometric and spectrophotometric titrations) and theoretical data (DFT-PBE0/def-2 TZVP, water CPCM). The lowest-energy conformer for each differently protonated species is reported.
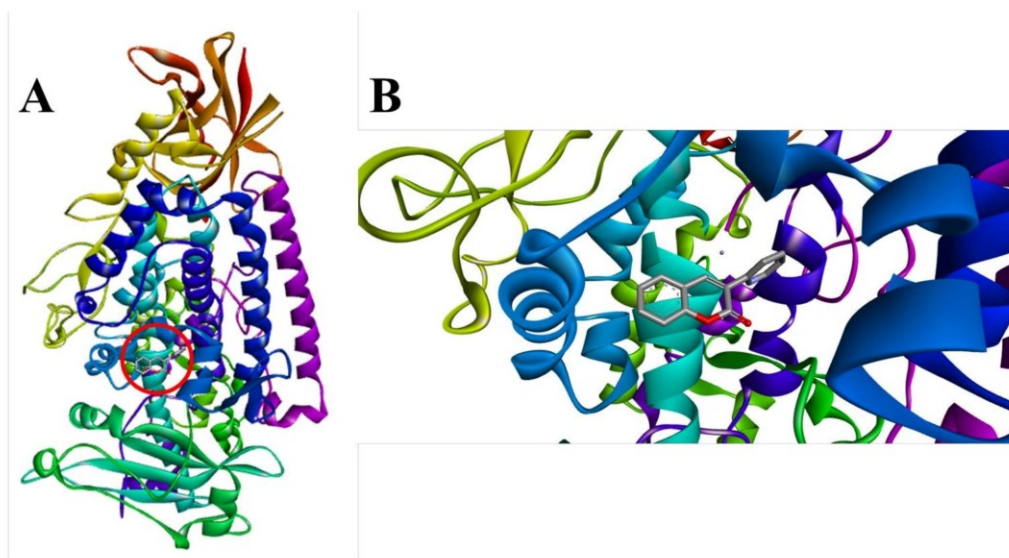

Fig. S32. Full view of the complex between the highest-ranking score of **1** and soybean lipoxygenase (**A**); zoom of the binding pocket occupied by the highest-ranking score of **1** and soybean lipoxygenase (**B**).

31
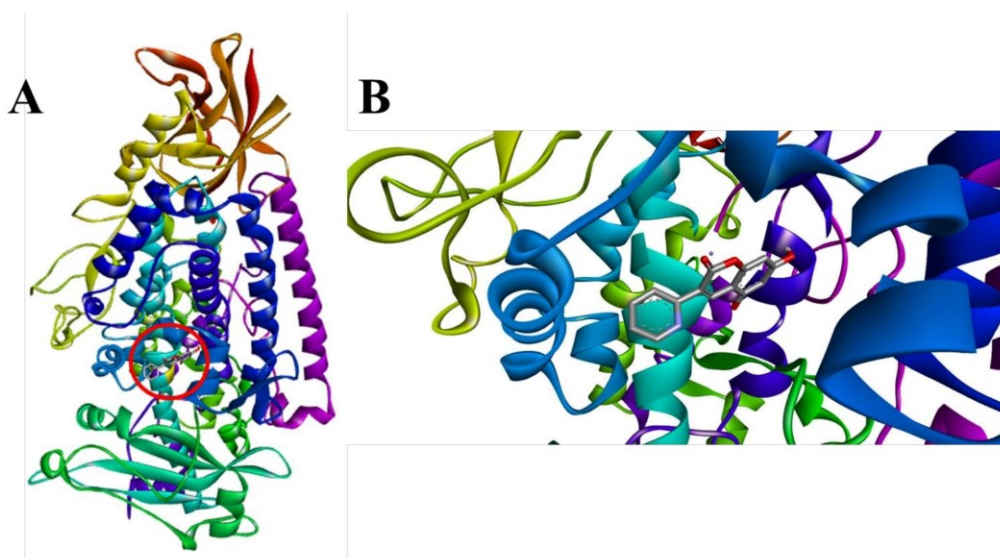
Fig. S33. Full view of the complex between the highest-ranking score of **3** (in its monoanionic form **HL**⁻) and soybean lipoxygenase (**A**); zoom of the binding pocket occupied by the highest-ranking score of **3** (in its monoanionic form **HL**⁻) and soybean lipoxygenase (**B**).
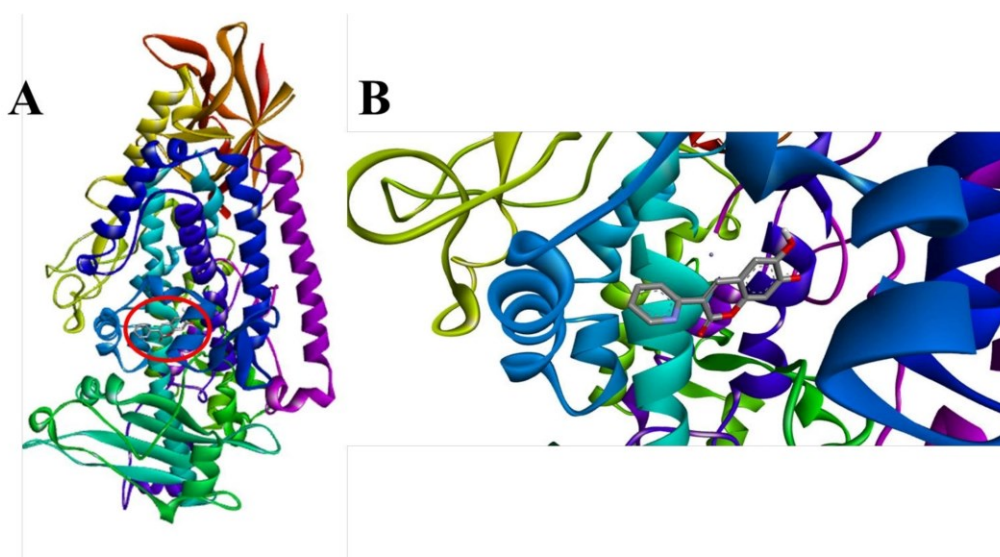
Fig. S34. Full view of the complex between the highest-ranking score of **4** (in its monoanionic form **HL**⁻) and soybean lipoxygenase (**A**); zoom of the binding pocket occupied by the highest-ranking score of **4** (in its monoanionic form **HL**⁻) and soybean lipoxygenase (**B**).

32
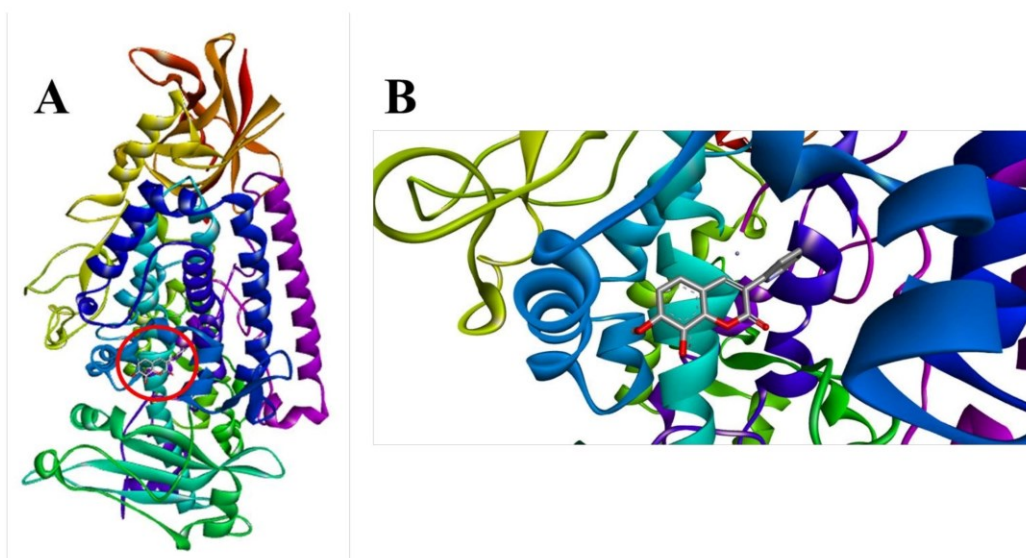
Fig. S35. Full view of the complex between the highest-ranking score of **5** (in its monoanionic form **HL⁻**) and soybean lipoxygenase (**A**); zoom of the binding pocket occupied by the highest-ranking score of **5** (in its monoanionic form **HL⁻**) and soybean lipoxygenase (**B**).

Table S1. Selected optimized bond distances (Å) and angles (°) for DFT-optimized structure of **1** (gas phase) and corresponding X-Ray structural parameters. Atom labelling scheme as in **Fig. 4A**.

	1	
	Structural parameters	**DFT-optimized**
C8-O2	1.370	1.348
O2-C7	1.374	1.378
C7-O1	1.204	1.201
C7-C6	1.476	1.466
C6-C5	1.488	1.482
C5-N1	1.355	1.339
N1-C1	1.324	1.321
C8-O2-C7	123.87	124.06

O2-C7-C6	117.25	116.62
O2-C7-O1	115.74	116.04
C7-C6-C5	120.55	121.43
C6-C5-N1	114.21	114.97
C5-N1-C1	117.96	119.02
C7-C6-C5-N1	169.59	173.96
C8-O2-C7-O1	179.77	179.68

Table S2. Selected optimized bond distances (Å) and angles (°) for DFT-optimized structure of **2** (gas phase). Atom labelling scheme as in **Fig. 4B**.

2

C8-O2	1.345	O2-C7-O1	115.58
O2-C7	1.384	C7-C6-C5	121.53
C7-O1	1.201	C6-C5-N1	115.04
C7-C6	1.461	C5-N1-C1	119.07
C6-C5	1.481	O3-C13-C14	122.27
C5-N1	1.339	O3-C13-C12	116.95
N1-C1	1.321	C7-C6-C5-N1	179.64
O3-C13	1.348	C8-O2-C7-O1	179.99
O3-H6	0.961	O3-C13-C12-C11	-179.99
C8-O2-C7	124.02	O3-C13-C14-C8	179.99
O2-C7-C6	116.58		

Table S3. Selected optimized bond distances (Å) and angles (°) for DFT-optimized structure of **3** (gas phase). Atom labelling scheme as in **Fig. 4C**.

3

C8-O2	1.343	**C7-C6-C5**	121.52
O2-C7	1.386	**C6-C5-N1**	115.11
C7-O1	1.201	**C5-N1-C1**	119.09
C7-C6	1.459	**O3-C13-C14**	112.20
C6-C5	1.480	**O3-C13-C12**	116.46
C5-N1	1.339	**O4-C11-C9**	116.72
N1-C1	1.321	**O4-C11-C12**	122.49
O3-C13	1.348	**C7-C6-C5-N1**	179.34
O4-C11	1.347	**C8-O2-C7-O1**	179.92
O3-H6	0.962	**O3-C13-C12-C11**	-179.99
O4-H8	0.961	**O3-C13-C14-C8**	179.99
C8-O2-C7	124.39	**O4-C11-C12-C13**	-179.99
O2-C7-C6	116.49	**O4-C11-C9-C10**	-0.05

Table S4. Selected optimized bond distances (Å) and angles (°) for DFT-optimized structure of **4** (gas phase). Atom labelling scheme as in **Fig. 4D**.

4

C8-O2	1.348	**C6-C5-N1**	115.07
O2-C7	1.379	**C5-N1-C1**	119.07
C7-O1	1.202	**O3-C13-C12**	114.94
C7-C6	1.462	**O3-C13-C14**	123.84
C6-C5	1.481	**O4-C12-C11**	120.60
C5-N1	1.339	**O4-C12-C13**	120.18

N1-C1	1.321	**C7-C6-C5-N1**	177.95
O3-C13	1.357	**C8-O2-C7-O1**	179.96
O4-C12	1.352	**O4-C12-C111-C9**	-179.99
O3-H6	0.961	**O4-C12-C13-C14**	179.99
O4-H7	0.964	**O3-C13-C12-C11**	179.99
O3···H7	2.126	**O3-C13-C14-C8**	-179.99
C8-O2-C7	123.92	**O3-C13-C12-O4**	-0.01
O2-C7-C6	116.47	**O4-C12-C13-O3**	0.01
C7-C6-C5	121.47		

Table S5. Selected optimized bond distances (Å) and angles (°) for DFT-optimized structure of **5** (gas phase). Atom labelling scheme as in **Fig. 4E**.

<div align="center">

5

</div>

C8-O2	1.350	**C6-C5-N1**	115.01
O2-C7	1.387	**C5-N1-C1**	119.09
C7-O1	1.200	**O3-C14-C13**	117.98
C7-C6	1.460	**O3-C14-C8**	123.20
C6-C5	1.481	**O4-C13-C14**	120.06
C5-N1	1.339	**O4-C13-C12**	119.70
N1-C1	1.321	**C7-C6-C5-N1**	179.58
O3-C14	1.356	**C8-O2-C7-O1**	179.97
O4-C13	1.345	**O4-C13-C12-C11**	-179.99
O3-H5	0.965	**O4-C13-C14-C8**	179.99
O3-H6	0.965	**O3-C14-C8-C9**	-179.99
O3···H6	2.174	**O4-C14-C13-C12**	179.99
C8-O2-C7	123.49	**O3-C14-C8-O2**	0.01

O2-C7-C6	116.23	**O3-C14-C13-O4**	-0.01
C7-C6-C5	121.27	**O4-C13-C14-O3**	0.01

Table S6. Selected atomic charges, calculated at Mulliken and NPA levels, of **1**. Atomic scheme as in **Fig. 4A.**

1

	Mulliken	NPA
O1	-0.318	-0.555
O2	-0.147	-0.422
N1	-0.233	-0.426

Table S7. Selected atomic charges, calculated at Mulliken and NPA levels, of **2**. Atomic scheme as in **Fig. 4B.**

2

	Mulliken	NPA
O1	-0.320	-0.557
O2	-0.152	-0.426
O3	-0.369	-0.643
H6	0.326	0.480
N1	-0.232	-0.423

Table S8. Selected atomic charges, calculated at Mulliken and NPA levels, of **3**. Atomic scheme as in **Fig. 4C**.

3

	Mulliken	NPA
O1	-0.321	-0.558
O2	0.148	-0.423

37

336

	Mulliken	NPA
O3	-0.372	-0.626
O4	-0.372	-0.627
H6	0.328	0.481
H8	0.326	0.483
N1	-0.231	-0.427

Table S9. Selected atomic charges, calculated at Mulliken and NPA levels, of **4**. Atomic scheme as in **Fig. 4D.**

	4	
	Mulliken	**NPA**
O1	-0.325	-0.562
O2	-0.152	-0.424
O3	-0.429	-0.658
O4	-0.383	-0.633
H6	0.334	0.492
H7	0.335	0.491
N1	-0.231	-0.428

Table S10. Selected atomic charges, calculated at Mulliken and NPA levels, of **5**. Atomic scheme as in **Fig. 4E.**

	5	
	Mulliken	**NPA**
O1	-0.321	-0.557
O2	-0.223	-0.453
O3	-0.434	-0.662

38

O4	-0.374	-0.623
H5	0.347	0.506
H6	0.340	0.495
N1	-0.233	0.429

Table S11. Energy values (eV) of the frontier Molecular Orbitals of the studied compounds in gas phase, ethanol, and water at the DFT level (PBE0, def-2 TZVP).

compound	gas		ethanol		water	
	HOMO	**LUMO**	**HOMO**	**LUMO**	**HOMO**	**LUMO**
1	-6.64	-2.27	-6.73	-2.25	-6.78	-2.25
2	-6.34	-2.09	-6.38	-2.09	-6.39	-2.09
3	-6.21	-1.97	-6.29	-2.05	-6.29	-2.06
4	-6.18	-2.08	-6.21	-2.10	-6.21	-2.10
5	-6.30	-2.17	-6.30	-2.12	-6.30	-2.12

Table S12. Calculated thermochemical descriptors for the studied compounds in gas, ethanol, and water (DFT PBE0/def-2TZVP level). Atom labelling arrangement as in **Scheme 1**.

COMPOUND	*SITE*	*BDE (kcal/mol)*		
		Gas	**Ethanol**	**Water**
2	**7-OH**	84.66	85.72	85.75
3	**5-OH**	84.28	85.18	85.20
	7-OH	84.32	85.53	85.57
4	**6-OH**	84.12	82.43	82.43
	7-OH	74.26	77.28	78.03
5	**7-OH**	84.06	81.84	81.72
	8-OH	78.65	77.94	77.87
COMPOUND	*SITE*	*PA (kcal/mol)*		
		Gas	**Ethanol**	**Water**
2	**7-OH**	322.40	33.80	34.58
3	**5-OH**	326.10	33.47	34.23
	7-OH	325.32	33.63	34.44
4	**6-OH**	339.27	40.66	41.20
	7-OH	315.52	28.35	29.35
5	**7-OH**	329.27	34.87	35.52
	8-OH	328.33	33.39	34.02
COMPOUND	*SITE*	*ETE (kcal/mol)*		

COMPOUND	SITE	Gas	Ethanol	Water
2	7-OH	72.67	102.82	102.35
3	5-OH	71.56	102.58	102.15
	7-OH	72.38	102.78	102.32
4	6-OH	58.23	92.64	92.34
	7-OH	72.11	100.41	99.86
5	7-OH	68.24	97.85	97.38
	8-OH	63.81	95.43	95.02

COMPOUND	SITE	SPLET (kcal/mol)		
		Gas	Ethanol	Water
2	7-OH	395.07	136.62	136.93
3	5-OH	397.66	136.05	136.37
	7-OH	397.70	136.41	136.76
4	6-OH	397.50	133.30	133.54
	7-OH	387.63	128.76	129.21
5	7-OH	397.51	132.72	132.90
	8-OH	392.14	128.82	129.04

COMPOUND	IP (kcal/mol)		
	Gas	Ethanol	Water
2	174.69	128.92	126.10
3	171.14	126.46	123.67
4	171.16	124.82	121.93
5	173.58	127.34	124.41

COMPOUND	SITE	PDE (kcal/mol)		
		Gas	Ethanol	Water
2	7-OH	223.35	258.80	10.86
3	5-OH	226.51	260.72	12.71
	7-OH	226.56	261.07	13.09
4	6-OH	226.35	259.61	11.61
	7-OH	216.48	255.06	7.29
5	7-OH	223.86	256.50	8.50
	8-OH	218.57	252.53	4.64

COMPOUND	SITE	SETPT (kcal/mol)		
		Gas	Ethanol	Water
2	7-OH	387.04	387.72	136.96
3	5-OH	397.65	387.18	136.38
	7-OH	397.70	387.53	136.76
4	6-OH	397.51	384.43	133.54
	7-OH	387.64	379.88	129.22
5	7-OH	397.44	303.84	132.91
	8-OH	392.15	379.87	129.05

Results and discussion

Article 8.

Hydroxylated coumarin-based thiosemicarbazones as dual anti-tyrosinase and antioxidant agents

Abstract

The discovery of novel anti-tyrosinase agents appears extremely important in both medical and industrial sectors, since an irregular production of melanin is related with the insurgence of several skin-related disorders (e.g., melanoma) and the browning process of fruit and vegetables. Considering that melanogenesis involve also non-enzymatic processes, the development of dual antioxidant and anti-tyrosinase agents appears extremely important. In this work we evaluated the antioxidant and tyrosinase inhibition ability of a panel of variably hydroxylated derivatives of (1*E*)-2-(1-(2-oxo-2*H*-chromen-3-yl)ethylidene)hydrazine-1-carbothioamide (**T1**). Interestingly, these molecules have more potent tyrosinase inhibitory properties compared to reference compound kojic acid. Moreover, the antioxidant activity appears to be influenced according to the number and substitution pattern of the hydroxyl groups.[*]

Hydroxylated coumarin-based thiosemicarbazones as dual anti-tyrosinase and antioxidant agents

Maria Grazia Cabiddu[1], Benedetta Era[2], Sebastiano Masuri[1], Enzo Cadoni[1], Tiziana Pivetta[1], Antonella Fais[1*]

[1] Department of Chemical and Geological Sciences, University of Cagliari, Cittadella Universitaria, 09042, Monserrato, Cagliari, Italy.
[2] Department of Life and Environmental Sciences, University of Cagliari, Cittadella Universitaria, 09042, Monserrato, Cagliari, Italy.

*Corresponding author: afais@unica.it

To be submitted

Introduction

Melanin, the pigment mainly responsible for skin coloration, is an heterogenous biopolymer that is produced in melanocytes through a well-known process called melanogenesis. Tyrosinase is a key enzyme for melanin production, due to its involvement in the rate-limiting step of melanogenesis. This enzyme catalyses the oxidation of phenols and diphenols thanks to the presence of a binuclear Copper-based catalytic site. During melanogenesis, Tyrosinase is involved in the biosynthesis of Dopaquinone, which can take place directly from L-tyrosine through the diphenolase catalytic cycle or passing through the hydroxylation of the same substrate to obtain L-dihydroxyphenylalanine (L-DOPA) by means of the monophenolase cycle.[1]

The development of novel tyrosinase inhibitors is of great importance for both medical and technological applications. Indeed, an irregular expression of tyrosinase will determine the accumulation of melanin, which is related to the onset of several skin pigmentation disorders, such as freckles, senile spots, melasma, and even malignant melanoma tumours.[1,2] In addition, tyrosinase is also involved in the browning process of fruits and vegetables, thus tyrosinase inhibitors could find potential applications as food preservatives.[3]

Many natural coumarins, such as umbelliferone (7-hydroxy-2-*H*-chromen-2-one) have proved to act as tyrosinase inhibitors.[4] Thanks to both their synthetic accessibility, and higher versatility in terms of biological properties, tuneable according to the nature and position of the substituents in the coumarinic skeleton, many scientists have evaluated the anti-tyrosinase activity of several coumarinic derivatives.[1,5]

We have previously shown how the insertion of hydroxyl groups in the structure of 3-aryl and heteroarylcoumarins allows to obtain novel antioxidant compounds with potent tyrosinase inhibitory properties.[6–8] Considering that melanogenesis involves also non-enzymatic oxidative process, the development of novel compounds with dual antioxidant and tyrosinase inhibitory properties appears quite useful.[9,10]

Under this framework, we aimed to investigate on the antioxidant and tyrosinase inhibition ability on a series of variably hydroxylated derivatives (**T2-5**, **Figure 1**) of (1*E*)-2-(1-(2-oxo-2*H*-chromen-3-yl)ethylidene)hydrazine-1-carbothioamide (**T1**, **Figure 1**), which appears to inhibit tyrosinase at micromolar concentration level, as previously observed.[11] All the studied compounds have more potent tyrosinase inhibitory properties compared to Kojic Acid, a known tyrosinase inhibitor of natural origin, with tuneable antioxidant activity according to the number and substitution pattern of the hydroxyl groups in the 2-*H*-chromen-2-one scaffold.
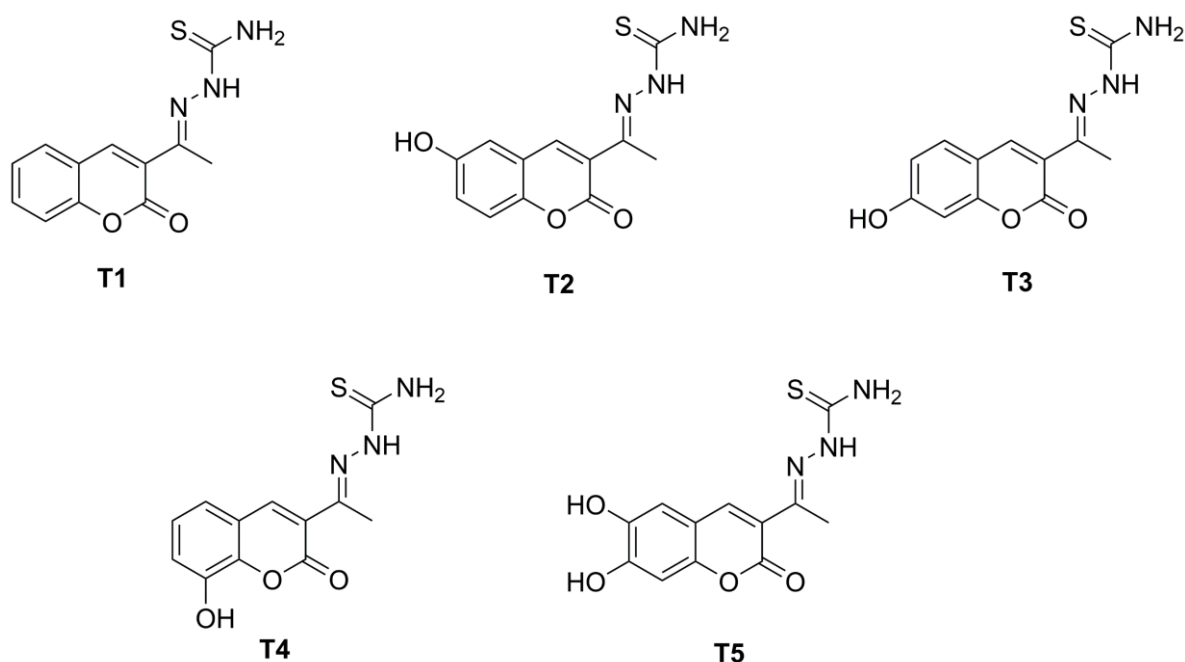
Figure 1. Structure and acronyms of the studied compounds

Experimental

Materials and methods

Ethyl acetoacetate, deuterated dimethyl sulfoxide, salicylaldehyde and its hydroxylated derivatives were purchased from Alfa Aesar. Absolute ethanol, piperidine, 1,1-diphenyl-2-picrylhydrazyl free radical (DPP·), deuterated chloroform, thiosemicarbazide and acetic acid were purchased from Merck (Milan, Italy).

NMR spectra were acquired using a Bruker Avance III HD 600 spectrometer at room temperature with tetramethylsilane (TMS) as the internal standard in DMSO d6 or CDCl3. Low resolution ESI mass spectra were recorded using a triple quadrupole QqQ Varian 310-MS mass spectrometer. High resolution ESI mass spectra were acquired on a Thermofisher ORBITRAP-ELITE. Melting points were acquired on a Kofler Hot Stage and are uncorrected.

Synthesis

General procedure for the synthesis of substituted 3-acetil-2H-chromen-2-one derivatives

Salycilaldehyde derivatives (7.24 mmol, 1.0 eq) and ethylacetoacetate (8.64 mmol, 1.2 eq) were dissolved in 2.6 mL of ethanol and Piperidine (0.15 mmol, 0.02 eq) was then added. The reaction mixture was left under stirring at reflux for 5 hours. For compounds **1-4** the reaction mixture was then cooled to room temperature, affording a precipitate that was filtered and recrystallized from methanol. For compound **5**, the reaction mixture was poured in cold water and treated with HCl 10% till acidic pH. A dark brown solid precipitated after a few minutes under stirring. The former one was filtered, dried, then repeatedly washed with Et2O and used as such for the next step.

3-acetyl-2*H*-chromen-2-one (1). Light yellow solid. Yield 81 %. Experimental results are in accordance with those reported in the literature.[11] Melting point: 178-180 °C. ^{1}H-NMR (600 MHz, CDCl$_3$, δ, ppm, **Figure S1**): 8.51 (d, J = 0.7 Hz, 1H), 7.69 – 7.63 (m, 2H), 7.40 – 7.32 (m, 2H), 2.73 (s, 3H). .LR ESI-MS (calculated, found, *m/z*): 211.0, 211.0 [M+Na]$^+$.

6-hydroxy-3-acetyl-2*H*-chromen-2-one (2). Yellow solid. Yield 63 %. Experimental results are in accordance with those reported in the literature.[12] Melting point: 244-245 °C. ^{1}H-NMR (600 MHz, DMSO d6, δ, ppm, **Figure S2**): 9.89 (s, 1H), 8.57 – 8.54 (m, 1H), 7.31 (d, J = 8.9 Hz, 1H), 7.24 (d, J = 2.9 Hz, 1H), 7.17 (dd, J = 8.9, 2.9 Hz, 1H), 2.58 (s, 3H). LR ESI-MS (calculated, found, *m/z*): 203.0, 203.0 [M-H]$^-$.

7-hydroxy-3-acetyl-2*H*-chromen-2-one (3). Light brown solid. Yield 34 %. Experimental results are in accordance with those reported in the literature.[13] Melting point: 243-244 °C. ^{1}H-NMR (600 MHz, DMSO d6, δ, ppm, **Figure S3**): 11.10 (br. s, 1H), 8.59 (d, J = 0.7 Hz, 1H), 7.78 (d, J = 8.6 Hz, 1H), 6.85 (dd, J = 8.6, 2.3 Hz, 1H), 6.75 (dd, J = 2.3, 0.7 Hz, 1H), 2.55 (s, 3H). LR ESI-MS (calculated, found, *m/z*): 203.0, 203.1 [M-H]$^-$.

8-hydroxy-3-acetyl-2*H*-chromen-2-one (4). Brown solid. Yield 57 %. Experimental results are in accordance with those reported in the literature.[14] Melting point: 253-255 °C. ^{1}H-NMR (600 MHz, DMSO d6, δ, ppm, **Figure S4**): 10.35 (s, 1H), 8.59 (s, 1H), 7.36 (dd, J = 5.8, 3.4 Hz, 1H), 7.24 – 7.18 (m, 2H), 2.59 (s, 3H). LR ESI-MS (calculated, found, *m/z*): 205.0, 204.9 [M+H]$^+$.

6,7-dihydroxy-3-acetyl-2*H*-chromen-2-one (5). Dark brown solid. Yield 61 %. Melting point: 192-194 °C. ^{1}H-NMR (600 MHz, DMSO d6, δ, ppm, **Figure S5**): 10.87 (s, 1H), 9.67 (s, 1H), 8.54 (s, 1H), 7.21 (s, 1H), 6.79 (s, 1H), 2.54 (s, 3H). LR ESI-MS (calculated, found, *m/z*): 219.0, 219.0 [M-H]$^-$

General procedure for the synthesis of substituted of substituted (1E)-2-(1-(2-oxo-2H-chromen-3-yl)ethylidene)hydrazine-1-carbothioamide compounds.[11]

The proper 3-acetilcoumarin derivative (2.5 mmol, 1.0 eq) was dissolved in 10 mL of ethanol, then thiosemicarbazide (2.5 mmol, 1.0 eq) and Acetic Acid (0.12 mL) were added. The reaction mixture was left under stirring at reflux for 6 hours. The reaction mixture was then cooled to room temperature, affording a precipitate that was filtered and recrystallized from ethanol.

(1*E*)-2-(1-(2-oxo-2*H*-chromen-3-yl)ethylidene)hydrazine-1-carbothioamide (T1). Yellow solid. Yield: 98 %. Experimental data were consistent with those reported in literature.[11] Melting point: 196-198 °C. ^{1}H-NMR (600 MHz, DMSO d6, δ, ppm, **Figure S6**): 10.44 (s, 1H), 8.48 (s, 1H), 8.40 (br. s, 1H), 7.94 (br. s, 1H), 7.77 (dd, J = 7.8, 1.6 Hz, 1H), 7.65 (ddd, J = 8.7, 7.3, 1.6 Hz, 1H), 7.44 (d, J = 8.3 Hz, 1H), 7.40 (td, J = 7.5, 1.1 Hz, 1H), 2.26 (s, 3H). HR ESI-MS (calculated, found, *m/z*): 262.0650, 262.0646 [M+H]$^+$.

(1*E*)-2-(1-(6-hydroxy-2-oxo-2*H*-chromen-3-yl)ethylidene)hydrazine-1-carbothioamide (T2). Yellow solid. Yield: 82 %. Melting point: 222-224 °C (with decomposition). ^{1}H-NMR (600 MHz, DMSO d6, δ, ppm, **Figure S7**): 10.40 (s, 1H), 9.80 (s, 1H), 8.36 (s, 2H), 7.95 (s, 1H), 7.27 (d, J = 8.3, 1H), 7.09 – 7.04 (m, 2H), 2.24 (s, 3H). ^{13}C-NMR (151 MHz, DMSO d6, δ, ppm, **Figure S8**): 179.69, 159.84, 154.36, 147.27, 146.73, 142.41, 126.28, 120.98, 119.92, 117.33, 113.33, 16.56. HR ESI-MS (calculated, found, *m/z*): 278.0599, 278.0591 [M+H]$^+$.

(1*E*)-2-(1-(7-hydroxy-2-oxo-2*H*-chromen-3-yl)ethylidene)hydrazine-1-carbothioamide (T3). Yellow-brown earth solid. Yield: 80 %. Melting point: 222-224 °C (with decomposition). ^{1}H-NMR (600 MHz, DMSO d6, δ, ppm, **Figure S9**): 10.73 (s, 1H), 10.34 (s, 1H), 8.36 (s, 2H),

8.39 (s, 1H), 8.34 (br. s, 1H), 7.90 (br. s, 1H), 7.59 (d, J = 8.6 Hz, 1H), 6.84 (dd, J = 8.5, 2.3 Hz, 1H), 6.74 (d, J = 2.2 Hz, 1H), 2.24 (s, 3H). ^{13}C-NMR (151 MHz, DMSO d6, δ, ppm, **Figure S10**): 179.55, 162.37, 159.99, 155.98, 147.05, 143.10, 131.06, 121.50, 114.15, 111.90, 102.23, 16.50. HR ESI-MS (calculated, found, *m/z*): 278.0599, 278.0594 [M+H]$^+$.

(1*E*)-2-(1-(8-hydroxy-2-oxo-2*H*-chromen-3-yl)ethylidene)hydrazine-1-carbothioamide (T4). Light yellow solid. Yield: 93 %. Melting point: 208-210 °C (with decomposition). ^{1}H-NMR (600 MHz, DMSO d6, δ, ppm, **Figure S11**): 10.73 (s, 1H), 10.41 (s, 1H), 8.41 (s, 1H), 8.38 (br. s, 1H), 7.94 (br. s, 1H), 7.20 – 7.17 (m, 2H), 7.14 – 7.11 (m, 1H), 2.26 (s, 3H). ^{13}C-NMR (151 MHz, DMSO d6, δ, ppm, **Figure S12**): 179.71, 159.53, 146.64, 144.83, 142.90, 142.53, 126.12, 125.17, 120.35, 119.55, 119.12, 16.54. HR ESI-MS (calculated, found, *m/z*): 278.0599, 278.0595 [M+H]$^+$.

(1*E*)-2-(1-(6,7-dihydroxy-2-oxo-2*H*-chromen-3-yl)ethylidene)hydrazine-1-carbothioamide (T5). Dark brown solid. Yield: 44 %. Melting point: 228-230 °C (with decomposition). ^{1}H-NMR (600 MHz, DMSO d6, δ, ppm, **Figure S13**): 10.38 (s, 1H), 10.30 (s, 1H), 9.52 (s, 1H), 8.32 (s, 2H), 7.90 (s, 1H), 7.04 (s, 1H), 6.77 (s, 1H), 2.23 (s, 3H). ^{13}C-NMR (151 MHz, DMSO d6, δ, ppm, **Figure S14**): 179.50, 160.29, 151.76, 149.28, 147.42, 143.68, 143.05, 121.51, 113.17, 111.42, 102.69, 15.92. HR ESI-MS (calculated, found, *m/z*): 294.0548, 294.0545 [M+H]$^+$.

Antioxidant assay

The DPPH antioxidant assay procedure reported is based on previously reported procedures with some modifications.[15,16] Each test compound was dissolved in DMSO at 1.0 mM concentration, and then diluted with absolute ethanol in the 500-2.0 μM concentration range. DPP· solution (0.1 mM, absolute ethanol) was prepared freshly, stored in the dark

and used in a few hours. Each test solution (1500 μL) was vigorously mixed to an equal volume of DPP$^.$ inside a tube and left in the dark for 30 minutes. The absorbance of the resulting solutions was measured at 517 nm. Each concentration was evaluated in three independent experiments. Results are reported as IC_{50} values (e.g., concentration of antioxidant required to quench 50% of DPP$^.$ under the selected experimental conditions). Ascorbic acid was used as reference inhibitor.

Tyrosinase inhibition assay

The inhibition of mushroom tyrosinase was evaluated as previously described, with slight modifications:[17] 50 mM phosphoric acid buffer solution (pH 6.8), a solution of mushroom tyrosinase (100 U/ml final concentration; Sigma Chemical Co., Milan, Italy) and dimethyl sulfoxide (DMSO) with or without the sample. The mixture was incubated at 25°C for 10 min. Then, L-DOPA solution (0.5 mM final) was added, and the reaction was monitored at 492 nm for 5 min, following the increase in absorbance at 492 nm, resulting from the formation of the dopachrome product. The IC_{50} value, e.g. concentration giving 50% inhibition of tyrosinase activity, was determined by interpolation of dose-response curves. Kojic acid was used as a reference tyrosinase inhibitor.

Results and Discussion

Chemistry

Target compounds **T1-5** were successfully obtained according to the 2-step synthetic strategy outlined in the **Scheme 1**. In brief, salicylaldehyde and its hydroxylated derivatives were subjected to Knoevenagel condensation in presence of ethyl acetoacetate (as active methylene compound) and piperidine (as base) to afford the 3-acetylcoumarins **1-5**. The

former intermediates were easily converted in the corresponding thiosemicarbazones by reacting them with thiosemicarbazide in presence of acetic acid as catalyst. The yields, for both **1-6** intermediates and **T1-5** target compounds, ranged from moderate to good. The structure and purity of both the intermediates and final compounds were confirmed from ¹H NMR and MS data. For target compounds **T2-5** we included the ¹³C NMR spectra to fully characterized them, since they have never been reported in literature. NMR spectra for both intermediates and final products are shown in the Supporting (**Figure S1-15**).

Y = 6,7,8 -H (**T1**)   Y = 7 -OH (**T3**)   Y = 6,7 -OH (**T5**)

Y = 6 -OH (**T2**)   Y = 8 -OH (**T4**)
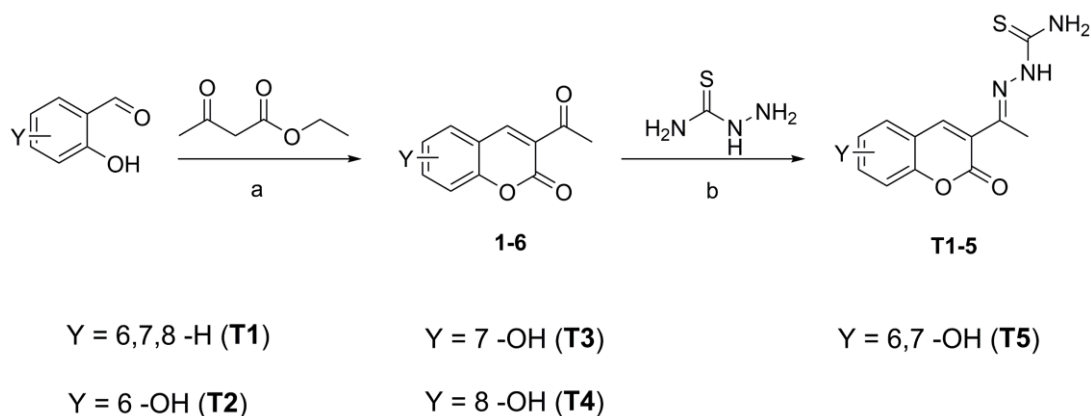
Scheme 1: reaction scheme and structures of the synthesized compounds. Reaction conditions: (**a**) Piperidine, EtOH, reflux, 5 hrs. (**b**) Acetic Acid, EtOH, reflux, 5 hrs.

Antioxidant assay

The antioxidant activity of **T1** and its hydroxylated derivatives **T2-6** was evaluated by means of the DPPH assay, which is based on the ability of the stable 1,1-diphenyl-picrylhydrazyl (DPP·) radical species to be converted in its diamagnetic form (DPPH) by accepting a H· from the tested compound. In ethanol, the DPP· radical shows an intense violet colouration (with a λ_{max} at 517 nm), while the DPPH specie is yellow coloured in the same solvent. From evaluation of the relative decrease in absorbance at different

concentrations of each tested compound, the antioxidant activities were evaluated by reporting their IC_{50} values, as shown in **Table 1**.

In comparison with Ascorbic Acid (used as reference), compounds **T1-3** are devoid of any radical scavenging capability while in **T4**, where the –OH occupy the 8th position of the coumarinic scaffold we observe a modest antioxidant ability. As expected, the molecule having a catechol-like motif (**T5**) is the most potent antioxidant of the series.

Table 1. IC_{50} values, determined from the antioxidant assay (reduction of the DPP· Radical), for the studied compounds. Ascorbic acid was used as reference compound.

Compound	IC_{50} (μM)[a]
T1	> 250
T2	> 250
T3	> 250
T4	28 ± 2
T5	7.1 ± 0.3
Ascorbic Acid	18.6 ± 0.6

[a] Concentration of antioxidant required to quench 50% of DPP· under the selected experimental conditions. Each IC_{50} value is expressed as mean ± the Standard Error of the Mean (SEM) of 3 independent experiments.

Tyrosinase inhibition assay

The anti-tyrosinase activity of the studied compounds was preliminary evaluated using mushroom tyrosinase as protein model. Results from IC_{50} values (**Table 2**), show that **T2** possess comparable tyrosinase inhibitory activity compared to Kojic Acid, while all the other molecules are more potent tyrosinase inhibitors than the reference. Apart from **T2**, it seems that the insertion of hydroxyl groups in the coumarinic skeleton plays little effect on the anti-tyrosinase potency observed. This doesn't exclude that the structural modifications introduced could influence the mode of interaction of the studied molecules towards

tyrosinase. Additional studies are currently ongoing to determine the enzymatic inhibition mechanisms.

Table 2. IC_{50} values, determined from the tyrosinase assay, for the studied compounds. Kojic Acid was used as reference compound.

Compound	IC_{50} (μM)[a]
T1	4 ± 2
T2	14 ± 7
T3	5 ± 2
T4	5.7 ± 0.8
T5	6 ± 2
Kojic Acid	18 ± 1

[a] concentration giving 50% inhibition of tyrosinase activity. Each IC_{50} value is expressed as mean ± the Standard Deviation (SD) of 3 independent experiments.

Conclusions

The results reported in this study evidence how the insertion of hydroxyl groups in the structure of the coumarin-based thiosemicarbazone **T1** has allowed to obtain a panel of novel dual anti-tyrosinase and antioxidant agents. It is interesting to point out how these molecules possess higher anti-tyrosinase potency compared to the known inhibitor Kojic Acid, with a tuneable antioxidant ability according to the substitution pattern of the hydroxyl groups. More studies are currently in progress to determine the mode of enzymatic inhibition exerted by the studied compounds. Moreover, their cytotoxicity on melanocytes will be studied with the aim of determining their potential applications in the biomedical and industrial fields.

Author contributions

Conceptualization: S.M., M.G.C, B.E., A.F., T.P.; Methodology: S.M., M.G.C, B.E., A.F., T.P.; Investigation: S.M., M.G.C, B.E., E.C.,; Formal analysis: S.M., M.G.C, B.E., A.F.; Validation:

S.M., M.G.C, B.E.; Visualization: S.M.; Writing – original draft: S.M.; Writing – review and editing: S.M., T.P.; Resources: T.P., E.C., A.F., B.E.; Supervision: S.M., M.G.C, B.E., A.F., T.P.

Acknowledgments

References

1   J. Li, L. Feng, L. Liu, F. Wang, L. Ouyang, L. Zhang, X. Hu and G. Wang, *Eur. J. Med. Chem.*, , DOI:10.1016/j.ejmech.2021.113744.

2   F. Solano, S. Briganti, M. Picardo and G. Ghanem, *Pigment Cell Res.*, 2006, **19**, 550–571.

3   M. R. Loizzo, R. Tundis and F. Menichini, *Compr. Rev. Food Sci. Food Saf.*, 2012, **11**, 378–398.

4   Y. Masamoto, Y. Murata, K. Baba, Y. Shimoishi, M. Tada and K. Takahata, *Biol. Pharm. Bull.*, 2004, **27**, 422–425.

5   S. Zolghadri, A. Bahrami, M. T. Hassan Khan, J. Munoz-Munoz, F. Garcia-Molina, F. Garcia-Canovas and A. A. Saboury, *J. Enzyme Inhib. Med. Chem.*, 2019, **34**, 279–309.

6   M. J. Matos, L. Santana, E. Uriarte, G. Delogu, M. Corda, M. B. Fadda, B. Era and A. Fais, *Bioorganic Med. Chem. Lett.*, 2011, **21**, 3342–3345.

7   M. J. Matos, C. Varela, S. Vilar, G. Hripcsak, F. Borges, L. Santana, E. Uriarte, A. Fais,

A. Di Petrillo, F. Pintus and B. Era, *RSC Adv.*, 2015, **5**, 94227–94235.

8   F. Pintus, M. J. Matos, S. Vilar, G. Hripcsak, C. Varela, E. Uriarte, L. Santana, F. Borges, R. Medda, A. Di Petrillo, B. Era and A. Fais, *Bioorganic Med. Chem.*, 2017, **25**, 1687–1695.

9   L. Denat, A. L. Kadekaro, L. Marrot, S. A. Leachman and Z. A. Abdel-Malek, *J. Invest. Dermatol.*, 2014, **134**, 1512–1518.

10   T. M. Lu, H. H. Ko, L. T. Ng and Y. P. Hsieh, *Chem. Biodivers.*, 2015, **12**, 963–979.

11   J. Liu, F. Wu, L. Chen, L. Zhao, Z. Zhao, M. Wang and S. Lei, *Food Chem.*, 2012, **135**, 2872–2878.

12   F. Martínez-Martínez, R. Razo-Hernández, A. Peraza-Campos, M. Villanueva-García, M. Sumaya-Martínez, D. Cano and Z. Gómez-Sandoval, *Molecules*, 2012, **17**, 14882–14898.

13   Š. Starčević, P. Brožič, S. Turk, J. Cesar, T. Lanišnik Rižner and S. Gobec, *J. Med. Chem.*, 2011, **54**, 248–261.

14   X. Liu, J. Fan, Y. Liu and Z. Shang, *J. Zhejiang Univ. Sci. B*, 2008, **9**, 990–995.

15   S. Masuri, E. Cadoni, M. G. Cabiddu, F. Isaia, M. G. Demuru, L. Moráň, D. Buček, P. Vaňhara, J. Havel and T. Pivetta, *Metallomics*, 2020, **12**, 891–901.

16   S. Masuri, M. G. Cabiddu, E. Cadoni and T. Pivetta, *New J. Chem.*, 2021, **45**, 10749–10760.

17   B. Era, S. Floris, V. Sogos, C. Porcedda, A. Piras, R. Medda, A. Fais and F. Pintus, *Plants*, 2021, **10**, 151.

Hydroxylated coumarin-based thiosemicarbazones as dual anti-tyrosinase and antioxidant agents

Maria Grazia Cabiddu[1], Benedetta Era[2], Sebastiano Masuri[1], Enzo Cadoni[1], Tiziana Pivetta[1], Antonella Fais[1*]

[1] Department of Chemical and Geological Sciences, University of Cagliari, Cittadella Universitaria, 09042, Monserrato, Cagliari, Italy.

[2] Department of Life and Environmental Sciences, University of Cagliari, Cittadella Universitaria, 09042, Monserrato, Cagliari, Italy.

SUPPLEMENTARY INFORMATION
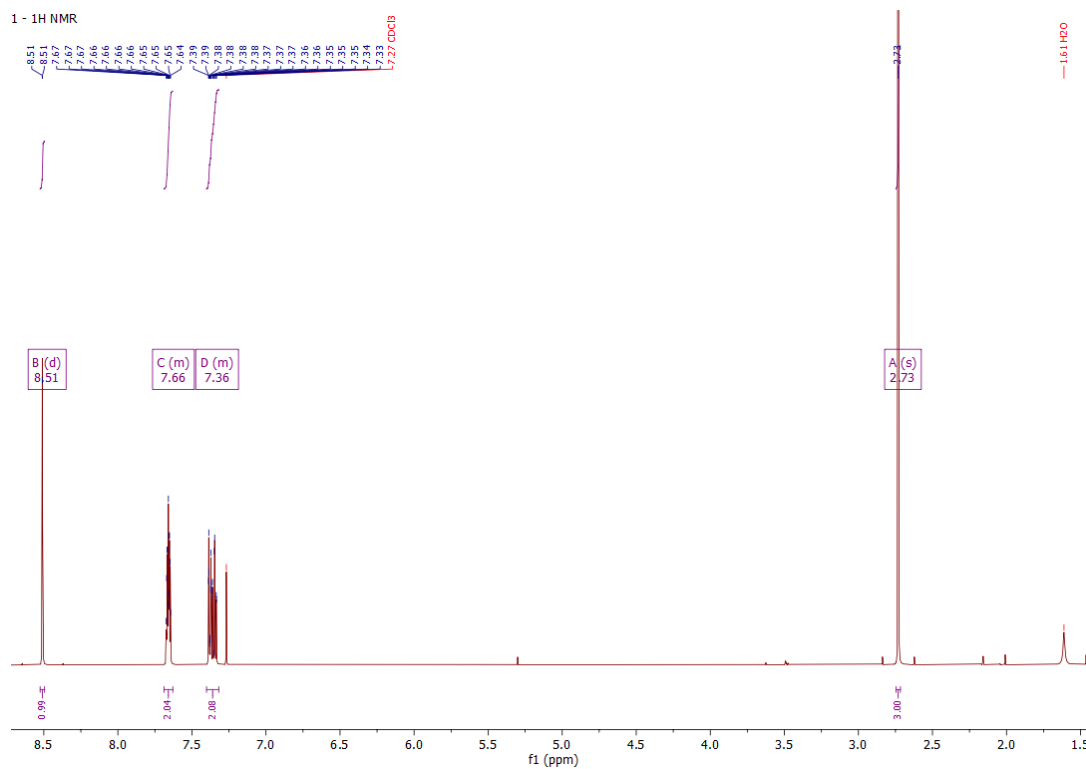
Figure S1. ^{1}H-NMR of **1**, 3-acetyl-2*H*-chromen-2-one (600 MHz, CDCl$_3$).
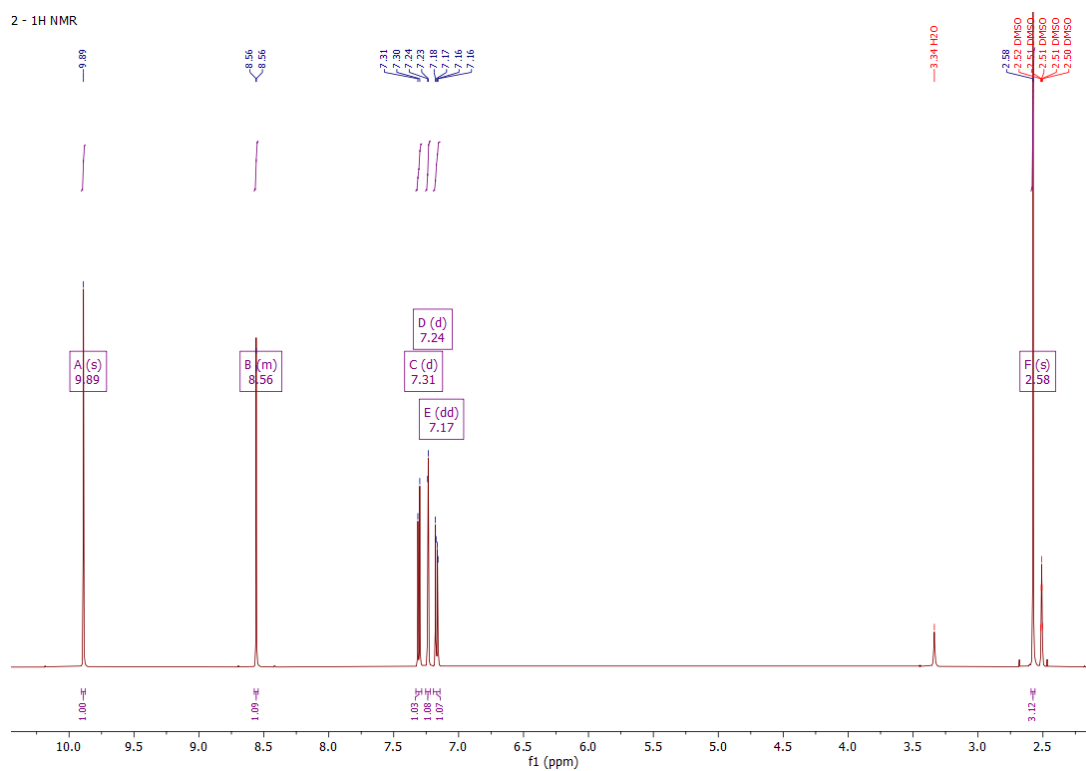
Figure S2. ^{1}H-NMR of **2**, 6-hydroxy-3-acetyl-2*H*-chromen-2-one (600 MHz, DMSO d6).
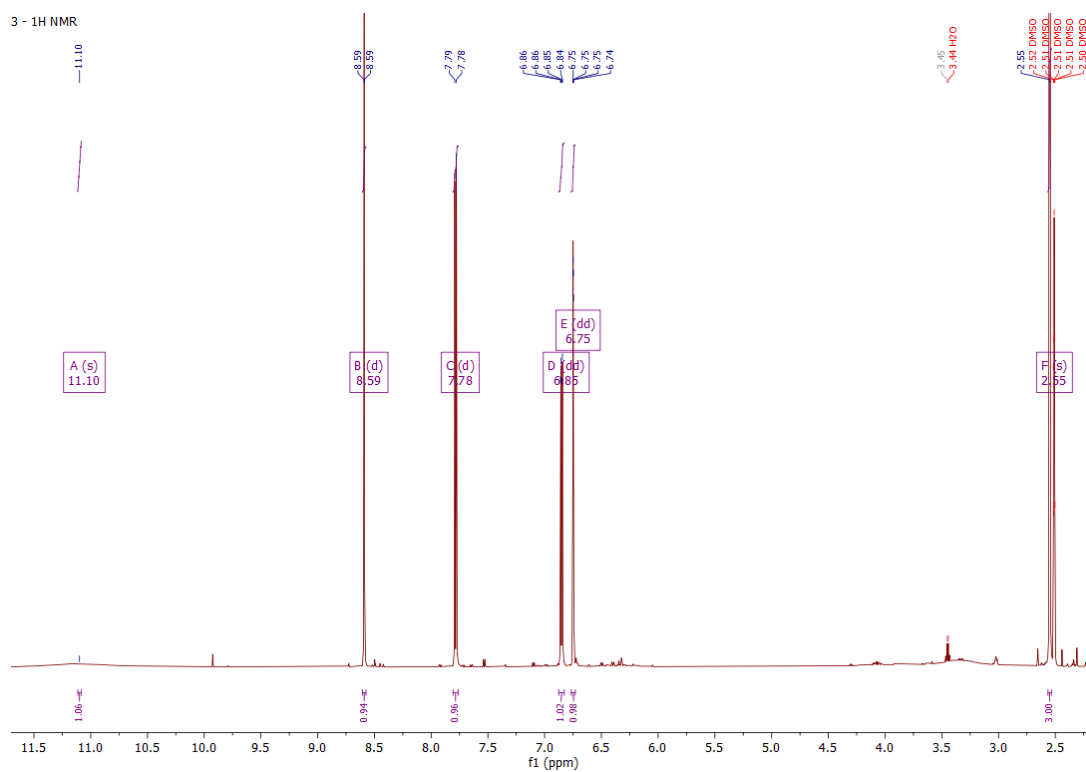
Figure S3. ¹H-NMR of **3**, 7-hydroxy-3-acetyl-2*H*-chromen-2-one (600 MHz, DMSO d6).
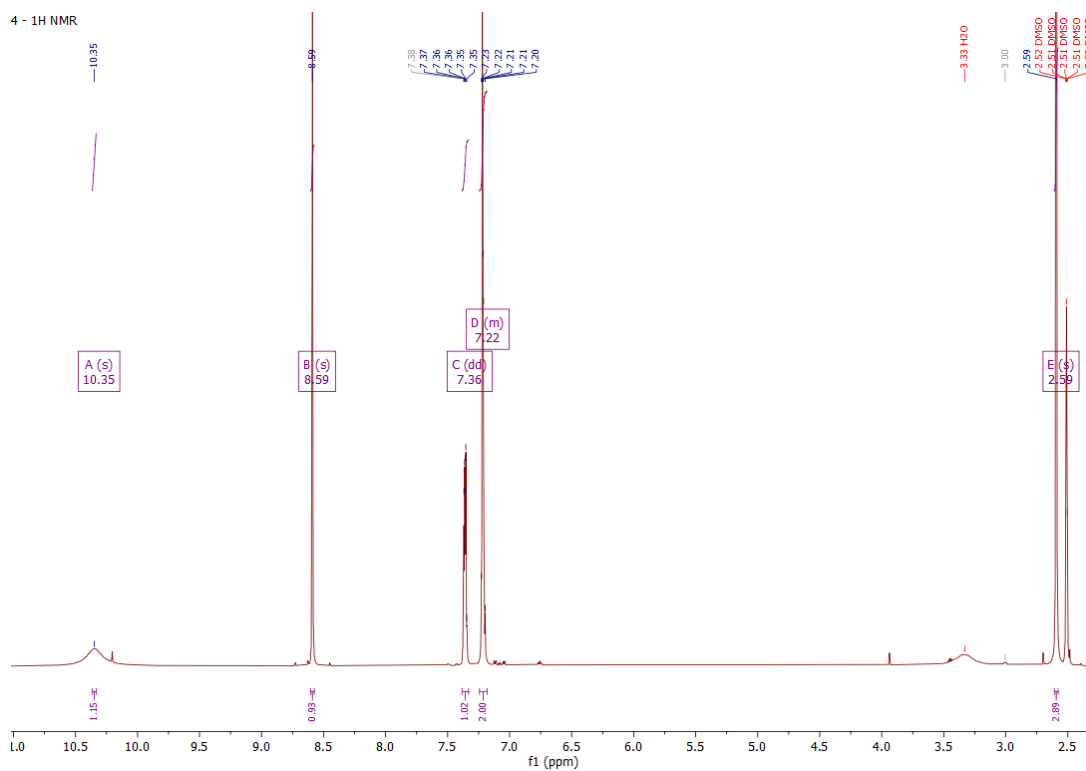
Figure S4. ¹H-NMR of **4**, 8-hydroxy-3-acetyl-2*H*-chromen-2-one (600 MHz, DMSO d6).
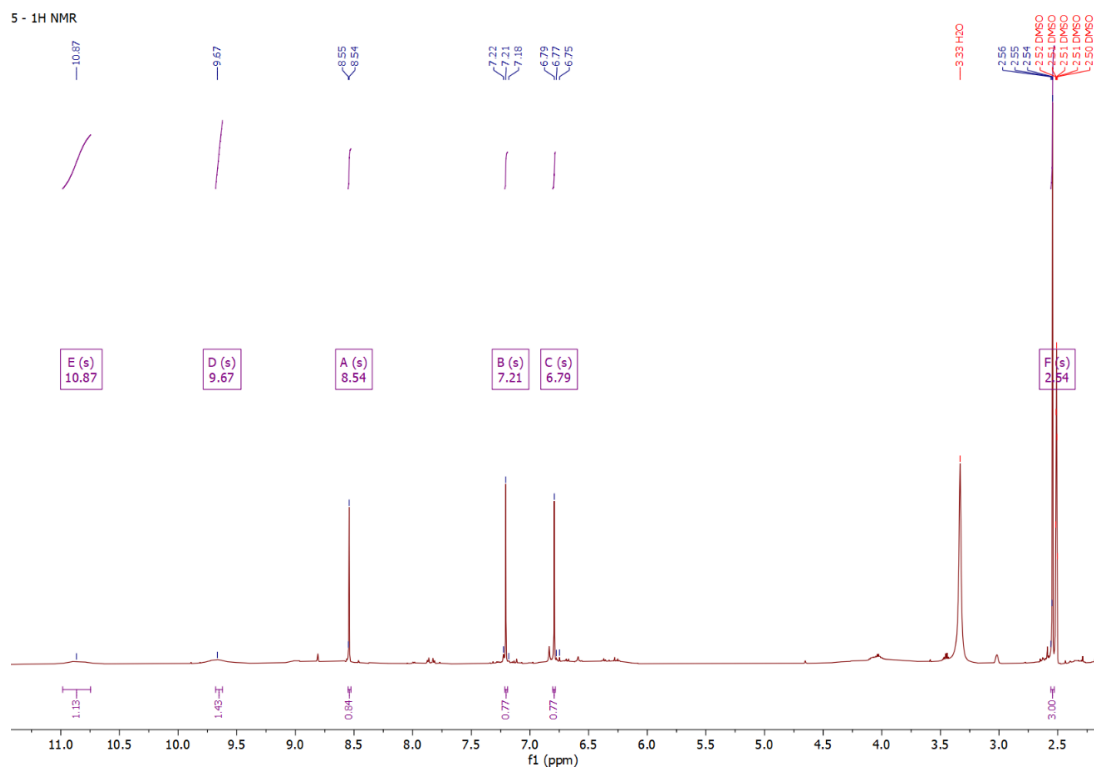
Figure S5. ¹H-NMR of **5**, 6,7-dihydroxy-3-acetyl-2*H*-chromen-2-one (600 MHz, DMSO d6).
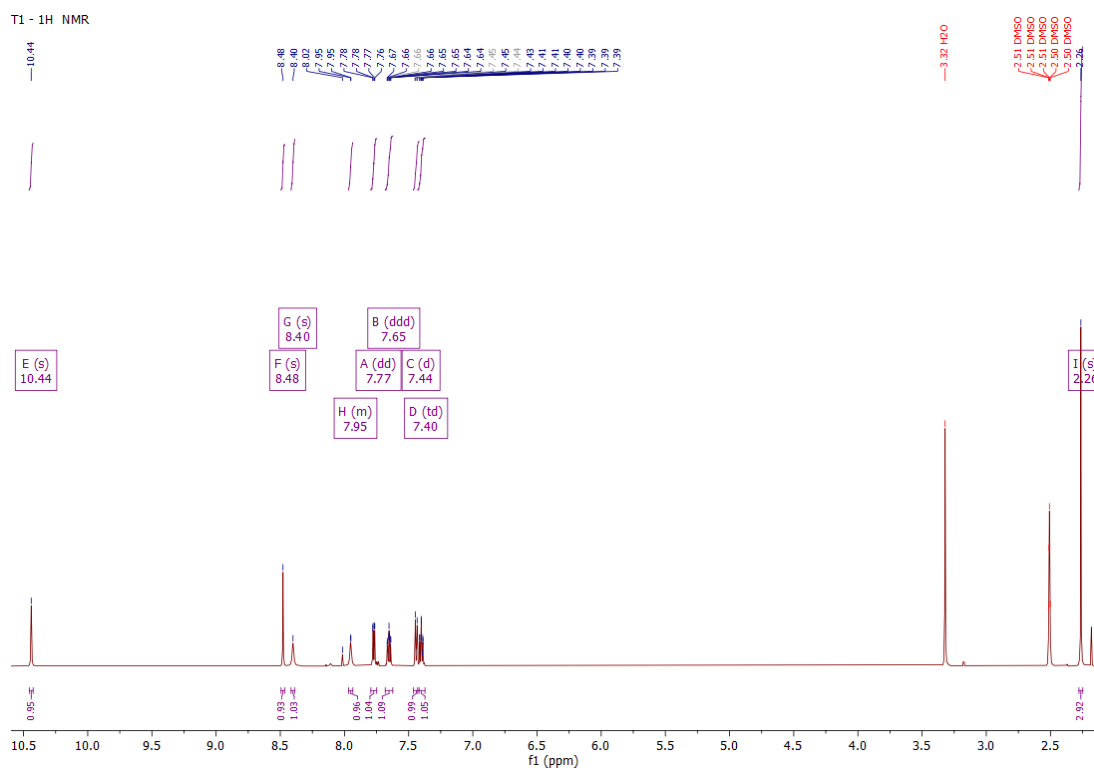
Figure S6. ¹H-NMR of **T1**, (1*E*)-2-(1-(2-oxo-2*H*-chromen-3-yl)ethylidene)hydrazine-1-carbothioamide (600 MHz, DMSO d6).
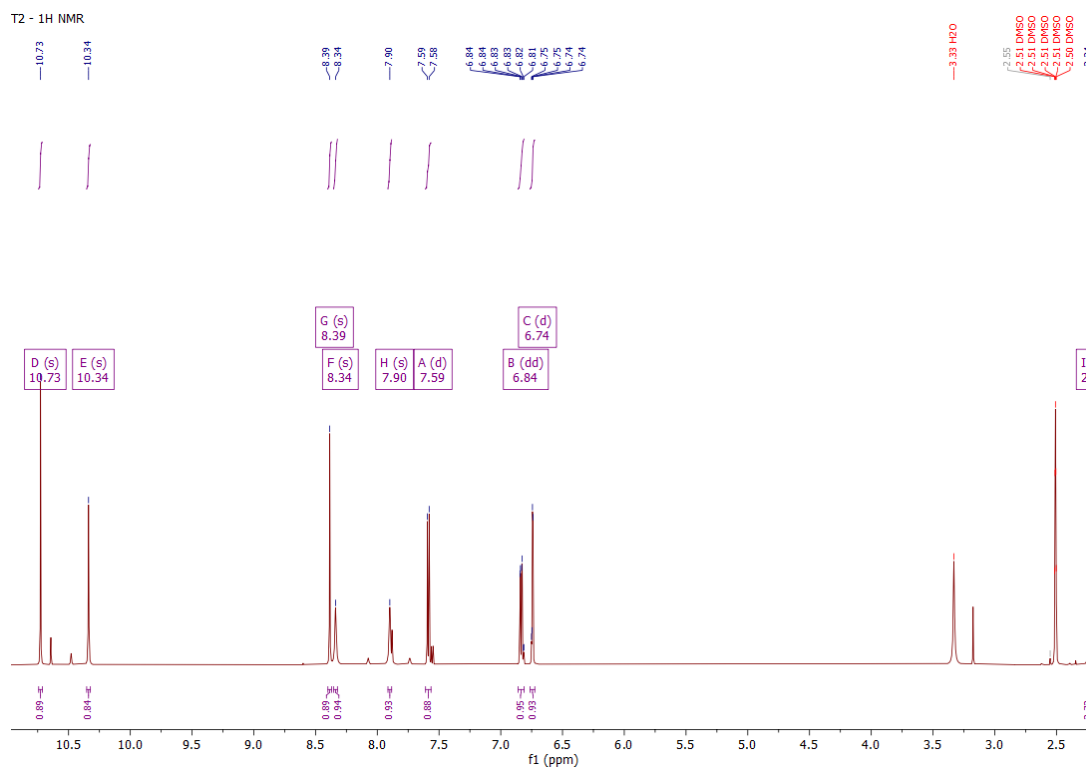
Figure S7. ¹H-NMR of **T2**, (1*E*)-2-(1-(6-hydroxy-2-oxo-2*H*-chromen-3-yl)ethylidene)hydrazine-1-carbothioamide (600 MHz, DMSO d6).
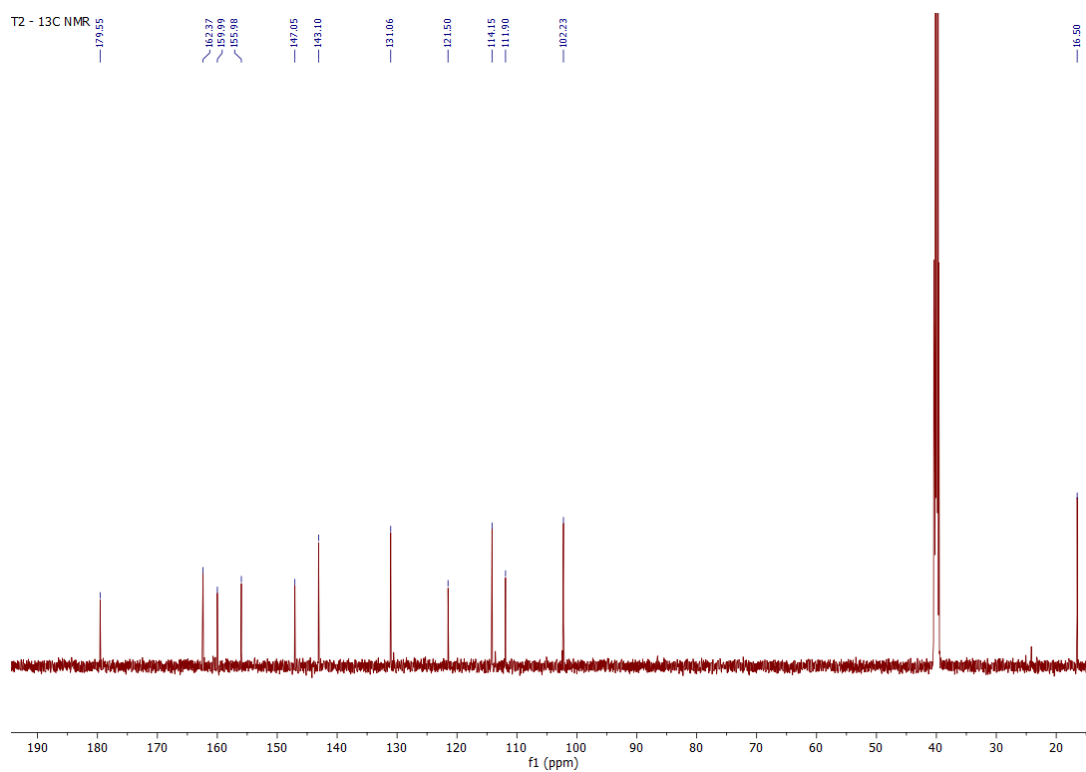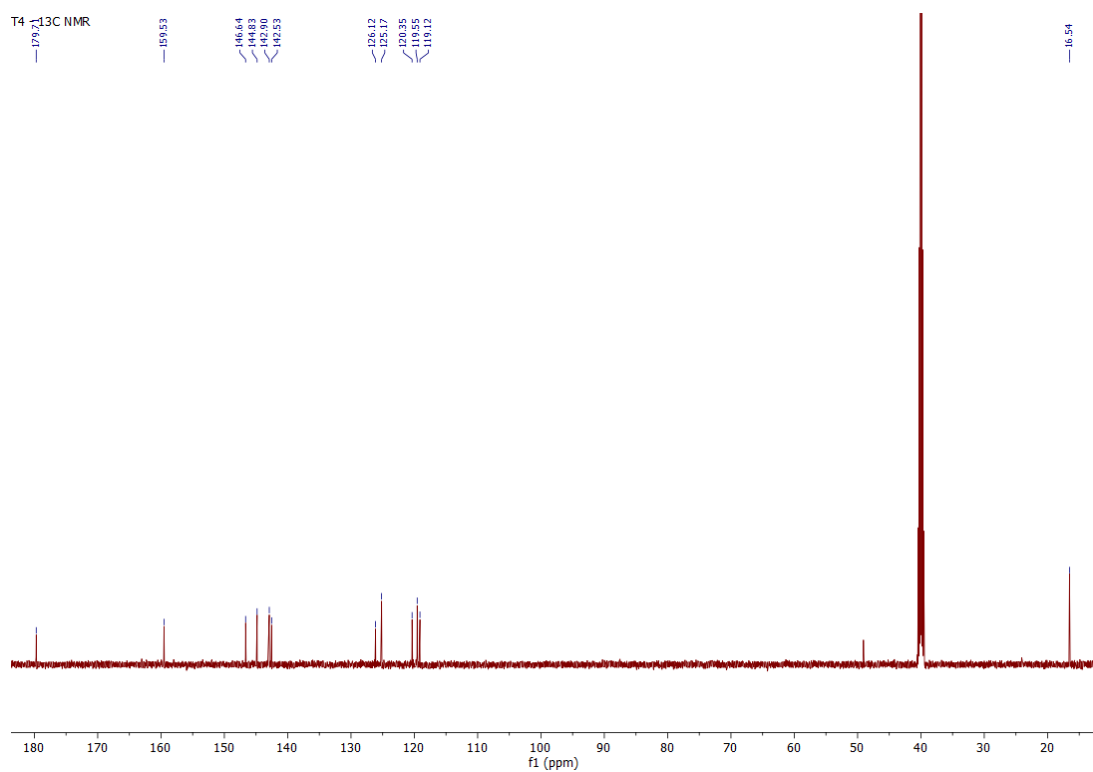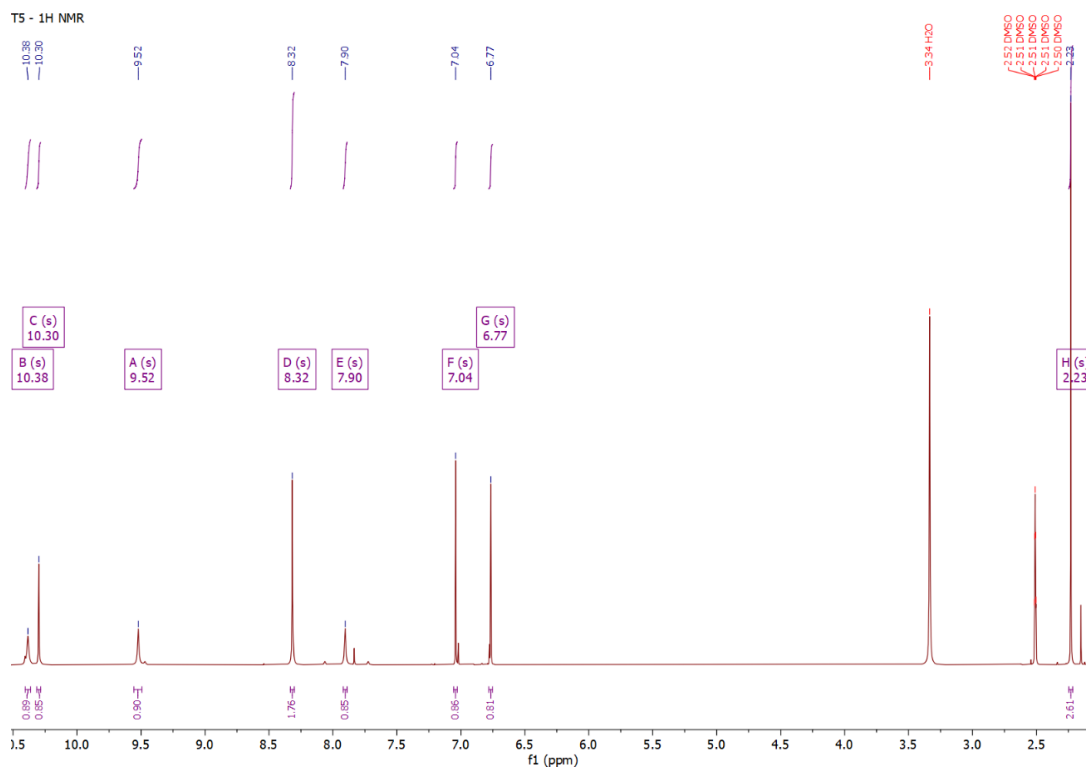

Figure S8. ¹³C-NMR of **T2**, (1*E*)-2-(1-(6-hydroxy-2-oxo-2*H*-chromen-3-yl)ethylidene)hydrazine-1-carbothioamide (151 MHz, DMSO d6).
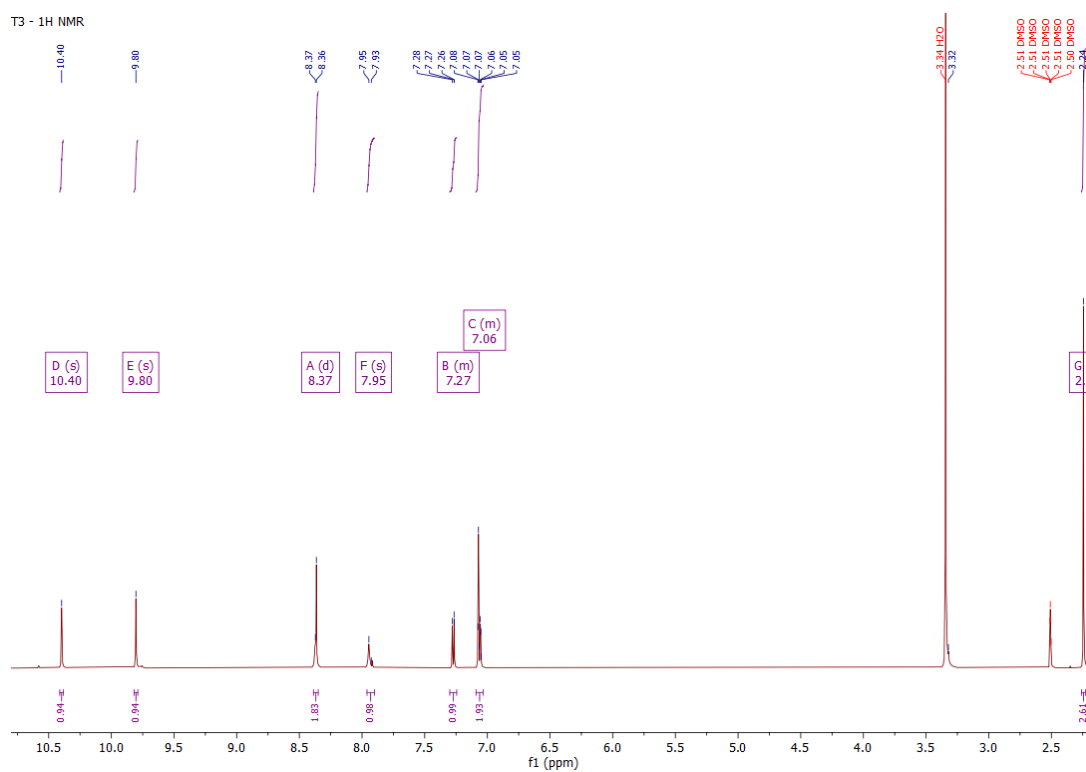
Figure S9. ^{1}H-NMR of **T3**, (1*E*)-2-(1-(7-hydroxy-2-oxo-2*H*-chromen-3-yl)ethylidene)hydrazine-1-carbothioamide (600 MHz, DMSO d6).
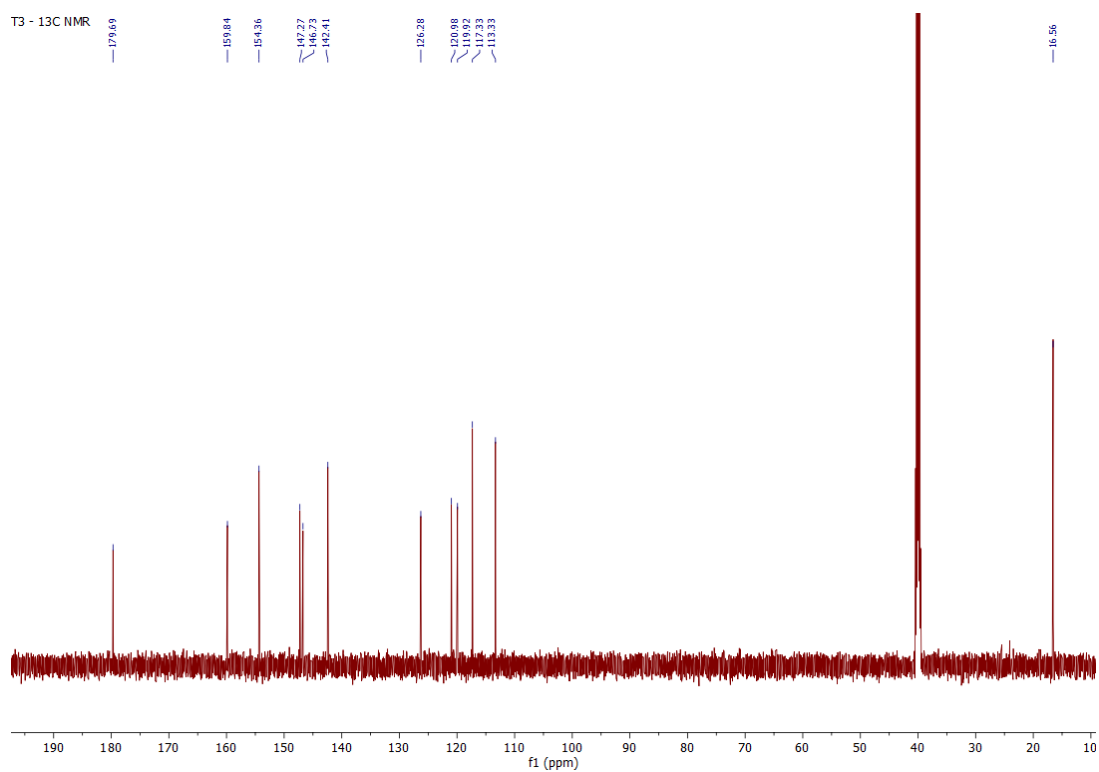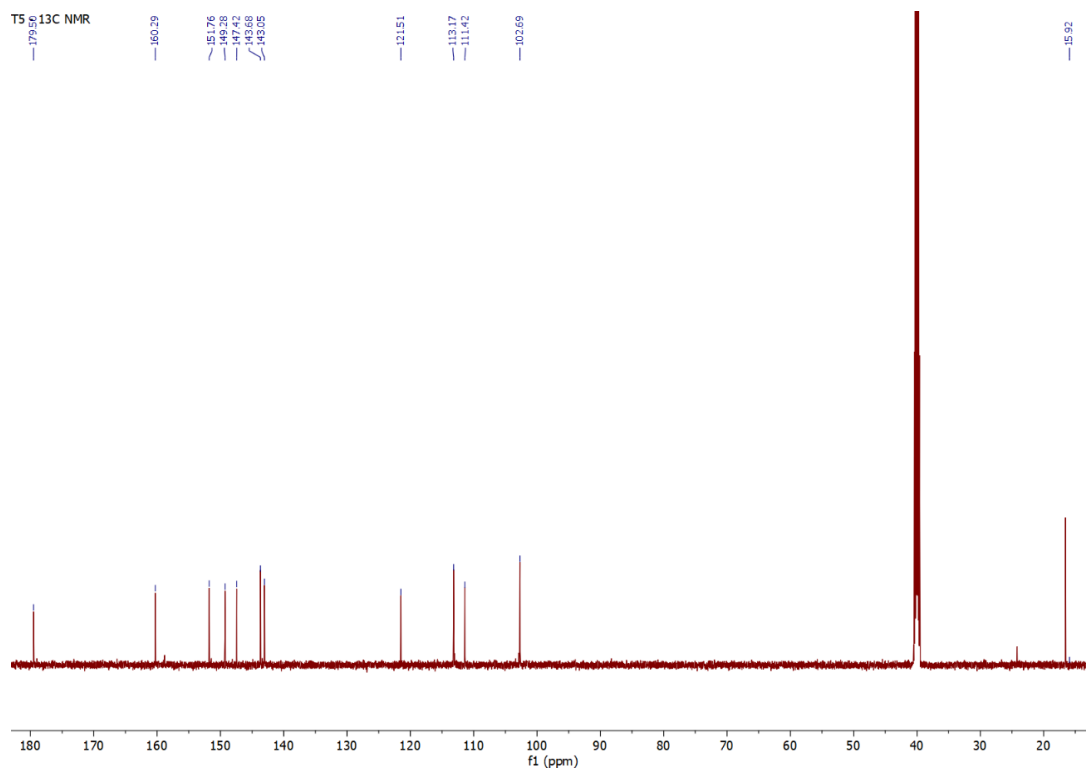

Figure S10. ^{13}C-NMR of **T3**, (1*E*)-2-(1-(7-hydroxy-2-oxo-2*H*-chromen-3-yl)ethylidene)hydrazine-1-carbothioamide (151 MHz, DMSO d6).
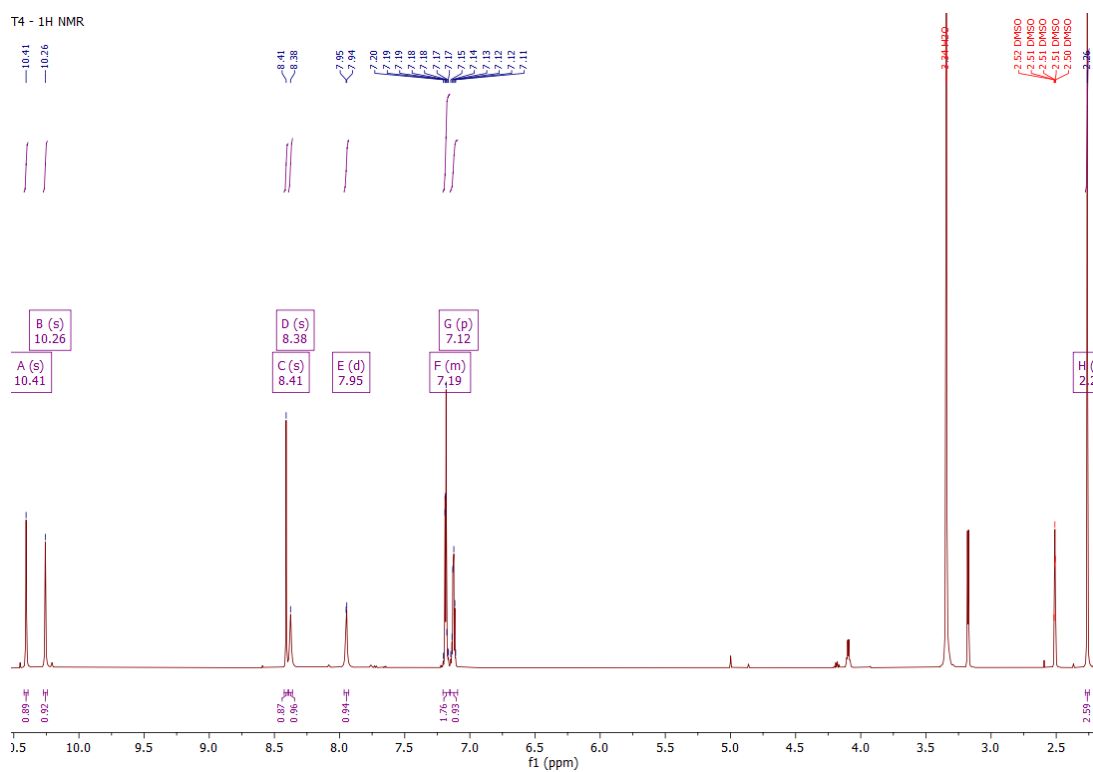
Figure S11. ^{1}H-NMR of **T4**, (1*E*)-2-(1-(8-hydroxy-2-oxo-2*H*-chromen-3-yl)ethylidene)hydrazine-1-carbothioamide (600 MHz, DMSO d6).

Figure S12. ^{13}C-NMR of **T4**, (1*E*)-2-(1-(8-hydroxy-2-oxo-2*H*-chromen-3-yl)ethylidene)hydrazine-1-carbothioamide (151 MHz, DMSO d6).

Figure S13. ¹H-NMR of **T5**, (1*E*)-2-(1-(6,7-dihydroxy-2-oxo-2*H*-chromen-3-yl)ethylidene)hydrazine-1-carbothioamide (600 MHz, DMSO d6).

Figure S14. ¹³C-NMR of **T5**, (1*E*)-2-(1-(6,7-dihydroxy-2-oxo-2*H*-chromen-3-yl)ethylidene)hydrazine-1-carbothioamide (151 MHz, DMSO d6).

Conclusions

This work was focused on the study of different classes of organic ligands and metal complexes with potential applications in the environmental and biological fields.

I've prepared a panel of 6th substituted derivatives of 3-(pyridin-2-yl)coumarin with a "ratiometric" and "turn-on" fluorescent behaviour for Fe(III).

Considering that the fluorescence response observed could be related with metal ion complexation, I've studied the Fe(III) complex formation processes at both solid and solution states. The most promising ligand of this panel has shown selectivity towards Fe(III) even in competition with other metal ions, with a LOD of 2.4 µM and a linear response to 35 µM of Fe(III). The fluorescence response observed in solution was observed on cellulose paper strip too, thus suggesting a potential application of this chemosensor for the determination of Fe(III) in liquid samples.

I've prepared and characterized a series of heteroleptic Cu(II) bis-phenanthroline complexes bearing different classes of organic ligands, such as imidazolidine-2-thiones, coumarin-based molecules and ER-stress modulators, such as Ursodeoxycholic acid and Salubrinal. The studied complexes showed anticancer potency in the micromolar/sub-micromolar concentration level against different cancer cell lines, such as ovarian (A-2780, SKOV-3), pancreatic (PANC-1), and renal (HEK-293). The mechanism of action of these compounds has been partially unveiled, showing how these compounds can interfere at the Endoplasmic Reticulum level by activating the pro-apoptotic branch of the Unfolded Protein Response. It is interesting to point out how the cytoprotective activity of the ER-

stress modulator Salubrinal is completely reverted when complexed to the $[Cu(phen)_2]^{2+}$ core, as observed with the cytotoxic complex **C0SAL**.

I've designed and synthesized a series of hydroxylated derivatives of 3-(pyridin-2-yl)coumarin and evaluated their antioxidant and soybean lipoxygenase inhibitory activity, showing how the number and relative position of the hydroxyl groups influences the biological properties of these molecules. As evidenced from the calculation of specific thermochemical descriptors (determined from DFT data), the antioxidant activity of the studied compounds would take place preferentially via the Hydrogen Atom Transfer mechanism. Moreover, by merging the experimental study of the protonation constants with the calculated molecular properties, I've preliminary evaluated the potential sites of absorption and distribution of these molecules.

The insertion of hydroxyl groups in the structure of **T1** has allowed me to design and synthesize novel coumarin-based thiosemicarbazones with dual antioxidant and anti-tyrosinase activity. Further studies are currently ongoing to determine the enzymatic inhibitory mode adopted by these molecules.

Perspectives

Based on the results so far achieved, it would be interesting to extend the study of the anticancer properties of the Cu(II) complexes reported towards other cancer cell lines or using *in-vivo* models. In addition, the study of their interaction with transport proteins (e.g., albumin) or endogenous ligands would help in understanding the transport mechanism and their speciation in biological fluids. The design and synthesis of novel ternary Cu(II) - phenanthroline complexes bearing other ER-stress modulators would also be worth of interest.

As regards the tyrosinase inhibitors, studies are currently ongoing to determine the mode of enzymatic inhibition exerted by these molecules. In addition, it would be necessary to study their cytotoxicity on melanocytes to evaluate their potential applications in the biomedical field.

Acknowledgments